

Shielding Aspects of Accelerators, Targets and Irradiation Facilities – SATIF 5

Workshop Proceedings
Paris, France
18-21 July 2000



Nuclear Science

Proceedings of the Fifth Meeting of the Task Force on
**Shielding Aspects of Accelerators,
Targets and Irradiation Facilities**

*Paris, France
18-21 July 2000*

Jointly organised by

OECD Nuclear Energy Agency (NEA)
CNRS – Institut de physique nucléaire d'Orsay (IPNO/IN2P3)
Radiation Safety Information Computational Centre (RSICC)
Shielding Working Group of the Reactor Physics Committee of Japan

NUCLEAR ENERGY AGENCY
ORGANISATION FOR ECONOMIC CO-OPERATION AND DEVELOPMENT

ORGANISATION FOR ECONOMIC CO-OPERATION AND DEVELOPMENT

Pursuant to Article 1 of the Convention signed in Paris on 14th December 1960, and which came into force on 30th September 1961, the Organisation for Economic Co-operation and Development (OECD) shall promote policies designed:

- to achieve the highest sustainable economic growth and employment and a rising standard of living in Member countries, while maintaining financial stability, and thus to contribute to the development of the world economy;
- to contribute to sound economic expansion in Member as well as non-member countries in the process of economic development; and
- to contribute to the expansion of world trade on a multilateral, non-discriminatory basis in accordance with international obligations.

The original Member countries of the OECD are Austria, Belgium, Canada, Denmark, France, Germany, Greece, Iceland, Ireland, Italy, Luxembourg, the Netherlands, Norway, Portugal, Spain, Sweden, Switzerland, Turkey, the United Kingdom and the United States. The following countries became Members subsequently through accession at the dates indicated hereafter: Japan (28th April 1964), Finland (28th January 1969), Australia (7th June 1971), New Zealand (29th May 1973), Mexico (18th May 1994), the Czech Republic (21st December 1995), Hungary (7th May 1996), Poland (22nd November 1996), Korea (12th December 1996) and the Slovak Republic (14 December 2000). The Commission of the European Communities takes part in the work of the OECD (Article 13 of the OECD Convention).

NUCLEAR ENERGY AGENCY

The OECD Nuclear Energy Agency (NEA) was established on 1st February 1958 under the name of the OEEC European Nuclear Energy Agency. It received its present designation on 20th April 1972, when Japan became its first non-European full Member. NEA membership today consists of 27 OECD Member countries: Australia, Austria, Belgium, Canada, Czech Republic, Denmark, Finland, France, Germany, Greece, Hungary, Iceland, Ireland, Italy, Japan, Luxembourg, Mexico, the Netherlands, Norway, Portugal, Republic of Korea, Spain, Sweden, Switzerland, Turkey, the United Kingdom and the United States. The Commission of the European Communities also takes part in the work of the Agency.

The mission of the NEA is:

- to assist its Member countries in maintaining and further developing, through international co-operation, the scientific, technological and legal bases required for a safe, environmentally friendly and economical use of nuclear energy for peaceful purposes, as well as
- to provide authoritative assessments and to forge common understandings on key issues, as input to government decisions on nuclear energy policy and to broader OECD policy analyses in areas such as energy and sustainable development.

Specific areas of competence of the NEA include safety and regulation of nuclear activities, radioactive waste management, radiological protection, nuclear science, economic and technical analyses of the nuclear fuel cycle, nuclear law and liability, and public information. The NEA Data Bank provides nuclear data and computer program services for participating countries.

In these and related tasks, the NEA works in close collaboration with the International Atomic Energy Agency in Vienna, with which it has a Co-operation Agreement, as well as with other international organisations in the nuclear field.

© OECD 2001

Permission to reproduce a portion of this work for non-commercial purposes or classroom use should be obtained through the Centre français d'exploitation du droit de copie (CCF), 20, rue des Grands-Augustins, 75006 Paris, France, Tel. (33-1) 44 07 47 70, Fax (33-1) 46 34 67 19, for every country except the United States. In the United States permission should be obtained through the Copyright Clearance Center, Customer Service, (508)750-8400, 222 Rosewood Drive, Danvers, MA 01923, USA, or CCC Online: <http://www.copyright.com/>. All other applications for permission to reproduce or translate all or part of this book should be made to OECD Publications, 2, rue André-Pascal, 75775 Paris Cedex 16, France.

FOREWORD

Accelerators play an increasingly important role in technological, energy and medical applications. As accelerators become more widely used and as their power increases, challenging new problems arise that require attention from the point of view of the characterisation of radiation environments and radiological safety.

The Nuclear Science Committee of the OECD Nuclear Energy Agency has sponsored a series of meetings on "Shielding Aspects of Accelerators and Irradiation Facilities (SATIF)" which have been held every 18-24 months since 1994. SATIF-1 was held on 28-29 April 1994 in Arlington, Texas; SATIF-2 on 12-13 October 1995 at CERN in Geneva, Switzerland; SATIF-3 on 12-13 May 1997 at Tohoku University in Sendai, Japan; SATIF-4 on 17-18 September 1998 in Knoxville, Tennessee; and SATIF-5 on 17-21 July 2000 at the OECD in Paris, France. SATIF-6 is scheduled for September 2002 at SLAC in Stanford, California.

The now established tradition of holding these meetings by rotation in different continents and in locations where there are many experts and important facilities available has proven to be beneficial and has allowed improved contacts and information exchange as well as the development of collaborative work among experts.

At the opening of the SATIF-5 meeting, and on the occasion of the 100th birthday of Frédéric Joliot (1900-1958), François Clapier, the Chairman, provided a brief historical background related to the early days in France when accelerator facilities were first being built and shielding aspects considered. Frédéric Joliot and his wife Irène Joliot-Curie were awarded the Nobel Prize for Chemistry for the synthesis of new radioactive isotopes in 1935. These discoveries revealed the possibility of using artificially produced radioactive isotopes to follow chemical changes and physiological processes, and such applications were soon successful, in particular for tracing the metabolism of the organism. In 1937 Frédéric Joliot was appointed professor at the Collège de France where he devoted part of his activities to the production of new radiation sources. The construction of electrostatic accelerators at Arcueil-Cachan and at Ivry, as well as a 7 MeV cyclotron at the Collège de France, were among the outstanding achievements of that period. With Jean Perrin, they laid the foundations for what would later become the *Centre National de la Recherche Scientifique* (CNRS). He and Irène Joliot-Curie took an active part in the development of nuclear reactors and the establishment of the *Commissariat à l'Énergie Atomique* (CEA).

The most recent accelerator project in France concerns the S3G – *Synchrotron de 3ème génération (Projet Soleil)*. The objective is fundamental and applied research of inert and biological matter. Thanks to its specificity of producing coherent radiation, it is particularly suitable to investigate the structure of matter. Its flexibility offers a vast field of applications in physics, material science, biology, chemistry, etc. It will be built on the Saclay plateau, next to the CEA research centre of the same name.

Throughout the meeting participants examined progress achieved during the last two years on issues such as radiation safety, activation, shield modelling and design of accelerator systems including electron-, proton- and ion-accelerators, and spallation sources. Relevant topics addressed included:

- experimental data for protons in the 0.8-2.6 GeV range impinging on different targets (Al, Mg, Na, Pb, W, Hg) needed for future high-power proton accelerators;
- improved estimation of neutron attenuation length and deep penetration experiments;
- studies on realistic beam loss scenarios for storage rings;
- experimental measurements of neutron production;
- determination of high fission yields for future radioactive neutral beam facilities;
- calculations and data presented for activation of soil, ground water, air, targets and cooling water relevant for personnel radiation safety and environmental impact;
- calculations for radiation damage to electronic components for future high-power machines.

Fifty-five specialists from nine countries attended the meeting, among them physicists, engineers and technicians from laboratories, institutes, universities and industries.

As part of the meeting a technical visit was arranged to the AGLAE (*Accélérateur Grand Louvre pour l'Analyse Élémentaire*) accelerator facilities of the *Laboratoire de Recherche des Musées de France*. Participants learned about the accelerator-based techniques (ion beam analysis) applied to study materials in art and archaeology. These methods are employed to identify the origin and authenticity of works of art and the techniques used by artists over the whole history of art. This provides additional insight into how techniques developed for scientific/technical applications benefit research in other domains, such as visual and plastic arts, and how these applications have lent to the improvement of methods in fields as varied as medicine and art restoration.

In conjunction with SATIF-5, the fifth seminar on Simulating Accelerator Radiation Environments (SARE) was held on 17-18 July 2000. The special topic of SARE-5 concerned “Models and Codes for Spallation Neutron Sources (SNS)”, and was chaired by Detlef Filges of Germany. The proceedings will be published in a separate volume by FZ Jülich, Germany.

The current proceedings provide a summary of the discussions, decisions and conclusions together with the text of the presentations made at the SATIF-5 meeting.

This text is published on the responsibility of the Secretary-General of the OECD. The views expressed do not necessarily correspond to those of the national authorities concerned.

Acknowledgements

The secretariat for these activities was conducted for the last three SATIF meetings by Pedro Vaz. The success of the meetings is due in a large extent to his dedication and organisational efforts. He has since left the OECD/NEA, and on behalf of the members of the SATIF expert group we thank him here for his outstanding services and wish him success in his new responsibility.

Acknowledgements are also due to the members of the SATIF-5 Technical Programme Committee, F. Clapier (Chairman), A. Fassò, D. Filges, T. Gabriel, H. Hirayama, N. Ipe, B. Kirk, N. Mokhov, T. Nakamura, E. Sartori, M. Silari, G. Stevenson, P. Vaz and L. Waters, for their contribution in shaping the technical programme, and to all participants who contributed valuable work and the ideas described in these proceedings. Special thanks go to Amanda Costa for her dedication in editing the contributions and her efforts to improve the layout of the text.

TABLE OF CONTENTS

FOREWORD	3
EXECUTIVE SUMMARY	9
<i>Appendix 1 – Agenda</i>	19
<i>Appendix 2 – Expert Group on Shielding Aspects of Accelerators, Targets and Irradiation Facilities (SATIF)</i>	23
<i>Appendix 3 – Brief Summary of the Workshop on Models and Codes for Spallation Neutron Sources</i>	25
SESSION I Proton and Ion Accelerator	27
<i>Chairs: N. Ipe, M. Silari</i>	
<i>Yu.E. Titarenko, O.V. Shvedov, V.F. Batyaev, E.I. Karpikhin, V.M. Zhivun, A.B. Koldobsky, R.D. Mulambetov, D.V. Fishchenko, S.V. Kvasova, A.M. Voloschenko, S.G. Mashnik, R.E. Prael, H. Yasuda</i>	
Threshold Reaction Rates Inside and on the Surface of Thick W-Na Target Irradiated with 0.8 GeV Protons.....	29
<i>Yu.E. Titarenko, O.V. Shvedov, Yu.V. Trebukhovsky, V.F. Batyaev, V.M. Zhivun, D.V. Fishchenko, V.A. Korolyov, G.N. Smirnov, S.G. Mashnik, R.E. Prael, A.J. Sierk, H. Yasuda</i>	
Spectral Measurements of Neutrons from Pb, W and Na Targets Irradiated by 0.8 and 1.6 GeV Protons.....	37
<i>H. Vincke, G.R. Stevenson</i>	
Production of Radioactive Isotopes in Molasse.....	47
<i>T. Nakamura, H. Sato, H. Iwase, T. Kurosawa, N. Nakao, Y. Uwamino, A. Fukumura</i>	
Neutron Production from Thin and Thick Targets by High-energy Heavy Ion Bombardment.....	59
<i>Yu.E. Titarenko, O.V. Shvedov, V.F. Batyaev, V.M. Zhivun, E.I. Karpikhin, R.D. Mulambetov, D.V. Fishchenko, S.V. Kvasova, S.G. Mashnik, R.E. Prael, A.J. Sierk, H. Yasuda</i>	
Study of Residual Product Nuclide Yields in 1.0 GeV Proton-irradiated ²⁰⁸ Pb and 2.6 GeV Proton-irradiated ^{nat} W Thin Targets	69

SESSION II	Electron Accelerator and Photon Sources	89
	<i>Chairs: T. Nakamura, N. Pauwels</i>	
	Synchrotron Radiation Facilities	91
	<i>N.E. Ipe, S. Mao, A. Fassò, J. Arthur, A. Toor, R. Tatchyn, D. Walz, W. Kroutil</i>	
	The Linac Coherent Light Source.....	93
	<i>P. Berkvens, P. Colomp</i>	
	Shielding Issues Around the ESRF Storage Ring.....	103
	High-energy Electron Machines	113
	<i>S.H. Rokni, J.C. Liu, S. Roesler</i>	
	Radiation Studies for the Environmental Protection at the Beam Delivery System of the Next Linear Collider	115
	<i>S. Roesler, J.C. Liu, S.H. Rokni</i>	
	Radiation Damage to Electronics in the Beam Tunnel of the Next Linear Collider.....	127
	<i>A. Leuschner, H. Dinter, K. Tesch, D. Dworak, J. Loskiewicz</i>	
	Calculation of Hadron Yields Around Thick Targets and Doses Behind Concrete Shielding of High-energy Electron Accelerators	139
SESSION III	High Intensity Medium-energy Accelerators	151
	<i>Chairs: D. Filges, H. Hirayama</i>	
	<i>D. Ridikas, W. Mittag, A.C.C. Villari</i>	
	Comparative Study of the Direct and Converter Methods for High Fission Yields	153
	<i>Yu.E. Titarenko, O.V. Shvedov, V.F. Batyaev, V.M. Zhivun, E.I. Karpikhin, R.D. Mulambetov, D.V. Fischenko, S.V. Kvasova, S.G. Mashnik, R.E. Prael A.J. Sierk, H. Yasuda</i>	
	Study of Residual Product Nuclide Yields from 0.1, 0.2, 0.8 and 2.6 GeV Proton-irradiated ^{nat} Hg Targets.....	165
	<i>V. Lacoste, A. Ferrari, M. Silari, V. Vlachoudis</i>	
	Activation Studies and Radiation Safety for the n_TOF Experiment.....	175
SESSION IV	Shielding Benchmark Calculations and Results	185
	<i>Chairs: P. Berkvens, L. Ulrici</i>	
	Neutron Attenuation Length	187
	<i>H. Hirayama, Attenuation Length Sub-working Group in Japan</i>	
	Intercomparison of Medium Energy Neutron Attenuation in Iron and Concrete (3)	189

<i>Deep Penetration Experiment</i>	203
<i>H. Handa, R. Tayama, K. Hayashi, H. Nakashima, Y. Sakamoto, N. Sasamoto, T. Abe, K. Yamada</i>	
Deep Penetration Calculations of Neutrons up to 1.5 GeV	205
<i>N. Nakao, T. Shibata, T. Nunomiya, T. Nakamura, E. Kim, T. Kurosawa, S. Taniguchi, M. Sasaki, H. Iwase, Y. Uwamino, S. Ito, P. Wright, D.R. Perry</i>	
Deep Penetration Experiment at ISIS	217
<i>Neutron Dosimetry Benchmark</i>	229
<i>M.R. Sutton, N.E. Hertel, L.S. Waters</i>	
A High-energy Neutron Depth-dose Experiment Performed at the LANSCE/WNR Facility	231
<i>Y. Nakane, Y. Sakamoto</i>	
Benchmark Experiments of Absorbed Dose in a Slab Phantom for Several Tens MeV Neutrons at the TIARA Facility.....	241
<i>N. Yoshizawa, Y. Sakamoto, S. Iwai, H. Hirayama</i>	
Benchmark Calculation with Simple Phantom for Neutron Dosimetry	253
<i>Electron-photon Benchmark (BEEP)</i>	265
<i>H. Hirayama, S. Ban, Y. Namito</i>	
Current Status of a Low-energy Photon Transport Benchmark.....	267
<i>Photon-neutron Production Benchmark</i>	279
<i>H. Vincke, E. Gschwendtner, C.W. Fabjan, T. Otto</i>	
Benchmarking of the Simulations of the ATLAS Hall Background	281
SESSION V Dosimetry and Dose Calculations	293
<i>Chairs: M. Pelliccioni, V. Batyaev</i>	
<i>Dose Conversion Coefficients for “High-energy” Radiations</i>	295
<i>M.R. Sutton, N.E. Hertel, L.S. Waters</i>	
Fluence-to-effective Dose Conversion Coefficients for High-energy Radiations Calculated with MCNPX.....	297
<i>Y. Sakamoto, S. Tsuda, O. Sato, N. Yoshizawa</i>	
Evaluation of Dose Conversion Coefficients for High-energy Radiation in Japan after SATIF-4	313
<i>Anthropomorphic Computational Models</i>	325
<i>M. Pelliccioni, M. Silari, L. Ulrici</i>	
Effective Dose and Organ Doses Due to Gas Bremsstrahlung from Electron Storage Rings	327

SESSION VI Additional Topics	339
<i>Chairs: B. Kirk, A. Leuschner</i>	
<i>E. Sartori, P. Vaz, J.B. Mannes Schmidt, H.T. Hunter, B.L. Kirk</i> Progress Report on the Collection of Computer Codes and Data Sets for Accelerator Shielding Analysis.....	341
<i>H. Vincke</i> FLUKACAD/PIPSICAD: Three-dimensional Interfaces Between FLUKA and AUTOCAD.....	361
<i>H. Nakano, R. Tayama, T. Tsukiyama, H. Handa, K. Hayashi, K. Shin, H. Hirayama, H. Nakashima, F. Masukawa, N. Sasamoto, Y. Sakamoto, K. Yamada, T. Abe</i> Development of DUCT-III Code for Duct Streaming Calculation Up to 3 GeV.....	371
<i>D. Ridikas, G. Fioni, P. Goberis, O. Déruelle, M. Fadil, F. Marie, S. Röttger, H. Faust</i> On the Fuel Cycle and Neutron Fluxes of the High Flux Reactor at ILL Grenoble	383
<i>S. Rollet, P. Batistoni</i> Shielding Aspects of a Tokamak Reaching Ignition.....	395
<i>E. Canetta, G. Maino, E. Menapace</i> Evaluation of Nuclear Data for Radiation Shielding by Model Calculations and International Co-operation Aspects	405
LIST OF PARTICIPANTS	417

EXECUTIVE SUMMARY

Scope

The expert group deals with multiple aspects related to radiation safety, activation and shielding modelling and design of accelerator systems including electron, proton and ion accelerators, spallation sources and the following type of facilities: synchrotron radiation facilities, transmutation sources, accelerator-driven systems, free electron lasers, high power targets and dumps.

Objectives

The main objectives of the SATIF meetings are:

- To promote the exchange of information among scientists in this particular field.
- To identify areas in which international co-operation could be fruitful.
- To carry on a programme of work in order to achieve progress in specific priority areas.
- To encourage free access to computer codes sources and cross-section and integral experiments data, and making them available at information centres.

Background and past achievements

The first SATIF meeting (SATIF-1) took place in Arlington, Texas (USA) on 29-30 April 1994, the second meeting (SATIF-2) was held on 12-13 October 1995 at CERN (European Laboratory for Particles Physics) in Geneva, Switzerland, the third meeting took place on 12-13 May 1997 at Tohoku University (Sendai, Japan) and the fourth meeting was held in Knoxville, Tennessee (USA) on 17-18 September 1998.

As a consequence of the success of these conferences, the seventh meeting of the NEA Nuclear Science Committee, held on 29-30 May 1996, approved the establishment of a specific task force on shielding aspects of accelerators, targets and irradiation facilities. Consequently, the SATIF specialists meetings became regular meetings of this task force. Following the fourth meeting it was decided to organise SATIF meetings every two years.

It is generally recognised that the four SATIF meetings preceding SATIF-5 have fostered considerable and significant co-operative actions and efforts at the international level, in areas such as:

- *Basic data*: New measurements, compilation of existing neutron, proton, light ion and pion cross-section data in the intermediate energy range above a few dozens of MeV, forward bremsstrahlung yields from thick targets at energies above 100 MeV, photoproduction data

(namely photonuclear cross-sections and photonuclear yields and angular distributions for all common elements at all energies), photo-pion yields and angular distributions at energies above 200 MeV, isotope production data, etc.

- *Nuclear models and computer codes in the intermediate energy range*: Code validation, intercomparison of codes, comparison between experimental data and predictions from existing computer codes implementing nuclear models.
- *Shielding experiments*: Measurements of forward and lateral attenuation of iron and concrete for proton and ion accelerators up to a few tens of GeV and as deep as possible, i.e. at least 5-6 meters, measurement of forward and lateral attenuation at electron accelerators.
- *Benchmark data*: Organisation of new benchmark exercises, compilation of existing benchmark data sets, etc.
- *Anthropomorphic computational models*: Compilation of existing models, phantom geometry and material compositions, evaluation of effective and organ doses.
- *Dose conversion coefficients for “high-energy” radiation*: Evaluation of fluence-to-effective dose conversion coefficients for high-energy radiation.

The last four SATIF meetings were held in conjunction with SARE (Simulating Accelerator Radiation Environment) meetings. The two meetings are complementary in their subject matter and the participants in both meetings are experts coming from different fields of science and technology. SATIF was originally designed as a forum of discussion and exchange of information in order to identify areas in which international co-operation is needed or needs to be strengthened. In the past, special attention has been paid to:

- The availability and compilation of experimental data for different applications.
- The organisation of international benchmark exercises.
- The availability of computer codes and data libraries for the use of the scientific community involved in various aspects related to accelerator shielding and applications.
- Identifying areas in which international co-operation can contribute to solve existing problems.

The presentations made at the successive SATIF meetings can generally be categorised according to the following topics:

- Data.
- Benchmarks.
- Computer codes and models.
- Facilities.
- Shielding techniques.
- Conversion coefficients.

- Code intercomparisons.
- Status of codes.

The fifth meeting – SATIF-5

The fifth meeting of the SATIF task force (SATIF-5) took place in Paris, France, at the OECD headquarters in the Château de la Muette, from 18-21 July 2000, and was jointly organised by:

- OECD Nuclear Energy Agency.
- Institut de Physique Nucléaire d'Orsay (IPNO).
- Radiation Safety Information Computational Centre (RSICC).
- Shielding Working Group of the Reactor Physics Committee of Japan.

Fifty-five specialists attended the meeting, among them physicists, engineers and technicians from laboratories, institutes, universities and industries in Belgium (Univ. Liège), France (CEA, GANIL, IN2P3), Germany (DESY, KFZ – Jülich, Hahn-Meitner Institute – Berlin, Univ. Hannover), Italy (INFN, ENEA), Japan (CYRIC, JAERI, KEK, RIKEN, Universities of Kyoto and Tohoku, Mitsubishi and Hitachi Corporations), USA (LANL, RSICC, SLAC, Georgia Institute of Technology), the Russian Federation (ITEP), Israel (Soreq Nuclear Data Centre), as well as representatives from international organisations (CERN, ESRF and OECD/NEA). The detailed list of participants is provided at the end of this publication.

The SATIF-5 meeting was preceded by the Workshop on Models and Codes for Spallation Neutron Sources, imbedded in the SARE-5 meeting, and organised on the same premises (please refer to Appendix 3 for a short summary of the workshop).

The SATIF-5 meeting was organised in seven sessions, each addressing different issues:

- *Session 1*: Proton and Ion Accelerators.
- *Session 2*: Electron Accelerators and Photon Sources.
- *Session 3*: High Intensity Medium Energy Accelerators.
- *Session 4*: Shielding Benchmark Calculations and Results.
- *Session 5*: Dosimetry and Dose Calculations.
- *Session 6*: Additional Topics.
- *Session 7*: Discussions and Future Actions.

A detailed agenda of the SATIF-5 meeting is provided in Appendix 1. Thirty-two papers were presented during the first six (topical) sessions. Highlights from the presentations performed and subjects discussed are as follows:

- Experimental data (reaction rates, residual product nuclei yield and neutron spectra) for 0.1-2.6 GeV protons impinging on different targets (Al, Mg, Na, Pb, W, Hg). This data is useful for future high-power proton accelerators. Status:
 - Data analysis still in progress.
 - Further measurements are planned.
 - Discrepancies between codes and measurements need to be reconciled.
 - Programme needs support.
- Neutron attenuation length and deep penetration experiments and benchmarks. Status:
 - Good progress has been accomplished.
 - Uncertainties on neutron attenuation lengths (for protons incident on concrete and iron) need to be resolved.
 - Need to understand differences in codes.
 - Extend neutron dose attenuation to tens of GeV to confirm asymptotic value.
- FLUKA calculations on hadron yields from high-energy electrons around thick targets and dose attenuation in concrete and resulting parameterisation is useful for electron accelerator shielding.
- Beam loss scenarios for storage rings should be realistic and include Monte Carlo simulations and beam optics.
- Experimental measurements of neutron production from deuterons (up to 200 MeV) incident on Be, C and U targets show some discrepancies with calculations.
- Determination of high fission yields for future RNB facilities.
- Calculations and data presented for activation of soil, ground water, air, targets and cooling water. Status:
 - These data are relevant for personnel radiation safety and environmental impact.
 - In general there is less activation data available for electron machines than proton machines.
- Calculations for radiation damage to electronic components is important for future high-power machines.

- Benchmarking neutron dosimetry in simple phantoms:
 - Results indicate large discrepancies between codes.
 - Code experts need to resolve these differences.
 - Need for experiments on N and C targets to help reconcile differences.
- Completed collection of experimental data of neutron spectra and yield from thin and thick target bombardment with heavy ions up to 800 MeV/nucleon. Status:
 - This data is useful for benchmarking of future Monte Carlo codes that will deal with heavy ion transport (space research application, medical application, etc.).
- Several papers on dosimetry confirm that $H^*(10)$ is not always the best estimator of effective dose for both broad and narrow beams:
 - Comparisons were made between experiments and Monte Carlo calculations.
- Improvements of low-energy photon transport (keV) in EGS4 were verified with measurements between 20-40 keV. Status:
 - This data is very useful for synchrotron radiation facilities.
- Assessment of induced activity in accelerator structures is important for decommissioning efforts.
- Specific examples of application of Monte Carlo techniques in complex problems such as Atlas background and n_TOF experiments.
- Non-accelerator applications. They included:
 - Tokamak shielding aspects.
 - Neutron fluxes of high flux reactor.
- Computer codes for accelerator shielding design and modelling. Status:
 - Several of the major experts on intranuclear reactions (INC, evaporation, fissions) attended the meeting; however, the absence of experts on internuclear transport calculations was strongly felt.
 - Graphical interfaces between FLUKA and Autocad for geometry plotting and particle tracking appear promising to FLUKA users.
 - Duct-III code would facilitate design of ducts and labyrinths and therefore should be made available.
 - Developments in codes should include:
 - ⇒ Electron and photon transport (with polarisation) down to 0.1 keV (for light sources).
 - ⇒ Reflectivity and refractivity of mirrors (for light sources).

- ⇒ Time dependence of radiation fields (for light sources).
- ⇒ Ion transport.
- ⇒ Residual nuclei decay mode for direct calculation of radiation exposure.

Discussion, proposals, conclusions

An extensive discussion took place during Session VII, with the following pre-established objectives:

- To review the progress achieved since the SATIF-4 meeting.
- To monitor the status of the agreed actions (on experiments, benchmark organisation, compilation of basic data, codes and methods) undertaken since then.
- To identify and initiate new co-operative actions.
- To improve common understanding of problems that have technical and safety significance.
- To review the current organisation of the SATIF meetings and to discuss the organisation of future meetings.
- To review the scope, objectives and deliverables of SATIF, in order to adjust them to the new needs expressed in the Member countries.
- To prepare and discuss a work programme for the next two years, which will be proposed for approval by the NSC together with the revised scope and objectives.

Follow-up of action items from SATIF-4

Progress was monitored on the following actions, decided at SATIF-4 (or earlier meetings):

- The BEEP benchmark (electron/photon transport benchmark, group chaired by A. Bielajew):
 - A paper reporting on low-energy photon results conducted at Japan in the framework of BEEP was presented at SATIF-5 by H. Hirayama.
 - A progress report by A. Bielajew is in preparation.
- Conversion coefficients, anthropomorphic computational models (group chaired by N. Yoshizawa):
 - Excellent progress has been obtained, four papers were presented during SATIF-5.
- Attenuation length (extension to other codes and to higher energies, group chaired by H. Hirayama):
 - Excellent progress has been achieved, three papers were presented during SATIF-5.

- Ground activation (work conducted at CERN):
 - A paper by H. Vincke was presented at SATIF-5 reporting on the results obtained so far.
- Deep penetration problems – different approaches (work by G. Stevenson and J. Bull).
 - No status report was presented.
- Compilation of photonuclear cross-sections (work by A Fassò):
 - No status report was presented.

Organisation of benchmark and intercomparison exercises

Results were presented on:

- The intercomparison of neutron transmission benchmark analysis for iron and concrete in TIARA and on the intercomparison of the medium-energy neutron attenuation in these materials.
- The Benchmark Calculation with a Simple Phantom for Neutron Dosimetry.

It was decided to continue the collaborative work already undertaken, namely on:

- Conversion coefficients, anthropomorphic computational models (N. Yoshizawa).
- Attenuation length (H. Hirayama).

New benchmarks were proposed, discussed and accepted, as follows:

- Deep penetration shielding benchmarks (proposed by T. Nakamura):
 - *ISIS experiment*
800 MeV – protons, 90°
Materials: Concrete, iron
Determination of λ values, neutron spectrum (Bonner ball, C- and Bi-activation)
 - *LANSCE/WNR experiment*
800 MeV – protons, 90°
Materials: Iron
Determination of λ values
 - *HIMAC experiment* (proceeding now)
400 MeV/nucleon – C on Cu target, 0°
Materials: Neutron spectrum (NE-213, self TOF, Bi-activation) in concrete (2 m), iron (1 m).
- CERN experiment (proposed by M. Silari):
 - High energy mixed proton/pion beam on thick Cu target, complex shielding structure, FLUKA predictions and neutron spectral measurements.

- Activation cross-sections of neutrons (proposed by T. Nakamura – follow up by E. Menapace and S. Rokni):
 - Collection of data.
 - Data library above threshold especially for light nuclei in air, water and soil. Check for:
 - ⇒ LANL (what data is available?).
 - ⇒ MENDL (place it into information centres).
 - ⇒ Measurement.
- Residual nuclei production cross-section and reaction rates for high-energy (0.04-2.6 GeV) protons (proposed by Yu. Titarenko, V. Batyaev, *et. al.*):
 - Experimental data from ITEP Moscow (Titarenko).
 - LANL calculations (Mashnik, Prael).
- Heavy ions (F. Clapier):
 - Neutron production from:
 - ⇒ Thick target (Data collection and compilation – HIMAC, Cecil, Heilbronn).
 - ⇒ Thin target (Cecil, RIKEN, HIMAC).

Follow-up of agreed actions

It was recognised that follow-up of agreed actions needs to become more effective. The follow-up should be made by the NEA Secretariat together with the co-ordinators assigned for specific activities or topics. In particular benchmarks should be distributed officially through the OECD/NEA to ensure an official status and strengthen participation. The setting up of specific listserver and web pages has been proposed as a tool to accomplish this.

Listserver and web pages

The following proposal for a listserver was submitted and accepted by the SATIF-5 participants:

- Address: satif@nea.fr.
- Members: all SATIF participants.
- Characteristics: Moderated (focussed, pertinent, of general interest to SATIF); web page with searchable archive of messages to be used to facilitate communication and follow-up actions

Further development of the web pages already existing has been discussed, in order to provide information on:

- Scope and objectives, deliverables.
- Membership and organisation.
- Next meeting and other relevant meetings.
- List of relevant publications or links to them.
- Summary records/actions.
- Downloading of benchmark specifications.
- Links to relevant web sites.
- Open questions/answers via notebook.

Computer codes and data libraries for shielding design and modelling

With regard to the state-of-the-art computer codes and data libraries available for use by scientists in the field of radiation shielding, an exhaustive and updated list of computer codes, data libraries and databases has been produced which is included in these proceedings. This compilation issued by RSICC in collaboration with the NEA Data Bank is a valuable reference for the community of users.

Among other actions decided upon at the discussion session were:

- To pursue the collection of experimental data sets available.
- To continue the activities on data compilations, giving particular emphasis to data availability for the user community.
- To further develop the activities on intercomparison exercises, between modelling methods (e.g. computer codes) available and experimental data.
- To encourage free access to computer codes sources and cross-section and integral experiments data, and making them available at information centres.

Future meetings of the SATIF task force

Concerning the organisation of future SATIF meetings, it was agreed by the majority of the SATIF participants that:

- Future SATIF meetings will typically last three days. They should contain, besides presentations of progress in work carried out at different research institution relevant to the scope of SATIF, specific sessions related to agreed collaborative work. During these it should be clarified, what has been achieved, what is in progress, what needs emerge for further work.

- A specific topical workshop addressing an issue of particular interest is organised in connection or embedded in SATIF meetings. The organisation of such topicals is under the responsibility of the Chair.

The next meeting (SATIF-6) is scheduled for September 2002 at SLAC, Stanford, CA, USA. The meeting will be held if possible in connection with the ANS RP&S Division Topical to be held in September 2002 in Santa Fe, NM, USA. A topical meeting embedded in SATIF-6, the topic of which is synchrotron radiation and free electron laser (FEL) light sources, has been proposed.

Acknowledgements are due to the members of the Technical Programme Committee of SARE-5 and SATIF-5, F. Clavier (Chairman), A. Fassò, D. Filges, H. Hirayama, N. Ipe, B. Kirk, N. Mokhov, T. Nakamura, E. Sartori, M. Silari, G. Stevenson, P. Vaz and L. Waters, for their contribution in shaping the technical programme.

Appendix 1

AGENDA

Tuesday, 18 July 2000

Welcome and opening remarks for the SATIF-5 meeting

Session I Proton and Ion Accelerator

Co-chairs: N. Ipe, M. Silari

V. Batyaev

Reaction Rates Inside and on the Surface of a 0.8 GeV Proton-irradiated Thick W-Na Target

V. Batyaev

Neutron Spectra Generated in W and Na Targets by 0.8 GeV Proton Irradiation

Heinz Vincke

Production of Radioactive Isotopes in Molasse

T. Nakamura

Neutron Production from Thin and Thick Targets by High-energy Heavy Ion Bombardment

N. Pauwels

Experimental and Calculated Neutrons Production by Deuterons Impinging on Be, C and U Thick Targets (200, 160, 80, 28, 20 and 17 MeV)

Yu. Titarenko

Study of Residual Product Nuclide Yields in GeV Proton-irradiated Thin ^{208}Pb and $^{\text{nat}}\text{W}$ Targets

Wednesday, 19 July 2000

Session II Electron Accelerator and Photon Sources

Co-chairs: T. Nakamura, N. Pauwels

Synchrotron Radiation Facilities

N. Ipe

The Linac Coherent Light Source

P. Bervkens

Shielding Issues Around the ESRF Storage Ring

High Energy Electron Machines

S. Rokni

Radiation Studies for the Personnel and Environment Protection for the Next Linear Collider Project

S. Roesler

Radiation Damage to Electronics in the Beam Tunnel of the Next Linear Collider

A. Leuschner

Calculation of Hadron Yields Around Thick Targets and Doses Behind Concrete Shielding of High-energy Electron Accelerators

Session III High Intensity Medium Energy Accelerators

Co-chairs: D. Filges, H. Hirayama

D. Ridikas

High Intensity Fission Yields by the Use of the Flowing Lithium Target-converter (Neutron Source)

V. Zhivun

Study of Residual Product Nuclide Yields in 0.1-1.6 GeV Proton-irradiated Thin Hg Targets

V. Lacoste

Activation Studies and Radiation Safety for the n-TOF Experiment

C. Volant

Experimental Spallation Reaction Results

Thursday, 20 July 2000

Session IV Shielding Benchmark Calculations and Results

Co-chairs: P. Berkvens, L. Ulrici

Neutron Attenuation Length

H. Hirayama

Intercomparison of the Medium-energy Neutron Attenuation in Iron and Concrete

Deep Penetration Experiment

Y. Sakamoto

Deep Penetration Calculations of Neutrons Up to 1.5 GeV

N. Nakao

Deep Penetration Experiment at ISIS

Neutron Dosimetry Benchmark

*M. Sutton**

Final Results of a High-energy Neutron Depth-dose Experiment Performed at the LANSCE/WNR Facility

Y. Sakamoto

Benchmark Experiments of Absorbed Dose in a Slab Phantom for Several Tens MeV Neutrons at the TIARA Facility

N. Yoshizawa

Benchmark Calculation with Simple Phantom for Neutron Dosimetry

Electron-photon Benchmark (BEEP)

H. Hirayama

Current Status of Low-energy Photon Benchmark Experiments at KEK

Photon-neutron Production Benchmark

H. Vincke

Benchmarking of the Simulations of the Atlas Hall Background

Session V Dosimetry and Dose Calculations

Co-chairs: M. Pelliccioni, V. Batyaev

Dose Conversion Coefficients for “High-energy” Radiations

*M. Sutton**

Fluence-to-effective Dose Conversion Coefficients for High-energy Radiations Calculated with MCNPX

* *This paper was not presented orally at the SATIF-5 workshop, but has been included in the final publication.*

Y. Sakamoto

Evaluation of Dose Conversion Coefficients for High-energy Radiation in Japan after SATIF-4

Anthropomorphic Computational Models

L. Ulrici

Effective Dose and Organ Doses Due to Gas Bremsstrahlung from Electron Storage Rings

Session VI Additional Topics

Co-chairs: B. Kirk, A. Leuschner

E. Sartori

Status of Computer Codes, Cross-sections and Data Libraries for Accelerator Shield Modelling

H. Vincke

Flukacad/Pipsicad: Three-dimensional Interfaces between FLUKA and AutoCAD

H. Hirayama

Development of DUCT-III Code for Duct Streaming Calculation up to 3 GeV

D. Ridikas

On the Fuel Cycle and Neutron Fluxes of the High Flux Reactor at ILL Grenoble

S. Rollet

Shielding Aspects of a Tokamak Reaching Ignition

E. Menapace

Nuclear Data Evaluation by Model Calculations for Radiation Shielding Purposes in the Framework of the International Co-operation

Friday, 21 July 2000

Session VII Discussion Session*

N. Ipe, M. Silari

Summary and Conclusions of the Meeting

Future Developments of SARE and SATIF

F. Clapier

Closing Remarks

* *The conclusions discussed during Session VII have been incorporated into the Executive Summary; so as not be redundant, this session has thus been eliminated from the Table of Contents.*

Appendix 2

EXPERT GROUP ON SHIELDING ASPECTS OF ACCELERATORS, TARGETS AND IRRADIATION FACILITIES (SATIF)*

<i>Present chair:</i>	F. Clapier (IPNO, France)
<i>Next chair:</i>	N. Ipe (SLAC, USA)
<i>Members:</i>	All NEA Member countries
<i>Date of creation:</i>	June 2000
<i>Duration:</i>	To 13 th NSC meeting (2003)

Scope

The expert group deals with multiple aspects related to radiation safety, activation and shielding modelling and design of accelerator systems including electron-, proton-, ion-accelerators, spallation sources and the following type of facilities: synchrotron radiation facilities, transmutation sources, accelerator driven systems, free electron lasers, high power targets and dumps.

Objectives

- To promote the exchange of information among scientists within the defined scope.
- To identify areas in which international co-operation could be fruitful.
- To carry on a programme of work in order to achieve progress in specific agreed priority areas.
- To encourage free access to computer codes sources and cross-section and integral experiments data, and making them available at information centres.

Deliverables

- Assessment of needs in experimental data for the validation of models and codes.
- Assessment of needs for evaluated nuclear data and processed data libraries.
- Organisation of shielding experiments.
- Collection and compilation of experimental data sets.

* *Discussed at SATIF-5 (July 2000) and transmitted for endorsement to NSC.*

- Assessment of models, computer codes, parameterisations and techniques available for accelerator shielding design purposes.
- Validation of computer codes and models available to perform particle transport simulation.
- Meeting at least once every two years and publication of proceedings.
- Reporting to the NEA Nuclear Science Committee.

Appendix 3

BRIEF SUMMARY OF THE WORKSHOP ON MODELS AND CODES FOR SPALLATION NEUTRON SOURCES*

The SARE-5 meeting officially started on Monday morning, 17 July 2000. François Clapier, co-organiser of both the SARE-5 and SATIF-5 meetings, welcomed the participants. Enrico Sartori and Pedro Vaz, of the OECD/NEA, represented the secretariat of the meeting.

The special topic of SARE-5 is “Models and Codes for Spallation Neutron Sources (SNS)”. Detlef Filges of Germany, General Chair for SARE-5, gave the introduction. He briefly discussed the three major projects on SNS: the European Spallation Source (ESS), the US SNS, and the Japanese Spallation Source. The latter will start at 1 MW, as compared to 5 MW for the ESS. Filges said that there is a need to identify important processes in support of engineering design. Problems in spallation studies include the difficulty in estimating microscopic quantities from macroscopic quantities and also the difficulty in generating measured quantities from calculated ones. Major computer code systems used in spallation analysis are: CALOR (US/ORNL), HERMES (Germany), Lahet Code System (LCS) (US/LANL) and MCNPX (US/LANL). There is a great need to improve these codes so that they can handle higher energy transport for incident protons in the GeV range.

The first session covered experimental observations. C.M. Herbach of Hahn-Meitner-Institut, Germany, presented a comparison of calculations using three different codes: Intra Nuclear Cascade (INC) coupled with GEMINI, LAHET and HERMES. He compared measured observations against those computed by these three codes. Measured observations are for production cross-sections of neutrons and charged particles, carried out between 0.8 and 2.5 GeV. The measurements were done with the neutron scintillation tank and silicon (NESSI) ball detector in Jülich.

R. Michel of Hannover University presented excitation functions of residual nuclide production of light heavy ions and neutron double differential cross-sections. S. Leray of CEA Saclay showed results on neutron double-differential cross-sections measured at SATURNE Saclay on different thin and thick targets up to 1.6 GeV and on isotope production on Pb measured at GSI Darmstadt. Computer simulations were produced using LAHET (Bertini and ISABEL options), Liège INC and TIERCE including the different INC models Bertini, Cugnon or Isabel. Neutron data are rather well reproduced when using Cugnon INC model, however no single computer code can model the isotopic distributions correctly.

The next session covered Intra Nuclear Cascade (INC) models. Three INC models were presented: Liège INC, ISABEL and BRIC. J. Cugnon of the University of Liège, Belgium, discussed the Liège INC model. INC was developed for heavy ion collisions in 1980. INC continues to be developed, but is available through Cugnon.

* *Held in Paris, France at the OECD headquarters in Château de la Muette on 17-18 July 2000, embedded in the SARE-5 meeting.*

Y. Yariv of Israel (Soreq Nuclear Research Centre) discussed his modifications to the ISABEL code – an INC model for hadrons. ISOBAR is a precursor of ISABEL. It calculates properties of single high-energy particles with a complex nucleus, using Monte Carlo simulations. The cascading of particles was discussed at length – particles are terminated when they leave the target or get below a certain energy cut-off. ISABEL is a generalisation to nucleus-nucleus collisions. A new version of ISABEL is available through Y. Yariv.

H. Duarte of CEA BRC discussed the BRIC 1.0 code. BRIC is a new INC code which calculates hadron nucleus reactions by Monte Carlo in the 150 MeV-1.5 GeV range. BRIC 1.0 results were compared with experiments and had good agreement.

F. Goldenbaum of FZ-Jülich discussed several nuclear transport models. HERMES and LCS were compared on neutron multiplicity distribution for 1.2 GeV on lead. The results were good for 2 cm, 15 cm and 35 cm. The agreement was still good for 2.5 GeV. The INC (Cugnon) code was then compared with LAHET (Bertini) and ISABEL using a gold target. These codes appear to be in agreement up to 400 MeV, but differ in the GeV range.

The latest developments in MCNPX were presented by S. Mashnik of LANL.

Y. Kadi of CERN then presented the Energy Amplifier Monte Carlo (EA-MC) code developed at CERN. EA-MC follows spallation neutrons generated by FLUKA-99. EA-MC keeps track of about 2 550 isotopes in a database. Of these isotopes, 393 have transport cross-sections.

A general summary of models used in accelerator-driven systems was presented by S. Mashnik.

A general discussion followed on Tuesday morning. The SARE-5 group felt that there is a need to concentrate on the following:

- Proton on mercury, lead, bismuth, iron and gold.
- Energy range $0.3 < E < 3$ GeV.
- For thin targets, double differential cross-sections.
- For thick targets, same as for thin plus distribution of residual nuclei.
- Provision of intermediate quantities from INC models.
- List of suggestions for experiments.
- Set up a web site to facilitate communication (Guenter Sterzenbach of Germany will do this).
- Keep these facilities in mind: LANSCE (800 MeV), Mol (350 MeV), ESS and SNS (1 GeV), JAERI/KEK (2-5 GeV).

SESSION I

Proton and Ion Accelerator

Chairs: N. Ipe, M. Silari

**THRESHOLD REACTION RATES INSIDE AND ON THE SURFACE
OF THICK W-NA TARGET IRRADIATED WITH 0.8 GeV PROTONS**

**Yury E. Titarenko, Oleg V. Shvedov, Vyacheslav F. Batyaev,
Evgeny I. Karpikhin, Valery M. Zhivun, Aleksander B. Koldobsky,
Ruslan D. Mulambetov, Dmitry V. Fishchenko, Svetlana V. Kvasova**
Institute for Theoretical and Experimental Physics
B. Cheremushkinskaya 25, Moscow 117259, Russia

Andrey M. Voloschenko
Keldysh Institute of Applied Mathematics
Miusskaya Sq. 4, 125047 Moscow, Russia

Stepan G. Mashnik, Richard E. Prael
Los Alamos National Laboratory
Los Alamos, NM 87545, USA

Hideshi Yasuda
Japan Atomic Energy Research Institute
Tokai, Ibaraki, 319-1195, Japan

Abstract

The preliminary results are presented of the experimental determination of threshold reaction rates in experimental samples made of Al, Co, Bi, In, Au, to name but a few, placed both inside and on the surface of extended thick W-Na target irradiated with 0.8 GeV protons. The target consists of 26 alternating discs each 150 mm in diameter: six tungsten discs are 20 mm thick, seven tungsten discs are 40 mm thick and 13 sodium discs are 40 mm thick. The relative position of discs is matched with the aim of flattening the neutron field along the target surface. The comparison is made of the measured rates with results of their simulation using the LAHET and KASKAD-S codes, and the ENDF/B6, MENDL2, MENDL2P, SADKO-2 and ABBN-93 databases. The results are of interest both in terms of integral data collection and to test the up-to-date predictive power of the codes applied in designing of hybrid accelerator-driven systems (ADS) that use tungsten targets cooled with sodium [1,2].

Foreword

Quantitative information on interaction of accelerated protons with different targets is necessary to design ADS. Application of hadron-nucleus process simulations should be tested by special experiments in which irradiation conditions, target material composition and location approximate the design type to the limit. There are several projects, [1], for example, where tungsten cooled by sodium is considered to be used as target material. This served as the basis for conducting experiments with micromodels of such targets. Comparison of experimental data obtained on such micromodels with corresponding calculated values will give us valuable information both for modifications of codes and databases and for assessment the calculation accuracy of the target part of the relevant ADS facility designs.

Experiment plan

The target with alternating adherent tungsten and sodium discs was designed in our micromodel. The location of these discs, which was specially chosen, facilitates the maximum flattening of the neutron field along the target. Experimental samples made of Al, Co, In, Au, Bi, ^{63}Cu , ^{65}Cu , ^{93}Nb , ^{64}Zn , ^{19}F (CF_2), ^{12}C , Ta and Tm manufactured by punching the corresponding foils or by moulding fine powders, 10.5 mm in diameter and 0.1-0.3 mm thick, were placed inside the target and on its surface.

The layout of tungsten and sodium discs is shown in Figure 1. All discs are 150 mm in diameter, disc thickness and sequence is listed in Table 1. The tungsten discs have a special design providing insertion of special bars with round recesses for experimental samples to be placed inside the target. The discs are located on a special adjustment table which provides alignment of target and proton beam axes with an accuracy of the order of 1 mm. The proton beam size examination has been performed by using in tentative exposures to radiation aluminium cut foils and Polaroid film.

Figure 1. Layout of W and Na discs and experimental samples

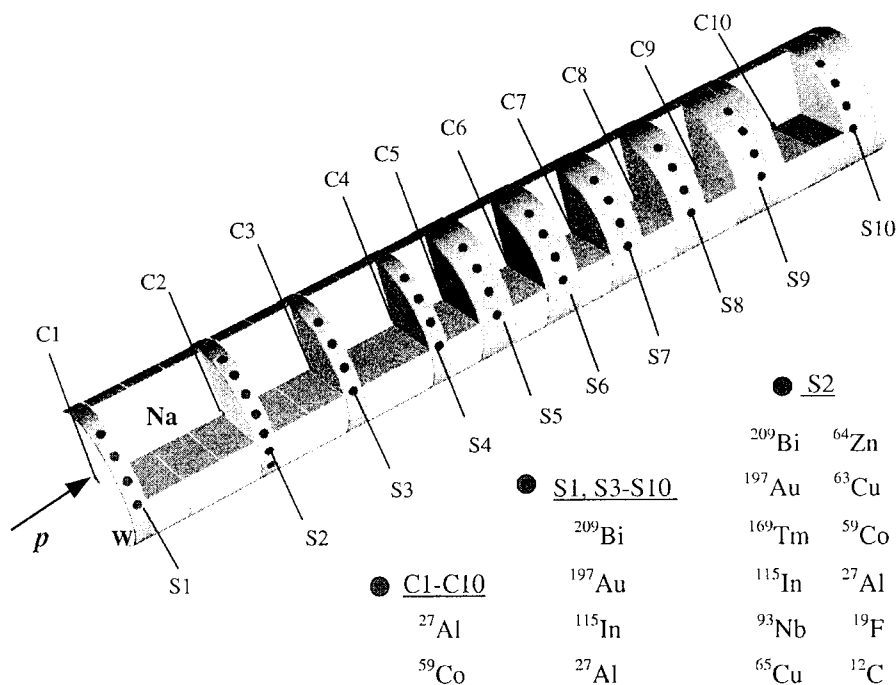


Table 1. Disc sequence, thickness and experimental samples layout

Disc number	Material	Thickness, mm	Samples	
			Inside	Outside
W1	W	20	5Al*, Co	Al, In, Bi, Au, Ta
Na1	Na	3*40=120	–	–
W2	W	20	5Al, Co	Al, In, Bi, Au, ¹⁶⁹ Tm, ⁶³ Cu, Ta, ⁶⁵ Cu, ⁹³ Nb, ⁶⁴ Zn, ¹⁹ F, ¹² C, Co
Na2	Na	2*40=80	–	–
W3	W	20	5Al, Co	Al, In, Bi, Au, Ta
Na3	Na	2*40=80	–	–
W4	W	20	5Al, Co	Al, In, Bi, Au, Ta
Na4	Na	40	–	–
W5	W	40	5Al, Co	Al, In, Bi, Au, Ta
Na5	Na	40	–	–
W6	W	40	5Al,Co	Al, In, Bi, Au, Ta
Na6	Na	40	–	–
W7	W	40	5Al, Co	Al, In, Bi, Au, Ta
Na7	Na	40	–	–
W8	W	40	5Al, Co	Al, In, Bi, Au, Ta
Na8	Na	40	–	–
W9	W	40+20=60	5Al, Co	Al, In, Bi, Au, Ta
Na9	Na	40	–	–
W10	W	2*40=80	5Al, Co	Al, In, Bi, Au, Ta
Total		W: 380	50 Al,	¹⁰ Al, ¹⁰ In, ¹⁰ Bi, ¹⁰ Au, ¹⁰ Co ¹⁰ Ta, ¹⁶⁹ Tm,
		Na: 520	10 Co	^{63u,65} Cu, ⁹³ Nb, ⁶⁴ Zn, ¹⁹ F, ¹² C, Co
		900		123 samples**

* “Al” designates a single Al sample; “5Al” designates five Al samples, etc.

** There are samples (made of Al) beside those specified in Table 1, for measuring the proton beam density distribution across the front (Al) surface and to control the neutron field uniformity along discs that form the target.

W (97.5%), Ni (1.75%), Fe (0.75%), and less than 0.2% of impurities are incorporated in tungsten discs. The average density of the tungsten discs is of 18.6 g/cm³. Sodium discs represent metallic sodium placed into a steel container with 0.4 mm thick walls. Impurities content in Na is less than 0.02%.

Target irradiation was performed with 0.8 GeV protons over a period of 10 hours at an average intensity equal to $4.8 \cdot 10^{10}$ p/cm² · pulse using the ITEP synchrotron. The pulse repetition rate is of 15 pulses per minute. Changes in the proton beam intensity over the irradiation period are presented in Figure 2. After a short decay lag, experimental samples were extracted from the target’s surface and inside volume and packaged into labelled polyethylene packages. Subsequent gamma spectra measurements were performed using several spectrometers. The absolute value for different threshold reaction rates were determined using the PCNUDAT decay database after gamma-spectra processing with the GENIE2000 code (see Table 2).

Simulation of reaction rates

To simulate the measured reaction rates, the LAHET Code System (LCS) [3] was used which involves the LAHET code for simulating hadron-nuclei interactions, the HMCNP code for simulating neutron transport at energies below 20 MeV, and the PHT code for simulating hard photon transport. Both neutron and proton spectra were calculated in all points where experimental samples are located.

Figure 2. Changes in the proton beam intensity over the period of irradiation

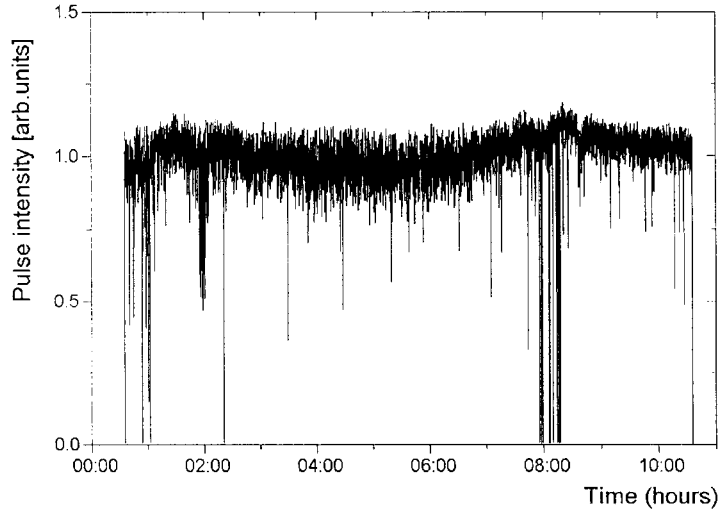


Table 2. Thresholds and main parameters of products for reaction rates being measured

Reaction	E_{th} (MeV)	Product	$T_{1/2}$	E_{γ} (keV) (Y_{γ} (%))
$^{115}\text{In}(n,n')$	0.335	^{115m}In	4.49h	336.2 (45.8)
$^{27}\text{Al}(n,p)$	1.89	^{27}Mg	9.46m	843.7 (71.8)
$^{64}\text{Zn}(n,p)$	2.1	^{64}Cu	12.70h	511.00 (35.8)
$^{59}\text{Co}(n,p)$	2.6	^{59}Fe	44.50d	1 099.3 (56.5)
$^{27}\text{Al}(n,ff)$	3.26	^{24}Na	15.02h	1 368.5 (100)
$^{197}\text{Au}(n,2n)$	8.5	^{196}Au	6.18d	355.7 (86.9)
$^{115}\text{In}(n,p)$	9	^{115}Cd	2.23d	527.9 (27.5)
$^{115}\text{In}(n,2n)$	9	^{114}In	49.51d	191.6 (16)
$^{65}\text{Cu}(n,2n)$	10.1	^{64}Cu	12.70h	511.00 (35.8)
$^{63}\text{Cu}(n,3n)$	~15	^{61}Cu	3.408h	656.0 (10.7)
$^{59}\text{Co}(n,2n)$	11	^{58}Co	70.92d	810.8 (99.4)
$^{19}\text{F}(n,2n)$	11.1	^{18}F	1.83h	511 (194)
$^{64}\text{Zn}(n,2n)$	12.4	^{63}Zn	38.1m	669.6 (8.40)
$^{12}\text{C}(n,2n)$	~20	^{11}C	20.38m	511 (162)
$^{209}\text{Bi}(n,4n)$	22.6	^{206}Bi	6.24d	803.1 (98.9)
$^{197}\text{Au}(n,4n)$	23	^{194}Au	39.5m	328.4 (63)
$^{169}\text{Tm}(n,4n)$	25.5	^{166}Tm	7.7h	778.82 (19.9)
$^{209}\text{Bi}(n,5n)$	29.6	^{205}Bi	15.31d	1 764.3 (32.5)
$^{93}\text{Nb}(n,4n)$	31	^{90}Nb	14.6h	1 129.2 (92.7)
$^{115}\text{In}(n,5n)$	35	^{111}In	2.83d	245.4 (94)
$^{209}\text{Bi}(n,6n)$	38	^{204}Bi	11.22h	899.2 (98.5)
$^{209}\text{Bi}(n,7n)$	45.3	^{203}Bi	11.76h	820.2 (29.6)

Another code system applied to simulate the experiment is the KASKAD-S code [4] which uses a discrete ordinate algorithm for coupled charges/neutral particle transport calculations in 2-D pencil beam problems. The multi-group cross-section library SADKO-2 for nucleon-meson cascade calculations coupled with the CONSYST/ABBN-93 neutron and gamma-ray cross-section libraries below 20 MeV is used.

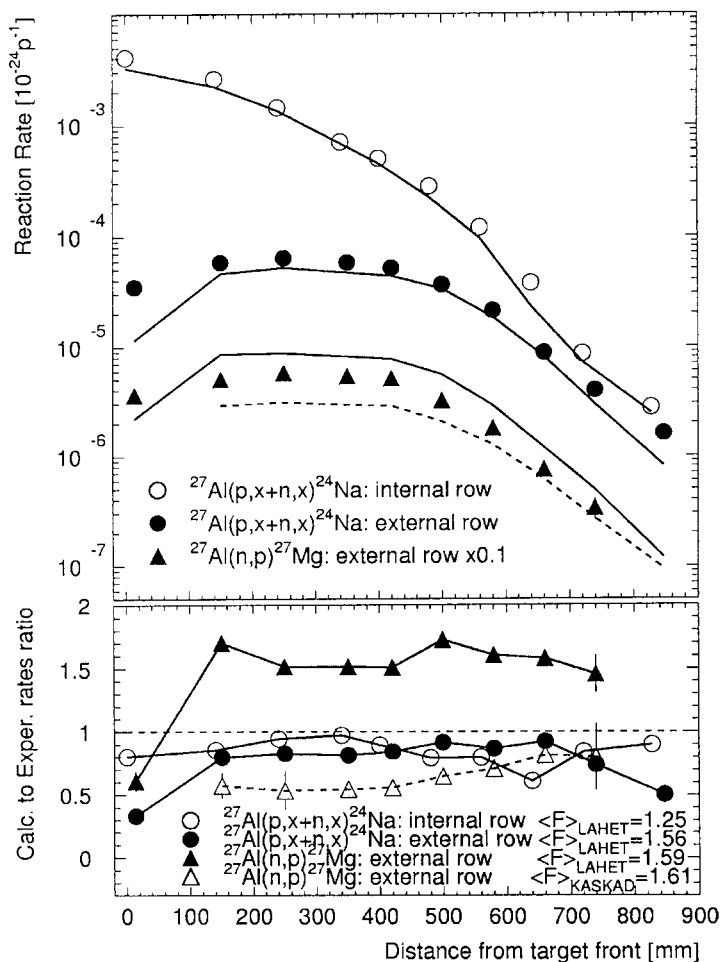
Reaction cross-sections for neutrons with energies up to 100 MeV and protons with energies up to 200 MeV were taken from MENDL2 [5] and MENDL2P [6] libraries, respectively. Reaction rates are obtained via integral product of spectra and cross-sections ($R = \int \phi(E)\sigma(E)dE$). The discrepancy between calculated and experimental results was estimated using the root mean square discrepancy factor, $\langle F \rangle$, defined in [7].

Results

The preliminary processing of gamma spectra from Al samples placed on the target outside surface and in the target centre makes it possible to estimate the generation rates of ^{24}Na and ^{27}Mg . Experimental and calculated values obtained using the LAHET code are presented in Figure 3. Measurements of gamma-spectra for all the samples irradiated are still in progress and all the reaction rates listed in Table 2 are expected to be determined after the completion of gamma-spectra processing.

Figure 3. Reaction rates of $^{27}\text{Al}(p,x+n,x)^{24}\text{Na}$ and $^{27}\text{Al}(n,p)^{27}\text{Mg}$ at the target axis and on the surface (top plot)

Calculations by LAHET and KASKAD-S are shown by solid and dashed lines, respectively. The ratios of reaction rate calculated values to the measured data are shown on the bottom plot.



Convergence of calculated and experimental values

The rates for ^{24}Na in Al foils predicted by LAHET are in satisfactory agreement with experimental values (except the first and last points on the surface), as shown in Figure 3. Whereas, the predicted rates for ^{27}Mg generation on the target surface are systematically overestimated compared to the measured values (by a factor of 1.6, on average), except the first point. At the same time, the ^{27}Mg production rates predicted by KASKAD-S are underestimated on average by a factor of 1.6. The observed discrepancies would be better understood only after the complete processing of gamma spectra for the rest of samples and determining both (n,p) – purely “neutron” and (p,n) – purely “proton” reactions.

Acknowledgements

The work was carried out under the ISTC Project #1145 and was supported by JAERI (Japan) and, partially, by the US Department of Energy.

REFERENCES

- [1] T. Takizuka, *et al.*, “Conceptual Design Study of Accelerator-driven Systems for Nuclear Waste Transmutation”, Proc. of the Second Int. Conf. on Accelerator-driven Transmutation Technologies and Applications, 3-7 June 1996, Kalmar, Sweden, pp. 179-185.
- [2] G.J. Van Tuyle and D.E. Beller, “Accelerator Transmutation of Waste Technology and Implementation Scenarios”, Proc. of the Third Int. Topical Meeting on Nuclear Applications of Accelerator Technology (AccApp'99), Long Beach, CA, 14-18 November 1999, pp. 337-346.
- [3] R.E. Prael and H. Lichtenstein, “User Guide to LCS: The LAHET Code System”, LANL Report LA-UR-89-3014, Los Alamos, MN (1989).
- [4] M. Voloschenko, “An Algorithm for Spallation Target Neutronics and Shielding Calculations”, Proc. Int. Conf. on Mathematics and Computations, Reactor Physics and Environmental Analyses in Nuclear Applications, 27-30 September 1999, Madrid, Spain, Vol. 2, p. 975; A.M. Voloschenko, E.I. Yefimov, T.T. Ivanova, V.P. Kryuchkov and O.V. Sumaneev, “Using Discrete Ordinate Method in the Spallation Target Neutronics and Shielding Calculations”, Proc. 3rd Int. Conf. on Accelerator-driven Transmutation Technologies and Applications, 7-11 June 1999, Pruhonice, Czech Republic, paper We-O-E12.
- [5] Yu.N. Shubin, *et al.*, “Cross-section Data Library MENDL-2 to Study Activation and Transmutation of Materials Irradiated by Nucleons of Intermediate Energies”, IAEA Report INDC(CCP)-385, Vienna, May 1995.

- [6] Yu.N. Shubin, *et al.*, “Cross-section Data Library MENDL-2P to Study Activation and Transmutation of Materials Irradiated by Nucleons of Intermediate Energies”, Proc. Int. Conf. on Nuclear Data for Science and Technology (Trieste 1997), IPS, Bologna, 1997, Vol. 1, p. 1054.
- [7] Yu.E. Titarenko, *et al.*, “Experimental and Theoretical Study of the Yields of Radionuclides Produced in ^{209}Bi Thin Target Irradiated by 1 500 MeV and 130 MeV Protons”, *Nucl. Instr. and Meth.*, A414 (1998) 73; Yu.E. Titarenko, *et al.*, “Study of Residual Product Nuclide Yield in 1.0 GeV Proton Irradiated ^{208}Pb and 2.6 GeV Proton Irradiated ^{187}W Thin Targets”, these proceedings.

**SPECTRAL MEASUREMENTS OF NEUTRONS FROM Pb, W,
AND Na TARGETS IRRADIATED BY 0.8 AND 1.6 GeV PROTONS**

**Yury E. Titarenko, Oleg V. Shvedov, Yury V. Trebukhovskiy, Vyacheslav F. Batyaev,
Valery M. Zhivun, Dmitry V. Fishchenko, Vladimir A. Korolyov, Gennady N. Smirnov**
SSC Institute for Theoretical and Experimental Physics
Moscow, 117259, Russia

Stepan G. Mashnik, Richard E. Prael, Arnold J. Sierk
Los Alamos National Laboratory
Los Alamos, NM 87545, USA

Hideshi Yasuda
Japan Atomic Energy Research Institute
Tokai, Ibaraki, 319-1195, Japan

Abstract

Preliminary results of neutron spectra measurements from Pb, W and Na targets irradiated by 0.8 and 1.6 GeV protons are presented. Measurements have been carried out using the proton beam extracted from the ITEP synchrotron and the TOF technique. Neutron registration has been carried out using BICRON MAB-511 liquid scintillation counters. Spectra measured at angles of 30°, 60°, 90°, 120°, and 150° have been compared with results of their simulation using the LAHET code system and the code CEM2k. The results are of interest both from data gathering viewpoint and as a benchmark of the up-to-date predictive powers of codes applied to design the hybrid accelerator-driven systems (ADS) using lead or lead-bismuth targets and sodium-cooled targets.

Foreword

Data on neutrons and charged particles generated from proton beam interactions with targets and structure materials are necessary when designing the present-day ADS facilities with proton beam energy of ~1-2 GeV [1,2]. Requirements concerning the data accuracy are rather strict because such data determine the external source term of the ADS. Besides, the neutron and proton data determine the calculation accuracy requirements of such principal ADS blanket parameters as the k_{eff} , safety control system efficiency, energy deposition of the fuel assembly and the minor actinide transmutation rates. These data are also important in calculating radiation resistance of structure materials exposed to high-energy particles.

What is said above determines the necessity for further experimental investigations of particle generation cross-sections and conducting more accurate measurements of these cross-sections at energies of bombarding protons up to several GeV. Such results are important, first, as nuclear constants by themselves and, second, in verifying the computational codes used in practice to calculate the parameters of ADS facilities.

All known experiments in measuring double-differential cross-sections of neutrons generated as a result of interaction of protons of intermediate energies with thin and thick targets made of different materials are tabulated in Table 1.

Table 1. Neutron spectra experiments at proton energies above 100 MeV

E_{inc} , MeV	Target nuclei	Neutron energy, MeV	Laboratory angle, degrees	Institute/year	Refs.
585	C, Al, Fe, Nb, In, Ta, Pb, U	$0.9-E_{\text{max}}$	30, 90, 150	PSI/87	[3]
120, 160	Al, Zr, Pb	≥ 30	0-145	IUCF/90	[4]
113	Be, C, O, Al, Fe, W, Pb, U	$0.5-E_{\text{max}}$	7.5-150	LANL/89	[5]
256	Be, C, O, Al, Fe, Pb, U	$0.5-E_{\text{max}}$	7.5-150	LANL/92	[6]
256, 800	Li, Al, Zr, Pb	$20-E_{\text{max}}$	7.5-150	LANL/93	[7]
318, 800	Al, Pb, U	$5-E_{\text{max}}$	7.5, 30	LANL/86	[8]
597	Be, B, C, N, O, Al, Fe, Pb, U	$0.5-E_{\text{max}}$	30-150	LANL/93	[9]
800	Be, B, C, N, O, Al, Fe, Cd, W, Pb	$0.3-E_{\text{max}}$	30-150	LANL/92	[10]
800, 1 500, 3 000	C, Al, Fe, In, Pb	$1-E_{\text{max}}$	15-150	KEK/97	[11]
2 200	Cu	3.3-200	60	KEK/83	[12]
500, 1 500	Pb	$1-E_{\text{max}}$	150-150	KEK/95	[13]
800, 200, 1 600	C, Fe, Zr, Pb, Th	$2-E_{\text{max}}$	0-160	SATURNE/98	[14]
600-1 600	Al, Cu, Zr, Pb	3-200	30-150	ITEP/96	[15]
750, 1 280, 2 200	Cu, Pb, U	7.5-70	119	ITEP/83	[16]

An analysis of the data presented in these works shows that double-differential cross-sections of neutrons for lead measured at proton energy of 0.8 GeV at LANL, KEK and SATURNE agree well with each other. They agree rather well with results of calculations performed with different codes. The agreement is worse for targets with small mass numbers where discrepancy may reach 100%. With incident proton energy increased to several GeV, the discrepancy between experimental and calculation data increases too.

Additional measurements of neutron spectra and yields in the proton energy range up to 2 GeV for different materials are necessary to study causes of mentioned discrepancies and to further improve available models and codes. Such experiments for measuring neutron double-differential cross-sections from Pb(p,xn), W(p,xn), and Na(p,xn) reactions in thick targets bombarded by protons with energies of 0.8 and 1.6 GeV were performed at the Institute of Theoretical and Experimental Physics (ITEP), Moscow. Measurements were performed using time-of-flight (TOF) techniques, and neutron spectra were measured at angles of 30°, 60°, 90°, 120° and 150° in the laboratory frame of reference.

The data obtained were compared with results of calculations by the LAHET code system [17] and the code CEM2k [18].

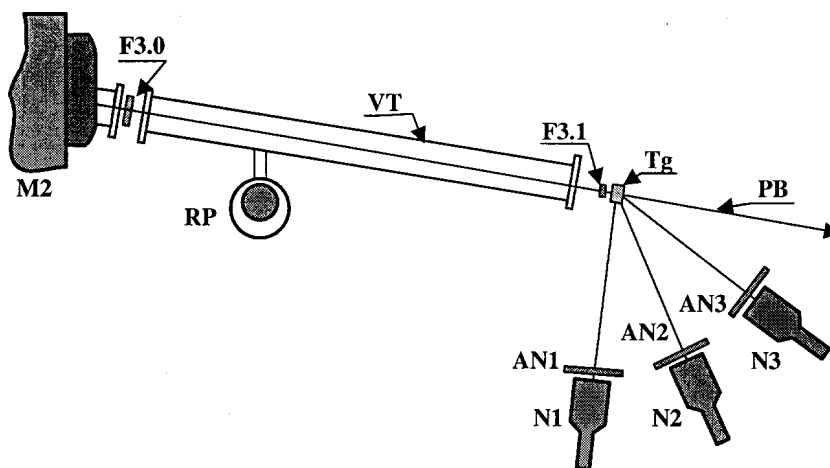
Description of the experiment

The experiment was carried out using the time-of-flight (TOF) technique. The TOF spectrometers were located in the 512nd beam of the ITEP proton synchrotron with a maximum energy of 10 GeV. Detectors were located at a distance of 2.5 m from the floor and more than 5 m from the ceiling and walls. The beam intensity was of approximately 10^5 protons per pulse. The beam was focused at the centre of the investigated targets, its profile was close to an ellipse with axes of 2 cm \times 2.5 cm. The distance between the target and neutron detectors changes from 1.5 m to 3 m and is not evacuated. The target materials and sizes are listed in Table 2. The contents of impurities in tungsten and sodium were less than 0.2% and 0.02%, respectively. Sodium was placed in a cylindrical steel container with 0.4 mm thick walls. The experimental facility layout is shown in Figure 1, where PB is the proton beam, M2 is the bending magnet, Tg is the target under investigation, F3.0 and F3.1 are plastic scintillators.

Table 2. The target materials and sizes

Target material	Proton energy, GeV	Target size, cm
Pb	0.8	$\varnothing 6.0 \times 2.0$
Pb	1.6	$15 \times 15 \times 20$
W	0.8, 1.6	$\varnothing 5.0 \times 3.0$
Na	0.8, 1.6	$\varnothing 6.0 \times 20$

Figure 1. The experimental facility layout



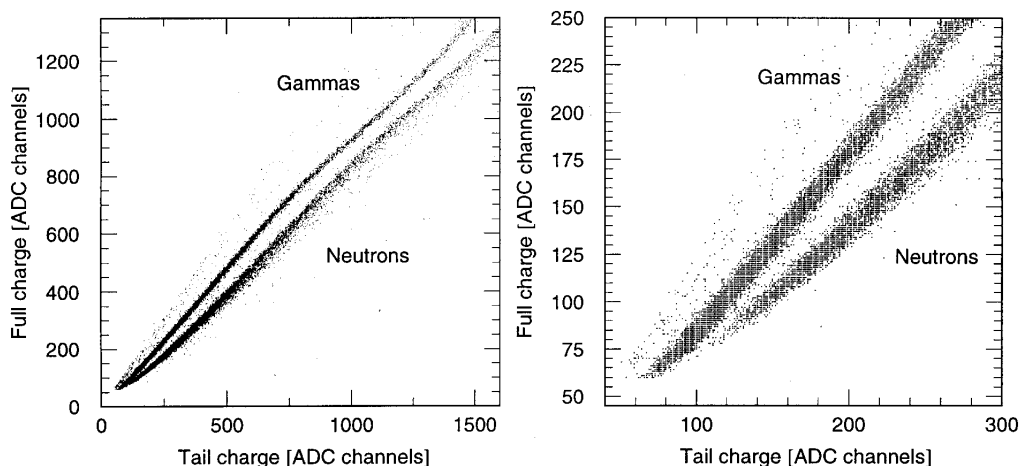
A 12 m distance was selected to minimise the effect of the great mass of large magnet M2 on the measurement results. The targets under investigation were located in the second focus of the beam at 80 m from the accelerator internal target.

The particles leaving the target are recorded by three detector assemblies (N1, N2, N3). Each of the assemblies consists of a 1 cm × 19 cm × 19 cm plastic scintillator (AN1, AN2, AN3) placed in the immediate proximity to, and ahead, a BICRON MAB-511 Ø 12.7 cm × 15.2 cm liquid neutron detector. There was no protection of the neutron detectors. Scintillators were turned on for coincidence with neutron detectors in charged particles spectra measurements and for anti-coincidence, in neutron spectra measurements.

Separation of neutrons and gammas were performed with an amplitude-amplitude analysis of the registered particle pulse (A(full charge) - A(tail charge)) within the recoil proton energy range of 2.5~10 MeV and an amplitude-time (A(full charge) - T(pulse duration)) analysis within the recoil proton energy range of ~10-300 MeV. The first method provides reliable separation of the small amplitude pulses. This is shown in Figure 2. The second method separates large amplitude pulses (Figure 3), where the quality of the amplitude-amplitude separation is lost.

Figure 3 demonstrates the branch behaviour of the amplitude-time separation technique. One can see that with increasing the pulse amplitude the branches that corresponds to neutrons and gammas diverge and the quality of separation increases accordingly.

Figure 2. Separation of neutrons and gammas with the amplitude-amplitude analysis



Thus, an acceptable quality of separation was achieved in the range of small pulse amplitudes by appropriate matching the parameters, and in the range of large pulse amplitudes, by using the amplitude-time separation technique.

The neutron counter efficiency was calculated using the SCINFUL [19] and CECIL [20] codes. Because the SCINFUL code application is limited to 80 MeV and the CECIL code gives reliable results up to energies of several hundred of MeV, the results of calculation with the SCINFUL code were used for energies below 80 MeV and the results of calculation with the CECIL code were used for higher energies. The results of calculation using the CECIL code at 80 MeV and above were re-normalised for matching with the results of the SCINFUL code at 80 MeV (see Figure 4). The error in determining the efficiency is estimated to be equal to 10% at energies below 80 MeV and 15% at higher energies.

Figure 3. Separation of neutrons and gammas with the amplitude-time analysis

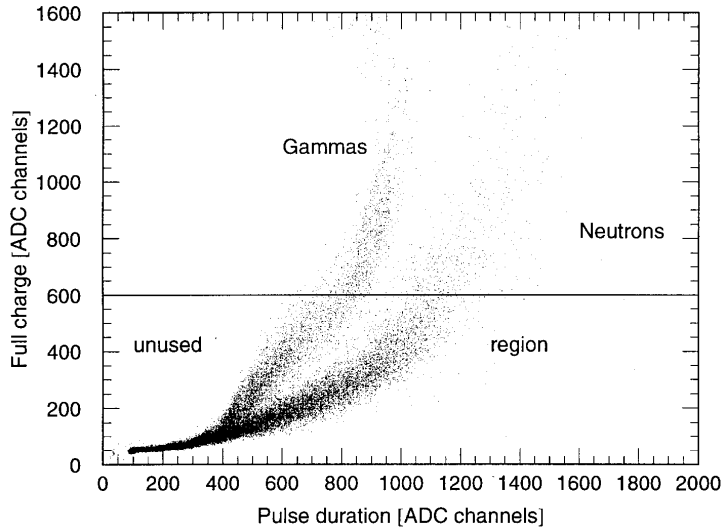
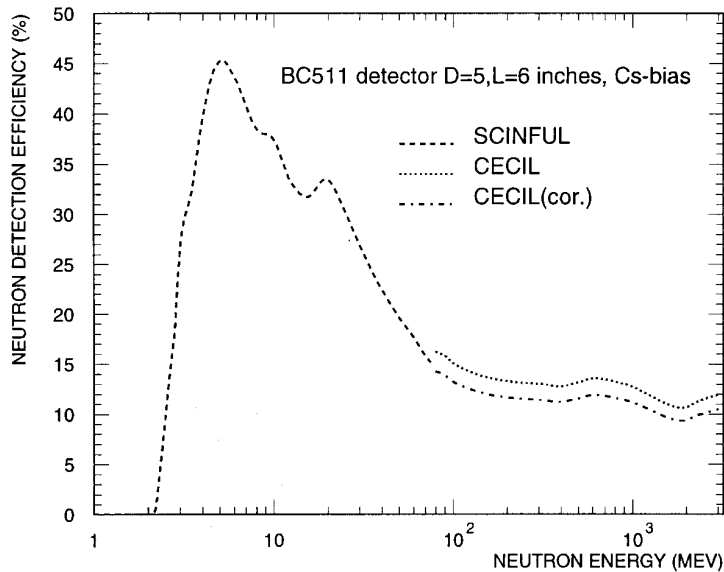


Figure 4. Efficiency of the BC511 detector used for neutron registration (detector size d5" × L6"). Calculation has been performed using the SCINFUL and CECIL codes at threshold corresponding to ¹³⁷Cs.



Simulation of neutron spectra

Because targets used in the present experiment can not be regarded as thin, simulations of neutron spectra by LAHET have included not only neutron generation from the proton-nucleus interactions, but also multiple scattering of primary protons together with the low energy (below 20 MeV) neutron transport by the HMCNP code. In the cases of lead and tungsten, elastic scattering of neutrons with energy above 20 MeV was taken into consideration as well.

Results

The measured neutron spectra from lead, tungsten, and sodium for proton energies of 0.8 and 1.6 GeV at angles of 30°, 60°, 90°, 120° and 150° are shown in Figures 5-7. The experimental data from other works ([10] and [11], for Pb at 0.8 GeV; [14], for Pb at 1.6 GeV; [10], for W 0.8 GeV) and calculations by LAHET are shown in the figures as well.

Figure 5. Double-differential neutron spectra from ^{nat}Pb at proton energies of 0.8 and 1.6 GeV measured in the present work (○), in previous works ([10] and [11], for 0.8 GeV and [14], for 1.6 GeV), together with the results of calculation by LAHET

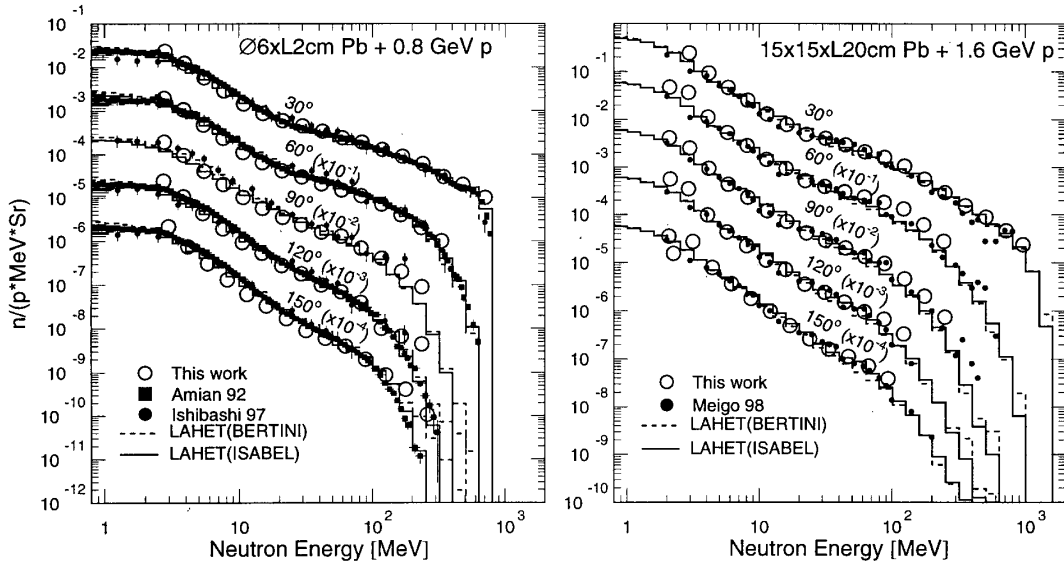


Figure 6. Double-differential neutron spectra from ^{nat}W at proton energies of 0.8 and 1.6 GeV measured in the present work (○), in a previous work ([10], for 0.8 GeV), together with calculations by LAHET

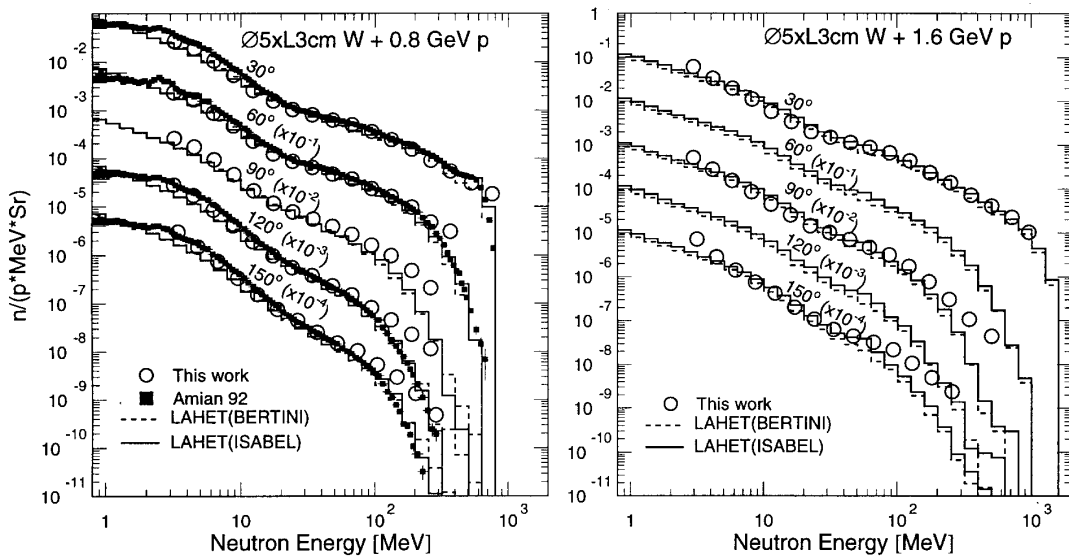
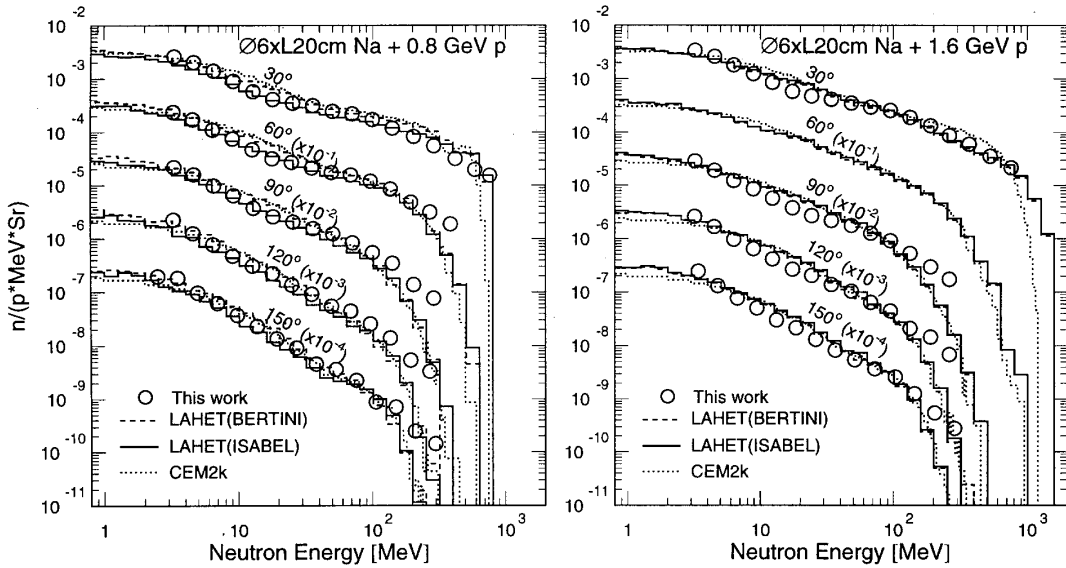
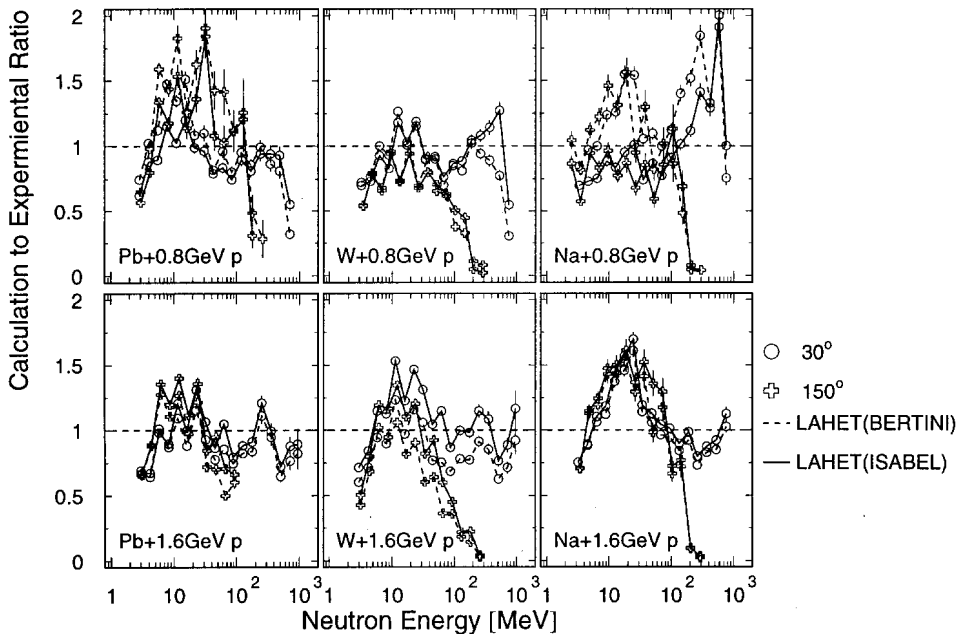


Figure 7. Double-differential neutron spectra from Na at proton energies of 0.8 and 1.6 GeV measured in the present work (○) together with the result of calculations by LAHET and CEM2k codes



Comparison of experimental and calculation results shows a satisfactory agreement for the heavy nuclei targets, W and Pb (Figure 8), at both proton energies. Exceptions may be seen for neutrons with energy above 100 MeV at angles 60°, 90° and 120° for $T_p = 1.6$ GeV and for energetic neutrons at 90°, 120° and 150° for $T_p = 0.8$ GeV. The agreement of calculated results with the data is worse with transfer to sodium. Traditionally, this is explained by problems for the most of theoretical models to describe high-energy hadron interactions with nuclei of low masses.

Figure 8. Calculation-to-experimental data ratios of neutron spectra at 30° and 150° from Pb, W and Na, as indicated



As an example, for the lightest element measured, Na, where the thickness of target should be of the least importance for the measured neutrons, we also show calculations with the last version of the Improved Cascade-Exciton Model code, CEM2k [18], simulating pure proton-nucleus reactions, without taking into account any internuclear interactions (Figure 7). One can see that for neutron energies above several MeV, where the thickness of target no longer affects significantly the measured spectra, CEM2k agrees with the data quite well, though some discrepancies in the very tails of the spectra still remain to be understood. Calculations with LAHET (both ISABEL and Bertini options) take into account the thickness of targets, therefore agree somewhere better than CEM2k with this data. Nevertheless, some disagreements between LAHET results and the data at the high-energy tails of most spectra and around ~20 MeV at forward angles for Na have yet to be understood. At a glance, it appears as though we obtained (with both LAHET and CEM2k) too many pre-equilibrium neutrons at forward angles and too few high-energy neutrons at backward angles; the latter could be an indication that the local Fermi distribution for intranuclear nucleons used by all models may be a too rough approximation. But these points require a further, more detailed investigation.

Acknowledgements

The authors are indebted to Dr. S. Meigo (JAERI) for his assistance in calculating the detection efficiency, to Dr. O.A. Shcherbakov (PINP, Gatchina) for helpful discussions of the measurement techniques, to Dr. V.L. Romadanov (MEPhI, Moscow) for his 14 MeV neutron source used in detector calibration, to Drs. V.N. Kostromin and I.A. Vorontsov (ITEP, Moscow) for their assistance in carrying out the experiments and to Dr. F.E. Chukreev (KIAE, Moscow) for discussions of results.

The work has been carried out under the ISTC Project #1145 and was supported by JAERI (Japan) and, partially, by the US Department of Energy.

REFERENCES

- [1] T. Takizuka, *et al.*, "Conceptual Design Study of Accelerator-driven Systems for Nuclear Waste Transmutation", Proc. of the Second Int. Conf. on Accelerator-driven Transmutation Technologies and Applications, 3-7 June 1996, Kalmar, Sweden, pp. 179-185.
- [2] G.J. Van Tuyle and D.E. Beller, "Accelerator Transmutation of Waste Technology and Implementation Scenarios", Proc. of the Third Int. Topical Meeting on Nuclear Applications of Accelerator Technology (AccApp'99), Long Beach, CA, 14-18 November 1999, pp. 337-346.
- [3] D. Filges, *et al.*, Joint Kernforschungsanlage Jülich and Kernforschungszentrum Karlsruhe Report Jul-1960/ KfK 3779, 1984; S. Cierjacks, *et al.*, *Phys. Rev.*, C 36, 1976 (1987).
- [4] W. Scobel, *et al.*, *Phys. Rev.*, C 41, 2010 (1990).
- [5] M.M. Meier, *et al.*, *Nucl. Sci. Eng.*, 102, 310 (1989).

- [6] M.M. Meier, *et al.*, *Nucl. Sci. Eng.*, 110, 299 (1992).
- [7] S. Stamer, *et al.*, *Phys. Rev.*, C 47, 1647 (1993).
- [8] M.M. Meier, *et al.*, *Radiation Effects*, 96, 73 (1986).
- [9] W.B. Amian, *et al.*, *Nucl. Sci. Eng.*, 115, 1 (1993).
- [10] W.B. Amian, *et al.*, *Nucl. Sci. Eng.*, 112, 78 (1992).
- [11] K. Ishibashi, *et al.*, *Nucl. Sci. Technol.*, 34, 529 (1997).
- [12] T.A. Shibata, *et al.*, *Nucl. Phys.*, A 408, 525 (1983).
- [13] Shin-ichiro Meigo, *et al.*, “Measurements of Spallation Neutron from a Thick Target Bombarded with 0.5 and 1.5 GeV Protons”, Proc. 13th Meeting of the International Collaboration on Advanced Neutron Sources (ICANS-XIII), 11-15 October 1995, PSI, Villien, Switzerland, Vol. II, p. 442 (1995).
- [14] Shin-ichiro Meigo, “Spallation Neutron Experiment at SATURNE”, Proc. 3rd Specialists Meeting on High-energy Nuclear Data, 30-31 March 1998, JAERI, Tokai, Japan, JARI-Conf 98-016, 1998, pp. 30-36; P. Pras, *et al.*, “Spallation Neutron Status at SATURNE”, Proc. Int. Conf. on Sub-critical Accelerator-driven Systems, 11-15 October 1999, ITEP, Moscow, pp. 161-169.
- [15] I.A. Vorontsov, *et al.*, *Issues of the Atomic Science and Technology, Ser. Nuclear Reactor Physics, TIYaS-X1*, 120 (1997); Yu.V. Trebukhovskiy, “Measurements of Neutron Spectra Induced by Intermediate Energy Protons in the Target Materials for Accelerator-driven Transmutation Systems”, Proc. Int. Conf. on Sub-critical Accelerator-driven Systems, 11-15 October 1999, ITEP, Moscow, pp. 212-216.
- [16] Yu.D. Bayukov, *et al.*, Preprint ITEP No. 172, Moscow (1983).
- [17] R.E. Prael and H. Lichtenstein, “User Guide to LCS: The LAHET Code System”, LANL Report LA-UR-89-3014, Los Alamos, MN (1989).
- [18] The code CEM2k is briefly surveyed in S.G. Mashnik, L.S. Waters and T.A. Gabriel, “Models and Codes for Intermediate Energy Nuclear Reactions”, Proc. 5th Int. Workshop on Simulating Accelerator Radiation Environments (SARE5), 17-18 July 2000, OECD Headquarters, Paris, France, and will be described by S.G. Mashnik and A.J. Sierk in a future paper.
- [19] J.K. Dickens, Report ORNL No. 6452, Oak Ridge (1988).
- [20] R.A. Cecil, *et al.*, *Nucl. Instr. & Methods*, 161, 439 (1979).

PRODUCTION OF RADIOACTIVE ISOTOPES IN MOLASSE

Heinz Vincke and Graham R. Stevenson

CERN, European Organisation for Nuclear Research, Switzerland

Abstract

This paper describes the production of radioactivity in molasse rock exposed to high-energy hadronic radiation. The molasse samples were irradiated by secondaries from 450 GeV protons interacting in a beryllium target. Detailed gamma spectroscopy provided the activities of the various radionuclides produced in the samples. Additionally, the Monte Carlo program FLUKA was used to simulate the irradiation experiment in order to determine conversion factors between inelastic nuclear interactions and the production of radioactive isotopes.

Introduction

The CERN site is located in the Geneva Basin, which is filled by sedimentary deposits collectively called molasse. For an environmental impact study of the CERN Neutrino Beam to Gran Sasso (CNGS) project, and for the Large Hadron Collider (LHC) the amount of radioactivity which will be produced in the molasse rock is of importance. Several samples of molasse were therefore taken from two different locations and were irradiated in the TCC2 area near the T4 target station of the CERN Super Proton Synchrotron (SPS). The radiation emitted by radioisotopes produced were measured afterwards with a Ge detector. This experiment was also simulated with the Monte Carlo program FLUKA, in order to determine conversion factors between inelastic nuclear interactions (star) and the production of radioactive isotopes. These factors are known as K_i values. The simulation permitted an estimation of the number of stars, hadron fluence distribution in energy and the production of residual nuclei in the molasse samples which can be used for the determination of such conversion factors. The present simulations were carried out using FLUKA97 (see [1,2] and the references therein).

Molasse samples

The molasse samples used for the irradiation were taken from two drillings, namely SLHC-43 and SLHC-44, see Figure 1. The natural radioactivity in the samples was measured. The main contribution to this natural radioactivity comes from ^{40}K (0.45 Bq/g) with small contributions from the thorium (0.027 Bq/g) and uranium (0.023 Bq/g) decay series. These results are in good agreement with the activity concentrations given in Refs. [3,4]. For the calculations of the induced radioactivity it was also necessary to know the chemical composition of the molasse rock. Thus, four samples were sent for the chemical analysis to the EMPA laboratory in Dübendorf [5]. The results of this chemical assay are shown in Table 1.

Figure 1. Layout of CNGS at CERN including the two positions of the drillings SLHC-43 and SLHC-44

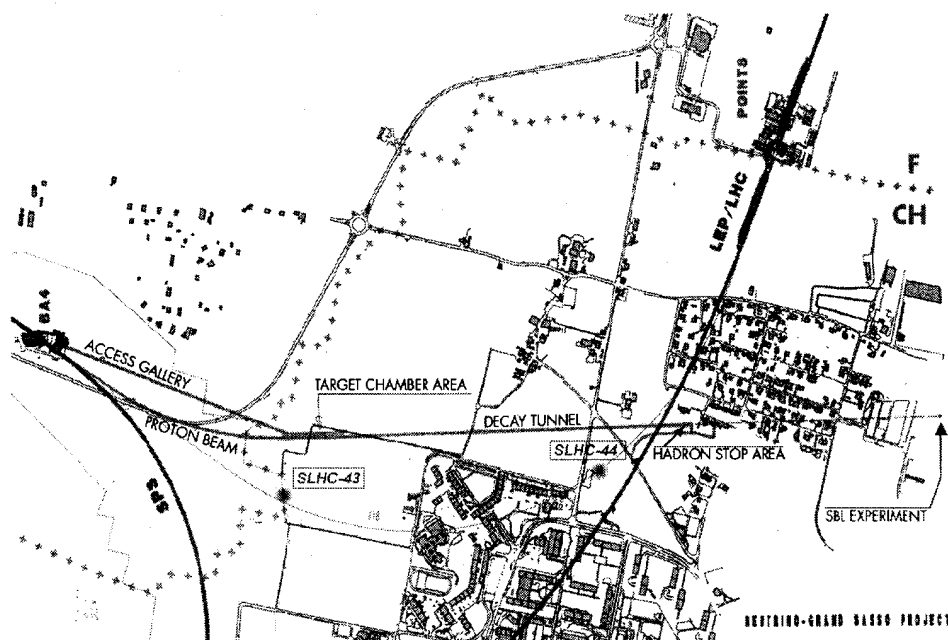


Table 1. Chemical composition of molasse from SLHC-43 and SLHC-44

Element	SLHC-43 in g/100g	SLHC-44 in g/100g
O	49.2	49.3
Si	19.8	19.6
Ca	9.3	10.0
Al	6.35	6.35
C	4.9	5.0
Fe	4.1	3.7
Mg	3.5	2.9
K	1.9	1.6
Na	0.57	0.37
Mn	0.135	0.06
Ti	0.07	0.07
P	0.04	0.02
Sr	0.04	0.08
Cr	0.016	0.018
Rb	0.014	0.009
Zn	0.01	0.009
Ni	0.009	0.01
V	0.007	0.009
Ba	0.006	0.006
Cu	0.004	0.004
Co	0.003	0.002
Ce	0.002	0.003
Eu	0.00007	0.00008

Most of the elements in molasse were detected using a common X-ray fluorescence spectroscopy (WD-XRF), but for Eu and Co plasma fluorescence spectroscopy (ICP-MS) had to be used. These two elements were of special interest because radioactive isotopes of these elements were found in a previous molasse irradiation experiment at CERN.

Data for molasse from 1992

Estimates of radioactivity induced in the rock were previously made by using data from the 1992 studies for the LHC [6]. These data were derived from earlier rock and soil activation studies. The radionuclides considered to be important for rock activation are shown in Table 2 together with the production probabilities K_i per star, defined as:

$$K_i = \frac{\Sigma_i}{\Sigma_{ie}} \quad (1)$$

where Σ_i is the macroscopic cross-section for the i^{th} radionuclide and Σ_{ie} is the total macroscopic inelastic cross-section for molasse.

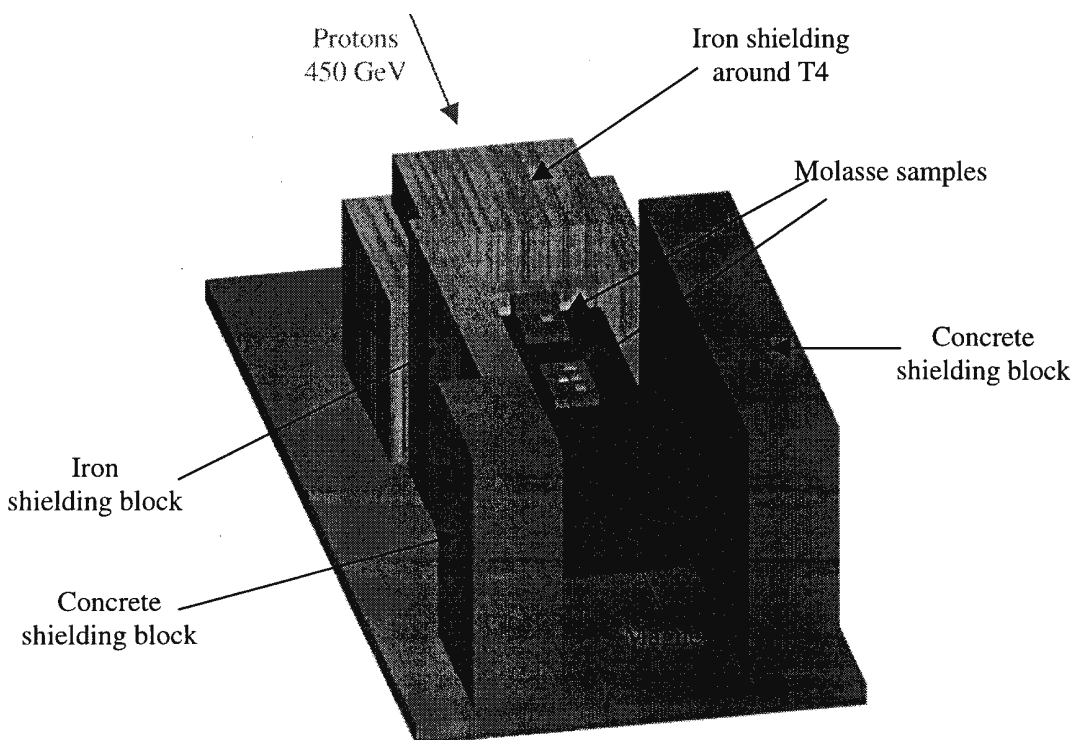
Table 2. Data for radionuclides produced in molasse from 1992

Nuclide	Half-life	Atoms per star (K_i)
^3H	12.4 y	0.05
^7Be	53.3 d	0.003
^{22}Na	2.60 y	0.011
^{45}Ca	163 d	0.006
^{46}Sc	83.8 d	0.0005
^{54}Mn	313 d	0.004
^{60}Co	5.27 y	0.003
^{152}Eu	13.3 y	0.01
^{154}Eu	8.8 y	0.0006

Irradiation

The irradiation of the five molasse rock samples took place in the TCC2 area from the end of July to the beginning of September 1998. Cylindrical plastic containers (6 cm in diameter, 2 cm in height) were filled with powdered molasse. The containers, weighing about 60 g, were then exposed on the first magnet downstream of the T4 target (see Figure 2). This location was chosen because of the high intensity needed for this experiment. The number of 450 GeV protons on the $200 \times 160 \times 2 \text{ mm}^3$ beryllium target in T4 was typically 4.0×10^{12} - 5.0×10^{12} per pulse (every 14.4 s). The samples were placed on small concrete blocks in order to better simulate the radiation environment in the rock around the LHC and CNGS structures.

Figure 2. Layout of the irradiation area at the T4 target station at CERN



Details of the FLUKA simulations

The irradiation experiment was simulated using FLUKA97 to follow the cascades from 450 GeV to the energy of thermal neutrons. The following sections define the essential parameters for these simulations.

Material assignments

The concrete shielding blocks were assumed to have a density of 2.35 g/cm^3 and the following chemical composition (the values in brackets give the corresponding mass fractions): oxygen (51.1%), silicon (35.8%), calcium (8.6%), aluminium (2.0%), iron (1.2%), hydrogen (0.6%), carbon (0.4%) and sodium (0.3%). The shielding around the T4 target and alongside the magnet was taken to be cast iron, with a density of 7.2 g/cm^3 , and to contain 5% of carbon. The magnet was assumed to be pure iron, with a density of 7.88 g/cm^3 . The coil of the magnet was made of copper with a density of 8.96 g/cm^3 . All other regions were filled with air at STP.

Particle energy thresholds

The simulations were aimed at determining star densities and radioisotope production in the different samples; the lower thresholds for particle transport were therefore set to 10 MeV for all hadrons, with the exception of neutrons which were followed down to thermal energies. Neutral pions, electrons, photons and neutrinos were not transported in the simulations, as they do not significantly contribute to the production of radioactive nuclei.

Biasing

Significant use of region-importance biasing was made in order to enhance the statistical accuracy of the results. In addition, the survival probability of thermal neutrons was set to be 0.9 in order to avoid undue time being wasted on tracking them.

Scoring

The number of stars (inelastic interactions of hadrons having kinetic energies greater than 50 MeV) in the molasse samples was recorded. The production of the residual nuclei was calculated directly in a FLUKA simulation, eliminating the need for relevant partial cross-sections. Furthermore, the track-lengths of neutrons below 19.6 MeV (the upper energy limit of the low energy neutron libraries in FLUKA) were scored by summing particle track-lengths in two of the molasse samples according to the FLUKA multi-group energy structure below this energy. Dividing the total track-lengths by the volume in which they were calculated gives the particle fluence.

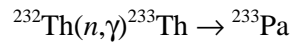
Gamma spectroscopy

The gamma-rays from the radioisotopes induced in the molasse samples were measured with a Ge detector. The gamma spectroscopy was carried out using the Canberra Genie-2000 spectroscopy software and the PROcount-2000 counting procedure software. This is a comprehensive software package for data acquisition, display and analysis. The Genie-2000 Gamma Analysis Software, which is part of the whole package, includes a set of advanced spectrum analysis algorithms which provide a

complete analysis of gamma-ray spectra (nuclide identification, interference correction, weighted mean activity, background subtraction and efficiency correction). The software is also capable of resolving overlapping peaks into individual components.

After the molasse samples had been irradiated, their activity was first measured after three days, then after one week and, finally, after 30 days. The peaks in the spectra, coupled with a precise energy calibration, could be used to determine the nuclides in the sample. The software provides nuclide identification through peak searches of spectra and scans of standard and user-generated nuclide libraries. In this study, a user-generated library was used which was based on the chemical composition of the rock samples and all the possible isotopes which could be created in the irradiation. The final step in nuclide analysis was to determine the activity of each isotope, corrected for decay to the time of the end of the irradiation.

The measured production of the gamma emitting radioactive isotopes in the molasse samples are indicated in the first and third columns of Table 6, normalised to the number of stars determined in the Monte Carlo simulations. Details concerning the measured radioactivities are to be found in [7]. From this report it can be concluded that the radioactivity coming from radioisotopes which have half-lives greater than 50 days is dominated by ^7Be , ^{46}Sc and ^{59}Fe after a few months of cooling. ^7Be is produced by spallation whereas ^{46}Sc is formed by both spallation and low-energy neutron capture. Like many other isotopes, ^{59}Fe is mainly produced by the capture of thermal neutrons. It is interesting to note that ^{233}Pa was detected in the irradiated molasse samples. This isotope is produced by thermal neutron capture followed by a β decay. Note that no chemical analysis was requested for ^{232}Th and therefore this isotope is not contained in Table 1.



Residual nuclei

The production rate of isotopes in the molasse samples was calculated with FLUKA by scoring the residual-nuclei production. In an energy range between 0.02 and 2.5 GeV, the hadron-nucleus interactions are described by a pre-equilibrium model. This includes an accurate model of the nuclear potentials. It must be noted that multi-fragmentation is not implemented in FLUKA, which is negligible for light target isotopes but can lead to an underestimation of the yield of light isotopes produced by interactions on medium- and high-mass targets. The radionuclides are produced mainly by spallation reactions or by radiative neutron capture. The (γ,n) reactions usually have only small cross-sections and are only of little importance in proton accelerators.

A complete list of the K_i values determined from the residual nucleus calculation in FLUKA is given in Table 6. The measured and the calculated activities for those nuclei where both measurement and calculation exist are compared in Table 3. For most isotopes this ratio is unity to within 2σ (which include the experimental measurement error from counting statistics and the estimated error from the FLUKA calculation based on running many similar calculations with different starting random numbers). The low value for ^{46}Sc is due to missing $^{45}\text{Sc}(n,\gamma)^{46}\text{Sc}$ cross-sections in the FLUKA data library.

Neutron spectra

Many of the produced isotopes in molasse come from low energy neutron activation. Some of them are pure β -emitters and, therefore, they can not be detected with the Ge detector. In order to study in more detail the production of ^{45}Ca and ^{55}Fe , which are of significant interest, it was essential

Table 3. Comparison: FLUKA “residual nuclei” – experiment

Nuclide	Half-life	FLUKA/experiment ratio \pm error
⁷ Be	53.3 d	0.93 \pm 0.06
²² Na	2.60 y	1.07 \pm 0.04
⁴⁶ Sc	83.8 d	0.034 \pm 0.004
⁴⁸ V	24.0 d	1.08 \pm 0.16
⁵¹ Cr	27.7 d	0.83 \pm 0.1
⁵² Mn	5.59 d	0.76 \pm 0.06
⁵⁴ Mn	313 d	1.56 \pm 0.13
⁵⁹ Fe	44.5 d	0.54 \pm 0.11
⁵⁶ Co	78.8 d	1.16 \pm 0.14
⁵⁷ Co	271 d	0.35 \pm 0.05
⁵⁸ Co	70.8 d	0.57 \pm 0.06
⁶⁰ Co	5.27 y	0.22 \pm 0.05

to calculate the track-length of neutrons in the samples down to thermal energies. The spectra were scored in Sample 1 and Sample 5 and are given in Figure 3. These two samples were chosen because the calculated low energy neutron flux ($E < 19.6$ MeV) differed at these positions. The yield Y of a radionuclide, produced by neutron capture in the sample, is calculated from:

$$Y = \int n\sigma(E)\Lambda(E)dE \quad \text{Bq} \quad (2)$$

where n is the atomic concentration of the isotope in molasse per cm^3 , $\sigma(E)$ is the energy dependent neutron capture cross-section for the production of the radionuclide and Λ is the track-length per proton of the neutron with energy E . In order to verify the results some calculations were carried out concerning the production of ⁴⁶Sc, ⁵⁹Fe, ⁶⁰Co and ¹⁵²Eu. These results are compared with the experimental data for the two selected samples in Table 4. Although FLUKA uses only a 72-group structure for low energy ($E < 19.6$ MeV) neutron transport, the results show an excellent agreement. As ⁴⁶Sc is produced by spallation and by neutron capture, the discrepancy between the experiment and the calculation can be explained because the latter does not contain the production of ⁴⁶Sc from spallation. The averaged K_i values determined from the low energy neutron spectra are given in the fifth column of Table 6.

Figure 3. Energy spectra of neutrons ($E < 19.6$ MeV) in Sample 1 and Sample 5 per primary proton

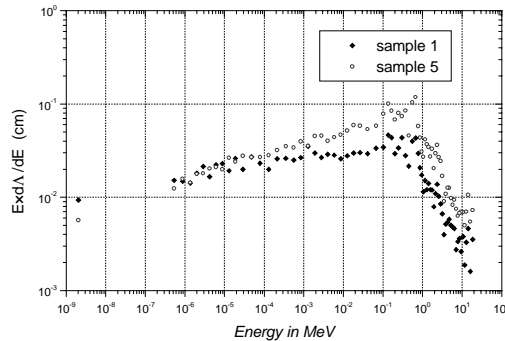


Table 4. Comparison of the production of selected radionuclides between the experiment and the FLUKA calculation (spectrum). All units are in Bq/g.

Nuclide	Sample 1		Sample 5		Ratio Spectrum/Experiment
	Experiment	Spectrum	Experiment	Spectrum	
⁴⁵ Ca	Not measurable	62.4	Not measurable	181.6	–
⁴⁶ Sc	38.5	25.2*	178.0	75.9*	0.54
⁵⁵ Fe	Not measurable	23.0	Not measurable	74.7	–
⁵⁹ Fe	22.0	24.1	92.0	81.8	0.99
⁶⁰ Co	4.5	4.0	17.9	15.7	0.88
¹⁵² Eu	1.4	1.4	5.0	4.3	0.93

* See section entitled *Neutron spectra*.

The neutron capture cross-sections used for the calculation are based on ENDF/B-VI cross-section data sets, except the ⁴⁴Ca(n,γ)⁴⁵Ca cross-sections, which were extracted from the JENDL-3.1 data. All data was obtained from the IAEA's Nuclear Data Centre, see [8].

Comparison between the 1992 and 1999 data

Table 5 shows the comparison between the data from 1992 and from 1999. Be aware that the soil composition of the 1992 data is based on glacial till. This table shows differences from the 1992 data in the production probabilities per star of ³H (factor 1.67 lower), ⁷Be (factor 4 higher), ⁴⁶Sc (factor 9 higher) and ⁶⁰Co (factor 3 higher) compared to the values obtained from a previous irradiation experiment. We gain reasonable confirmation of old values for the production of ²²Na, ⁴⁵Ca, ⁵⁴Mn, ¹⁵²Eu and ¹⁵⁴Eu.

Table 5. Comparison between the K_i from the 1992 study and from the 1999 study

Nuclide	Half-life	Data 1992, atoms per star (K_i)	Data 1999, atoms per star (K_i)
³ H	12.4 y	0.05	0.03
⁷ Be	53.3 d	0.003	0.012
²² Na	2.60 y	0.011	0.0084
⁴⁵ Ca	163 d	0.006	0.007
⁴⁶ Sc	83.8 d	0.0005	0.0044
⁵⁴ Mn	313 d	0.004	0.0045
⁶⁰ Co	5.27 y	0.003	0.009
¹⁵² Eu	13.3 y	0.01	0.008
¹⁵⁴ Eu	8.8 y	0.0006	0.0006

Conclusions

This paper summarises a comprehensive study of the production of radioactive isotopes in molasse. It can be concluded that the results from the FLUKA calculations are in a reasonable agreement to the experimental data. Note that for these radionuclides which are produced dominantly by low energy and thermal neutrons, the production probability per star can vary somewhat because the low energy and the thermal energy neutron fluences are not directly proportional to the star density rate. This indicates the special care to be taken when using an atom per star factor K_i for elements

produced by low energy neutron capture. Moreover, it is worth mentioning that in the new study 40 isotopes were identified whereas only nine isotopes were considered in the old 1992 data. Some of the new isotopes have half-lives greater than a year, and although they are produced in smaller quantities, they contribute to the remaining radioactivity over long times scales.

Table 6. Data for radionuclides produced per star in molasse with half-lives greater than five days

Radionuclide	Half-life	Experiment	Resnuc	Spectrum	K_i 1992	K_i 1999
³ H	12.4 y	–	0.03 ± 4%	–	0.05	0.03
⁷ Be	53.3 d	0.0118 ± 5%	0.011 ± 4%	–	0.003	0.012
¹⁰ Be	1.60 × 10 ⁶ y	–	0.006 ± 5%	–	–	0.006
¹⁴ C	5730 y	–	0.016 ± 1%	–	–	0.016
²² Na	2.60 y	0.0084 ± 2.5%	0.009 ± 3%	–	0.011	0.0084
²⁶ Al	7.16 × 10 ⁵ y	–	0.015 ± 4%	–	–	0.015
³² P	14.3 d	–	0.0019 ± 7%	–	–	0.0019
³³ P	25.4 d	–	0.0023 ± 6%	–	–	0.0023
³⁵ S	87.44 d	–	0.00066 ± 3%	–	–	0.00066
³⁶ Cl	3.01 × 10 ⁵ y	–	0.015 ± 4%	–	–	0.015
³⁷ Ar	35.02 d	–	0.027 ± 3%	–	–	0.027
³⁹ Ar	269 y	–	0.013 ± 3%	–	–	0.013
⁴¹ Ca	1.03 × 10 ⁵ y	–	0.19 ± 2%	–	–	0.19
⁴⁵ Ca	163 d	–	0.007 ± 2%	0.0065 ± 54%	0.006	0.007
⁴⁶ Sc	83.8 d	0.0044 ± 9%	0.00015 ± 7%	–	0.0005	0.0044
⁴⁴ Ti	47.3 y	–	0.00002 ± 17%	–	–	0.00002
⁴⁸ V	24.0 d	0.00053 ± 12%	0.00057 ± 9%	–	–	0.00053
⁴⁹ V	330 d	–	0.0012 ± 6%	–	–	0.0011*
⁵¹ Cr	27.7 d	0.0036 ± 6%	0.003 ± 9%	–	–	0.0036
⁵² Mn	5.59 d	0.00086 ± 4%	0.00065 ± 7%	–	–	0.00086
⁵⁴ Mn	313 d	0.0045 ± 3%	0.007 ± 8%	–	0.004	0.0045
⁵⁵ Fe	2.70 y	–	0.023 ± 8%	0.0146 ± 48%	–	0.023
⁵⁹ Fe	44.5 d	0.0013 ± 19%	0.0007 ± 9%	0.0008 ± 53%	–	0.0013
⁵⁶ Co	78.8 d	0.00006 ± 7%	0.00007 ± 9%	–	–	0.00006
⁵⁷ Co	271 d	0.000057 ± 5%	0.00002 ± 12%	–	–	0.00006
⁵⁸ Co	70.8 d	0.000052 ± 2%	0.00003 ± 10%	–	–	0.00005
⁶⁰ Co	5.27 y	0.0088 ± 20%	0.0025 ± 11%	0.0034 ± 58%	0.003	0.009
⁶³ Ni	96 y	–	0.00017 ± 19%	–	–	0.00017
⁶⁵ Zn	244 d	0.00037 ± 20%	–	–	–	0.0004
⁸⁶ Rb	19 d	0.0015 ± 14%	–	–	–	0.0015
¹³⁴ Cs	2.06 y	0.0031 ± 18%	–	–	–	0.003
¹³¹ Ba	11.8 d	0.000075 ± 7%	–	–	–	0.00008
¹³³ Ba	10.7 y	–	–	–	–	0.00008 ²
¹⁴¹ Ce	32.5 d	0.000098 ± 18%	–	–	–	0.0001
¹⁵² Eu	13.3 y	0.00796 ± 15%	–	0.0045 ± 66%	0.01	0.008
¹⁵⁴ Eu	8.8 y	0.00063 ± 32%	–	–	0.0006	0.0006
¹⁶⁰ Tb	72.3 d	0.000214 ± 16%	–	–	–	0.0002
¹⁸¹ Hf	42.0 d	0.000046 ± 18%	–	–	–	0.00005
¹⁸² Ta	115 d	0.00038 ± 17%	–	–	–	0.0004
²³³ Pa	27.0 d	0.00053 ± 19%	–	–	–	0.0005

* See [7].

Acknowledgements

We would like to thank Ian Dawson, Stefan Roesler and Helmut Vincke for many discussions. Furthermore, we are grateful to Y. Donjoux, L. Ulrici, G. Roubaud, P. Vojtyla and J. Wolf for their help during the gamma spectroscopy measurements. We would like to thank all the authors of FLUKA and especially Alfredo Ferrari and Paola Sala for many helpful discussions.

REFERENCES

- [1] A. Fassò, A. Ferrari, J. Ranft and P.R. Sala, “New Developments in FLUKA Modelling of Hadronic and EM Interactions”, in Proceedings of the Third Workshop on Simulating Accelerator Radiation Environments (SARE-3), KEK, Tsukuba, Japan, 1997, p. 32, (1997).
- [2] A. Ferrari, T. Rancati and P.R. Sala, “FLUKA Applications in High-energy Problems: From LHC to ICARUS and Atmospheric Showers”, in Proceedings of the Third Workshop on Simulating Accelerator Radiation Environments (SARE-3), KEK, Tsukuba, Japan, 1997, p. 165 (1997).
- [3] United Nations Scientific Committee on the Effects of Atomic Radiation, “Sources, Effects and Risks of Ionizing Radiation”, 1988 Report to the General Assembly, with annexes.
- [4] Bernard Shleien, “The Health Physics and Radiological Health Handbook” (1992).
- [5] EMPA, Swiss Federal Laboratory for Materials Testing and Research, Ueberlandstrasse 129, Ch-8600 Duebendorf.
- [6] G.R. Stevenson and J.M. Zazula, “The Estimation of Parameters of Radiological Interest in the LHC Beam Dump and its Surroundings”, CERN Internal Report CERN/TIS-RP/IR/92-02 (1992).
- [7] H. Vincke and G.R. Stevenson, “Production of Radioactive Isotopes in Molasse”, CERN Internal Report CERN/TIS-RP/IR/99-20 (1999).
- [8] IAEA’s Nuclear Data Centre, <http://iaeaand.iaea.or.at/>

Additional references

- [9] P.A. Aarnio, A. Fassò, A. Ferrari, H.-J. Möhring, J. Ranft, P.R. Sala, G.R. Stevenson and J.M. Zazula, “FLUKA: Hadronic Benchmarks and Applications”, in Proceedings of the International Conference on Monte Carlo Simulation in High Energy and Nuclear Physics, MC’93, Tallahassee, USA, 1993, P. Dragovitsch, S.L. Linn and M. Burbank, eds., p. 88, World Scientific, Singapore (1994).
- [10] C. Birattari, E. De Ponti, A. Esposito, A. Ferrari, M. Pelliccioni and M. Silari, “Measurements and Characterization of High-energy Neutron Fields”, *Nuclear Instruments and Methods*, A338 (1994), 534.

- [11] C. Birattari, E. De Ponti, A. Esposito, A. Ferrari, M. Magugliani, M. Pelliccioni, T. Rancati and M. Silari, "Measurements and Simulations in High-energy Neutron Fields", in Proceedings of the 2nd Specialists Meeting on Shielding Aspects of Accelerators, Targets and Irradiation Facilities, CERN, Geneva, Switzerland, 1995, p. 171, published by OECD Nuclear Energy Agency (1996).
- [12] A. Ferrari, P.R. Sala, R. Guaraldi and F. Padoani, "An Improved Multiple Scattering Model for Charged Particle Transport", *Nuclear Instruments and Methods*, B71 (1992), 412.
- [13] F. Pirotte, M. Silari and L. Ulrici, "Induced Radioactivity in Concrete and Rock in BA4 and TCC6 (BA7)", CERN Internal Report CERN/TIS-RP/IR/96-03 (1996).
- [14] A.H. Sullivan, "Ground Activation Around the AA and ACOL Target Areas", Internal report CERN TIS-RP/IR/87-34.
- [15] R.H. Thomas and G.R. Stevenson, "Radiological Safety Aspects of the Operation of Proton Accelerators", Technical Report Series No. 283, IAEA Vienna (1988).
- [16] H. Vincke, "Flukacad/Pipsicad: Three-dimensional Interfaces Between FLUKA and AutoCAD", these proceedings.

NEUTRON PRODUCTION FROM THIN AND THICK TARGETS BY HIGH-ENERGY HEAVY ION BOMBARDMENT

Takashi Nakamura, Hisaki Sato, Hiroshi Iwase
Department of Quantum Science and Energy Engineering
Tohoku University, Japan

Tadahiro Kurosawa
Electrotechnical Laboratory, Japan

Noriaki Nakao
High-energy Accelerator Research Organisation, Japan

Yoshitomo Uwamino
Institute of Physical and Chemical Research, Japan

Akifumi Fukumura
National Institute of Radiological Sciences, Japan

Abstract

We measured neutrons produced from thin and thick targets bombarded by high-energy heavy-ions. The angular and energy distributions of neutrons produced by 100 and 180 MeV/nucleon He, 100, 180, 400 MeV/nucleon C, 100, 180, 400 MeV/nucleon Ne, 400 MeV/nucleon Ar, Fe and Xe, and 800 MeV/nucleon Si ions stopping in thick carbon, aluminium, copper and lead targets were measured using the Heavy-ion Medical Accelerator in Chiba (HIMAC) of the National Institute of Radiological Sciences (NIRS), Japan. The experimental results are compared with calculations using the HIC code, and the calculated results agree with the measured results within a factor of 2. The double differential cross-sections (DDX) of neutron production from thin C, Al, Cu and Pb targets bombarded by 135 MeV/nucleon C ion were measured using the RIKEN ring cyclotron of the Institute of Physical and Chemical Research, Japan. The experimental spectra were compared with the calculations using the HIC and the QMD codes.

Introduction

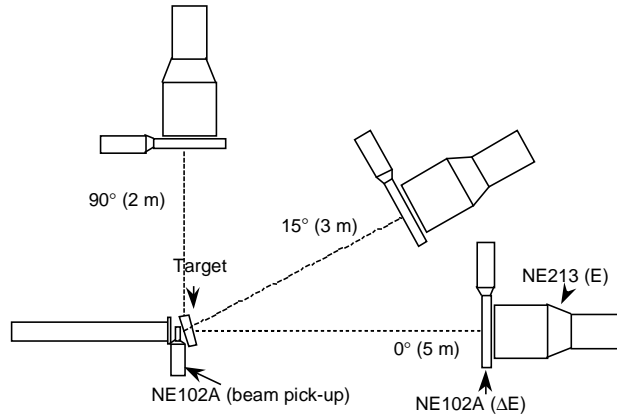
Recently, high-energy heavy ions have been used in various fields of nuclear physics, material physics and medical application, especially cancer therapy. At the National Institute of Radiological Sciences (NIRS) in Chiba, Japan, the Heavy Ion Medical Accelerator in Chiba (HIMAC) has been used for heavy ion cancer therapy for the last three years, and the Gesellschaft für Schwer Ionen (GSI) in Germany has just begun heavy ion cancer therapy. Several institutes in the world have started or plan to build radioactive beam facilities in which high-energy radioactive heavy ions are used for investigating exotic nuclei, nuclear synthesis and so on. To design these facilities, radiation shielding is essential to protect workers and nearby inhabitants from the penetrating neutrons produced by high-energy heavy ions. The data on the energy/angle distribution of secondary neutrons from a thick target which fully stops heavy ions, so-called thick target neutron yield (TTY), are indispensable to estimate radiation source terms for accelerator shielding design [1]. For projectiles of energy higher than 100 MeV/nucleon, several experimental results on TTY have been published on neutron production from proton incidence [2-6]. For heavier ions, however, there is only one set of experimental data on TTY for 160 and 177.5 MeV/nucleon helium ions [7]. Recently, Heilbronn, *et al.* published two reports on TTY for 155 MeV/nucleon He and C, and 272, 435 MeV/nucleon Nb ions [8,9]. There also exists one published work on the double differential cross-section (DDX) of neutron production for 337 MeV/nucleon Ne ions on C, Al, Cu and U targets [10]. In this work, we present a systematic study on TTY using the HIMAC for 100, 180 MeV/nucleon He, 100, 180, 400 MeV/nucleon C, 100, 180, 400 MeV/nucleon Ne, 400 MeV/nucleon Ar, Fe, Xe and 800 MeV/nucleon Si ions, and the double differential cross-sections (DDX) of neutron production from thin C, Al, Cu and Pb targets bombarded by 135 MeV/nucleon C ions using the RIKEN ring cyclotron of the Institute of Physical and Chemical Research. The measured TTY data are compared with those calculated with the heavy ion code (HIC) [11] based on intranuclear cascade and evaporation models. The DDX data are compared with the calculation using the two heavy ion Monte Carlo codes HIC and the quantum molecular dynamics model (QMD) [12].

Experimental procedure

Thick target experiment

The energy of neutrons produced in the target was measured by the time-of-flight (TOF) method. Figure 1 shows the experimental geometry of a typical arrangement of three neutron counters. A thin NE102A plastic scintillator (30 mm diameter by 0.5 mm thick) was placed just behind the end window of the beam line as a beam pick-up scintillator. The output pulses from this scintillator were used as the start signal of the TOF measurement. These output pulses were also used to count the absolute number of projectiles incident on the target. A target was set on the beam line 10 cm behind the beam pick-up scintillator. The beam spot size incident on the target was about 1.5 cm in diameter and the beam height was 1.25 m above the concrete floor of the experimental area. The NE213 liquid scintillator (12.7 cm diameter by 12.7 cm thick), which is designed to expand the dynamic range of output pulses for high-energy neutron measurements [14], was used for neutron detector (E counter). The NE102A plastic scintillator (15 cm by 15 cm square and 0.5 cm thick) for ΔE counter was placed in front of the E counter to discriminate charged particles from non-charged particles, neutrons and photons. Three sets of E and ΔE counters were used for simultaneous angular distribution measurements at three different angles. The detectors were located 2 m at large angles to 5 m at small angles away from the target to provide better energy resolutions in the forward directions where there are larger yields of high-energy neutrons. In order to minimise neutrons in-scattering, no local shielding was used near the detectors. By interposing an iron shadow bar (15 cm by 15 cm square and 60 cm thick) between the target and the detector, the background neutron components from room scattering were measured.

Figure 1. Thick target experimental arrangement at HIMAC



The incident energies of heavy ions and the target materials with their thickness are given in Table 1. Target materials are C (1.77 g/cm³), Al (2.7 g/cm³), Cu (8.93 g/cm³) and Pb (11.34 g/cm³) and each target has a shape of 10 cm by 10 cm square and its thickness was determined to stop the incident particles completely. When the measurements were carried out at large angles, the target was set at 45° to the beam line to minimise the attenuation effect of neutrons through the target.

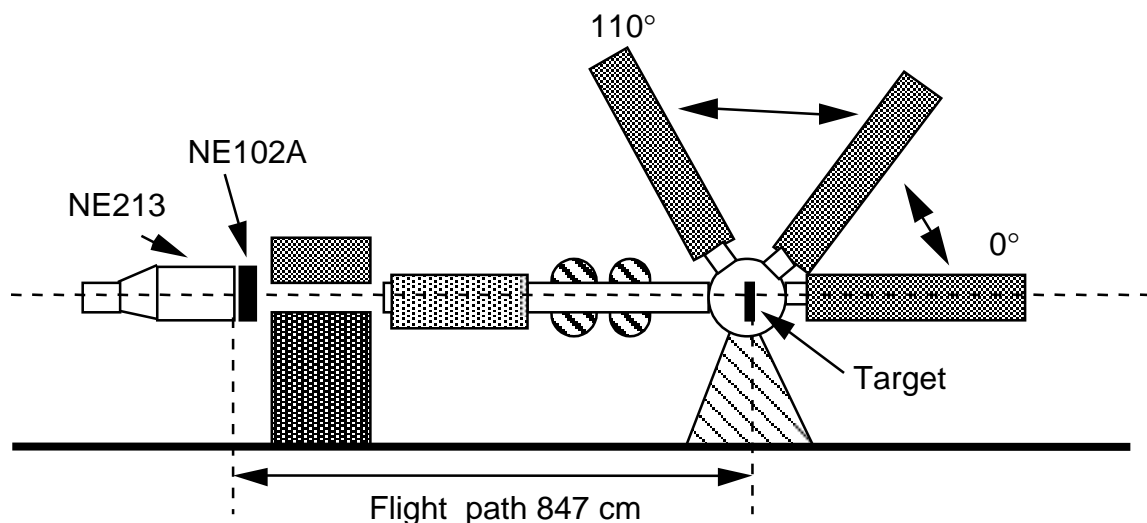
Table.1 Projectile types with their incident energy per nucleon and target thickness that was estimated to stop the incident particles completely

Incident particle type and energy [MeV/u]	Target thickness [cm]
He [100]	C [5.0], Al [4.0], Cu [1.5], Pb [1.5]
He [180]	C [16.0], Al [12.0], Cu [4.5], Pb [5.0]
C [100]	C [2.0], Al [2.0], Cu [0.5], Pb [0.5]
C [180]	C [6.0], Al [4.0], Cu [1.5], Pb [1.5]
C [400]	C [20.0], Al [15.0], Cu [5.0], Pb [5.0]
Ne [100]	C [1.0], Al [1.0], Cu [0.5], Pb [0.5]
Ne [180]	C [4.0], Al [3.0], Cu [1.0], Pb [1.0]
Ne [400]	C [11.0], Al [9.0], Cu [3.0], Pb [3.0]
Ar [400]	C [7.0], Al [5.5], Cu [2.0], Pb [2.0]
Fe [400]	C [4.0], Al [3.0], Cu [1.5], Pb [1.5]
Xe [400]	C [3.0], Al [2.0], Cu [1.0], Pb [1.0]
Si [800]	C [23.0], Al [17.0], Cu [6.5], Pb [6.5]

Thin target experiment

The measurements were carried out at the RIKEN ring cyclotron. A schematic view of the experimental set-up is shown in Figure 2. The ΔE-E counter, which was the same detector as those of the thick target experiment, was used for neutron measurements. The target thickness is 1 mm of C, 0.6 mm of Al, 0.3 mm of Cu and 0.3 mm of Pb. The direction of incident beam was rotated around the target from 0° to 110° through the beam swinger magnet in order to measure the energy-angle distribution of neutrons produced from the target by the time-of-flight (TOF) method having the flight

Figure 2. Schematic view of the thin target experimental set-up



path of 847 cm. The charged particles passed through the target were bent down to the beam dump by the clearing magnet. In order to shield the spurious scattered neutrons, the neutrons produced directly from the target were introduced into the detector through the iron-concrete collimator (20 cm \times 20 cm aperture) of 120 cm thickness. The measurements were carried out at 0°, 15°, 30°, 50°, 80° and 110°.

Data acquisition electronics

The timing signal from the beam pick-up scintillator was divided into two pulses, and one pulse was fed to a constant fraction discriminator (CFD) to start a 2 048 channel CAMAC time-to-digital converter (TDC) and to count the number of incident beam particles. The other pulse was fed to a charge-integrated type 2249A analogue to digital converter (ADC) to get pulse height data. The anode signal from each E counter was split into three pulses. One signal was fed to a CFD to produce the stop signal of TDC and the gate of ADC. Two signals of the E counter were sent through different delay cables to two channels of ADC to measure the total and slow light components. The anode signal from each ΔE counter was also fed to ADC to get pulse height data. These digital data from the CAMAC system were recorded event by event on a 3.5 inch magneto-optical disk with the personal computer using the Kakuken On-line Data Acquisition System (KODAQ) [13].

Monte Carlo analysis of thick target experiment

These experimental results were compared with the Monte Carlo calculations. The neutron spectra were calculated by using the Heavy Ion Code (HIC) [11]. The HIC code is a Monte Carlo code that calculates continuum state transitions between projectile and target in heavy ion reactions at energies above 50 MeV/nucleon. The assumption in the model is that the reaction can be represented by the interaction of two Fermi gases that pass through each other. In this code, an intranuclear cascade and an evaporation model are used. Since the HIC code only gives the double differential neutron production cross-section, the so-called thin target yield, the calculations were performed for a series of thin target yield calculations. These were then summed to obtain the neutron yields from heavy ions stopping in a thick target, considering the projectile continuous energy loss and the projectile number attenuation in the target, as follows:

$$\frac{d^2\phi}{dEd\Omega} = \sum_{i=1}^m \sigma_m NP_m \Delta E_m / \left(\frac{\Delta E_m}{\Delta x_m} \right) \quad (1)$$

$$P_m = P_{m-1} \exp(-\sigma_m^{\text{Tot}} N \Delta x_m) \quad (2)$$

where σ_m is the double differential neutron production cross-section calculated by HIC, N is the atomic density of target, P_m is the number of beam particles in the target ($P_0 = 1.0$), $\Delta E_m/\Delta x_m$ is the stopping power calculated by the SPAR code [14], σ^{Tot} is the total reaction cross-section given as an experimental formula by Shen, *et al.* [15], and Δx_m is the thickness of thin target divided. In Eq. (2), the neutron production from the extranuclear cascade is still neglected, and this approximation can hold in the relatively lower energy region.

Results and discussion

Thick target results

Energy spectra

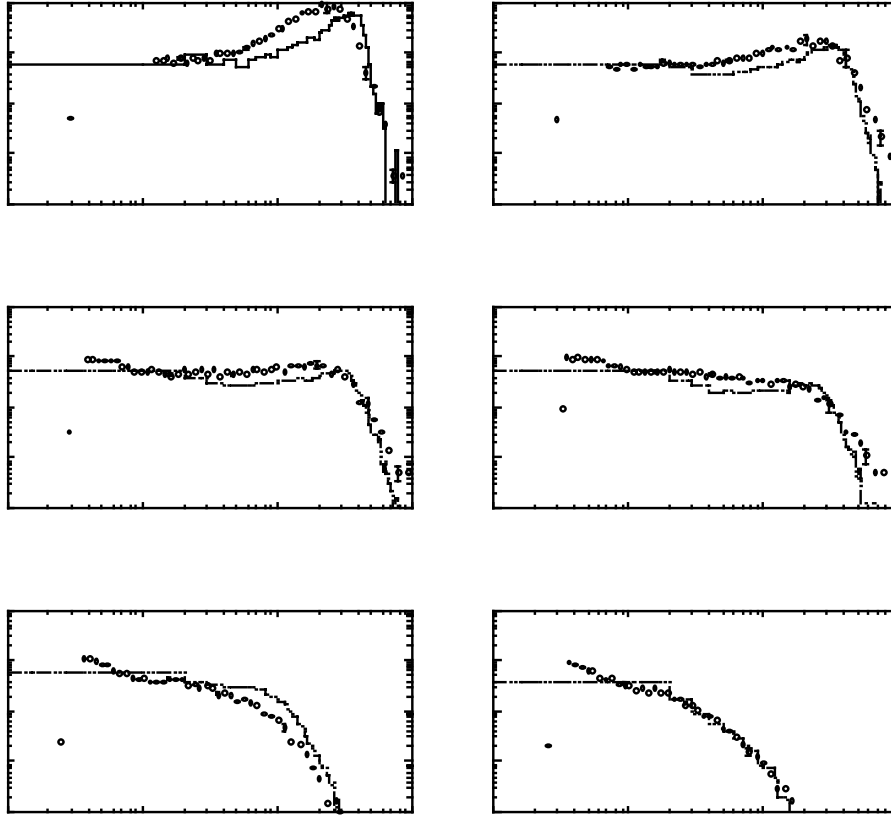
The measured neutron energy spectra for C target bombarded by 400 MeV/nucleon C projectile are shown in Figure 3, as examples. Neutron spectra measured in the forward direction have a broad peak at the high-energy end, especially a large bump at 0° , and this peak becomes more prominent for a lighter target and for a higher projectile energy. The peak energy of this bump is about 60-70% of the projectile energy per nucleon. This means that these high-energy neutron components produced in the forward direction by a break-up process and the momentum transfer from projectile to target nuclei are both higher for lighter nucleus and higher projectile energies than for heavier nucleus and lower projectile energy. The energy of the neutrons in the forward direction extends to more than twice that of the incident particle energy per nucleon. The neutron spectra have two components, one below about 10 MeV corresponds to neutrons produced isotropically in the centre of mass system mainly by the equilibrium process, and the other above 10 MeV corresponds to those produced by the pre-equilibrium process. Since the neutron emission by the pre-equilibrium process has forwardness in the angular distribution, the neutron spectra become softer at large emission angles, where the equilibrium process is prominent.

The calculated spectra are also shown in Figure 3 with the experimental results. These figures clarified that a broad high-energy peak in the forward direction appears around the incident particle energy per nucleon, while on the other hand the measured peak appears about 60-70% of that as described before. This marked discrepancy may come from the fact that the HIC calculation, which does not include the effects of the nuclear potential and the viscosity of nuclear matter, fails to express the break-up process. The superposition of thin target yields in the calculation provides fairly well (roughly within a factor of 2) the measured thick target yield at large neutron emission angle where the break-up process is negligibly small, although the extranuclear cascade reaction is neglected in this superposition.

Angular distribution

Figure 4 shows the neutron yields integrated above 5 MeV for each emission angle. All of the results suggest that the angular distribution becomes more forward peaked for higher energies of the incident projectiles, and that neutron yield is larger for a lighter target nucleus in the forward direction,

Figure 3. Neutron spectra from the 400 MeV/nucleon C ion in the C target



and at large angles the yields become larger for a heavier target nucleus. This reveals again that the neutron production at the forward angles mainly occurs through the direct reaction process that reduces in magnitude with an increase of emission angle and at large angles the low energy neutrons via equilibrium process dominate the yields.

Total yields

The total neutron yields above 5 MeV were integrated over a hemisphere from 0-90°, and they are shown in Figure 5. The total neutron yields become slightly larger with increase of the target mass, but their dependence on the target mass is very small compared with the difference of neutron numbers of the target. The difference in neutron yields between He, C and Ne ion projectiles is also very small, but the yields from Ar and Fe ion projectiles are larger than from those lighter ions. These differences in neutron yields might be caused by the neutron production cross-section, the thickness of the target and neutrons produced by secondary charged particles.

Thin target results

We obtained neutron energy spectra for C, Al, Cu and Pb targets bombarded by 135 MeV/nucleon C ion. These experimental results were compared with the calculation using the HIC [11] and the QMD [12] codes. Figure 6 shows the experimental and calculated double differential cross-sections of neutron production from C, Al, Cu and Pb targets, respectively. Neutron energy spectra measured

Figure 4. Angular distribution of neutron yields integrated above 5 MeV for 100, 180 MeV/nucleon He, 100, 180, 400 MeV/nucleon C and 100, 180, 400 MeV/nucleon Ne

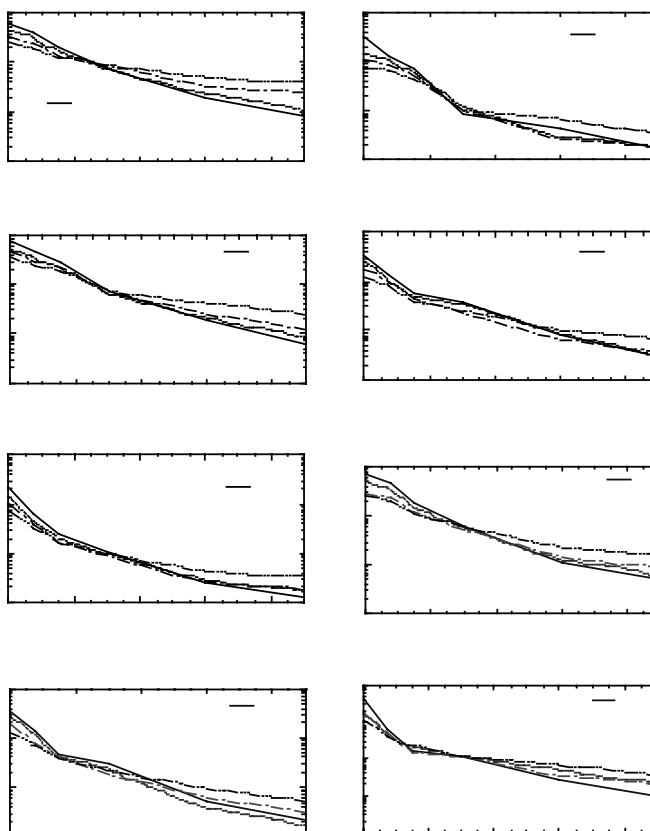


Figure 5 Total neutron yields above 5MeV integrated for hemisphere from 0-90°

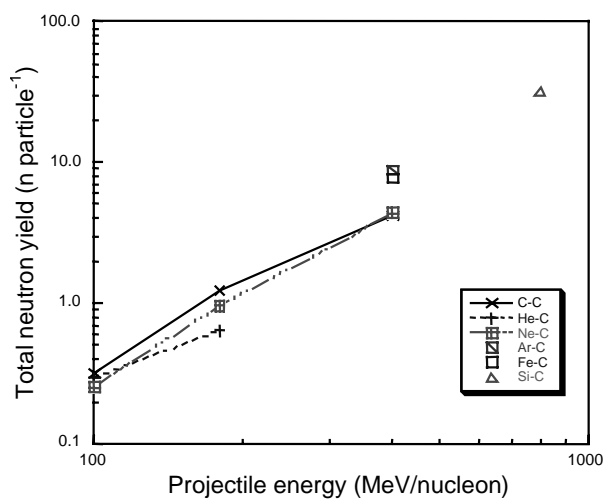
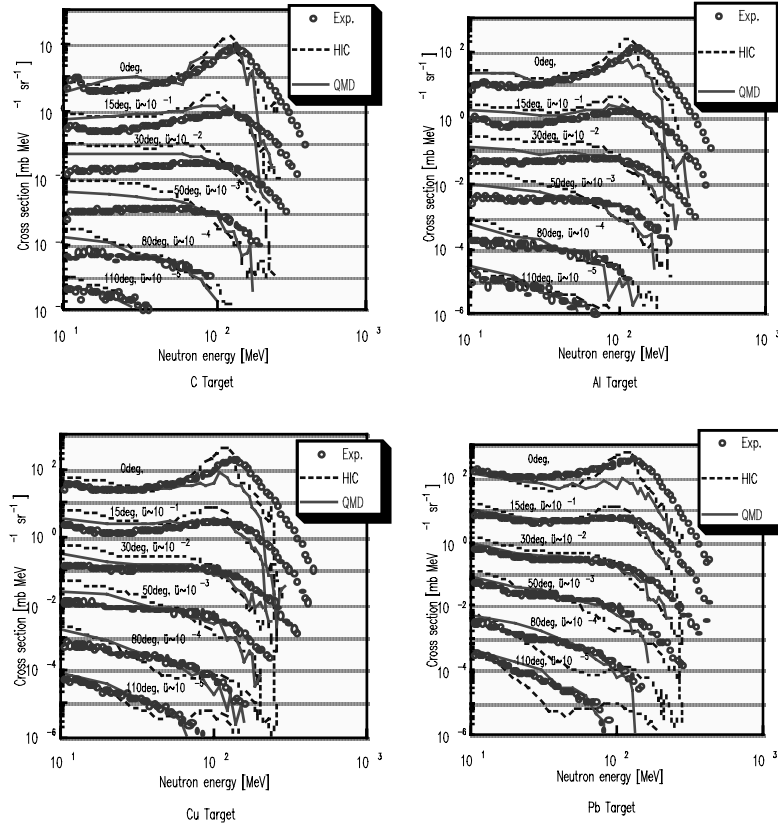


Figure 6. Measured and calculated neutron production cross-section for 135 MeV/nucleon C ion



in the forward direction have a peak near the projectile energy per nucleon. This peak is due to a knock-on process in which a neutron is knocked out by the direct collision between the target nucleon and the projectile nucleon. This peak becomes more prominent in the forward direction and for a lighter target, since the momentum transfer from projectile to target nuclei is higher for lighter nucleus than for heavier nucleus [16]. The high-energy end of neutrons in the forward direction reaches about 300-400 MeV. This reflects the Fermi motion of a nucleon in a nucleus. The neutron spectra have another two components based on cascade pre-equilibrium emission process and evaporation-equilibrium emission process. At small angles the knock-on process is dominant, and at large angles the evaporation process is dominant. Two calculations of HIC and QMD show a tendency to underestimate the high-energy neutron components beyond the peak at all angles. The HIC overestimates the peak, while the QMD underestimates the peak. At large angles, the calculated spectra reach good agreement with the measured spectra. In general, the QMD gives better agreement with the experimental results, especially for heavy targets, than the HIC.

Conclusion

We measured angular and energy distributions of neutrons produced by 100 and 180 MeV/nucleon He, 100, 180, 400 MeV/nucleon C, 100, 180, 400 MeV/u Ne, 400 MeV/nucleon Ar, Fe and Xe, and 800 MeV/nucleon Si ions stopping in carbon, aluminium, copper and lead targets. The neutron spectra in the forward direction have a broad peak at about 60-70% of the incident particle energy per nucleon due to break-up process and extend up to almost twice the projectile energy per nucleon. The experimental results were also compared with the calculations using the HIC code, and the

calculated results agree with the measured results roughly within a factor of 2 margin of accuracy. This is the first systematic study on neutron production from thick targets by heavy ions, and it will be useful for the shielding design of high-energy heavy ion accelerator facilities.

We also measured double differential cross-sections of neutron production from thin C, Al, Cu and Pb targets bombarded by 135 MeV/nucleon C ion. The experimental spectra were compared with the calculations using the HIC and the QMD codes. The calculated spectra tend to underestimate the high-energy neutron region. At large angles, the calculated spectra, particularly the QMD, are in rather good agreement with the measured spectra. These experimental results will be useful as the benchmark data for investigating the accuracy of nuclear reaction model used in the high-energy particle transport calculation code.

REFERENCES

- [1] T. Kato, T. Nakamura, *Nucl. Instr. and Meth.*, A311, 548 (1992).
- [2] J.W. Wachter, W.A. Gibson, W.R. Burrus, *Phys. Rev.*, C6, 1496 (1972).
- [3] M.A. Lone, *et al.*, *Nucl. Instr. and Meth.*, A256, 135 (1987).
- [4] M.M. Meier, *et al.*, *Nucl. Sci. Eng.*, 102, 310 (1989).
- [5] M.M. Meier, *et al.*, *Nucl. Sci. Eng.*, 104, 339 (1990).
- [6] J.V. Siebers, *et al.*, *Nucl. Sci. Eng.*, 115, 13 (1993).
- [7] R.A. Cecil, *et al.*, *Phys. Rev.*, C21, 2471 (1980).
- [8] L. Heilbronn, *et al.*, *Nucl. Sci. Eng.*, 132, 1 (1999).
- [9] L. Heilbronn, *et al.*, *Phys. Rev.*, to be published.
- [10] R.A. Cecil, *et al.*, *Phys. Rev.*, C24, 2013 (1981).
- [11] W.H. Bertini, ORNL-TM-4134.
- [12] J. Aichelin, *Physics Report*, 202, 233 (1991).
- [13] Kazuo Omata, Yuuzou Fujita, INS-T-496 (1990).
- [14] T. Nakane, *et al.*, JAERI-M 93-152 (1993).
- [15] Shen Wen-qing, *et al.*, *Nucl. Phys.*, A491, 130 (1989).
- [16] T. Kurosawa, *et al.*, *Nucl. Instrum. Methods*, A430, 440 (1999).

STUDY OF RESIDUAL PRODUCT NUCLIDE YIELDS IN 1.0 GeV PROTON-IRRADIATED ^{208}Pb AND 2.6 GeV PROTON-IRRADIATED $^{\text{nat}}\text{W}$ THIN TARGETS

**Yury E. Titarenko, Oleg V. Shvedov, Vyacheslav F. Batyaev, Valery M. Zhivun,
Evgeny I. Karpikhin, Ruslan D. Mulambetov, Dmitry V. Fischenko, Svetlana V. Kvasova**

Institute for Theoretical and Experimental Physics
B. Cheremushkinskaya 25, 117259, Moscow, Russia

Stepan G. Mashnik, Richard E. Prael, Arnold J. Sierk
Los Alamos National Laboratory, Los Alamos, NM 87545, USA

Hideshi Yasuda
Japan Atomic Energy Research Institute, Tokai, Ibaraki, 319-1195, Japan

Abstract

One-hundred thirteen (113) residual product nuclide yields in a 1.0 GeV proton-irradiated thin monoisotopic ^{208}Pb sample and 107 residual product nuclide yields in a 2.6 GeV proton-irradiated $^{\text{nat}}\text{W}$ sample have been measured and simulated by eight different codes. The irradiations were performed using proton beams extracted from the ITEP synchrotron. The nuclide yields were γ -spectrometered directly using a high-resolution Ge-detector. The γ -spectra were processed by the GENIE-2000 code. The ITEP-developed SIGMA code was used together with the PCNUDAT nuclear decay database to identify the γ -lines and to determine the cross-sections. The $^{27}\text{Al}(p,x)^{22}\text{Na}$ reaction was used to monitor the proton flux. The measured yields are compared with calculations of the LAHET (with ISABEL and Bertini options), CEM95, CEM2k, CASCADE, CASCADE/INPE, INUCL and YIELDX codes. Estimates of the mean deviation factor are used to demonstrate the predictive power of the codes. The results obtained may be of interest in studying the parameters of the Pb and W target modules of the hybrid accelerator-driven system (ADS) facilities.

Introduction

At present, the Pb-Bi eutectic and W are regarded as the most promising target materials for ADS facilities [1-3]. As a result, the high-energy irradiation mode of using the materials necessitates additional studies of the nuclear physics characteristics of Pb, Bi and W, particularly the yields of residual product nuclei under proton irradiation in a broad range of energies from a few MeV to 2-3 GeV. Results of such studies are extremely important when designing even demonstration versions of the ADS facilities.

Undoubtedly, computational methods will play an important role when forming a set of nuclear constants for ADS facilities. Therefore, verification of the most extensively used simulation codes has proved to be of a high priority.

Basic definitions and computational relations

The formalism of representing the reaction product yields (cross-sections) in high-energy proton-irradiated thin targets is described in sufficient detail in [4]. In terms of the formalism, the variations in the concentration of any two chain nuclides produced in an irradiated target ($N_1 \xrightarrow{\lambda_1} N_2 \xrightarrow{\lambda_2} \rightarrow$) may be presented to be a set of differential equations that describe the production and decays of the nuclides. By introducing a formal representation of the time functions, F_i , of the form $F_i = (1 - e^{-\lambda_i \tau}) \frac{1 - e^{-\lambda_i KT}}{1 - e^{-\lambda_i T}}$, ($i = 1, 2$ and Na or another monitor product; τ is the duration of a single proton pulse; T is the pulse repetition period; K is the number of pulses within the irradiation period), which characterises the nuclide decays within the irradiation time, and by expressing (similar to the relative measurements) the proton fluence size via the monitor reaction cross-section, σ_{st} , we can present the cumulative and independent yields as:

$$\sigma_1^{cum} = \frac{A_0}{\eta_1 \varepsilon_1 N_{Na}} \frac{N_{Al}}{N_T} \frac{F_{Na}}{\lambda_{Na}} \sigma_{st} \quad (1)$$

$$\sigma_1^{cum} = \frac{A_1}{v_1 \eta_2 \varepsilon_2 F_1 N_{Na}} \frac{N_{Al}}{N_T} \frac{\lambda_2 - \lambda_1}{\lambda_2} \frac{F_{Na}}{\lambda_{Na}} \sigma_{st} \quad (2)$$

$$\sigma_2^{ind} = \left(\frac{A_2}{F_2} + \frac{A_1 \lambda_1}{F_1 \lambda_2} \right) \frac{1}{\eta_2 \varepsilon_2 N_{Na}} \frac{N_{Al}}{N_T} \frac{F_{Na}}{\lambda_{Na}} \sigma_{st} \quad (3)$$

$$\sigma_2^{cum} = \sigma_2^{ind} + v_1 \sigma_1^{cum} = \left(\frac{A_1}{F_1} + \frac{A_2}{F_2} \right) \frac{1}{\eta_2 \varepsilon_2 N_{Na}} \frac{N_{Al}}{N_T} \frac{F_{Na}}{\lambda_{Na}} \sigma_{st} \quad (4)$$

where σ_1^{cum} is the cumulative cross-section of the first nuclide; σ_2^{ind} and σ_2^{cum} are the independent and cumulative cross-sections of the second nuclide; N_{Al} and N_T are the numbers of nuclei in the monitor (standard) and in experimental sample, respectively; η_1 and η_2 are the γ -line yields; ε_1 and ε_2 are the spectrometer efficiencies at energies E_{γ_1} and E_{γ_2} ; v_1 is the branching ratio of the first nuclide; λ_1 , λ_2 and λ_{Na} are, respectively, the decay constants of the first and second nuclides and of the monitor product (^{22}Na and/or ^{24}Na).

The factors A_0 , A_1 and A_2 are calculated through fitting the measured counting rates in the total absorption peaks, which correspond to energies E_{γ_1} (the first nuclide) and E_{γ_2} (the second nuclide), by exponential functions. It should be noted that Eqs. (1)-(4) were derived on the assumption that the γ -intensities of the two nuclides produced under irradiation are recorded up to the desired accuracy within an interval of time from the irradiation end to the moment of the ultimate detectable intensity. If, for some reason, the factor A_1 cannot be found, then the factor A_2 will be used together with expression (14) from [4] to determine the quantity σ_2^{cum*} , which we called the supra cumulative yield:

$$\sigma_2^{cum*} = \sigma_2 + \frac{\lambda_2}{\lambda_1 - \lambda_2} v_1 \sigma_1^{cum} = \frac{A_2}{\eta_2 \epsilon_2 F_2 N_{Na}} \frac{N_{Al}}{N_T} \frac{F_{Na}}{\lambda_{Na}} \sigma_{st} \quad (5)$$

The resultant value of σ_2^{cum*} may prove to be very different from σ_2^{cum} . Nevertheless, the supra cumulative yield can be either used directly to verify the codes, or determined further up to σ_2^{cum} if the needed data are obtained elsewhere (for example, from inverse kinematics experiments).

Experimental techniques

A 10.5 mm diameter, 139.4 mg/cm² monoisotopic ²⁰⁸Pb metal foil sample (97.2% ²⁰⁸Pb, 1.93% ²⁰⁷Pb, 0.87% ²⁰⁶Pb, < 0.01% ²⁰⁴Pb, < 0.00105% of chemical impurities) and a 38.1 mg/cm² natW metal foil sample (99.95% W, < 0.05% of chemical impurities), both of 10.5 cm diameter, were proton-irradiated. As monitors, 139.6 mg/cm² and 139.1 mg/cm² Al foils of the same diameter were used. Chemical impurities of the monitor did not exceed 0.001%.

The samples were irradiated by the external proton beam from the ITEP U-10 synchrotron [4]. The average flux densities during irradiation of Pb and W samples were of 1.4×10^{10} p/cm² and 2.8×10^{10} p/cm², respectively.

Our measurements were supported by extra researches aimed at reducing the systematic errors in the experimental results. These researches included:

- Experiments to specify the neutron component in the extracted proton beams.
- Experiments to specify the ²⁷Al(p,x)²⁴Na monitor reaction cross-section.
- Studies to specify the dependence of the γ -spectrometer detection efficiency on the position geometry of irradiated sample.
- Studies to optimise the γ -spectrum simulation codes.

Figures 1 and 2 show the results of measuring the neutron component in the extracted proton beams, i.e. the neutron-to-proton flux density ratio, $\Phi_n = \Phi_p$. Figure 3 presents the monitor reaction cross-sections measured here and in other works*. The height-energy dependence of the detection efficiency is displayed in Figure 4.

* MI85 – *Nucl. Phys.*, A 441 (1985), 617; MI86 – *NIM*, B 16 (1986), 61; MI89 – *Analyst*, 114 (1989), 287; MI90 – NEANDC(E)-312-U(1990) 46; MI93 – INDC(GER)-037/LN(1993) 49; MI95 – *NIM*, B 103 (1995), 183; MI96 – *NIM*, B 114 (1996), 91; MI97 – *NIM*, B 129 (1997), 153.

Figure 1. The neutron backgrounds around the extracted proton beams that irradiate thin experimental samples

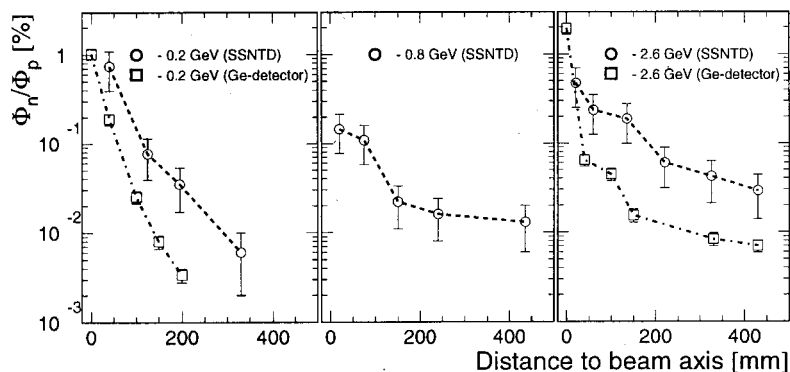


Figure 2. Neutron component in the extracted proton beams of different energies

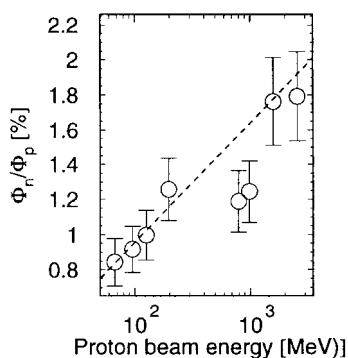


Figure 3. The $^{27}\text{Al}(p,x)^{24}\text{Na}$ monitor reaction cross-sections measured in this and other works

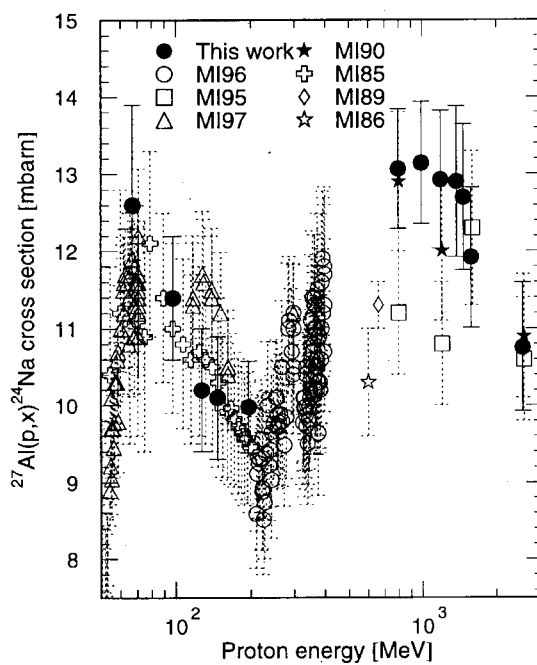
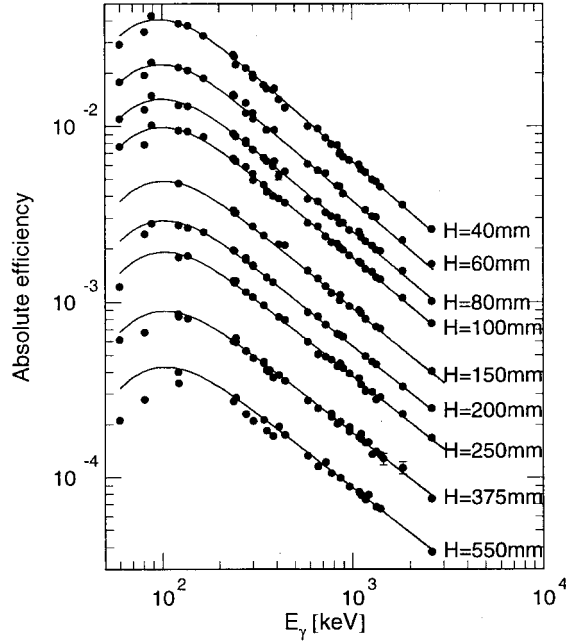


Figure 4. The experimental and calculated detection efficiency of the spectrometer



The discrepancies between the two sets of high-energy data in Figure 3 have yet to be studied. The analytical expression of the spectrometer detection efficiency as a function of energy and sample position height is:

$$\varepsilon(E, H) = \varepsilon_{base}(E) \cdot \left[\frac{(q_1 + q_2 \cdot \ln E + H_{base})}{(q_1 + q_2 \cdot \ln E + H)} \right]^2 \quad (6)$$

where q_1 and q_2 are parameters defined by fitting the experimental results. An analysis of the γ -spectrum processing codes has shown that the GENIE-2000 code is superior to the others because of its interactive mode of fitting the peaks, which permits correction of the automated computer-aided processing; therefore, we chose it for our work.

Experimental results and measurement errors

Tables 1 and 2 present the results of measuring the reaction product yields in the 1 GeV proton-irradiated ^{208}Pb and 2.6 GeV proton-irradiated ^{nat}W samples. One-hundred thirteen (113) yields from ^{208}Pb have been obtained, of which, six independent yields (i), 17 independent yields of metastable states (m), 15 independent yields of metastable and ground states ($\Sigma m_j + g$), 64 cumulative yields (c), and 11 supra cumulative yields, when the addend may exceed the determination error (c*). One-hundred seven (107) yields from ^{nat}W are presented, of which, six independent yields (i), nine metastable state yields (m), 5 yields of metastable and ground states ($\Sigma m_j + g$), 86 cumulative yields (c), and 1 supra cumulative yield (c*).

From Tables 1 and 2 one can see that the experimental errors range within $\sim(6-35)\%$. The main contribution to the total error is from uncertainties in the nuclear data, namely, in the absolute quantum yields and cross-sections of the monitor reactions.

Table 1. Experimental product nuclide yields in 1 GeV proton-irradiated ^{208}Pb

Product	T_{1/2}	Type	Yield (mb)
^{206}Bi	6.243d	i	4.60 ± 0.29
^{205}Bi	15.31d	i	6.20 ± 0.40
^{204}Bi	11.22h	i(m1+m2+g)	5.29 ± 0.80
^{203}Bi	11.76h	i(m+g)	4.84 ± 0.59
$^{204\text{m}}\text{Pb}$	67.2m	i(m)	11.0 ± 1.0
^{203}Pb	51.873h	c	31.5 ± 2.1
^{201}Pb	9.33h	c*	26.9 ± 2.4
^{200}Pb	21.5h	c	18.2 ± 1.2
^{198}Pb	2.4h	c	8.9 ± 2.1
$^{197\text{m}}\text{Pb}$	43.0m	c*	17.9 ± 4.0
^{202}Tl	12.23d	c	18.9 ± 1.2
^{201}Tl	72.912h	c	43.7 ± 2.9
^{200}Tl	26.1h	c	40.6 ± 2.6
^{200}Tl	26.1h	i(m+g)	22.7 ± 1.5
^{199}Tl	7.42h	c	38.5 ± 5.2
$^{198\text{m}}\text{Tl}$	1.87h	i(m1+m2)	17.6 ± 3.6
^{198}Tl	5.30h	c	35.9 ± 5.0
$^{196\text{m}}\text{Tl}$	84.6m	i(m)	34.8 ± 4.4
^{203}Hg	46.612d	c	4.03 ± 0.27
$^{197\text{m}}\text{Hg}$	23.8h	i(m)	10.7 ± 0.7
$^{195\text{m}}\text{Hg}$	41.6h	i(m)	13.6 ± 2.0
$^{193\text{m}}\text{Hg}$	11.8h	i(m)	18.9 ± 2.5
^{192}Hg	4.85h	c	35.2 ± 2.8
$^{198\text{m}}\text{Au}$	54.48h	i(m)	1.01 ± 0.14
^{198}Au	64.684h	i(m+g)	2.11 ± 0.22
^{198}Au	64.684h	i	1.09 ± 0.30
^{196}Au	6.183d	i(m1+m2+g)	4.13 ± 0.35
^{195}Au	186.098d	c	48.7 ± 5.5
^{194}Au	38.020h	i(m1+m2+g)	7.06 ± 0.75
^{192}Au	4.94h	c	46.9 ± 6.6
^{192}Au	4.94h	i(m1+m2+g)	11.6 ± 1.7
^{191}Pt	69.6h	c	40.1 ± 4.4
^{189}Pt	10.87h	c	46.8 ± 4.8
^{188}Pt	10.2d	c	40.5 ± 2.9
^{190}Ir	11.78d	c	0.69 ± 0.06
^{188}Ir	41.5h	c	43.2 ± 3.2
^{188}Ir	41.5h	i(m+g)	2.93 ± 0.69
^{186}Ir	16.64h	c*	20.8 ± 1.9
^{185}Ir	14.4h	c*	34.8 ± 2.3
^{184}Ir	3.09h	c*	39.5 ± 3.0
^{185}Os	93.6d	c	41.8 ± 2.8
$^{183\text{m}}\text{Os}$	9.9h	i(m)	23.2 ± 1.5
^{182}Os	22.1h	c	42.0 ± 2.8

Table 1. Experimental product nuclide yields in 1 GeV proton-irradiated ^{208}Pb (cont.)

Product	T_{1/2}	Type	Yield (mb)
^{183}Re	70.0d	c	41.7 ± 2.9
^{182}Re	12.7h	c	45.2 ± 3.7
^{181}Re	19.9h	c	43.1 ± 5.9
^{179}Re	19.7m	c*	47.8 ± 4.2
^{177}W	2.25h	c	30.1 ± 3.5
^{176}W	2.30h	c	30.8 ± 4.3
^{176}Ta	8.09h	c	34.5 ± 3.6
^{173}Ta	3.14h	c	31.0 ± 3.9
^{172}Ta	36.8m	c*	17.3 ± 2.3
^{175}Hf	70.0d	c	31.3 ± 2.3
^{173}Hf	23.6h	c	28.4 ± 2.6
^{172}Hf	683.017d	c	24.1 ± 1.6
^{171}Hf	12.1h	c	18.2 ± 2.8
^{170}Hf	16.01h	c	22.1 ± 6.8
^{172}Lu	6.7d	c	23.9 ± 1.7
^{172}Lu	6.7d	i(m+g)	0.19 ± 0.05
^{171}Lu	8.24d	c	26.1 ± 1.8
^{170}Lu	48.288h	c	21.7 ± 2.9
^{169}Lu	34.06h	c	18.6 ± 1.2
^{169}Yb	32.026d	c	20.9 ± 1.5
^{166}Yb	56.7h	c	16.1 ± 1.1
^{167}Tm	9.25d	c	19.4 ± 4.0
^{165}Tm	30.06h	c	14.4 ± 1.4
^{160}Er	28.58h	c	8.8 ± 0.6
^{157}Dy	8.14h	c	5.73 ± 0.45
^{155}Dy	9.90h	c*	3.66 ± 0.27
^{155}Tb	5.32d	c	4.16 ± 0.39
^{153}Tb	56.16h	c*	2.52 ± 0.25
^{152}Tb	17.50h	c*	2.10 ± 0.17
^{153}Gd	241.6d	c	2.60 ± 0.23
^{149}Gd	9.28d	c	2.24 ± 0.18
^{146}Gd	48.27d	c	1.26 ± 0.09
^{147}Eu	24.0d	c	0.98 ± 0.31
^{146}Eu	4.59d	c	1.63 ± 0.11
^{146}Eu	4.59d	i	0.37 ± 0.05
^{143}Pm	265.0d	c	1.02 ± 0.13
^{139}Ce	137.64d	c	0.83 ± 0.06
$^{121\text{m}}\text{Te}$	154.0d	i(m)	0.44 ± 0.04
^{121}Te	16.78d	c	1.11 ± 0.11
$^{119\text{m}}\text{Te}$	4.7d	i(m)	0.40 ± 0.04
$^{120\text{m}}\text{Sb}$	5.76d	i(m)	0.54 ± 0.05
$^{114\text{m}}\text{In}$	49.51d	i(m1+m2)	0.95 ± 0.19

Table 1. Experimental product nuclide yields in 1 GeV proton-irradiated ^{208}Pb (cont.)

Product	$T_{1/2}$	Type	Yield (mb)
$^{110\text{m}}\text{Ag}$	249.79d	i(m)	1.12 ± 0.09
$^{106\text{m}}\text{Ag}$	8.28d	i(m)	0.89 ± 0.08
^{105}Ag	41.29d	c	0.65 ± 0.12
^{105}Rh	35.36h	c	4.63 ± 0.54
$^{101\text{m}}\text{Rh}$	4.34d	i(m)	1.29 ± 0.16
^{103}Ru	39.26d	c	3.84 ± 0.26
^{96}Tc	4.28d	i(m+g)	1.20 ± 0.09
^{95}Tc	20.0h	c	1.38 ± 0.13
^{96}Nb	23.35h	i	2.31 ± 0.19
^{95}Nb	34.975d	c	5.41 ± 0.34
^{95}Nb	34.975d	i(m+g)	3.03 ± 0.20
^{95}Zr	64.02d	c	2.34 ± 0.15
^{89}Zr	78.41h	c	2.30 ± 0.16
^{88}Zr	83.4d	c	0.76 ± 0.08
$^{90\text{m}}\text{Y}$	3.19h	i(m)	4.82 ± 0.39
^{88}Y	106.65d	c	4.03 ± 0.27
^{88}Y	106.650d	i(m+g)	3.41 ± 0.25
^{87}Y	79.8h	c*	2.94 ± 0.23
^{85}Sr	64.84d	c	2.76 ± 0.22
^{86}Rb	18.631d	i(m+g)	5.48 ± 0.66
^{83}Rb	86.2d	c	3.46 ± 0.28
$^{82\text{m}}\text{Rb}$	6.472h	i(m)	2.73 ± 0.30
^{82}Br	35.3h	i(m+g)	2.17 ± 0.14
^{75}Se	119.77d	c	1.34 ± 0.09
^{74}As	17.77d	i	1.86 ± 0.18
^{59}Fe	44.503d	c	0.91 ± 0.08
^{65}Zn	244.26d	c	0.79 ± 0.19
^{46}Sc	83.81d	i(m+g)	0.35 ± 0.06

Table 2. Experimental product nuclide yields in 2.6 GeV proton-irradiated $^{\text{nat}}\text{W}$

Product	$T_{1/2}$	Type	Yield (mb)
^{177}W	2.25h	c	13.9 ± 1.9
^{176}W	2.30h	c	9.9 ± 2.9
^{184}Ta	8.7h	c	4.44 ± 0.43
^{183}Ta	5.1d	c	10.5 ± 1.0
^{182}Ta	114.43d	c	12.9 ± 1.3
$^{178\text{m}}\text{Ta}$	2.36h	i(m)	8.1 ± 1.3
^{176}Ta	8.09h	c	29.3 ± 3.3
^{175}Ta	10.5h	c	26.0 ± 2.8
^{174}Ta	63m	c	25.8 ± 2.8
^{181}Hf	42.39	c	1.26 ± 0.12
^{173}Hf	23.6h	c	29.9 ± 2.5
^{171}Hf	12.1h	c	19.6 ± 2.4
^{170}Hf	16.01h	c	19.6 ± 4.0

Table 2. Experimental product nuclide yields in 2.6 GeV proton-irradiated ^{nat}W (cont.)

Product	T _{1/2}	Type	Yield (mb)
¹⁷² Lu	6.7d	i(m+g)	4.32 ± 0.56
¹⁷¹ Lu	8.24d	c	30.1 ± 2.46
¹⁷¹ Lu	8.24d	i(m+g)	10.8 ± 2.0
¹⁷⁰ Lu	48.288h	c	24.8 ± 2.2
¹⁶⁹ Lu	34.06h	c	22.2 ± 1.8
¹⁶⁷ Lu	51.5m	c	23.4 ± 2.4
¹⁶⁷ Yb	17.5m	c	24.9 ± 2.8
¹⁶⁶ Yb	56.7h	c	24.6 ± 2.1
¹⁶⁶ Tm	7.7h	c	27.2 ± 2.3
¹⁶⁶ Tm	7.7h	i	2.36 ± 0.46
¹⁶⁵ Tm	30.06h	c	27.1 ± 2.4
¹⁶³ Tm	1.81h	c	26.3 ± 3.3
¹⁶¹ Tm	33m	c	21.0 ± 2.5
¹⁶¹ Er	3.21h	c	24.3 ± 2.5
¹⁶⁰ Er	28.58h	c	23.9 ± 2.2
¹⁵⁷ Er	25m	c	26.4 ± 5.9
¹⁵⁶ Er	19.5m	c	15.9 ± 2.4
^{160m1} Ho	5.02h	i(m1+m2)	24.9 ± 2.3
¹⁵⁷ Ho	12.6m	c	26.1 ± 6.8
¹⁵⁶ Ho	56m	c	19.6 ± 1.8
¹⁵⁷ Dy	8.14h	c	24.2 ± 2.2
¹⁵⁵ Dy	9.90h	c	22.1 ± 1.9
¹⁵³ Dy	6.4h	c	14.0 ± 1.9
¹⁵² Dy	2.38h	c	15.6 ± 1.3
¹⁵⁵ Tb	5.32d	c	22.7 ± 1.9
¹⁵³ Tb	56.16h	c	18.9 ± 1.7
¹⁵² Tb	17.50h	c	16.2 ± 1.3
¹⁵¹ Tb	17.609h	c	16.7 ± 1.4
¹⁴⁹ Tb	4.118h	c	6.85 ± 0.62
¹⁴⁷ Tb	1.70h	c	2.15 ± 0.34
¹⁵¹ Gd	124.0d	c	19.0 ± 2.2
¹⁴⁹ Gd	9.28d	c	20.4 ± 1.7
¹⁴⁷ Gd	38.1h	c	18.6 ± 1.6
¹⁴⁶ Gd	48.27d	c	19.4 ± 1.6
¹⁴⁵ Gd	23.0m	c	12.9 ± 1.4
¹⁴⁹ Eu	93.1d	c	26.7 ± 3.4
¹⁴⁷ Eu	24.0d	c	22.4 ± 2.0
¹⁴⁶ Eu	4.59d	c	23.0 ± 1.9
¹⁴⁶ Eu	4.59d	i	3.62 ± 0.31
¹⁴⁵ Eu	5.93d	c	17.8 ± 1.6
¹³⁹ Nd	5.5h	c	2.87 ± 0.43
¹³⁹ Ce	137.64d	c	19.8 ± 1.6
¹³⁵ Ce	17.7h	c	17.8 ± 1.5
¹³² Ce	3.51h	c	16.3 ± 2.7

Table 2. Experimental product nuclide yields in 2.6 GeV proton-irradiated ^{nat}W (cont.)

Product	T_{1/2}	Type	Yield (mb)
¹³² La	4.8h	c	14.5 ± 1.6
¹³¹ Ba	11.50d	c	16.2 ± 1.3
¹²⁶ Ba	100m	c	7.9 ± 1.1
¹²⁹ Cs	32.06h	c	18.7 ± 1.6
¹²⁷ Xe	36.4d	c	15.4 ± 1.3
¹²⁵ Xe	16.9h	c	14.2 ± 1.2
¹²³ Xe	2.08h	c	15.6 ± 1.3
¹²² Xe	20.1h	c	11.7 ± 1.0
¹²¹ Te	16.78d	c	10.7 ± 1.1
¹¹⁹ Te	16.03h	c	9.17 ± 0.74
^{119m} Te	4.7d	i(m)	1.97 ± 0.17
¹¹⁷ Te	62m	c	8.81 ± 0.77
^{118m} Sb	5.0h	i(m)	1.08 ± 0.22
¹¹⁵ Sb	32.1m	*	9.85 ± 0.88
¹¹³ Sn	115.09d		7.55 ± 0.67
¹¹¹ In	2.8049d		7.44 ± 0.74
^{110m} In	4.9h	i(m)	3.29 ± 0.29
¹⁰⁹ In	4.2h	c	5.12 ± 0.43
^{106m} Ag	8.28d	i(m)	1.70 ± 0.16
¹⁰⁵ Ag	41.29d	c	5.33 ± 0.69
¹⁰⁰ Pd	87.12h	c	1.24 ± 0.27
¹⁰⁰ Rh	20.8h	c	3.97 ± 0.44
¹⁰⁰ Rh	20.8h	i	2.68 ± 0.28
^{99m} Rh	4.7h	c	2.41 ± 0.28
⁹⁷ Ru	69.6h	c	3.13 ± 0.28
⁹⁶ Tc	4.28d	i(m+g)	1.73 ± 0.20
^{93m} Mo	6.85h	i(m)	1.61 ± 0.13
⁹⁰ Nb	14.6h	c	2.58 ± 0.22
⁸⁹ Zr	78.41h	c	3.46 ± 0.28
⁸⁸ Zr	83.4d	c	2.56 ± 0.27
⁸⁸ Y	106.65d	c	3.49 ± 0.34
⁸⁸ Y	106.65d	i(m+g)	1.56 ± 0.22
⁸⁷ Y	79.8h	c	4.13 ± 0.34
⁸³ Sr	32.41h	c	1.96 ± 0.93
⁸⁴ Rb	32.77d	i(m+g)	1.31 ± 0.14
⁸³ Rb	86.2d	c	3.34 ± 0.58
^{82m} Rb	6.472h	i(m)	1.89 ± 0.17
⁷⁷ Kr	74.4m	c	1.71 ± 0.18
⁷⁵ Se	119.77d	c	2.38 ± 0.22
⁷³ Se	7.15h	c	1.03 ± 0.11
⁷⁴ As	17.77d	c	1.38 ± 0.16
^{69m} Zn	13.76h	i(m)	0.42 ± 0.038
⁵⁴ Mn	312.12d	i	2.51 ± 0.42
⁵¹ Cr	27.704d	c	4.5 ± 1.4

Table 2. Experimental product nuclide yields in 2.6 GeV proton-irradiated ^{nat}W (cont.)

Product	T _{1/2}	Type	Yield (mb)
⁴⁸ V	15.973d	c	0.557 ± 0.062
⁴⁸ Sc	43.67h	i	0.668 ± 0.091
⁴³ K	22.3h	c	0.681 ± 0.084
²⁸ Mg	20.91h	c	0.91 ± 0.089
²⁴ Na	14.959h	c	4.09 ± 0.34
⁷ Be	53.29d	i	8.7 ± 1.0

Comparison with experimental data obtained elsewhere

Table 3 and Figure 9 compare some of the present results with experimental data of other laboratories published in [6].

Table 3. The yields (mb) of some products in the 1 GeV proton-irradiated ²⁰⁸Pb inferred from measurements at different laboratories; the ZSR and GSI data are taken from [6], the ITEP data are our present results

Product nuclide	ZSR Hannover	ITEP	GSI Darmstadt
²⁰⁰ Tl	22.3 ± 6.1	22.7 ± 1.5	17.0 ± 0.4(1.6)
¹⁹⁶ Au	3.88 ± 0.47	4.13 ± 0.35	4.0 ± 0.1(0.4)
¹⁹⁴ Au	6.85 ± 0.92	7.06 ± 0.75	6.3 ± 0.2(0.6)
¹⁴⁸ Eu	0.104 ± 0.04	–	0.075 ± 0.005(0.010)
¹⁴⁴ Pm	0.068 ± 0.013	–	0.036 ± 0.003(0.006)

Simulation of experimental results

Simulation techniques are of essential importance when forming the set of nuclear constants to be used in designing the ADS facilities, because they are universal and save much time and labour. At the same time, the present-day accuracy and reliability of the simulated results are inferior to experiment. Besides, the simulation codes are of different abilities to work when used to study the reactions that are of practical importance.

Considering the above, the present work is primarily aimed at verifying the simulation codes used most extensively for the above purpose with a view to not only estimating their ability to work when applied to the issues discussed here, but also opening up ways to improve them.

The following eight simulation codes were examined to meet these requirements:

- The CEM95 cascade/exciton code [7].
- The CASCADE cascade/evaporation/fission/transport code [8].
- The INUCL cascade/pre-equilibrium/evaporation/fission code [9].
- The LAHET (ISABEL and Bertini options) cascade/evaporation/fission code [10].

- The YIELDX semi-phenomenological code [11].
- The CASCADE/INPE cascade/pre-equilibrium/evaporation/fission/transport code [12].
- The CEM2k cascade/exciton code [16], a last modification of the CEM95 code.

Contrary to the simulation results, the experimental data include not only the independent, but also (and mainly) cumulative and the supra cumulative yields of residual product nuclei. To obtain a correct comparison between the experimental and simulation results, theoretical cumulative yields must be calculated on the basis of the simulated independent yields.

Since any branched isobaric chain can be presented to be a superposition of a few linear chains, the simulated cumulative and supra cumulative yields of a n-th nuclide can be calculated as:

$$\sigma_n^{cum} = \sigma_n^{ind} + \sum_{i=1}^{n-1} \sigma_i^{ind} \prod_{j=i}^{n-1} v_j \quad (7)$$

$$\sigma_n^{cum*} = \sigma_n^{ind} + \frac{\lambda_{n-1}}{\lambda_{n-1} - \lambda_n} v_{n-1} \times \left[\sigma_{n-1}^{ind} + \sum_{i=1}^{n-2} \left(\sigma_i^{ind} \prod_{j=i}^{n-2} v_j \right) \right] \quad (8)$$

The branching ratios of the decay chains were retrieved from [13]. To obtain a correct comparison between results by different codes, the calculations were re-normalised to unified cross-sections for proton-nucleus inelastic interactions from [14].

If an experiment/simulation difference of not above 30% ($0.77 < \sigma_{calc}/\sigma_{exp} < 1.3$) is taken to be the coincidence criterion [15], the simulation accuracy can be presented to be the ratio of the number of such coincidences to the number of the comparison events. The 30% level meets the accuracy requirements of the cross-sections for nuclide production to be used in designing the ADS plants, according to [15]. The mean simulated-to-experimental data ratio can be used as another coincidence criterion:

$$\langle F \rangle = 10 \sqrt{\left\langle \log(\sigma_{cal,i}/\sigma_{exp,i})^2 \right\rangle} \quad (9)$$

with its standard deviation:

$$S(\langle F \rangle) = \left\langle \left(\log(\sigma_{cal,i}/\sigma_{exp,i}) - \log(\langle F \rangle) \right)^2 \right\rangle \quad (10)$$

where $\langle \rangle$ designates averaging over all N_s number of the experimental and simulated results used in a comparison.

The mean ratio $\langle F \rangle$ together with its standard deviation $S(\langle F \rangle)$ defines the interval $[\langle F \rangle : S(\langle F \rangle), \langle F \rangle \times S(\langle F \rangle)]$ that covers about 2/3 of the simulation-to-experiment ratios.

The two criteria are considered sufficient to derive conclusions about the predictive power of a given code. The default options were committed to practical usage of the simulation codes.

Comparison of data with simulation results

The results obtained with the above-mentioned codes are presented in:

- Figures 5 and 6, which show results of a detailed comparison between the simulated and experimental radioactive product yields.
- Figures 7 and 8, which show the simulated mass distributions of reaction products together with the measured cumulative (and supra cumulative) yields of the products that are at an immediate proximity to the stable isobar of a given mass (the sum of such yields from either sides in case both left and right-hand branches of the chain are present). Obviously, the displayed simulation results do not contradict the experimental data if calculated values run above the experimental data and follow a general trend of the latter. This is because the direct γ -spectroscopy method used here identifies only radioactive products, that, as a rule, represents a significant fraction of the total mass yield, but, should a stable isobar of the given mass be produced, the γ -spectroscopy data are never equal to the total mass yield.
- In Figure 9, that shows the experimental and simulated independent yields of reaction products in the form of isotopic mass distributions for several elements.

Table 4 presents the statistics of our comparison between the experimental and simulated reaction product yields in the thin ^{208}Pb and $^{\text{nat}}\text{W}$ samples irradiated by 1.0 GeV and 2.6 GeV protons, respectively. Namely, it shows the total number of measured yields, N_T ; the number of the measured yields selected to compare with calculations, N_G ; the number of the product nuclei whose yields were simulated by a particular code, N_S ; the number of the comparison events when the simulated data differ from the experimental results by not above 30%, $N_{C_{1.3}}$; the number of the comparison events when the simulated data differ from the experimental results by not more than a factor of 2.0, $N_{C_{2.0}}$.

Table 4. Comparison statistics for ^{208}Pb and $^{\text{nat}}\text{W}$

Code	Pb, $E_p = 1.0$ GeV $N_T = 116, N_G = 95$			W, $E_p = 2.6$ GeV $N_T = 107, N_G = 93$		
	$N_{C_{1.3}}/N_{C_{2.0}}/N_S$	$\langle F \rangle$	$S(\langle F \rangle)$	$N_{C_{1.3}}/N_{C_{2.0}}/N_S$	$\langle F \rangle$	$S(\langle F \rangle)$
LAHET	41/65/90	2.06	1.78	13/51/90	2.52	1.83
CEM95	–	–	–	28/66/81	2.51	2.23
CEM2k	38/58/66	1.62	1.44	17/60/84	2.24	1.73
CASCADE	33/60/86	2.28	1.90	48/71/91	2.24	2.04
CASCADE/INPE	36/66/84	1.84	1.56	–	–	–
INUCL	29/54/90	2.87	2.16	38/58/86	3.78	3.23
YIELDX	30/54/90	2.87	2.24	25/60/93	2.04	1.58

Since about 30% of all measured secondary nuclei are not spallation reaction products, an important criterion of the codes is their ability to simulate the high-energy fission and fragmentation processes. Among the codes used here, LAHET, CASCADE, INUCL, CASCADE/INPE and YIELDX simulate both spallation and fission. The CEM95 and CEM2k codes simulate spallation only, which is explicitly reflected in a smaller number of the products simulated (the parameter N_S in Table 4 and in the shapes of the simulation curves in Figures 5-8).

The following conclusions follow from our analysis of the experiment-to-simulation comparison results presented in Table 4 and in Figures 5-9:

- 1) Generally, all codes can quite adequately simulate the weak spallation reactions (the $A \geq 180$ products for ^{208}Pb and the $A \geq 150$ products for $^{\text{nat}}\text{W}$), with the simulation results differing from experimental data within a factor of 2.
- 2) In the deep spallation region ($150 < A < 180$ for ^{208}Pb and $110 < A < 150$ for $^{\text{nat}}\text{W}$), the simulation codes are of very different predictive powers, namely:
 - The LAHET (when not shown explicitly as “Bertini”, all results by LAHET are of the ISABEL option), CEM2k, CASCADE/INPE and YIELDX predictions are actually the same as the experimental data.
 - The CASCADE code simulates the $A > 160$ product yields adequately. Below $A = 160$, however, the simulated data get underestimated progressively (up to a factor of 5) compared with experiment (see Figure 7).
 - The INUCL code underestimates the yields of all the products by a factor of 2-10 in all the above mass ranges (see Figures 7 and 8).
- 3) In the mass range characteristic of the fission products ($50 < A < 150$ for ^{208}Pb and $30 < A < 110$ for $^{\text{nat}}\text{W}$), the INUCL code predictions are in the best agreement with experiment when describing the yields from ^{208}Pb . As a rule, the INUCL-simulated results differ from the data by not above a factor of 1.5. In the case of $^{\text{nat}}\text{W}$, however, the prediction quality deteriorates substantially. The LAHET-simulated yields are underestimated by a factor of 1.5-10.0 for Pb (Figures 5 and 7) in the whole fission product mass region and for $A < 60$ in the case of W (Figures 6 and 8) but are overestimated several times for fission fragments with $A > 60$ from W. The YIELDX-simulated yields are either under or overestimated by a factor of up to 30 without showing any physical regularities. The CASCADE/INPE-simulated yields of the $130 < A < 150$ reaction products are strongly underestimated (up to 1-2 orders of magnitude), while the simulated $40 < A < 130$ product yields agree with the data within a factor of 2, as a rule. Generally, all the codes exhibit the feature noted above for INUCL, namely, the yield prediction quality in the case of $^{\text{nat}}\text{W}$ is much worse compared with ^{208}Pb , probably, because the fission cross-sections of high-excited compound nuclei with very low fissility are difficult to calculate.
- 4) The last version of the improved cascade/exciton model code, CEM2k [16], shows the best agreement with the 1 GeV Pb-data in the spallation region, especially for the isotopic mass distributions (Figure 9). At 2.6 GeV (W-target), it overestimates the expected experimental fission cross-section of about 41 mb [17] by a factor of 6. This overestimation of the fission cross-section causes an underestimation of the yield of nuclei which are most likely to fission (with a very low fissility) at the evaporation stage of a reaction, after the cascade and pre-equilibrium stages, i.e. for $147 < A < 175$ (see Figure 6). Similar disagreement with the 2.6 GeV W-data one can see as well for LAHET and CEM95, that is also related with an overestimation of the fission cross-section at 2.6 GeV (see Figures 6 and 8). The code CEM2k is still under development, its problem with the overestimation of fission cross-sections at energies above 1 GeV has yet to be solved, and it has to be complemented with a model of fission fragment production, to be able to describe as well fission products.

Figure 5. Product comparison between the experimental (closed symbols) and simulated (open symbols) yields of radioactive reaction products from ^{208}Pb irradiated with 1 GeV protons. Cumulative yields are labelled with a “c” when the respective independent yields are also shown.

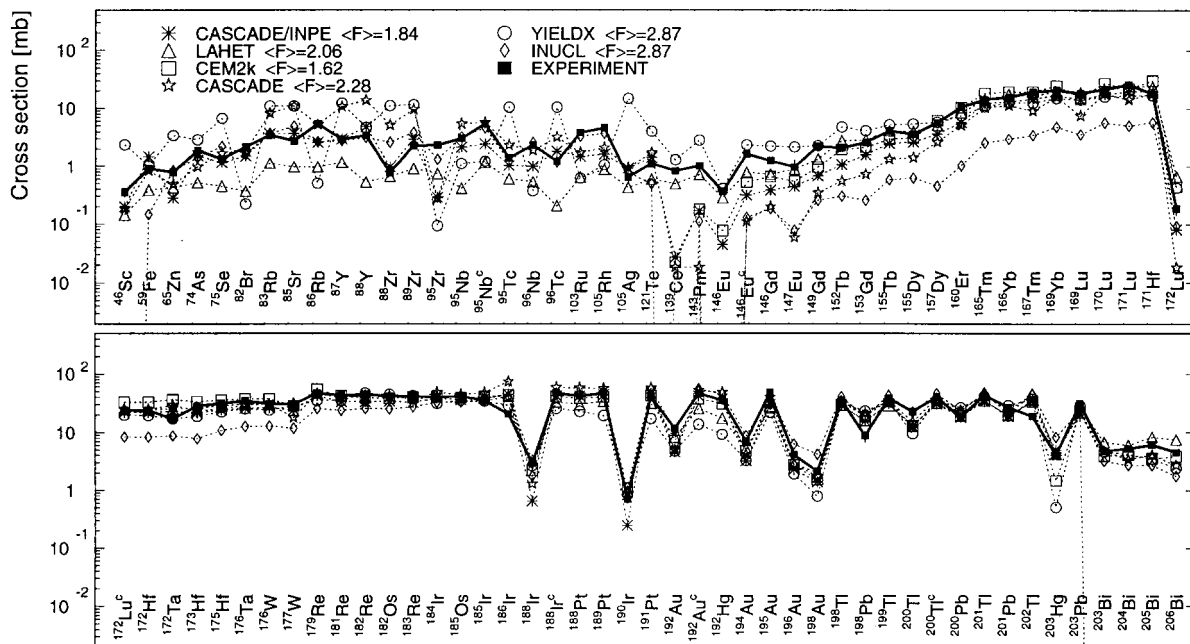


Figure 6. Product comparison between the experimental (closed symbols) and simulated (open symbols) yields of radioactive reaction products from ^{nat}W irradiated with 2.6 GeV protons. Cumulative yields are labelled with a “c” when the respective independent yields are also shown.

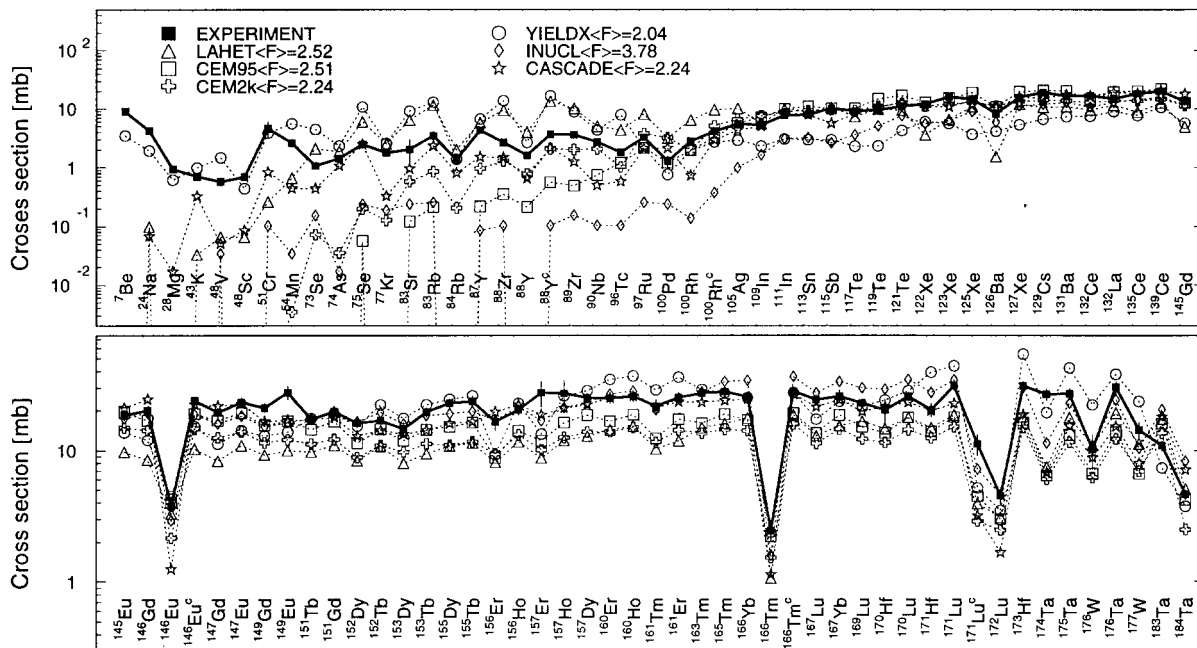


Figure 7. Measured and calculated by the codes mass product yields from ^{208}Pb irradiated with 1.0 GeV protons. For comparison, the GSI data from [6] are shown as well.

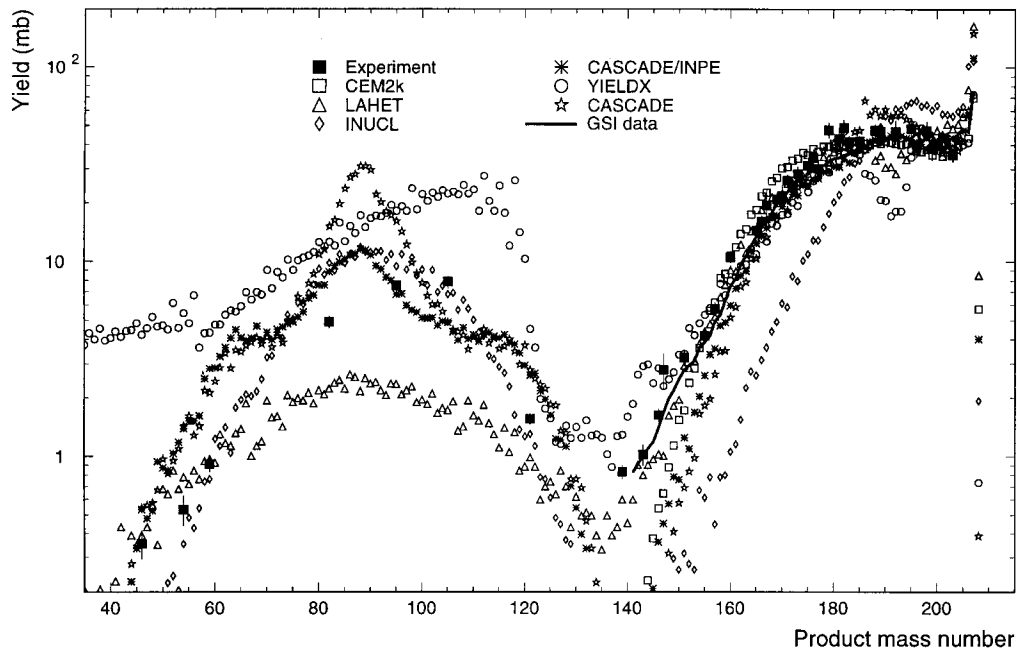


Figure 8. Measured and calculated via the codes mass product yields from ^{nat}W irradiated with 2.6 GeV protons

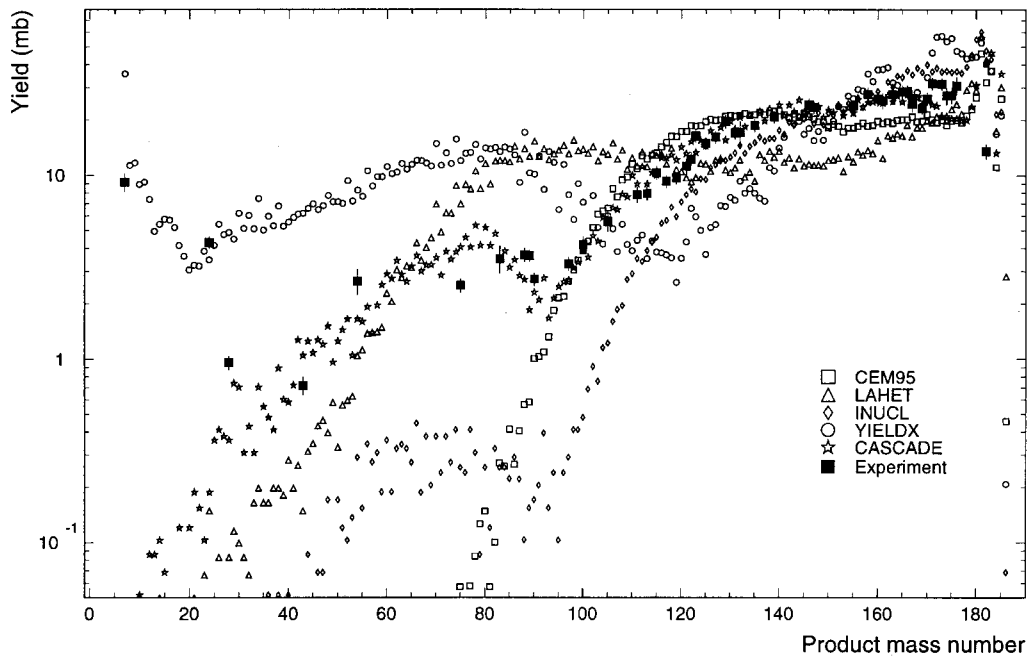
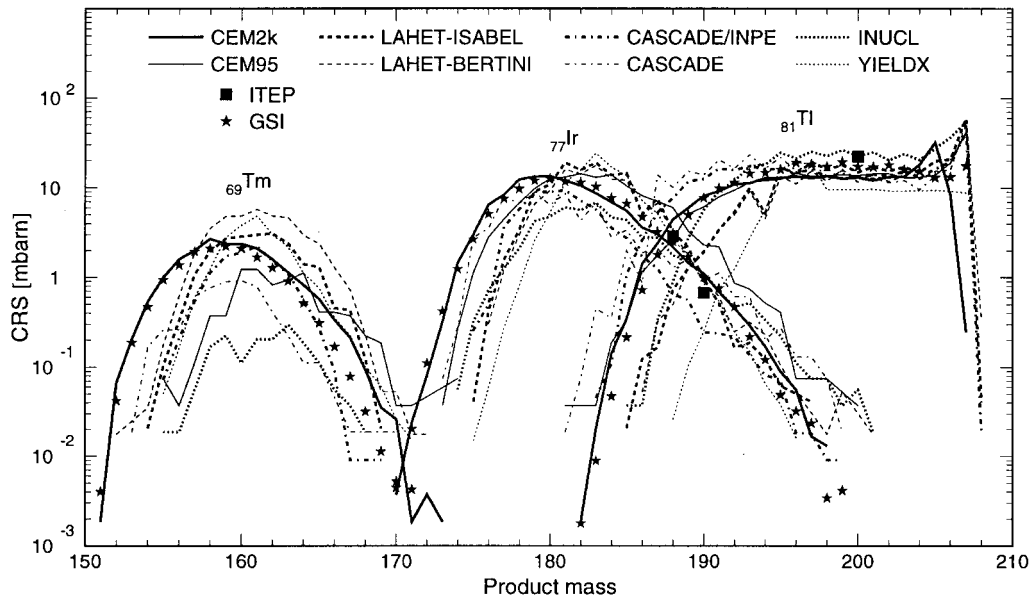


Figure 9. Isotopic mass distributions of the reaction products in ^{208}Pb . The rich, inverse-kinematics, GSI data from [6] are shown by filled stars.



Conclusion

The trends shown by the advances in the nuclear transmutation of radioactive wastes and spallation neutron source (SNS) facilities permit us to expect that the accumulation and analysis study of nuclear data for ADS facilities will have the same rise of academic interest and practical commitments as in the nuclear reactor data during the last five decades. Therefore, the experimental data on the yields of the proton-induced reaction products as applied to the ADS and SNS main targets and structure materials are urgent to accumulate. It should be emphasised that the charge distributions in the isobaric decay chains are important to study as well. The data thus obtained would make it possible, first, to raise the information content of the comparisons between the experimental and simulated results and, second, to lift the uncertainties in experimental determination of the cumulative yields by establishing unambiguous relations between σ^{cum} and σ^{cum*} for many of the reaction product masses.

Regarding the codes benchmarked here, one may conclude that none of them agree well with the data in the whole mass region of product nuclides and all should be improved further. The new CEM2k code developed recently at Los Alamos [16] agrees with our data in the spallation region the best of the codes tested. But CEM2k has yet to be completed by a model of fission fragmentation, to become applicable in the fission-product region as well.

Acknowledgements

The authors are grateful to Professor Vladimir Artisyuk (Tokyo Institute of Technology) for consulting and discussion our results on simulation-to-experimental comparisons.

The work was carried out under the ISTC Project #839 supported by the European Community, Japan (JAERI), Norway and, partially, by the US Department of Energy.

REFERENCES

- [1] Gregory J. Van Tuyle, "ATW Technology Development & Demonstration Plan", LANL Report LA-UR-99-1061, Los Alamos (1999); "ATW Technology & Scenarios", LANL Report LA-UR-99-771, Los Alamos (1999).
- [2] T. Mukaiyama, "OMEGA Program in Japan and ADS Development at JAERI", Proc. 3rd Int. Conf. on Accelerator-driven Transmutation Technologies and Applications (ADTT'99), Praha, 7-11 June 1999, paper Mo-I-5.
- [3] M. Salvatores, "Strategies for the Back-end of the Fuel Cycle: A Scientific Point of View", Proc. 3rd Int. Conf. on Accelerator-driven Transmutation Technologies and Applications (ADTT'99), Praha, 7-11 June 1999, paper Mo-I-4.
- [4] Yu.E. Titarenko, O.V. Shvedov, M.M. Igumnov, S.G. Mashnik, E.I. Karpikhin, V.D. Kazaritsky, V.F. Batyaev, A.B. Koldobsky, V.M. Zhivun, A.N. Sosnin, R.E. Prael, M.B. Chadwick, T.A. Gabriel and M. Blann, "Experimental and Computer Simulation Study of the Radionuclides Produced in Thin ²⁰⁹Bi Targets by 130 MeV and 1.50 GeV Proton-induced Reactions", *Nucl. Instr. Meth.*, A 414, 73 (1998).
- [5] M. Gloris, R. Michel, U. Herpers, F. Sudbrok, and D. Filges, "Production of Residual Nuclei from Irradiation of Thin Pb-targets with Protons up to 1.6 GeV", *Nucl. Instr. Meth.*, B 113, 429 (1996); R. Michel, M. Gloris, H.-J. Lange, I. Leya, M. Lüpke, U. Herpers, B. Dittrich-Hannen, R. Rösel, Th. Schiekkel, D. Filges, P. Dragovitsch, M. Suter, H.-J. Hofmann, W. Wölfli, P.W. Kubik, H. Baur and R. Wieler, "Nuclide Production by Proton-induced Reactions on Elements ($6 \leq Z \leq 29$) in the Energy Range from 800 to 2 600 MeV", *Nucl. Instr. Meth.*, B 103, 183 (1995).
- [6] W. Wlazlo, T. Enqvist, P. Armbruster, P. Armbruster, J. Benlliure, M. Bernas, A. Boudard, S. Czajkowski, R. Legrain, S. Leray, B. Mustapha, M. Pravikoff, F. Rejmund, K.-H. Schmidt, C. Stéphan, J. Taieb, L. Tassan-Got and C. Volant, "Cross-sections of Spallation Residues Produced in 1A GeV ²⁰⁸Pb on Proton Reactions", *Phys. Rev. Lett.*, 84, 5736 (2000).
- [7] K.K. Gudima, S.G. Mashnik and V.D. Toneev, "Cascade-exciton Model of Nuclear Reactions", *Nucl. Phys.*, A 401, 329 (1983); S.G. Mashnik, "User Manual for the Code CEM95", JINR, Dubna, 1995; OECD Nuclear Energy Agency Data Bank, Paris, France (1995), to be found at <http://www.nea.fr/abs/html/iaea1247.html>; RSIC-PSR-357, Oak Ridge, TN (1995).
- [8] V.S. Barashenkov, Le Van Ngok, L.G. Levchuk, Zh.Zh. Musul'manbekov, A.N. Sosnin, V.D. Toneev and S.Yu. Shmakov, "Cascade Program Complex for Monte Carlo Simulation of Nuclear Processes Initiated by High-energy Particles and Nuclei in Gaseous and Condensed Matter", JINR Report R2-85-173, Dubna (1985); V.S. Barashenkov, F.G. Zheregi and Zh.Zh. Musul'manbekov, "The Cascade Mechanism of Interactions of High-energy Nuclei", *Yad. Fiz.*, 39 (1984) 1133; V.S. Barashenkov, B.F. Kostenko and A.M. Zadorogny, "Time-dependent Intranuclear Cascade Model", *Nucl. Phys.*, A 338, 413 (1980).

- [9] G.A. Lobov, N.V. Stepanov, A.A. Sibirtsev and Yu.V. Trebukhovskii, “Statistical Simulation of Interaction of Hadrons and Light Nuclei with Nuclei. Intranuclear Cascade Model”, Preprint ITEP-91, Moscow (1983); A.A. Sibirtsev, N.V. Stepanov and Yu.V. Trebukhovskii, “Interaction of Particles with Nuclei. Evaporation Model”, Preprint ITEP-129, Moscow (1985); N.V. Stepanov, “Statistical Simulation of High-excited Nuclei Fission. I. Model Formulation”, Preprint ITEP-81, Moscow (1987); N.V. Stepanov, “Statistical Simulation of High-excited Nuclei Fission. II. Calculation and Comparison with Experiment”, (in Russian) Preprint ITEP-55-88, Moscow (1988).
- [10] R.E. Prael and H. Lichtenstein, “User Guide to LCS: The LAHET Code System”, LANL Report LA-UR-89-3014, Los Alamos (1989); also: <http://www-xdiv.lanl.gov/XTM/lcs/lahet-doc.html>.
- [11] C.H. Tsao, private communication; R. Silberberg, C.H. Tsao and A.F. Barghouty, “Updated Partial Cross-sections of Proton-nucleus reactions”, *Astrophys. J.*, 501, 911 (1998); R. Silberberg and C.H. Tsao, “Partial Cross-sections in High-energy Nuclear Reactions, and Astrophysical Applications. I. Targets With $Z \leq 28$ ”, *Astrophys. J., Suppl.*, No. 220, 25, 315 (1973); “Partial Cross-sections in High-energy Nuclear Reactions, and Astrophysical Applications. II. Targets Heavier Than Nickel”, *ibid.*, p. 335.
- [12] V.S. Barashenkov, A.Yu. Konobeev, Yu.A. Korovin and V.N. Sosnin, “CASCADE/INPE Code System”, *Atomnaya Énergiya*, 87, 283 (1999).
- [13] N.G. Gusev and P.P. Dmitriev, *Radioactive Chains: Handbook*, Energoatomizdat, Moscow, 1988.
- [14] J.R. Letaw, R. Silberberg and C.H. Tsao, “Proton-nucleus Total Inelastic Cross-sections: An Empirical Formula for $E > 10$ MeV”, *Astrophys. J., Suppl.*, 51, 271 (1983).
- [15] A. Koning, “Nuclear Data Evaluation for Accelerator-driven Systems”, Proc. 2nd Int. Conf. on Accelerator-driven Transmutation Technologies and Applications, 3-7 June 1996, Kalmar, Sweden, pp. 438-447.
- [16] The code CEM2k is briefly surveyed in S.G. Mashnik, L.S. Waters and T.A. Gabriel, “Models and Codes for Intermediate Energy Nuclear Reactions”, Proc. 5th Int. Workshop on Simulating Accelerator Radiation Environments (SARE5), 17-18 July 2000, OECD Headquarters, Paris, France, and will be described by S.G. Mashnik and A.J. Sierk in a future paper.
- [17] A.V. Prokofiev, “Compilation and Systematics of Proton-induced Fission Cross-section Data”, *Nucl. Instr. Meth., A*, submitted in December 1998, to be published in September 2000.

SESSION II

Electron Accelerator and Photon Sources

Chairs: T. Nakamura, N. Pauwels

Synchrotron Radiation Facilities

THE LINAC COHERENT LIGHT SOURCE

N.E. Ipe, S. Mao, A. Fassò, J. Arthur, A. Toor*, R. Tatchyn D. Walz and W. Kroutil

Stanford Linear Accelerator Centre, Stanford, CA

*Lawrence Livermore National Laboratory, Livermore, CA

Abstract

The Linac Coherent Light Source is a self-amplified spontaneous emission based free electron laser to be built at the Stanford Linear Accelerator Centre by a multi-laboratory collaboration. This facility will provide ultra-short pulses of coherent X-ray radiation with the fundamental harmonic energy tuneable over the energy range of 0.82 to 8.2 keV. In addition to the coherent X-ray radiation, which will have an extremely high peak and average brightness, a continuous spectrum of spontaneous synchrotron radiation (SR) of high brightness will also be produced. The characteristics of the LCLS and its associated radiological issues are discussed.

Introduction

A multi-laboratory collaboration comprised of the Stanford Linear Accelerator Centre (SLAC), Argonne National Laboratory (ANL), Brookhaven National Laboratory (BNL), Los Alamos National Laboratory (LANL), Livermore National Laboratory (LLNL) and the University of California at Los Angeles (UCLA) proposes to build a self-amplified spontaneous emission based free electron laser (FEL) called the Linac Coherent Light Source (LCLS) at SLAC [1]. This facility will provide ultra-short pulses of coherent X-ray radiation with the fundamental harmonic energy tuneable over the energy range of 0.82 to 8.2 keV. The coherent X-ray radiation will have an extremely high peak and average brightness. In addition, a continuous spectrum of spontaneous synchrotron radiation (SR) of high brightness extending to above 1 MeV with decreasing intensity will also be produced. The radiological issues associated with the LCLS include radiation effects peculiar to the high peak power density of the FEL, general radiation safety concerns encountered at both electron linear accelerator and SR facilities and radiation background for detectors.

Self-amplified spontaneous emission (SASE)

Relativistic electrons circulating in a storage ring emit synchrotron radiation when they are deflected in the magnetic fields of bending magnets or special structures called insertion devices (IDs). An ID (wiggler or undulator), usually located in the straight sections of the storage rings, consists of a series of short magnets with alternating magnetic fields, which cause the particles to oscillate as they pass through the device. Since the particles are forced to change direction many times in a short distance the brightness of the SR is greatly enhanced. The spectrum from a bending magnet is continuous. The spectrum from a wiggler is much brighter because of the linear superposition from each electron oscillation. The beam emanating from an undulator has a much smaller angular spread and is therefore even brighter. Owing to interference effects photons are concentrated according to their energies at specific angles from the axis of the beam. The spectrum is enhanced at certain energies. An electron traversing through an undulator emits electromagnetic (EM) radiation at the wavelength λ [1], where: $\lambda = \lambda_u(1 + K^2/2)/2\gamma^2$, λ_u = undulator period, K = undulator parameter, $\gamma = E/mc^2$, E = beam energy, and mc^2 = rest mass energy.

For the brightest SR storage ring, the electron beam emittance is large compared to hard X-ray wavelengths. At longer wavelengths the electron emittance can match the photon emittance for an FEL. There are many existing IR FELs in existence, using storage rings. The electron beam density in phase space is low, i.e. the electrons are separated by a distance greater than the fundamental undulator emission wavelength, λ . The transverse electric field of the spontaneous radiation produced by the magnet or insertion device is not strong enough to significantly effect the electron beam path or density in phase space [2]. Each electron radiates independently, and not coherently with the others. The intensity of the spontaneous SR radiation is proportional to the number of electrons.

For an FEL to work the electron beam density in phase space must be very high. There must also be a strong electromagnetic field bathing the electron beam. The interaction of the field and the bright electron beam leads to amplification of the field. One way to generate the initial strong EM field is through spontaneous radiation from a very long undulator. This process is known as self-amplified spontaneous emission (SASE). The periodic magnetic field of the undulator causes the electron beam to follow an oscillatory path thus producing spontaneous SR. The transverse electric field of the spontaneous radiation is strong enough to slightly deflect the oscillatory motion of the electrons. This deflection leads to longitudinal bunching of the electrons when there is proper phase matching (a condition that is satisfied at the odd harmonics of undulator fundamental emission frequency). The bunched electrons then tend to produce SR, which is coherently phased with the electromagnetic

field. The field in turn produces more bunching which results in a stronger field, which in turn leads to more bunching. The process continues and saturates when enough energy is removed from the electron beam to cause it to lose phase matching with the electromagnetic field. The micro bunching of the electrons causes them to radiate collectively, resulting in the onset and amplification of coherent radiation. The intensity of the FEL radiation is proportional to the square of the number of electrons. Thus, SASE occurs when the spontaneous radiated field becomes strong enough to induce bunching and gain saturation in a single pass through the undulator.

The Linac Coherent Light Source

Figure 1 shows a layout of the proposed LCLS facility [3]. A new injector consisting of a gun and a short linac will inject electrons into the last one-third section of the existing SLAC two-mile long linear electron accelerator. The electron beam energy is tuneable from 4.53 to 14.35 GeV. After passing through two stages of magnetic bunch compression, the electron beam has peak energy of 14.35 GeV (maximum), a peak current of 3 400 A and a normalised emittance of 1.5 mm-mrad at the exit of the linac. The beam is transferred into a 121 m long undulator, housed in the final focus test beam (FFTB) tunnel by means of a transfer line. The electron beam is then deflected into a beam dump while the photon beam produced in the undulator enters the experimental area. Table 1 lists the LCLS parameters.

Figure 1. A schematic of the LCLS

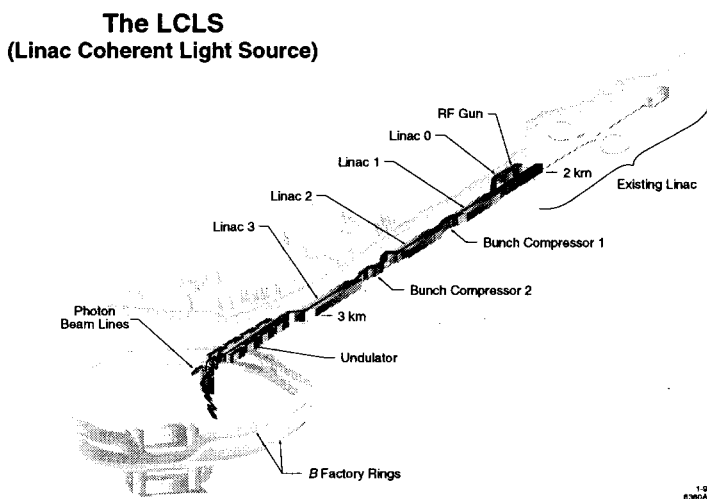


Table 1. LCLS parameters

Electron energy	14.35 GeV
Normalised emittance	1.5π mm-mrad
Peak current	3 400 A
Repetition rate	120 Hz
Pulse width	233 fs (FWHM)
Undulator length	121 m
Undulator field	1.32 Tesla
Undulator parameter, K	3.7
No. of undulator periods	3 328

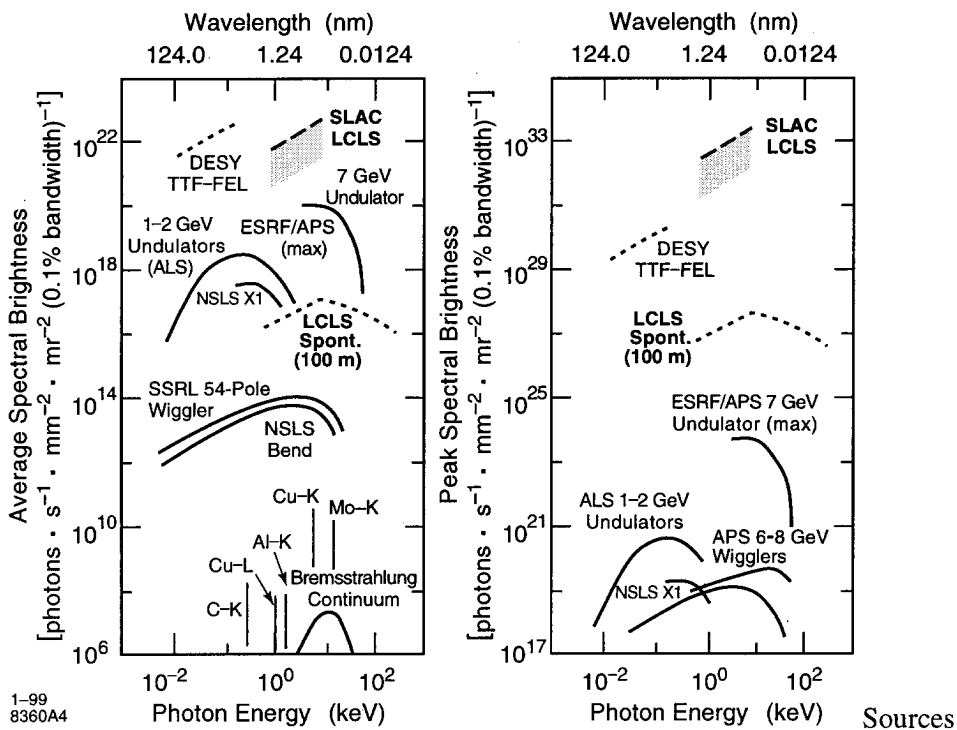
Table 2 shows the FEL and spontaneous radiation parameters for electron energies of 4.53 and 14.35 GeV. With the undulator design that is being contemplated for the LCLS, the first harmonic of the FEL radiation will be linearly polarised.

Table 2. FEL and spontaneous radiation parameters for electron energies of 4.53 and 14.35 GeV

Radiation type	FEL		Spontaneous SR	
	4.53	14.35	4.53	14.35
Electron energy (GeV)	4.53	14.35	4.53	14.35
Fundamental energy (keV)	0.82	8.2	0.82	8.2
Peak power/pulse (GW)	11	9	8.1	81
Average power (W)	0.36	0.31	0.27	2.7
Transverse beam size – 1 st harmonic (μm)	37	31	52	33
Divergence – 1 st harmonic (μrad)	3.2	0.38	6.2	2.0
Peak brightness (γ/s/mm ² /mr ² /0.1% bandwidth)	1.2×10^{32}	12×10^{32}	0.1×10^{28}	1×10^{28}
Average brightness (γ/s/mm ² /mr ² /0.1% bandwidth)	0.42×10^{22}	4.2×10^{22}	0.1×10^{17}	1×10^{17}

Figure 2 shows the average and peak brightness for various X-ray sources, storage rings and FELs. The top curves apply to FELs that are either proposed or under construction, and represent calculated values. The shading around the LCLS curve indicates an estimated range of uncertainty, allowing for possible errors in electron optics. In general the middle curves apply to existing SR sources, and are also calculated values. One curve in the middle shows the expected peak brightness of the LCLS spontaneous SR. The peak brightness of the LCLS is about 10 orders of magnitude greater than currently achieved in third-generation SR sources. The curves at the bottom show the brightness for conventional X-ray sources.

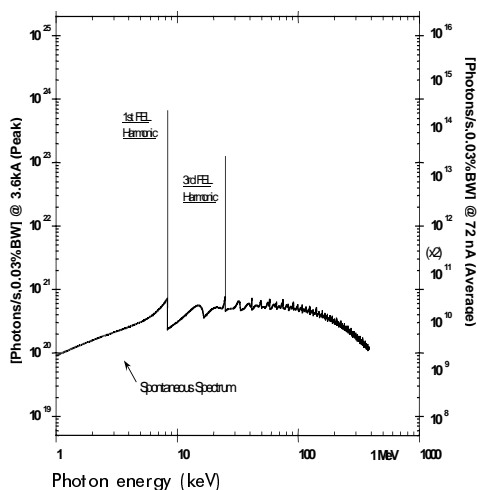
Figure 2. Average and peak brightness as a function of photon energy for various sources



1-99
8360A4

Figure 3 shows the calculated spectrum for the LCLS. The FEL fundamental wavelength is 1.5 Å corresponding to photon energy of 8.2 keV. FEL amplification is also possible at the third harmonic wavelength as shown in the figure, however the gain is much less than the fundamental.

Figure 3. Calculated spectrum for the LCLS



Radiological considerations

Radiological considerations include radiation effects, general radiation safety and detector background.

Radiation effects

The peak coherent power for the LCLS is 9 GW with average powers of the order of 1 W. The pulse length is approximately 230 fs while the peak power of the spontaneous radiation is 81 GW. The high brightness and peak power density of both the laser and the spontaneous radiation will provide unusual challenges in the design of optics, safety systems and beam line components. Power damage can be mitigated by the use of absorption cells, small incidence angles and long beam lines. Calculations indicate that the dose in eV/atom along the beam line for the FEL's fundamental harmonic at start-up wavelength (15 Å or 0.82 keV) is so high that no solid matter will survive undamaged at normal incidence.

Tests performed at LLNL with a circularly polarised laser (0.5 J/cm², 150 fs, 1 μm) incident on stainless steel, indicate that above a threshold fluence the mechanism of damage is unexpected and unexplainable. One of the initial tasks of the LCLS experimental programme will be to carefully study the physics of the interaction between very high peak power X-ray pulses and matter. A method for continuously varying the pulse power will be important for these studies. Sophisticated absorption cells have been proposed (and patented by LLNL) that will reduce the power density/heat load on beam line optics and safety system devices such as beam stops and shutters. In addition to interlocked absorption cells, the safety systems will also require burn-through monitors (BTMs) that are described in the following section. Separate absorption cells have been designed for the FEL and the spontaneous SR. The absorption cells will be filled with a pressurised gas such as xenon. Calculations have been performed with the Monte Carlo code FLUKA to study the radial and longitudinal dose distribution in

the absorption cell. The technical difficulties associated with multiple scattering models in a high-Z, high pressure gas can be avoided with the use of single scattering. Preliminary results indicate that the walls of the absorption cell do not require cooling. The photon beam dump will also be equipped with an absorption cell. The beam dump will be comprised of materials with increasing Z, since the damage increases with increasing Z.

In order to eliminate spontaneous synchrotron radiation from the useful laser beam, a series of collimators will be inserted into the photon beam lines. These collimators will be operated at grazing angle incidence and coated with thin layers of material in order to mitigate the heat load from the extreme power densities. Energy deposition in these thin layers needs to be determined. FLUKA is currently being used to determine energy deposition profile from photo-electrons for grazing incidence in order to study material response, heating of mirrors downstream of the undulator and photo-electrons that escape into vacuum and re-enter the target due to electrostatic charge build-up on target. The implementation of reflection and refraction properties of low-energy X-rays in codes such as FLUKA used for this purpose will be very useful.

The narrow vacuum chamber (outer diameter ~0.25 inch) of the undulator will attenuate the low-energy spontaneous synchrotron radiation, but radiation damage to the undulator (made out of rare earth magnetic material – NdFeB) from the remaining synchrotron radiation and electron beam losses must be considered. No field degradation has been observed in remnant field for up to 290 rads of 60 Co gamma rays [4]. However, field degradation has been observed for 17 MeV electron fluences of about $8.75 \times 10^{15} \text{ e}^-/\text{cm}^2$ with the loss depending on magnet grade and manufacturer. Monte Carlo simulations performed to determine energy deposition would need to consider the near field spectrum from the undulator.

Radiation safety

The FFTB is shielded with 1.2 m of concrete laterally and 1 m of concrete on the roof. The shielding is sufficient for the LCLS electron beam, which has an average power of 1.4 kW at 14.35 GeV. Radiation safety for the LCLS covers radiation concerns that are normally encountered at both high-energy electron linacs and synchrotron radiation facilities and includes the following [5]:

- *Bremsstrahlung and neutron production from primary electron beam interactions with beam line components upstream of and along the undulator.* A protection collimator upstream of the undulator made of copper with internal diameter of 0.1 cm and thickness 0.15 cm will be used to protect the undulator from a mis-steered beam and particles from the electron beam halo. The collimator continuously intercepts 1% of the beam.

A profile monitor made of tungsten, of thickness 20 μ , may be inserted upstream of the undulator. The profile monitor intercepts 20% of the beam and can be a significant source of radiation when it is inserted into the beam.

Intensity monitors may be inserted along the various sectors of the undulator. The monitor made of diamond, of thickness 0.05 cm, will be inclined at an angle of 45° to the beam. It will intercept the full beam and is expected to be the largest source of radiation when inserted into the beam.

The walls and roof of the experimental enclosures will require shielding against the bremsstrahlung and neutrons and muons. The photon stoppers will provide protection against bremsstrahlung.

- *Gas bremsstrahlung arising from interactions of residual gas molecules with the electron beam in the 121 m length of the undulator.* The average electron beam current for the LCLS is 0.95 nA, whereas typically in a storage ring the stored beam current varies from 100 to 500 mA. The beam current in LCLS is therefore six orders of magnitude lower than in a storage ring. The residual pressure in LCLS is 10^{-7} torr while in a storage ring it is usually around 10^{-9} torr. The pressure in LCLS is two orders of magnitude greater than in a storage ring. Typical insertion device lengths are about 5 m, while the LCLS undulator is about 20 times longer. Overall the gas bremsstrahlung from LCLS is expected to be lower than that encountered in storage rings, however it may not be negligible. Therefore a full Monte Carlo simulation of the gas bremsstrahlung is warranted.
- *Muon production from the electron beam dump and upstream electron beam losses.* Electron beam losses upstream of the undulator and electrons incident on the beam dump can result in the production of muons. The forward directed muons could be shielded with iron. The stoppers will also provide shielding against the muons.
- *Skyshine and boundary dose.* Once the beam losses have been identified the skyshine and boundary dose from the operation of the LCLS will have to be studied.
- *Scattered and forward directed FEL and synchrotron radiation.* The walls and the roof of the experimental enclosures will be shielded for scattered and forward directed FEL and SR. The photon stoppers and the photon dump will provide protection against the forward directed SR and FEL radiation.
- *Activation.* The average beam power for the electron beam is 1.4 kW. Activation will occur in areas of beam loss and will have to be evaluated.
- *Personnel protection system and beam containment system.* The personnel protection system (PPS) consists of electrical interlocks and mechanical barriers that prevent personnel from entering beam shielding enclosures when particle beams may be operating. The beam containment system (BCS) ensures that the beam does not reach occupied areas, and consists of devices that contain the beam and limit the beam power and beam loss.

Figure 4 shows a plan view of the FFTB tunnel. The PPS stoppers, D2, 60 and 61 provide protection against radiation from upstream beam losses for entry into the FFTB tunnel. The muon shield provides shielding against muons produced from upstream beam losses. Immediately downstream of the undulator are five permanent magnets and two DC magnets that bend the electron beam into a dump. The magnets allow the deflection of electron beams ranging in energy from 4.53 to 14.35 GeV into the electron beam dump.

Figure 5 shows an elevation view of the beam dump and the LCLS experimental hall. Because of the high peak coherent power of the LCLS all safety systems such as collimators, beam dumps (mechanical beam containment devices) and PPS stoppers are protected by BTMs. Collimators are placed in critical locations where the beam can be steered. BTMs are devices which are wired into the PPS to turn the beam off if the mechanical beam containment device that it is protecting has burned through. These monitors are stainless steel pressurised gas-filled vessels that are placed at shower maximum. They rupture when the associated mechanical beam containment device (such as the collimator) burns through. Loss of gas is detected with a pressure switch shuts off the beam.

Figure 4. Plan view of the FFTB tunnel

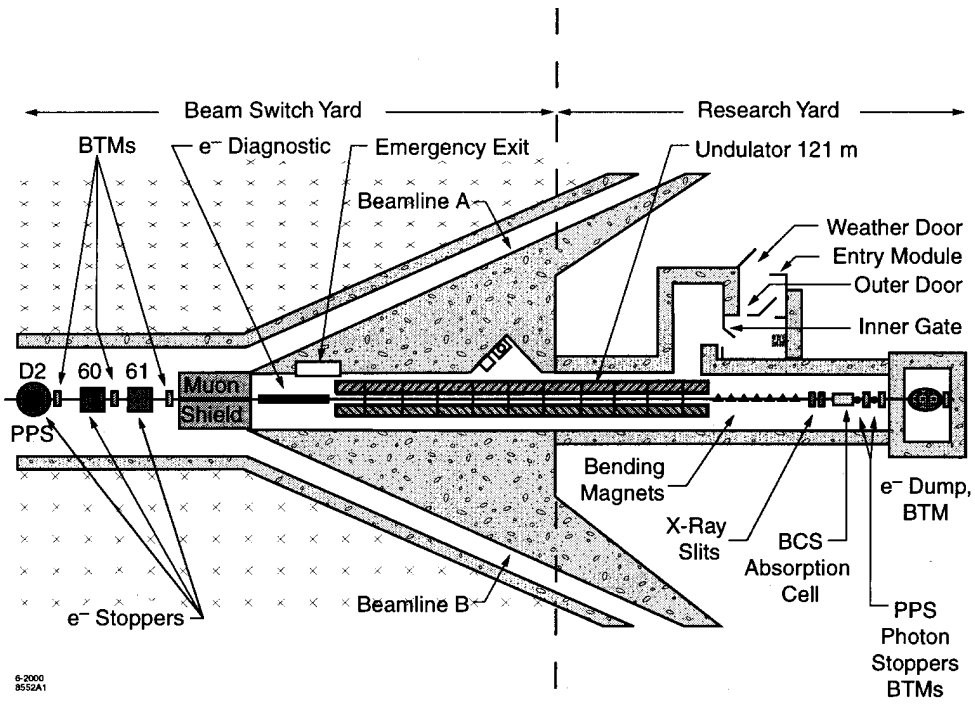
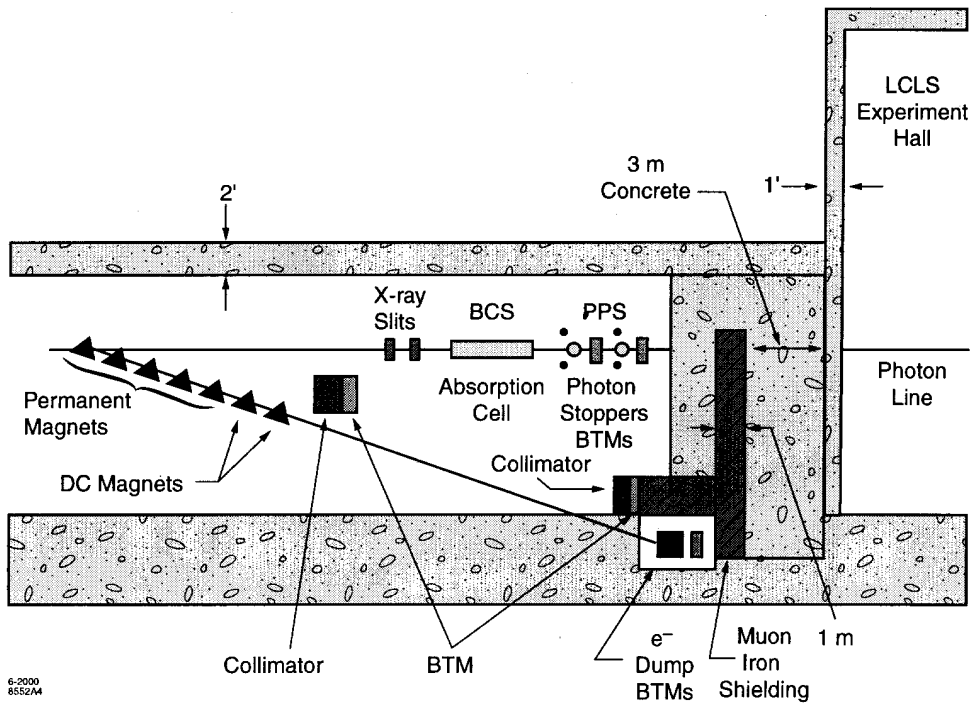


Figure 5. Elevation view of beam dump



Conclusions

The characteristics of the LCLS and associated radiological issues have been discussed. Future needs of the LCLS include Monte Carlo codes that incorporate electron and photon transport down to 0.1 keV, polarisation of photons, reflectivity and refractivity of mirrors and time dependence of radiation fields.

Acknowledgements

Gratitude is expressed to the SLAC Publications Department and Betty Eaton of Radiation Physics for their help with the preparation of this paper.

This work was performed under the auspices of the US Department of Energy by Stanford University, Stanford Linear Accelerator Centre under contract No. DE-AC03-76SF00515 and by the University of California Lawrence Livermore National Laboratory under contract No. W-7405-Eng-48.

REFERENCES

- [1] M. Cornacchia, "The LCLS X-ray FEL at SLAC", SLAC-PUB-8053, February 1999.
- [2] J. Arthur, "Prospects for an X-ray FEL Light Source and Some Possible Scientific Applications", in X-ray and Inner-shell Processes, AIP Conf. Proc. 506, p. 597 (2000).
- [3] M. Cornacchia, "X-ray Free Electron Lasers and the LCLS Project", in AIP Conf Proc. 521, p. 441 (1999).
- [4] T. Ikeda and S. Okuda, *Nucl. Instrum. Meth.*, A407 (1998), 439.
- [5] LCLS Design Study Report, SLAC-R-521, UC-414, April 1998.

SHIELDING ISSUES AROUND THE ESRF STORAGE RING

Paul Berkvens, Patrick Colomp
European Synchrotron Radiation Facility, France

Abstract

This paper deals with various shielding issues concerning the European Synchrotron Radiation Facility (ESRF) storage ring. Three main radiation sources can be identified: photon and neutron radiation outside the concrete storage ring tunnel produced by electron beam losses, scattered gas bremsstrahlung outside the beam line optics hutches and scattered X-rays outside the beam line hutches. The results of some shielding experiments are discussed and compared with preliminary results from Monte Carlo simulations and with the commonly used models for shielding calculations. A dedicated beam line has been installed at the ESRF to carry out gas bremsstrahlung measurements. Results from these measurements are also presented in this paper, including comparisons with Monte Carlo calculations. Finally, the shielding calculations for the synchrotron radiation beam lines are briefly mentioned.

Introduction

The European Synchrotron Radiation Facility (ESRF) operates a 6 GeV electron storage ring used to produce X-ray beams for 40 experimental beam lines. The experimental hall around the storage ring at the ESRF is classified as a free access area. Therefore the annual dose limits for the public must be guaranteed. Three main radiation sources can be identified: photon and neutron radiation outside the concrete storage ring tunnel produced by electron beam losses, scattered gas bremsstrahlung outside the beam line optics hutches and scattered X-rays outside the beam line hutches.

Evaluation of the storage ring concrete shielding

Introduction

Shielding requirements for high-energy electron accelerators are usually evaluated using the well-known model for local losses [1]:

$$H = \frac{S e^{-d/\lambda}}{R^2}$$

where H is the dose equivalent at a distance R metres from the particle beam interaction point, after the scattered radiation has passed through a thickness d of a shielding with a corresponding attenuation length λ .

The source term for the gamma dose rate under 90° due to bremsstrahlung is given by [1]:

$$S_{90} = 50 \text{ Sv}\cdot\text{h}^{-1}\cdot\text{kW}^{-1} \text{ at } 1 \text{ m}$$

and an attenuation length of 21 cm can be used for photons in ordinary concrete (2.35 g/cm^3) [1].

This model was essentially developed for linear accelerators in which the beam impinges on well-defined targets or beam stops. However, when this model is used for shielding calculations for storage rings the geometry is not so clear, and certain very approximate beam loss assumptions must therefore be made. Very often uniform losses around the ring are assumed, and these uniform losses are then used in the above model as a number of identical local losses, distributed uniformly along the machine, e.g. one loss point per unit cell.

In the design study of the ESRF [2], the shielding for the storage ring was defined such as to respect dose limits outside the shield wall for Category A radiation workers (50 mSv/y or $25 \text{ }\mu\text{Sv/h}$). After a few years of operation the experimental hall has been reclassified as a free access area because it was demonstrated that radiation limits for the public could be easily maintained (5 mSv/y or $2.5 \text{ }\mu\text{Sv/h}$). With the new European radiation protection legislation, ESRF now needs to demonstrate to the French authorities that the new limits for the public (1 mSv/h or $0.5 \text{ }\mu\text{Sv/h}$) can still be guaranteed.

In this context a number of shielding experiments have been carried out, which are described in the following paragraphs.

Experimental results

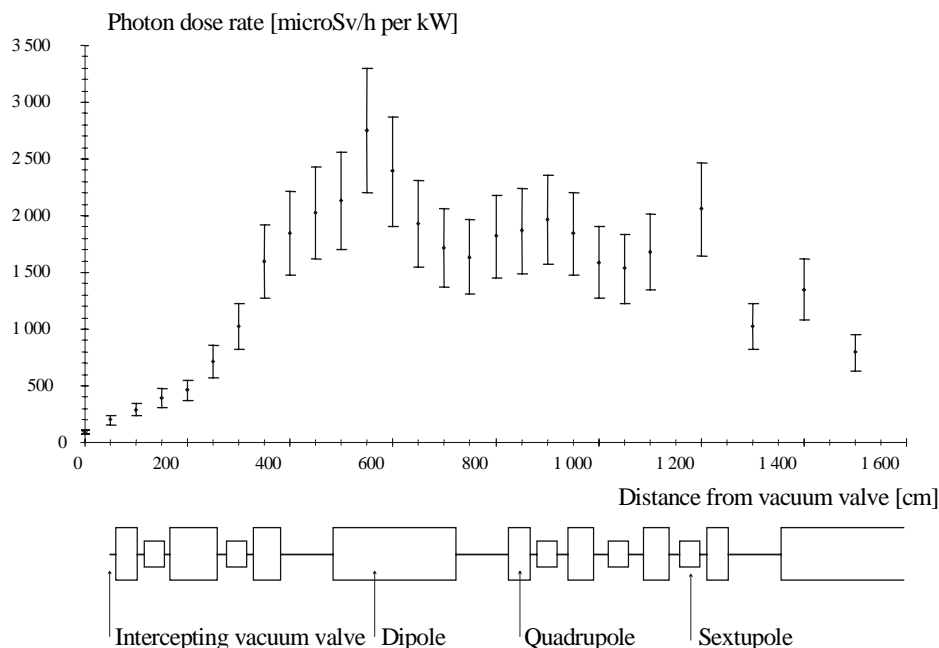
The clearly very pessimistic predictions from the design study compared to the real dose levels could be explained partly by over-conservative beam loss assumptions: the injection efficiency now

reaches values above 90% and the lifetime now stands at over 50 hours at 200 mA compared to the design value of 8 hours at 100 mA. However, a further decrease by a factor of five in the radiation limits could not be expected from these improved machine performances. Therefore more detailed measurements were required to relate measured dose levels to beam loss values.

To obtain such quantitative data, exactly known localised beam losses were created and the corresponding dose rate distributions were measured outside the concrete shielding. The losses were produced by injecting 6 GeV electrons (i.e. the nominal energy of the ESRF storage ring) and losing these electrons on a closed vacuum valve. The photon equivalent doses were measured on the storage ring roof, using ionisation chambers in analogical integration mode.

One example of such a photon dose profile is shown in Figure 1. The dose values are expressed in dose rate [$\mu\text{Sv/h}$] per intercepted beam power [kW]. We show an error bar of $\pm 20\%$ corresponding to the uncertainty of the injection efficiency and of the first turn losses in the storage ring upstream of the interaction point.

Figure 1. Measured photon dose profiles on top of the storage ring roof tunnel, for a 6 GeV beam intercepted on a vacuum valve



From the results two observations are immediately obvious. The measured dose profile is completely different from the one predicted by the model. Indeed the model predicts a maximum dose level approximately above the vacuum valve, and a rapid $1/R^2$ decrease, further enhanced by the increasing effective shield thickness. The second observation is the absolute value of the measured dose levels. The height between the beam axis and the tunnel ceiling is 1 m, and the roof is made of 1 m ordinary concrete. With these values, the model predicts a maximum dose rate of:

$$H_{\max} = \frac{50 \cdot 10^6 \cdot e^{-100/21}}{2^2} = 1.07 \cdot 10^5 \mu \text{ Sv} \cdot \text{h}^{-1} \text{ per kW}$$

which is nearly 40 times higher than the measured maximum value.

Monte Carlo simulation

Why are the measured results so different from the dose profile predicted by the macroscopic model? The reason is obviously the fact that, in a high-energy electron storage ring such as that operated at the ESRF, the electron beam is not intercepted by a so-called “optimised” target, but essentially interacts with a small thickness target. In the case of the experiment this target is the central 1 mm stainless steel part of the vacuum valve. Other examples of thin targets are the scraping of the beam due to aperture limitations of the vacuum vessel, or the interaction of the beam with the residual gas molecules producing gas bremsstrahlung. These thin targets will essentially degrade the energy of the primary beam via bremsstrahlung production and induce multiple scattering. The majority of the electrons, however, will travel further down the storage ring, and will be finally stopped downstream, depending on their energy and the magnetic lattice of the machine. Some electrons will even do a few turns before being stopped. The majority of them will be stopped in the magnets (dipoles, quadrupoles and sextupoles), and the yokes of these magnets will make up for the real targets, but at the same time present a non-negligible amount of local shielding.

From the above it is obvious that a Monte Carlo code describing the electromagnetic cascade alone cannot correctly simulate the present case. Indeed, only a program combining both the electromagnetic cascade development and the magnetic transport of the electrons (positrons) through the storage ring lattice can be expected to give correct results. Therefore it was decided to develop such a code.

As the starting point we used a Monte Carlo code written some years ago essentially to do gas bremsstrahlung simulations. This code is largely inspired by the EGS4 code [3] and is basically a simplified version of the latter. The program is only meant to give dose values behind shield walls, and is not intended to give accurate dose distributions for therapy beams. Therefore, wherever possible, simplified sampling schemes for cross-sections and secondary particle distributions are implemented, making use of interpolations from pre-calculated values, in order to reduce CPU time. Also over-sampling is largely used to improve statistics for thick shield wall transmission or for dose calculations at large angles. The program calculates fluences of photons and electrons/positrons behind the shield wall, and then uses fluence to dose equivalent conversion factors to obtain values for the effective dose equivalent.

To this program we have now added a module describing the transport of the electrons and positrons through the magnetic elements of the storage ring. The particle trajectories are obtained via second-order numerical integration. Typical integration steps of a few cm are used, with a step refinement at the point of impact, to locate the interaction point with the thin wall vacuum vessels with sufficient accuracy. A central sub-routine manages the overall particle transport, checking whether a particle moves inside a vacuum vessel, inside a vessel wall or a magnet yoke, whether a magnetic field is present, etc.

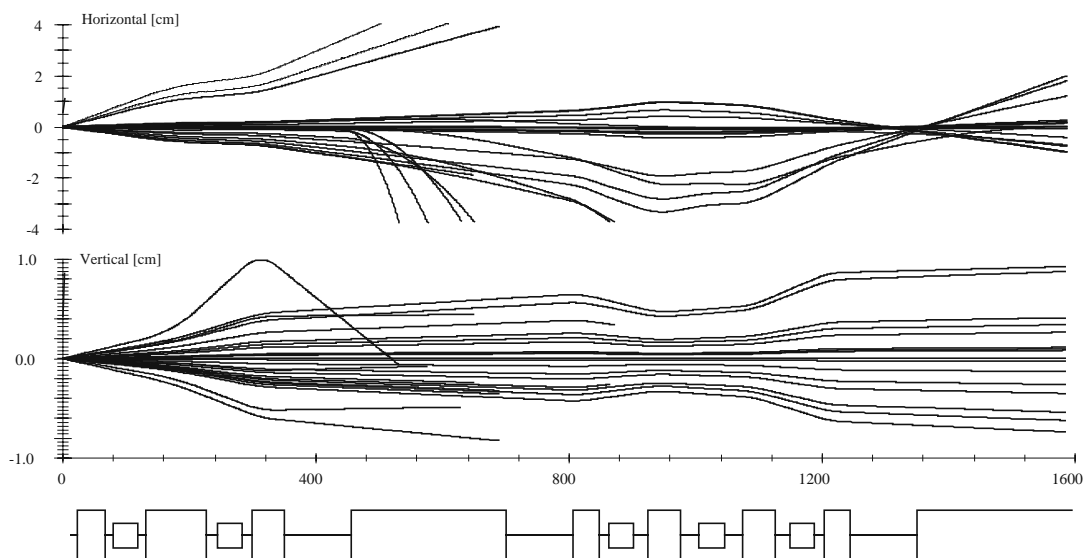
The code is written in C++, using the CodeWarrior Integrated Development Environment. A typical result shown in Figure 4 requires about four hours of CPU time when running on a DELL Latitude 650 MHz PC. The first results were only obtained a few weeks ago. The agreement between experimental results and calculated values is satisfactory. At present major developments concern essentially a more accurate description of the complex geometries of quadrupole and sextupole yokes, as well as a more performing ray-tracing description of low energy electrons (< 20 MeV) or electrons with large transverse velocities (e.g. cascade electrons/positrons scattered out of the yokes back in the magnetic regions). With these improvements we expect to obtain a better agreement between experiments and simulations.

Example of a simulation

To illustrate the program we simulate the experiment described in Figure 1.

Figure 2 shows the trajectories of a few electrons coming out of the vacuum valve, clearly showing the effect of the dipole field (and to a lesser extent of the quadrupoles).

Figure 2. Trajectories of electrons emitted from the vacuum valve



The actual electron loss pattern is shown in Figure 3. Few electrons are lost immediately downstream of the vacuum valve. These are essentially electrons which received a large deflection due to multiple scattering. The main losses, however, appear in the dipole magnet; the energy of the electrons has been reduced due to bremsstrahlung production in the vacuum valve, and these electrons are deflected by the dipole magnet in the vacuum vessel. The peak at the end of the dipole magnet can be explained by the reduction of the horizontal vacuum vessel aperture at this place. The second sharp peak corresponds to the downstream absorber (aperture reduction). The losses in the first part of the achromat are directly explained by the increasing dispersion of the magnetic lattice. Finally, some smaller losses again occur in the second dipole.

Figure 4 finally compares the calculated photon dose rates with the measured ones. On the same figure we have also represented the dose profile predicted by the local-loss model. We see that the agreement between the experiment and the Monte Carlo simulation is relatively good. As mentioned above, we are presently improving the geometrical modelling of the rather complex quadrupoles and sextupoles yokes, as well as writing a better tracing code for low energy electrons and/or electrons with large transverse momentum. With these improvements the agreement will certainly improve.

Conclusions

The first results obtained with this Monte Carlo code are very promising. We believe that the use of such Monte Carlo calculations can be useful for the definition of shielding requirements for future storage rings, because it will allow the use of more realistic beam loss assumptions. Indeed, the use of

Figure 3. Electron linear loss profile

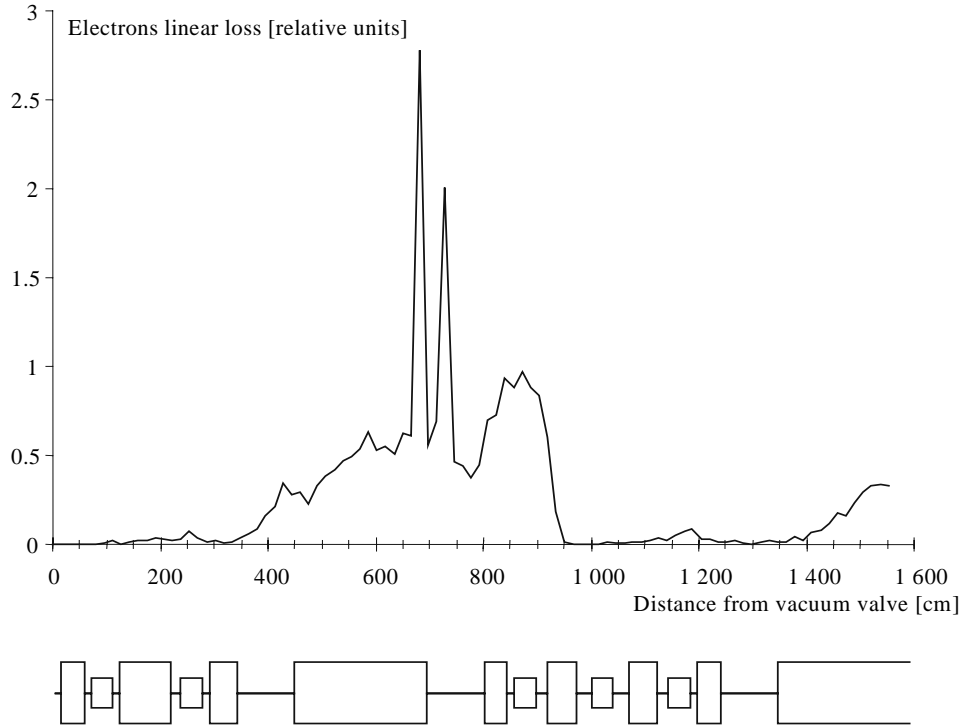
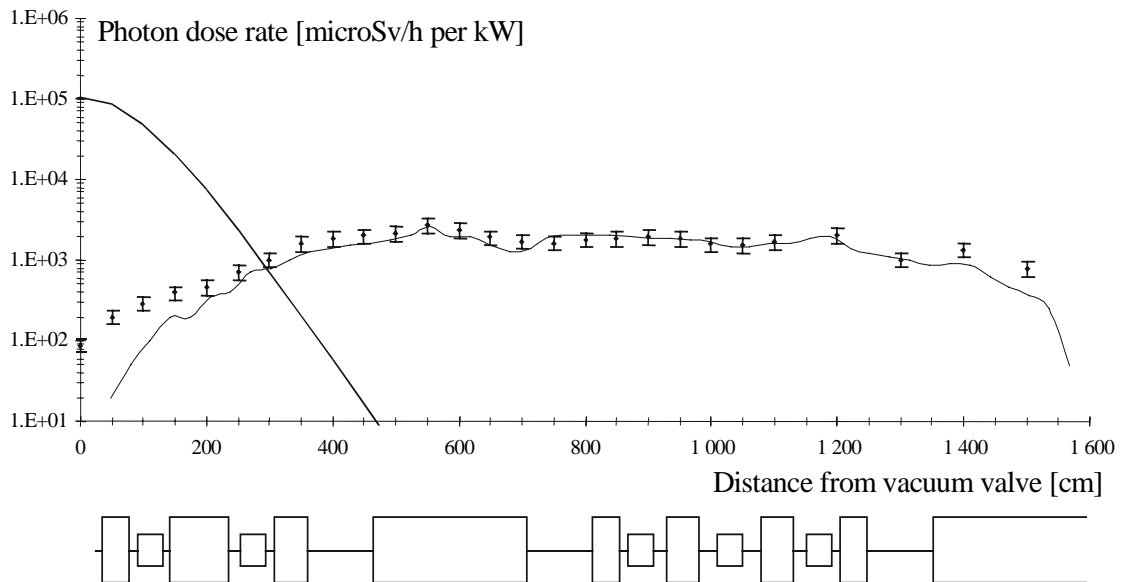


Figure 4. Comparison between the experimental results (dots) and the Monte Carlo results (solid line). The predicted profile from the local-loss model is also shown.



the analytical model results in prohibitively thick shields, and therefore one tends to use unrealistic loss patterns to arrive at acceptable wall thickness. However, the experience at the ESRF has clearly shown that during the lifetime of a storage ring, regular modifications and upgrades take place which often lead to changed loss profiles, and local losses of several tens of per cent of the total losses, both during injection and stored beam conditions, can be observed.

The next step will be to also include neutron production and transport in the code, because neutron doses often dominate outside the shield walls of high-energy electron storage rings.

Gas bremsstrahlung

Introduction

Radiation levels outside the optics hutches of the undulator beam lines at the ESRF are almost entirely due to scattered radiation coming from gas bremsstrahlung. Indeed, the important length of the straight sections (15 m from dipole to dipole) on the one hand and the degrading vacuum conditions inside the ID vessel due to their reduced vertical apertures has led to a situation in which this radiation source becomes predominant, and has required further attention due to the decrease in the legal dose limits.

It was therefore decided to build a temporary dedicated beam line downstream of one of the straight sections to carry out gas bremsstrahlung measurements with the view of providing a valuable diagnostic tool for the evaluation of prototype vacuum vessels.

Description of the experimental set-up

To characterise the bremsstrahlung radiation produced in an insertion device vacuum vessel, a very simple experimental set-up is required. At the ESRF our standard measurement consists of measuring the on-axis dose using TLDs inside a PMMA phantom.

Even in the absence of insertion devices on the straight section, there will always be some synchrotron radiation produced in the upstream and downstream dipoles. It is therefore mandatory to put a minimum shielding in front of the phantom, otherwise the bremsstrahlung measurements will be completely polluted by this synchrotron radiation. Figure 5 shows the results of some simulations carried out to determine the required lead thickness. A thickness of 3 mm of lead is a good compromise, because it sufficiently reduces the X-rays, while it does not alter too strongly the bremsstrahlung spectrum. We therefore put the PMMA phantom behind a 3 mm thick lead screen; the TLDs can be placed inside the phantom at different depths.

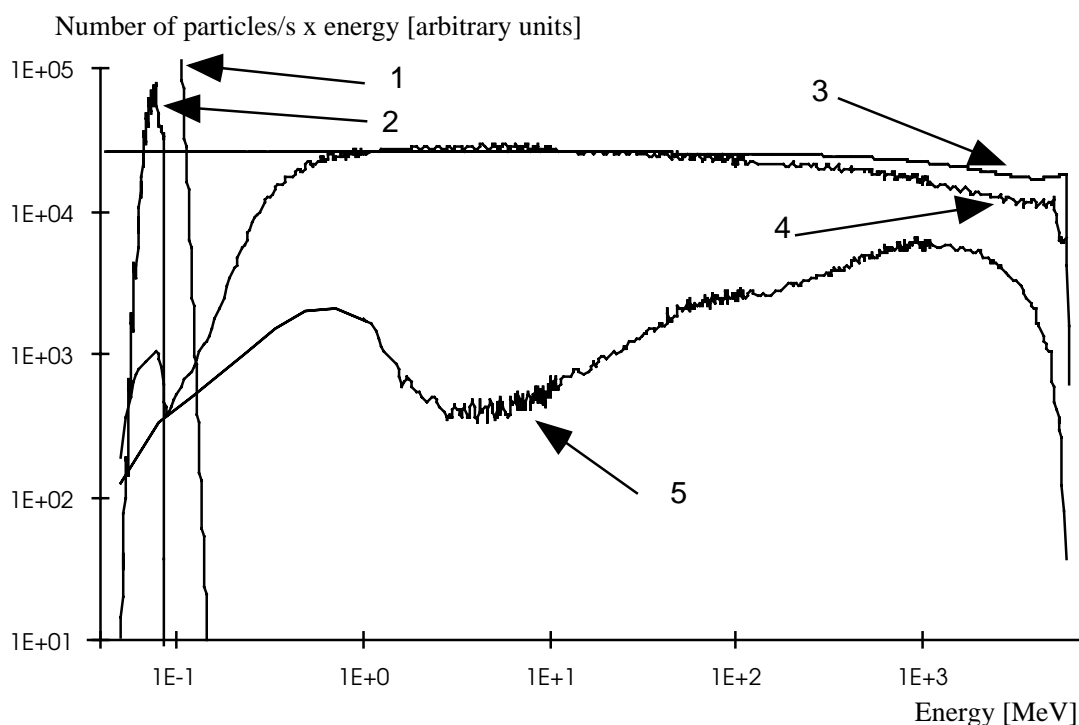
Monte Carlo simulations

Since the on-axis gas bremsstrahlung measurement is the only objective way to obtain a realistic value for the average pressure in the straight section, we have simulated the experimental set-up, to find a relation between the measured dose rates and the pressure.

We use our electromagnetic shower Monte Carlo code described above. The direct sampling of gas bremsstrahlung photons is in principle a very inefficient way. We therefore calculate the photon spectrum, using an analytical expression for the bremsstrahlung cross-section and taking into account

Figure 5. Calculated bremsstrahlung and synchrotron radiation spectra before and after a 3 mm thick lead shield

Unattenuated (1) and attenuated (2) synchrotron radiation spectra; unattenuated (3) and attenuated (4) bremsstrahlung photon spectra and electron + positron spectra behind the lead shield (5)



all the relevant storage ring parameters: energy, current, emittance, residual gas analysis data. The total pressure will be the remaining parameter used to normalise our calculated dose profile to the measured ones, thus yielding a conversion factor between dose rate and average total pressure.

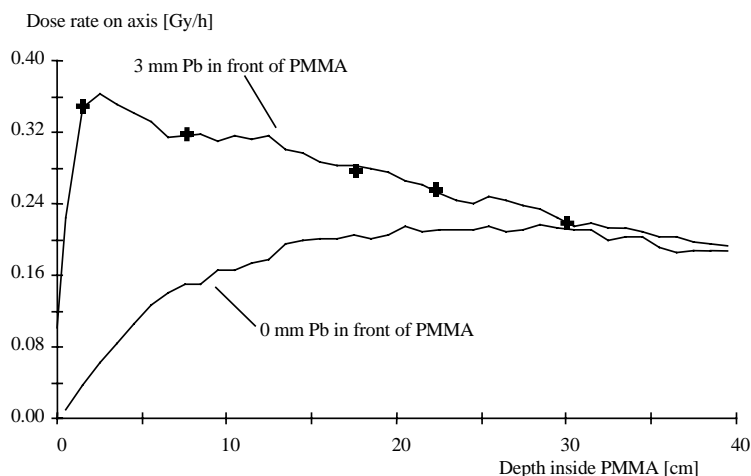
Figure 6 shows an example. Normalising the calculated dose profile to a pressure of 2.10^{-9} mbar gives a good agreement with the measured data. Figure 6 clearly shows that one must be extremely careful when comparing results of this kind at different facilities. The experimental conditions must be exactly the same, otherwise the comparison is completely meaningless. Our simulations have shown indeed that the thickness of the lead shield, as well as its exact position with respect to the phantom, greatly influence the dose profile.

In 1999 gas bremsstrahlung measurements were carried out at the same beam line using lead glass scintillators from APS. This measurement provides a direct measurement of the gas bremsstrahlung photon count rate, therefore also allowing to determine a value for the average total pressure. These measurements and the Monte Carlo simulations of the TLD set-up yielded values for the total pressure which agreed within 20%.

Shielding for X-ray hutches

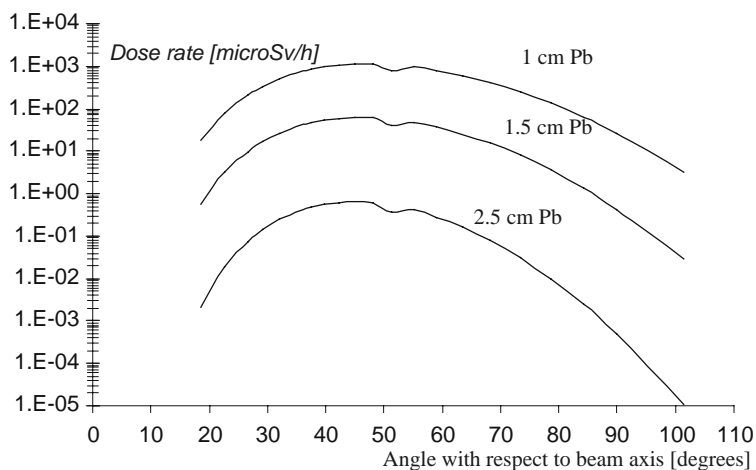
For completeness we mention the shielding calculations used for the definition of the lead hutches. The shielding against scattered bremsstrahlung is done using the Monte Carlo code mentioned above. The shielding against X-rays is done using a simple analytical code which calculates the X-ray

Figure 6. Measured gas bremsstrahlung dose rates in PMMA phantom (crosses) and calculated values (solid lines)



spectrum for a given beam line, taking into account the storage ring parameters and the characteristics of the insertion device or bending magnet. The program calculates the scattered radiation for a given scattering source and calculates the attenuation through the shield wall using total attenuation cross-sections (photo-electric effect + Compton scattering). This simplification gives accurate enough results, because, as we have verified using Monte Carlo simulations, the build-up inside the lead hutch walls (thickness a few mm up to a few cm) is negligible. In the past, and even nowadays the program PHOTON [4] has often been used to calculate shielding for synchrotron radiation. This program however gives completely wrong results for hard X-ray facilities such as ESRF, because it does not take into account the angular distribution of the Compton scattering. It uses the differential cross-section at 90° , and with it the energy of the scattered radiation also at 90° . Due to the Compton shift the maximum dose level is obtained for angles at about 45° with respect to the primary beam axis. This is illustrated in Figure 7; in the case of this 28.7 keV critical energy wiggler the predicted Pb thickness (using only the 90° value, which corresponds roughly to the value given by PHOTON) is more than 1 cm smaller than the actual required value.

Figure 7. Dose rates behind a lead shield side wall for synchrotron radiation from a 1.5 m long, 125 mm period 1.2 T wiggler and a 200 mA, 6 GeV beam, scattered from a Cu target, as a function of the angle with respect to the impinging beam direction



REFERENCES

- [1] A.H. Sullivan, “A Guide to Radiation and Radioactivity Levels Near High-energy Particle Accelerators”, *Nuclear Technology Publishing*, 1992.
- [2] Note descriptive de l’ESRF, Étude de Sécurité, Grenoble, 1988.
- [3] W.R. Nelson, *et al.*, “The EGS4 Code System”, Stanford Linear Accelerator Centre Report SLAC-265, 1985.
- [4] Dean Chapman, “Photon: A User’s Manual”, NSLS report BNL 40822, 1988.

High-energy Electron Machines

**RADIATION STUDIES FOR THE ENVIRONMENTAL PROTECTION
AT THE BEAM DELIVERY SYSTEM OF THE NEXT LINEAR COLLIDER**

S.H. Rokni, J.C. Liu, S. Roesler
Stanford Linear Accelerator Centre
Stanford, CA 94309, USA

Abstract

The concentration of induced radionuclides in the soil and groundwater around, and air inside, the collimation section of the beam delivery system of the Next Linear Collider are calculated with the FLUKA Monte Carlo code. The concentration of ^3H and ^{22}Na in groundwater are comparable to the drinking water limits. The fluence of particles (photon, neutron, proton and pion) in the air inside the tunnel for the collimation section is also calculated with FLUKA. The induced activities of ^3H , ^7Be , ^{11}C , ^{13}N , ^{15}O and ^{41}Ar are then estimated by folding the particle fluences with various nuclear cross-sections. The worker exposure during access after accelerator shutdown and the general public dose from radioactivity released to the environment are studied. The concern is for the short-lived radioisotopes of ^{13}N and ^{15}O , produced mainly by photons, and ^{41}Ar produced by thermal neutrons. The results show that the radiological consequences from the air activation are minor.

Introduction

The collimation section of the beam delivery system (BDS) for the Next Linear Collider (NLC) [1] eliminates particles at large amplitude that could cause unacceptable levels of background in the detector. The collimation section consists of a series of spoilers and absorbers that are designed to continuously absorb 0.1% (10 kW) of the total beam power. The calculation of the amount of induced radioactivity in the soil that could leach out and eventually reach public drinking water supplies is an important factor in the design of shielding for the BDS. Studies have shown that only ^3H and ^{22}Na could contribute significantly to the activity in groundwater and need to be considered [2,3]. Other radionuclides either have very short half-lives or are strongly absorbed in the soil (e.g. ^7Be , ^{45}Ca , ^{54}Mn).

Another significant factor in the design of shielding for the BDS is the amount of radionuclides produced in the air inside the tunnel for the collimation section. The airborne radionuclides in the tunnel could constitute a radiological hazard for workers accessing the tunnel after a shutdown. Additionally, if the radionuclides are released to the environment the general public may receive dose from various pathways.

This paper summarises the results from various methods used in the calculation of the induced activity of several radionuclides in the soil and gives the initial estimates for the concentration of ^3H and ^{22}Na in the groundwater around the collimation section of the BDS. The induced radioactivity in the air inside the tunnel is also calculated, and the radiological consequences from the air activation are presented. A detailed analysis of the methods used in calculating the soil, groundwater and air activation is discussed elsewhere [4,5].

The FLUKA calculations

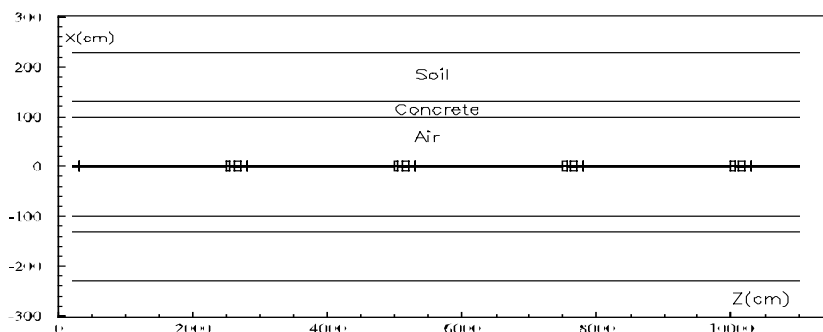
The calculations were performed using the 99 version of the Monte Carlo particle interaction and transport code FLUKA [6]. The program is used to simulate the electromagnetic and hadronic particle cascades in the beam line components, walls and soil around, and the air inside the BDS tunnel. In the following sections some aspects of the simulations that are relevant to the present study are discussed.

The geometry and materials

A cylindrical concrete shell (inner radius = 100 cm, outer radius = 130 cm) surrounded by a 100 cm thick cylindrical layer of soil (Figure 1) was used to approximate the 300 meter long tunnel for the BDS. The collimation region is comprised of six sections, each one having two spoilers (vertical/horizontal) and two absorbers (horizontal/vertical). Each spoiler (inner radius = 0.0061 cm, length = 0.357 cm) is followed by an absorber (inner radius = 0.05 cm, length = 50 cm) located 2 200 cm down-beam that is protecting a (focusing/de-focusing) quadrupole magnet (inner radius = 0.7 cm, length = 100 cm) that is located 50 cm down-beam of the absorber. In the FLUKA geometry, spoilers and absorbers were assumed to consist entirely of copper and magnets were made of iron. The beam pipe is a cylindrical shell made of iron (inner radius = 0.5 cm, outer radius = 0.6 cm). The outer radii of the spoilers, the absorbers and the magnets are all 10 cm. For soil, density = 2.1 g cm^{-3} , and the following chemical composition and mass fractions are used: O (54.6%), Si (30.7%), Al (4.2%), K (2.5%), Fe (1.8%), Mg (1.7%), H (1.6%), Na (1.3%), Ca (1.2%), Mn (0.003%). The water content of the soil is assumed to be 30% by volume. Air fills the rest of the tunnel.

The lower kinetic energy transport cut-off for electrons/positrons and for photons were all set at 5 MeV. Neutrons were transported down to the lowest thermal group of the 72 energy group neutron cross-section of the ENEA data set. The transport threshold for all other hadrons was set to be 10 keV.

Figure 1. Cross-section of the tunnel for the collimation section of the NLC beam delivery system



The threshold for scoring the hadron inelastic reactions was set at 50 MeV. The interaction length for nuclear inelastic interactions of photons was reduced by a factor of 50 in all materials to increase photo-hadron production. Full leading particle biasing was activated for all electromagnetic processes for photons, electrons and positrons below 500 GeV in all regions. The region importance biasing for neutrons was activated in concrete and soil. The magnetic field option in FLUKA was used to set a field gradient of 9.56 kG/cm for focusing and de-focusing quadrupole magnets. The incident beam was assumed to have a δ -function size and to strike the first vertical spoiler at $x = 0.0066$, $y = 0.0$ and $z = 299.99$ parallel to the z -axis.

Calculated quantities

Three approaches using FLUKA were considered to estimate the induced radioactivity in the soil. The first approach was to estimate the radionuclide production by folding the FLUKA-calculated neutron fluence with the appropriate nuclear cross-sections. The second method was to calculate directly with FLUKA the production of residual-nuclei in the soil. The third approach was to calculate the number of stars, then convert it to the number of radionuclides in the soil using appropriate atom per star factors. These approaches are compared with each other by calculating the induced activity in a small region of soil with each method. This region (inner radius = 130 cm, outer radius = 140 cm, length = 50 cm, starting at $z = 5\,000$ cm) is across the absorber that intercepts most of the scattered beam, thus good statistical significance of the results is expected. The approaches considered in the present study are described further in the rest of this section.

- *Method 1.* The number of atoms of ^3H , ^7Be and ^{22}Na per gram of soil per primary electron was obtained by folding the FLUKA calculated neutron fluence (see Figure 2a) in the small region of soil with the nuclear cross-sections for production of these isotopes from oxygen and silicon nuclei. Since the tunnel is shielded with a 30 cm thick concrete layer the activation of the soil outside this shield is mainly due to neutron interactions with its constituents, oxygen and silicon [7,8]. Measured cross-sections for the $^{16}\text{O}(n,x)^3\text{H}$ and $^{28}\text{Si}(n,x)^3\text{H}$ reactions are not available, thus the results from an evaluation of the existing cross-sections for the proton-induced reactions by Tesch [7] (see Figure 2b) were substituted for the unavailable neutron-induced cross-sections. Therefore, results obtained with this method could have large uncertainties associated with them. Results of ^3H activity in the soil from folding of the neutron fluence spectrum with the above cross-sections show that only the spallation neutrons in the approximate energy range of 20 MeV to 200 MeV contribute to the ^3H production from oxygen and silicon (see Figure 2c).

Figure 2a. Neutron fluence in the small scoring region in the soil

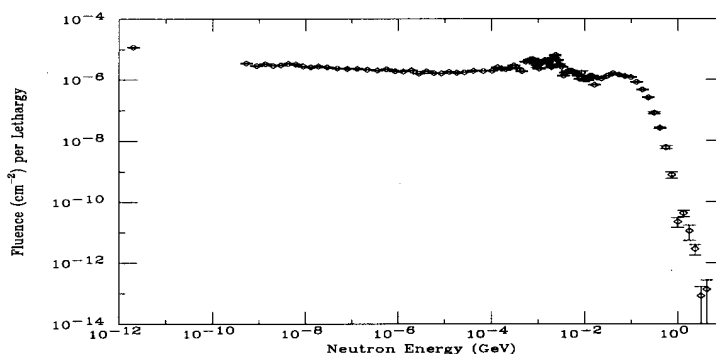


Figure 2b. Cross-sections used to calculate ^3H production from silicon and oxygen [7]

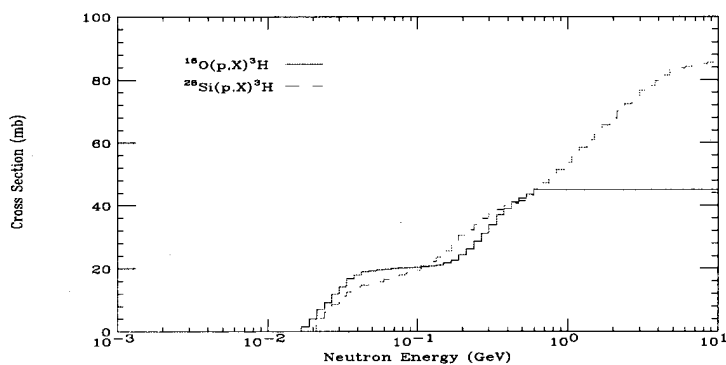
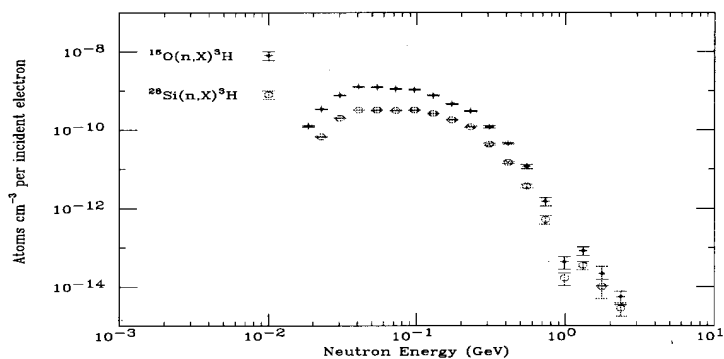


Figure 2c. Contribution of oxygen and silicon to the activity of ^3H in soil



- *Method 2.* The production of residual isotopes was directly calculated with the RESNUCLE option of FLUKA. The physics implemented in the code does not include a nuclear multi-fragmentation model, therefore the yield of nuclides with mass numbers far from the parent nuclei in medium-mass targets could be underestimated.
- *Method 3.* The number of stars (defined as the inelastic interactions of hadrons with kinetic energies greater than 50 MeV) was calculated with FLUKA. This number was converted to the number of radionuclides using the radionuclide per star factors that can be obtained from the ratio of the measured (or calculated) activity to the calculated number of stars [9,10].

Table 1 shows the activity concentration for ^3H , ^7Be and ^{22}Na calculated by the three methods described above and for the other radionuclides calculated with Methods 2 and 3 in the small scoring region in the soil. The percentage values represent the statistical uncertainty of the results. For the column labeled “Star method”, the values of atom per star from Vincke, *et al.* [11] have been used. Note that for ^7Be , ^{22}Na and ^{54}Mn , these values are based on measurements on Molasse.

Table 1. Comparison of radionuclide production rate (atoms/cm³ per incident electron) in the small scoring region in soil (volume = $4.2 \times 10^5 \text{ cm}^3$) calculated with different methods

Nuclide	Spectrum	Direct isotope production	Star method
^3H	2.8×10^{-9}	5.0×10^{-10} (8%)	1.2×10^{-9}
^7Be	5.1×10^{-10}	1.8×10^{-10} (19%)	4.6×10^{-10}
^{22}Na	6.1×10^{-10}	2.9×10^{-10} (6%)	3.2×10^{-10}
^{45}Ca	–	1.1×10^{-9} (13%)	2.7×10^{-10}
^{54}Mn	–	1.5×10^{-10} (22%)	1.7×10^{-10}
^{56}Fe	–	4.1×10^{-9} (22%)	8.9×10^{-10}

The BDS soil activation

The average induced activity over the entire 300 meter long, 100 cm thick soil layer (with a volume equalling $3.39 \times 10^9 \text{ cm}^3$) that surrounds the collimation section of the BDS was then calculated by multiplying the number of stars calculated with FLUKA in this region ($1.10 \pm 0.2\%$) with the appropriate radionuclide per star factors. These factors are the ratios of the number of different isotopes in the small scoring region, calculated with the RESNUCLE option in FLUKA, over the number of stars in the same region. Calculation of activity using the direct production of residual nuclei in the entire volume of soil around the BDS is much more CPU intensive than calculating the star density.

Assuming that 0.1% of the beam intensity (1.25×10^{11} electrons/second) is lost on the first spoiler, the average activity concentration for different radionuclides was calculated. Table 2 shows the activation for various nuclei after 10 years of NLC operation (6 000 hours of continuous operation followed by 2 760 hours of downtime) and four different cool-off periods. The natural activity concentration of the soil varies from 0.3 to 1 Bq gm⁻¹, much smaller than the total induced activity immediately after shutdown. However, this value is dominated by ^{24}Na , which has a 15 hour half-life and decays away in less than a week. Ten years after shutdown the total induced activity is close to the natural background with only ^3H , ^{22}Na and ^{55}Fe contributing to the soil activity. With 50 years of cool-off, the total induced activity in the soil is much less than the natural activity of the soil. Additionally, some of the radionuclides (e.g. ^3H) could leach out of the soil and add to the activity of groundwater, thus the activity remaining in the soil would be reduced even further. It should be pointed out that currently there are no limits for soil activation in the federal, state or local government regulations in the US.

Groundwater activation

The concern from activity in groundwater is mainly due to ^3H and ^{22}Na [2,3,7,8]. Here, it is assumed that 100% of ^3H and 15% of ^{22}Na is leached out of the soil [7,8] and is dissolved in the groundwater. After 10 years of NLC operation the activities of these two radionuclides will be

Table 2. Average induced activity in the soil around the BDS tunnel

Nuclide	Half-life	Activity concentration (Bq gm ⁻¹)				
		Saturation	Shutdown	1 year	10 years	50 years
³ H	12.3 y	0.25	0.07	0.07	4.2 × 10 ⁻²	4.5 × 10 ⁻³
⁷ Be	53.3 d	0.09	0.09	–	–	–
²² Na	2.6 y	0.14	0.10	0.07	6.6 × 10 ⁻³	1.6 × 10 ⁻⁷
²⁴ Na	15.0 h	9.37	9.37	–	–	–
⁴⁵ Ca	163.8 d	0.55	0.45	0.10	8.9 × 10 ⁻⁸	–
⁵⁴ Mn	312.1 d	0.08	0.06	0.03	1.7 × 10 ⁻⁵	1.5 × 10 ⁻¹⁹
⁵⁵ Fe	2.7 y	2.05	1.34	1.04	1.1 × 10 ⁻¹	4.1 × 10 ⁻⁶
Activity concentration		12.53	11.48	1.31	1.5 × 10 ⁻¹	4.5 × 10 ⁻³

0.52 Bq cm⁻³ and 0.10 Bq cm⁻³, respectively. It is unlikely that there will be drinking water wells close to the NLC tunnel. However, should that be the case, the calculated tritium concentration is comparable to the Environmental Protection Agency (EPA) standard for the tritium concentration in drinking water [12], 0.74 Bq cm⁻³. The calculated concentration level for ²²Na in water outside the BDS is below the Department of Energy (DOE) Derived Concentration Guide of 0.37 Bq cm⁻³ [13]. With the inclusion of dilution factors and accounting for residence time of water near the collimation section the concentration of the induced activity in groundwater would be reduced to levels well below these limits. The total activity of ³H and ²²Na in the water (1.0 × 10⁹ cm³) outside the entire BDS is 0.6 GBq at the shutdown which is far lower than the 185 GBq limit for release to waste water per year [14].

Air activation

FLUKA was also used to calculate the fluence of particles (photon, neutron, proton and pion) capable of producing radionuclides in the air inside the tunnel for the collimation section of the BDS. These fluences were then folded with appropriate nuclear cross-sections to estimate the number of radionuclides produced in air [5]. The spectrum lethargy plot in Figure 3a shows that in the energy range between 10 MeV and 100 MeV the photon fluence dominates over hadron fluence by 2-3 orders of magnitude. In the calculations air is assumed to have a density of 0.001225 g cm⁻³ with the following composition (weight fraction): nitrogen (75.58%), oxygen (23.17%) and argon (1.25%).

The radionuclides ¹³N and ¹⁵O are produced predominantly in the giant resonance reactions, and ¹¹C, ³H and ⁷Be in photon and hadron-induced spallation reactions on nitrogen and oxygen atoms in air. Additionally, ⁴¹Ar is produced in the ⁴⁰Ar(n,γ)⁴¹Ar reaction with a cross-section of 550 mb for thermal neutrons. For the giant resonance reactions of ¹⁴N(γ,n)¹³N and ¹⁶O(γ,n)¹⁵O, the evaluation of the measured cross-sections by Fassò, *et al.* [15], and for the photo-spallation reactions of ¹⁶O(γ,x)¹¹C, ¹⁶O(γ,x)³H, and ¹⁶O(γ,x)⁷Be the evaluation of the measured cross-sections by Tesch [16] were used. For hadron induced reactions (e.g. ¹⁶O(n,x)³H, ¹⁶O(n,x)⁷Be) the cross-sections evaluated by Huhtinen [17] using FLUKA95 were used. This was in part due to the lack of measured cross-sections for the neutron-induced reactions.

Figure 3b compares the nuclear cross-sections of ¹⁶O and ¹⁴N for neutron and photon leading to ¹⁵O or ¹³N. The giant resonant reactions of ¹⁴N(γ,n)¹³N and ¹⁶O(γ,n)¹⁵O have maximum cross-sections up to 15 mb peaked at ~20 MeV. Since the photon and neutron cross-sections are comparable in this case, the photon component is expected to dominate the production of ¹³N and ¹⁵O completely and the contribution of hadrons is negligible. On the other hand, nuclear cross-sections for production of ¹¹C from ¹⁶O and ¹⁴N are dominated by hadron induced reactions. However, due to the much higher fluence

Figure 3a. Particle fluence spectra in the NLC BDS tunnel air region [5]

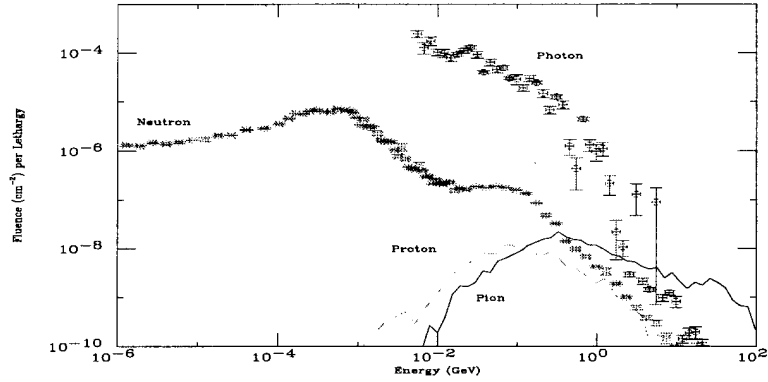


Figure 3b. Nuclear cross-sections of ^{16}O and ^{14}N for neutron and photon leading to ^{15}O or ^{13}N [5]

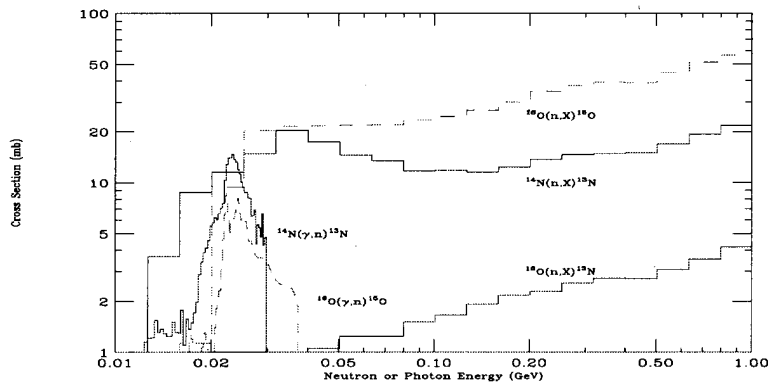
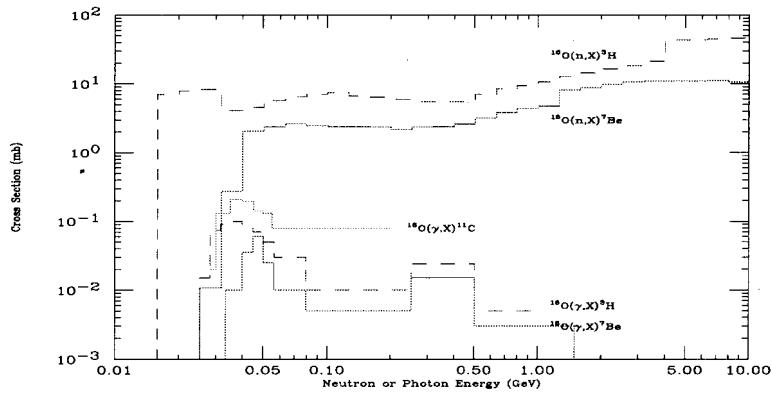


Figure 3c. Nuclear cross-sections for ^3H or ^7Be production by neutrons and photons on ^{16}O . The reaction $^{16}\text{O}(\gamma,x)^{11}\text{C}$ is also shown for comparison [5]



of photons, production of ^{11}C from oxygen and nitrogen is mainly due to photo-spallation reaction in the energy range from 30 MeV to 100 MeV. In Figure 3c the neutron cross-sections for ^{16}O leading to ^3H or ^7Be are shown. Again, due to much higher fluence, photons are the major contributor to the production of ^3H and ^7Be in air. However, the hadron contribution to the total yield is not negligible in this case (e.g. 45% for ^3H) [5]. The yields of radionuclides in air (atom/beam particle) inside the tunnel for the collimation section of the NLC BDS are listed in Table 3.

Table 3. Worker dose estimation from air activation in the collimation section of the NLC BDS tunnel (volume = $9.4 \times 10^8 \text{ cm}^3$)

Radionuclide	^{11}C	^{13}N	^{15}O	^{41}Ar	^3H	^7Be
Half-life	20.4 min	10 min	2 min	1.83 h	12.3 y	53.3 day
Atom/beam particle	0.0010	0.016	0.0028	0.0018	0.00077	0.00016
A_c (Bq cm^{-3})	0.14	2.1	0.37	0.24	0.00048	0.0068
DAC (Bq cm^{-3})	0.148	0.148	0.148	0.111	0.740	0.296
A_c/DAC	0.94	14	2.5	2.1	0.00065	0.023
A_c/DAC after 1 h	0.12	0.22	0.000	1.5	0.0006	0.02

Worker exposure during access

The worker exposure during access after the accelerator shutdown was estimated based on the assumption that 1.25×10^{11} electrons per second are lost on the first spoiler. In Table 3, the activity concentration in air inside the collimation section (A_c) at the end of a one-month long operation are compared with the derived air concentration (DAC) values [18]. Note that dose from exposure of 2 000 DAC-h is 0.05 Sv.

For these calculations it has been assumed that each access would follow one month of continuous operation with no ventilation during the operation or shutdown. The ratios of A_c/DAC for ^{13}N , ^{15}N and ^{41}Ar are higher than 1. However, a waiting period of one hour before access would reduce most activity concentrations to minimal levels. In that case only the concentration for the ^{41}Ar would exceed its DAC value.

Effluent dose to general public

To estimate the dose to the general public from radioactivity released to the environment it is assumed that, in contrast to the previous section, the total activity in the tunnel is vented out immediately after a shutdown. Therefore, the annual activity released for each type of radionuclide (A_y) is 12 times the activity at the end of a one-month long operation. The airborne effluent dose to the public per unit activity released as a function of distance (50 m to 10 km) from the release point was calculated using the DOE-certified CAP88 computer code [19]. SLAC specific parameters and Nuclear Regulatory Commission (NRC) terrestrial food chain model parameters were used in place of the yet unknown NLC location specific parameters.

Table 4 shows that the annual dose to the Maximum Exposed Individual (H_{mei}) is dominated by ^{13}N , $1.9 \mu\text{Sv/y}$. The dose to the MEI, which in this case is an individual who lives 50 m from the release point, is much less than the NESHAPS [20] legal limit of $100 \mu\text{Sv/y}$. However, it is required by EPA [18] to have a continuous radioactivity monitoring system for air emission if the dose to MEI is more than $1 \mu\text{Sv/y}$. A holding period of 1 hour before air release would reduce the dose significantly such that the maximum annual dose is $0.25 \mu\text{Sv/y}$, caused mainly by ^{41}Ar . Note that the dose to general public is proportional to the activity released annually. Therefore, if the tunnel is not sealed during the operation, the actual dose could be much higher.

Table 4. Effluent dose estimation from air activation in the collimation section of the BDS tunnel

Radionuclide	¹¹ C	¹³ N	¹⁵ O	⁴¹ Ar	³ H	⁷ Be
Half-life	20.4 min	10 min	2 min	1.83 h	12.3 y	53.3 day
A _y (MBq/y)	1568	24000	4200	2700	5.4	76
H _{mei} /A _y (pSv/MBq)	84	78	68	103	75	581
H _{mei} (μSv/y)	0.1	1.9	0.3	0.3	0.0004	0.04
H _{mei} (μSv/y), hold 1 h	0.02	0.03	0.000	0.25	0.0004	0.04

Conclusions

FLUKA has been used to estimate the concentration of induced activity in the soil and groundwater around, and air inside, the collimation section of the NLC beam delivery system. Different methods are used to calculate the activity concentrations for ³H, ⁷Be and ²²Na in the soil. Following 10 years of NLC operation, the activity concentration in the soil drops to the same level as the natural background after a 10 year cool-off period. The activity concentration for ³H and ²²Na in groundwater are also estimated. After 10 years of operation, the concentration levels for ³H are below the EPA drinking water limit. Dilution factors, not considered here, are expected to lower the concentration levels significantly below the applicable EPA and DOE limits. The total activity in groundwater from this section of the NLC is far below the limit for release to waste water.

The FLUKA calculations also show that the photon fluence dominates the radioactivity production in the air due to its much higher intensity than hadrons. Photons with energy between 10 and 100 MeV contribute the most to the production of ³H, ⁷Be, ¹¹C, ¹³N, ¹⁵O in air. However, for ⁴¹Ar, it is the thermal neutron component that dominates the activation. The worker exposure during access after one month of operation is not a major concern (dose dominated by the short-lived radioisotopes of ¹³N, ¹⁵O, and ⁴¹Ar), and if desired can be easily mitigated by waiting for one hour before access. Assuming that all radioactivity in the air at the end of one-month long operation is released to a meteorological and ecological environment that is same as that of SLAC, the annual dose to the general public was found to be minor (again the dose comes from ¹³N, ¹⁵O and ⁴¹Ar). The hazard can be mitigated by means of decay (e.g. wait one hour prior to the release) and in that case the hazard will be mainly due to ⁴¹Ar.

Acknowledgements

We wish to thank the authors of FLUKA for making the code available to us, and would like to acknowledge helpful discussions with A. Fassò and L. Keller. This work was supported by Department of Energy contract DE-AC03-76SF00515.

REFERENCES

- [1] NLC Design Group, "Zeroth-order Design Report for the Next Linear Collider", SLAC Report 474 (LBNL-PUB-5424) (1996).
- [2] T.B. Borak, M. Awschalom, W. Fairman, F. Iwami, J. Sedlet, "The Underground Migration of Radionuclide Produced in Soil Near High-energy Proton Accelerators", *Health Phys.* 23:679-687 (1972).
- [3] S. Baker, J. Bull, D. Gross, "Leaching of Accelerator Produced Radionuclides", *Health Phys.*, 73:912-918 (1997).
- [4] S. Rokni, J.C. Liu and S. Roesler, "Initial Estimates of the Activation Concentration of the Soil and Groundwater Around the NLC Beam Delivery System Tunnel", SLAC RP Note RP-00-04, May (2000).
- [5] J.C. Liu, S. Roesler, S. Rokni and R. Sit, "Evaluation of Radiological Consequence from Air Activation at NLC BDS Tunnel", SLAC RP Note RP-00-05, May (2000).
- [6] A. Fassò, A. Ferrari, J. Ranft and P.R. Sala, "New Developments in FLUKA Modeling of Hadronic and EM Interactions", Proceedings of the Third Workshop on Simulating Accelerator Radiation Environments (SARE-3), KEK, Tskuba, Japan, p. 32 (1997).
- [7] K. Tesch, "Production of Radioactive Nuclides in Soil and Groundwater Near Dump of a Linear Collider", DESY Internal Report-DESY, D3-86, January (1997).
- [8] B. Racky, H. Dinter, A. Leuschner and K. Tesch, "Radiation Environment of the Linear Collider TESLA", Proceedings of the Fourth Workshop on Simulating Accelerator Radiation Environments (SARE-4), Knoxville, Tennessee, USA, p. 14 (1998).
- [9] J. Ranft, K. Goebel, "Estimation of Induced Radioactivity Around High-energy Accelerators from Hadronic Cascade Star Densities Obtained from Monte Carlo Calculations", CERN HP-70-92, 1970.
- [10] A.H. Sullivan, "Groundwater Activation Around the AA and ACOL Target Areas", CERN Internal Report CERN/TIS-RP/IR/87-34 (1987).
- [11] H. Vincke and G.R. Stevenson, "Production of Radioactive Isotopes in Molasse", CERN Internal Report CERN/TIS-RP/IR/99-20 (1999).
- [12] US Environmental Protection Agency, Code of Federal Regulations, Washington DC, US Government Printing Office, 40CFR part 141 (1992).
- [13] US Department of Energy, "Radiation Protection of the General Public and the Environment", 10CFR834, Federal Register (1993).

- [14] California Code of Regulation (CCR), Title 17, Public Health, Division 1, Chapter 5, Subchapter 4, Group 3, Article 30287 (1994).
- [15] A. Fassò, A. Ferrari, P.R. Sala, "Total Giant Resonance Photonuclear Cross-sections for Light Nuclei: A Database for the FLUKA Monte Carlo Transport Code", Proceedings of the Third Specialists Meeting on Shielding Aspects of Accelerators, Targets and Irradiation Facilities (SATIF-3), Tohoku University, Sendai, Japan, 12-13 May 1997, p. 61, OECD/NEA (1998).
- [16] K. Tesch and H. Dinter, "Production of Radioactive Nuclides in Air Inside the Collider Tunnel and Associated Doses in the Environment", DESY Internal Report DESY-D3-88, January (1998).
- [17] M. Huhtinen, "Determination of Cross-sections for Assessments of Air Activation at LHC", CERN Internal Report CERN/TIS-RP/TM/96-29 (1997).
- [18] US Department of Energy, Occupational Radiation Protection, 10CFR835, Federal Register, Final Rule, November (1998).
- [19] B. Parks, CAP88 PC Code (Version 1), US Department of Energy, Germantown, MD (1992).
- [20] 40CFR61, National Standards for the Emission of Radionuclides Other than Radon from Department of Energy Facilities (NESHAPS), Code of Federal Regulation, Subpart H (1989).

RADIATION DAMAGE TO ELECTRONICS IN THE BEAM TUNNEL OF THE NEXT LINEAR COLLIDER

S. Roesler, J.C. Liu and S.H. Rokni
Stanford Linear Accelerator Centre
Stanford, CA 94309, USA

Abstract

Radiation damage to electronics in the linac tunnel of the Next Linear Collider due to ionising and non-ionising effects has been estimated with detailed FLUKA simulations. Results for total dose deposited in silicon and for displacement damage by neutrons, protons and charged pions are presented. It is shown that non-radiation-hard electronics could be severely damaged unless sufficiently shielded against radiation. A scenario is proposed in which the electronic components are located in niches in the beam tunnel wall which are shielded by layers of polyethylene.

Introduction

Due to beam losses along the accelerator structures in the main linac tunnel of the Next Linear Collider (NLC) [1] showers of secondary particles – predominantly electrons, positrons, photons and neutrons – will be created. Any mechanical or electrical component installed in the beam tunnel will therefore be exposed to and possibly damaged by this secondary radiation.

In order to reduce the damage to electronic components different scenarios have been proposed. They typically differ in whether the electronics are installed inside the beam tunnel or outside, i.e. in parallel tunnels, sector alcoves, on the surface, etc. Advantages and disadvantages of each scenario have to be estimated carefully since in general large cost-factors are involved. Whereas the former solutions require the installation of radiation-hard electronics and/or local shielding, the latter solutions allow the use of conventional, non-radiation-hard electronics but involve the construction of additional tunnels and long cable runs.

The present study aims toward estimating the radiation damage to semiconductors installed at various locations inside the beam tunnel. In particular, the installation of the electronics in niches in the beam tunnel wall is proposed. Ionising and non-ionising cumulative effects on electronics are estimated by calculating the total dose delivered to silicon and the displacement damage by hadrons using the Monte Carlo code FLUKA [2]. Single event effects are not considered in this study.

The FLUKA calculations

The calculations were carried out with the '99 version of the particle interaction and transport code FLUKA. The program has been used to simulate the electromagnetic and hadronic particle cascade in the NLC beam tunnel and walls, as well as in various components and magnets which will be installed in the vicinity of the beam pipe. In the following, details of the calculations are discussed which are of importance for the present study.

The geometry and materials

The complex geometry of a 12 m long section of the beam tunnel has been modelled in detail with the ALIFE geometry editor [3, 4]. The geometry is described in a right-handed orthogonal system with its origin centred in the beam pipe at the front face of the tunnel section, as the vertical axis and z pointing down-beam. An elevation view of the geometry is shown in Figure 1. The installations close to the beam pipe include: two quadrupole magnets, two electronics racks supported by hollow iron cylinders underneath the magnets, a space frame, a support structure and three ion pumps mounted on hollow cylindrical structures above the space frame. A three-dimensional view of the FLUKA geometry is shown in Figure 2.

As can be seen in Figures 2 and 3, three cylindrical niches in the beam tunnel wall at a height of 90 cm above beam line level were also modelled. They are embedded in the wall under a horizontal angle of 45 degrees backwards, i.e. against the direction of the beam, and have a length of about 70 cm. Two different diameters were studied: 15 cm and 30 cm (Figure 3 shows the 15 cm niches). In both cases Niche 2 was shielded by a layer of polyethylene of 7.5 cm thickness.

Three locations for electronics installations were considered (see Figure. 3 and 4): (i) at the ion pumps above the beam line; (ii) on racks below the magnets; and (iii) in the tunnel-wall niches. In addition, the effect of shielding on the damage levels at the pump and rack locations was studied by

Figure 1. Vertical section through the geometry of the NLC beam tunnel used in the FLUKA calculations

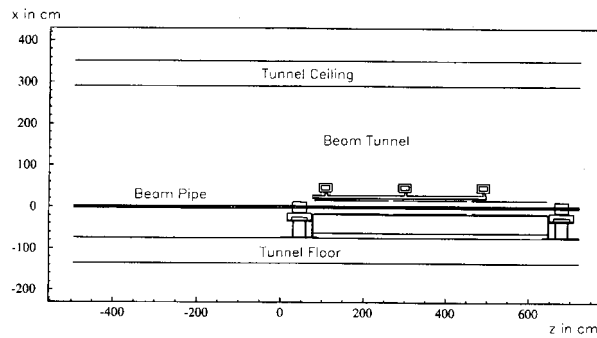


Figure 2. Three-dimensional representation of the FLUKA geometry created using FLUKACAD [5] and AutoCAD. In this view the z axis is pointing from the right to the left.

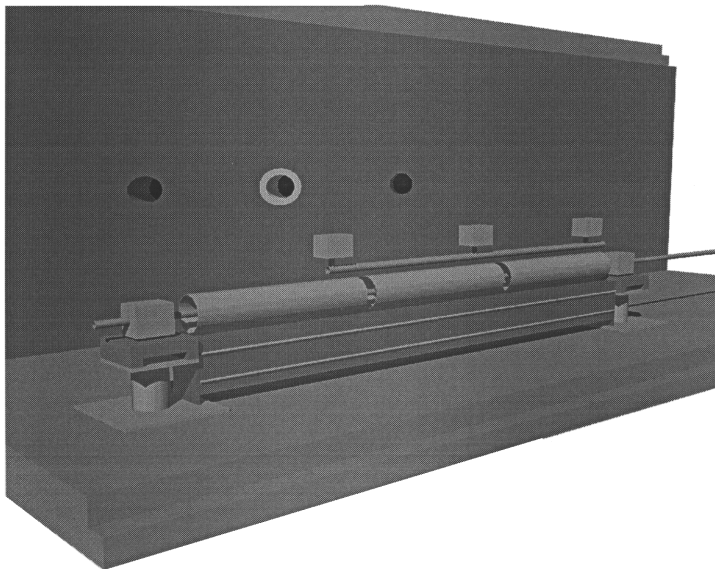


Figure 3. Horizontal section through the geometry of the niches used in the calculations (left figure). The set-up with niches of a diameter of 15 cm is shown. Niche 2 (right figure) is shielded by a layer of polyethylene.

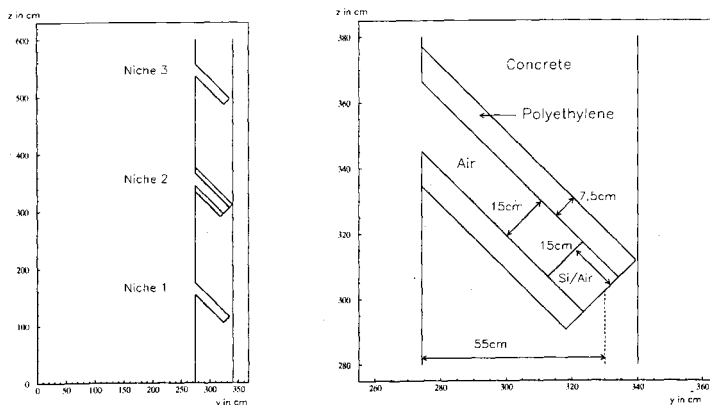
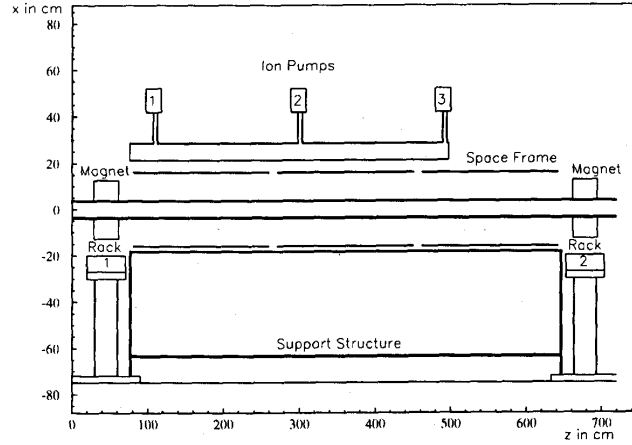


Figure 4. Vertical section through the simulated beam line installations. The three ion pumps and two racks were assumed to be possible locations for electronics.



assuming the pumps to be completely enclosed by 5 cm of lead and the racks to be covered by 10 cm of lead from the front, top and back. This set-up, shown in Figures 1 and 2, will be referred to below as “shielded” whereas the one without additional lead shielding (Figure 4) as “unshielded”. In the case of the niches the electronics was assumed to be located within the last 15 cm at the end of each niche (see Figure 3).

In order to estimate the total dose delivered to semiconductors, both the pumps and racks consisted completely of silicon. Similarly, in the niches 15 cm long silicon cylinders with the same diameter as the one of the niches were used.

Calculated quantities

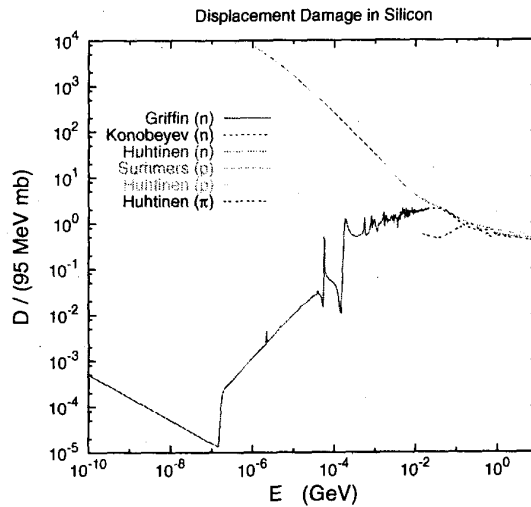
The damage by ionising radiation was estimated by calculating the total dose (electromagnetic and hadronic) to silicon at the respective locations in the tunnel.

Displacement damage is proportional to the non-ionising energy loss (NIEL) of a particle in the semiconductor lattice and can be expressed in terms of a displacement damage function $D(E)$. In order to characterise the damage efficiency of any particle for a given energy E , the values of D are usually normalised to the ones for 1 MeV neutrons (95 MeV mb). Figure 5 shows a compilation of damage efficiency functions for silicon [6,7] which are widely used to estimate radiation damage at LHC experiments (see for example [8]) and were also applied in this work. These data were implemented as a FLUKA user subroutine. This allowed to fold the hadron fluence Φ with the 1 MeV neutron displacement damage function:

$$\Phi_{\text{eq}}^{\text{1MeV}} = \int dE \frac{D(E)}{95\text{MeVmb}} \Phi(E) \quad (1)$$

and to score it in a three-dimensional mesh for any location in the NLC beam tunnel. The quantity $\Phi_{\text{eq}}^{\text{1MeV}}$ (in units of $\text{cm}^{-2} \text{s}^{-1}$) can be considered as the equivalent 1 MeV neutron fluence producing the same bulk damage.

Figure 5. Silicon displacement damage functions for neutrons, protons and pions [7] (see also [6] and references therein). Values are normalised to the displacement damage by 1 MeV neutrons (95 MeV mb).



Energy thresholds and biasing

In order to save CPU-time energy thresholds for the transport of electrons and photons in the displacement damage calculations were set higher than in the dose calculations. Since in the former calculations only the hadronic cascade was of interest the threshold for electron/positron transport was set to 20 MeV and the one for photon transport to 6 MeV, which corresponds approximately to the lower energy threshold for giant dipole resonance interactions. For dose calculations the thresholds were lowered to 1 MeV and 100 keV for electrons/positrons and photons, respectively.

Full leading particle biasing was activated in electromagnetic processes. Photonuclear interactions were biased with a reduction factor of 0.02 for the inelastic interaction length of photons. Particle splitting by region importance biasing was used in the concrete wall around the niches in order to enhance the statistical significance of the results in the niches.

Loss scenarios

Two beam-loss scenarios were considered: continuous losses of 500 GeV electrons over the full length of the beam pipe section (line source) and point losses at certain longitudinal locations in the pipe (point source). Whereas the former represents beam losses continuously occurring during normal operation the latter represents cases of mis-steered beam. In the calculations, the primary 500 GeV electrons were assumed to move parallel to the z -axis in positive z -direction hitting the accelerator irises at a distance from the z -axis of 0.8 cm.

Concerning the lost beam power the following assumptions were made: A power of 1.4 W is lost continuously per meter for 10 years and 300 days of NLC operation per year. This value was obtained in a study [9] from measurements combined with FLUKA calculations for the SLC linac tunnel which were scaled to the NLC beam power of 10 MW. Estimates for the maximum power which can be lost at a point are not available at present. In order to allow easy scaling the arbitrary assumption of a loss of 1 W was made.

Damage to electronics near the beam line

Results for the total dose deposited in silicon at the locations of Rack 2 and Pump 2 (see Figure 4) are given in Table 1. Note that results are average values for rather large silicon volumes (as compared to the size of electronics) of 2 106 cm³ for the pump and 20 022 cm³ (27 540 cm³) for the shielded (unshielded) rack and the actual dose value might therefore be underestimated due to self-attenuation in the silicon.

Table 1. Total dose to silicon at the location of Rack 2 and Pump 2. The second row under “Continuous loss” gives the values integrated over 10 × 300 days of NLC operation.

Rack 2		Unshielded	Shielded (10 cm Pb)
Continuous loss	Gy/h	2.6 ± 0.1	(2.4 ± 0.4) × 10 ⁻³
	Gy	1.9 × 10 ⁵	170
Point loss (z = 620 cm)	Gy/h	3.0	–
Pump 2		Unshielded	Shielded (5 cm Pb)
Continuous loss	Gy/h	1.0 ± 0.1	0.02 ± 0.01
	Gy	7.2 × 10 ⁴	1 600
Point loss (z = 200 cm)	Gy/h	0.3	–

The equivalent 1 MeV neutron fluence Φ_{eq}^{1MeV} was scored for neutrons, protons and charged pions in a mesh covering the whole tunnel section with a bin-size of 10 cm × 10cm × 10 cm. Figure 6 shows the results for neutrons for a vertical section through the beam tunnel containing the beam pipe. Values are averaged over 20 cm in y, i.e. over two bins in y from y = -10 cm to y = 10 cm. At any location shown the values have to be interpreted as the displacement damage a silicon material (e.g. semiconductor) would experience over ten years at that location. Studying the variation along z (keeping x fixed at, for example, 100 cm) it can be observed that the values increase (decrease) for z < -200 cm (z > 500 cm). This can be explained by the fact that only losses over a 12 m long section of the beam line were considered. Hence, contributions from losses upstream/downstream of the considered section are missing at locations z < -200 cm (z > 500 cm). Values vary from about 1 × 10¹⁴ cm⁻² close to the beam pipe to 5 × 10¹² cm⁻² underneath the tunnel ceiling. At the locations of the pumps and racks (shielded scenario) the 1 MeV neutron fluence is about 2 × 10¹³ cm⁻² and 4 × 10¹³ cm⁻², respectively. Displacement damage due to other hadrons is negligible as compared to that by neutrons (two orders of magnitude lower).

Damage to electronics in the niches

Dose to electronics in the niches

As mentioned above, in order to estimate the dose to electronics to be installed in the niches the last 15 cm of the niches were assumed to consist of silicon (see Figure 3). The corresponding silicon volumes are 2 651 cm³ and 10 603 cm³ for the 15 cm and 30 cm diameter niches, respectively. Dose values for the three niches and the two different diameters are listed in Table 2. The quoted errors reflect only the statistical uncertainties of the calculations.

Comparing the three values for either of the two diameters to each other it can be seen that the value for Niche 1 is lowest. This can be explained by the fact that most of the dose (> 90%) is deposited by the electromagnetic cascade which is strongly peaked in forward direction. Doses for

Figure 6. Displacement damage by neutrons in silicon for a loss of 1.4 W/m and 10×300 days of operation. Values are given for a vertical section through the NLC main linac tunnel containing the beam pipe.

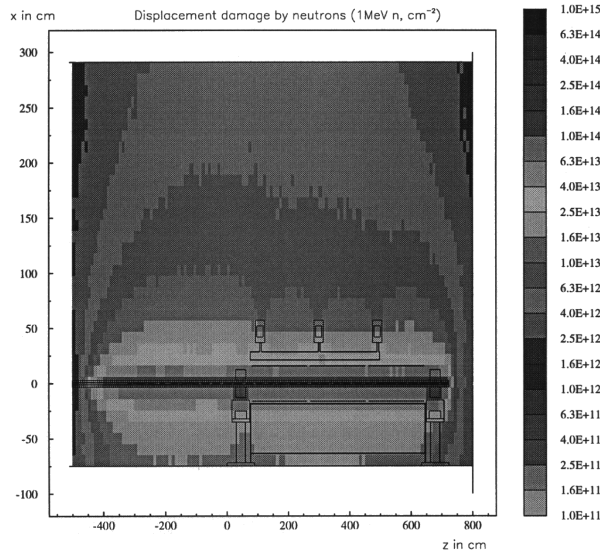


Table 2. Total dose deposited in silicon in the three niches. Values are given for a continuous loss of 1.4 W/m and 10×300 days of operation. Units are in Gy.

Diameter	15 cm		30 cm	
	Value	Error (stat.)	Value	Error (stat.)
Niche 1	33.0	15%	29.0	11%
Niche 2	56.0	13%	47.0	8%
Niche 3	38.0	9%	45.0	12%

Niche 1 are therefore underestimated because contributions from primary electrons lost upstream of the considered beam pipe section are missing. Furthermore, the energy deposition in Niche 2 is the highest of the three niches. This is somewhat misleading because the polyethylene around Niche 2 replaces what is concrete in the cases of the other two niches. Since concrete has a density which is about 2.5 times higher than that of polyethylene, replacing concrete by polyethylene effectively results in a reduction of the attenuation of the cascade component penetrating through the concrete.

Comparing the results for the two diameters to each other one would at first expect the doses to be larger the larger the diameter of the opening is. In contrast, the results are comparable to each other within their statistical uncertainties. This can be attributed to an artefact of averaging over the silicon cylinder and of keeping in addition the axes of the niches at the same locations. Due to the forward-peaked electromagnetic cascade the contribution to the total dose from particles penetrating through the concrete as compared to those streaming directly through the opening is therefore significant. Hence, doubling the diameter of the opening has a relatively small effect on the total dose. On the other hand, by increasing the diameter of the silicon cylinder and keeping the axis at the same place part of the additional silicon is now closer to the wall surface and part is deeper in the wall effectively leading to the same average doses.

As already mentioned above, the fact that the values quoted in Table 2 were obtained by averaging over rather large silicon volumes results in an underestimation of the dose to electronics which are of much smaller sizes due to self-attenuation in the silicon. Self-attenuation can however be corrected for if it is known for silicon. Here it is assumed that silicon and concrete have similar properties so that the dependence of energy deposition in the concrete wall around the niches on the depth calculated with FLUKA can be used which decreases exponentially with depth with a slope of 0.063 cm^{-1} . Assuming furthermore that the location inside the silicon cylinder which corresponds to the average value is shielded by at most 15 cm of silicon, the resulting correction factor would be $e^{0.063 \text{ cm}^{-1} \times 15 \text{ cm}} = 2.6$. Using this factor the actual dose delivered to an electronic component in Niche 2 (30 cm diameter) is $2.6 \times 47.0 \text{ Gy} = 122 \text{ Gy}$.

Displacement damage

Figures 7 and 8 show the results of the FLUKA calculations for Niches 1 and 2, respectively. In contrast to the dose calculations there was no need for the silicon volumes and the niches were left empty (i.e. the silicon was replaced by air). The equivalent 1 MeV neutron fluence caused by neutrons was scored in three meshes around the three niches with bin-sizes of $2 \text{ cm} \times 2 \text{ cm} \times 2 \text{ cm}$. The results are shown for horizontal sections and are averaged over 12 cm in x (i.e. vertically), from $x = 87 \text{ cm}$ to $x = 99 \text{ cm}$ (cf. the niches are centred at $x = 92.7 \text{ cm}$).

Two sources of radiation contribute to the displacement damage in the niches: (i) radiation penetrating through the shielding wall and (ii) radiation streaming through the niche openings. First of all it can be seen that the present design of the niches reduces the displacement damage by roughly an order of magnitude, from about $5 \times 10^{12} \text{ cm}^{-2}$ at the entrance to about $5 \times 10^{11} \text{ cm}^{-2}$ at the innermost locations. Furthermore the larger the diameter the bigger the contribution from neutrons steaming directly through the opening, and also the bigger the contribution through the concrete. The latter, of course, is due to the fact that the niche axes were kept at the same positions and only the diameter was changed. This causes the effective concrete shield to be thinner for the larger diameter providing less attenuation for neutrons.

Figure 7. Displacement damage by neutrons in silicon for Niche 1 (left figure: 15 cm diameter, right figure: 30 cm diameter) and a loss of 1.4 W/m during 10×300 days of operation.

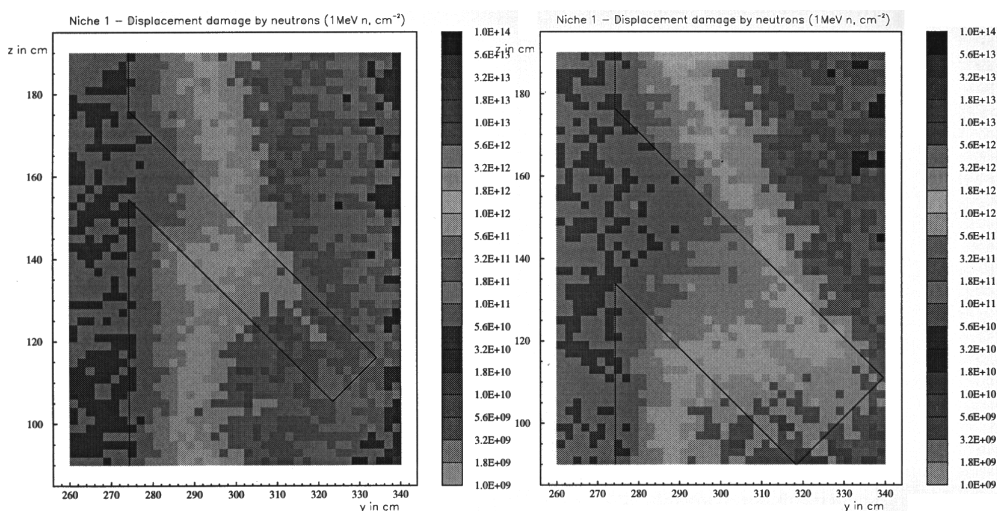
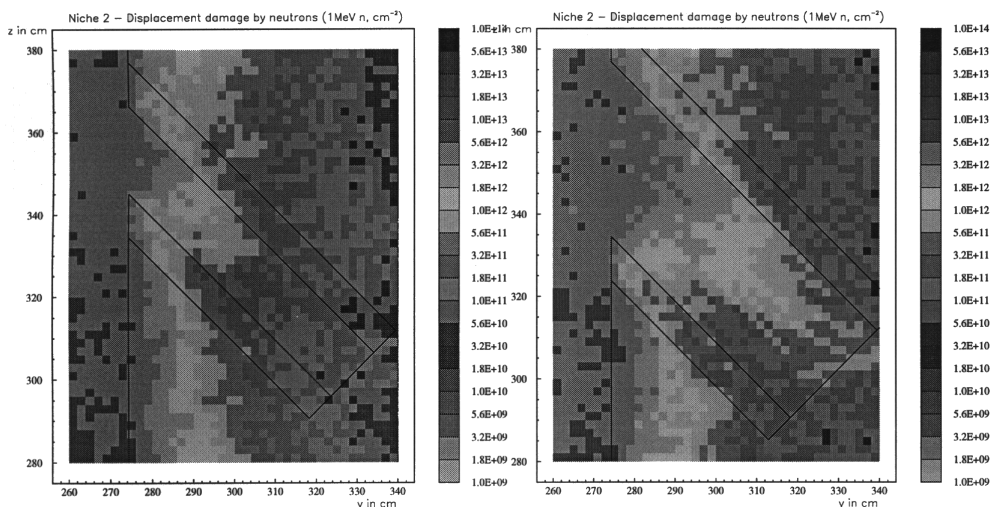


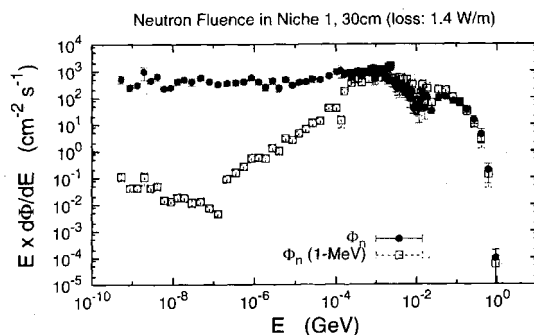
Figure 8. As in Figure 7, here for Niche 2



From a comparison of Figures 7 and 8 the effect of the polyethylene layer (thickness: 7.5 cm) can be seen. Whereas it is rather efficient in case of the 15 cm diameter, for the 30 cm diameter niche it only provides a “shadow” of about 7 cm on the side of the niche closest to the tunnel and its effect is compensated by the contribution steaming through the opening further inside.

In order to estimate the average displacement damage a silicon semiconductor might experience in these niches, values were averaged over the innermost 15 cm of each niche and the whole diameter. As an example, the average spectral neutron fluence rates obtained for Niche 1 and a diameter of 30 cm is shown in Figure 9. The spectral fluence rates have the typical shape of neutron spectra behind concrete shields: a $1/E$ behaviour below 1 MeV, a peak at about 1 MeV due to nuclear evaporation processes and a peak at about 80-100 MeV. The latter is due to the interplay of a decreasing (with increasing energy) inclusive neutron production spectrum with a mean free path distribution which has a broad minimum around 100-300 MeV and a steep decrease towards larger energies. In order to study which neutron energies cause most of the displacement damage the fluence rate in each energy bin was multiplied by the respective value $D(E) = 95 \text{ MeV mb}$ of the damage efficiency function (see Figure 5). This gives the equivalent 1 MeV neutron spectral fluence rates $\Phi_n(1 \text{ MeV})$ which are also shown in Figure 9. It follows that low energy neutrons with energies below about 100 keV are relatively unimportant and most of the damage is caused by neutrons of higher energies (1-100 MeV).

Figure 9. Neutron energy spectra in niche 1 for the 30 cm diameter and a continuous beam loss of 1.4 W/m (circles). In addition, the energy spectra multiplied with the silicon displacement damage function (see Figure 5) are given (squares).



Integrating $\Phi_n(1 \text{ MeV})$ over all energies and over 10 years of operations yields the values listed in Table 3. As mentioned above the values for Niche 3 underestimate the actual values since losses downstream of the simulated tunnel section that would also contribute to the fluence in that niche are not considered. Those are low energy neutrons mainly streaming in a backward direction directly through the niche opening. Therefore, the difference between Niches 1 and 3 is more pronounced for the larger (30 cm) opening. The differences between the values for Niche 1 and 2 are due to the polyethylene layer at Niche 2 which reduces the equivalent 1 MeV neutron fluence by about a factor of 1.8. It should again be emphasised that these values are *averages* over rather large volumes and that local values can be higher or lower by a factor of two as can be seen in Figures 7 and 8.

Table 3. Equivalent 1 MeV neutron fluence $\Phi_{\text{eq}}^{1\text{MeV}}$ in silicon for neutrons at the locations of the three niches. Values are given for a continuous loss of 1.4 W/m and 10×300 days of operation. Units are in cm^{-2} .

Diameter	15 cm		30 cm	
	Value	Error (stat.)	Value	Error (stat.)
Niche 1	2.5×10^{11}	12%	7.4×10^{11}	7%
Niche 2	1.3×10^{11}	12%	4.1×10^{11}	9%
Niche 3	2.1×10^{11}	12%	4.8×10^{11}	6%

Conclusions

The present study provides estimates for the radiation damage to electronics in the main linac tunnel of the NLC due to cumulative effects. Total doses delivered to silicon and equivalent 1 MeV neutron fluences are calculated with FLUKA for different locations in the tunnel. Results are given for continuous losses as well as point losses and are normalised to lost beam powers of 1.4 W/m and 1 W, respectively. Whereas the former value is based on measurements performed at the SLC linac the latter value of 1 W is arbitrarily chosen in order to allow a convenient scaling for occasional mis-steering scenarios.

During 10 years of 300 days of operation of the NLC electronics installed close to the beam line might receive a total dose of more than 200 kGy which can only be reduced by significant lead shielding. For example, a shielding thickness of 10 cm reduces this value for Rack 2 by about three orders of magnitude.

On the other hand, the average dose values to silicon in the niches are only of the order of 50 Gy. Realistic (surface) dose values may reach 150 Gy. These values are mainly due to energy deposition by electromagnetic particles and could be reduced by additional lead shielding. The equivalent 1 MeV neutron fluence is estimated to be about $7.4 \times 10^{11} \text{ cm}^{-2}$ for a 30 cm diameter niche and $2.5 \times 10^{11} \text{ cm}^{-2}$ for a 15 cm diameter niche. A layer of 7.5 cm polyethylene reduces these values by about a factor of two. No attempt has been made to estimate single-event effects [10].

Acknowledgements

The authors are grateful to Alfredo Ferrari for providing the FLUKA code, as well as to Martin Breidenbach and Alberto Fassò for many stimulating discussions. This work was supported by the Department of Energy under contract DE-AC03-76SF00515.

REFERENCES

- [1] The NLC Design Group, “Zeroth-order Design Report for the Next Linear Collider”, SLAC Report 474 (1996).
- [2] A. Fassò, A. Ferrari, J. Ranft and P.R. Sala, “New Developments in FLUKA Modeling of Hadronic and EM Interactions”, in Proceedings of the Third Workshop on Simulating Accelerator Radiation Environments (SARE-3), KEK, Tsukuba, Japan, p. 32 (1997).
- [3] A. Morsch, “ALIFE: A Geometry Editor and Parser for FLUKA”, November (1997).
- [4] A. Morsch and S. Roesler, “Radiation Studies for the ALICE Environment Using FLUKA and ALIFE”, in Proceedings of the Fourth Workshop on Simulating Accelerator Radiation Environments (SARE-4), Knoxville, Tennessee, USA, p. 229 (1998).
- [5] H. Vincke, “Flukacad/Pipsicad: Three-dimensional Interfaces Between FLUKA and AutoCAD”, these proceedings.
- [6] G. Lindström, M. Moll and E. Fretwurst, “Radiation Hardness of Silicon Detectors – A Challenge from High-energy Physics, *Nucl. Instrum. Meth.*, A426 (1999), 1.
- [7] M. Huhtinen, private communication (2000). The data tables were downloaded from the WWW site (<http://sesam.desy.de/~gunnar/Si-dfuncs-general.html>).
- [8] P.A. Aarnio and M. Huhtinen, “Hadron Fluxes in Inner Parts of LHC Detectors”, *Nucl. Instrum. Meth.*, A336 (1993), 98.
- [9] S. Rokni, J.C. Liu and S. Mao, “Preliminary Estimates of the Radiation Levels Inside the Next Linear Collider Linac Tunnel”, SLAC Radiation Physics Note RP-98-14 (1998).
- [10] M. Huhtinen and F. Faccio, “Computational Method to Estimate Single Event Upset Rates in an Accelerator Environment”, submitted to Elsevier Preprint (see the following site: <http://atlas.web.cern.ch/Atlas/GROUPS/FRONTEND/radhard.htm>).

CALCULATION OF HADRON YIELDS AROUND THICK TARGETS AND DOSES BEHIND CONCRETE SHIELDING OF HIGH-ENERGY ELECTRON ACCELERATORS

A. Leuschner, H. Dinter, K. Tesch

Deutsches Elektronen-synchrotron DESY, Hamburg, Germany

D. Dworak, J. Loskiewicz

Institute of Nuclear Physics, Cracow, Poland

Abstract

The field of neutrons, protons and pions produced by high-energy electrons hitting thick targets is studied by means of the FLUKA Monte Carlo code. Particle spectra and dependencies of fluences on primary energy (1-250 GeV), on angle (20-150°) and on target mass number are calculated. As an example the total number of low energy neutrons and of high-energy neutrons per electron are given. The attenuation of the total hadron dose equivalent in concrete and dose ratios of the main components are calculated. All results are parameterised and expressed by simple formulae.

Introduction

Monte Carlo codes have proved to be the most important tools in calculating particle production and shielding. With modern computers significant results can be gained even in complicated geometries and moderately thick shieldings up to the highest primary energies. However, the effort in using comprehensive code systems is considerable and computing times are always high. Therefore it is desirable to have simple formulae at hand for cases in which the actual situation can be approximated by a simplified geometry. In many cases this procedure is sufficient for existing or future accelerator shielding design, and more accurate calculations may be unnecessary in view of the fact that very often the accuracy of calculated doses does not depend on any calculational method but on the insufficient knowledge of the number of absorbed primary particles. Such formulae can be derived from Monte Carlo calculations.

Formulae of this kind are available for calculation of hadron doses at proton accelerators, see [1] for lateral shielding and [2] for longitudinal shielding, and papers quoted there. Other recent shielding calculations are given in [3] and [4]. Photon doses behind concrete shielding at proton accelerators are calculated in [5]. Numerous publications are addressed to neutron shielding, recent papers are [6,7].

For electron accelerators the lateral shielding of the electromagnetic component (e^\pm, γ) is studied in [8]. This dose depends strongly on target geometry, therefore several target configurations and materials were examined and the results condensed to formulae covering the angular range $5-140^\circ$. Electron-photon doses behind absorbers (in beam direction) are calculated in [9].

Missing are simple equations for calculating hadron doses around shielded targets at electron accelerators. For the past few years, the hadron production by photons has been incorporated in the well-known FLUKA Monte Carlo code [10]. We used this possibility to calculate dose equivalents of neutrons, protons and pions (and also of electrons and photons) around thick targets of different materials and their attenuation in concrete in the angular region $20-150^\circ$ for primary electron energies E_0 between 1-250 GeV. The results were parameterised to receive simple equations for calculating the total dose equivalent. Detailed results are compiled in an internal report [12].

Target geometry

When an electron beam hits a target, the produced electron-photon doses depend strongly on its shape, see e.g. [8], where several target geometries are studied. When dealing with hadron doses the target should be rather thick so that the maximum number of hadrons is produced whereas the internal absorption of hadrons is still low. This implies a target which is just large enough for the electromagnetic cascade to be fully developed.

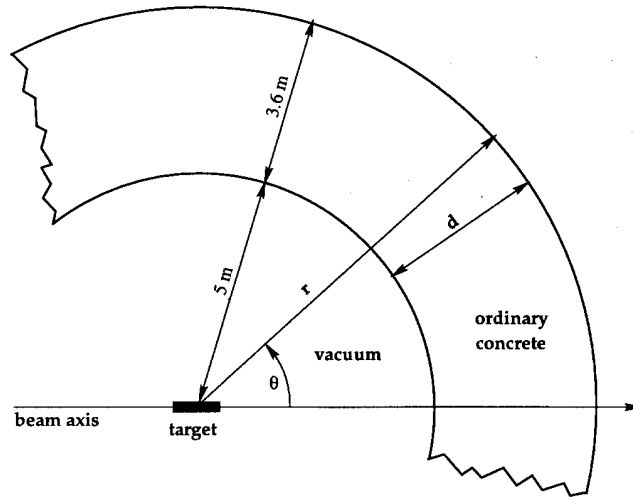
We used targets of cylindrical shape; the length is chosen so that 10% of the radially integrated energy is lost longitudinally, and the radius is chosen so that 10% of the longitudinally integrated energy is lost radially. The resulting dimensions for all primary energies are shown in Table 1, and the used cascade data are taken from [13]. These cylinders are hit on axis by a one-dimensional electron beam. Fluences and doses are calculated in a spherical geometry at large distances compared to the target dimensions where the target can be regarded as a point source of secondary radiation. Figure 1 contains a sketch of the geometry.

The calculated doses around these thick targets can be representative for cases when a beam hits an obstacle, e.g. a collimator or any other machine component because of beam mis-steering. They may be the basis for discussing worse-case scenarios.

Table 1. Dimensions of targets used in the calculations

Material	Radius [cm]	Length [cm] for a primary energy of					
		1 GeV	3 GeV	10 GeV	30 GeV	100 GeV	250 GeV
Al	12	70	85	100	112	125	137
Cu	4	14	17	20	22	24	26
Nb	5	12	15	16	19	20	22
Pb	2	7	7	7	8	8	8

Figure 1. Sketch of the spherical geometry used for the calculations with the target in the centre



Radiation field around targets

Before considering the attenuation of hadron doses in concrete we studied the radiation field around the targets in the total angular range for all four target materials and for all six primary energies (see Table 1). The FLUKA code was used in fully analogue manner to calculate fluences of neutrons, protons and pions. The boundary-crossing estimator was used. Low energy cuts were set at 1 MeV for electrons, positrons and photons, at 10 MeV for protons and pions, and neutrons were calculated down to thermal energy. Some of the results are presented in the following.

First we studied the shape of the fluence spectra of neutrons, protons and pions and their dependence on primary energy E_0 and on target material. A typical example is shown in Figure 2. At large angles (80-100°) the typical contribution of particles from the intranuclear cascade (around 100 MeV) and the low energy neutrons show up. It turns out that the shapes of all spectra at large angles (80-100°) are independent of E_0 and material in the considered primary energy range. This is also true at 20-30° if $E_0 \geq 30$ GeV, and for $E_0 \leq 10$ GeV the high-energy tail decreases as expected.

The dependence of the fluences on the primary energy is a simple power law $\Phi \sim E_0^a$; the exponent a is nearly the same for the angle-integrated fluences and for all fluences in a specified angular interval. For neutrons below 150 MeV the mean value a is 1.0 ± 0.06 , for neutrons of higher energies and for protons and pions a is 1.1 ± 0.06 . The values are higher than for incoming protons where a is 0.7 due to partitioning of the primary energy between the hadronic and the electromagnetic cascades [1].

Figure 2. Fluences of neutrons and protons per logarithmic energy interval per one 30 GeV electron, Cu target, distance 500 cm

Upper part: angular interval 20-30°. Lower part: angular interval 80-100°.

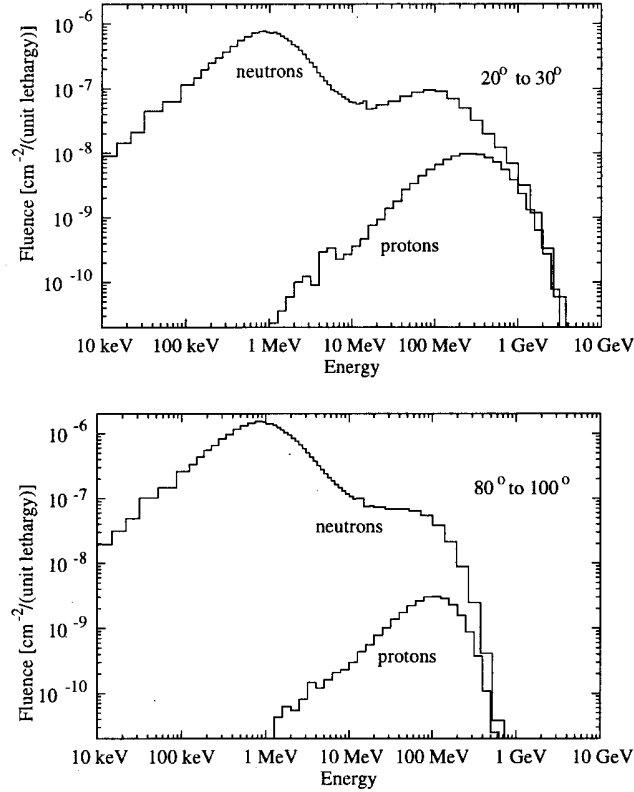


Table 2 demonstrates the dependence of hadron production on mass number A of the target for four hadron components. The expected increase of low energy ($E_n < 20$ MeV) neutron production with increasing A (see e.g. Ref. [14]) is somewhat reduced due to absorption in our thick targets. The production of high-energy neutrons and charged particles decreases with increasing A as a result of reduced radiation lengths within the electromagnetic cascade and enhanced intranuclear interactions at large A . The relative A -dependence agrees with measurements of neutrons above 25 MeV performed at $E_0 = 6.3$ GeV many years ago [15]. The variation in production numbers is small for $A > 90$, therefore we dropped shielding calculations for a lead target in section.

Table 2. Calculated numbers of particles produced by one 30-GeV electron in four targets with dimensions shown in Table 1

Target	A	Neutrons		Protons	Charged pions
		$E_n < 20$ MeV	$E_n > 20$ MeV	$E_p > 10$ MeV	$E_\pi > 10$ MeV
Al	27	2.2	0.28	0.020	0.035
Cu	64	4.2	0.19	0.011	0.018
Nb	93	8.2	0.16	0.008	0.013
Pb	207	8.2	0.14	0.012	0.012

The calculation of secondary particles around the targets gives the opportunity to compare the total number of produced neutrons with other calculations and with measurements. See Table 3, where the numbers of neutrons below and above 20 MeV per one 1 GeV primary electron are displayed; for high-energy neutrons the calculated data are derived from 10 GeV results and the experimental data from 6.3 GeV results, both scaled down to 1 GeV for comparison. The low energy data are in only moderate agreement. The experimental results seem to be higher than the calculated ones except in the recent work of Degtyarenko, *et al.* [16] in which a new nuclear fragmentation model was used. In this regard, a decision cannot be made, as new and better experiments are necessary. For comparison with the high-energy results we found only our rather old data [15], which we found somewhat reduced because of more recent information on the cross-section of the then-used activation reaction. Again the calculated values are smaller than the measured ones, about by a factor of 2.

Table 3. Number of neutrons produced per 1 GeV primary electron in thick targets

Target material	Neutron energy $E_n < 20$ MeV				$E_n > 20$ MeV		
	This work	Calculations		Measurements from compilation [13]	This work	Bathow [15]	
Swanson [20]		Mao, <i>et al.</i> [11]	Degtyar. [16]				
Al	0.074	0.10			Bathow 0.18	0.0088	0.02
Cu	0.14	0.19	0.16	~0.28	Bathow 0.35	0.0063	0.013
					DeStabler 0.19		
					Stevenson 0.33-0.45		
Pb	0.28	0.34	0.30		Bathow 0.41	0.0045	0.009

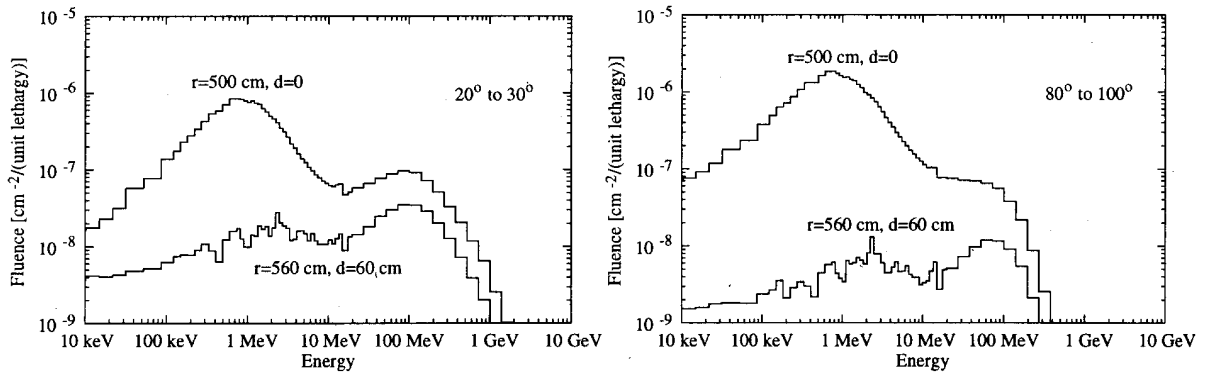
Doses behind concrete shielding

In order to calculate dose equivalents behind concrete shields and the associated dose equivalent attenuation coefficients, the targets described in Table 1 were surrounded by a spherical concrete shell with a thickness of 360 cm and positioned at a distance r between 500 cm and 860 cm from the midpoint of the target (see Figure 1). We could reduce the available parameter sets considerably according to the results of the preceding section. Only two primary energies were selected: $E_0 = 30$ GeV to receive results for $E_0 \geq 10$ GeV, and $E_0 = 3$ GeV for results with $E_0 \leq 10$ GeV. The change in spectra from the niobium target to the lead target is small, so we received the A -dependence for $A < 100$ from Al, Cu and Nb targets and took the niobium results as being representative of the $A > 100$ region. Four angular intervals $\Delta\theta$ were selected: 20-30°, 50-60°, 80-100° and 140-160°. One-way fluences of neutrons, protons and pions were calculated by the FLUKA code, and the hadron production cross-sections were artificially increased by a factor of 50. Dose equivalents were calculated from the fluences by multiplication with fluence-to-dose conversion factors; we used the same factors as in [1] to receive the maximum dose in a 30 cm phantom. In addition to hadrons, photon fluences with energies above 1 MeV and doses were also calculated in all cases. Examples of the neutron spectra are displayed in Figure 3 in a concrete depth $d = 60$ cm to show the shaping effect of the concrete.

Next we will discuss the attenuation of the total hadron dose and its components. An example of hadron dose equivalent attenuation is shown in Figure 4 for the four ranges of angle θ . A steep and a flat exponential decrease are observed. In Figure 5 the hadron dose is split into four components: neutrons above 20 MeV, neutrons below 20 MeV, protons and charged pions. One can see that at 90° the steeply decreasing component usually attributed to low energy neutrons is due to the charged

Figure 3. Neutron fluence spectra behind 60 cm concrete compared with the source spectra. Fluences are given per logarithmic energy interval per one 30 GeV electron, Cu target, distance $r = 500$ cm, concrete thickness $d = 0$ (source) and $r = 560$ cm, concrete thickness $d = 60$ cm.

Left part: angular interval 20-30°. Right part: angular interval 80-100°.



particles and to neutrons below 20 MeV. Incidentally the combined effect of both gives nearly the same dose equivalent attenuation coefficient $\lambda_1 = 28 \text{ g/cm}^2$ for all examined E_0 , A , and for angles θ with a pronounced steeply decreasing component (see below). This value is lower than 48 g/cm^2 recommended for low-energy neutrons [13], lower than 42 g/cm^2 measured with isotopic neutron sources [17], and somewhat lower than 33 g/cm^2 from other recent calculations in the lower GeV range [16]. The slowly decreasing hadron dose component is produced by high and low-energy neutrons being in radiation equilibrium behind concrete thickness larger than about 80 cm and by charged particles (at large angles by protons also in equilibrium with neutrons). The ratio of these components is of interest since in many cases only the dose of neutrons below 20 MeV is measured. Mean values are calculated for three targets, $E_0 = 3 \text{ GeV}$ and 30 GeV , $\theta = 25^\circ$ and 90° , $d > 80 \text{ cm}$ concrete. The dose equivalent ratio of neutrons above 20 MeV to dose of low-energy neutrons is 1.9 ± 0.2 , high-energy neutrons are the main neutron dose equivalent component in all considered cases. The dose ratio charged particles to low-energy neutrons decreases at small angles from 2.6 to 1.3 with increasing concrete thickness for $E_0 = 30 \text{ GeV}$, and from 1.4 to 0.3 for $E_0 = 3 \text{ GeV}$. At 90° it is 0.4 and independent of primary energy and shielding thickness. The charged particles are only protons at 90° and $d > 80 \text{ cm}$ concrete, at 25° pions contribute up to 200 cm concrete.

In Figure 5 the electron-photon dose H_γ is also shown. It is the dominating component behind thin concrete shielding. One should note, however, that H_γ depends strongly on target shape, so H_γ is better calculated from our earlier paper [8]. These earlier results agree with results of this work within a factor of 2 for roughly similar geometries. However, the hadrons deteriorate the purely exponential decrease of H_γ at larger thicknesses. The beginning of an equilibrium between hadron dose and photon dose is indicated in Figure 5 at a level of $H_\gamma/H_h \approx 0.02$.

The 90° curve of Figure 4 for high-energy neutrons and larger concrete thickness can be compared with our earlier paper [18] which is a compilation of earlier calculations and measurements of high-energy neutron doses. The attenuation coefficient is nearly the same, and the absolute values agree within a factor of 2. Another comparison can be made with the first hadron dose calculation behind thick shielding at electron accelerators [19]; here only star densities were calculated and a general ratio star density to dose assumed. At 25° and 55° a fair agreement with Figure 4 is achieved, and at 90° the values disagree because of a smaller attenuation coefficient in [19].

Figure 4. Attenuation of the total hadron dose equivalent in concrete at four angular intervals produced by one 30 GeV electron in the Cu target. The dose is multiplied by the squared distance from the target.

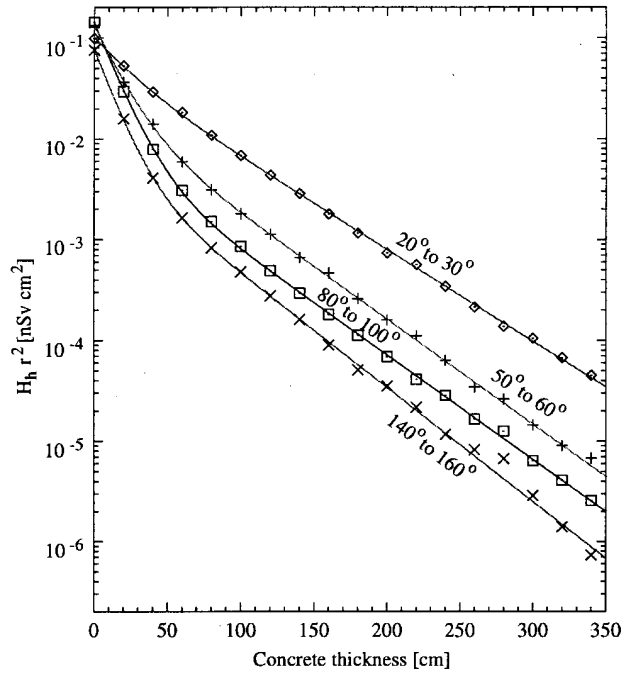
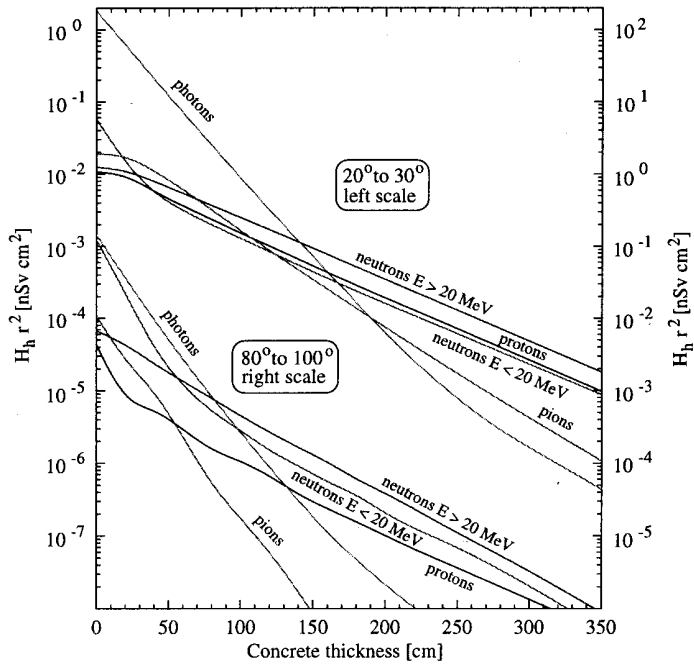


Figure 5. Attenuation of four hadron dose equivalent components in concrete at two angular intervals. The dose is multiplied by the squared distance from the target. $E_0 = 30$ GeV, Cu target. The electron-photon dose is added.



All total hadron dose equivalents per primary electron behind concrete shielding calculated up to $d = 360$ cm, for $E_0 = 3$ GeV and 30 GeV and for Al, Cu, and Nb targets can be expressed by:

$$H_h \cdot r^2 = a_1 \exp(-d/\lambda_1) + a_2 \exp(-d/\lambda_2) \quad (1)$$

d and r are concrete thickness and distance. The parameters $\lambda_{1,2}$ and $a_{1,2}$ were parameterised with the following results. λ_1 could be fixed for all cases (see above):

$$\lambda_1 = 28 \text{ g/cm}^2 \quad (2)$$

λ_2 depends weakly on angle θ but not on E_0 or mass number A .

$$\lambda_2 = [91 + 52 \exp(-\theta/33^\circ)] \text{ g/cm}^2 \quad (3)$$

The dependence of a_1 and a_2 on E_0 , A and θ was discussed qualitatively in the previous section.

$$a_1 = 0.29 A^{2/3} (E_0/1 \text{ GeV}) [0.33 + 0.67 \sin(\theta)] \text{ pSv cm}^2 \quad (4)$$

$$a_2 = 81 A^{-4/5} (E_0/1 \text{ GeV})^{1.1} [0.04 + 0.96 \exp(-\theta/24^\circ)] \text{ pSv cm}^2 \quad (5)$$

The hadron doses calculated from Eqs. (1)-(5) agree well with the original FLUKA results up to a primary energy of 250 GeV. The equations are valid for $\theta > 20^\circ$ and for $A < 100$, for $A > 100$ the results with $A = 100$ are a sufficient approximation.

If only neutron dose equivalents are of concern the best fits for a_1 and a_2 are:

$$a_1 = 0.24 A^{2/3} (E_0/1 \text{ GeV}) [0.33 + 0.67 \sin(\theta)] \text{ pSv cm}^2 \quad (6)$$

$$a_2 = 23 A^{-2/3} (E_0/1 \text{ GeV})^{1.1} [0.07 + 0.93 \exp(-\theta/31^\circ)] \text{ pSv cm}^2 \quad (7)$$

Neutron doses calculated with Eqs. (1)-(3), (6) and (7) can be compared with the most recent calculation of neutron doses for the energy range $E_0 = 0.2$ to 8 GeV [16]. The authors use the same fit as in Eq. (1). We compared both results for $E_0 = 3$ GeV. λ_1 , λ_2 and the θ -dependence of λ_2 are only slightly different from our results. The values of a_1 and a_2 of Ref. [16], however, are a factor 2.5 to 3 higher, as has already been discussed in the previous section and Table 3.

It is not easy to estimate the reliability of results received by Eqs. (1)-(7) quantitatively. The main reasons are the dramatic lack of published dose measurements behind shielding at high primary energies, the contribution of high-energy neutrons and (in several cases) of charged particles and the use of selected fluence-to-dose conversion factors in calculating dose equivalents. Guided by comparison with other calculations and by the considerations in the previous section we estimate an uncertainty of a factor of two in both directions.

Finally, we compare our λ_2 values with the corresponding values for primary protons calculated in [1] (see Table 4). For primary electrons the θ -dependence is weaker and the λ_2 are smaller at all angles. The reason is that the high-energy tail of the neutron dose spectrum from protons is shifted towards higher energies compared with that from electrons.

Table 4: Attenuation coefficients of hadron dose equivalents produced by 30 GeV electrons or 30 GeV protons hitting a copper target.

θ [degree]	λ [g/cm ²]	
	Primary electrons Eq. (3)	Primary protons Ref. [1]
20-30	115	150
30-40	108	139
40-50	103	137
50-60	101	127
60-70	99	123
70-80	96	113
80-100	94	110
100-120	94	103
120-140	92	117
140-160	92	113

Summary

A new generation of electron accelerators for high-energy physics as well as for the production of synchrotron radiation is under development. For a proper design of shielding requirements and for the assessment of environmental impacts the availability of reliable data for the production and the attenuation of secondary radiation is necessary.

In the present work such data were calculated by means of Monte Carlo simulations. For a set of thick targets of different materials the yields of hadrons (neutrons, protons, pions) were calculated in the range of 1-300 GeV beam energies and for emission angles between 20-150°. As a result, the total number produced neutrons agree well with data so far available.

The attenuation of secondary particles was studied in the same range of primary energies and angular emissions. An equilibrium radiation field of hadrons was found in concrete resulting in fluence spectra of independent shapes and attenuation coefficients being constant at least within the thickness of the shielding material concrete interesting for the praxis. This fact enables to parameterise the results in a way that hadron and neutron doses behind concrete may be easily obtained in the mentioned energy and angular regions.

Acknowledgements

All Monte Carlo calculations were performed at ACK CYFRONET AGH, Cracow, according to grant No. KBN/SPP/IFJ/065/1998 and No. KBN/S2000/IFJ/065/1998.

REFERENCES

- [1] H. Dinter, K. Tesch and D. Dworak, *Nucl. Instr. Meth.*, A384, 539, 1997.
- [2] K. Shin, H. Dinter and K. Tesch, “Longitudinal Attenuation of Dose Equivalent in a Concrete Shield for High-energy Proton Beams”, Internal Report DESY D3-85, 1996.
- [3] I.L. Azhgirey, I.A. Kurochkin, A.V. Sannikov and E.N. Savitskaya. *Nucl. Instr. Meth.*, A408, 535, 1998.
- [4] C. Birattari, E. DePonti, A. Esposito, A. Ferrari, M. Magugliani, M. Pelliccioni, T. Rancati and M. Silari, “Measurements and Simulations in High-energy Neutron Fields”, in SATIF-2, CERN, OECD/NEA, 1995.
- [5] D. Dworak, K. Tesch and J.M. Zazula, *Nucl. Instr. Meth.*, A321, 589, 1992.
- [6] Y. Nakane, Y. Sakamoto, K. Hayashi and T. Nakamura, “Intercomparison of Neutron Transmission Benchmark Analysis for Iron and Concrete Shields in Low, Intermediate and High-energy Proton Accelerator Facilities”, SATIF-3, Tokyo University Sendai, 1997, OECD/NEA.
- [7] H. Hirayama, “Intercomparison of the Medium-energy Neutron Attenuation in Iron and Concrete”, in SATIF-3, Tokyo University Sendai, 1997, OECD/NEA.
- [8] H. Dinter, J. Pang and K. Tesch, *Rad. Protection Dosimetry*, 25, 107, 1988.
- [9] H. Dinter, J. Pang and K. Tesch, *Rad. Protection Dosimetry*, 28, 207, 1989.
- [10] A. Fassò, A. Ferrari and P.R. Sala, “Designing Electron Accelerator Shielding with FLUKA”, in 8th Intern. Conf. Radiation Shielding, Arlington, 1994.
- [11] X. Mao, K.R. Kase and W.R. Nelson, *Health Physics*, 70, 207, 1996.
- [12] D. Dworak, J. Loskiewicz, H. Dinter, A. Leuschner and K. Tesch, “The Monte Carlo Calculated Spectra and Angular Distributions of Secondary Particles from 3, 30, 250 GeV Electron Interactions in Thick Al, Cu, Nb, and Pb Targets”, Report no. 1840/AP, Institute of Nuclear Physics, Krakow, January 2000.
- [13] Landolt-Börnstein, “Shielding Against High-energy Radiation”, *Numerical Data in Science and Technology*, Volume 11, Springer Verlag, 1990.
- [14] W.P. Swanson, “Radiological Safety Aspects of the Operation of Electron Linear Accelerators”, Technical Report Series 188, IAEA, Vienna, 1979.
- [15] G. Bathow, E. Freytag and K. Tesch, *Nucl. Phys.*, B2, 669, 1967.

- [16] P. Degtyarenko and G. Stapleton, "Parametrization for Shielding Electron Accelerators Based on Monte Carlo Studies", in Conf. Health Physics of Radiation-generating Machines, Health Physics Society, San Jose, 1997.
- [17] K. Tesch, *Particle Accelerators*, 9, 201, 1979.
- [18] K. Tesch, *Rad. Protection Dosimetry*, 22, 27, 1988.
- [19] A.Fassò, M. Höfert and A. Ioannidou, *Rad. Protection Dosimetry*, 38, 301, 1991.
- [20] W.P. Swanson, *Health Physics*, 37, 347, 1979.

SESSION III

High Intensity Medium-energy Accelerators

Chairs: D. Filges, H. Hirayama

COMPARATIVE STUDY OF THE DIRECT AND CONVERTER METHODS FOR HIGH FISSION YIELDS

D. Ridikas

CEA Saclay

F-91191 Gif-sur-Yvette Cedex, France

W. Mittig, A.C.C. Villari

GANIL

BP 5027, F-14076 Caen Cedex 5, France

Abstract

The aim of the considerations below is to estimate the orders of magnitude for the production of radioactive nuclear beams (RNBs) at GANIL with possible evolutions of the present accelerator complex within the next decade. This study was requested by the Conseil Scientific du GANIL. In this respect, the time scale considered is intermediate between long range plans such as Eurisol, a R&D programme that is just starting in a European collaboration, and the present SPIRAL facility, which should enter into operation at the end of 2000. In this context we consider and compare methods to produce ISOL beams by fission and/or low energy spallation with the main goal of reaching 10^{14} fissions/s in the RNB production target. Such RNBs would complement the present SPIRAL beams obtained by fragmentation of the projectile or the target, that are limited to light elements if high intensities are required. The coupled LAHET + MCNP + CINDER code system is used for simulations.

Introduction

Together with an increase in the accelerator power available, the new RNB targets will have to be designed to deal with high power densities. This is a problem of concern to a number of RNB facility concepts currently under consideration in various laboratories world-wide. One effective solution to this problem, as initially proposed by the Argonne National Laboratory group [1], is to decouple the heat dissipation from the nuclide production and release to the ion source. This can be achieved by stopping the primary beam on a converter target to produce an intense flux of neutrons to irradiate a secondary production target located behind the first one.

Here we consider and compare two main possibilities. One is neutron induced fission, in which the neutrons are produced in a converter from a primary proton or deuteron beam. The second method is close to the one used at CERN Isolde, where a high intensity proton beam directly hits a fissionable target. The energies for the primary beams were limited to 50 MeV for the first method, and to 200 MeV for the second, compatible with the time scale we intend to cover and without major modification of the GANIL accelerator complex.

All numerical calculations have been performed with a coupled LAHET + MCNP + CINDER code system described in more detail in Refs. [2-5].

The converter (C) method

Neutron yields: (d,xn) versus (p,xn)

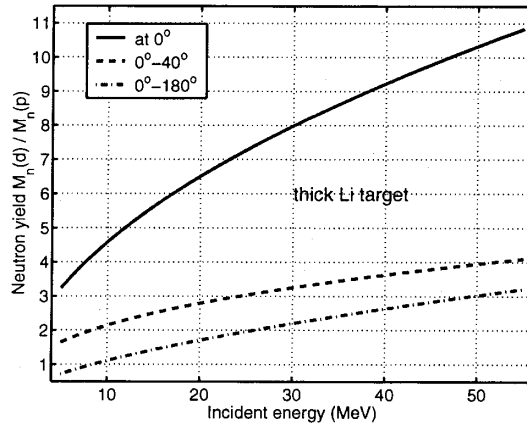
Extensive use has already been made of fast neutrons produced by bombarding light nuclei with deuterons or protons. As the choice of the targets between Li and Be, thermomechanical properties aside, there seems to be little basis for distinction. The forward neutron yields are similar [6]. For very intense primary beams (~1.0 MW), cooling requirements indicate the use of a liquid target, i.e. lithium (melting point 181°) rather than beryllium (melting point 1 287°). For this reason we will limit our discussion on neutron production via the d + Li and p + Li reactions only.

In Figure 1 we present the ratio of neutron yields from the d + Li reaction over p + Li reaction for thick Li target. It is clearly seen that for a given projectile energy the neutron yields at zero degrees (solid curve) are higher from the d + Li reaction than from p + Li. This difference increases with incident energy. The same holds for the average neutron energies at forward direction: more energetic neutrons are produced by deuteron induced reactions if compared to proton induced reactions [6]. Consequently the differences in neutron yields in the case of partially angle-integrated (dashed curve) and, furthermore 4 π -integrated yields (dashed-dotted curve) are less pronounced as clearly seen from Figure 1.

We note that high beam currents (> 10 mA) suggest the use of a linear accelerator, which means comparing protons and deuterons of equal energy. Figure 1 clearly shows that the total neutron yield from deuteron on lithium is 2-3 times higher than that from proton on the same target, i.e. deuteron is the better projectile. This final conclusion is even more convincing for the very forward neutron yields, which are actually of interest in this work. In this case the neutron production is favoured by deuterons by a factor of 4-10 (depending on incident energy).

Figure 1. Ratio of neutron yields from the d + Li reaction over the p + Li reaction as a function of the total incident energy

The neutron yields are extrapolated from Ref. [6] and references therein



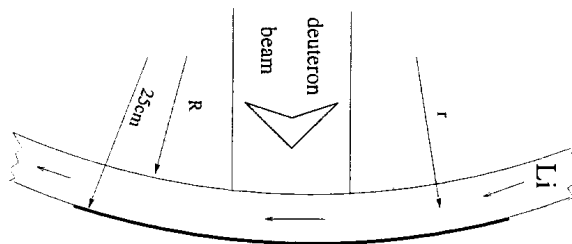
The target converter

Assuming a deuteron energy fixed by a proper match of the neutron-energy spectrum, the neutron yield can be increased linearly by increasing the deuteron beam current. We have chosen 1 MW as the maximum deuteron beam power we feel can be reached and deposited in the target within engineering constraints. The following discussion of a d-Li neutron source design is therefore addressed to a 28.6 MA, 35 MeV deuteron accelerator and a molten lithium target capable of dissipating the resulting 1 MW beam power.

An intensive study of target configuration that will withstand the 1 MW beam power deposited in the target has led to two possible designs [7,8]: one, a rotating Be wheel in a vacuum, cooled either by D₂O or lithium and the other, a fast flowing jet of lithium in vacuum. Of the two schemes, the rotating Be wheel has been rejected because of complexity, need for maintenance in a high radiation environment, and thermal and mechanical limitations. Therefore, the fast flowing lithium jet with an air-cooled heat exchanger was chosen for its simplicity and intrinsic reliability.

Figure 2 illustrates the principle. The accelerator-generated deuteron beam is directed toward a high-speed flowing jet of liquid Li. The Li flow passes through the beam interaction zone (defined by the beam size and shape), where it stops and absorbs the incident beam power and thus heats a portion of Li. The Li continues to flow to a drain channel in a tank where complete mixing occurs with the large volume of Li.

Figure 2. Schematic of a flowing lithium target interacting with a vertical deuteron beam



The studies in Ref. [9] show that the maximum temperature reached in the flowing lithium target can lead to film instabilities due to fast bubble growth (boiling). This situation could be avoided by providing the means to pressurise the flowing lithium sheet in its vacuum environment. Further investigation led to the idea of centrifugal force being the simplest approach to providing the pressure gradient in the flowing lithium [7]. If the liquid Li is ejected from its nozzle at velocity v , tangentially against a curved surface (see Figure 2), then the pressure P in (toor) at any point r will be:

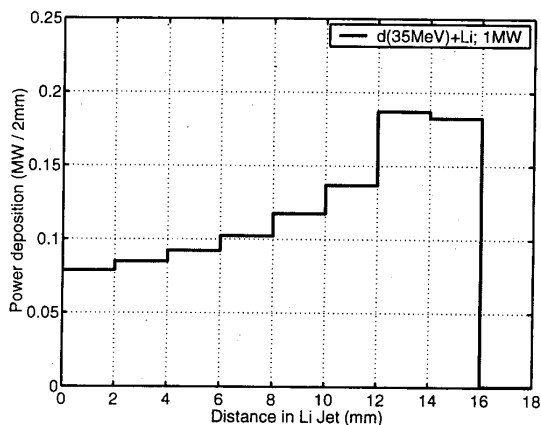
$$P(r) = 7.5 \times 10^{-3} \rho v^2 \ln r/R$$

where ρ is the density of the liquid, r is the major radius at $P(r)$ and R is the minor radius as shown in Figure 2. The target, then, will consist of a fast flowing liquid Li film, confined on three sides, between two vertical side plates and a curved vacuum window which separates the machine vacuum space from the experimental area. Due to the deuteron beam incident vertically on the target flowing Li is “attached” to the backside of the window simply by gravitational force in addition to the centrifugal force as discussed above.

The range of deuterons in the Li jet increases strongly with energy. Power density then increases substantially with decreasing deuteron energy. The Li jet thickness must be tailored to the deuteron’s initial energy to maximise neutron flux, minimise Li flow rate, and ensure the complete stopping of the incident beam. The amount of Li mass evaporated must be minimised to maintain vacuum integrity, reduce beam-vapour interaction, and minimise Li vapour deposition on accelerator and other components of the system. Higher deuteron energies could be favoured due to higher neutron yields. On the other hand, this would considerably increase the thickness of the flowing lithium, limiting its high performance (e.g. the range of 100 MeV deuterons in liquid Li is ~ 10 cm). One should also consider additional accelerator costs in the case of higher incident beam energies.

Figure 3 shows the energy deposition of 35 MeV (1 MW) deuteron beam in lithium. Varying the initial deuteron energy may be desirable to produce neutron spectra with different characteristics for a wide range of applications. As is discussed in more detail in [9], lower incident deuteron energies deposit their energy near the front surface, causing higher surface temperature and consequently a higher Li vaporisation mass. Therefore, higher incident deuteron energies are favoured. In addition, the thickness of the liquid lithium has to be slightly thicker than the actual stopping range of the deuterons in order to avoid the surface evaporation near the back surface of the target. Here the beam deposition power will be at the maximum as shown in Figure 3.

Figure 3. Beam power deposition of 35 MeV deuterons (28.6 mA) in liquid Li



At operating temperatures up to 400°C, stainless steel can be used for piping, valves, pumps, etc. in the loop with very little corrosion. Estimated temperatures of the lithium in the catch basin will not be higher than 300°C for liquid entering the target area at 200°C [7]. Further, the resulting flow rate also ensures that the maximum temperature at the hottest point in the film, near the end of the range of the 35 MeV deuterons at ~1.45 cm, does not exceed the saturated temperature of the lithium at that point of the film.

Based on the above discussion and Refs. [7,9], Table 1 lists the major Li target parameters. The expected neutron flux is of the order of 3×10^{14} n/s cm² in the forward direction at the backside of the target converter. We note that similar neutron fluxes are presently available only in the high flux nuclear reactors.

Table 1. Target converter parameters

Beam power/energy	1 MW/35 MeV
Beam dimension	3.82 cm diameter
Beam area	11.46 cm ²
Target cross-section	2.0 cm × 2.0 cm
Lithium flow rate	5.14 l/s
Lithium entrance/exit temperature	~200°C/~300°C

Finally, we add a few qualitative estimations concerning the liquid Li loop flow. With the target cross-section of 2 cm × 12 cm and 5.14 l/s of the liquid Li required for a power dissipation of 1 MW, it will be necessary to circulate ~18.5 m³/h of liquid lithium with its target velocity of 2.15 m/s. The bulk temperature of the lithium being ~300°C provides for a corrosion-free system. As such, the system will follow standard liquid-metal technology without the need for exotic materials. However, the “cleaning” of the Li lithium will be necessary due to its impurities (e.g. nitrogen [10]) as well as due to the d + Li reaction products. The major concern will be the production of radioactive elements such as tritium gas (T_{1/2} = 12.33 y) and ⁷Be (T_{1/2} = 53.29 d) as presented in Table 2. We estimate that nearly 50 µg of radioactive tritium gas will be produced during the irradiation period of 90 days (see Table 2 caption for irradiation conditions). On the other hand, the major auxiliaries needed for a lithium clean-up system have been thoroughly studied and can be fabricated (e.g. cold-trapping or hot-trapping units [10]) in order to remove lithium-deuteride and lithium-tritide which will be formed. Further detailed and quantitative analysis of the problematics as above is certainly needed.

Table 2. In-target activity of the pure ⁷Li target converter after 90 days of irradiation (28.6 mA deuterons of 35 MeV, i.e. 1 MW)

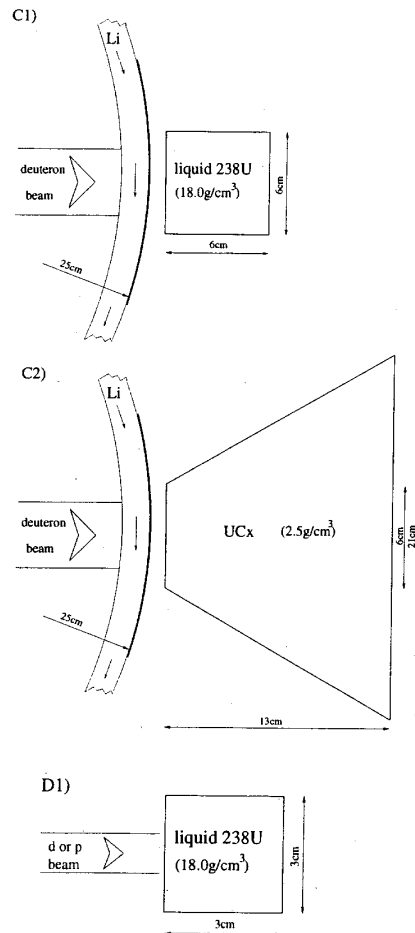
Cooling period	0 s	1 s	1 min	1 hour	1 day	14 days	30 days	90 days
³ H (Ci)	501	501	501	501	500	499	498	494
⁶ He (Ci)	11 477	4 860	0	0	0	0	0	0
⁸ Li (Ci)	347	152	0	0	0	0	0	0
⁷ Be (Ci)	4 189	4 189	4 189	4 168	4 135	3 491	2 835	1 299
Total (Ci)	16 513	9 701	4 689	4 687	4 635	3 991	3 333	1 793

The isotope production targets

Let us assume that the main goal for the future RNB factory is to reach fission rates of the order of $\sim 10^{14}$ fission/s. To obtain this number with a similar neutron source as above one needs to put a few kilograms of a fissionable material (e.g. liquid ^{238}U with $\rho = 18 \text{ g/cm}^3$). Another possibility is to use materials of much lower densities (e.g. UC_x with $\rho = 2.5 \text{ g/cm}^3$). In order to reach the wanted number of fissions in this case, one must keep a mass similar to that of the fissionable material. This leads to a less compact geometry of the production target, i.e. its volume increases considerably. Below we will present a few comparable examples of such target geometries to be used both with a target converter (neutron source as above) as well as a production target which interacts directly with the incident beam.

An example of the production target in its simplified geometry (cylinder) is presented in Figure 4-C1. Its length and radius have been adapted to the optimum fission rates depending on the neutron source performance. Figure 4-C2 shows a less compact geometry (cone) production target with $\rho = 2.5 \text{ g/cm}^3$. In both cases, $\sim 10^{14}$ fissions/s will result in $\sim 3 \text{ kW}$ fission power deposited in the production target. It should be noted that in the case of the converter method, the incident beam is decoupled from the production target, which now is heated only by “useful” fissions.

Figure 4. Flowing lithium target converter schematic (on the left) together with two possible production target geometries (C1 – cylinder and C2 – cone on the right). D1 represents a simplified production target (cylinder) based on the incident beam interacting directly with a fissionable material. All elements are symmetric along the beam axis.



The direct (D) method

In this particular case, when the incident beam hits the production target directly, it seems difficult to go much above the 10 kW limit power deposited in the target. The highest maximum value was obtained (~24 kW) and tested thermally by heating for the RIST target [11]. In Figure 4 we present a compact uranium cylinder (D1) which, with a combination of an incident deuteron beam, gives $\sim 10^{14}$ fissions/s and at the same time does not cross the “limiting” deposition of the beam power ~ 20 kW.

We limit our estimations to the maximum 200 MeV energy due to the following reasons:

- Higher incident energies would require thicker production targets due to increased stopping ranges of the projectiles.
- Fission cross-sections both for protons and deuterons saturate for energies higher than 100 MeV [12].
- The cross-section for certain fission yields (e.g. Ba, Zr, Ag) reaches its maximum around 200 MeV [13].
- 100 MeV per nucleon is still compatible with the present GANIL accelerator complex.

Comparison of the C and D methods

Tables 3 and 4 summarise the main beam and target characteristics for both converter and direct methods. We have also included protons in addition to deuterons as incident particles to have a quantitative comparison of the performance of both projectiles.

Table 3. Different projectile/target combinations to produce intensive RNB by the fission/spallation of heavy targets. In all cases 1×10^{14} fissions/s are expected.*

Scenario	Particle type	Energy	Min. primary beam power (current)	In-target power	Target type (material)
S1	d	35 MeV	196 kW (5.6 mA)	3.2 kW	C1 (liquid ^{238}U)
S2	p	35 MeV	525 kW (15 mA)	3.2 kW	C1 (liquid ^{238}U)
S3	d	35 MeV	560 kW (16 mA)	3.2 kW	C2 (solid UC_x)
S4	d	200 MeV	13.8 kW (69 μA)	17.0 kW	D1 (liquid ^{238}U)
S5	p	200 MeV	13 kW (65 μA)	16.2 kW	D2 (liquid ^{238}U)
S6	p	100 MeV	24.5 kW (245 μA)	27.7 kW	C1 (liquid ^{238}U)

* For different target types see Table 4.

Table 4. Different target types for the production of RNB by the fission/spallation reactions*

Target type	Density (g/cm^3)	Volume (cm^3)	^{238}U mass (g)	Geometry specification
C1	18.0	1 169	3 055	Cylinder ($r = 3$ cm, $l = 6$ cm)
C2	2.5	2 055	3 055	Cone ($r_1 = 3$ cm, $r_2 = 10.5$ cm, $l = 13$ cm)
D1	18.0	21	382	Cylinder ($r = 1.5$ cm, $l = 3$ cm)
D2	18.0	35	636	Cylinder ($r = 1.5$ cm, $l = 5$ cm)

* See Table 3 for details.

C – with converter, D– without converter (direct)

At low energies (~35 MeV) in the case of the C method, deuterons (Scenario 1) will require ~3 times lower beam intensities than protons (Scenario 2). At this point we refer to our discussion on neutron yields at forward direction. The use of UC_x production target even with deuterons (Scenario 3) will need higher beam intensities due to neutron characteristics inside the production target: carbon is known as an efficient moderator of neutrons. An interesting possibility in the case of the D method would be to use 200 MeV deuterons (Scenario 4) or protons (Scenario 5) at much lower incident beam power (~15 times) as compared to the C method. In this case deuterons are favoured since less uranium is needed to obtain the same number of fissions (compare D1 and D2 in Table 4). In our opinion, the question if ~20 kW beam deposition power on the production target can be handled still remains open. Finally, protons of 100 MeV already cross this limit (Scenario 6).

Fission yields

The in-target fission yields are presented in Table 5 for some isotopes and correspond to ~10¹⁴ fission/s in all three of the most attractive scenarios (S1, S3 and S4 as above). One has to keep in mind that these are in-target fissions, i.e. fission products still have to leave the production target in order to be really “useful”.

Table 5. Estimate of projected in-target fission yields.
The fission fragment intensities are normalised to a primary beam intensity which corresponds to ~10¹⁴ fissions/s in the production target.*

Beam	T_{1/2} (s)	Liquid U (S1) (at./s 6 mA p)	UC_x (S3) (at./s 18 mA p)	Liquid U (S4) (at./s 70 μA p)
⁹¹ ₃₆ Kr	8.57	3.2 × 10 ¹²	2.2 × 10 ¹²	1.1 × 10 ¹²
⁹² ₃₆ Kr	1.85	2.5 × 10 ¹²	1.8 × 10 ¹²	1.1 × 10 ¹²
⁹⁴ ₃₆ Kr	0.21	6.0 × 10 ¹¹	4.5 × 10 ¹¹	2.4 × 10 ¹¹
⁹⁷ ₃₇ Rb	0.17	2.2 × 10 ¹¹	3.4 × 10 ¹¹	1.1 × 10 ¹¹
¹¹⁷ ₄₇ Ag	72.8	6.7 × 10 ¹¹	4.6 × 10 ¹¹	1.1 × 10 ¹²
¹¹⁹ ₄₇ Ag	2.1	5.2 × 10 ¹¹	3.2 × 10 ¹¹	8.8 × 10 ¹¹
¹³² ₅₀ Sn	40.0	1.6 × 10 ¹²	1.2 × 10 ¹²	3.2 × 10 ¹¹
¹³³ ₅₀ Sn	1.44	5.3 × 10 ¹¹	4.1 × 10 ¹¹	1.1 × 10 ¹¹
¹³⁹ ₅₄ Xe	39.7	4.7 × 10 ¹²	3.8 × 10 ¹²	1.5 × 10 ¹²
¹⁴¹ ₅₄ Xe	1.73	2.5 × 10 ¹²	2.3 × 10 ¹²	5.9 × 10 ¹¹
¹⁴² ₅₄ Xe	1.22	1.3 × 10 ¹²	1.0 × 10 ¹²	2.9 × 10 ¹¹
¹⁴⁴ ₅₄ Xe	1.10	9.6 × 10 ¹⁰	7.4 × 10 ¹⁰	2.0 × 10 ¹⁰
¹⁴⁴ ₅₅ Cs	1.02	1.6 × 10 ¹²	1.3 × 10 ¹²	3.6 × 10 ¹¹

* See Tables 3 and 4 for details concerning the production targets for different scenarios.

It is clear that different fission fragments resulting from different target geometries will have different diffusion-effusion properties. Here we have considered the possibility of having solid UC_x and liquid U targets. The advantage of a liquid target compared with a solid one is its density. It is well known that liquid materials have better diffusion coefficients than solid ones, but the material to be

transversed is usually larger in the first case. This gives an overall efficiency of diffusion which is usually the best for very porous solid targets. In order to favour the fast diffusion in a liquid target, one could promote a fast convection of the medium. We have not yet reached a final agreement on the projected overall efficiency (i.e. release * delay * ion-source efficiency). It is expected to be around 10% for some elements with $T_{1/2} > 1$ s and around 1%-0.1% with $T_{1/2} < 1$ s. This means that the numbers in Table 5 have to be multiplied accordingly for the expected final RNB intensities.

Radioactivity management

Due to $\sim 10^{14}$ fissions/s a total activity of about 14 kCi is expected. Various parts of the installation will become highly radioactive. Hence, the management of this radioactivity is an important element in the design of the instrument. High radioactivity due to the noble gases and halogens will require a special treatment. Of course, one could fix the radioactivity at some places which are easy to shield or at some cooling places where the radioactivity will decay after irradiation. The aim of this report is beyond a detailed analysis of these activities and dose rates. Table 6 gives only the maximum activity of the source after 90 days of irradiation (see the case with a target type C2 from Tables 3-4). It is clear that this source will still be highly radioactive even after 90 days of cooling. Consequently a remote control system will be needed to dismount a used source, and to mount its replacement. We note separately that similar numbers were estimated in the case of the PIAFE [14] project where $\sim 10^{14}$ fissions/s were expected in the reactor driven RNB facility.

Table 6. In-target activity of the UC_x (case C2) ion source after 90 days irradiation by the use of a lithium converter interacting with 16 mA deuterons of 35 MeV

Cooling period	0 s	1 s	1 min	1 hour	1 day	14 days	30 days	90 days
Activity (kCi)	13.6	12.6	8.3	4.5	2.5	0.8	0.5	0.2

Towards the proton dripline

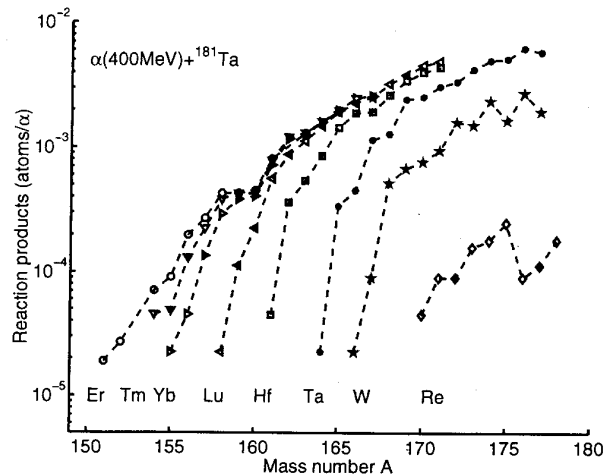
In order to produce nuclei on the proton-rich side of the mass valley, other reactions than nuclear fission should be explored. For example, having the accelerator facility with energies up to 100 MeV per nucleon (compatible with present GANIL accelerator complex), the proton rich nuclei could be efficiently produced with alpha induced reactions. The following reactions as $\alpha + Nb$, $\alpha + La$, $\alpha + Ta$ and $\alpha + Th$ would explore nearly entire proton dripline in the mass range of $A = 60-230$, where the data are sparse, and almost non-existent beyond $A = 84$.

In Figure 5 we present the isotopes produced in one of the reactions as above, namely $\alpha + Ta$ at $E_\alpha = 400$ MeV. Here only isotopes on the proton-rich side are shown. Similarly, by the use of targets with lower atomic numbers, the proton dripline could be searched in the lower mass region. More detailed and systematic calculations of the production of proton-rich nuclei would be very useful in this respect.

Conclusions

The results we presented show that very high fission yields may be obtained. The most efficient solution strongly depends on the target-ion source technology, and the extreme intensities wanted. Somewhat schematically one can resume the following: for big target-ion source volumes (~ 1 litre) the neutron induced fission from a converter can provide the best results. To achieve 10^{14} fissions/s, a

Figure 5. Isotopic distributions of the in-target production of proton rich isotopes from the $\alpha(400\text{ MeV}) + \text{Ta}$ (1 cm thick) reaction. Only the proton rich side of the reaction products is shown. The yields are normalised per incident alpha particle.



primary beam intensity of 196 kW and 525 kW for deuterons and protons of 35 MeV respectively is necessary. The total power dissipated in the target would be ~ 3 kW. It is clear that in this case a dedicated high intensity accelerator has to be built.

For smaller target volumes (~ 0.02 litre), a direct proton or deuteron beam is more efficient. With a deuteron beam of 200 MeV and only 14 kW, 10^{14} fissions/s could be reached. The total power dissipated in the target would be about 17 kW. An increase of the target volume would add a significant amount of secondary fissions induced by fast neutrons.

We note that the converter method may reach the highest final intensities if big target volumes may be handled. For example, 7.5×10^{14} fissions/s can be obtained employing a deuteron beam of 1.6 MW at 35 MeV resulting in 24 kW fission power deposition (perhaps being the limit) in the target. The direct bombardment by a beam of protons or deuterons would provide similar yields with smaller target volumes. However, 1×10^{14} fissions/s is already very close to the allowable heat deposition due to the primary beam and fissions combined (~ 17 kW). On the other hand, in this case heavy target materials other than U could be used (e.g. Nb, La, Ta, Th). Thus, this method provides a higher versatility than the converter method. In addition, the direct bombardment of these targets by a beam of alpha particles would lead to the production of proton-rich nuclei in the region where the nuclear data are sparse or non-existent.

A very promising technical aspect in the case of liquid targets could be the use of beams incident vertically on the target. This would avoid the very hostile combined conditions of a high intensity beam on a window separating the vacuum and a high temperature liquid. A vertical beam could create a very high temperature inside the liquid, with moderate temperatures of the container walls. Along with convection currents, this should favour fast and efficient effusion. Similar conditions could be created in the target with the converter method. More detailed calculations and some exploratory experiments are necessary in this domain.

Finally, we add that the radioactivity problems will be crucial in the construction of such a radioactive beam facility.

REFERENCES

- [1] J.A. Nolen, Proceedings of the 3rd International Conference on RNB, Gif-sur-Yvette, France, 24-27 May 1993, D.J. Morrissey, ed., Edit. Front. (1993), 111.
- [2] R.E. Prael, H. Lichtenstein, "User Guide to LCS: The LAHET Code System", LANL report LA-UR-89-3014 (September 1989); R.E. Prael, private communication (May 1999).
- [3] J. Briesmeister for Group X-6, "MCNP-A, A General Monte Carlo Code for Neutron and Photon Transport", Version 4A, LA-12625-M, LANL (1993).
- [4] W.B. Wilson, T.R. England, K.A. Van Riper, "Status of CINDER'90 Codes and Data", LANL pre-print LA-UR-99-361 (1999); Proc. of 4th Workshop on Simulating Accelerator Radiation Environments, 13-16 September 1998, Knoxville, Tennessee, USA; W.B. Wilson, private communication (April 2000).
- [5] D. Ridikas, "Optimization of Beam and Target Combinations for Hybrid Reactor Systems and Radioactive Ion Beam Production by Fission", PhD thesis, GANIL report GANIL-T 99 04 (October 1999).
- [6] M.A. Lone, A.J. Ferguson, B.C. Robertson, *Nucl. Instr. & Meth.*, 189 (1981), 515.
- [7] P. Grand, S.N. Goland, *Nucl. Instr. & Meth.*, 145 (1977), 49.
- [8] C.M. Logan, R. Booth, R.A. Nickerson, *Nucl. Instr. & Meth.* 145 (1977), 77.
- [9] A. Hassanein, *Journal of Nuclear Materials*, 233-237 (1996), 1547.
- [10] Ch. Latge, private communication, CEA Cadarache (May 2000).
- [11] J.R.J. Bennett, *Nucl. Instr. & Meth.*, B 126 (1997), 126; J.R.J. Bennett, *et al.*, *Nucl. Instr. & Meth.*, B 126 (1997), 105.
- [12] P.C. Stevenson, H.G. Hicks, W.E. Nervik, D.R. Nethaway, *Phys. Rev.*, 111 (1958), 886.
- [13] M. Lindner, R.N. Osborne, *Phys. Rev.*, 94 (1954), 1323.
- [14] PIAFE Collaboration, "Technical Report of the Project Covering the Period 1993-1996", ISN 97-52 (July 1997).

**STUDY OF RESIDUAL PRODUCT NUCLIDE YIELDS FROM
0.1, 0.2, 0.8 AND 2.6 GeV PROTON-IRRADIATED ^{NAT}Hg TARGETS**

**Yury E. Titarenko, Oleg V. Shvedov, Vyacheslav F. Batyaev, Valery M. Zhivun,
Evgeny I. Karpikhin, Ruslan D. Mulambetov, Dmitry V. Fischenko, Svetlana V. Kvasova**

Institute for Theoretical and Experimental Physics
B. Chermushkinskaya 25, 117259, Moscow, Russia,

Stepan G. Mashnik, Richard E. Prael, Arnold J. Sierk

Los Alamos National Laboratory
Los Alamos, NM 87545, USA

Hideshi Yasuda

Japan Atomic Energy Research Institute
Tokai, Ibaraki, 319-1195, Japan

Abstract

The direct γ -spectrometry method is used to measure more than 350 residual product nuclide yields from 0.1, 0.2, 0.8 and 2.6 GeV proton irradiated ^{NAT}HgO targets. The γ -spectrometer resolution is of 1.8 keV at the 1332 keV γ -line. The resultant γ -spectra are processed by the GENIE2000 code. The γ -lines are identified, and the cross-sections calculated, by the ITEP-designed SIGMA code using the PCNUDAT radioactive database. The ²⁷Al(p,x)²²Na reaction is used as monitor. The experimental results are compared with calculations by the LAHET, CEM95, CEM2k, INUCL, CASCADE and YIELDX codes.

Introduction

Mercury is planned to be used as a target material in all the present-day designs of the Spallation Neutron Source (SNS) facilities [1-3], thus necessitating that the proton-Hg interaction characteristics should be studied in a broad energy range from a few MeV to 2-3 GeV. Among the characteristics, the yields of residual product nuclei are of particular importance. They are independent nuclear constants to be used in practical calculations as well as to verify the codes for calculating the SNS facility design parameters, such as radioactivity (both current and residual), deterioration of resistance to corrosion, yields of gaseous products, poisoning, etc.

Experiment

The experimental samples are 10.5 mm diameter discs manufactured by pressing fine-dispersed ^{nat}HgO powder. The weight contents of impurities in the samples do not exceed 0.16%, of which 0.01% Si, 0.03% Cl, 0.02% Ca, 0.04% Ti, 0.03% Fe and 0.01% Ba. The total content of the remaining 60 elements, found by the spark mass spectrometry, is below 0.02%.

The measurements were made using the relative method, employing the $^{27}\text{Al}(p,x)^{22}\text{Na}$ reaction to monitor the process. The monitors are 10.5 mm Al foils having chemical impurities below 0.001%. Two independent proton beams from the ITEP U-2 synchrotron are used to irradiate the samples, namely, the low-energy (70-200 MeV) and high-energy (800-2600 MeV) beams.

Table 1 presents the characteristics of the experimental samples and monitors along with the main irradiation parameters.

Table 1. Parameters of experimental samples and monitors, irradiation conditions and monitor reaction cross-sections

Proton energy, GeV	Sample thickness, mg/cm ²	Monitor thickness, mg/cm ²	Irradiation time, min	Mean proton flux density, p/cm ² /s	$^{27}\text{Al}(p,x)^{22}\text{Na}$ cross-section, mb
0.10	536.0	138.2	60	$2.5 \cdot 10^9$	19.1 ± 1.3
0.20	537.4	137.3	45	$7.1 \cdot 10^9$	15.1 ± 0.9
0.80	529.3	139.1	15	$1.5 \cdot 10^{10}$	15.5 ± 0.9
2.6	536.3	137.0	60	$4.9 \cdot 10^{10}$	11.7 ± 0.9

The techniques for irradiating the samples and for processing the γ -spectra are presented in [4] together with formulas used to determine the fragment nuclide yields.

Results

More than 350 yields of residual nuclei (from $^{22}\text{Na}^*$ to ^{203}Hg) from 0.1, 0.2, 0.8 and 2.6 GeV proton-irradiated ^{nat}Hg have been measured. Figures 1-9 show the products that were measured at all the four energies.

* The ^{22}Na and ^{24}Na yields have been determined disregarding the contributions from the Al monitor samples.

The experimental data were compared with the LAHET, CEM95, CEM2k, INUCL, CASCADE and YIELDX code-simulated yields. The comparison method and a short description of all codes together with further references may be found in [4]. It should be noted that all these codes do not calculate the independent and cumulative yields individually for the ground and metastable states of the produced radionuclides, whereas the yields of either ground or metastable states alone are often measured. Therefore, those particular measurement results were excluded from the comparison procedure. The only exclusion is the case of measuring both states, so the total yields can be compared with the simulation results. Table 2 and Figures 1-4 present the results of a detailed nuclide-by-nuclide comparison.

Table 2. Statistics of the experimental-to-simulated yield comparisons

Code	$E_p = 0.1 \text{ GeV}, N_T = 48, N_G = 35$			$E_p = 0.2 \text{ GeV}, N_T = 66, N_G = 49$		
	$N_{C_{1.3}}/N_{C_{2.0}}/N_S$	$\langle F \rangle$	$S(\langle F \rangle)$	$N_{C_{1.3}}/N_{C_{2.0}}/N_S$	$\langle F \rangle$	$S(\langle F \rangle)$
LAHET	13/21/30	2.24	1.92	22/36/48	1.99	1.69
CEM95	6/15/28	2.29	1.61	20/31/38	1.79	1.56
CEM2k	9/18/28	1.96	1.52	22/31/38	1.66	1.48
INUCL	10/19/33	2.74	2.05	12/27/48	2.25	1.66
CASCADE	16/24/33	2.36	1.98	21/35/48	2.33	1.95
YIELDX	–	–	–	14/35/49	2.10	1.66
	$E_p = 0.8 \text{ GeV}, N_T = 106, N_G = 88$			$E_p = 2.6 \text{ GeV}, N_T = 142, N_G = 121$		
	$N_{C_{1.3}}/N_{C_{2.0}}/N_S$	$\langle F \rangle$	$S(\langle F \rangle)$	$N_{C_{1.3}}/N_{C_{2.0}}/N_S$	$\langle F \rangle$	$S(\langle F \rangle)$
LAHET	42/63/87	2.06	1.73	23/80/118	2.02	1.49
CEM95	30/46/59	2.35	2.13	46/77/91	2.27	2.11
CEM2k	26/51/63	1.65	1.43	32/77/101	2.73	2.29
INUCL	26/42/82	2.74	1.95	37/77/115	2.55	2.03
CASCADE	35/59/84	2.52	2.10	56/93/114	1.76	1.55
YIELDX	32/62/88	2.21	1.82	26/65/120	2.52	1.78

In Table 2, N_T is the total number of the measured yields, N_G is the number of the measured yields selected to be used in comparison with calculations, N_S is the number of the products whose yields were simulated by a particular code, $N_{C_{1.3}}$ is the number of the comparison events when the simulation-experiment difference does not exceed 30% and $N_{C_{2.0}}$ is the number of the comparison events when the simulation-experiment difference does not exceed a factor of 2.

Figures 1-4 show the results of the nuclide-by-nuclide comparison of the experimental data with the LAHET, CEM95, CEM2k, CASCADE, INUCL and the YIELDX code-simulated results. One can see that all codes (except YIELDX) adequately predict the $A > 170$ product yields for 100, 200 and 800 MeV protons and the $A > 120$ product yields for 2 600 MeV protons. The yields simulated by all the codes in the remaining ranges of masses, i.e. in the fission and fragmentation regions, are very different from experiment, with the most significant differences observed in the $80 < A < 103$ range for 100 and 200 MeV protons, in the $48 < A < 130$ range for 800 MeV protons, and in the $28 < A < 100$ range for 2 600 MeV protons. It should be noted that CEM95 and CEM2k do not calculate the process of fission itself, and do not provide fission fragments and a further possible evaporation of particles from them. When, during a Monte Carlo simulation of a compound stage of a reaction using the evaporation and fission widths these codes have to simulate a fission, they simply remember this event (that permits them to calculate fission cross-section and fissility) and finish the calculation of this event without a real subsequent calculation of fission fragments. Therefore, the results from CEM95 and CEM2k shown here reflect the contribution to the total yields of the nuclides only from deep spallation processes of successive emission of particles from the target, but do not

Figure 1. Nuclide-by-nuclide comparison between the experimental and simulated results for 0.1 GeV protons. The cumulative yields are labelled with a “c” when the respective independent yields are also shown.

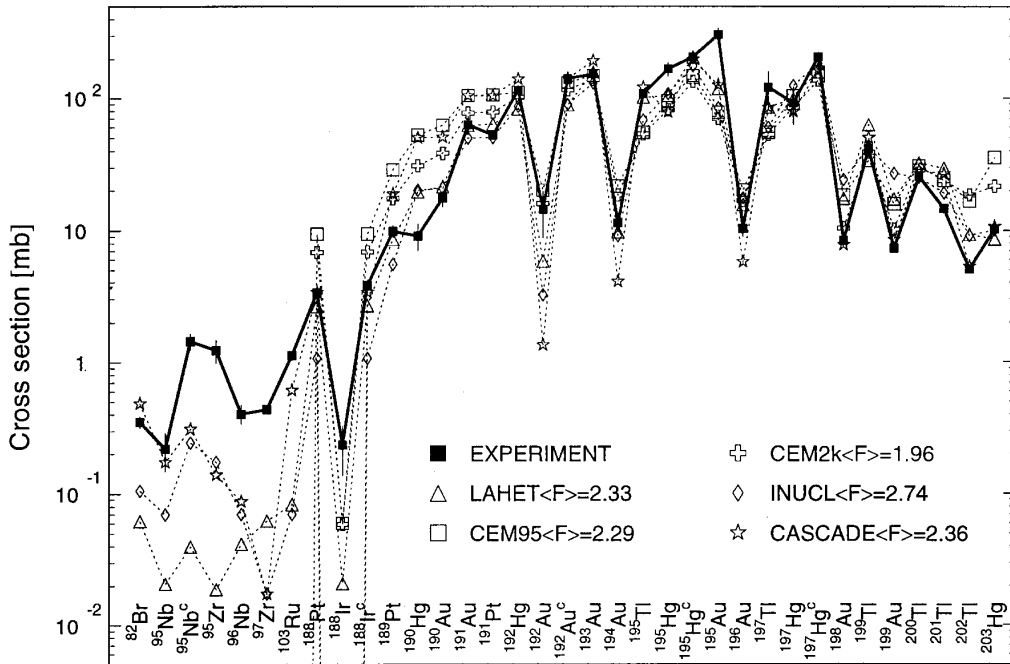


Figure 2. Product-by-product comparison between the experimental and simulated results for 0.2 GeV protons. The cumulative yields are labelled with a “c” when the respective independent yields are also shown.

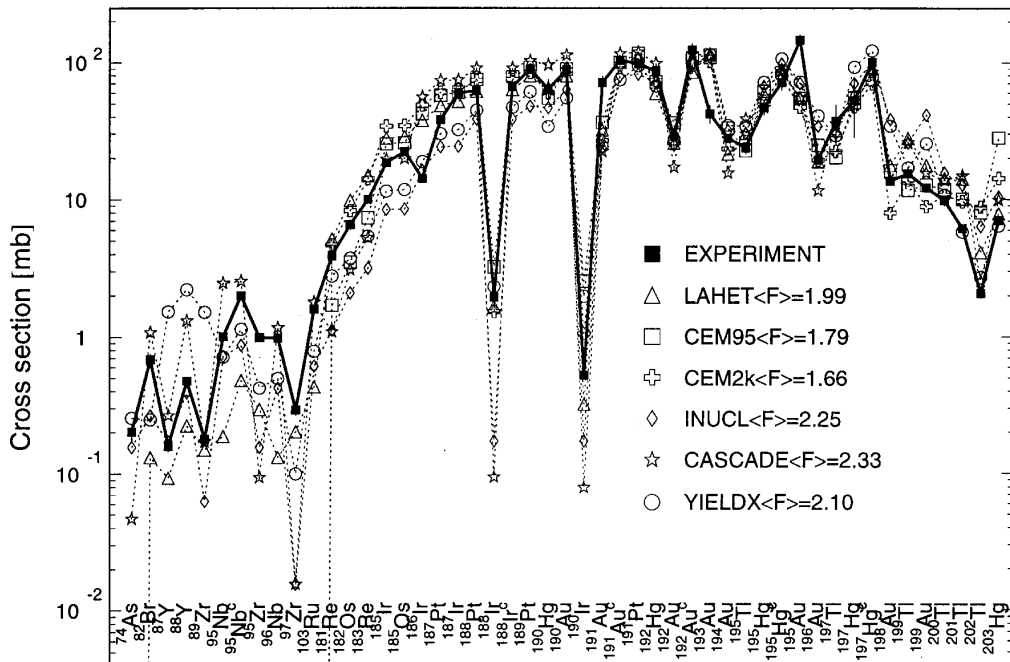
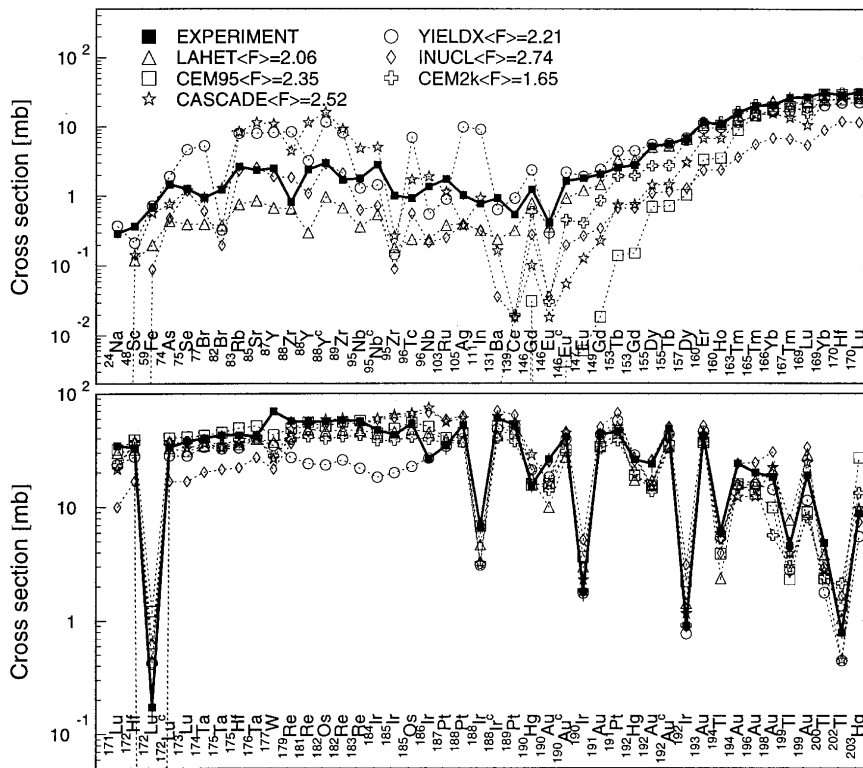


Figure 3. Nuclide-by-nuclide comparison between the experimental and simulated results for 0.8 GeV protons. The cumulative yields are labelled with a “c” when the respective independent yields are also shown.



contain fission products. To be able to describe nuclide production in the fission region, these codes have to be extended by incorporating a model of high-energy fission (e.g. in the transport code MCNPX, where these code are used, they are complemented by the RAL fission model).

Figures 5-8 show the simulated mass yield of the reaction products. The experimental cumulative yields, which are often equal to the mass yields within measurement errors, are also shown for comparison. The following conclusions may be drawn from the comparison between the experimental and simulated mass yields:

- In the case of 0.1 GeV protons and $A > 190$, all codes predict the mass curve shape quite adequately.
- In the case of 0.2 GeV protons and $A > 180$, all code-simulated yields are in a good agreement with the data.
- In the case of 0.8 GeV protons, the best agreement with experiment is obtained by YIELDX, for $A > 130$ and by INUCL, for $A < 130$.
- In the case of 2.6 GeV protons and $A > 100$, the CEM95 and CASCADE results agree with the data, while the LAHET calculations are underestimated and the YIELDX and INUCL yields represent the mass curve shape erroneously. None of the codes can describe well the experimental curve shape at $A < 100$.

Figure 4: Nuclide-by-nuclide comparison between the experimental and simulated results for 2.6 GeV protons. The cumulative yields are labelled with a “c” when the respective independent yields are also shown.

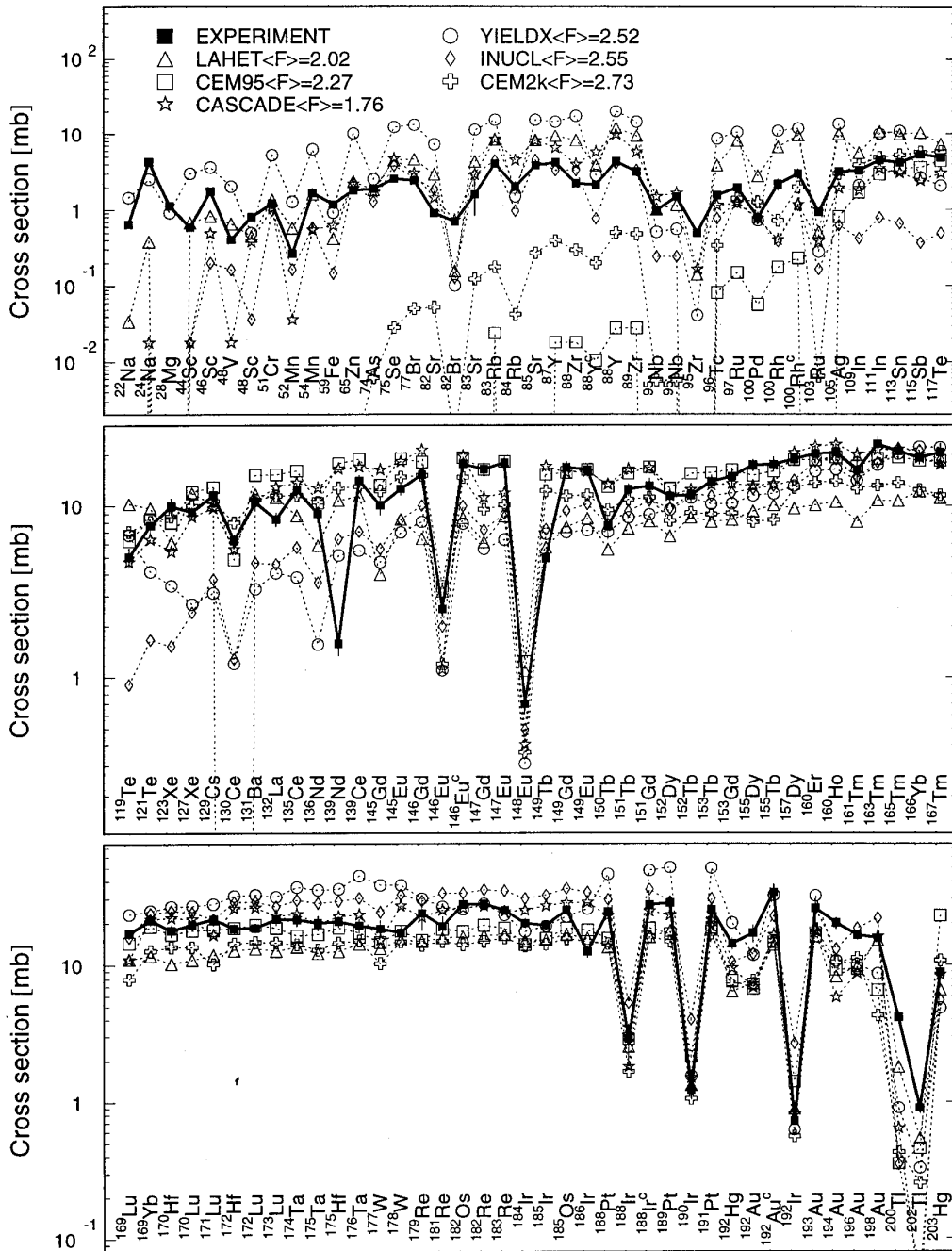


Figure 5. The simulated and experimental mass yields at 0.1 GeV

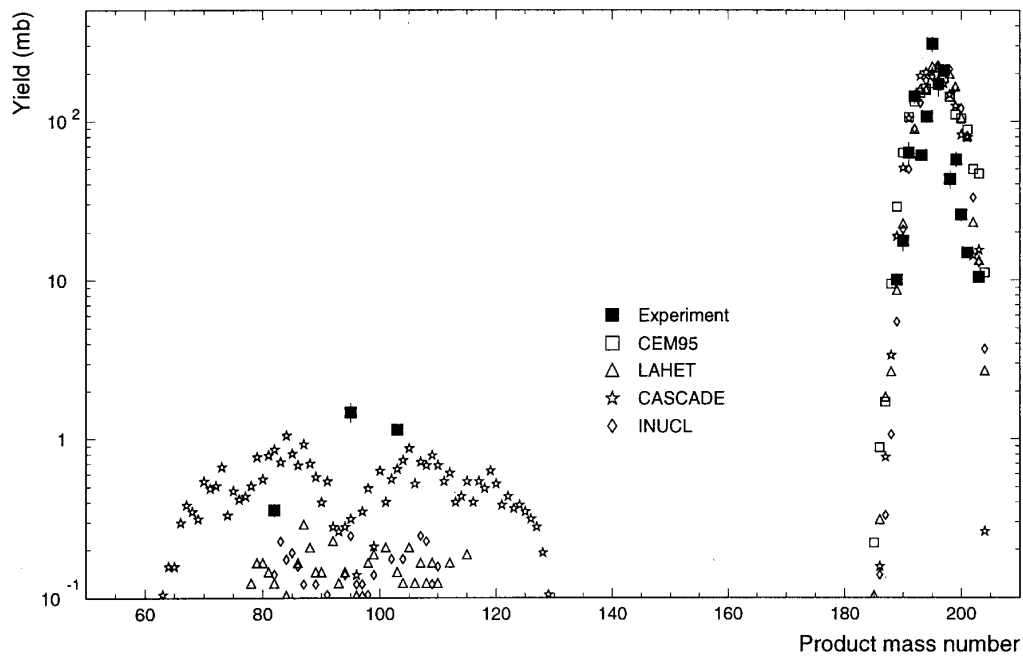


Figure 6. The simulated and experimental mass yields at 0.2 GeV

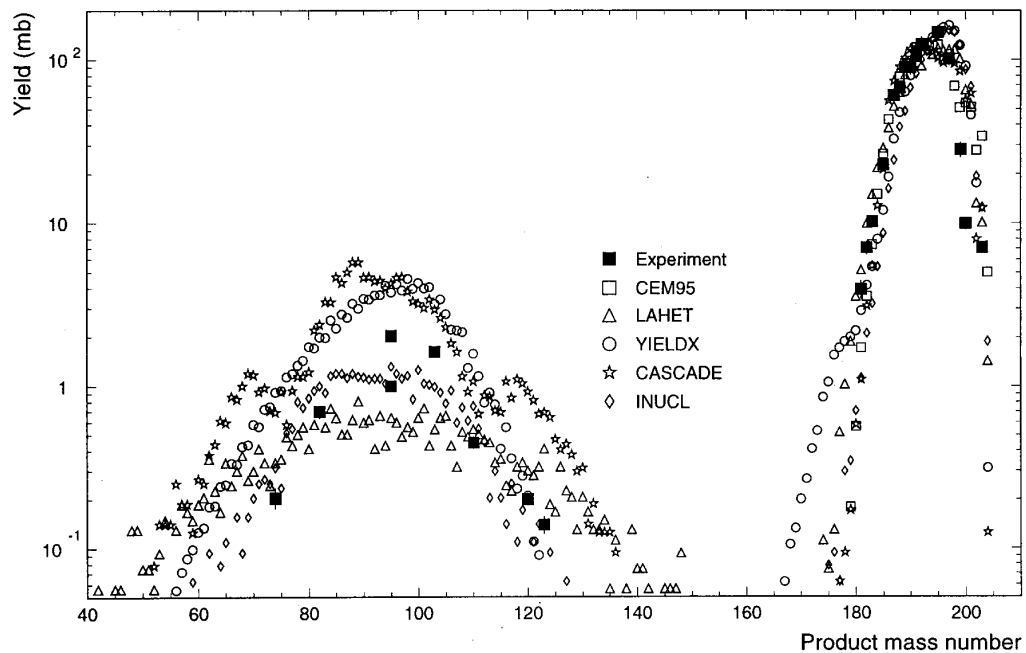


Figure 7. The simulated and experimental mass yields at 0.8 GeV

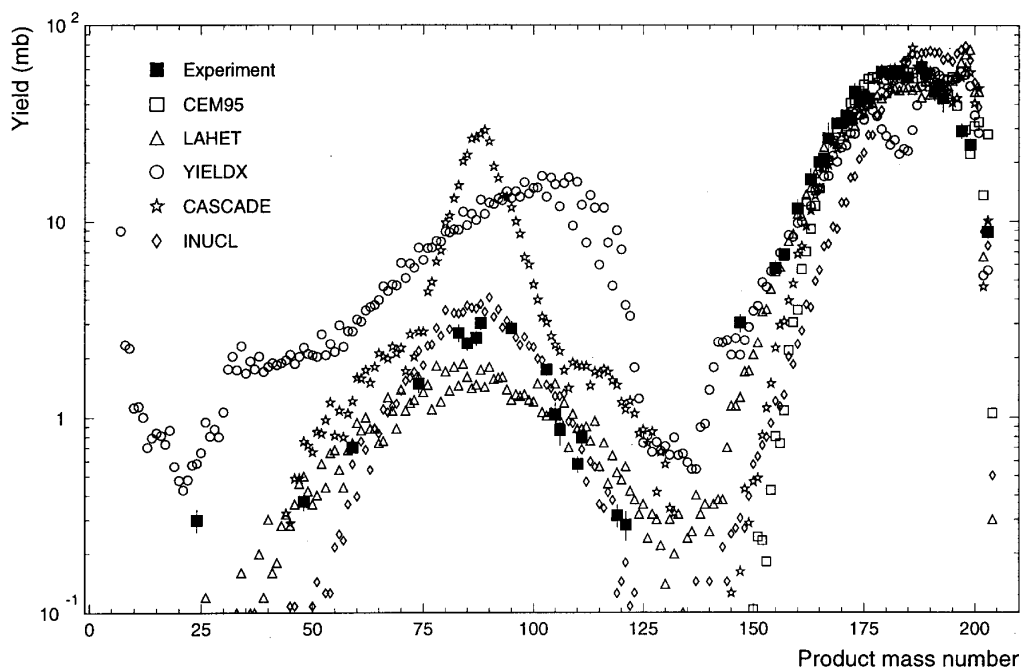


Figure 8. The simulated and experimental mass yields at 2.6 GeV

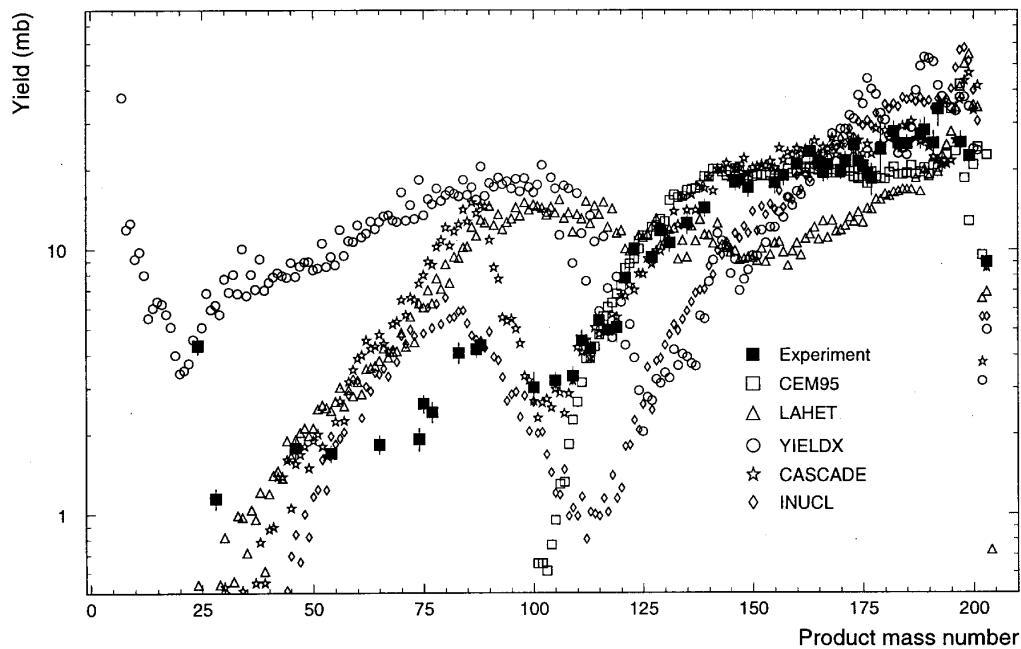


Figure 9. Some experimental and simulated yields versus the proton energy

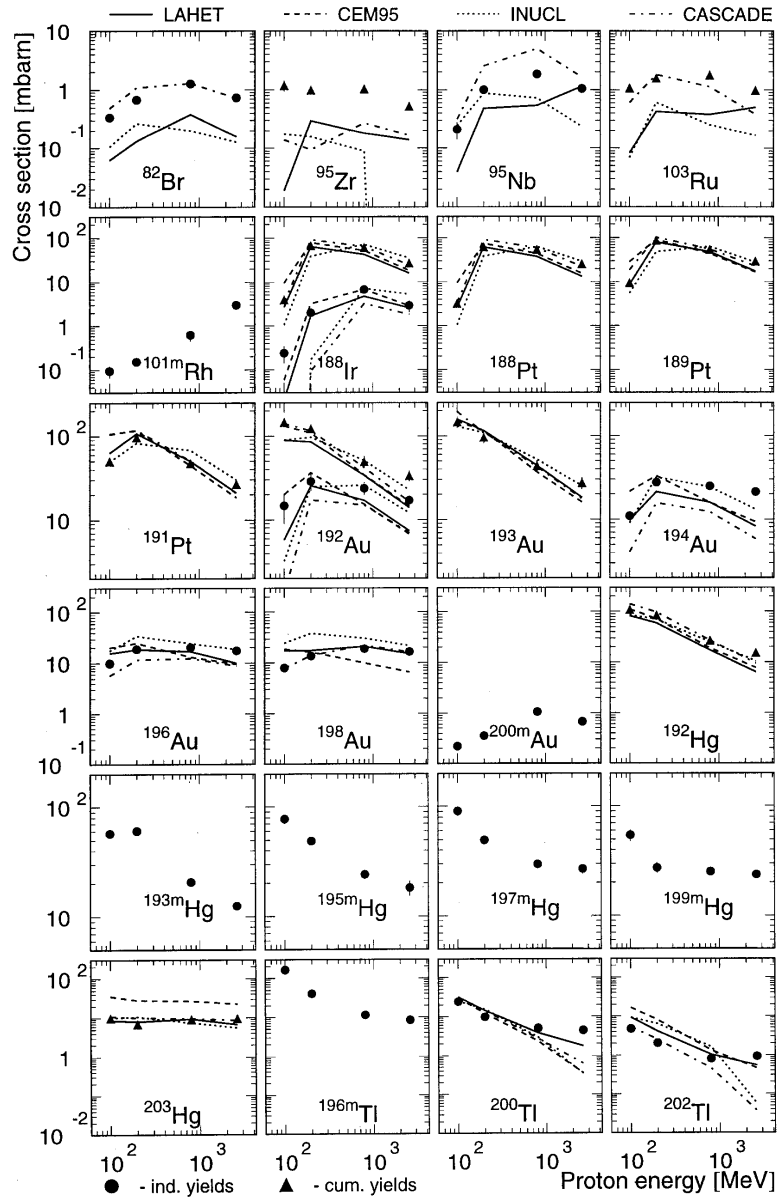


Figure 9 illustrates the dependence of a part of measured yields on the proton energy, i.e. excitation functions. These data will be analysed further after a final release of all the experimental results.

Conclusion

Our experiment-to-simulation comparison has shown that, on the whole, the simulation codes can but poorly predict the experimental results. In some cases, the differences reach an order of magnitude or even more. The last version of the improved cascade-exciton model code, CEM2k [5], shows the best agreement with the data in the spallation region at all energies except 2.6 GeV, where the model overestimates the expected experimental fission cross-section of about 75 mb [6] by a factor of 4. This overestimation of the fission cross-section causes an underestimation of the yield of nuclei which

are most likely to fission at the evaporation stage of a reaction, after the cascade and pre-equilibrium stages, i.e. for $170 < A < 185$. (Similar disagreement with the data one can see as well for LAHET and CEM95, that is also related with an overestimation of the fission cross-section at 2.6 GeV.) CEM2k is still under development, its problem with the overestimation of fission cross-sections at energies above 1 GeV has yet to be solved, and it has to be complemented with a model of fission fragment production as mentioned above, to be able to describe as well fission products.

This means that the nuclear data must be accumulated persistently in the above-mentioned ranges of energies and masses, to help improve hadron-nucleus interaction models released in codes used in applications.

Acknowledgements

The work was carried out under the ISTC Project #839 supported by the European Community, Japan (JAERI), Norway and, partially, by the US Department of Energy.

REFERENCES

- [1] W. Braeutigam, *et al.*, "The Status of the European Spallation Neutron Source (SNS) R&D Programme", Proc. 3rd Int. Topical Meeting on Nuclear Applications of Accelerator Technology, Long Beach, CA, 14-18 November 1999, pp. 225-231.
- [2] J.R. Alonso, "The Spallation Neutron Source (SNS) Project: Introduction", Proc. 2nd Int. Topical Meeting on Nuclear Applications of Accelerator Technology, 20-23 September 1998, Gatlinburg, TN, pp. 197-201.
- [3] N. Watanabe, *et al.*, "Recent Progress in Design Study of Japanese Spallation Neutron Source", Proc. 8th Int. Conf. on Nuclear Engineering (ICONE 8), Baltimore, MD, 2-6 April 2000, CD ROM, ICONE-8457.
- [4] Yu.E. Titarenko, *et al.*, "Experimental and Computer Simulation Study of the Radionuclides Produced in Thin ^{209}Bi Targets by 130 MeV and 1.50 GeV Proton-induced Reactions", *Nucl. Instr. Meth.*, A 414, 73 (1998); Yu.E. Titarenko, *et al.*, "Study of Residual Product Nuclide Yields in 1.0 GeV Proton Irradiated ^{208}Pb and 2.6 GeV Proton-irradiated ^{nat}W Thin Targets", these proceedings.
- [5] The code CEM2k is briefly surveyed in S.G. Mashnik, L.S. Waters, and T.A. Gabriel, "Models and Codes for Intermediate Energy Nuclear Reactions", Proc. 5th Int. Workshop on Simulating Accelerator Radiation Environments (SARE5), 17-18 July 2000, OECD Headquarters, Paris, France, and will be described by S.G. Mashnik and A.J. Sierk in a future paper.
- [6] A.V. Prokofiev, "Compilation and Systematics of Proton-induced Fission Cross-section Data", *Nucl. Instr. Meth.*, A, submitted in December 1998, to be published in September 2000.

ACTIVATION STUDIES AND RADIATION SAFETY FOR THE n_TOF EXPERIMENT

V. Lacoste, A. Ferrari, M. Silari, V. Vlachoudis
CERN, European Organisation for Nuclear Research, Switzerland

Abstract

The Neutron Time-of-flight (n_TOF) facility, whose installation is about to be completed at CERN, will use a high intensity proton beam (7×10^{12} protons per bunch, one or four bunches allowed per 14.4 s at 20 GeV/c). Through the spallation process onto a solid lead target ($80 \times 80 \times 60 \text{ cm}^3$), a high flux of neutrons, charged particles and photons is produced. Intensive simulation studies with the FLUKA Monte Carlo code were undertaken to calculate the radioactivity induced in the target and in the surrounding structures as well as in the cooling water. Shielding calculations were also performed for the various critical locations along the 200 m long tunnel which houses the proton beam line, the target and the TOF tube. In particular, extensive simulations were required to define the shielding of the target area and the dimensions of the access labyrinths.

Introduction

The Neutron Time-of-flight (n_TOF) is a high flux spallation neutron source followed by a 200 m time-of-flight basis. The aim of the n_TOF facility at CERN is to measure the cross-sections needed for the design of innovative ADS applications like the incineration of nuclear waste [1], energy production [2], radioisotope production for medical applications [3] and many other basic science subjects, in particular astrophysics [4]. As a result of the studies reported in a precedent work [5] and its addendum [6], the neutron time-of-flight facility has been proposed at the CERN PS [4] delivering a maximum intensity of 2.8×10^{13} protons within a 14.4 s supercycle at a momentum of 20 GeV/c. This allows to study – systematically and with excellent resolution – neutron cross-sections of almost any element using targets of very modest mass, necessary for unstable or otherwise expensive materials, in the interval from 1 eV to 250 MeV. The n_TOF facility uses a high intensity proton beam which, through the spallation process, produces a high neutron flux as well as charged particles and photons [7]. The radiation protection aspects of such a facility are clearly a major concern. Therefore, intensive simulation studies were undertaken to calculate the activity and the dose equivalent rates at different locations of the facility. These simulations cover different topics, such as the activation of the lead target, the cooling water, the dose rates around the target area and near the charged particles sweeping magnet. The neutrons streaming in a service tunnel linking the n_TOF tunnel (TT2A) to a laboratory located in the basement of an adjacent building as well as the dose rate in this tunnel have been estimated and will also be discussed below.

Simulation studies on activation

Activation of the lead target

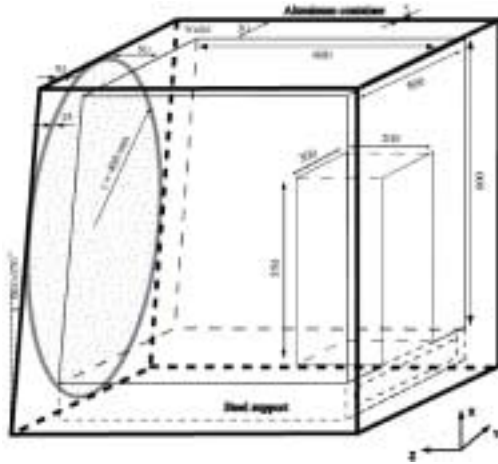
The target is made with pure lead blocks and its shape is $80 \times 80 \times 60 \text{ cm}^3$, except for the spallation area where a volume of $30 \times 55 \times 20 \text{ cm}^3$ was removed to have the nominal design dimension [8] (Figure 1a). The exit plane is at an angle of -0.676° with respect to the vertical. The target is mounted on a steel support and is submerged in water contained in an aluminium alloy vessel. The water layer surrounding the lead block is 3 cm thick except at the exit face of the target, at which point it is 5 cm thick. The walls of the aluminium container are 0.5 cm thick, except the exit wall that consists of a thin single metallic window [8]. This aluminium window mounted onto the water tank is 1.6 mm thick and 80 mm in diameter.

In order to calculate the activity of the target the residual nuclei produced by inelastic hadronic interactions in the lead volume were scored. The intensity of the beam was assumed to be 7×10^{12} protons per bunch. Two cases were considered, the first with a bunch every 14.4 s (supercycle duration), the second with four bunches every 14.4 s. Two representative irradiation periods were considered, one lasting one month and the other nine months. The beam intensity is supposed to be constant and equal to the average value (i.e. 4.9×10^{11} and 1.94×10^{12} protons per second for one and four bunches per supercycle, respectively). At the end of the irradiation the activity of the lead target is about 800 Ci for the one bunch scenario (Figure 1b). After one year of decay, the total activity is about 1 Ci for one month of irradiation, and about 7 Ci for nine months of irradiation. For four bunches the values are obviously four times larger.

The dose equivalent rate after an irradiation of one month and one day of cooling is estimated to be at maximum 25 Sv/h on the exit face of the lead target. This result is obtained by using the ω factor [9], which converts star density to dose rate in contact with an extended target. The star density

Figure 1

a) Geometry of the lead target



b) Activity of the target vs. cooling time after one month and nine months of irradiation with one or four bunches per 14.4 s, 7×10^{12} protons per bunch

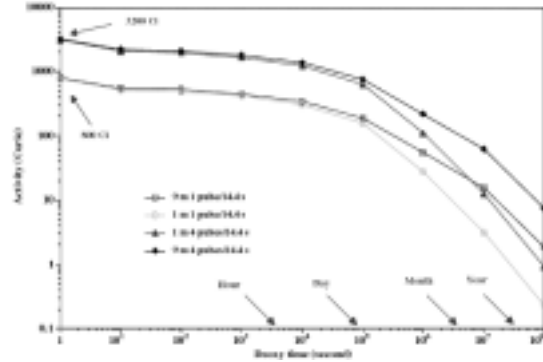


Table 1. Maximum dose equivalent rates on the exit face of the lead target expressed in Sv/h, for different irradiation and cooling times

$I = 1.94 \times 10^{12}$ p/s	$T_c = 1$ day	$T_c = 10$ days	$T_c = 30$ days
$T_{irr} = 1$ month	25	4	2
$T_{irr} = 1$ year	30	11	8

rate (hadron inelastic interaction per cm^3/s) is calculated by Monte Carlo (the FLUKA code [10] in our case). The dose rates obtained after different irradiation and cooling periods, for a beam intensity of 1.94×10^{12} protons/s (four bunch scenario) are given in Table 1.

Activation of the cooling water

The activation of the cooling water was calculated under the same conditions described previously for the target activation. The total volume of water used in the cooling system is about 700 l; the aluminium container contains 20% of this volume. At the end of the irradiation, the activity is about 2.7 Ci for the one bunch scenario. After one year of decay, the total activity is around 5 mCi for one month of irradiation and about 20 mCi for nine months of irradiation. For four bunches, the values are four times larger. The activity decreases rapidly after one day because of the short half-life of most of the produced radionuclides (Figure 2).

We can reasonably assume that the specific activity of the whole water volume is five times lower than the specific activity in the water inside the container, as this water permanently circulates in the cooling system. The radionuclides dominating the activity are given in Table 2 (one month of irradiation). After one day of decay, the activity is mainly due to ^7Be and tritium, with 53.3 d and 12.33 y half-lives respectively.

Figure 2. Activity of the cooling water versus cooling time after one month and nine months of irradiation with one or four bunches per PS supercycle, 7×10^{12} protons per bunch

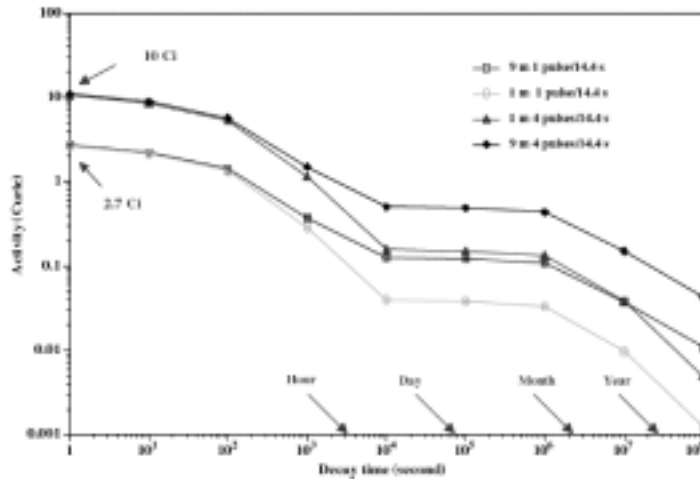


Table 2. Radionuclides dominating the total activity of the cooling water irradiated for a period of one month

Tcooling	Residual nuclei	Becquerel	A (%)
Day	^7Be (ec mode, $T_{1/2} = 53.3$ d)	1.3×10^9	96.1
	^3H (β^- mode, $T_{1/2} = 12.33$ y)	5.3×10^7	3.9
Month	^7Be	9.1×10^8	94.5
	^3H	5.3×10^7	5.5
Year	^7Be	1.2×10^7	19.8
	^3H	5.0×10^7	80.2

Radiation safety

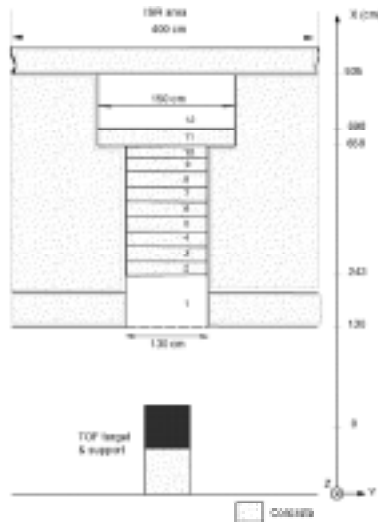
Target shielding

The lead target is situated at a depth of 9 m under the ISR tunnel, which is a supervised area. The dose rate allowed in this region must be less than $2.5 \mu\text{Sv/h}$; the design value for the shielding was taken at $1 \mu\text{Sv/h}$. FLUKA [10] simulations were performed to determine the shielding requirements.

The TOF target will be removed from the TT2A tunnel via a shaft set in concrete and linking a service tunnel located in between TT2A and the ISR, which will serve as a storage area for the target. The concrete's thickness between TT2A and this service tunnel is 5.5 m. FLUKA simulations were performed to estimate the dose in the ISR during the TOF operation. Only neutrons have been transported without any energy cut-off.

Simulations were performed of the neutrons transmitted through the shielded shaft. For this purpose the 130 cm diameter shaft was assumed to be filled with 4.55 m of concrete, divided into 10 slices and 12 regions for simulation purposes (Figure 3) [8]. The density of the concrete is 2.35 g/cm^3 . An average quality factor of five was applied to convert absorbed dose in Gray to dose equivalent in Sievert. We considered one bunch and four bunches every 14.4 s with an intensity of 7×10^{12} protons per bunch.

Figure 3. Geometry of the shaft used in the FLUKA simulation



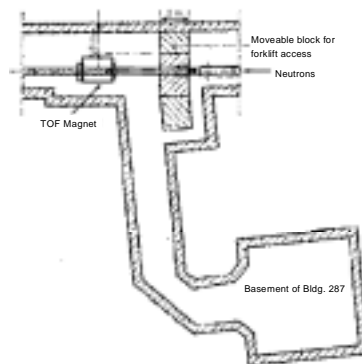
In Region 1, 1.3 m above the target and before any shielding, the dose equivalent rate is about 80 Sv/h for the one bunch scenario. In Region 12, the dose equivalent rate is around 3 mSv/h. For the four bunch scenario the values are obviously four times higher. The dose equivalent rate in the ISR with the shaft “plugged” with 4.55 m of concrete is clearly far too high. To reduce it to the design value, additional shielding has to be installed on top of the target. Additional calculations have shown that a shielding consisting of 80 cm iron plus 2.4 m concrete placed in the service tunnel in between the shaft and the ISR will reduce the dose equivalent rate to below 1 μ Sv/h.

Shielding of the basement of Building 287

Initial dose rate estimation

A laboratory routinely occupied by personnel is located at the same level of the TOF TT2A tunnel. This room, located in the basement of Building 287 (Figure 4), is linked to TT2A by a 12 m long tunnel, which serves as an emergency exit and therefore cannot be completely blocked off. The way to reduce neutron streaming from TT2A into Building 287 is to install a properly designed labyrinth. As Building 287 is a supervised area, the ambient dose equivalent rate in the laboratory must not exceed 2.5 μ Sv/h.

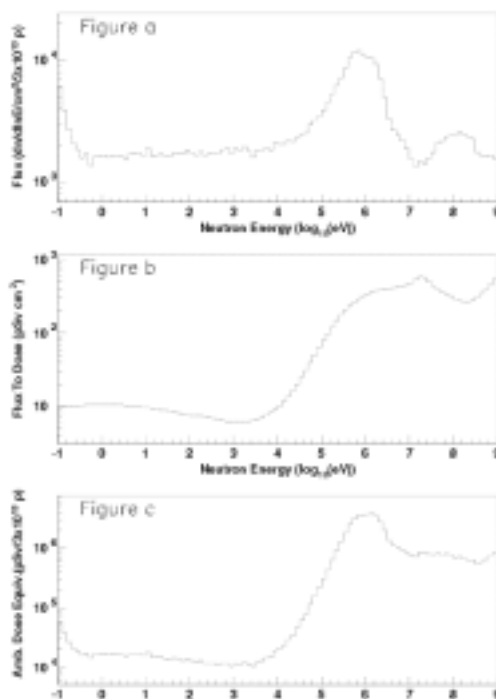
Figure 4. TT2A and service tunnel linking to the basement of Building 287



A collimator and the TOF sweeping magnet are located near the tunnel aperture, about 140 m from the TOF target. The integral neutron background fluence in the tunnel (outside the neutron tube) versus the flight distance has been estimated at around 10^5 n/cm²/3 × 10¹³ protons. The neutron spectrum at the entrance of the service tunnel is shown in Figure 5a. This neutron fluence has then been folded with the neutron fluence to ambient dose equivalent conversion factors (Figure 5b) given by [12]. The total dose equivalent for four bunches is 1.3 × 10⁷ pSv, or a rate of 3.25 mSv/h for four bunches every 14.4 s.

Figure 5

- a) Background neutron flux in the TOF tunnel at 140 m from the lead target
- b) Neutron fluence to dose equivalent conversion factor
- c) Neutron ambient dose equivalent per isoenergic bin for four bunches



Simple estimate

A first estimate of the attenuation provided by a labyrinth made of concrete and consisting of two legs each of 5.60 m long, 0.9 m wide and about 2.5 m high (cross-sectional area $A = 2.30$ m²) was carried out using the attenuation curves given in [13]. The resulting dose equivalent rate is estimated to be less than 1 μSv/h. The attenuation factors and results are given in Table 3.

Table 3. Estimate of the dose rate in the labyrinth, in the case of 3 × 10¹³ protons/14.4 s

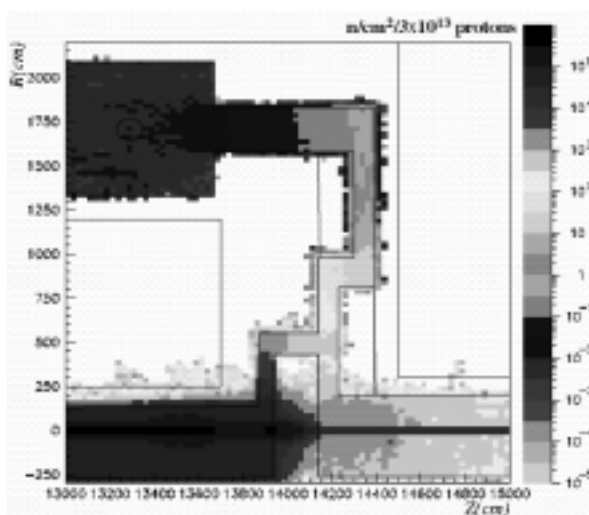
Leg dimensions: l = 5.60 m; A = 2.3 m²	Attenuation factor	Initial dose rate: 3.25 mSv/h
1 st leg	0.022	71.5 μSv/h
2 nd leg	0.009	0.6 μSv/h

Monte Carlo simulation

Due to the complexity of the problem, a Monte Carlo simulation was performed to estimate the neutron streaming in this tunnel, with the two concrete blocks of the labyrinth defined above (Figure 6).

At the tunnel entrance, 139 m after the lead target, the “background” neutron fluence is about $10^5 \text{ n/cm}^2/3 \times 10^{13}$ protons (four bunches per PS supercycle); these neutrons are mainly fast. The dose equivalent rate is about 7.5 mSv/h using the ambient dose equivalent conversion factor given by [12] for fast neutrons (300 pSv cm^2). At the entrance of the small experimental room, the neutrons are mainly thermal, the fluence is reduced by six orders of magnitude, and the dose rate estimated with the conversion factor for thermal neutrons is reduced to 0.2 nSv/h.

Figure 6. FLUKA simulation of the neutron fluence in the tunnel, with the concrete labyrinth



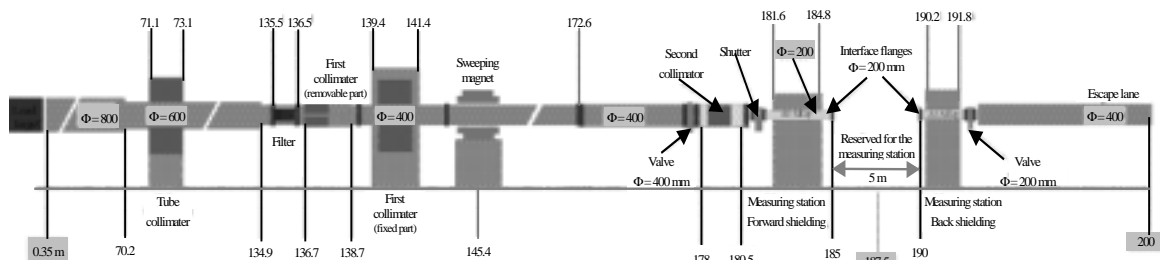
The dose equivalent rate obtained by the simple calculation is *a priori* three orders of magnitude higher than the rate obtained by simulation. The first estimate was done just by considering a 12 m long straight tunnel with two concrete legs, and taking an initial dose equivalent rate of 3.25 mSv/h at the entrance situated 142 m upstream from the target. The geometry of this area is in reality more complex (as shown in Figure 4), and the previous rate is obtained at 139 m, before the collimator wall (Figure 6). By considering the fast neutron fluence of $10^3 \text{ n/cm}^2/3 \times 10^{13}$ protons, the dose equivalent rate at 142 m is 0.22 mSv/h. This rate is reduced to 44 nSv/h after the two concrete legs, and should be reduced even more by the perpendicular shape of the passage leading to the laboratory. The results given by the calculation and simulation are consistent.

Dose rate estimate at the measuring station

The measuring station is located at 187.5 m from the lead target. After the proton beam is stopped, the background in the experimental area will be dominated by γ -rays emitted by the lead target and propagating through the TOF tube. The diameter of this tube will be 1.8 cm for the capture cross-section measurements and 15 cm for the fission cross-section measurements. Calculations were performed to determine the dose rate in this area and to design the lead shutter to be inserted at the end of the TOF tube.

Considering the dose equivalent rate of 25 Sv/h on the exit face of the target, an estimate of the rate at 187 m gives 0.5 μ Sv/h by considering the solid angle subtended by a surface of 10 cm in diameter. This simple calculation does not take into account the effects of the reductions and collimators at different places on the neutron TOF tube (Figure 7). A more detailed calculation was performed by means of a Monte Carlo simulation including the complex geometry of the n_TOF line.

Figure 7. TOF tube sections from the lead target up to the end of the TT2A tunnel



After an irradiation period of one month, the activity of the lead target saturates around 800 Ci, emitting 2.5×10^{13} γ /s. The photon energy distribution from the whole lead block was obtained using the activity of the residual nuclei from FLUKA and the intensity of the γ -rays corresponding to each nucleus, taken from the ENSDF database of nuclei decay modes [11]. These source photons were then transported with FLUKA from the lead target to the measuring station, taking into account the whole and detailed geometry of the 200 m long TOF tunnel. The calculated dose equivalent rate is about 1 nSv/h; this simulation was done with the photons isotropically distributed into the target and not transported from their creation point (co-ordinates of the residual nucleus).

The actual dose rate will most likely be in between the two values obtained by these extreme approaches. Further developments of the FLUKA Monte Carlo code should include the residual nuclei decay modes.

Conclusion

The n_TOF facility at CERN provides unique features for the study of neutron cross-sections. The CERN PS will deliver a maximum intensity of 2.8×10^{13} protons within a 14.4 s supercycle at a momentum of 20 GeV/c. The spallation process in the four tonne pure lead target will produce a high flux of neutrons, charged particles and photons. Intensive simulation studies with the FLUKA Monte Carlo code were undertaken to estimate the radioactivity induced in the target. The induced activity should reach 800 Ci after one month of running time with 7×10^{12} protons per supercycle (one bunch scenario); the dose equivalent rate on the exit face has been evaluated to 25 Sv/h, using the ω factor. The activity of the cooling water was estimated at about 2.7 Ci for the same irradiation conditions. The nuclei dominating the activity after one year of cooling down are ^7Be and ^3H .

Shielding calculations were also performed for the various critical locations around the lead target and along the 200 m neutron line. During the running period, the dose equivalent rate above the target due to neutrons was estimated at about 80 Sv/h, for one PS bunch per supercycle. A massive shielding is required to keep the ISR tunnel safe situated 9 m above the target. Results from FLUKA simulations show that the dose equivalent rate is decreased to 3 mSv/h with 4.55 m of concrete in the shaft above the target. This shaft is needed to allow the removal of the lead target for maintenance purposes. To reduce the dose rate to the design value of 1 μ Sv/h, additional shielding consisting of 80 cm of iron and 2.4 m of concrete was installed on top of the target.

Another critical location is the laboratory located in the basement of Building 287 and linked to the TOF tunnel by a 12 m long emergency exit tunnel. The ambient dose equivalent rate in this room must not exceed 2.5 $\mu\text{Sv/h}$. Simplified calculations and FLUKA simulations have shown that a labyrinth of two legs of 5.6 m in length and with a cross-section of 2.3 m^2 will efficiently reduce the neutrons streaming from the TOF tunnel to the laboratory. The dose equivalent rate of 3.25 mSv/h at the entrance of the 12 m long tunnel, situated at 140 m from the lead target, will be reduced to less than 1 $\mu\text{Sv/h}$ in the laboratory.

After the beam is stopped, γ -rays are emitted by all the activated materials mainly by the lead target. A fraction of these gammas will propagate through the n_TOF tube to the measuring station situated 187 m downstream from the target. A lead shutter of 5-10 cm in thickness will be needed to shield this residual photon flux.

The commissioning of the n_TOF experiment should start during the summer of 2000. A radiation monitoring system [8] was installed to measure the induced activity and the dose equivalent rates at the critical locations. The results of the measurements provided by the various monitors will be compared to the predictions of the present simulations.

REFERENCES

- [1] C. Rubbia, *et al.*, "A Realistic Plutonium Elimination Scheme with Fast Energy Amplifiers and Thorium-plutonium Fuel", CERN/AT/95-53 (ET); C. Rubbia, *et al.*, "Fast Neutron Incineration in the Energy Amplifier as Alternative to Geological Storage: The Case of Spain", CERN/LHC/97-01 (EET).
- [2] C. Rubbia, J-A. Rubio, S. Buono, F. Carminati, N. Fiétier, J. Galvez, C. Gelès, Y. Kadi, R. Klapisch, P. Mandrillon, J.-P. Revol and Ch. Roche, "Conceptual Design of a Fast Neutron Operated High Power Energy Amplifier", CERN/AT/95-44 (ET); see also C. Rubbia, "A High Gain Energy Amplifier Operated with Fast Neutrons", AIP Conference Proceedings 346, International Conference on Accelerator-driven Transmutation Technologies and Applications, Las Vegas, 1994.
- [3] C. Rubbia, "Resonance Enhanced Neutron Captures for Element Activation and Waste Transmutation", CERN/LHC/97-04 (EET).
- [4] "Proposal for a Neutron Time of Flight Facility", CERN/SPSC 99-8, SPSC/P 310, 17 Mar. 1999.
- [5] C. Rubbia, *et al.*, "A High Resolution Spallation Driven Facility at the CERN-PS to Measure Neutron Cross-sections in the Interval from 1 eV to 250 MeV", CERN/LHC/98-02 (EET), Geneva, 30 May 1998.
- [6] C. Rubbia, *et al.*, "A High Resolution Spallation Driven Facility at the CERN-PS to Measure Neutron Cross-sections in the Interval from 1 eV to 250 MeV: A Relative Performance Assessment", CERN/LHC/98-02 (EET)-Add. 1, Geneva, 15 June 1998.

- [7] C. Borcea, A. Ferrari, Y. Kadi, V. Lacoste, V. Vlachoudis, “Particle Distribution Entering the Vacuum Tube from a $80 \times 80 \times 60 \text{ cm}^3$ Lead Target”, SL-Note-2000-029 (EET), 30 March 2000.
- [8] “Neutron TOF Facility (PS 213) Technical Design Report”, CERN/INTC/2000-004, 11 February 2000.
- [9] M. Höfert, *et al.*, “The Prediction of Radiation Levels from Induced Radioactivity: Discussion of an Internal Dump Facility in the PS”, DI/HP/185 Health Physics Group, 27 January 1975.
- [10] A. Fassò, A. Ferrari, J. Ranft and P.R. Sala, Proc. of the Third Workshop on Simulating Accelerator Radiation Environments (SARE-3), Tsukuba (Japan), H. Hirayama, ed., KEK Proceedings 97-5 (1997), 32. A. Ferrari, T. Rancati and P.R. Sala, Proc. of the Third Workshop on Simulating Accelerator Radiation Environments (SARE-3), Tsukuba (Japan), H. Hirayama, ed., KEK Proceedings 97-5 (1997), 165.
- [11] J.K. Tuli, “Evaluated Nuclear Structure Data File – A Manual for Preparation of Data Sets”, Thomas W. Burrows, “The Program RADLST”, National Nuclear Data Center, Brookhaven National Laboratory, Upton, NY 11973, 29 February 1988.
- [12] A.V. Sannikov, E.N. Savitskaya, “Ambient Dose and Ambient Dose Equivalent Conversion Factors for High-energy Neutrons”, CERN/TIS-RP/93-14 (1993).
- [13] IAEA Technical Report Series No. 283, “Radiological Safety Aspects of the Operation of Proton Accelerators”, IAEA Vienna (1988).

SESSION IV

Shielding Benchmark Calculations and Results

Chairs: P. Berkvens, L. Ulrici

Neutron Attenuation Length

**INTERCOMPARISON OF MEDIUM ENERGY
NEUTRON ATTENUATION IN IRON AND CONCRETE (3)**

H. Hirayama

KEK, High Energy Accelerator Research Organisation
1-1 Oho, Tsukuba, Ibaraki, 305-0801 Japan
E-mail: hideo.hirayama@kek.jp

Attenuation Length Sub-working Group in Japan

Abstract

Expanding upon the results presented at SATIF-4, revised calculation problems were prepared by the Japanese Working Group and sent to the participants. So as to determine the energy dependence of the source neutrons, 1, 1.5 and 3 GeV neutrons were added. The secondary neutrons from 3 and 5 GeV protons, calculated by H. Nakashima, were also added. Additionally, the total and elastic cross-sections of H, O, Al, Si and Fe used at each code were requested to be included for comparisons. This paper presents a comparison of the cross-section data and the neutron attenuation length of iron and concrete sent from two groups to the organiser at the end of June, including the results presented at SARE-4 and the future themes which emerge from this intercomparison.

Introduction

Neutron attenuation at a medium energy below 1 GeV has not been well understood until now. It is desired to obtain common agreements concerning the behaviours of neutrons inside various materials. This is necessary in order to agree on definitions of the attenuation length, which is very important for shielding calculations involving high-energy accelerators. As a means of accomplishing this objective, Japanese participants of SATIF-2 proposed to compare the attenuation of medium-energy neutrons inside iron and concrete shields between various computer codes and data, this being cited as a suitable action for SATIF. The first results from three groups were presented at SATIF-3 [1]. The attenuation of neutrons above 20 MeV was compared for the planar geometry at SATIF-4 [2]. Secondary neutrons produced by medium-energy protons were also included as the source neutrons. The attenuation length itself varied slightly, but all results showed the same tendency towards an increase in attenuation length accompanying an increase of the neutron energy up to 500 MeV. It was found that differences existed in the attenuation tendencies of source neutrons between the codes used. Considering these results, revised calculation problems were prepared by the Japanese Working Group and sent to the participants. So as to determine the energy dependence of the source neutrons, 1, 1.5 and 3 GeV neutrons were added. The secondary neutrons from 3 and 5 GeV protons, calculated by H. Nakashima [3], were also added. Additionally, the total and elastic cross-sections of H, O, Al, Si and Fe used at each code were requested to be included for comparisons.

The results from two groups were sent to the organiser at the end of June. This paper presents a comparison of the cross-section data and the neutron attenuation length of iron and concrete, including the results presented at SARE-4 and the future themes which have emerged from this intercomparison.

Problems for an intercomparison (3)

Considering the results presented at SATIF-4 [2], the following revised problems were proposed to be calculated by various codes with their own databases. The total and elastic cross-section data were added to determine the reasons for the differences in the attenuation tendency of source neutrons. Secondary neutrons produced by 3 and 5 GeV protons toward lateral directions were also added, and were calculated by H. Nakashima [3] using the same procedure as from 0.5 and 1 GeV protons using FLUKA [4,5].

Neutron total and elastic cross-section comparison

- Material: H, O, Si, Al and Fe.
- Energy: 50, 100, 200, 500, 1 000, 2 000, 3 000 and 5 000 MeV.

Attenuation calculation

Source neutron energy

Source neutrons are uniformly distributed within the following energy regions:

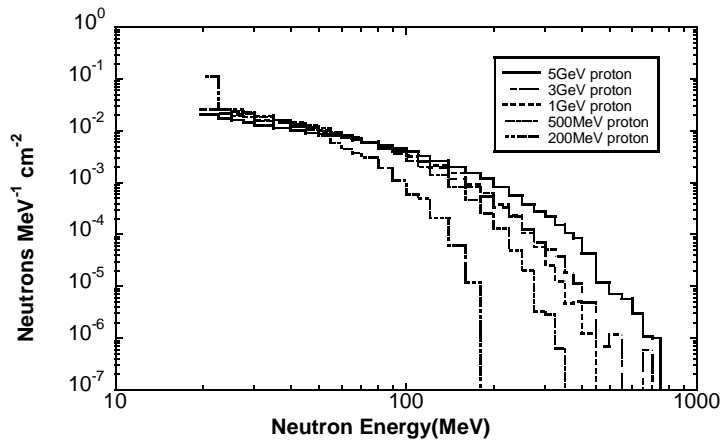
- 40-50 MeV.
- 90-100 MeV.
- 180-200 MeV.

- 375-400 MeV.
- 1 GeV.
- 1.5 GeV.
- 3 GeV.

Secondary neutrons (see Figure 1):

- From 200 MeV protons.
- From 500 MeV protons.
- From 1 GeV protons.
- From 3 GeV protons.
- From 5 GeV protons.

Figure 1. Secondary neutron at 90° from an iron target bombarded by protons (FLUKA calculations)



Geometry

Plane (6 m thick) with normal-incident parallel beams.

Shielding material

As typical shielding materials, iron and concrete were selected. The densities of the two materials and the composition of concrete are also presented (Table 1).

- Iron (density 7.87 g cm^{-3}).
- Concrete (density 2.27 g cm^{-3}) [Type 02-a, ANL-5800, 660 (1963)].

Table 1. Composition of concrete

Element	Atomic number density ($10^{24}/\text{cm}^{-3}$)	Weight per cent
H	1.3851E-2	1.02
C	1.1542E-4	1.00
O	4.5921E-2	53.85
Mg	1.2388E-4	0.22
Al	1.7409E-3	3.44
Si	1.6621E-2	34.21
K	4.6205E-4	1.32
Ca	1.5025E-3	4.41
Fe	3.4510E-4	1.41

Energy group and fluence to the dose-equivalent conversion factor

The energy group in Table 2 is presented as the standard; it is required that the neutron spectra be presented in this energy group, if possible.

In dose calculations, it is recommended to use the neutron flux-to-dose equivalent conversion factor (Table 3), so as to avoid any ambiguity due to the conversion factor used. The values given in Table 3 are conversion factors to the neutron energy corresponding to that given in Table 2.

Table 2. Upper energy of 66 neutron energy groups (MeV)

3.00E+3	2.50E+3	2.00E+3	1.90E+3	1.80E+3	1.70E+3	1.60E+3	1.50E+3
1.40E+3	1.30E+3	1.20E+3	1.10E+3	1.00E+3	9.00E+2	8.00E+2	7.00E+2
6.00E+2	5.00E+2	4.00E+2	3.75E+2	3.50E+2	3.25E+2	3.00E+2	2.75E+1
2.50E+2	2.25E+2	2.00E+2	1.80E+2	1.60E+2	1.40E+2	1.20E+2	1.10E+2
1.00E+2	9.00E+1	8.00E+1	7.00E+1	6.50E+1	6.00E+1	5.50E+1	5.00E+1
4.50E+1	4.00E+1	3.50E+1	3.00E+1	2.75E+1	2.50E+1	2.25E+1	2.00E+1

Table 3. Neutron flux-to-dose conversion factor [(Sv/hr)/(n/sec/cm²)]

ICRP51 (1987) [6], 20-3 000 MeV, Table 23

7.02E-6	6.72E-6	6.32E-6	6.22E-6	6.11E-6	5.98E-6	5.84E-6	5.69E-6
5.52E-6	5.34E-6	5.14E-6	4.94E-6	4.72E-6	4.47E-6	4.18E-6	3.78E-6
3.26E-6	2.72E-6	2.25E-6	2.20E-6	2.15E-6	2.10E-6	2.05E-6	1.99E-6
1.93E-6	1.86E-6	1.82E-6	1.79E-6	1.77E-6	1.74E-6	1.72E-6	1.70E-6
1.68E-6	1.67E-6	1.65E-6	1.64E-6	1.63E-6	1.62E-6	1.61E-6	1.60E-6
1.59E-6	1.58E-6	1.57E-6	1.56E-6	1.55E-6	1.54E-6	1.53E-6	1.52E-6

Quantities to be calculated

The following quantities must be calculated for intercomparisons:

- Dose equivalent due to neutrons above 20 MeV at 50, 100, 150, 200, 250, 300, 350, 400, 450 and 500 cm.
- Neutron spectrum in $\text{n}/\text{cm}^2/\text{MeV}/\text{source neutron}$ at 100, 200, 300, 400 and 500 cm.

Summary of contributors

Cross-section data

R.E. Prael presented a comparison of the nucleon cross-section data used in FLUKA, LAHET3 and MCNPX with several parameterisation methods at SARE-4 [7]. He prepared the cross-section data required upon a request of the organiser. Including these data, contributors are summarised in Table 4. B.S. Sychev published the evaluated the cross-sections of high-energy hadron interactions for various materials [8] after SATIF-4. His evaluated data were also used in the comparisons.

Table 4. Contributors for cross-section intercomparisons

Name of participant and organisation	Name of computer code or database
R.E. Prael (LANL)	FLUKA, LAHET3, NCMPX
H. Nakashima (JAERI)	NMTC/JAM [9,10,11]
N. Mokhov (FNAL)	MARS13(99)
Y. Sakamoto (JAERI)	HILOR

Neutron attenuation calculation

Although several groups tried to calculate the proposed problems, only two groups (see Table 5) sent results to the organiser. Other groups are continuing their calculations, and can send their results before the next meeting.

Table 5. Contributors providing calculation results

Name of participants and organisation	Name of computer code	Name of database used in the computer code
R. Tayama, etc. (Hitachi Eng. Co., Ltd. and Starcom Co., Ltd.)	NMTC/JAM	JAM
Y. Sakamoto (JAERI)	ANISN-JR	HILO-86

Results and discussions

Cross-section

Intercomparisons of the total and elastic cross-sections were proposed to determine the reasons for the variations in the attenuation tendency of the source neutrons. Figures 2 and 3 show comparisons of the total and elastic cross-sections of iron, respectively. To see the differences clearly, comparisons using evaluated data by Sychev are shown in Figures 4 and 5. The total cross-sections agree within about 10%, including HILO86R multi-group cross-section data. There are large differences in the elastic cross-section at 200 MeV up to 50%.

The cross-sections for concrete were calculated by the organiser using the atomic number density in Table 1 and those of H, O, Al, Si and Fe. Figures 6-9 show similar comparisons for iron. Generally, although the total cross-sections agree with each other, those of HILO86R are about 30% higher at 200 MeV. In the case of elastic cross-sections, relatively large differences of about 30% are shown from 100-5 000 MeV.

Figure 2. Comparison of iron total cross-section

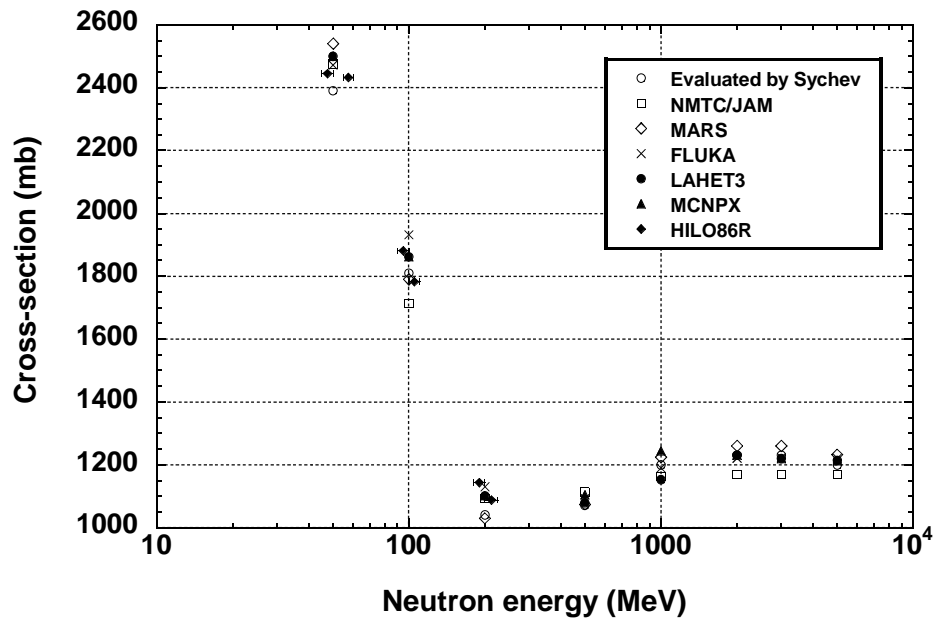


Figure 3. Comparison iron elastic cross-section

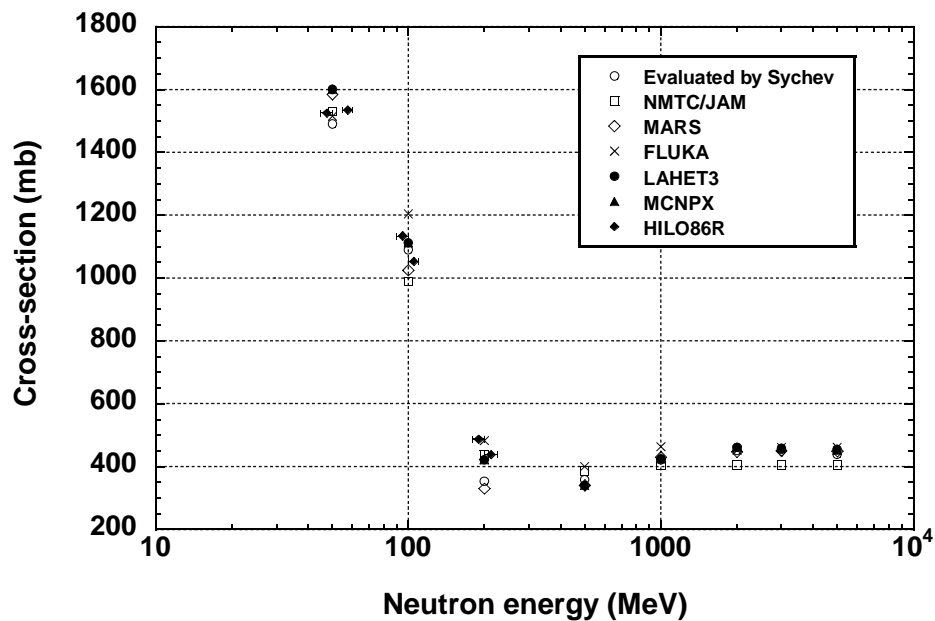


Figure 4. Comparison with the evaluated data by Sychev for the iron total cross-section

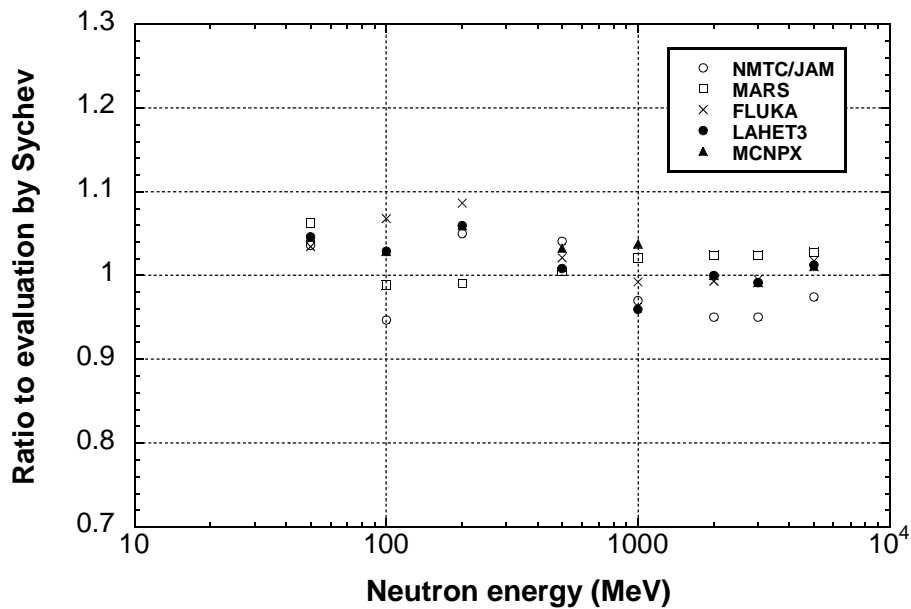


Figure 5. Comparison with the evaluated data by Sychev for the iron elastic cross-section

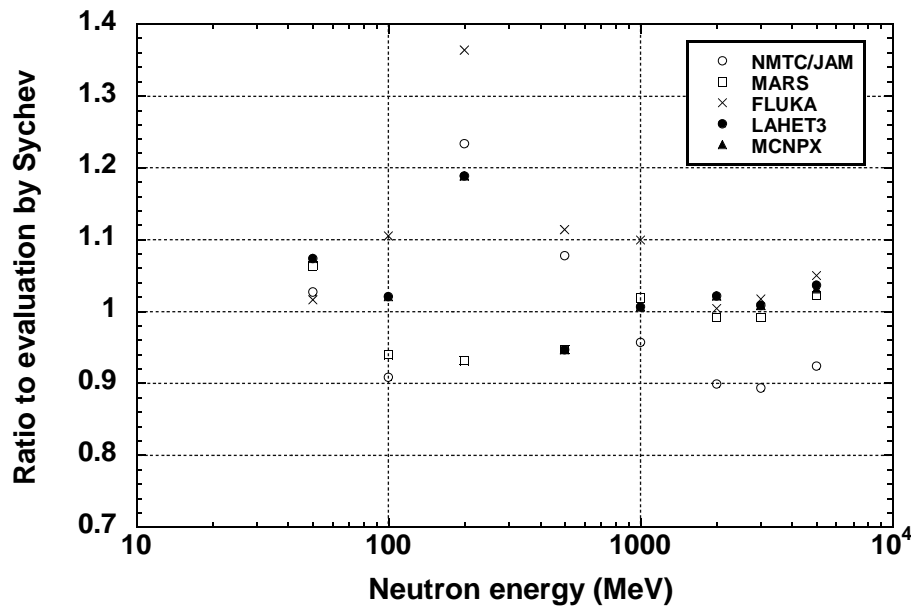


Figure 6. Comparison of the concrete total cross-section

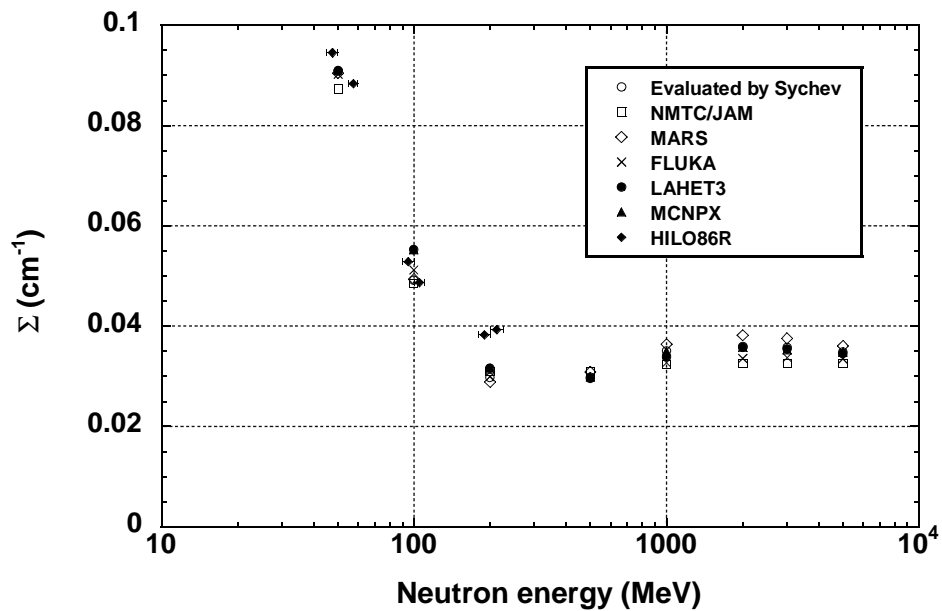


Figure 7. Comparison of the concrete elastic cross-section

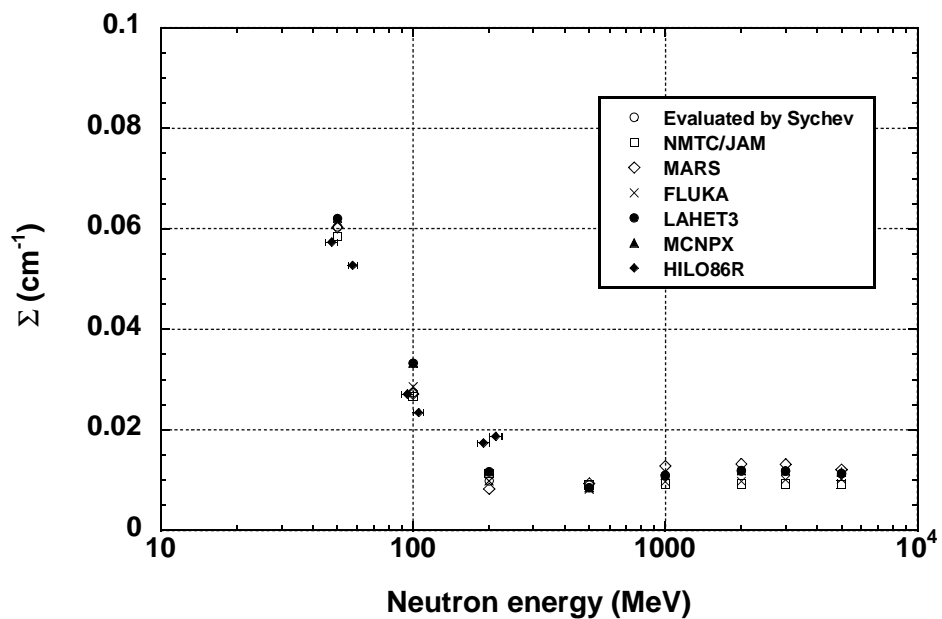


Figure 8. Comparison with the evaluated data by Sychev for the concrete total cross-section

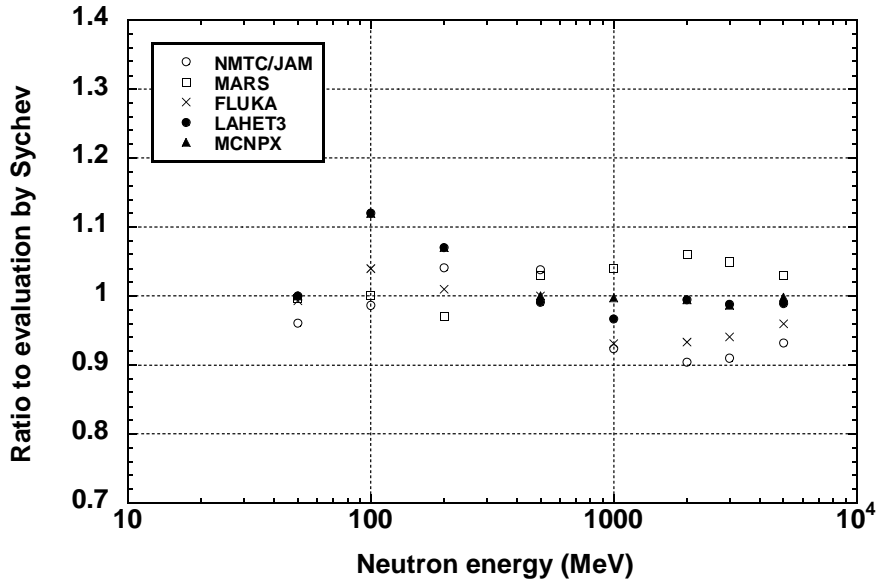
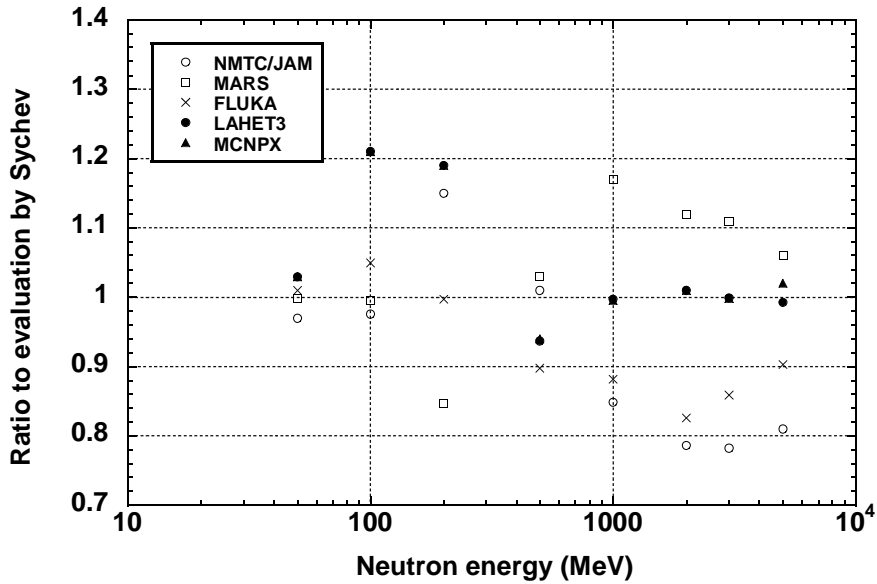


Figure 9. Comparison with the evaluated data by Sychev for the concrete elastic cross-section



H. Nakashima studied the effects of elastic scattering on the dose equivalents inside iron and concrete using NMTC/JAM with and without elastic scattering [12]. The difference for 200 MeV neutrons is about 30% at 2.5 m in iron and about 50% at 5 m in concrete. For 1 GeV neutrons, both results are almost the same. The difference becomes large for secondary neutrons, and is about a factor of 2 at 2.5 m in iron and 5 m in concrete.

At deep penetrations, differences of 10-20% at the total cross-section would also affect the results. In addition to Nakashima's studies, it is desired to study the effects of these differences in the fundamental data inside thick shields.

Attenuation length

The attenuation length (λ ; g cm^{-2}) for each case was obtained by a least-squares fitting. The neutron attenuation lengths of iron and concrete obtained using this method are shown in Figures 10 and 11, respectively. In these figures, the results presented at SATIF-4 are also plotted. The attenuation lengths of both iron and concrete still increase with increases of the source neutrons, even in the 5 000 MeV case. However the increase rate decreases compared with that below 500 MeV. It is supposed that the attenuation length reaches a constant value at around 10 GeV.

Figure 10. Comparison of the neutron attenuation length of iron

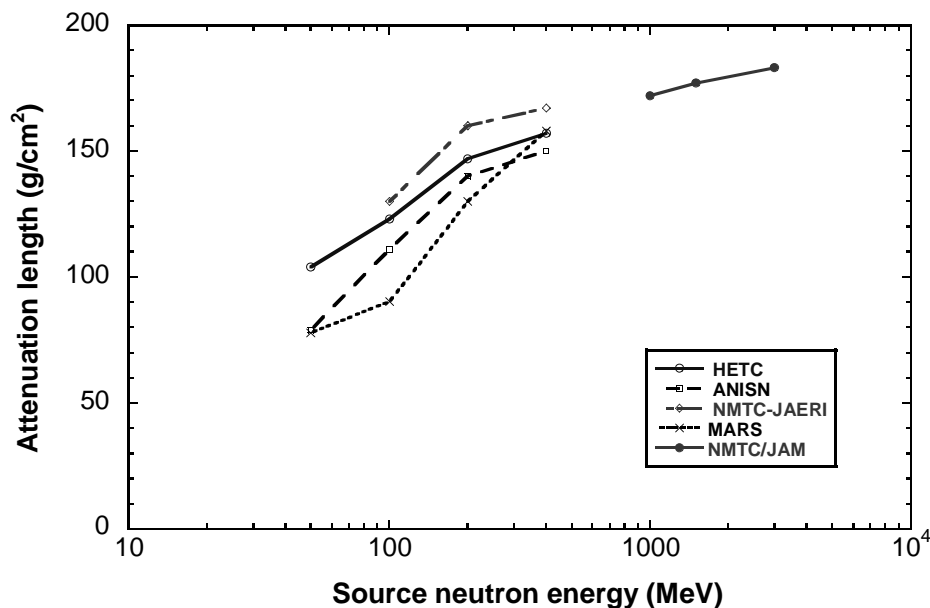
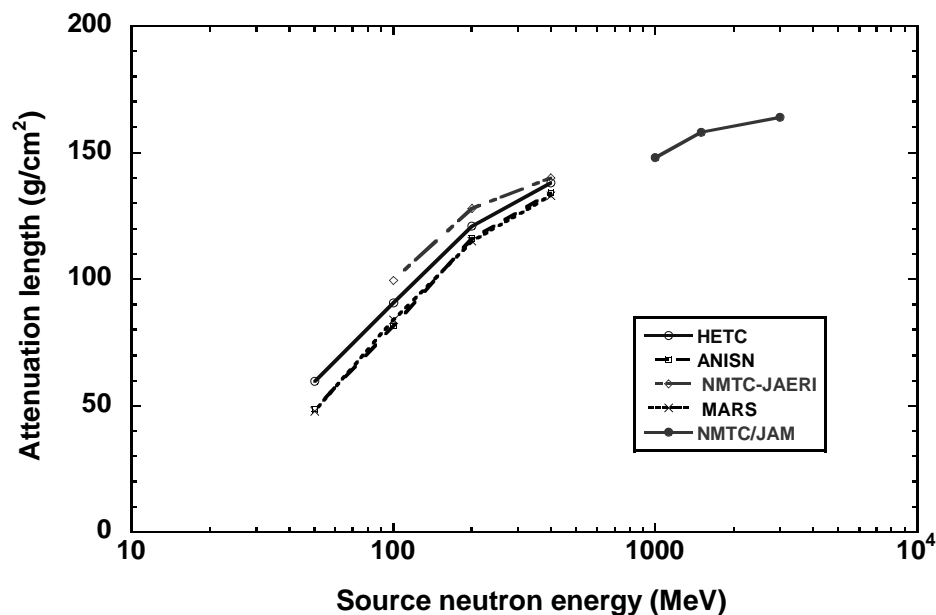


Figure 11. Comparison of the neutron attenuation length of concrete



The attenuation lengths of iron and concrete for secondary neutrons from high-energy protons are shown as the function of the proton energy in Figures 12 and 13, respectively. In these figures, the experimental results at ISIS [8] and LANSCE [9] are also plotted together with those presented at SARE-4. The attenuation lengths of both iron and concrete slightly increase with an increase in the proton energy, and seem to increase for higher-energy protons. The values of the experimental results are larger than those calculated. The secondary neutron spectrum presented was for neutrons emitted at 90° from the iron target (5 cm diameter, 60 cm length). In the case of both experiments, a heavy shield existed in the forward direction, and a shield was situated very close to the target. These differences are supposed to be the reasons for the difference, but this possibility must be verified.

Figure 12. Comparisons of the attenuation length of iron for secondary neutrons from the high-energy protons

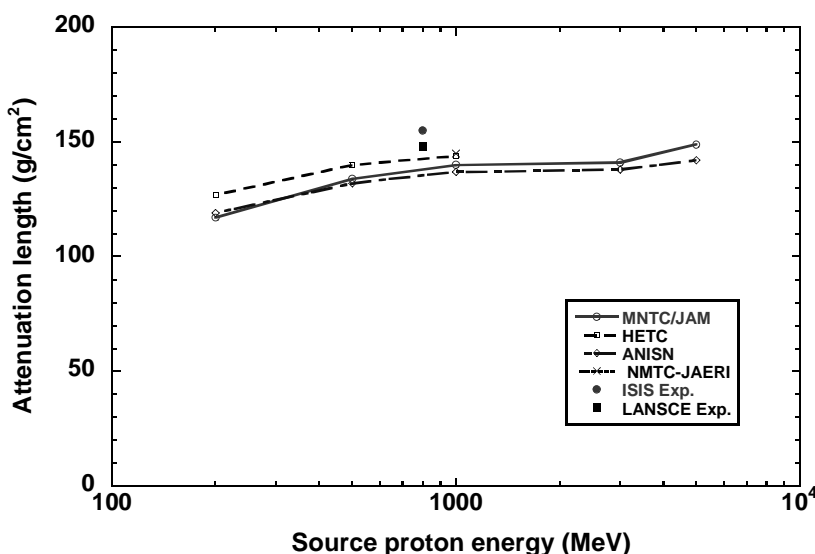
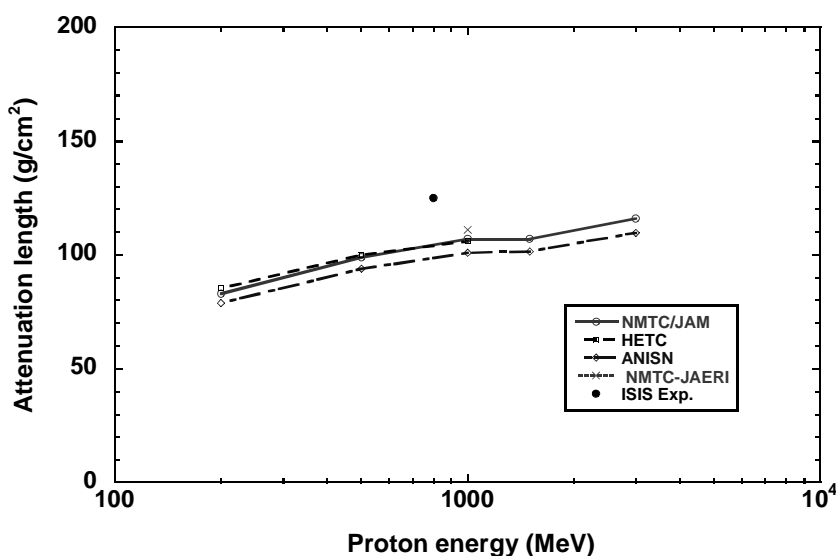


Figure 13. Comparison of the attenuation length of concrete for secondary neutrons from high-energy protons



Future themes

From the comparisons given above, it is necessary to discuss and perform the following themes as the next step:

- Compare with the results of other codes to confirm the tendency shown above. It is desired to receive the results from other groups.
- Neutron dose equivalent attenuation up to several tens of GeVs in order to confirm whether the attenuation length reaches a constant value or not.
- Select suitable problems to understand the attenuation length of secondary neutrons from high-energy protons.
- Intercomparisons of the cross-section data are important, but are not suitable for studies within this task. It is desired to create new groups for this theme.

REFERENCES

- [1] Hirayama, *et al.*, “Intercomparison of the Medium-energy Neutron Attenuation in Iron and Concrete”, Proceedings of Shielding Aspects of Accelerators, Targets and Irradiation Facilities, SATIF-3, Tohoku University, 12-13 May 1997, pp. 185-195.
- [2] Hirayama, *et al.*, “Intercomparison of the Medium-energy Neutron Attenuation in Iron and Concrete (2)”, Proceedings of Shielding Aspects of Accelerators, Targets and Irradiation Facilities, SATIF-4, Knoxville, Tennessee, USA, 17-18 September 1998, pp. 143-154.
- [3] H. Nakashima, private communication.
- [4] A. Fassò, A. Ferrari, J. Ranft and P.R. Sala, “FLUKA: Present Status and Future Developments”, Proc. IV Int. Conf. on Calorimetry in High-energy Physics, La Biodola (Isolad’Elba), 20-25 Sept. 1993, A. Menzione and A. Scribano, eds., World Scientific, p. 493.
- [5] A. Fassò, A. Ferrari, J. Ranft and P.R. Sala, “FLUKA: Performances and Applications in the Intermediate Energy Range”, Specialists Meeting on Shielding Aspects of Accelerators, Targets and Irradiation Facilities, Arkington, Texas, 28-29 April 1994.
- [6] ICRP Publication 51, “Data for Use in Protection Against External Radiation”, annals of the ICRP 17(2/3) (1987).
- [7] R.E. Prael, A. Ferrari, R.K. Tripathi and A. Polanski, “Comparison of Nucleon Cross-section Parameterization Methods for Medium and High Energies”, Proceedings of the Forth Workshop on Simulating Accelerator Radiation Environments, Knoxville, TN, USA, 14-16 Sept. 1998, pp. 171-181.

- [8] R.S. Sychev, "Cross-sections of High-energy Hadron Interactions on Nuclei", Russian Academy of Sciences, Moscow Radiotechnical Institute, translated by E. Gelfand (1999).
- [9] H. Takada, *et al.*, "An Upgraded Version of the Nucleon Meson Transport Code: NMTC/JAERI97", JAERI-DATA/CODE 98-005, 1998.
- [10] K. Niita, *et al.*, "Analysis of the Proton-induced Reactions at 150 MeV-24 GeV by High-energy Nuclear Reaction Code JAM", JAERI Tech 99-065 (1999) (in Japanese).
- [11] K. Niita, "High-energy Nuclear Reaction Code JAM", Proc. of Symp. on Nucl. Data, JAERI Tokai, 18-19 Nov. (1999).
- [12] H. Nakashima, private communication.

Deep Penetration Experiment

DEEP PENETRATION CALCULATIONS OF NEUTRONS UP TO 1.5 GeV

Hiroyuki Handa, Ryuichi Tayama, Katsumi Hayashi

Hitachi Engineering Co., Ltd.
Saiwai-cho, 3-2-1, Hitachi, Ibaraki 317-0073 Japan
E-mail: h_handa@psg.hitachi-hec.co.jp

Hiroshi Nakashima, Yukio Sakamoto, Nobuo Sasamoto

Japan Atomic Energy Research Institute
Tokai-mura, Ibaraki 319-1195 Japan

Teruo Abe, Koubun Yamada

Startcom Co., Ltd.
Hayamiya, 4-18-10, Nerima-ku, Tokyo 179-0085 Japan

Abstract

In order to optimise the shielding design of an accelerator facility, it is important to understand the shielding characteristics of the facility and its applicability to the design of calculation codes. From this point of view, deep penetration calculations were performed for three shielding benchmark problems:

- (a) The intercomparison problem.
- (b) The beam spill problem.
- (c) The full beam stop problem.

They were performed using the Monte Carlo codes NMTC, LAHET and MCNP, as well as an S_N code, ANISN. Consequently, useful insights regarding the accuracy of the ANISN code, the shielding characteristics of high-energy neutron penetration and the optimisation of the shield were obtained.

Introduction

The concept of all the facilities of the Centre for Neutron Science has been studied at the Japan Atomic Energy Research Institute (JAERI). In the shielding design of the accelerator facility and the neutron scattering facility, Monte Carlo methods and S_N methods will be used for deep penetration problems. However, these methods pose certain difficulties when applied to design calculations.

High-energy neutrons were generated corresponding to proton energy, and have become a major source for shielding in the facilities. Therefore, the characteristics of the neutron for deep penetration should be understood. It is also necessary to clarify the dependency of the neutron with respect to the different targets. Additionally, low energy neutrons may also be important in a deep penetration problem.

Monte Carlo methods have been improved so as to be applicable to deep penetration calculations. The next step is to accumulate the applicability experience of the Monte Carlo methods to actual design configurations. Since S_N methods will be utilised as an auxiliary tool with Monte Carlo methods, it is also necessary to determine the calculation accuracy of the S_N methods.

Three shielding benchmark problems of relatively thick bulk shield were analysed using Monte Carlo codes and an S_N code so as to better understand the shielding characteristics of the accelerator facility and the applicability of the calculation codes.

Outline of benchmark problems

The following three problems are analysed:

- (a) The intercomparison problem.
- (b) The beam spill problem.
- (c) The full beam stop problem.

Problem (a) was proposed by H. Hirayama at SATIF-4 [1], and was intended to investigate the fundamental penetrating characteristics of neutrons above 20 MeV through bulk shield. The geometry of the problem is a plane shield with normal incident parallel beams. The thickness and material of the shield is a 3 m thick iron or a 6 m thick ordinary concrete. The sources are the neutrons uniformly distributed within following energy regions: 375-400, 180-200, 90-100 and 45-50 MeV, as well as the secondary neutron spectrum produced from an iron target bombarded by 1 GeV proton.

Problem (b) and (c) are typical geometries encountered in the shielding design of the facility. Problem (b) is the problem for which penetrating characteristics of neutrons of the overall energy region can be estimated and is for the shielding design of the accelerator facility. Neutrons are generated from a supposed beam loss point. Then, a cylindrical iron target of 5 cm in diameter and 50 cm in length was modelled as a beam loss point as shown in Figure 1. The proton beam spill rate is 1 W/m. Incident proton energies are 100, 400, 800 MeV, 1 and 1.5 GeV.

Problem (c) addresses the penetrating characteristics of neutrons through a multi-layer shield and is for the shielding design of the neutron scattering facility. Neutrons are generated from the target by the full stop of a proton beam. The proton beam energy and power are 1.5 GeV and 5 MW. The target shown in Figure 2 is a cylindrical hydrargyrum with a diameter of 16 cm and a length of 60 cm. A lead

reflector with a thickness of 20 cm in the forward direction of the proton beam and a thickness of 30 cm in the radial direction surrounds the target. The following shield is assumed around the target in the configurations:

- Forward direction: 4 m thick iron + 1 m thick concrete.
- Radial direction: 3 m thick iron + 1 m thick concrete.

Intercomparison problem

Calculation method

The calculation was carried out using the Nucleon Meson Transport Code NMTC/JAERI97 [2]. The bulk shield was modelled to be a cylindrical geometry with a 3 m diameter and thickness for iron and 6 m for concrete. The source was a normal incident pencil beam to the bulk shield and was located at the centre of the shield. Circular surface crossing estimators with the same diameters as the bulk shields were used as detectors. The size of mesh intervals is 25 cm for iron and 50 cm for concrete, respectively. Calculations using the deterministic method were also performed using the ANISN-JR [3] code and the HILO86R [4] cross-section library.

Results

The attenuation of the calculated dose equivalents by NMTC and ANISN within iron and concrete are given in Figures 3 and 4, respectively. The dose equivalents of neutrons above 20 MeV decrease almost exponentially along with an increase in the thickness for all of the results. Apparent differences, however, can be seen in the attenuation tendency. NMTC provides larger result than ANISN. The differences become larger with a decrease in the source neutron energy, and for 100 MeV source neutron, NMTC gives results almost ten times as high as ANISN with 5 m thick concrete.

Beam spill problem

Calculation method

In the beam spill problem, LAHET [5] was applied to calculate the neutron flux above 20 MeV, as was NMTC. Then, the continuous energy Monte Carlo code MCNP-4A was used to calculate the neutron contribution with energies below 20 MeV using calculated results by LAHET and NMTC. The track length estimator was used as a detector. The values for an importance sampling technique were decided at intervals of 2.0.

ANISN calculations were also performed using a cylindrical geometry with the HILO86R cross-section library. As for a source term, boundary-crossing flux at the inner surface of the shield obtained from NMTC and MCNP calculations was used as an isotropic angular shell source only for the forward direction. The neutron component above 400 MeV was put to the first energy group of the library (400~375 MeV), because the upper energy of HILO86R is up to 400 MeV.

Results

As an example of the results, the attenuation of the neutron dose equivalents inside iron for the 1.5 GeV proton beam are given in Figure 5.

The energy spectrum (as shown in Figure 6) changes with an increase in the penetration depth and major energy component shifts to a relatively low-energy region owing to the elastic scattering and 24 keV resonance of iron. This effect of the change of energy spectrum is displayed in Figure 7. While the major energy region of the incident neutron (0.0-25.0 cm cell) to the shield contributed to dose rate is 10^{-1} ~ 10^0 MeV, the energy region shifts to about 20 keV and below it after 200 cm thick penetration (200.0-225.0 cm cell).

ANISN gives slightly higher results than Monte Carlo calculations, because although ANISN decreases almost exponentially, the attenuation curve of Monte Carlo calculations is slightly dented. As for the energy spectrum, the discrepancy between ANISN and Monte Carlo calculations becomes large, especially for high energy with an increase in the penetration depth. In this case, high-energy cross-section data should be reviewed.

As for the concrete shield shown in Figure 8, the ANISN calculation shows about one-fifth the result of the Monte Carlo calculations behind the 600 cm thick concrete. The different change of neutron spectrum with iron can be observed in Figures 9 and 10. With concrete, the major energy region contributed to a dose equivalent shift from 10^0 ~ 10^{-1} MeV to near 10^2 and 10^0 MeV with an increase in the penetration depth.

Full beam stop problem

Calculation method

In the full beam stop problem, the calculation method is almost the same as that of the beam spill problem. A track length estimator was used.

ANISN calculations were also performed using slab geometry for the beam incident direction and spherical and cylindrical geometries for the radial direction with similar isotropic angular shell sources as that of the beam spill problem.

Results

As an example of the results of the full beam stop problem, the attenuation of the neutron dose equivalents inside the radial shields is given in Figure 11. The calculated results give a more rapid attenuation tendency in the concrete than in the iron, and a higher shielding performance was observed in the concrete than in the iron. This tendency is different from the general knowledge of shielding performance for the high-energy neutrons as shown Figures 3 and 4. In an iron/concrete multi-layer shield, the required thickness of the concrete behind the iron can be reduced in comparison to just a single layer shield of concrete. For example, more than 1 m thick concrete to reduce the dose in a digit is necessary for a single concrete according to Figure 4, while just 25 cm thick concrete is needed for the multi-layer shield. This is because of a change in the neutron spectrum to low energy after deep penetration in iron. That is (as shown in Figure 12) a relatively low energy neutron below 24 KeV of iron resonance is major component in an incident neutron spectrum to the concrete shield after the deep penetration through an iron shield. In these low energy regions, concrete has a higher shielding performance than iron as a result of the elastic scattering effect of hydrogen contained in concrete.

As for a comparison between Monte Carlo codes and ANISN, spherical geometry gives lower results than the Monte Carlo calculations. On the other hand, the cylindrical geometry gives a slightly higher result than the Monte Carlo in the iron and gives almost the same result as the Monte Carlo in the concrete. Therefore, cylindrical geometry as for ANISN is suitable for design calculation in the problem.

Conclusions

Deep penetration calculations for three shielding benchmark problems were performed using Monte Carlo codes and an S_N code in an effort to understand the shielding characteristics of the accelerator facility and the applicability of the calculation codes. The following results were obtained:

- For the dose equivalents of neutrons above 20 MeV, NMTC shows higher results than ANISN in both iron and concrete.
- High-energy cross-section data should be reviewed as a result of the discrepancy between ANISN and Monte Carlo calculations.
- It is important to consider the change of the neutron energy spectrum in the deep penetration problems. Especially, low energy neutrons escaping from the 24 keV resonance window of iron are dominant components to dose equivalents in a thick iron shield.
- In an iron/concrete multi-layer shield, the required thickness of the concrete behind the iron can be reduced in comparison with a simple concrete shield.

Acknowledgements

The authors wish to thank Dr. H. Takada for his helpful advice with the use of NMTC/JAERI97.

REFERENCES

- [1] H. Hirayama, *et al.*, “Intercomparison of the Medium-energy Neutron Attenuation in Iron and Concrete (2)”, KEK Preprint 98-164, Oct. (1998).
- [2] H. Takada, *et al.*, JAERI-Data/Code 98-005 (1998).
- [3] K. Koyama, *et al.*, JAERI-M 6954 (1977).
- [4] H. Kotegawa, *et al.*, JAERI-M 93-020 (1993).
- [5] E.R. Prael, *et al.*, “User Guide to LCS: The LAHET Code System”, Sept. (1989).

Figure 1. Geometry for beam spill problem

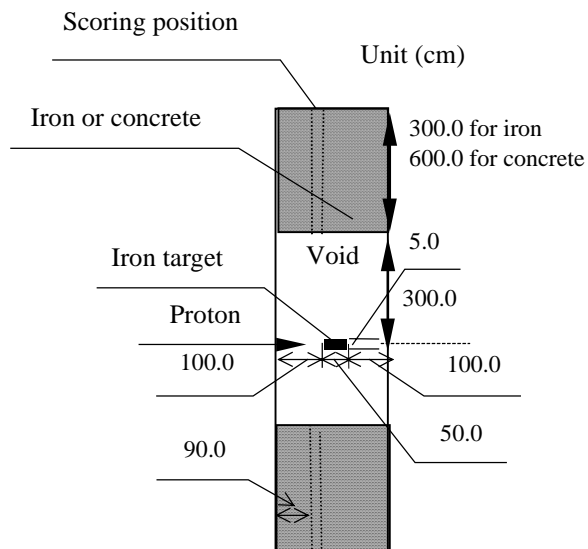


Figure 2. Geometry for full stop problem

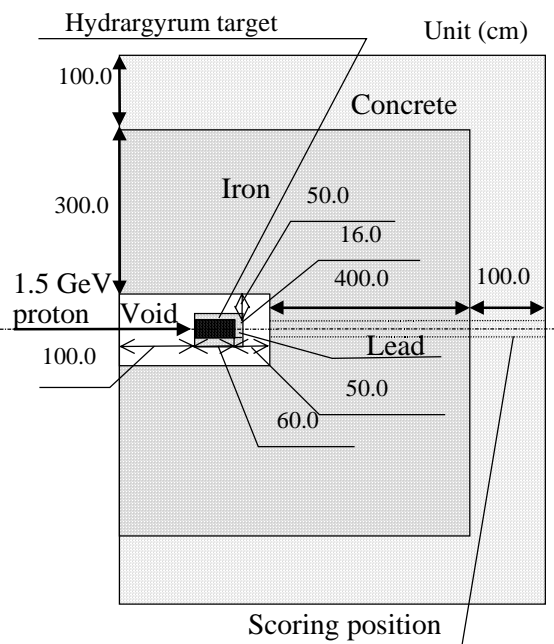


Figure 3. Attenuation of neutron dose equivalent inside iron for intercomparison problem

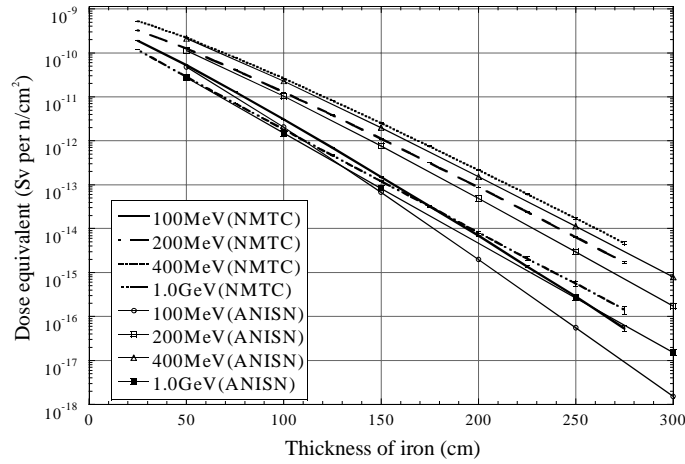


Figure 4. Attenuation of neutron dose equivalent inside concrete for intercomparison problem

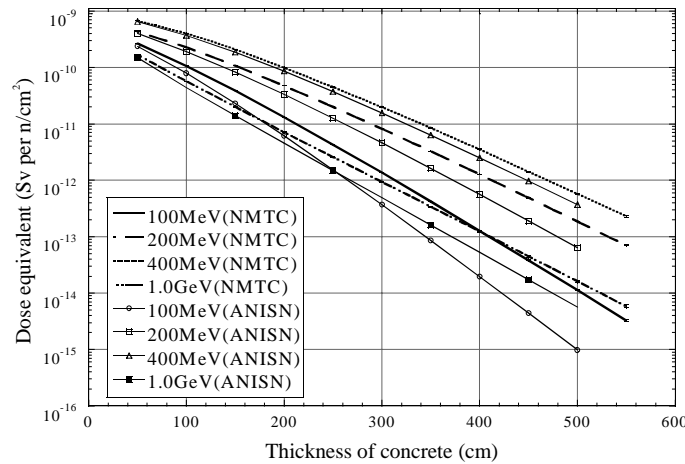


Figure 5. Attenuation of neutron dose equivalent inside iron for beam spill problem (1.5 GeV proton)

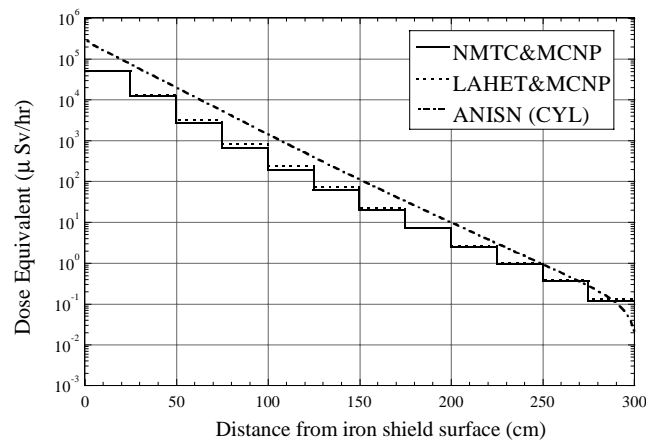


Figure 6. Neutron spectrum inside iron for beam spill problem

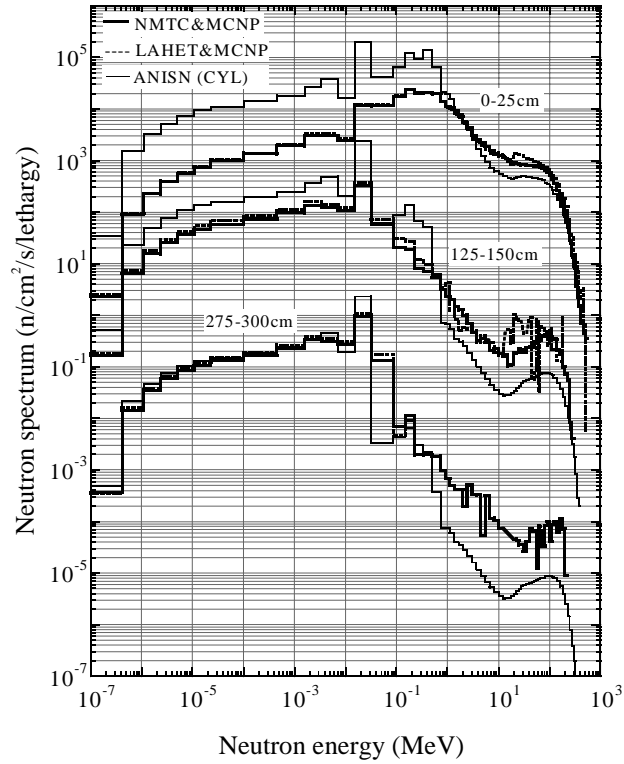


Figure 7. Percentage of dose contribution in each neutron energy component inside iron shield (1.5 GeV proton)

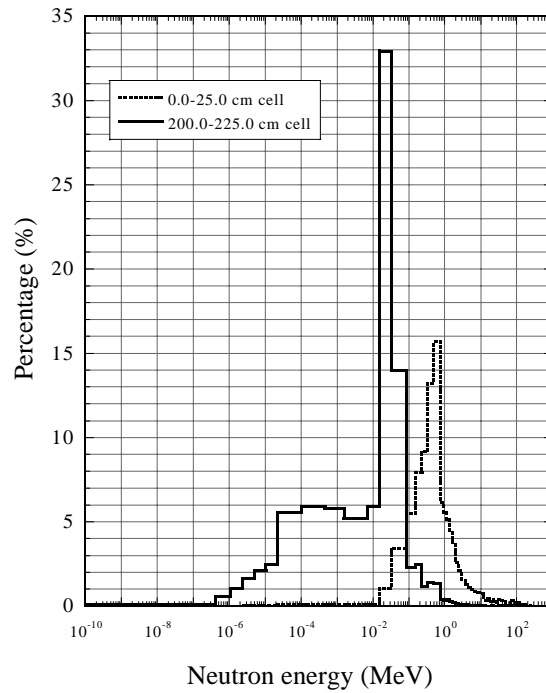


Figure 8. Attenuation of neutron dose equivalent inside concrete for beam spill problem (1.5 GeV proton)

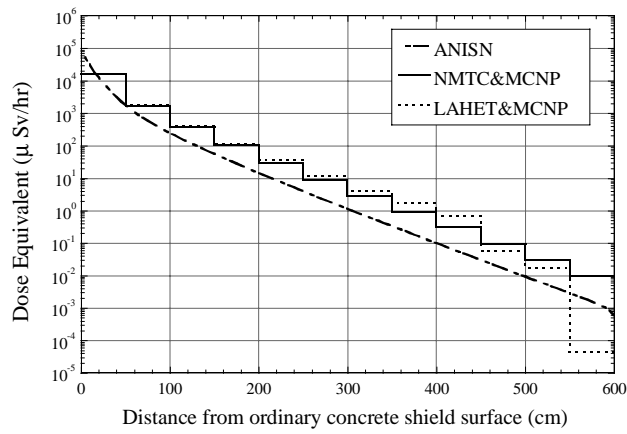


Figure 9. Neutron spectrum inside concrete for beam spill problem (1.5 GeV proton)

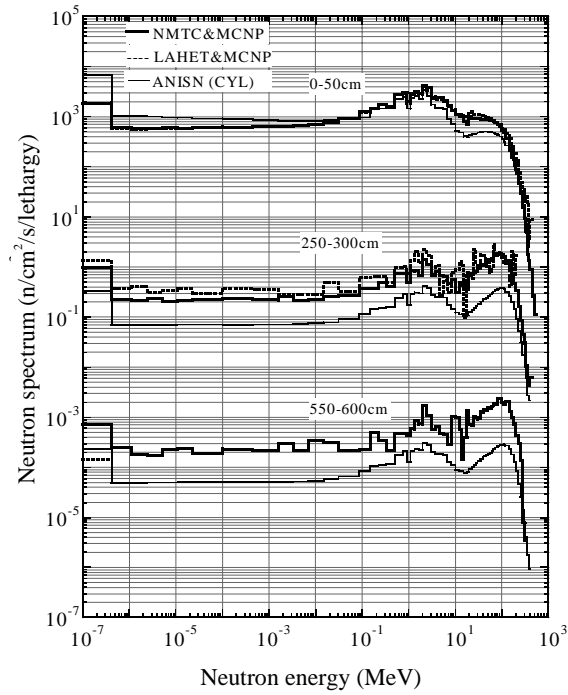


Figure 10. Percentage of dose contribution in each neutron energy component inside concrete shield (1.5 GeV proton)

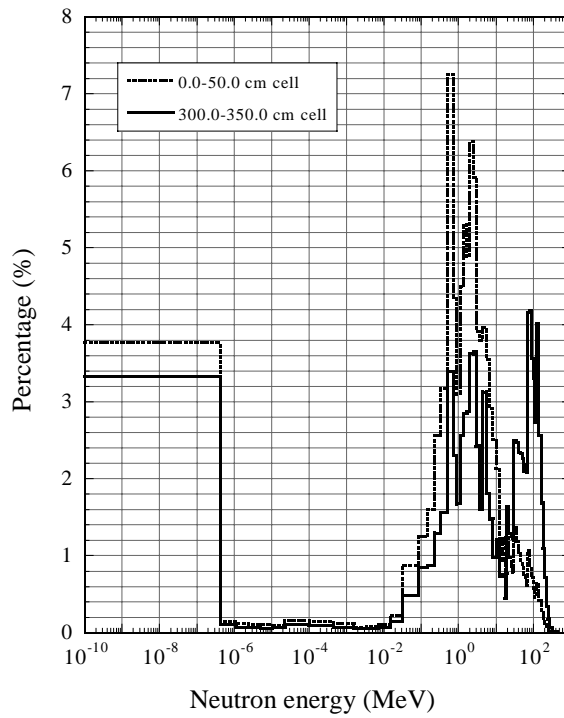


Figure 11. Attenuation of neutron dose equivalent inside radial shield for full beam stop problem

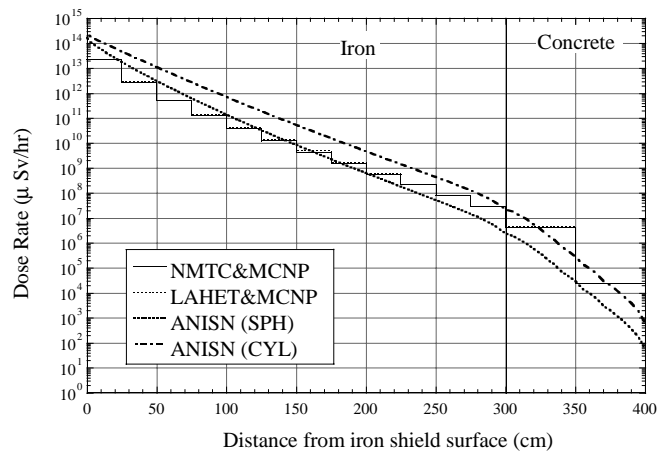
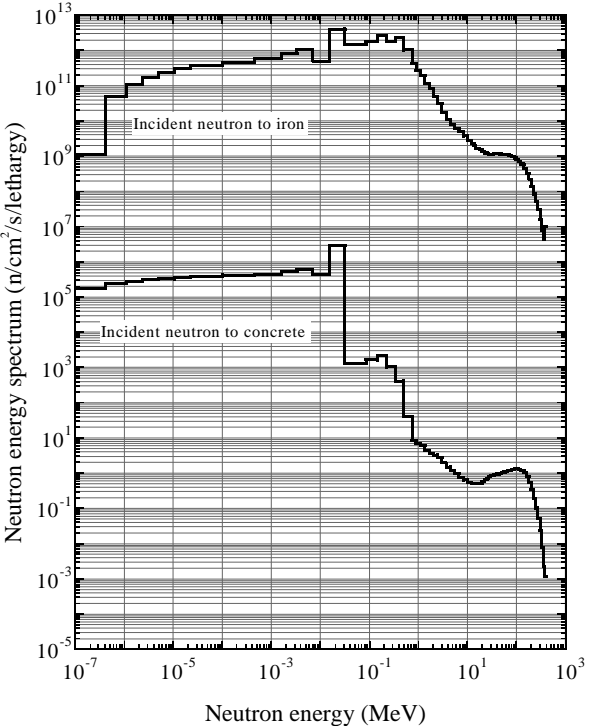


Figure 12. Energy spectrum of incident neutron to radial shield for full beam stop problem



DEEP PENETRATION EXPERIMENT AT ISIS

Noriaki Nakao*, **Tokushi Shibata**

High-energy Accelerator Research Organisation (KEK)

Oho 1-1, Tsukuba, Ibaraki 305-0801, Japan

*E-mail: noriaki.nakao@kek.jp

Tomoya Nunomiya, **Takashi Nakamura**, **Eunjoo Kim^a**,

Tadahiro Kurosawa^b, **Shingo Taniguchi^c**, **Michiya Sasaki**, **Hiroshi Iwase**

Tohoku University

Aoba, Aramaki, Aoba-ku, Sendai, 980-8579, Japan

Yoshitomo Uwamino, **Sachiko Ito**

The Institute of Physical and Chemical Research (RIKEN)

Hirosawa 2-1, Wako, Saitama 351-0198, Japan

Paul Wright, **David R. Perry**

Rutherford Appleton Laboratory (RAL)

Chilton, Didcot, Oxfordshire, OX11 0QX, UK

Abstract

A deep penetration experiment was performed at a spallation neutron source facility, ISIS. In the ISIS target station, a thick tantalum target is irradiated by 800 MeV-200 μ A protons, and is shielded by a 284 cm thick iron and 97 cm thick concrete in an upward direction. In the experiment, concrete slabs of up to 120 cm thickness or iron slabs of up to 60 cm thickness were additionally equipped at the top of the bulk shield. Neutrons leaked through the transverse bulk shield and additional shields were measured by various activation detectors using $^{12}\text{C}(n,2n)^{11}\text{C}$, $^{209}\text{Bi}(n,xn)^{210-x}\text{Bi}$ ($x = 4\sim 10$) and $^{27}\text{Al}(n,\alpha)^{24}\text{Na}$ reactions, and by an indium activation multi-moderator spectrometer. The reaction rates and the neutron energy spectra in a neutron energy range from thermal to 400 MeV for the various thicknesses of concrete and iron were obtained. These experimental data will be useful as benchmark data for neutron deep penetration. From the attenuation profiles established of $^{12}\text{C}(n,2n)$ and $^{209}\text{Bi}(n,xn)$ reaction rates, the attenuation lengths of high-energy neutrons produced at 90° by 800 MeV protons were estimated for concrete and iron.

The intra-nuclear cascade evaporation Monte Carlo calculations with the HETC-KFA2 code and the discrete-ordinates calculations with ANISN/DLC119 were also performed to compare with the experimental data. The calculations gave largely underestimated neutron fluxes for deep penetration, and gave about 10~20% shorter attenuation lengths.

^a Present address: Japan Atomic Energy Research Institute (JAERI), Toukai, Ibaraki 319-1195, Japan.

^b Present address: Electrotechnical Laboratory (ETL), Tsukuba, Ibaraki 305-8568, Japan.

^c Present address: Japan Synchrotron Radiation Research Institute (JASRI), Hyogo 679-5198, Japan.

Introduction

In high-intensity and high-energy hadron accelerator facilities, massive shields are required to reduce the leakage of high-energy neutrons having high penetrability. In order to estimate the deep penetration neutrons for shielding design of such facilities, the point kernel method, the Monte Carlo calculation and S_n calculation are usually used for shielding calculations. The calculations for such a large attenuation through a very thick shielding generally are largely in error with regard to the neutron flux. In the Monte Carlo calculation, a variance reduction method and a step-by-step calculation using multi-layer slabs are usually used for statistically good estimations of neutron flux outside a very thick shield. The accuracy of the calculation results are not well known, however, because the experimental data are very scarce. On the other hand, most of conceptual shielding designs for high-energy accelerator facilities have been generally performed using a point kernel method, that is the Moyer model, which is based on a single exponential attenuation of neutron dose equivalent behind a thick shield to be in a spectral equilibrium state. In this deep penetration problem, the dose attenuation length, which is ruled by high-energy neutrons above about 100 MeV, is an extremely important parameter of the Moyer model. Neutron shielding experiments at several accelerator facilities have been performed to get the attenuation length, but the reliable experimental data behind a very thick shield are still very scarce and dispersed [1-3].

Since 1992 deep penetration shielding experiments have been performed at an intense spallation neutron source facility, ISIS, of the Rutherford Appleton Laboratory [4,5]. A series of experiments were performed at the top surface of the bulk shield (shield top) just above the target to measure deep penetration neutrons through the transverse shield of 284 cm thick iron and 97 cm thick concrete. In the latest experiment in 1998, $^{12}\text{C}(n,2n)^{11}\text{C}$, $^{209}\text{Bi}(n,xn)^{210-x}\text{Bi}$ ($x = 4\sim 10$) and $^{27}\text{Al}(n,\alpha)^{24}\text{Na}$ reaction rates and neutron energy spectra outside the additionally equipped iron and concrete shields were measured, and attenuation profiles of high-energy neutrons produced by 800 MeV protons were obtained. This benchmark shielding experiment at an intense high-energy accelerator facility will also provide useful information for estimating the accuracy of the deep penetration transport calculations.

Experiment

ISIS facility

The experiment was performed at the ISIS spallation neutron source facility, RAL. The ISIS facility consists of a 70 MeV H^- linear accelerator, 800 MeV proton synchrotron and a spallation neutron target station. The beam intensity was about 170 μA at the target with a 50 Hz repetition rate. A cross-sectional view around the target station along the 800 MeV proton beam axis is shown in Figure 1. The tantalum target is placed at the centre of the stainless steel vessel and the moderators and reflectors are placed around the target. The spallation target is shielded with 284 cm thick iron and 97 cm thick ordinary concrete at an upward direction and the experiment was performed at the top of the shield just above the target. As shown in Figure 1, a big bent duct reaches the shield top through the bulk shield downstream from the target. Neutrons that leaked from the duct exit became large background components on our measurement. Therefore, as shown in Figure 2, an iron igloo (120 cm inner diameter, 60 cm thick and 196 cm high) was equipped to reduce the background, and additional shields of concrete or iron were piled up inside the igloo.

Shielding material

In this shielding experiment, the additional shielding blocks of ordinary concrete and iron were placed upon the top centre of the bulk shield just above the target as shown in Figure 2. Concrete

shields of 20, 40, 60, 80, 100 and 120 cm thickness were assembled by using blocks (119 cm diameter by 20 cm thick) of 2.36 g/cm^3 density, and iron shields of 10, 20, 30, 40, 50 and 60 cm thickness were assembled by using blocks (119 cm diameter by 10 cm thick) of 7.8 g/cm^3 density.

Detectors

The neutrons were produced from the target as the burst pulses corresponding to the 50 Hz synchrotron operation, and the pulse counters could not be used here because of the pulse pile-up problem. We therefore used the activation detectors. Large volume activation detectors were adopted in order to obtain high detection efficiencies. After irradiation, the energy spectra of gamma-rays from the detectors were measured with two HPGe detectors.

$^{12}\text{C}(n,2n)^{11}\text{C}$ activation detector

The disk type (8 cm diameter by 3cm thick) and the Marinelli-type detectors, as shown in Figure 3, were used in this experiment for measuring the spatial neutron flux distribution on the shield top and in the additional concrete and iron shields. The half-life of ^{11}C is about 20 minutes and the threshold energy of the reaction is about 20 MeV, which is a shortly activated good neutron flux monitor of energy above 20 MeV. The reaction cross-section has recently been measured by our group [5] as shown in Figure 4 and has an almost constant value of about 20 mb above 20 MeV.

$^{209}\text{Bi}(n,xn)^{210-x}\text{Bi}$ activation detector

The bismuth detector (8 cm diameter by 1.1 cm thick) was used to get the high-energy neutron spectrum by using the $^{209}\text{Bi}(n,xn)^{210-x}\text{Bi}$ ($x = 4\sim 10$) reactions. Their threshold energies are from 22 MeV to 70 MeV. Recent measurements of the cross-section data by our group in the energy range of 20~130 MeV is available from Ref. [6] and are in good agreement with those of the ENDF/B-VI high-energy library [7] (see Figure 5).

$^{27}\text{Al}(n,\alpha)^{24}\text{Na}$ activation detector

The Marinelli-type detectors, which are same shape as the graphite detector shown in Figure 3, were used in several measuring positions. The half-life of ^{24}Na is about fifteen hours and the threshold energy of the reaction is 3.25 MeV. Cross-section data shown in Figure 6 is calculated by the ALICE code.

Indium-activation multi-moderator spectrometer

The In_2O_3 powder is sealed in a spherical cavity of a small Lucite cylinder which is placed in spherical polyethylene moderators [8]. Five different moderators, Bonner sphere, of 9.8, 5.5, 3.2, 2.0 and 0 cm radius were used. A cross-sectional view of the detector with the smallest moderator is shown in Figure 7. The gamma-rays from the $^{116\text{m}}\text{In}$ nucleus produced by the $^{115}\text{In}(n,\gamma)^{116\text{m}}\text{In}$ reaction were measured. The response functions of the five detectors [8] are shown in Figure 8.

Monitoring of beam intensity

The relative proton beam current was monitored by the electromagnetic coil voltage at the muon target during the experiment. These data were converted to the beam current (Coulomb) and used in the analysis of the activation detectors.

Experimental procedure and data analysis

This experiment was performed employing various thicknesses of concrete and iron shields. The activation detectors were set upon the shield for irradiation. In order to obtain good statistics of photo-peak counts measured with two HPGe detectors, repeated irradiations and activity measurements were performed for each shielding material and thickness several times a day, and the photo-peak counts in the same condition were summed up to get the reaction rates. The peak efficiencies of the Ge detectors, including the self-absorption effect, were estimated using the EGS4 Monte Carlo code [9]. The thus obtained reaction rates of $^{115}\text{In}(n,\gamma)^{116\text{m}}\text{In}$ for five detectors of the Bonner sphere and $^{27}\text{Al}(n,\alpha)$, $^{12}\text{C}(n,2n)$ and $^{209}\text{Bi}(n,xn)$ ($x = 4\sim 10$) were unfolded by the SAND-2 code [10] with the response functions and the cross-section data, and the neutron energy spectra in the energy range down to thermal energy were analysed. Neutron energy spectra calculated by the ANISN code [11], which is described later, were used as initial guess spectra for the unfolding.

Calculation

Calculations of particle production from the target and deep penetration calculations were performed [12] to compare with the experimental data.

Particle production

The secondary particle production from a tantalum (Ta) target and the particle transmission through the target assembly were calculated with the HETC-KFA2 Monte Carlo code [13]. In the calculation, a simple cylindrical geometry of three strata having the same centre axis was employed, the strata consisting of a cylindrical Ta target of 90 mm diameter by 338.5 mm long, a target container of 182 mm diameter by 430 mm long and a reflector of 542 mm diameter by 790.5 mm long in order from the centre. The heterogeneous structure including heavy water in each stratum was homogeneously approximated so as to conserve the number of atoms and the average atomic density for representative materials.

Protons of 800 MeV were injected into the Ta target bottom surface, and an angular and energy distribution of neutron leakage from the outer surface of cylindrical assembly were estimated above 15 MeV neutron energy. The result for the angular interval of 85-95° was used for the following deep penetration calculations.

Deep penetration calculation

Neutron and photon transport calculations were carried out with a one-dimensional S_n code, ANISN [11]. Spherical geometry was adopted and the DLC119/HILO86 multi-group cross-section data library [14] was used in the calculation. The leakage neutron spectra from the Ta target was used as a source neutron spectrum, and energy distribution of neutrons inside and outside the bulk shield were calculated down to thermal energy.

A multi-layer calculation was carried out with the HETC-KFA2 Monte Carlo [13] for neutron deep penetration in an energy range above 15 MeV. A shield geometry was divided into approximately 100 cm thick slabs, and a step-by-step calculation was carried out for good statistics. The energy spectrum of leakage neutrons at 85-95° from the target assembly was used for the source neutron which impinged on the centre of the bottom surface of the first iron slab. This multi-layer calculation is equivalent to a calculation with a plane source and infinite slab, and all flux distributions were, therefore, divided by the square of the distance from the target in order to obtain the result for a point source at the target position.

Dose equivalent and $^{12}\text{C}(n,2n)$ reaction rate were estimated with the calculated energy distribution of neutron flux. The ICRP51 flux to dose conversion factor was used for dose estimation, and the cross-section data of $^{12}\text{C}(n,2n)$ which is based on the experimental cross-section data [6] was used for estimation of the reaction rate.

Results and discussions

Figure 9 shows the attenuation profiles of the $^{12}\text{C}(n,2n)^{11}\text{C}$ reaction rates with the concrete and iron thicknesses. The errors of the results are the statistical errors of the photo-peak counts of the 511 keV gamma-rays. This figure also gives the spatial distribution in the air along the vertical axis of the bulk shield upward from the tantalum target without any additional shield on the shield top. These three curves are the results on the centre of this vertical axis. We found that the data without additional shielding decreased with the square of the distance from the tantalum target.

Figure 10 shows the attenuation profiles of the $^{209}\text{Bi}(n,xn)^{210-x}\text{Bi}$ ($x = 4\sim 10$) reaction rates in the concrete shield. All experimental data are well fitted to a solid line of the same slope as that fitted to the $^{12}\text{C}(n,2n)$ reaction data, in spite of the different threshold energies of these reactions. This clarifies that the neutron energy spectrum behind this thick shield is in an equilibrium state. The attenuation lengths of these reaction rates correspond to those for neutron flux above 20 MeV, and are 125 g/cm² for concrete (2.36 g/cm³) and 161 g/cm² for iron (7.8 g/cm³). These values are just between the results given by Stevenson, *et al.*[1] and Ban, *et al.*[2] as seen in Figure 11.

Figure 12 shows the comparison of calculated and measured attenuation profiles of $^{12}\text{C}(n,2n)^{11}\text{C}$ reaction rate through bulk shield and additional concrete or iron shield. It can be found that the calculated results underestimated to the experiment. At the top of the target station with no additional shield, the ratios of the calculated reaction rates to those of experiment (C/E), 0.033 and 0.136 for the ANISN and HETC-KFA2 codes, respectively, were obtained. Calculated attenuation lengths, which were estimated from the attenuation profiles through the bulk shield region and additional shield region, were 17% and 11~15% shorter than those of experimental results for concrete and iron shields, respectively.

Measured neutron energy spectra on the shield top floor and on the additional shield were obtained with the indium activation Bonner sphere, and are shown in Figure 13, compared with the calculated results. Although discrepancies of the absolute values of the spectra were large between the measured and calculated results both by the HETC and ANISN codes, the spectrum shapes generally agree well, and two peaks due to cascade and evaporation can be clearly seen in the spectra.

Conclusion

The deep penetration experiment was performed at ISIS. The attenuation profiles through concrete and iron shields were clarified and attenuation lengths of high-energy neutrons produced at

90° by 800 MeV protons were estimated. The shielding configuration is rather simple and the measured attenuation lengths of concrete and iron are the good benchmark data for investigating the accuracy of deep penetration calculations.

The calculated results by HETC-KFA2 and ANISN/DLC119 gave largely underestimated neutron fluxes for deep penetration, and gave 10~20% shorter attenuation lengths than the experiment.

REFERENCES

- [1] G.R. Stevenson, K.L. Liu and R.H. Thomas, "Determination of Transverse Shielding for Proton Accelerators Using the Moyer Model", *Health Phys.*, Vol. 43, p. 13 (1982).
- [2] S. Ban, *et al.* "Measurement of Transverse Attenuation Length for Paraffin, Heavy Concrete and Iron Around an External Target for 12 GeV Protons", *Nucl. Instr. and Meth.*, Vol. 174, p. 271 (1980).
- [3] S. Ban, H. Hirayama and K. Katoh, "Measurement of Secondary Neutron Fluxes Around Beam Stop for 500 MeV Protons", *Nucl. Instr. and Meth.*, Vol. 184, pp. 409- 412 (1981).
- [4] Y. Uwamino, *et al.*, "Study on Bulk Shielding of an 800 MeV Proton Accelerator", Proc. of OECD/NEA Specialists Meeting on Shielding Aspects of Accelerators, Target and Irradiation Facilities (SATIF-1), Arlington, Texas (1994).
- [5] N. Nakao, T. Shibata, T. Ohkubo, S. Sato, Y. Uwamino, Y. Sakamoto and D.R. Perry, "Shielding Experiment at 800 MeV Proton Accelerator Facility", Proc. 1998 ANS Radiation Protection and Shielding Division Topical Conference, Nashville, Tennessee, Vol. 2, pp. 192-199 (1998).
- [6] E. Kim, T. Nakamura and A. Konno, "Measurements of Neutron Spallation Cross-sections of ^{12}C and ^{209}Bi in the 20 to 150 MeV Energy Range", *Nuclear Science And Engineering*, 129, pp. 209-223 (1998).
- [7] ENDF-B/VI, "Evaluated Nuclear Data File, ENDF-B/VI", National Neutron Cross-section Center, Brookhaven National Laboratory (1990).
- [8] Y. Uwamino, T. Nakamura and A. Hara, "Two Types of Multi-moderator Neutron Spectrometers: Gamma-ray Insensitive Type and High Efficiency Type", *Nucl. Instr. and Meth.*, A239 (1985) 299.
- [9] W.R. Nelson, H. Hirayama and D.W.O. Rogers, "The EGS4Code System", SLAC-265 (1985).
- [10] W.N. McElroy, S. Berg, T. Crockett, R.G. Hawkins, "A Computer Automated Iterative Method for Neutron Flux Spectra Determination by Foil Activation", AFWL-TR-67-41, Vol. 1-4, Air Force Weapon Laboratory (1967).

- [11] W.W. Engle Jr., "A Users's Manual for ANISN, A One-dimensional Discrete Ordinates Transport Code With Anisotropic Scattering", K-1693, Oak Ridge Gaseous Diffusion Plant, (1967).
- [12] N. Nakao and Y. Uwamino, "Deep Penetration Calculations Compared with the Shielding Experiment at ISIS", *J. Nucl. Sci. Technol.*, Supplement 1, pp. 162-166 (March 2000).
- [13] P. Cloth, *et al.*, "HERMES: A Monte Carlo Program System for Beam-materials Interaction Studies", KFA-IRE-E AN/12/88 (1988).
- [14] R.G. Alsmiller, Jr., *et al.*, "Neutron-photon Multi-group Cross-sections for Neutron Energies Up to 400 MeV (Revision 1)", ORNL/TM-9801, Oak Ridge National Laboratory (1986).

Figure 1. Cross-sectional view of neutron spallation target station with 800 MeV proton at ISIS

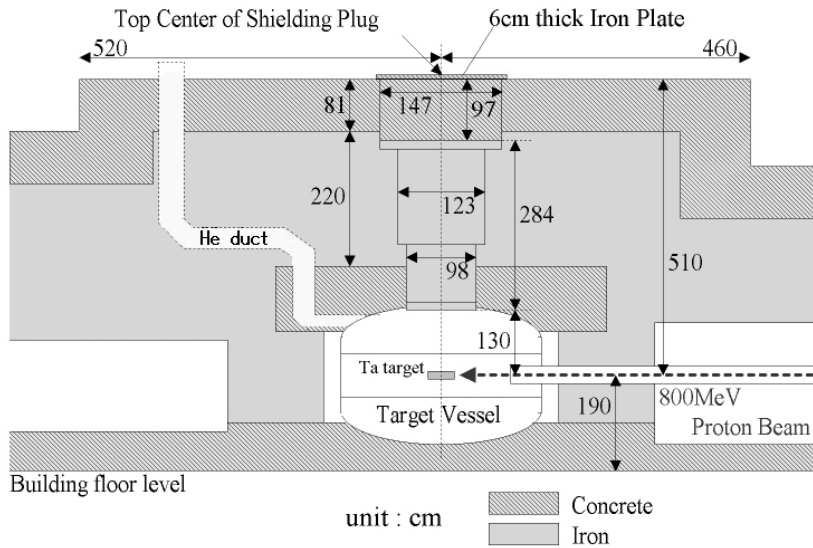


Figure 2. Experiment geometry with iron igloo to reduce the background neutrons

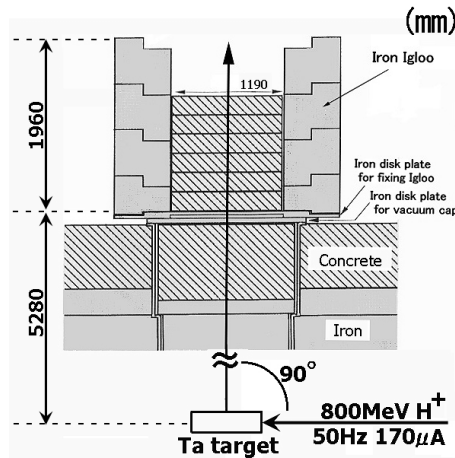


Figure 3. Cross-sectional view of graphite disk and Marinelli-type activation detector

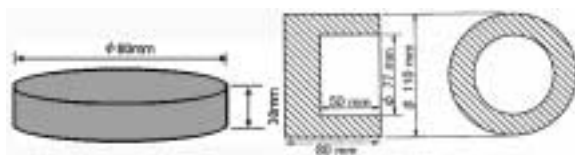


Figure 4. Cross-section of $^{12}\text{C}(n,2n)$ reaction

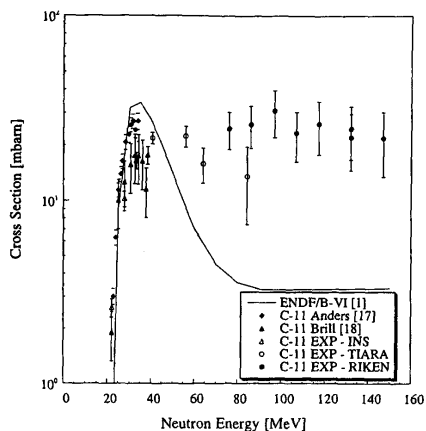


Figure 5. Cross-section of $^{209}\text{Bi}(n,xn)$ reaction

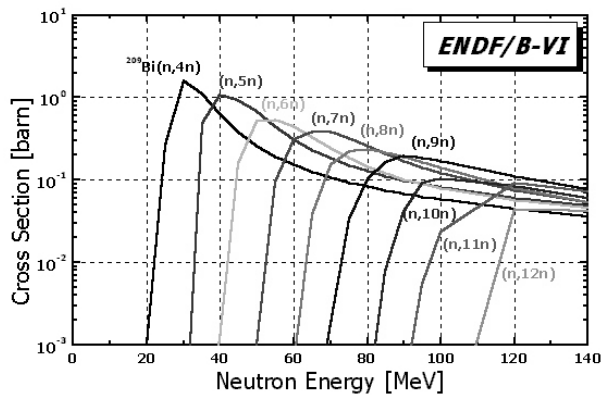


Figure 6. Cross-section of $^{27}\text{Al}(n,\alpha)^{24}\text{Na}$ reaction

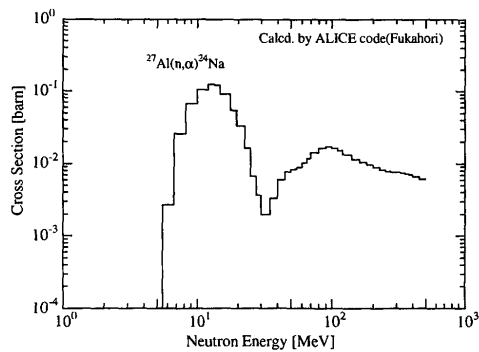


Figure 7. Cross-sectional view of indium activation Bonner sphere

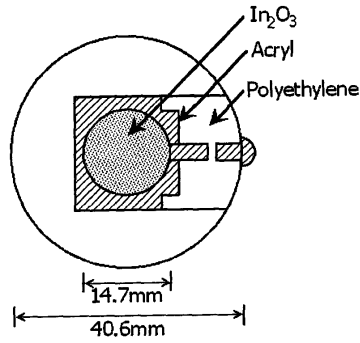


Figure 8. Response functions of indium activation Bonner sphere

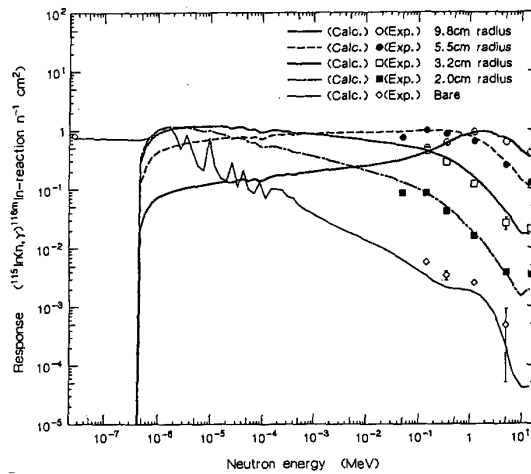


Figure 9. Attenuation profiles of $^{12}\text{C}(n,2n)^{11}\text{C}$ reaction

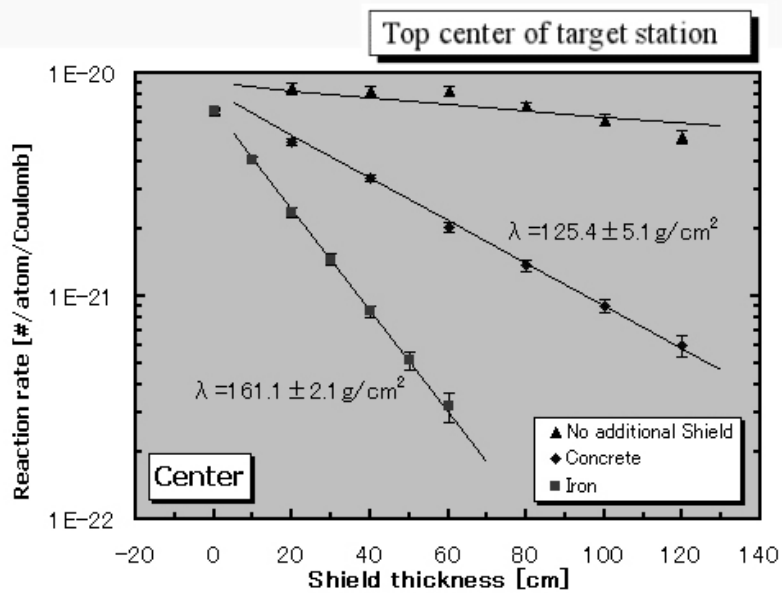


Figure 10. Attenuation profiles of $^{209}\text{Bi}(n,xn)$ reaction for concrete

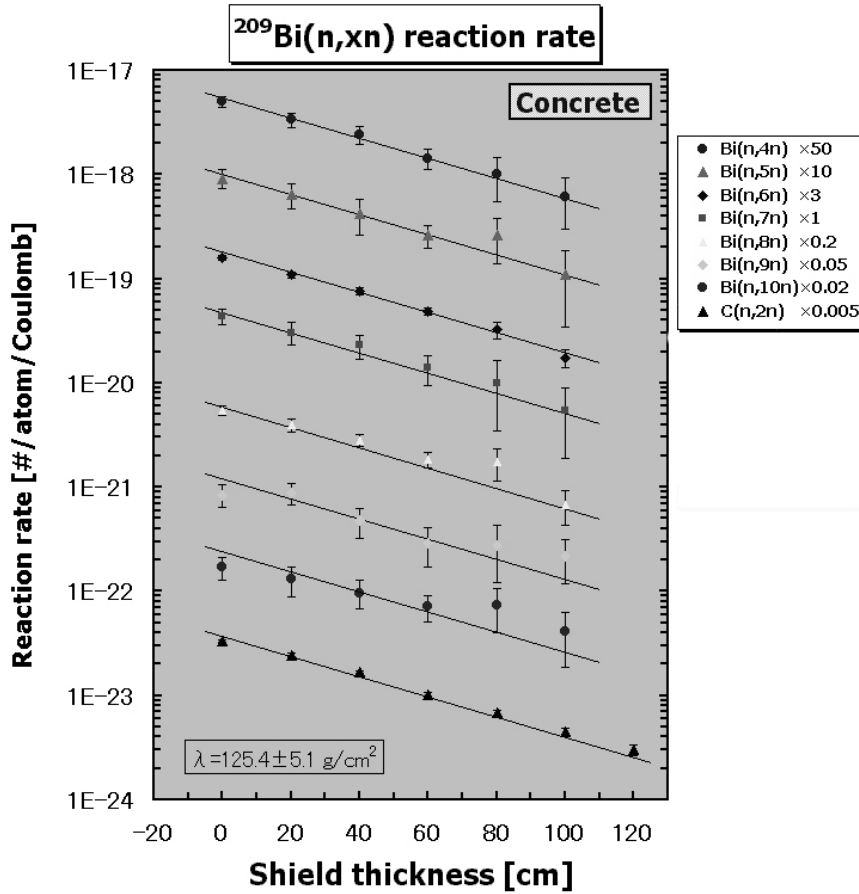


Figure 11. Comparison of various data on neutron attenuation length for concrete as a function of incident proton energy

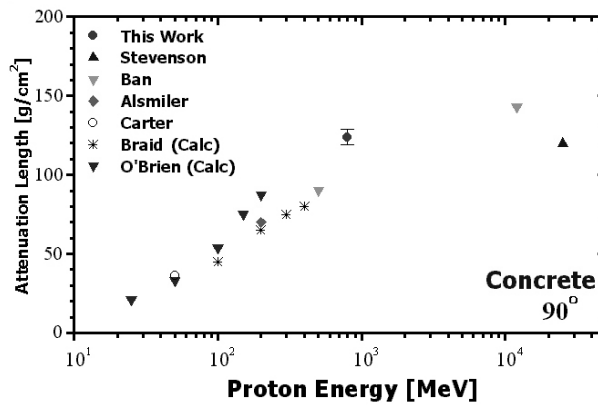


Figure 12. Comparison of calculated and measured attenuation profiles of $^{12}\text{C}(n,2n)$ reaction rate through bulk shield and additional shield

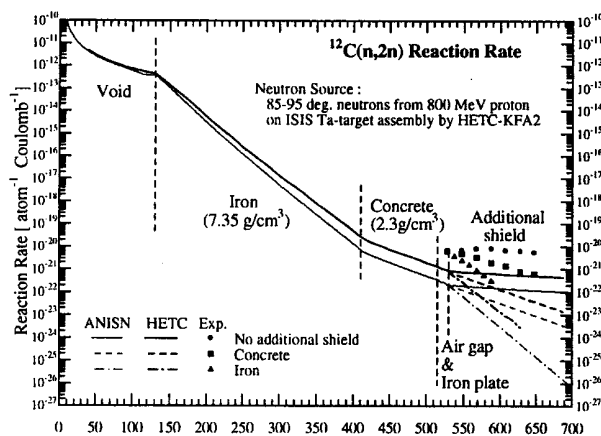
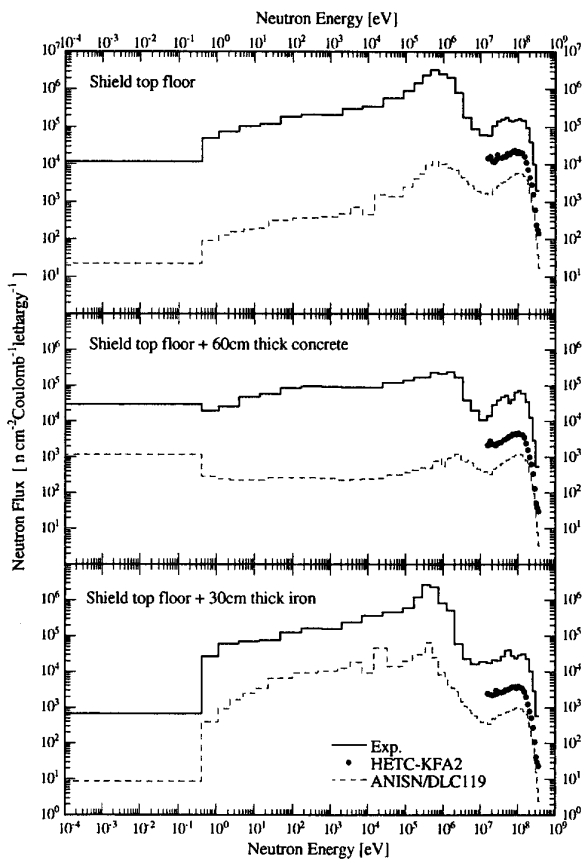


Figure 13. Comparisons of calculated and measured neutron energy spectra on the shield top floor, 60 cm thick additional concrete and 30 cm thick additional iron shield



Neutron Dosimetry Benchmark

**A HIGH-ENERGY NEUTRON DEPTH-DOSE EXPERIMENT
PERFORMED AT THE LANSCE/WNR FACILITY**

Michele R. Sutton and Nolan E. Hertel
Georgia Institute of Technology

Laurie S. Waters
Los Alamos National Laboratory

Abstract

A high-energy neutron depth-dose experiment was performed at Los Alamos Neutron Science Centre, Weapons Neutron Research (LANSCE/WNR) complex as part of a continuing effort to meet high-energy dosimetry needs and to test the validity of MCNPX in calculating high-energy dosimetric quantities. The experiment consisted of filtered beams of neutrons with energies up to 800 MeV impinging on a 30 cm³ tissue-equivalent phantom. The absorbed dose was measured in the phantom at various depths with tissue-equivalent ion chambers. The phantom and the experimental set-up were modelled using MCNPX. The results from the experiment and the simulation are presented and compared.

Introduction

Conversion coefficients for radiation protection quantities and operational quantities as well as other dosimetric quantities are often calculated using radiation transport codes such as MCNPX [1]. The acceptance of such calculations depends on the validity of the radiation transport code in calculating the most basic dosimetric quantity, absorbed dose. In an effort to test the validity of MCNPX in calculating absorbed dose, experiments were performed at the Los Alamos Neutron Science Centre, Weapons Neutron Research (LANSCE/WNR) facility in November 1998 and September 1999. The experiments consisted of filtered beams of high-energy neutrons impinging on the centre of a tissue-equivalent phantom. The absorbed dose distribution was measured with tissue-equivalent ion chambers. The experiment was modelled with MCNPX and the results were compared with the experimental results.

The neutron source

The neutron source used for the experiment was WNR Target 4. WNR Target 4 consists of a 3 cm $\varnothing \times 7.5$ cm water-cooled tungsten target suspended at the centre of a vacuum chamber and surrounded by a massive shield with penetrations for the neutron flight paths. An intense neutron source is produced from 800 MeV protons hitting the target [2]. The experiment was performed at WNR Flight Path 30 Left (FP30L) approximately 20 m from WNR Target 4.

The neutron beam was filtered with various thicknesses of polyethylene (40 cm and 60 cm) and lead (5 cm and 10 cm) to produce different neutron spectra. The beam profile was measured with imaging plates and was 16 cm in diameter at the surface of the phantom. The neutron spectrum was measured for each filter by WNR personnel using a fission chamber (15 cm in front of the phantom) and time-of-flight techniques (TOF) [3]. The measured neutron spectra for the various filtrations are shown in Figure 1. Sweeping magnets were placed in the beam line after the filters to remove charged particles. Low-energy neutron (< 1 MeV) and gamma spectral information were not measured. A graphical representation of the experimental set-up is shown in Figure 2.

Figure 1. The measured neutron spectra for various filters at WNR FP30L

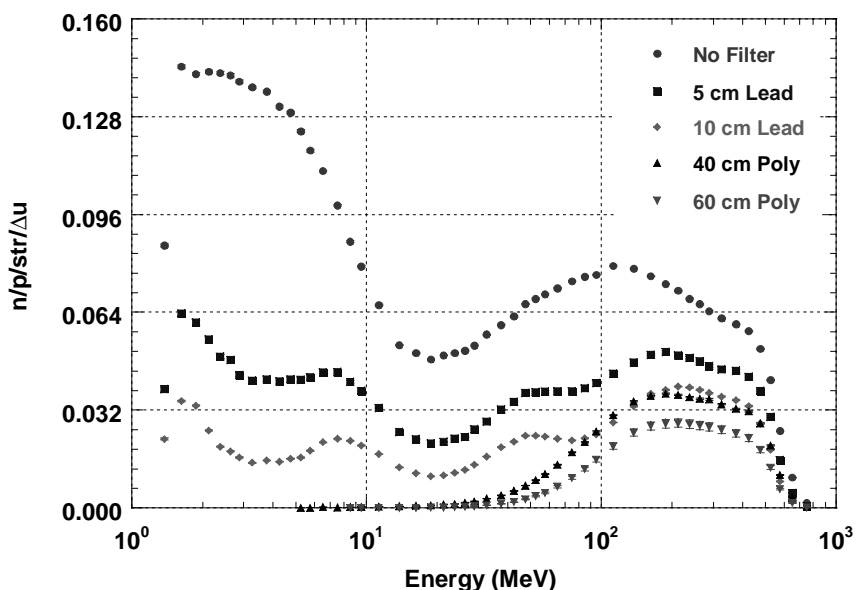
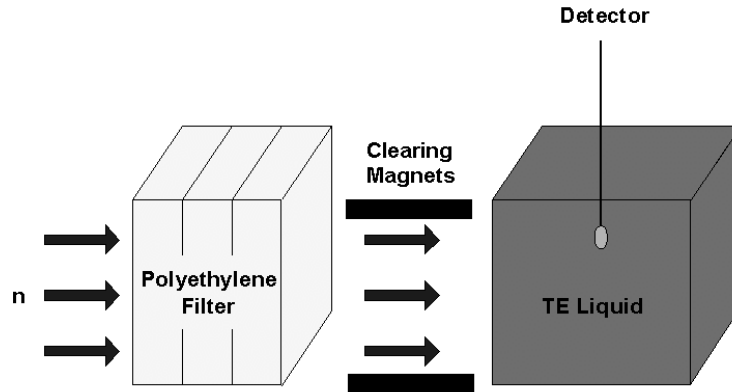


Figure 2. A graphical representation of the experimental set-up



The tissue-equivalent phantom

The phantom was a 30 cm cube with polymethylmethacrylate (PMMA) walls with a thickness of 5 mm filled with Goodman Liquid [4]. Goodman Liquid is a tissue substitute comprised of 10.2% hydrogen, 12.0% carbon, 3.6% nitrogen and 74.2% oxygen by weight. It is a clear liquid with a density of 1.07 g/cm³ and is recognised by the International Commission of Radiation Units and Measurements (ICRU) as an acceptable tissue substitute for neutrons [5].

Instrumentation and measurements

Three different sized (0.1 cm³, 2 cm³ and 5 cm³) tissue-equivalent (A-150) ion chambers were used to measure the absorbed dose in the phantom. The ion chambers were operated at a voltage of 295 V. Methane-based tissue-equivalent gas was flowed through the chambers at 8 cm³/min. The current was integrated using a Keithley Model 6517A programmable electrometer. The temperature and pressure were also recorded for each measurement.

The dose was measured along the centre axis of the phantom at various depths for the different filters. In 1998, dose measurements were made in the phantom with no filter, and 5 cm lead, 40 cm polyethylene and 60 cm polyethylene filters in the beam. Measurements were made approximately every 3 cm along the depth axis of the phantom. In 1999, more precise measurements were made with no filter, and 10 cm lead and 60 cm polyethylene filters in the beam at one centimetre intervals down the phantom centreline. Measurements were also made along the traverse axis of the phantom at depths of 3 cm, 15 cm and 27 cm for the unfiltered and filtered beams.

Experimental analysis

The dose was calculated using the following Bragg-Gray relation:

$$D = \frac{Q(\bar{w}/e)S_r d}{M} \quad (1)$$

where D is the absorbed dose (gray), Q is the collected charge (coulombs), \bar{w}/e is the average energy required to form an ion pair (joules/coulomb), S_r is the ratio of the mass stopping powers of the wall

and gas, M is the mass in the sensitive volume of the chamber (kg) and d is the chamber gas volume correction factor [6,7]. The mass of each ion chamber was determined by the method described in AAPM (American Association of Physicists in Medicine) Report No. 7 using a NIST traceable ^{60}Co source [8]. All other factors not measured were taken from the recommendations in the literature [6-9]. Temperature and pressure corrections were applied to the measurements. Each measurement was normalised to fission chamber counts. The total uncertainty in the absorbed dose derived from the ion chamber readings is 10%.

MCNPX calculations

Source spectra

A detailed computational model (Figure 3) of WNR Target 4 was created to develop a low-energy neutron tail for the neutron source and to create a gamma-ray source for the FP30L neutron beam. A comparison of the calculated and measured neutron spectra for the unfiltered beam is shown in Figure 4. The calculated gamma-ray spectra are shown in Figure 5. A combination of the calculated and measured neutron spectra was used to calculate the neutron source spectra for the different filters. The combined neutron spectrum for the unfiltered beam is shown in Figure 6. It includes the calculated spectrum below 2 MeV and the measured spectrum above 2 MeV. As expected, the calculated results yielded neutrons below 1 MeV for the lead filters but no neutrons below 1 MeV for the polyethylene filters.

Figure 3. The computational model of WNR Target 4 used for neutron and gammas spectral calculations

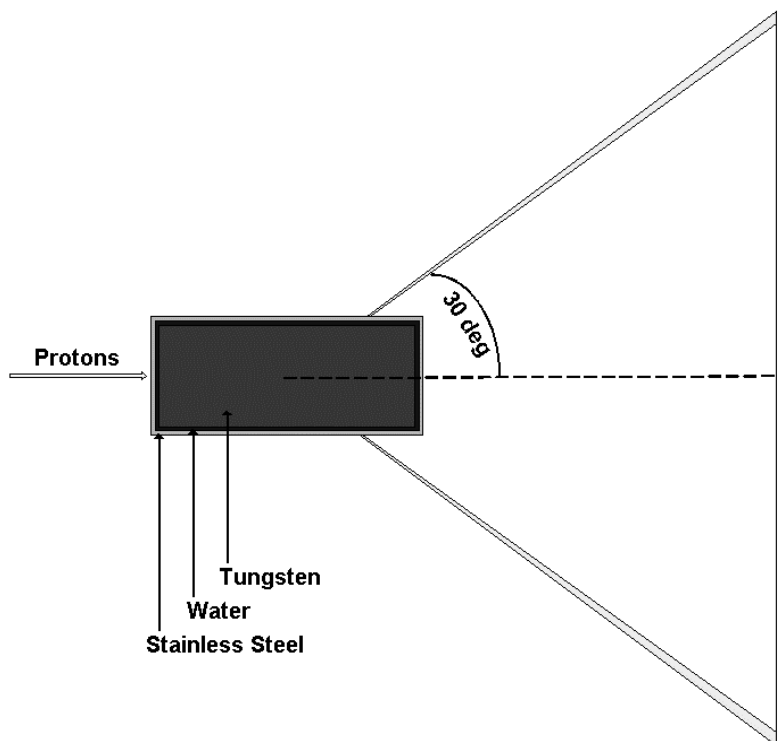


Figure 4. Neutron spectra measured at WNR FP30L compared with the neutron spectrum calculated with MCNPX

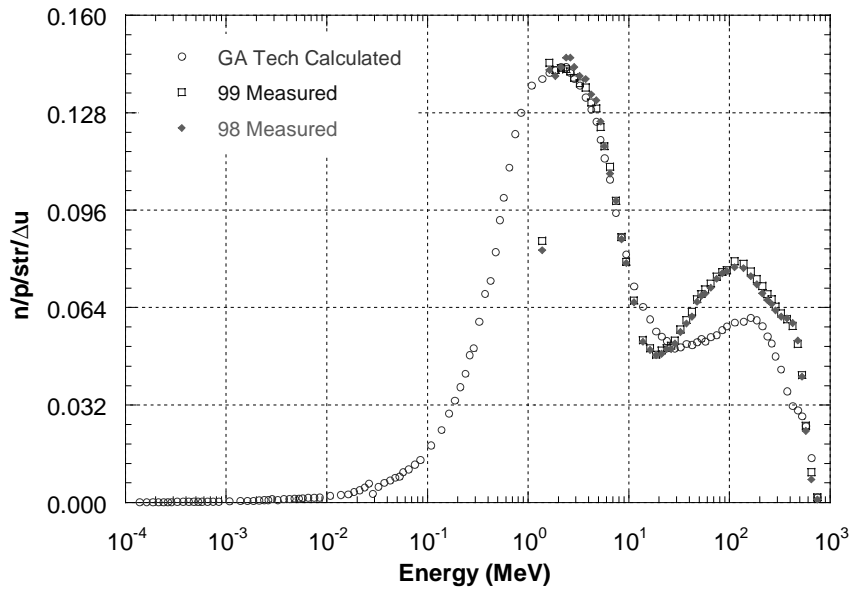


Figure 5. Gamma spectra of WNR Target 4 at FP30L for various filters calculated with MCNPX

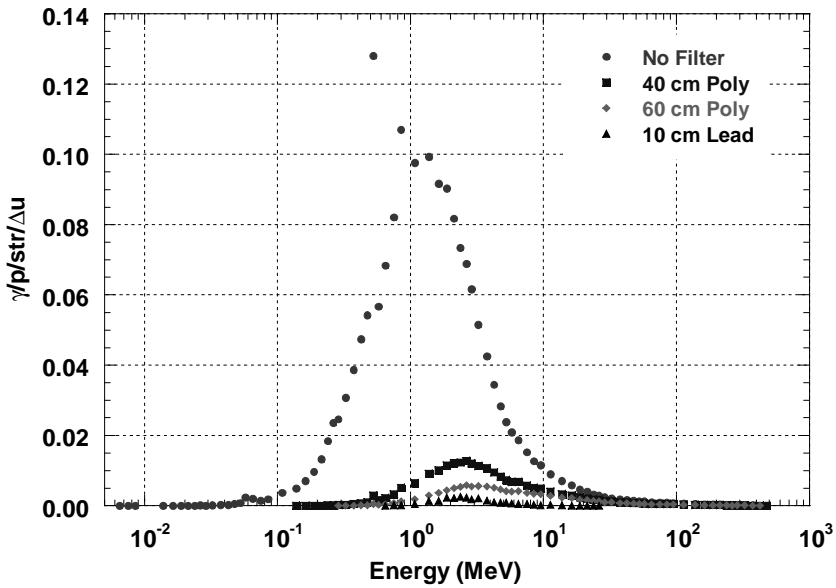
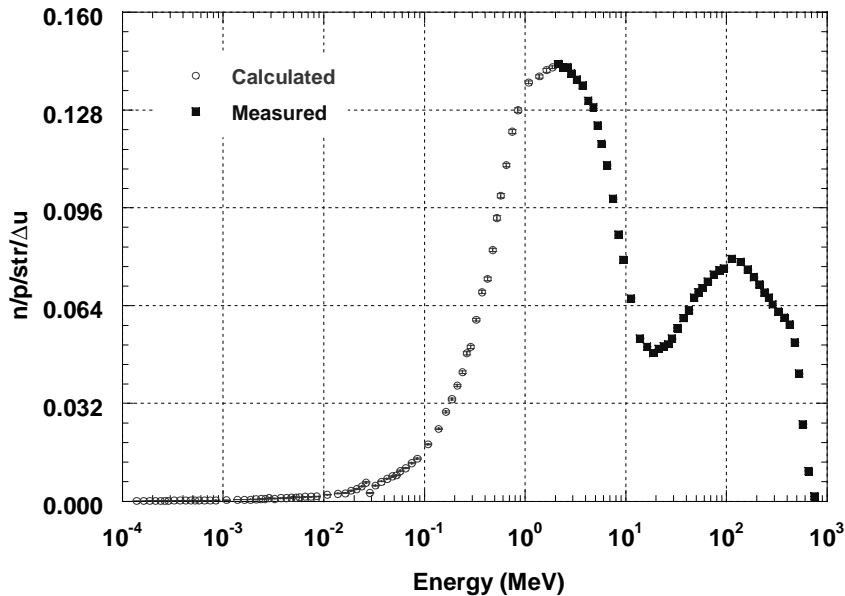


Figure 6. The neutron spectrum used to determine the low-energy neutron contribution to the dose distribution for the unfiltered beam



Depth-dose distribution

The depth-dose distribution was calculated using energy deposition tallies in 1 cm^3 cells centred at one centimetre increments along the depth axis of the phantom. The measured spectra were used as the source spectra. The source was uniformly distributed over a disk with a diameter of 16 cm and was placed 15 cm in front of the phantom in a vacuum.

The depth-dose distribution was also calculated using the measured neutron spectra with the low-energy tails added for the unfiltered and lead-filtered beams. The gamma depth-dose distribution for each filter was calculated using the gamma spectra in Figure 5 and added to the neutron absorbed dose to determine the total depth-dose distribution in the phantom.

Results and discussion

The depth-dose for each neutron spectra along with the computational results are shown in Figures 7-11. The calculated absorbed dose as a function of depth agrees well with the measurements for all of the neutron spectra. Figure 1 shows the results for the unfiltered beam. As can be seen in Figure 1, the absence of low-energy neutrons and gammas in the source description (i.e. the measured spectrum) for the calculation yields an under prediction of the total dose. Low-energy neutrons and gammas contribute 12% and 6%, respectively, to the total dose for the unfiltered beam.

A comparison of the experimental and calculated depth-dose for the lead-filtered beam is shown in Figures 8 and 9. Again, the absence of low-energy neutrons in the source description of the calculation yields an under prediction of the total dose. The addition of low-energy neutrons in the source description increases the dose by approximately 3%. The gamma contribution for the lead filters is negligible.

Figure 7. The experimental depth-dose results compared with calculated depth-dose results for the unfiltered beam. The calculated gamma depth-dose and the calculated depth-dose from the measured spectrum alone are also shown.

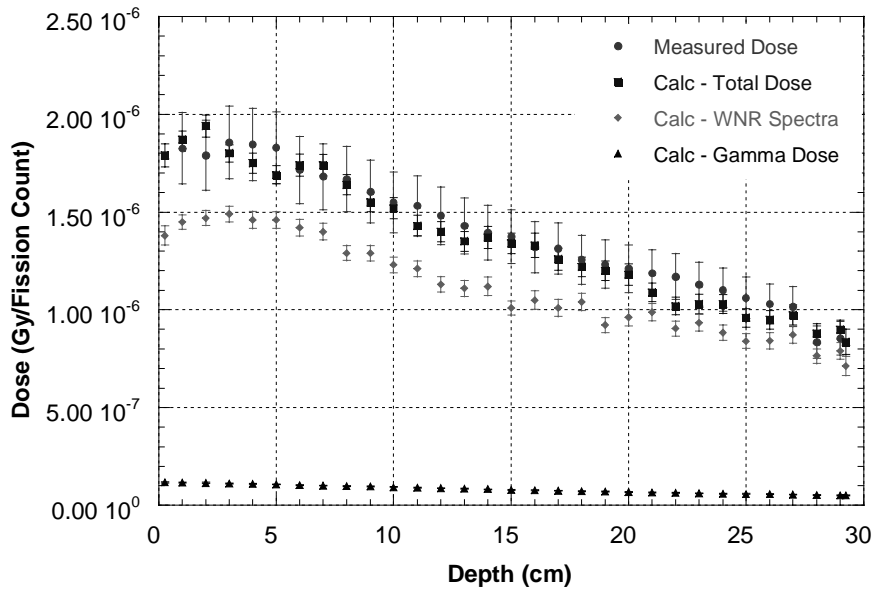


Figure 8. The experimental depth-dose results compared with the calculated depth-dose results for the 5 cm lead beam filter

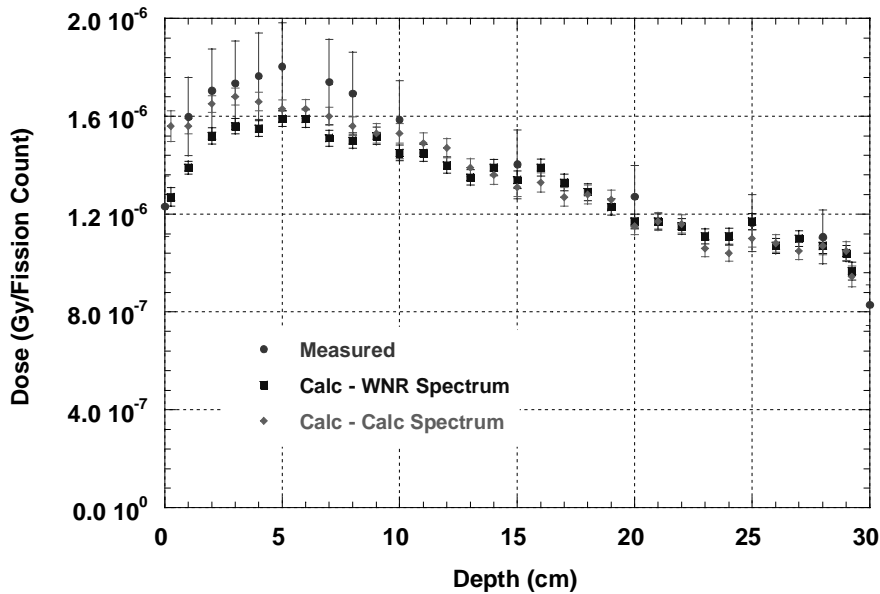


Figure 9. The experimental depth-dose results compared with the calculated depth-dose results for the 10 cm lead beam filter

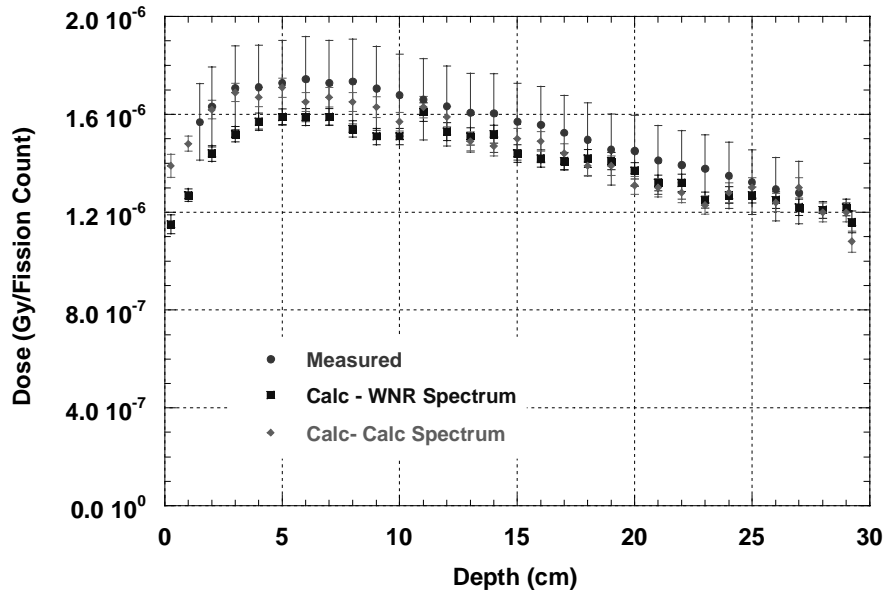


Figure 10. The experimental depth-dose results compared with the calculated depth-dose results for the 40 cm polyethylene beam filter

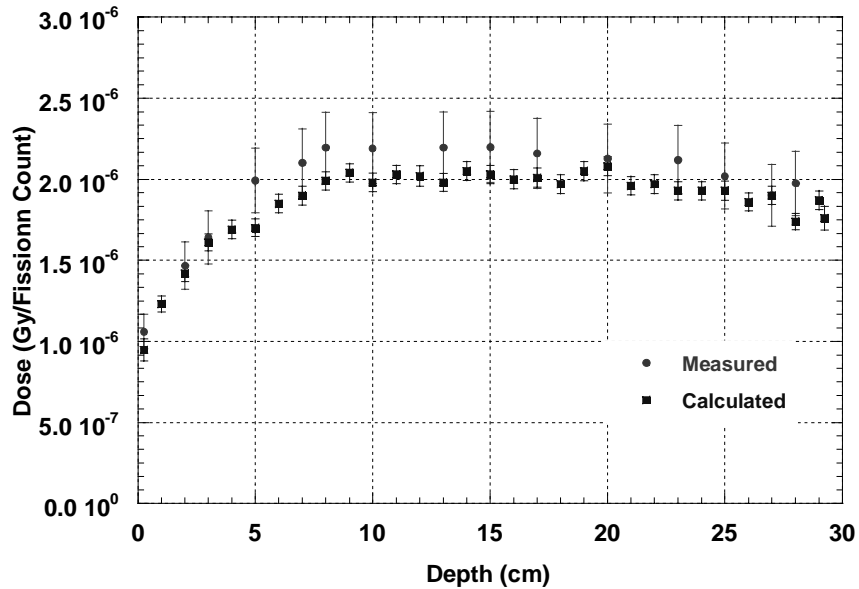


Figure 11. The experimental depth-dose results compared with the calculated depth-dose results for the 60 cm polyethylene beam filter

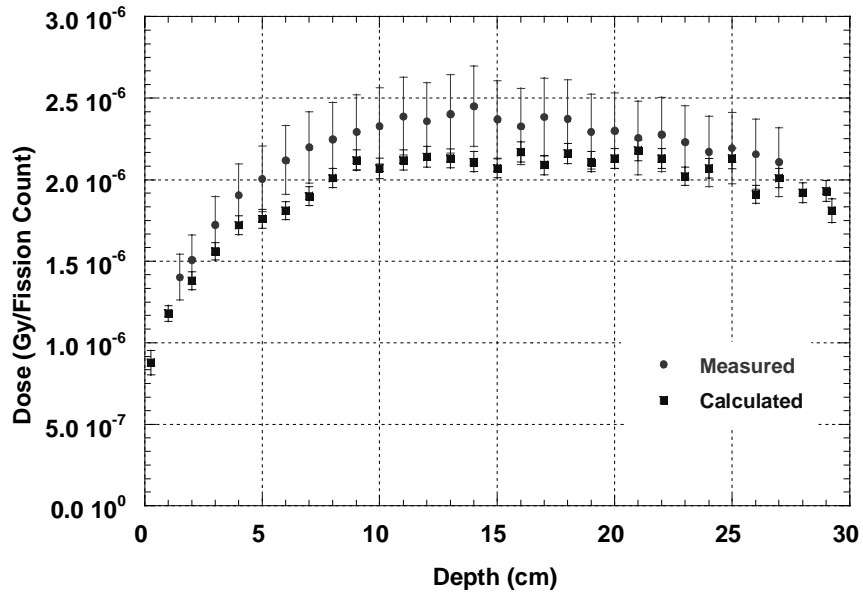
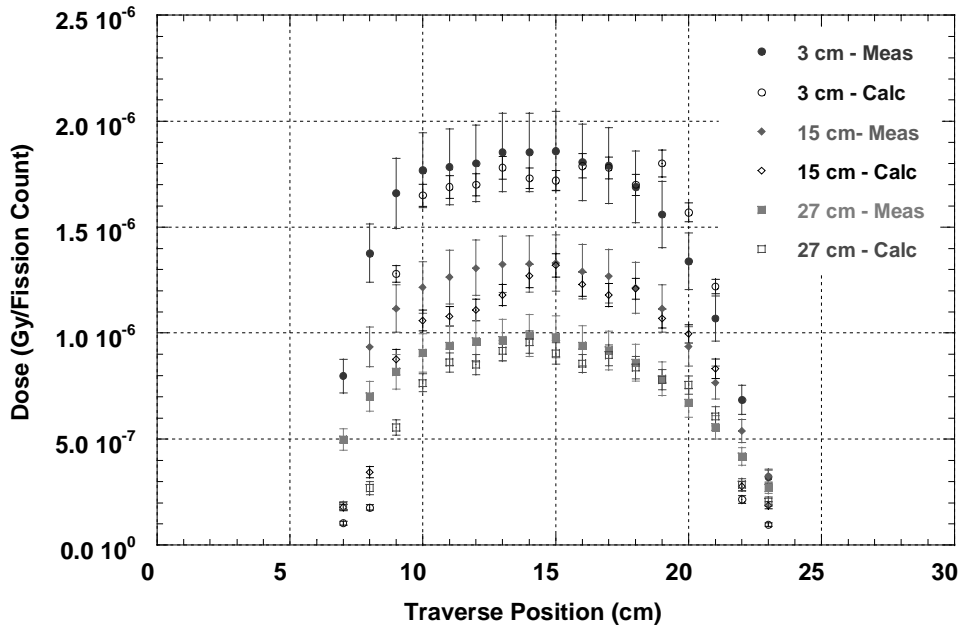


Figure 12. The experimental dose results compared with the calculated dose results along the traverse axis of the phantom for three different depths for the unfiltered beam



The results for the polyethylene-filtered beams are shown in Figures 10 and 11. The gamma dose for the polyethylene filters is negligible and low-energy neutrons are not present. The results of the traverse measurements and calculations for the unfiltered beam are shown in Figure 12. The comparison shows good agreement.

The computed depth-dose distributions compare well with the measured distributions. The actual beam distribution incident on the phantom is not uniform. A final refinement in the calculations will be undertaken to simulate the actual spatial distribution using image plate data. Another experiment is being planned to focus on the measurement of the low-energy neutron and gamma spectral information as well as the spatial distribution of the beam spot.

It has recently come to the authors' attention that the energy of proton recoils from collisions of neutrons and hydrogen may be locally deposited by the code [10]. This is not a significant effect at depths where charged particle equilibrium exists in the phantom; however, it does affect the absorbed dose calculation near the surface of the phantom.

REFERENCES

- [1] H.G. Hughes, R.E. Prael and R.C. Little, "MCNPX – The LAHET/MCNP Code Merger", XTM-RN(U) 97-012 (1997).
- [2] P.W. Lisowski, *et al.*, *Nucl. Sci. Eng.*, 106, p. 208 (1990).
- [3] S.A. Wender, *et al.*, *Nucl. Instrum. Methods*, A336, p.226 (1993).
- [4] L.J. Goodman, *Health Physics*, 16, p. 763 (1969).
- [5] ICRU Report 44, "Tissue Substitutes in Radiation Dosimetry and Measurement" (1989).
- [6] P.R. Almond and J.B. Smathers, "Neutron Dosimetry", NBS Special Publication #594 (1979).
- [7] AAPM Report No. 7, "Protocol for Neutron Beam Dosimetry", Medical Physics Publishing (1980).
- [8] ICRU Report 45, "Clinical Neutron Dosimetry Part I: Determination of Absorbed Dose in a Patient Treated by External Beams of Fast Neutrons" (1989).
- [9] M.B. Chadwick, *et al.*, *Med. Phys.*, 26 (6) (1999).
- [10] R.E. Little, personal communication, July 2000.

BENCHMARK EXPERIMENTS OF ABSORBED DOSE IN A SLAB PHANTOM FOR SEVERAL TENS MeV NEUTRONS AT THE TIARA FACILITY

Y. Nakane and Y. Sakamoto
Japan Atomic Energy Research Institute, Japan

Abstract

Absorbed dose distributions in a plastic phantom of $30 \times 30 \times 30 \text{ cm}^3$ slab were measured for 40 and 65 MeV quasi-monoenergetic neutrons at TIARA with tissue equivalent detectors. Distributions of energy deposition of charged particles and neutron energy spectra in the phantom were calculated by using Monte Carlo codes, HETC-3STEP and MORSE-CG/KFA, respectively. Measured dose distributions were compared with calculated ones obtained from the energy deposition and the neutron energy spectra with the neutron Kerma factor. In addition, fission rate distributions in the phantom were measured with a ^{238}U fission counter for comparison with measured and calculated neutron spectra.

Introduction

From the viewpoint of radiation shielding design at high-energy accelerator facilities, it is important to establish calculation methods for high-energy radiation above 20 MeV. As for the calculations of source-term and transportation, several calculation codes and nuclear data have been used for accelerator shielding design. Analyses of benchmark experiments are very useful for validating the accuracy of calculation methods. Therefore, intercomparisons of benchmark analyses by each organisation using individual methods were proposed at SATIF-2, and four kinds of neutron transmission benchmark problems for iron and concrete shields in low, intermediate and high-energy proton accelerator facilities were prepared [1]. Calculated results were summarised, presented and discussed at SATIF-3 [2]. The results have helped amend codes and estimate systematic errors and safety margins in the shielding design.

As for the dose evaluation, dose conversion coefficients for high-energy neutrons have been calculated using high-energy Monte Carlo codes [3-7]. The accuracy of the calculation methods for dose evaluations, however, has not been validated sufficiently for intermediate and high-energy neutrons because of scarce data suitable for the validation of the calculation codes. Most of the dose measurements using a tissue equivalent counter were for the measurement of the neutron Kerma factor with a thin material, though some cases of the measurements of dose distributions with a thick material can be found. Energy deposition spectra in a Plexiglas phantom have been measured with tissue equivalent counters for 50 MeV d-Be and 65 MeV p-Be neutron beams [8]. The purpose of the measurement was, however, only for the evaluation of mean quality factors for radiation protections in therapy. The results are not suitable for the validation of the calculation codes because dose distributions in the phantom were not measured, and also because the contribution of source neutrons above 20 MeV was small. For another example for dose measurements, dose distributions in a thick concrete shield have been measured for 230 MeV protons incident upon stopping-length aluminium, iron and lead targets [9]. In the measurement, however, energy spectra of source neutrons generated from the targets were not measured. It is desirable for the validation of calculation codes that measurements of dose distributions in a tissue equivalent material be performed for monoenergetic source neutrons, of which energy spectra were measured accurately.

In the present work, absorbed dose distributions in a plastic phantom were measured with a tissue equivalent proportional counter and a tissue equivalent ionisation chamber for 40 and 65 MeV quasi-monoenergetic neutrons at Takasaki Ion Accelerators for Advanced Radiation Application (TIARA) of Japan Atomic Energy Research Institute (JAERI). Measured dose distributions were compared with calculated ones obtained from energy depositions and neutron energy spectra with the neutron Kerma factor. In addition, fission rate distributions in the phantom were measured with a ^{238}U fission counter for the evaluation of neutron flux in the calculations.

Experiments

Experiments were performed in the quasi-monoenergetic neutron beam field at the AVF cyclotron facility, TIARA of JAERI. Figure 1 shows a cross-sectional view of the experimental arrangement. Quasi-monoenergetic source neutrons (“40 MeV” and “65 MeV”) of about 40 and 65 MeV were produced in 3.6 mm and 5.2 mm thick ^7Li targets (99.9% enriched) bombarded with 43 and 68 MeV protons, respectively. Source neutrons emitted in the forward direction reached an experimental room through a 10.9 cm diameter and 220 cm long iron collimator embedded in a shielding wall. The protons penetrating through the target were bent down toward a beam dump by a clearing magnet. An additional iron collimator with a 10.9 cm diameter and 85 cm long cylindrical hole was set on a movable stand in order to depress the neutron leakage through a shielding wall and a rotary shutter as shown in Figure 1. A copper plate of 3 mm thickness was set at the exit of the

additional collimator as a neutral proton beam stopper. The $30 \times 30 \times 30 \text{ cm}^3$ slab phantom made of polymethyl methacrylate (PMMA) was placed on the beam at the position of 558 cm from the Li target. Absorbed dose and microdosimetric spectra at the front surface and the depth of 2, 5, 10, 15, 20 and 25 cm in the phantom were measured along the centre line of the phantom by using a tissue equivalent proportional counter (TEPC – Far West Technology Inc., Model LET-SW1/2) for the “40 MeV” and “65 MeV” sources. The counter consists of a sphere of TE plastic wall, a collecting wire and an outer aluminium shell. The internal diameter and wall thickness of the sphere are 1.27 cm and 0.127 cm, respectively. The 0.18 mm thick and 2.0 cm outer diameter aluminium shell outside the TE sphere is used as a vacuum tight container. The counter was filled with a propane-based TE gas, the same as that in ICRU Report 26 [10], at a pressure of 9.03 kPa, which simulated a 2 μm diameter sphere of unit density tissue.

To compare with the TEPC measurements, the distributions at the same positions were measured by using a tissue equivalent ionisation chamber (TEIC – Far West Technology Inc., Model IC-17) for the “65 MeV” source. The detector has a spherical shape of TE plastic wall. The outer diameter and wall thickness are 2.29 cm and 0.127 cm, respectively. A methane-based TE gas, the same as that in ICRU-26, flowed at 5 cm^3/min in the plastic wall. The absorbed dose caused by both neutrons and gamma-rays in the wall surrounding a cavity was measured from the electrometer reading.

In addition, fission rates at the depth of 1, 3, 5, 10, 15, 20 and 25 cm in the phantom were measured with a ^{238}U fission counter (Centronic FC4A/1000) with a 6.4 mm diameter \times 69.9 mm long (active length was 24.8 mm) [11]. For the measurement, the phantom was placed on the beam at a position of 472 cm from the Li target with the additional iron collimator of 45 cm long. The absolute efficiency of the counter was 1.12×10^5 barn/ cm^2 /counts from the measurements at TIARA, which was 20% smaller than that measured with a ^{252}Cf neutron sources.

Source neutron spectra above 10 MeV have been measured by the TOF method with a 12.7 cm diameter \times 12.7 cm long BC501A liquid scintillation detector as shown in Figure 2 [12]. Source spectra below 10 MeV were measured with a spherical multi-moderator spectrometer, and evaluated at the phantom position using the MCNP-4B code [13] with the cross-section processed from the LA150 library [14] as shown in Figure 3. [15]. The absolute fluxes of source neutrons in the monoenergetic peak were measured using a proton recoil counter telescope (PRT) [16]. The intensity of the source neutrons was monitored with the Faraday cup and two fission counters placed near the target and the collimator, of which efficiencies had been calibrated for proton beam charge (μC) with the PRT. The error of neutron intensity monitoring was estimated to be less than 7%.

Calculation

Calculation codes

Two kinds of calculations were performed for the comparison of the experimental results of absorbed dose in the phantom. One is the calculation that the dose caused by neutrons for the energy above 15 MeV is calculated from a deposition energy of charged particles generated by the reaction with incident neutrons, while that for the energy below 15 MeV is calculated from neutron energy spectra and the Kerma factor. The other method is the calculation of the dose caused by neutrons for the whole energy region from neutron energy spectra and the Kerma factor.

The absorbed dose caused by neutrons above 15 MeV was obtained from the deposition energy of charged particles from the induced reaction of neutrons calculated by the HETC-3STEP code [17], and that below 15 MeV was obtained from the neutron energy spectra calculated with the MORSE-CG/KFA code [18] and the neutron Kerma factor for the A-150 plastic given in ICRU Report 26. The grouped

cross-section processed from JENDL 3.1 [19], having the energy structure of 100 groups from thermal to 14.9 MeV for neutrons and 36 groups up to 14 MeV for gamma-rays, was used for the calculation with MORSE-CG/KFA. For the comparison, absorbed dose distributions for the whole energy region of neutrons from thermal to peak region were also obtained from the neutron Kerma factor and the neutron energy spectra calculated by the MORSE-CG/KFA code with the DLC119/HILO86 multi-group cross-section library [20]. In the calculations, the neutron Kerma factor for the A-150 plastic was prepared for the neutron energy region from 30-70 MeV from that evaluated for hydrogen by Bassel [21], for carbon, nitrogen and oxygen by Chadwick [22,23], while that listed in ICRU Report 26 was used for the energy region up to 30 MeV.

Fission rates in the phantom were obtained from transported neutron energy spectra and ^{238}U fission cross-sections from JENDL-3 [19] for below 20 MeV and the data [24] for above 20 MeV. Two kinds of calculations, the same as for absorbed dose, were performed for neutron energy spectra.

For comparison with the measured ones, calculated results were normalised to the proton beam charges in the unit of micro Coulomb.

Calculation geometry

Three-dimensional calculation geometry, as shown in Figure 4, was used for the dose calculations of the HETC-3STEP and the MORSE-CG/KFA codes. The energy spectra of source neutrons evaluated for the surface of the phantom in the previous section were used in the calculation. The source neutron beams impinge on the phantom at its centre. A neutron beam spreading is 3.89×10^{-4} sr as shown in Figure 4(a), which means the neutron beam spread of 10.9 cm diameter at the beam exit, 490 cm from the Li target. The detector reproduced from TEPC was placed at the measured position in the phantom. The detector is assumed to be a sphere of 2.0 cm in diameter, and consists of an aluminium shell, TE gas and TE plastic wall as shown in Figure 4(b). A sphere of 15.24 mm in diameter, integrated into the TE plastic wall and TE gas in the wall, was used as an estimator in the calculation. The energy deposition in the estimator was calculated with the HETC-3STEP code. A track length estimator of the sphere was used as the flux estimator for the MORSE-CG/KFA calculation.

The same geometry was used for the fission rate calculations. The phantom was placed at 472 cm from the source, and a neutron beam spreading is 4.78×10^{-4} sr for the use of 45 cm thick additional collimator. A 6.4 mm diameter \times 24.8 mm long cylinder was defined as a track length estimator used for the calculations, and set at the measured positions in the phantom.

Results and discussion

Microdosimetric spectra from the measurements

Figures 5 and 6 show the microdosimetric spectra obtained from the TEPC measurement at the surface of the phantom, and 5 and 25 cm depth positions in the phantom for the “40 MeV” and the “65 MeV” sources, respectively, where the $d(y)$ is normalised to unity. From the figures, it can be seen that the peak position for the “65 MeV” source of about 7 keV/ μm , is lower than that for the “40 MeV” source of about 10 keV/ μm , as a result of the small dE/dx for high-energy protons. The contribution of each particle to the absorbed dose for the “40 MeV” and the “65 MeV” sources can be roughly estimated from the y value region as shown in Tables 3 and 4, respectively. It is found that the contribution of protons to total dose is 76-85%, and that inside the phantom is 5-10% larger than that on the phantom because of recoil protons produced in the phantom.

Comparison of fission rates in the phantom

Figure 7 shows the measured and calculated fission rate distributions in the phantom. Fission rates calculated from the energy spectra by the HETC-3STEP and MORSE-CG codes agree well with the experimental ones at the depth up to 15 cm in the phantom, while overestimate 33% and 22% at the depth of 25 cm for the “40 MeV” and the “65 MeV”, respectively. On the other hand, those calculated from the energy spectra by only the MORSE-CG code agree with the experimental ones within 15% at the depth up to 25 cm. From the comparison of two kinds of calculated spectra, the spectra calculated with HETC-3STEP for neutron energy above 15 MeV were higher than those with MORSE-CG at the deep position of the phantom, as shown in Figure 8.

Comparison of absorbed dose in the phantom

Measured and calculated absorbed dose distributions in the phantom for the “40 MeV” and the “65 MeV” source neutrons are shown in Figures 9 and 10, respectively. In the figures, results on the phantom position were shown for the depth of 0 cm.

For the comparison between the measurements of TEPC and TEIC for the “65 MeV” source, two results are in good agreement with each other within an error of 14%. The TEPC can measure the absorbed dose caused by neutrons only, while the TEIC can measure that caused by both neutrons and gamma-rays. From the results of TEPC measurements, the dose caused by gamma-rays was estimated to be only 0.2-0.3% of that by neutrons.

For the comparison between the measurements and the calculations, calculated results using the HETC-3STEP and the MORSE-CG codes agree with the measured ones within an error of 10%, with the exception of the depth of 25 cm for the “40 MeV”, for which the calculated result is 18% higher than the measured one. This can be attributed to the overestimation of spectrum in the calculation of HETC-3STEP at the depth of 25 cm because the same results are obtained for fission rates in the previous section.

The absorbed dose distributions inside the phantom calculated from the neutron spectra for the whole energy region using only the MORSE-CG code are in good agreement with the experimental ones within 13% at depths up to 25 cm because the calculated fission reaction rates agree well with the measured ones within 15% at that depth for the “40 MeV” and the “65 MeV” source neutrons. The absorbed dose distributions on the surface of the phantom are, however, 38% and 60% higher than the measured ones for the “40 MeV” and the “65 MeV” source neutrons, respectively. These disagreements are ascribed to the Kerma approximation, in which the charged particles and recoil nuclide are assumed to lose the energy very near the reaction point. On the other hand, the absorbed dose on the surface of the phantom calculated by HETC-3STEP and MORSE-CG agrees well with the measured one because it was obtained from the energy deposition of charged particles calculated using the HETC-3STEP code for neutrons above 15 MeV.

Conclusion

Absorbed dose distributions in the slab phantom were measured with the TEPC and the TEIC for 40 and 65 MeV quasi-monoenergetic neutrons, and the measured results were compared with those calculated using the HETC-3STEP and the MORSE-CG codes. Good agreement was obtained between the measured results of absorbed dose and the calculated ones from the deposition energy of charged particles from induced reactions by the HETC-3STEP code for the neutron energy above 15 MeV and those from the Kerma factor and neutron energy spectra calculated by the MORSE-CG code for the

energy below 15 MeV. The results of absorbed dose obtained for the whole energy region of neutrons from neutron energy spectra and the Kerma factor also agree well with the measured ones inside the phantom, while those on the surface of the phantom are higher than the measured ones because of the application of the Kerma approximation to intermediate energy neutrons. From the comparison of measured and calculated fission rates in the phantom, neutron flux calculated with the HETC-3STEP code tends toward overestimation, but not smaller than that for absorbed dose evaluations.

Acknowledgements

The authors would like to thank Mr. M. Takada of the National Institute of Radiological Sciences, Dr. H. Nakashima, Dr. N. Sasamoto and Mr. T. Hiruta of JAERI, Dr. S. Iwai of Nuclear Development Corp. and Professor T. Nakamura of Tohoku University for their useful suggestions and discussions about dose measurements. We also wish to thank Dr. N. Yoshizawa of the Mitsubishi Research Institute for his suggestions and discussions concerning the calculation by the HETC-3STEP code. The collaboration of Mr. Y. Harada of JAERI, Mr. S. Tanaka of JAERI Takasaki and the operation staff of TIARA facility in the experiments at the TIARA is also greatly appreciated.

REFERENCES

- [1] Y. Nakane, *et al.*, JAERI-Data/Code 96-029 (1996).
- [2] Y. Nakane, *et al.*, Proc. SATIF-3 meeting (1997).
- [3] B.K. Nabelssi and N.E. Hertel, *Radiat. Prot. Dosim.*, 48 (1993), 227.
- [4] A. Ferrari and M. Pelliccioni, *Radiat. Prot. Dosim.*, 76 (1998), 215.
- [5] V. Mares, *et al.*, *Radiat. Prot. Dosim.*, 70 (1997), 391.
- [6] N. Yoshizawa, *et al.*, *J. Nucl. Sci. Technol.*, 35 (1998), 928.
- [7] A.V. Sannikov and E.N. Savitskaya, *Radiat. Prot. Dosim.*, 70 (1997), 386.
- [8] P. Pihet, *et al.*, *Radiat. Prot. Dosim.*, 9 (1984), 241.
- [9] J.V. Sievers, *et al.*, *Nucl. Sci. Eng.*, 115 (1993), 13.
- [10] "Neutron Dosimetry for Biology and Medicine", ICRU Report 26 (1977).
- [11] Y. Nakane, *et al.*, *Radiat. Meas.*, 28 (1997), 479.
- [12] N. Nakao, H. Nakashima, T. Nakamura, Sh. Tanaka, Su. Tanaka, K. Shin, M. Baba, Y. Sakamoto and Y. Nakane, *Nucl. Sci. Eng.*, 124 (1996), 228.

- [13] "MCNP – A General Monte Carlo n-Particle Transport Code," Version 4B, LA-12625-M, Los Alamos National Laboratory (1997).
- [14] M.B. Chadwick, *et al.*, *Nucl. Sci. Eng.*, 131 (1999), 293.
- [15] Y. Nakane and Y. Sakamoto, submitted to *Nucl. Instr. Meth.* (2000).
- [16] M. Baba, *et al.*, *Nucl. Instr. Meth.*, A 428 (1999), 454.
- [17] N. Yoshizawa, K. Ishibashi and H. Takada, *J. Nucl. Sci. Technol.*, 32 (1995), 601.
- [18] P. Cloth, *et al.*, KFA-IRE-EAN 12/88 (1988).
- [19] K. Shibata, *et al.*, JAERI 1319 (1990).
- [20] R.G. Alsmiller, Jr., J.M. Barnes and J.D. Drischler, ORNL/TM-9801 (1986).
- [21] R.H. Bassel and G.H. Herling, *Radiat. Res.*, 69 (1977), 210.
- [22] M.B. Chadwick, *et al.*, *Nucl. Sci. Eng.*, 123 (1996), 17.
- [23] M.B. Chadwick and P.G. Young, *Nucl. Sci. Eng.*, 123 (1996), 1.
- [24] P.W. Lisowski, *et al.*, Proceedings of Specialists Meeting on Neutron Cross-Section Standards for Energy Region above 20 MeV, Uppsala Sweden, 21-23 May (1991), 177.

Figure 1. Cross-sectional view of the experimental arrangement

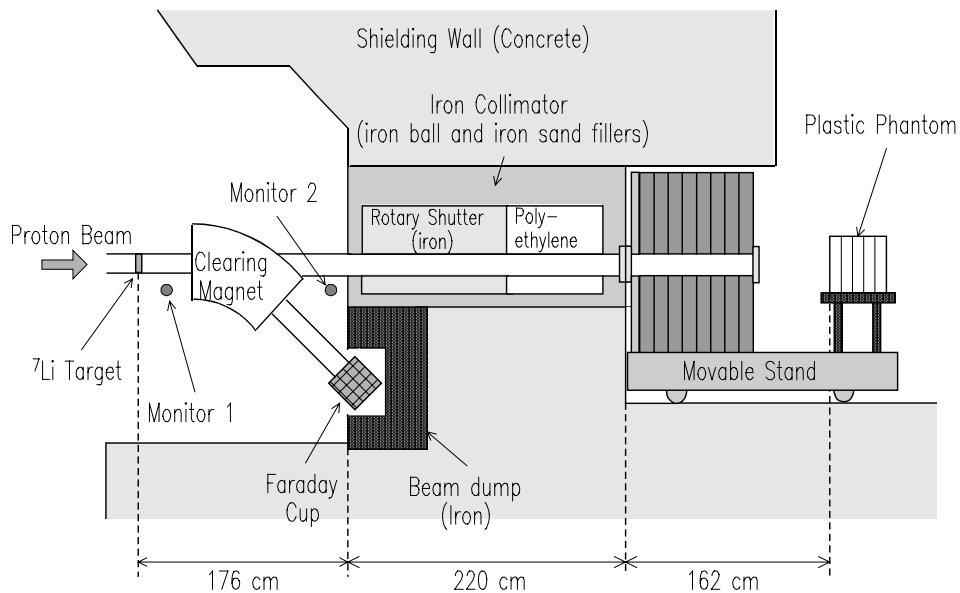


Figure 2. Source neutron spectra measured with BC501A counter [12]

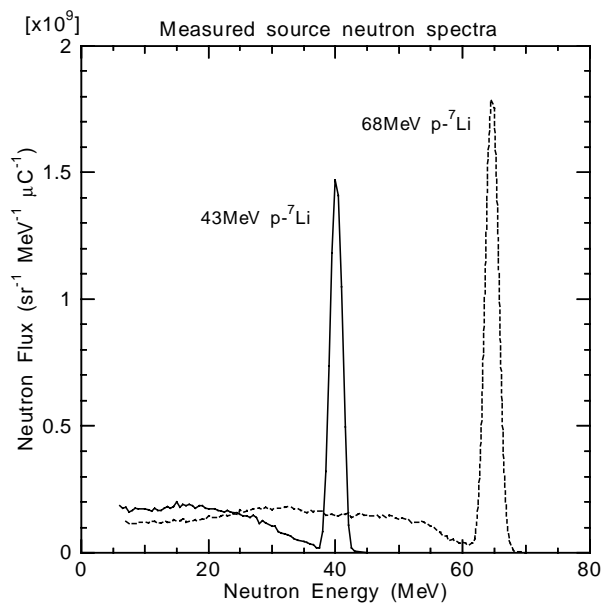


Figure 3. Evaluated source spectra at the surface of the phantom

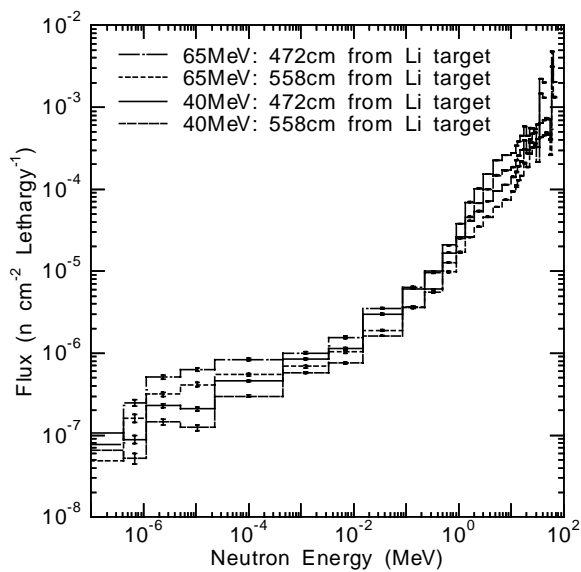
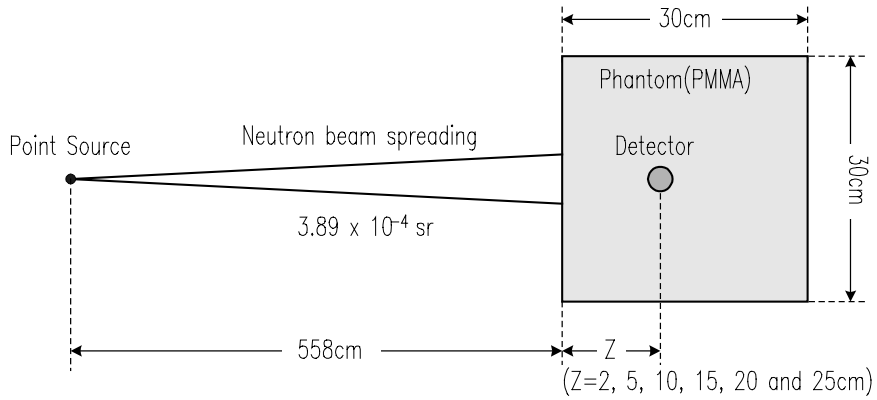


Figure 4. Calculation geometry used for absorbed dose calculation

(a) Side view of the calculation geometry



(b) Enlargement of the detector in the calculation geometry

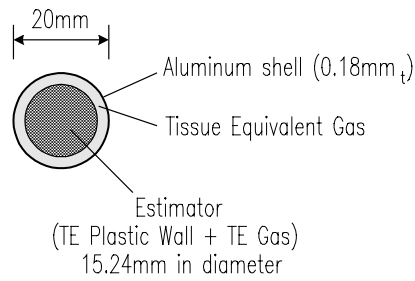


Figure 5. Microdosimetric spectra for the “40 MeV” source

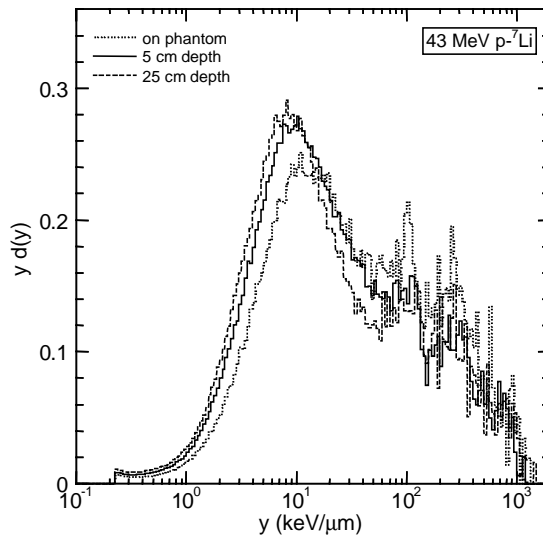


Figure 6. Microdosimetric spectra for the “65 MeV” source

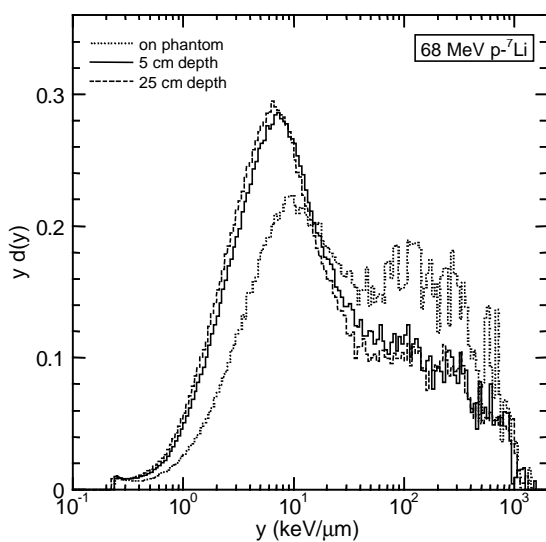


Figure 7. Measured and calculated fission rates of ²³⁸U in the phantom

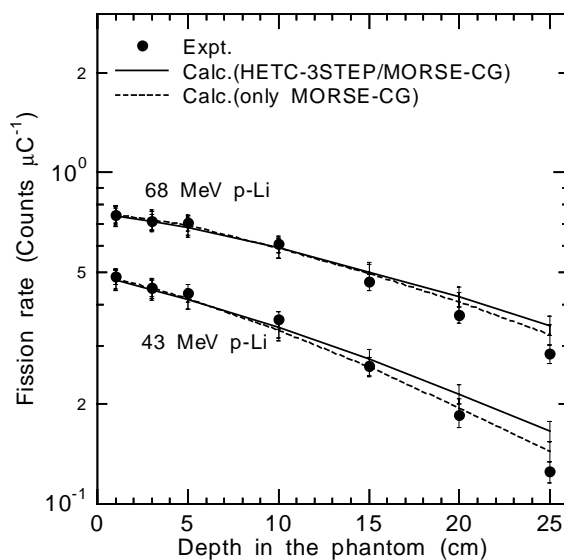


Figure 8. Calculated energy spectra in the phantom for the “40 MeV”

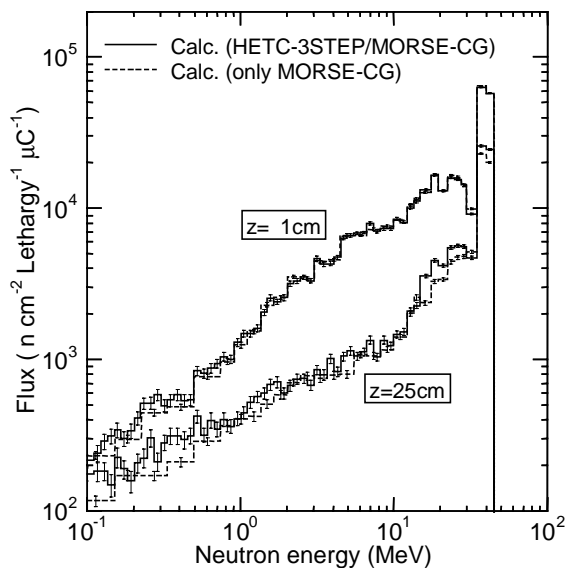


Figure 9. Measured and calculated absorbed dose in the phantom for the “40 MeV”

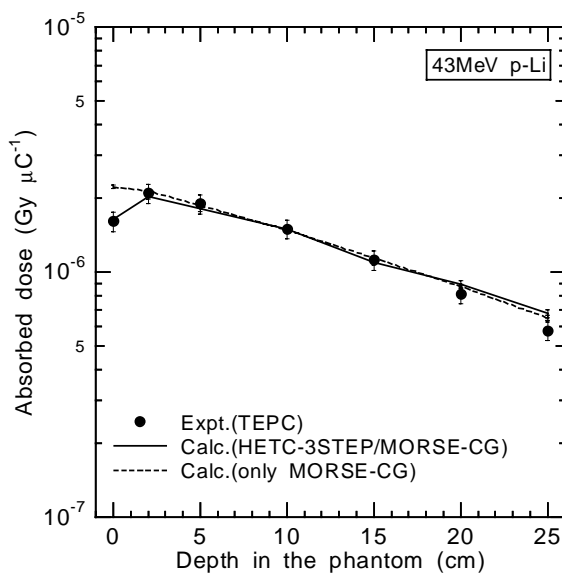
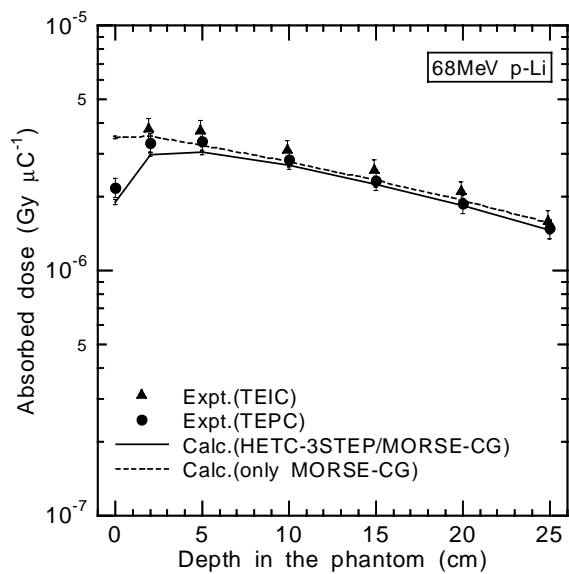


Figure 10. Measured and calculated absorbed dose in the phantom for the “65 MeV”



BENCHMARK CALCULATION WITH SIMPLE PHANTOM FOR NEUTRON DOSIMETRY

Nobuaki Yoshizawa

MRI, Mitsubishi Research Institute, Japan

Yukio Sakamoto

JAERI, Japan Atomic Energy Research Institute, Japan

Satoshi Iwai

NDC, Nuclear Development Corporation, Japan

Hideo Hirayama

KEK, High-energy Accelerator Research Organisation, Japan

Abstract

Benchmark calculations for high-energy neutron dosimetry were performed. Neutron-induced energy deposition in a cylinder phantom (radius 100 cm, depth 30 cm) was calculated. Incident neutron energies were from 100 to 10 000 MeV. Four single-element (hydrogen, carbon, nitrogen and oxygen) phantoms and ICRU four-element tissue phantom were used. The depth dose distributions in the central region ($R = 0-1$ cm) and the whole region ($R = 0-100$ cm) were calculated. Calculated results of FLUKA, MCNPX and HETC-3STEP were compared. There were large differences among calculated results especially for the single-element phantom up to a factor of seven.

Introduction

Subsequent to the recommendations of ICRP Publication 60 [1], effective doses for high-energy neutrons were calculated by some authors using several computer codes. Unfortunately, above 20 MeV there are few cross-section libraries due to a lack of experimental data. Consequently, computer codes that do not need cross-section data were used for effective dose calculation for high-energy neutrons. In those computer codes, theoretical models or empirical formulae are used to calculate cross-sections.

Fluence to effective dose conversion coefficients for AP irradiation geometry [2-5] is displayed in Figure 1. Effective dose conversion coefficients for PA and ISO were also reported. Ratios of maximum to minimum value of effective dose are presented in Figure 2 for AP, PA and ISO. The maximum value of the ratio is about 1.8 at 2 GeV for AP irradiation. To investigate performance of computer codes for high-energy neutron dosimetry calculations, simple benchmark calculations were planned and calculation results for neutron dose were compared.

Benchmark calculations

Neutron-induced energy deposition in a cylinder phantom (radius 100 cm, depth 30 cm) was calculated. Four single-element (hydrogen, carbon, nitrogen and oxygen) phantoms and the ICRU four-element tissue phantom were used to calculate neutron dose. The depth dose distributions in the central region ($R = 0-1$ cm) and the whole region ($R = 0-100$ cm) were calculated. A detailed description of this benchmark is presented in Appendix A.

Computer codes

Three computer codes were used in this benchmark calculation. The names of the participants are shown below.

Participant	Organisation	Code	Additional information
M. Pelliccioni	INFN (Italy)	FLUKA [6]	
M. Sutton	Georgia Institute of Tech. (USA)	MCNPX [7]	LA150 library [10]
N. Yoshizawa	MRI (Japan)	HETC-3STEP [8] MORSE-CG/KFA [9]	JENDL-3.1 library [11]

Results of calculations

Depth dose

Figures 3-6 show the results of dose in each element as a function of the phantom. Maximum errors of calculation were about 2%, 3% and 4% for FLUKA, MCNPX and HETC-3STEP, respectively. For the hydrogen phantom, calculated results agree well up to 1 000 MeV, except for 0-3 cm depth at 100 MeV. Above 3 000 MeV, systematic differences appear. For the carbon, nitrogen and oxygen phantoms, results are very similar. For almost all energy regions, maximum results emerge from the HETC-3STEP calculations and minimum results from the FLUKA calculations for both the central and the whole region of the phantom. The largest difference is about a factor of seven in the central region at 3 000 MeV. For the whole region, the differences among the results are up to a factor of three. For the tissue phantoms, maximum differences for the whole region are within a factor of six at 10 000 MeV. At the same neutron energy, maximum differences for the central region are about a factor of three.

Total energy deposition

Figure 7 shows the total energy deposition in the phantoms for the central and the whole region as a function of incident neutron energy. For the hydrogen phantom, the results agree well up to 1 000 MeV. Above 3 000 MeV, differences become greater with increasing neutron energy. For the carbon, nitrogen and oxygen phantoms, results are very similar. The results of FLUKA and MCNPX agree well at 100 MeV. As neutron energy increases, the results of MCNPX become similar to the results of HETC-3STEP. There are large differences between the results of HETC-3STEP and FLUKA at 100 MeV. Total energy deposition in the central region calculated by HETC-3STEP is larger than energy deposition calculated by FLUKA in the whole region for the carbon, nitrogen and oxygen phantoms. For the whole region of the tissue phantom, the results agree within about a factor of three. For the central region, differences become larger with increasing neutron energy. The reason that HETC-3STEP and FLUKA results tend to agree is that the overestimation of energy deposition from neutron-hydrogen interaction calculated by FLUKA is cancelled out by an underestimation of energy deposition from the neutron-oxygen interaction. Hydrogen and oxygen are the main elements of the tissue phantom, as shown in Table A.1.

Summary

A simple benchmark for high-energy neutron dosimetry was set up. Calculated neutron doses in the simple cylinder phantom were compared in the energy range from 100 MeV to 10 000 MeV. It was found that there were large differences among calculated results, especially for the single-element phantom. There were also large differences for dose distributions in the central and whole region.

As a result of this benchmark, it is recommended perform some studies so as to better predict the accuracy of predictions by the computer codes for high-energy neutron dosimetry calculation. Some studies listed below are needed in the future.

- Comparison of partial energy deposition by p, d, t, ^3He , alpha and other particles.
- Comparison of calculated cross-section for H, C, N, O.
- Comparison of treatment of physical process to deposit particle energy in the phantom.
- Experimental approach is also needed [ex. 5,12].

Acknowledgement

We wish to thank Dr. M. Pelliccioni and Dr. M. Sutton for their contribution to this benchmark.

REFERENCES

- [1] International Commission on Radiological Protection, "1990 Recommendations of the International Commission on Radiological Protection", ICRP Publication 60, Pergamon Press, Oxford (1991).
- [2] B.K. Nabelssi, N.E. Hertel, *Radiat. Prot. Dosim.*, 48 (3), 227 (1993).
- [3] A. Ferrari, *et al.*, *Radiat. Prot. Dosim.*, 71 (3), 165 (1997).
- [4] N. Yoshizawa, *et al.*, *J. Nucl. Sci. and Technol.*, 35, 928 (1998).
- [5] M.Sutton, *et al.*, *J. Nucl. Sci. and Technol.*, S1, 753 (2000).
- [6] A. Fassò, *et al.*, "FLUKA: Hadronic Benchmarks and Applications", Proc. MC93 Monte Carlo Conference, 22-26 February 1993, Tallahassee (Florida), P. Dragovitsch, S.L. Linn, M. Burbank, eds., p. 88 (1994).
A. Fassò, *et al.*, "An Update about FLUKA", Proc. 2nd Workshop on Simulating Accelerator Radiation Environments, CERN, Geneva, Switzerland, 9-11 Oct. 1995, G.R. Stevenson, ed., CERN Report TIS-RP/97-05, pp. 158-170 (1995).
A. Fassò, *et al.*, "New Developments in FLUKA Modelling Hadronic and EM Interactions", Proc. 3rd Workshop on Simulating Accelerator Radiation Environments, KEK, Tsukuba, Japan, 7-9 May 1997, H. Hirayama, ed., KEK Proceedings 97-5, pp. 32-43 (1997).
A. Ferrari, *et al.*, "The Physics of High-energy Reactions", Proc. of the Workshop on Nuclear Reaction Data and Nuclear Reactors Physics, Design and Safety, International Centre for Theoretical Physics, Miramare-Trieste, Italy, 15 April-17 May 1996, A. Gandini and G. Reffo, eds., World Scientific (1998).
- [7] H.G. Hughes, *et al.*, "MCNPX – The LAHET/MCNP Code Merger", XTM-RN(U) 97-012 (1997).
- [8] N. Yoshizawa, K. Ishibashi, H. Takada, *J. Nucl. Sci. and Technol.*, 32, 601 (1995).
- [9] P. Cloth, *et al.*, KFA-IRE-EAN 12/88 (1988).
- [10] M.B.Chadwick, *et al.*, *Nucl. Sci. Eng.*, 131, 293 (1999).
- [11] T. Nakagawa, *et al.*, *J. Nucl. Sci. and Technol.*, 32, 1259 (1995).
- [12] Y. Nakane, *et al.*, "Dose Distributions in a Plastic Phantom Irradiated by 40- and 65-MeV Quasi-monoenergetic Neutrons", Proc. of the 10th International Congress of the International Radiation Protection Association (IARP10), Hiroshima, Japan, P-3b-155, 14-19 May (2000).

Figure 1. Comparison of neutron fluence to effective dose for AP irradiation

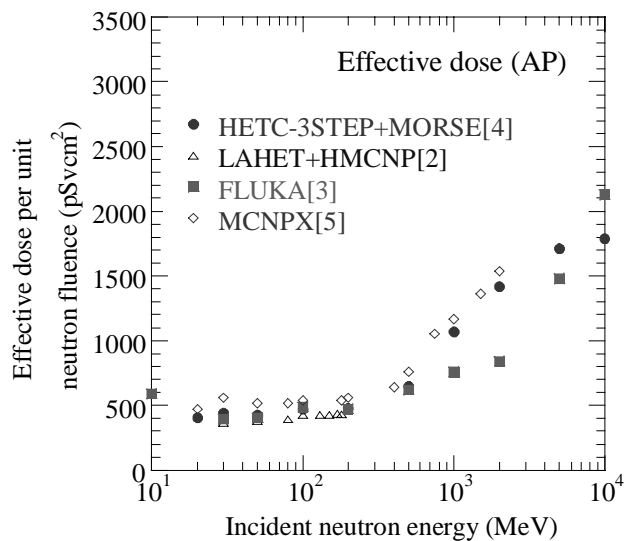


Figure 2. Ratios of maximum to minimum value of calculated effective dose as a function of incident neutron energy

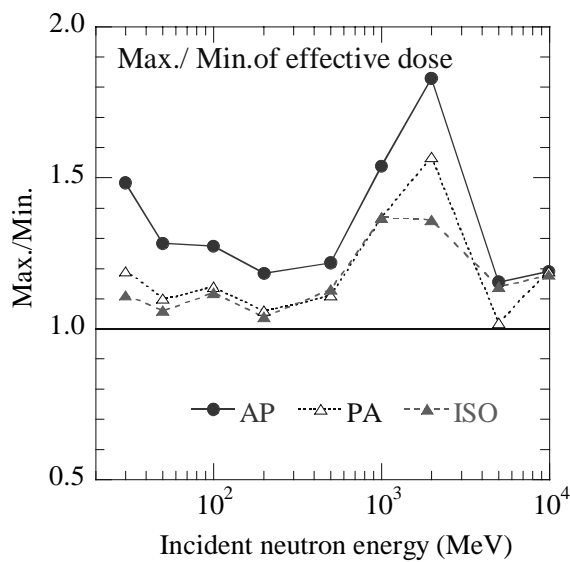


Figure 3. Comparison of neutron dose distribution in (a) hydrogen, (b) carbon, (c) nitrogen, (d) oxygen and (e) tissue cylinder phantom (radius 100 cm, depth 30 cm)

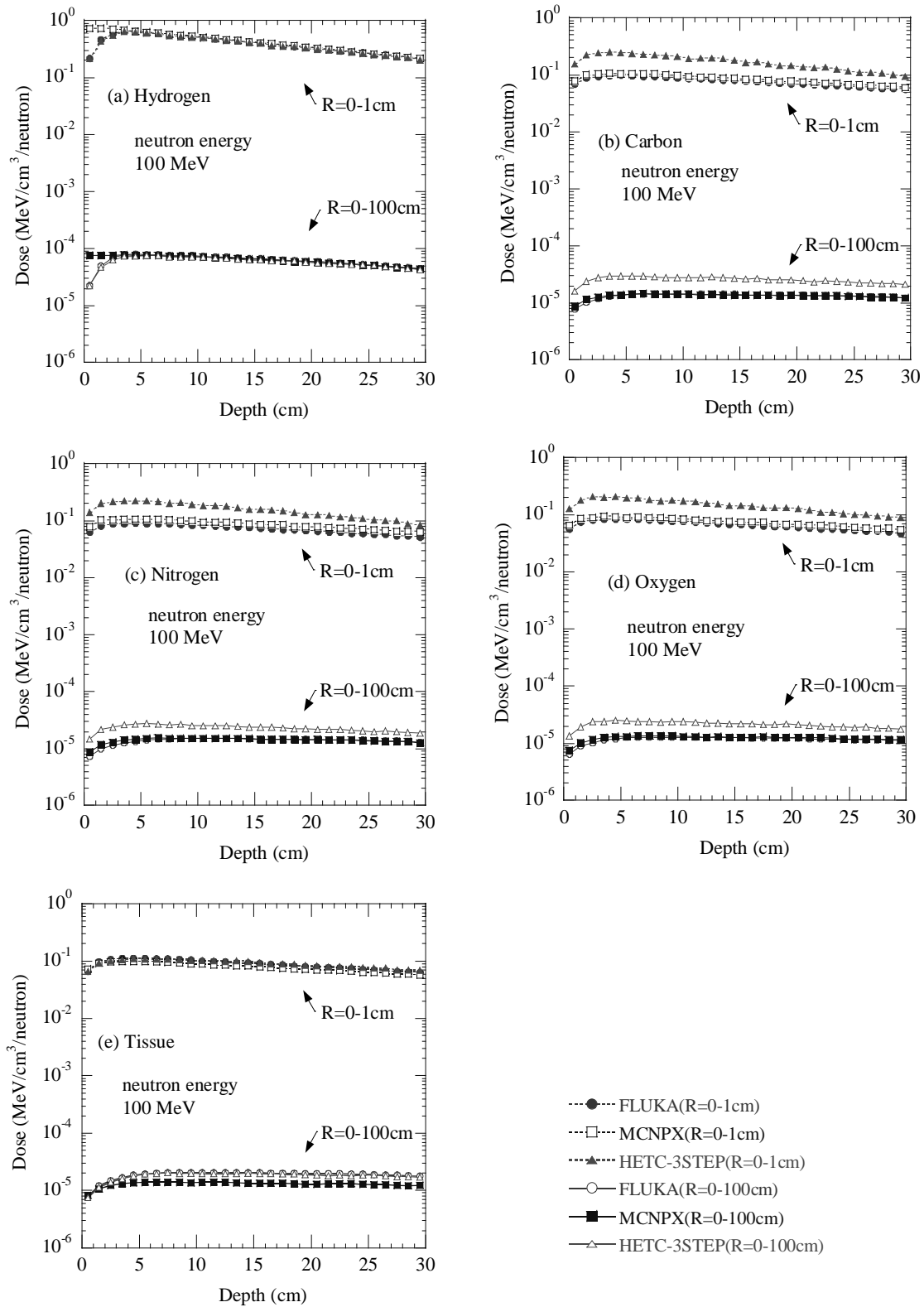


Figure 4. Comparison of neutron dose distribution in (a) hydrogen, (b) carbon, (c) nitrogen, (d) oxygen and (e) tissue cylinder phantom (radius 100 cm, depth 30 cm)

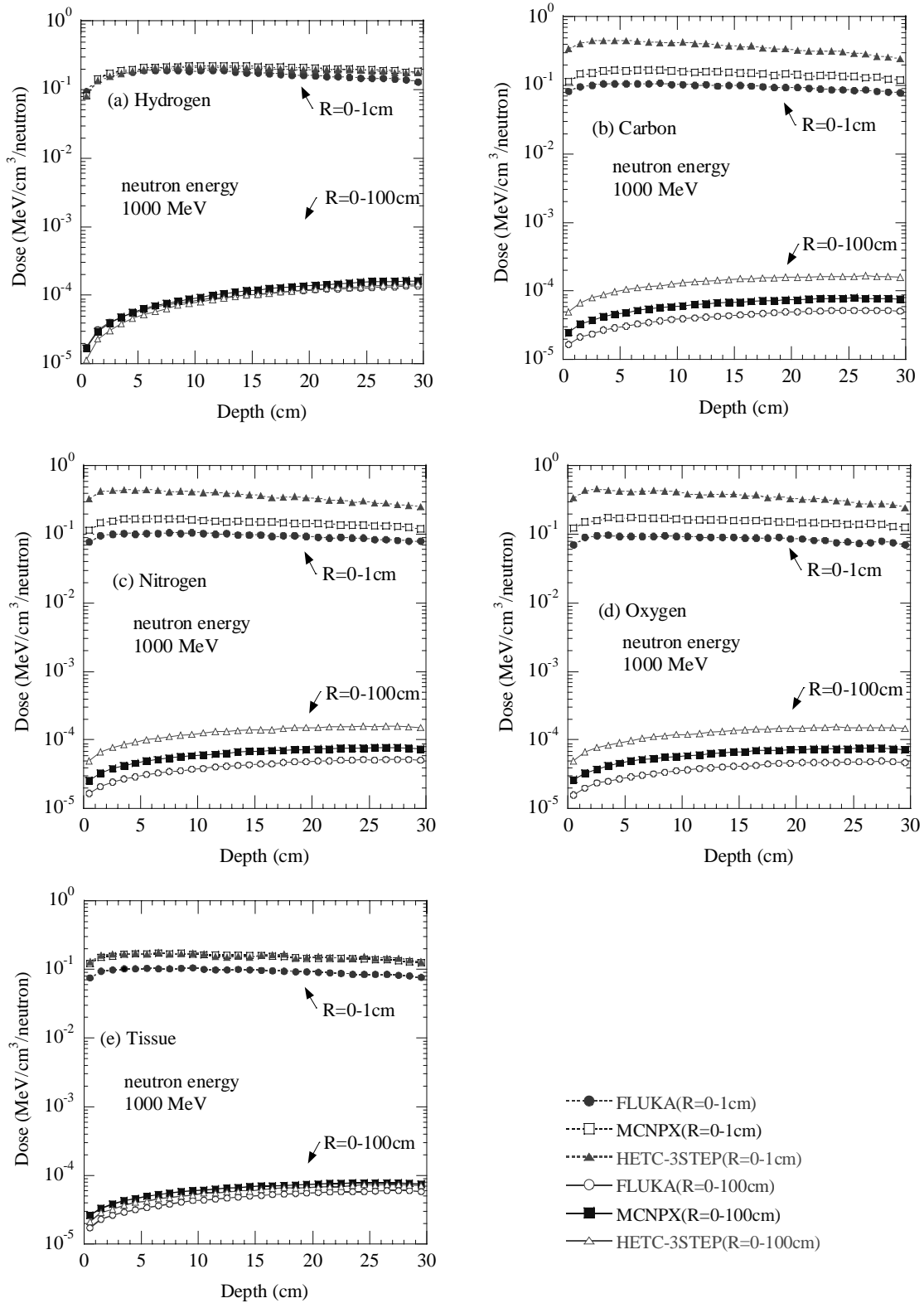


Figure 5. Comparison of neutron dose distribution in (a) hydrogen, (b) carbon, (c) nitrogen, (d) oxygen and (e) tissue cylinder phantom (radius 100 cm, depth 30 cm)

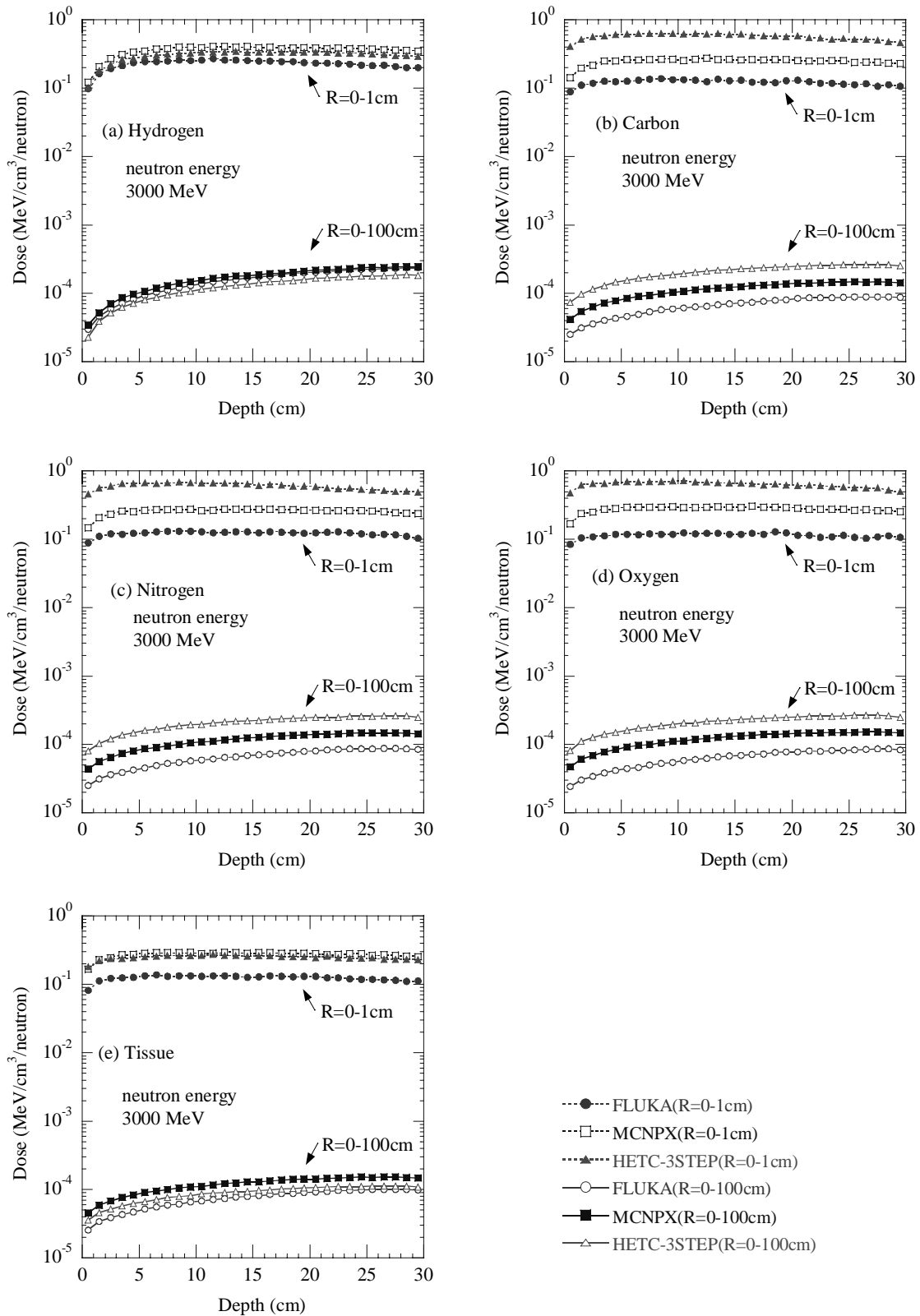


Figure 6. Comparison of neutron dose distribution in (a) hydrogen, (b) carbon, (c) nitrogen, (d) oxygen and (e) tissue cylinder phantom (radius 100 cm, depth 30 cm)

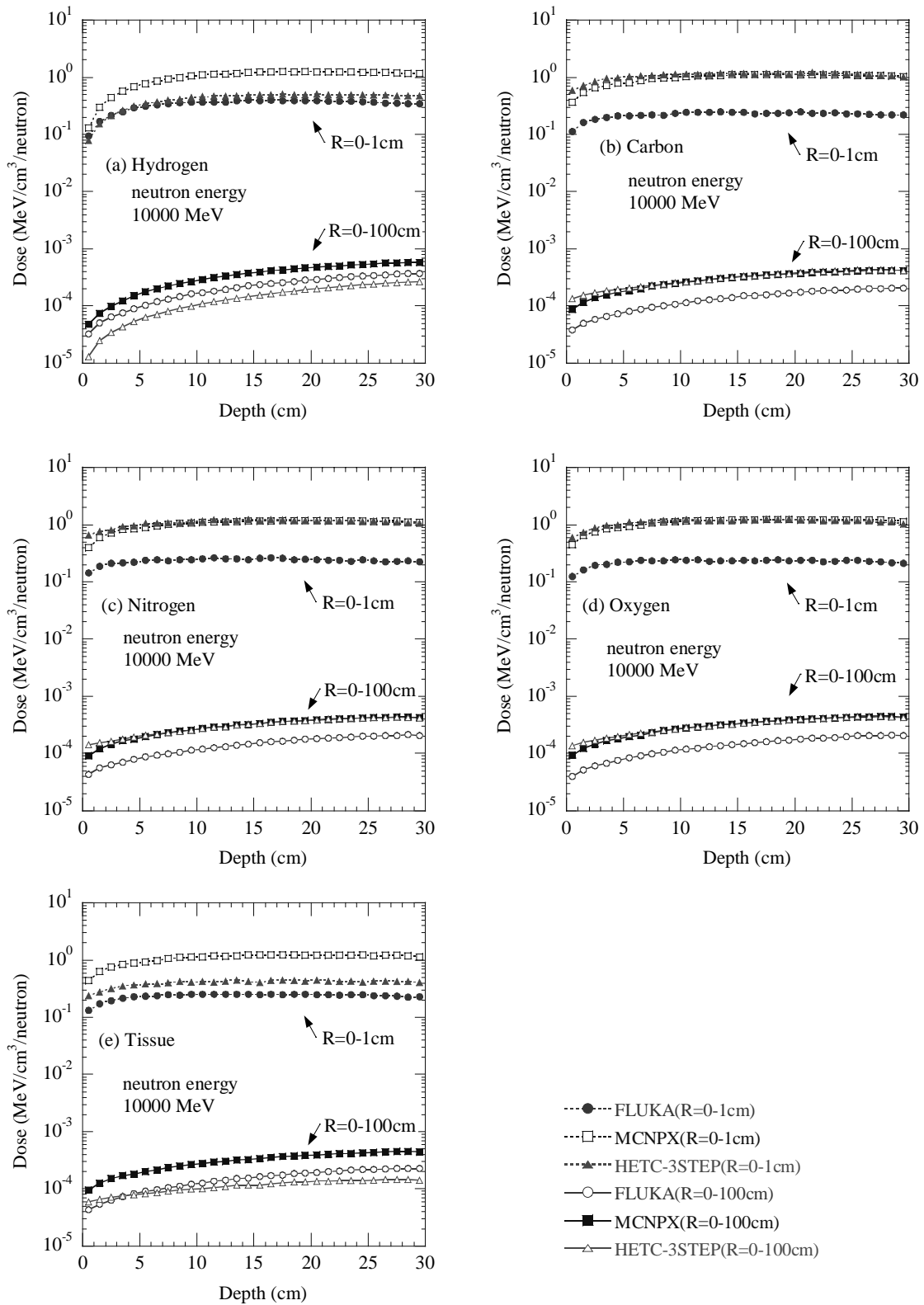
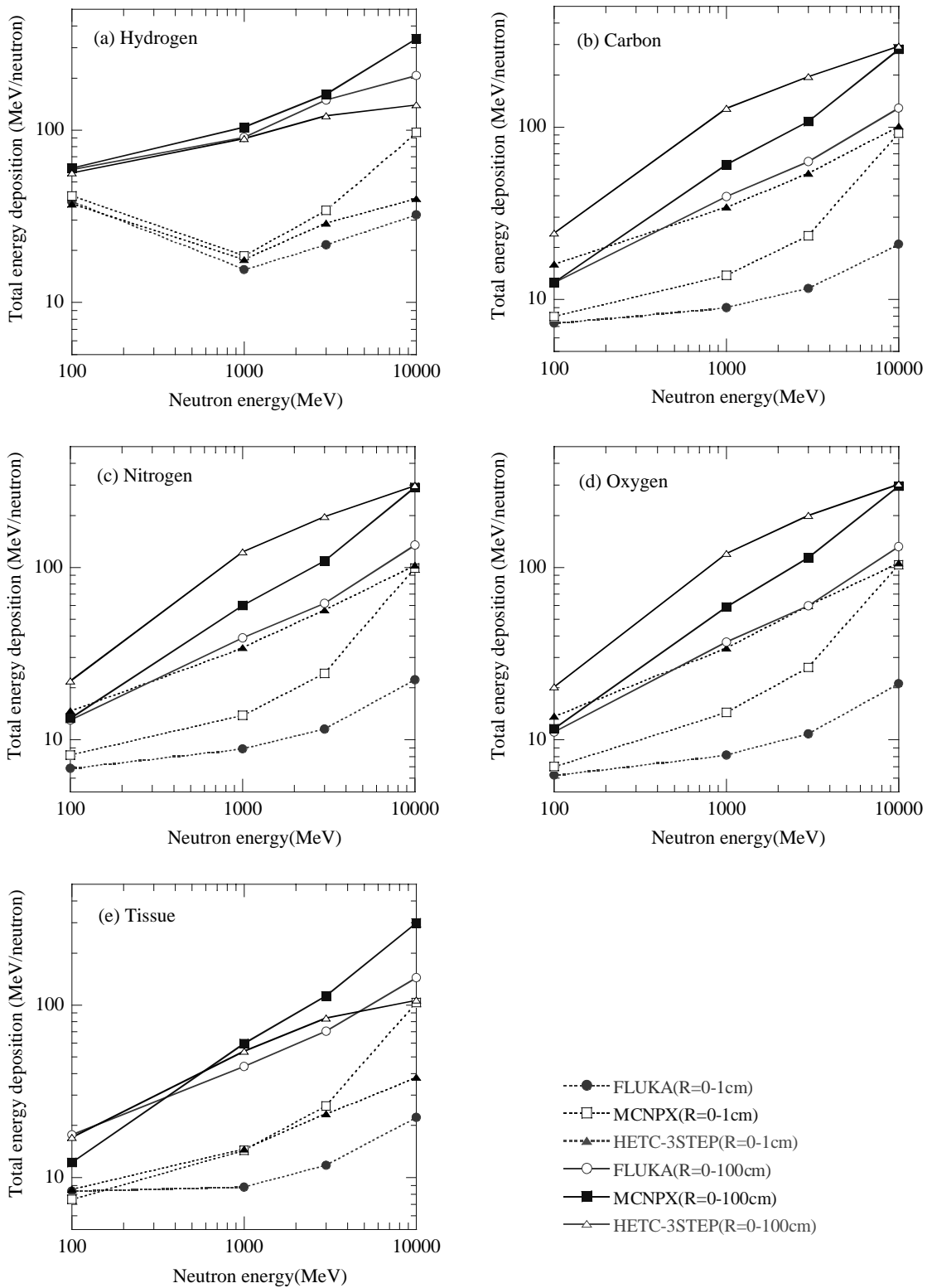


Figure 7. Comparison of total energy deposition for (a) hydrogen, (b) carbon, (c) nitrogen, (d) oxygen and (e) tissue cylinder phantoms in the regions R = 0-1 cm and R = 0-100 cm



Appendix A
Benchmark problem for neutron dosimetry

Geometry

Cylinder (radius 100 [cm] × depth 30 [cm]) (*please see Figure A.1*).

Material

Table A.1. Condition of elements for phantoms*

Elements	Z	A	[g/cm ³]	wt. %	[atoms/cm ³ /1E+24]
(1) H	1	1	1.0	100	6.022E-01
(2) C	6	12	1.0	100	1.004E-01
(3) N	7	14	1.0	100	8.603E-02
(4) O	8	16	1.0	100	7.528E-02
(5) ICRU four-element tissue			1.0		
H	1	1		10.1	6.082E-02
C	6	12		11.1	5.570E-03
N	7	14		2.6	1.118E-03
O	8	16		76.2	2.868E-02

* *Solid phase*

Beam conditions

Neutron pencil beam, energy = 100, 1 000, 3 000, 10 000 [MeV].

Requested results

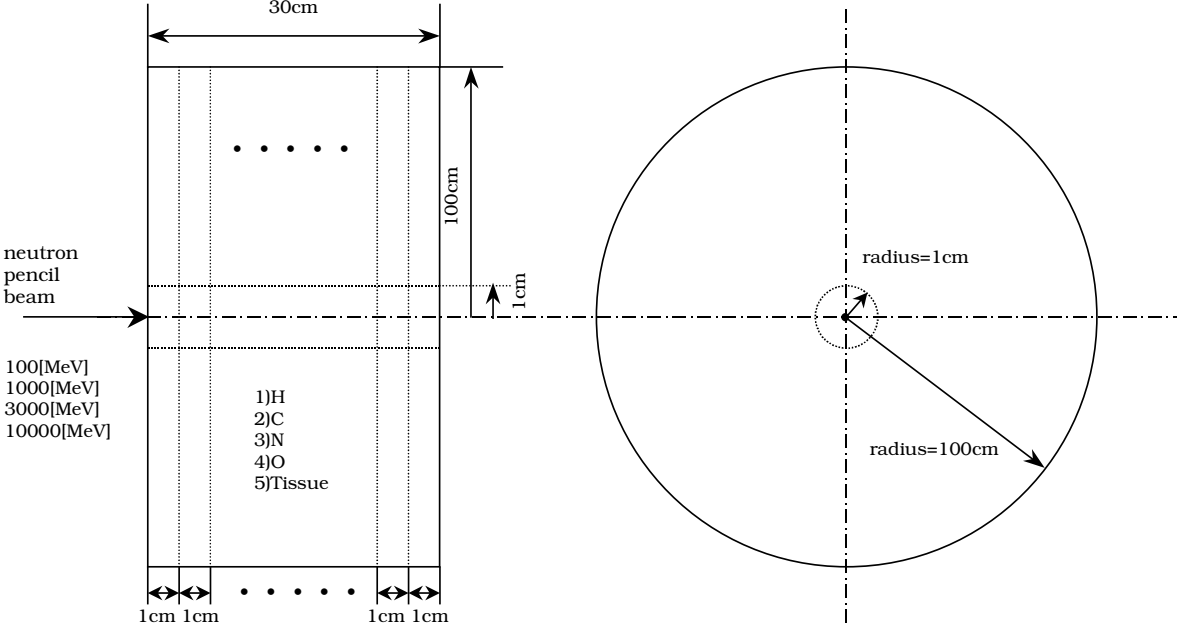
1) Total dose [MeV/cm³].

2) Region:

R = 0-1 cm, D = 0-1 cm, 1-2 cm,...29-30 cm (30 regions).

R = 0-100 cm, D = 0-1 cm, 1-2 cm,...29-30 cm (30 regions).

Figure A.1. Geometry of the simple phantom for the benchmark calculations



*Electron-photon
Benchmark (BEEP)*

CURRENT STATUS OF A LOW-ENERGY PHOTON TRANSPORT BENCHMARK

H. Hirayama, S. Ban and Y. Namito

KEK, High-energy Accelerator Research Organisation

Oho, Tsukuba, Ibaraki, 305-0801 Japan

E-mail: hideo.hirayama@kek.jp

Abstract

The scattered-energy spectra of monochromised synchrotron-radiation photons toward 90° by samples (C, Cu, Pb) were measured using high-purity Ge detectors. The incident photons were in a linearly polarised beam of 20, 30 and 40 keV. To investigate the validity of the EGS4 code regarding photon transport in the keV region, we performed systematic comparisons of measurements and EGS4. EGS4 calculations were performed in default status and with improvements of low-energy photon transport (linearly polarised photon scattering, Doppler broadening, L-X and K-X). The measurement and calculations were compared in absolute values. Both the intensity and the shape of the peaks were compared. EGS4 calculations with improvements in low-energy photon transport agreed well with the measurements.

Introduction

Measurements of 20-40 keV photon transport were performed using monochronised synchrotron radiation. The merits of monochronised synchrotron radiation are the use of mono-energy and mono-direction photons. This type of experiment is free from scattering inside the source or by the source holder, which is inevitable in any experiment using a radioisotope source. Thus, this experiment is performed under much clearer conditions compared to the one using a radioisotope source. Also, the geometry is simple and well defined. The measurement value is given in absolute values. Thus, this experimental data may be useful as a benchmark in the few ten keV region to examine the validity of a photon transport code.

The Rayleigh scattered, Compton-scattered, multiply scattered photons, and fluorescent photons (K-rays and L-X-rays) are included in the photon spectra. The scattering is influenced by the photon linear polarisation, and the Compton scattering is influenced by electron binding and Doppler broadening. By simulating this experiment, it is possible to check the calculation program regarding these points.

Expansion of the general-purpose electron-photon Monte Carlo transport code EGS4 [1] is being continued. One subject concerning the expansion is a detailed treatment of photon transport in the keV region. The purpose of this comparison is to verify the validity of the EGS4 code in this energy region.

Measurement

Experimental details

A measurement was performed at a BL-14C in the 2.5 GeV synchrotron light facility (KEK-PF). The experimental arrangement is shown in Figure 1. Photons from a vertical wiggler were used after being monochronised by a Si(1,1,1) double-crystal monochromator. The incident beams were 20, 30 and 40 keV linearly polarised photons. The polarisation vector was in the vertical direction and the degree of linear polarisation (P) is shown in Table 1. Depending on the detune of the monochromator, P is subject to a change by a few per cent.

In Figure 1, the propagation and polarisation vectors of an incident photon are shown as \vec{k}_0 and \vec{e}_0 . Incident photons passed through a collimator (C_0) with an opening diameter (D_0) of 2 mm and a free air ionisation chamber (FAIC), and were scattered by the sample (S). The photon intensity was monitored by the FAIC, which was calibrated by a calorimeter [2]. After passing an air layer and Kapton film, photons entered the vacuum chamber (VC). The thickness of air and Kapton are summarised in Table 2.

A list of the samples and their thickness is given in Table 3. The normal vector of the samples was $(-\cos\xi\sin\eta, -\sin\xi, \cos\xi\cos\eta)$. While the design values of ξ and η were 45° and 45° , the actual values of ξ and η were 45.88° and 45° . Thus, the actual value of the normal vector were $(-0.492, -0.718, 0.492)$. The effective thickness for incident photons of the Cu and Pb samples were more than ten mean free paths for all of the photon energies used; these samples could be treated as infinitely thick samples. The samples were contained in a vacuum chamber, and vacuum pipes were placed between the vacuum chamber and the Ge detectors in order to reduce any scattering due to air.

Photons through collimators (C_1 and C_2) located in the X and Y directions were detected by Ge detectors (Ge-1 and Ge-2). Before entering Ge detectors, photons passed through a Kapton film and an air layer. The distances from the surface of the sample to the exits of the collimators (L_1 and L_2) were

424 and 436 mm, respectively, and the opening diameters of the collimators (D_1 and D_2) were 5.01 and 5.04 mm, respectively. The scattered photon intensity had an azimuth angle dependence, since the incident photon beam comprised linearly polarised photons. To observe the effect of linear polarisation, the scattered photon intensity was measured by two Ge detectors located in two different azimuth angle directions. Two high-purity Ge low-energy photon detectors (ORTEC GLP16195/10 and GLP16195/10P) were used for the measurement; the former and the later were used as Ge-1 and Ge-2, respectively. The absorbing layers of Ge detectors are summarised in Table 4 [3].

The signal from the detector was amplified by an ORTEC 572 amplifier, passed through a 1850-ADC (Seiko EG&G) and stored in 4 k memory in a Model-7800 multi-channel analyser (Seiko EG&G). The typical accumulation time was 600 seconds.

Data analysis

An energy calibration of the measured counts of scattered photon was performed. The L_{α} ($L_{\alpha_1} + L_{\alpha_2}$) peak of Pb and the K_{α_1} peak of Pb were used for the energy calibration. The K_{α_1} of Pb was emitted due to the photoelectric effect of higher harmonic incident photons from the monochrometer.

Based on the measured counts of scattered photons, ($n_x(k)$ and $n_y(k)$), the photon counts per incident photon per solid angle toward the x and y directions (C_x and C_y) were derived as:

$$C_x(k) = \frac{1}{\Omega_x} \left(\frac{n_x(k)}{I_0} - \frac{n_x^{bg}(k)}{I_0^{bg}} \right)$$

$$C_y(k) = \frac{1}{\Omega_y} \left(\frac{n_y(k)}{I_0} - \frac{n_y^{bg}(k)}{I_0^{bg}} \right)$$

Here, k is the scattered photon energy, Ω_x and Ω_y are the opening solid angles of the collimators and n_x^{bg} and n_y^{bg} are the background counts obtained from a no-sample run. The background count was negligibly small ($< 0.2\%$ of sample run). I_0 and I_0^{bg} are the number of incident photons during a sample run and a no-sample run. The attenuation of incident photons due to air and Kapton film between FAIC and VC was considered when I_0 and I_0^{bg} were calculated. A dead-time correction was made using the ratio of the live time and the real time of ADC. The dead time was controlled to be less than 2%. A correction for pile up is not considered here. The pile up was controlled to be less than 1%.

The statistical error is shown in the figures, and is not included here. The major sources of errors are the monitor (1.4%), the orientation of the sample (1%), the solid angle of collimators (1%), and P (2%). The error in P strongly affects $C_y(k)$, because they are proportional to $(1 - P)$, and P is about 0.8. In total, the errors of $C_x(k)$ and $C_y(k)$ are estimated to be about 3% and 10%, respectively (1σ).

The fluctuation of the measured value is about the same as these estimated errors, except for the Rayleigh scattered photons.

Measurements were performed for nine conditions (three samples times three energies). Figures 3-6 show the measured photon spectra for an incident energy of 40 keV.

EGS4 calculation

Improvement

The EGS4 code with the low-energy photon transport expansion developed at KEK was used. In addition to the physical processes in the standard EGS4 code, we considered the following physical processes in the calculation:

- Up to ten K-X-rays are considered.
- Effect of linear polarisation on the Compton and Rayleigh scattering [4,6].
- Doppler broadening of a Compton-scattered photon [5,6].
- L-X-rays. Some of the authors (HH, YN and SB) released a preliminary version of a program to treat L-X-rays in EGS4 [7]. After that, the following improvements to the physical model were made:
 - The energy dependence of the sub-shell ionisation cross-sections (L_I , L_{II} and L_{III}) is treated by approximately treating the cross-sections in a log-log fitting. The agreement of the measured and calculated L-X-rays from L_I (ex. L_{γ}) was apparently improved by this treatment.
 - Experimental L relative X-ray emission rates, summarised by Salem, *et al.* [8] were used. The theoretical L relative X-ray emission rates, calculated by Scofield [9], were used for L-X-rays, which Ref. [8] does not mention. We did not use the L-X relative X-ray emission rates in Ref. [10].
 - The photon cross-section and branching ratio in an energy bin which contains the K-edge or L-edge is determined using extrapolation from a higher or lower energy bin.

In the calculation, we ignored the following points, which may have some effect on the measurement:

- Interference of Rayleigh scattering.
- Interference of Compton-scattered photons [11].

This last phenomenon has not yet been studied well.

Two-step calculation

The calculation was divided into two steps. In the first step, photon transport inside the sample was performed and scattered photons toward 90° were scored. In the second step, photon transport inside the Ge detector was performed using the scattered photon spectra obtained in the first step as the incident photons. The energy deposition in the Ge region was scored and compared with the measured pulse height spectra.

An EGS4 calculation without any low-energy photon transport expansion is shown in Figure 2. An EGS4 calculation with a low-energy photon transport expansion is shown in Figures 3-6.

Comparison

A comparison of the measured and calculated photon spectra for 40 keV incident photons is shown in Figures 3-6. The ratio of the measured and computed intensities of Compton-scattered, Rayleigh-scattered, L-X-ray and K-X-ray are shown in Figures 7-10.

The results of comparisons of the measurement and EGS4 calculations were as follows:

- *Compton scattering*. Both the intensity and the spectra agreed well.
- *Rayleigh scattering*. Agreed reasonably well. In some cases, C/M reaches 0.8 or 1.2. This was due to interference. This was verified by observing the interference pattern using an imaging plate.
- *Multiple scattering*. Agreed well.
- *L-X-rays*. Major three L-X-rays agreed well. Other three L-X-rays differ up to 50%.
- *K-X*. Agreed well.

REFERENCES

- [1] W.R. Nelson, H. Hirayama and D.W.O. Rogers, SLAC-265 (Stanford University, Stanford, 1985).
- [2] H. Nakashima, S. Tanaka, M. Yoshizawa, H. Hirayama, S. Ban, Y. Namito and N. Nariyama, *Nucl. Instrum. and Meth.*, A310 (1991), 696.
- [3] "Solid-state Photon Detector Operators Manual" (EG&G ORTEC).
- [4] Y. Namito, S. Ban and H. Hirayama, *Nucl. Instr. Meth.*, A332 (1993), 277.
- [5] Y. Namito, S. Ban and H. Hirayama, *Nucl. Instr. Meth.*, A349 (1994), 489.
- [6] Y. Namito, S. Ban and H. Hirayama, *KEK Internal*, 95-10 (1995).
- [7] H. Hirayama, Y. Namito and S. Ban, *KEK Internal*, 96-10 (1996).
- [8] S.I. Salem, S.L. Panossian and R.A. Krause, *Atomic Data and Nucl. Data Tables*, 14 (1974), 91.
- [9] J.H. Scofield, *Atomic Data and Nucl. Data Tables*, 14 (1974) 121.
- [10] R.B. Firestone, *Table of Isotopes, 8th ed.*, John Wiley & Sons, Inc., Table 7b-7d (1996).
- [11] W. Schülke and S. Mourikis, *Acta Cryst.*, A42 (1986), 86.
- [12] Y. Namito, S. Ban and H. Hirayama, "Low-energy Photon Transport Benchmark Problems", KEK Report (in preparation).

Table 1. Source conditions

Energy (keV)	40	30	20
Linear polarisation P	0.856	0.840	0.828
Energy width $\Delta E/E$		10^{-3}	
Intensity ($\gamma/\text{sec}/\text{cm}^2$)		10^{11}	

Table 2. Thickness of the absorbing layer in measurements for element samples

Place	Kapton (g/cm^2)	Air (cm)
FAIC-VC	3.58×10^{-3}	8.7*
VC-Ge-1	3.58×10^{-3}	3.5
VC-Ge-2	3.58×10^{-3}	5.0

* Between the centre of FAIC and Kapton film.

Table 3. Thickness of the samples (in g/cm^2)

C	Cu	Pb
0.1325	1.79	0.568

Table 4. Absorbing layers of the Ge detector

	Be	Inactive Ge (μm)
GLP-16195/10	0.5	~ 0.3
GLP-16195/10P	0.127	~ 0.3

Figure 1. Experimental arrangement

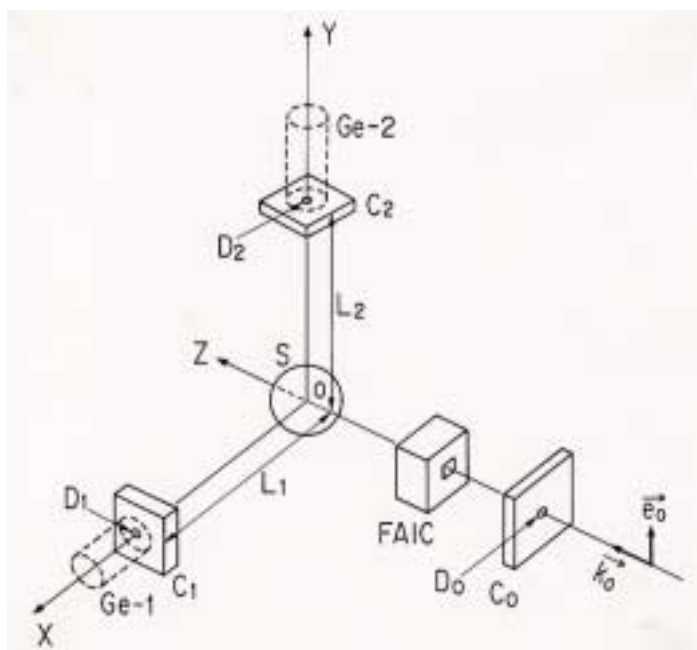


Figure 2. Photons from a C target

Incident energy, $k_0 = 40$ keV. "Default" means the EGS4 code without any low-energy photon-transport expansion. The calculated values are Gauss-smearred with $\sigma = 0.35$ keV.

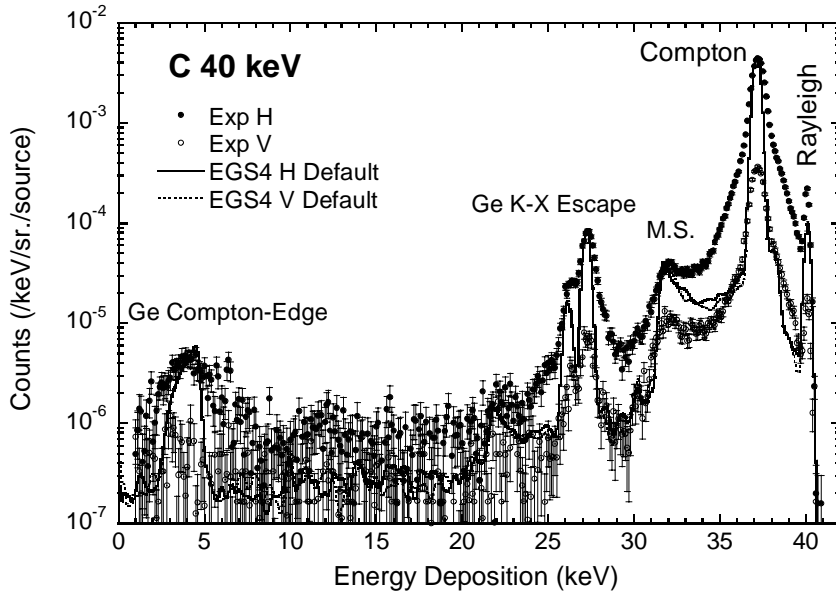


Figure 3. Photons from a C target

The incident energy, $k_0 = 40$ keV. LP + DB means that linearly polarised photon scattering and Doppler broadening were considered in the calculation. The calculated values are Gauss-smearred with $\sigma = 0.35$ keV.

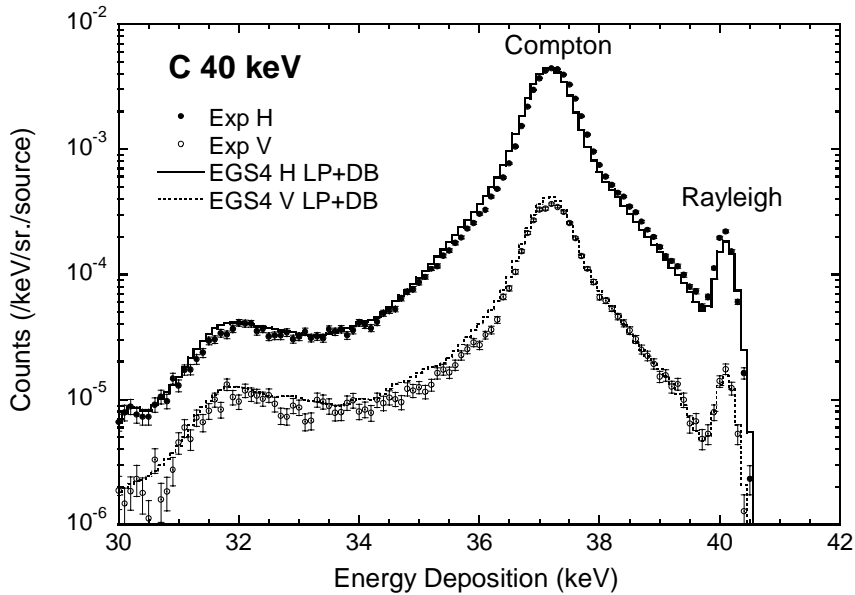


Figure 4. Photons from a Cu target

See caption of Figure 3 concerning the measurement and calculation conditions

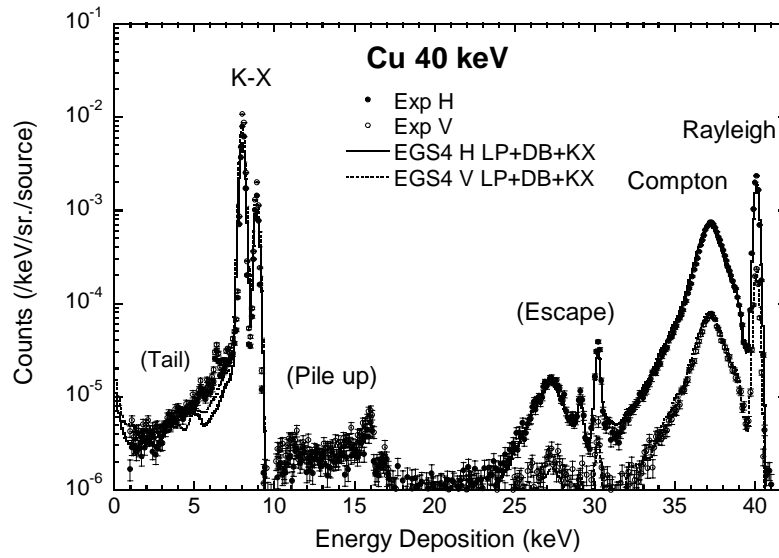


Figure 5. Photons from a Pb target. LX means that the L-X-ray was considered in the calculation.

See the caption of Figure 3 concerning the measurement and calculation condition

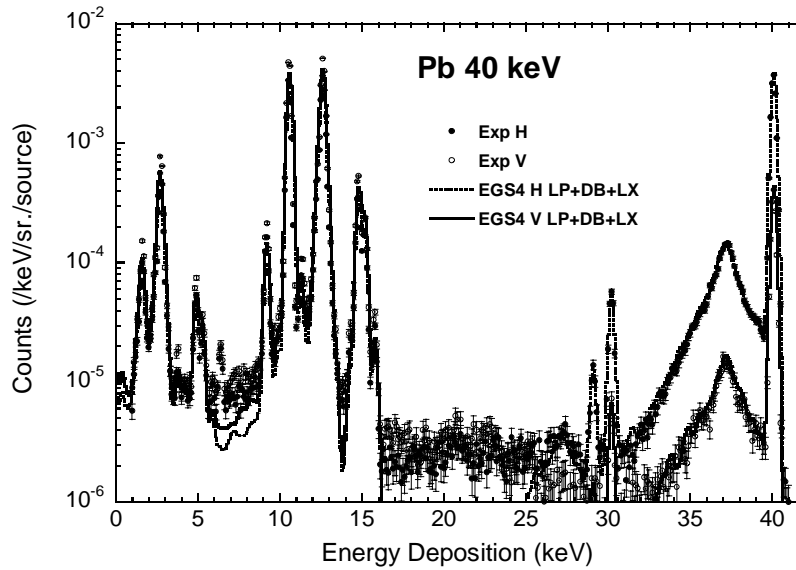


Figure 6. L-X photons from a Pb target

$k_0 = 40 \text{ keV}$. The calculated values are Gauss-smearred with $\sigma = 0.27 \text{ keV}$.

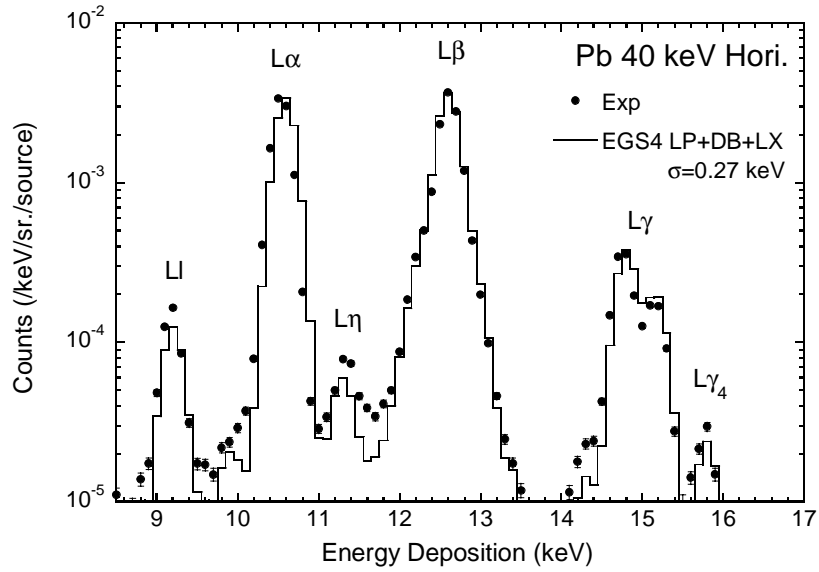


Figure 7. Ratio of the measured and computed intensity of Compton-scattered photons

H+V means that the sum of the horizontal and vertical components was compared

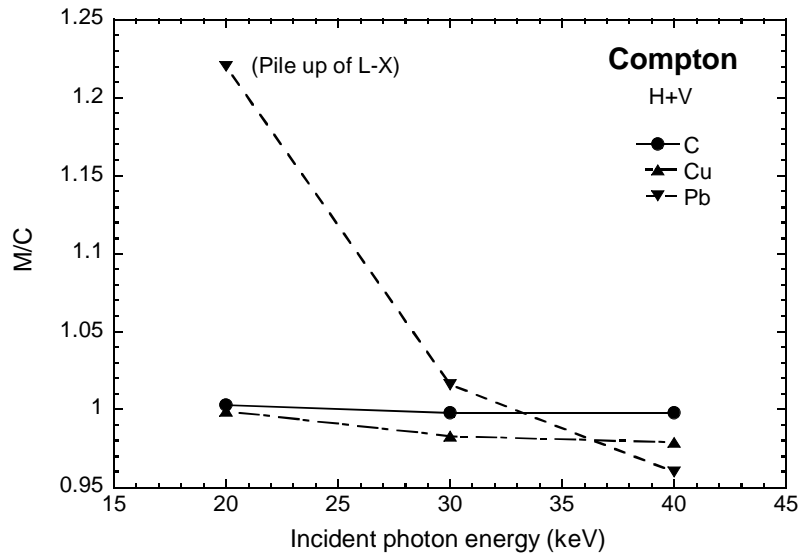


Figure 8. Ratio of the measured and computed intensity of the Rayleigh-scattered photons

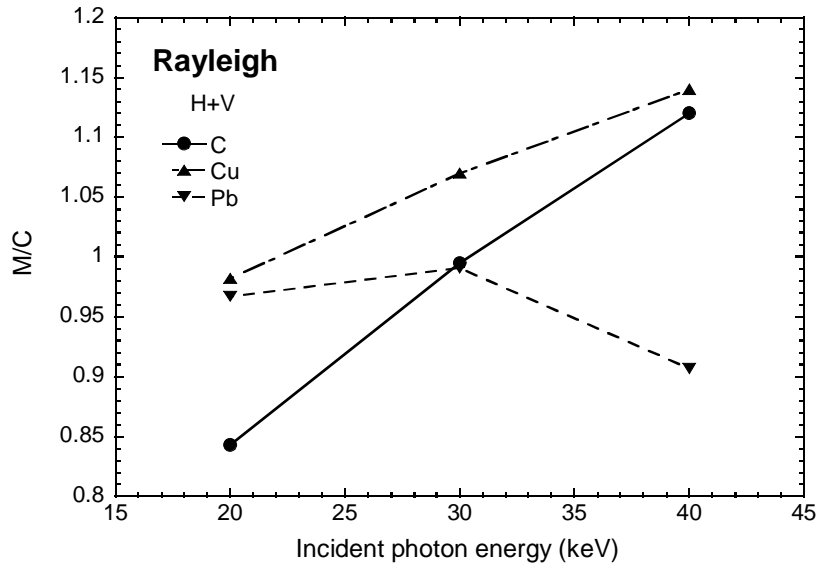


Figure 9. Ratio of the measured and computed intensity of L-X-rays

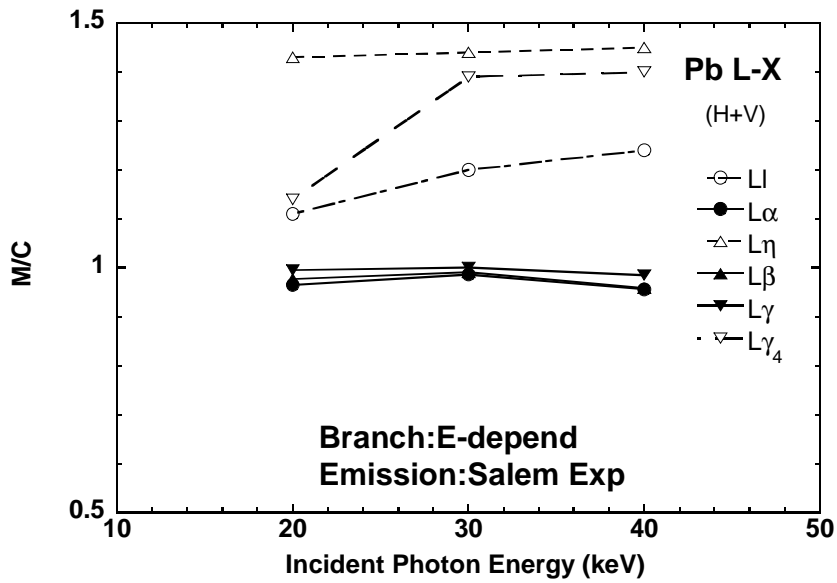
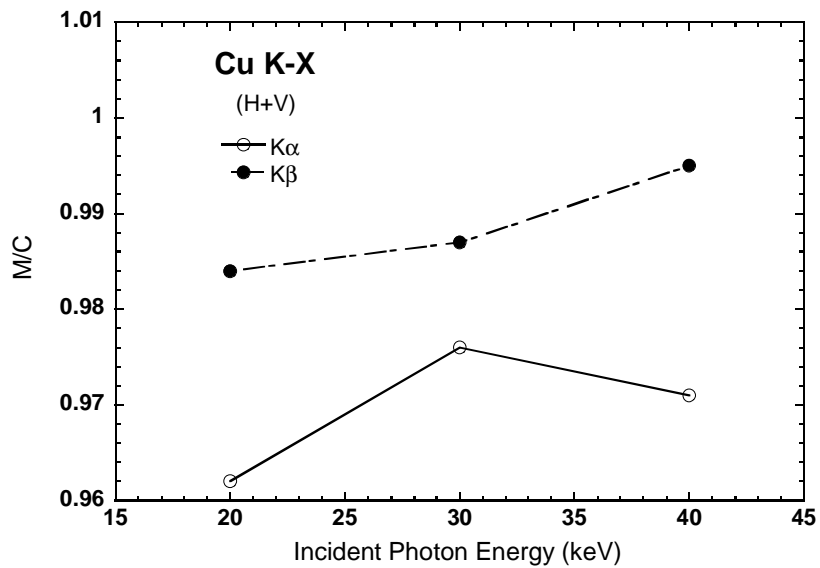


Figure 10. Ratio of the measured and computed intensity of the K-X-rays



*Photon-neutron
Production Benchmark*

BENCHMARKING OF THE SIMULATIONS OF THE ATLAS HALL BACKGROUND

Helmut Vincke, Edda Gschwendtner, C.W. Fabjan, Thomas Otto
CERN, Geneva

Abstract

The ATLAS [1] experiment has to be operated during 15 years in the presence of a mixed photon and neutron background [up to 10^4 particles/(cm²s)] in an energy range from thermal energies to several MeV. This background has been estimated through extensive evaluations with the Monte Carlo code FLUKA [2]. We present the simulation of the photon and neutron background in an experimental environment, which can be compared to the ATLAS shielding set-up. The aim is to benchmark FLUKA in order to reduce the existing uncertainties of the ATLAS background simulations. The paper explains how this experiment was modelled very accurately in the simulation. It describes the necessary steps for obtaining reliable results. Finally, the comparison with the measurements is discussed.

Introduction

In 2005, the Large Hadron Collider (LHC) will be operational at CERN as a new instrument for discovery in particle physics. The LHC will be a p-p collider with a centre of mass energy of 14 TeV. At a luminosity of $10^{34} \text{ cm}^{-2} \text{ s}^{-1}$ beam crossing points will provide experiments with collision rates at the 10^9 Hz level, producing 10^{11} particles per second. Due to the high rate of p-p collisions the level of the background is so high that it becomes a major design criterion for ATLAS.

Background in the ATLAS environment

The background emanating from the calorimeter and the shielding material is one of the main constraints of the muon spectrometer instrumentation layout and operation. It influences parameters such as the rate capability of the muon trigger detectors, radiation damage of detector components, the pattern recognition efficiency and the momentum resolution. Two main classes of background hits can be distinguished. First there are primary collision products such as hadronic debris of calorimeter showers. Second we find low energetic neutrons, originating from primary hadrons interacting with the forward calorimeter, the shielding, the beam pipe and other machine elements. These low energetic neutrons escape from the absorber and create via nuclear processes low-energy photons. The consequence of this reaction cycle is that a kind of “radiation gas” consisting of low-energy photons and neutrons surrounds the outer parts of the ATLAS detector (muon chambers). At rapidity $\eta = 2$ ($\theta = 15^\circ$) in the area of the muon chambers the photon background produces count rates of about 100 Hz/cm^2 , whereas the muon rate is only 10^{-3} Hz/cm^2 .

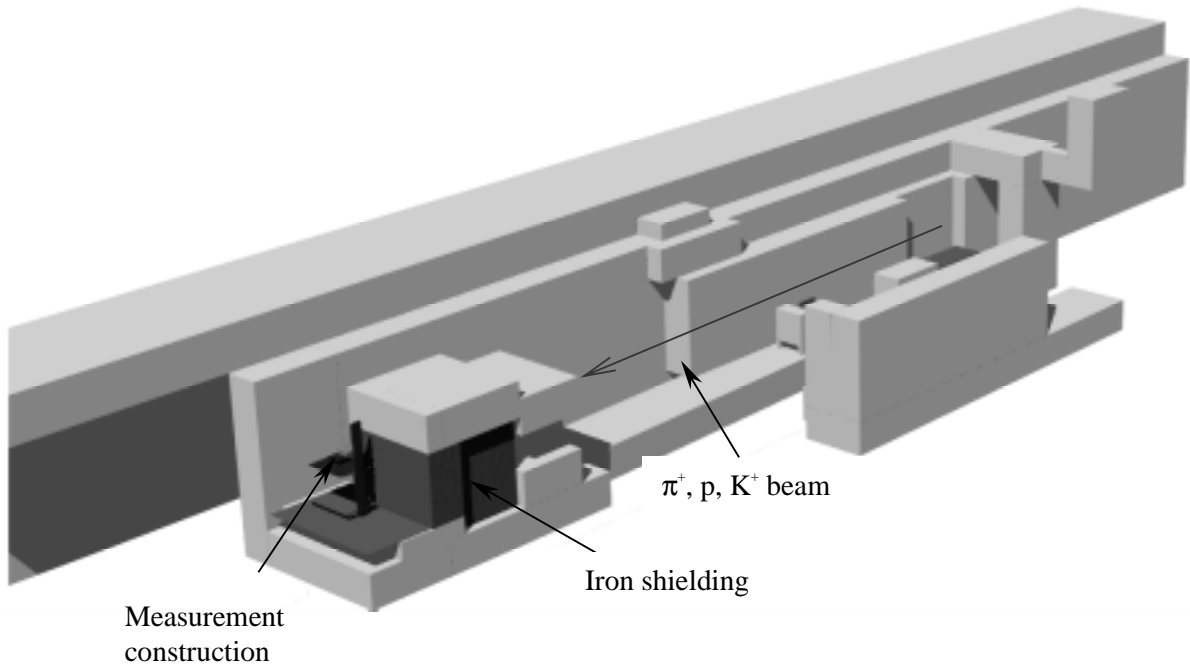
The ATLAS background calculations, performed with FLUKA, were multiplied with a safety factor of five in order to cover all possible simulation uncertainties. These uncertainties are a combination of limited knowledge concerning the p-p cross-sections at 14 TeV, MDT detector efficiency and an existing uncertainty concerning the shower calculations. In order to reduce the uncertainty contribution of the simulated shower processes, benchmarking simulations were performed with the corresponding measurements.

Benchmarking simulations

General description of the simulated measurement set-up

We simulated an experimental set-up, which should be comparable to the ATLAS environment, including its background. For the implementation of this aim the following experimental construction was chosen: a cast iron wall with a thickness of 200 cm (11λ) and 240 cm (14λ), respectively, was irradiated by a mixed positive charged hadron beam (π^+ , protons, K^+) with a momentum of 40 and 120 GeV/c. The iron represents the material of the forward ATLAS calorimeter. The beam energies are close although higher to the typical secondary particle energies in the forward region of ATLAS. Behind this cast iron wall a measurement set-up, including a cylindrical BGO scintillator, was installed. The dimensions of the BGO crystal were 1.5 inches in height and diameter. Two positions for the BGO were chosen. The first position was between 6 and 10 cm (BGO crystal position) off beam axis and is called in this paper “mid position”. The second measurement position, called “side position” is located between 56 and 60 cm off beam axis. The measurements were performed in the H6 area at CERN. The simulated set-up (240 cm cast iron wall) can be found in Figure 1.

Figure 1. Simulated set-up for the ATLAS background benchmarking (240 cm cast iron, BGO at side position) created using FLUKACAD [3] and AutoCAD. The outer shielding of the H6 area was partly removed to show the internal structure of the experimental set-up.



The simulations of counting rates in the BGO were generally performed in three steps:

- 1) Simulation of the shower processes induced by the primary beam particles. Information about particles hitting the BGO is written to a file. This file contains details concerning position, flight direction, energy, statistical weight and information concerning the origin of the single particles.
- 2) The stored particles are shot during a second run to the BGO in order to simulate the energy deposition induced in the BGO crystal.
- 3) The obtained BGO energy deposition spectrum is converted into a real BGO spectrum in order to compare it with the BGO measurement result.

Simulation of the shower processes induced by the primary beam particles

Simulations with the BGO at mid positions

In order to receive the particles entering the BGO one has to distinguish between measurement locations of the BGO in mid position and in side position. In the mid position only analogue runs can be performed. The reason for this is as follows: very close to the beam axis late hadronic shower processes occur, which produce – among other particles – π^0 . These π^0 decay almost at the position of their production into two high energetic γ , which induce an electromagnetic shower in the absorber. Many low-energy γ , electrons and positrons can be found at later stages of this EM shower. In case such a π^0 production happens close to the BGO, the crystal can be hit by many particles at the same time. To calculate the following energy deposition in the crystal correctly, all shower particles originating from the same primary beam particle hitting the BGO have to be simulated together in one

stage. That means that all particles of the same shower can induce at most one count. In a biased run the correlation between the primary beam particles and the shower particles entering the crystal is lost. Therefore a biased simulation for this kind of situation would lead to incorrect results. Only if almost no “multi-events” occur, a biased execution of the first run is acceptable. In Figure 2 an electromagnetic shower induced by a hadronic interaction with following π^0 decay in mid position is shown. This picture shows an event consisting of more than one particle, hitting the BGO crystal (highlighted cylinder).

Figure 2. Electromagnetic shower induced by a hadronic interaction with subsequent π^0 decays. The first 20 cm of the inner part of the iron wall is removed in order to show the beginning of the shower. This and all following geometry pictures were created using FLUKACAD [3], PIPSICAD [3] and AutoCAD.



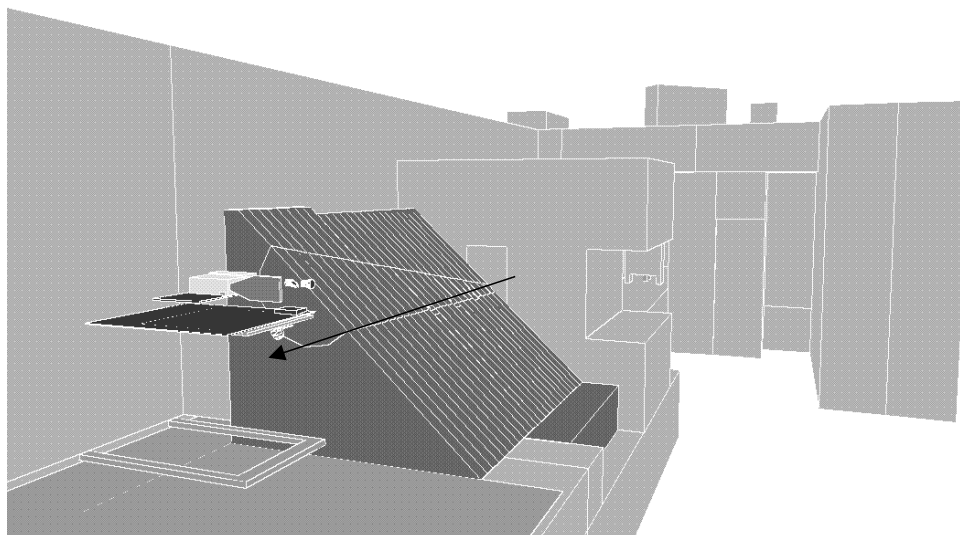
Simulations with the BGO at side positions

To receive BGO counting rates, analogue runs were also performed for the side positions. The number of particles hitting the BGO crystal, however, is far too small to obtain an energy dependent rate spectrum. Therefore, runs including sophisticated biasing techniques were performed. This procedure is justified at side positions, because at these locations the amount of multi-events can be neglected. Therefore the particles, including all necessary information, are stored on a file and will be treated in the second run according to their statistical weight. The biasing areas in the iron absorber are shown in Figure 3. In order to show the different biasing regions, a cut through the absorber was performed in this picture. To increase the amount of particles reaching the BGO, a cone inside the absorber, containing regions with higher biasing importance, was installed. The small end of this cone is hit by the beam. To bias the particle shower in the direction of the BGO, the large end of the cone is shifted in the direction of the measurement construction. Furthermore a general increase of the biasing importance with increasing absorber width, starting at beam entry position was performed. To prevent weight fluctuations of the particles entering the BGO detector, “weight windows” were installed at the necessary positions.

Simulation of energy deposition in the BGO crystal

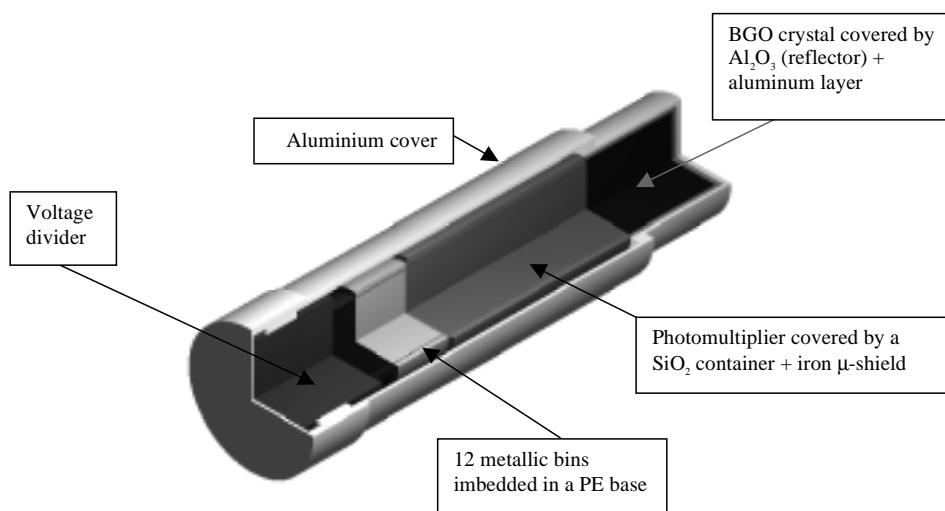
The particles stored during the first run are loaded as primary particles in the second run. In this run energy depositions induced by each primary beam particle are simulated via using the FLUKA input card “DETECT”. The result of this procedure is an energy dependent spectrum of counts

Figure 3. Cut through the cast iron block in order to show the biasing situation at side positions. The arrow shows the direction of the beam. Regions inside the cone have increased biasing importance. Parts of the construction, which would hide the view into the direction of the BGO, were removed in this picture.



induced in the BGO (1 024 energy dependent channels). The calculated spectrum would be comparable to a real measurement taken with a BGO with infinite energy resolution. A cross-section through the simulated BGO is shown in Figure 4. The shower induced by a beam particle (already calculated in the first run) cannot produce more than one count. To take this into consideration one has to distinguish between a particle file, which was produced by an analogue first run and a particle file, which was produced via a biased first run. In case of an analogue first run, particles originating from the same primary particle have to be loaded together on the stack. This procedure guarantees that each primary beam particle cannot produce more than one entry in the histogram.

Figure 4. Cross-section through the simulated BGO scintillator (crystal dimension: 1.5 inches in height and diameter)

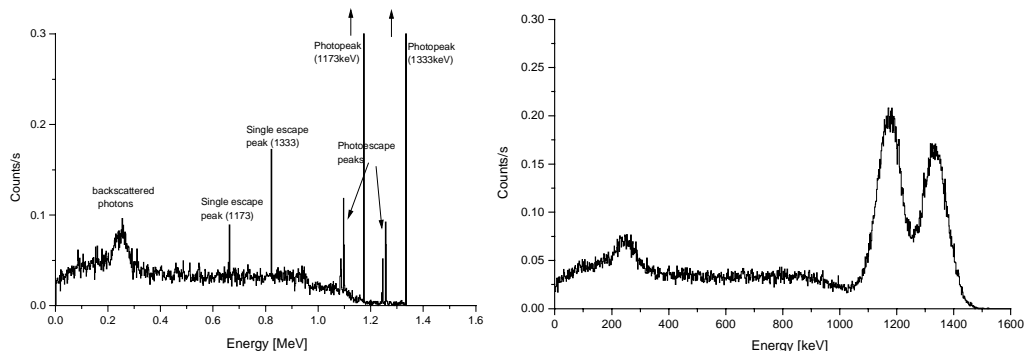


In case of a biased first run (no multi-events are expected) the particles have to be treated in the following way. The fact that each stored particle has different statistical weight has to be taken into account for the second run. A particle with a certain statistical weight has to be converted into a proper number of particles with a weight of 1.0 in order to perform the second run in a fully analogue mode. After the simulation of the energy deposition of each particle, the result (number of induced counts) has to be adapted to the number of primary beam particles and the factor induced by the particle weight conversion. In order to get the number of counts per primary beam particle one has to divide the result of Run 2 by the number of primary particles times the multiplication factor induced by the weight adaptation. To clarify this procedure we discuss the following example. In the first run, the shower of three beam particles was calculated in biased mode. As result of this run a particle file is produced, which contains ten shower particles hitting the BGO. Four of them are calculated to have a statistical weight of 0.30, whereas the remaining six particles have a weight of 0.75. In the energy deposition run all particles with a weight of 0.3 are processed three times (weight multiplication with 10) and each particle of the second kind is processed seven times. For all particles of the second kind a statistical weight of 0.05 is still left and also has to be taken into consideration. The remaining weight of 0.05 of these particles gives another six particles of the second kind a 50% chance to be started. The energy deposition run has to be done in a fully analogue way (FLUKA card "DETECT" is used); therefore all particles are given the weight 1.0. To obtain the entries in the histogram normalised to the number of beam particles (three), the result has to be divided by 30 [= 3 · 10 (weight multiplication factor)].

Convoluting the BGO energy deposition spectrum with the BGO resolution function

The received energy deposition spectrum of the BGO corresponds to a measured spectrum with infinite energy resolution. To adapt the result to the real BGO, including electronic instrumentation, a proper convolution of the single energy dependent entries has to be done. A simple example can be found in Figure 5, where the BGO is irradiated by an ^{60}Co source.

Figure 5. BGO energy deposition spectrum induced by a Co source before (left) and after conversion (right). Entries in 1 024 channels (1.76 keV width) were convoluted with the proper resolution.



Procedure of conversion

In a real BGO detector a specified energy deposition induced by a particle with a certain energy will be measured with a detector dependent energy resolution. The measured spectrum around an obtained mean value shows a Poisson distribution. The reason for this behaviour can be found in detector dependent fluctuations concerning the measurement procedure of energy depositions. The standard

variation of the measured spectrum, induced by an energy deposition, is energy dependent and can be elicited via a measurement of one mono-energetic source. To adapt the calculated energy deposition to the real spectrum, a calibration measurement with a ^{137}Cs source was performed. The measured energy, including the spectrum resolution concerning the BGO used, is shown in Table1:

Table1. Parameters of the measured BGO spectrum received by using a ^{137}Cs source

Energy	σ around energy mean value
662 keV	36.15 keV

In order to receive the energy resolution for all energies, this measurement result has to be extrapolated via the following procedure. The Poisson statistic applies the well known counting behaviour for the detector:

$$\sqrt{\text{counts}} = \sigma$$

where *counts* means the number of counted scintillation events produced during the measurement of one energy deposition. The mean value of these counts complies a certain energy deposition. With a knowledge of the amount of the energy deposition (662 keV) plus the measured standard variation (36.15 keV) and the fact that this counting procedure follows the Poisson statistic, the average minimal energy unit (E_{min}) to produce countable scintillation events can be calculated.

$$\sqrt{\frac{\overline{E}}{E_{min}}} = \frac{\sigma(E)}{E_{min}}$$

where $\sigma(E)$ is the standard variation in energy units and E is the amount of energy deposition.

The average minimal energy unit of the detection process in the BGO is therefore 1.974 keV. With this information one can calculate the σ for each energy via the following equation:

$$\sigma(E) = \sqrt{E_{min}} \cdot \sqrt{\overline{E}} = 1.405 \cdot \sqrt{E(\text{keV})}$$

For example, a ^{137}Cs photon (= 662 keV) produces in average 335.35 scintillation processes, which are detected by the electronics in the BGO. The appropriate counting σ of this energy is 18.3, which corresponds to an energy of 36.15 keV (= 18.3 · 1.974 keV).

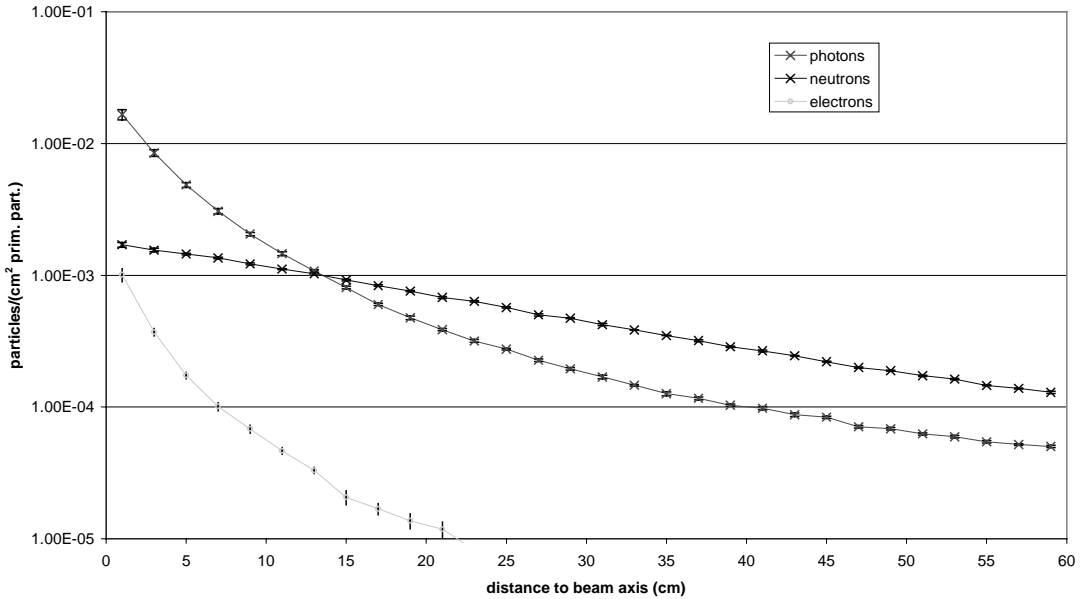
To convert the energy deposition spectrum into a real BGO spectrum the mean energy of each channel and the proper sigma is calculated. The events which are stored in each channel will be Gaussian smeared with the proper sigma around the actual channel. Therefore the sharp energy deposition peaks get a real detector dependent shape.

Results

Fluences behind the shielding

The different particle fluences behind the 200 cm cast iron absorber, induced by a 40 GeV/c mixed hadron beam, can be found in Figure 6. Close to the beam axis the photon fluence is much stronger than the neutron fluence. On the other hand the neutron fluence decreases more slowly with

Figure 6. Fluences behind a 200 cm thick cast iron absorber induced by an hadronic beam with an energy of 40 GeV/c



increasing distance to the beam axis. This behaviour of the fluences can be explained as follows. Close to the beam axis high-energy particle collisions occur. In these interactions π^0 are produced, which decay into two γ . These two γ are the beginning of an electromagnetic shower. Because of the lack of high-energetic particles in outer regions, the π^0 production fades with further distance to the hadronic collision centre (beam axis). Neutrons are also mainly produced close to the beam axis. But the survival probability of a particle which undergoes a collision with an iron or carbon atom is much higher in the case of a neutron than in the case of a photon. The neutrons in the simulations were calculated down to thermal energies and the threshold for the photons was set to 100 keV.

Characterisation of events hitting the BGO

In Figure 7 two different event scenarios are shown. The one, concerning the mid position, shows a high multi-event rate. This means that mostly more than one particle, originating from the same primary particle, hit the BGO together. The average number of particles entering the BGO per event in mid position is 2.6. The situation at the side position is completely different. Due to the lack of high-energetic collisions followed by π^0 decays close to the BGO position, mainly single particle events occur. The average number of particles entering the BGO per event in this situation is 1.05. This fact and the low reaction probability between the entering particles and the BGO crystal ($\gamma \sim 40\%$, $n \sim 10\%$) justifies a biased shower calculations at the side position.

Hadronic origin of particles entering the BGO

In Table 2 the situations concerning the origin of the photons entering the BGO are shown. The first column describes the situation behind the cast iron wall of 2 m, which is irradiated by a 40 GeV/c hadron beam. The BGO is located in mid position. Eighty per cent of all photons entering the BGO originate from π^0 decays. The remaining 20% are produced via (n,γ) reactions or other inelastic

Figure 7. Classification of the events hitting the BGO behind the 200 cm cast iron absorber in mid (left) and side (right) position. The momentum of the beam particles is 40 GeV/c.

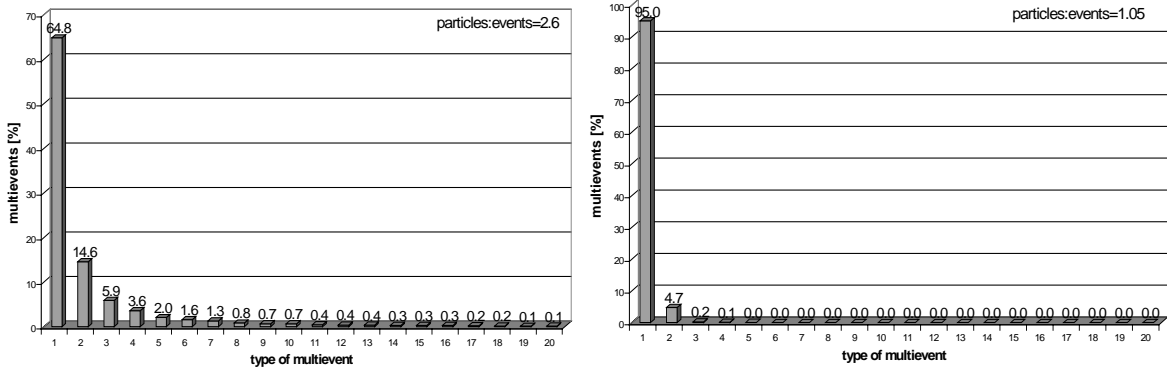


Table 2. Hadronic origin of photons entering the BGO behind the 200 cm cast iron absorber in mid and side position. The momentum of the beam particles is 40 GeV/c.

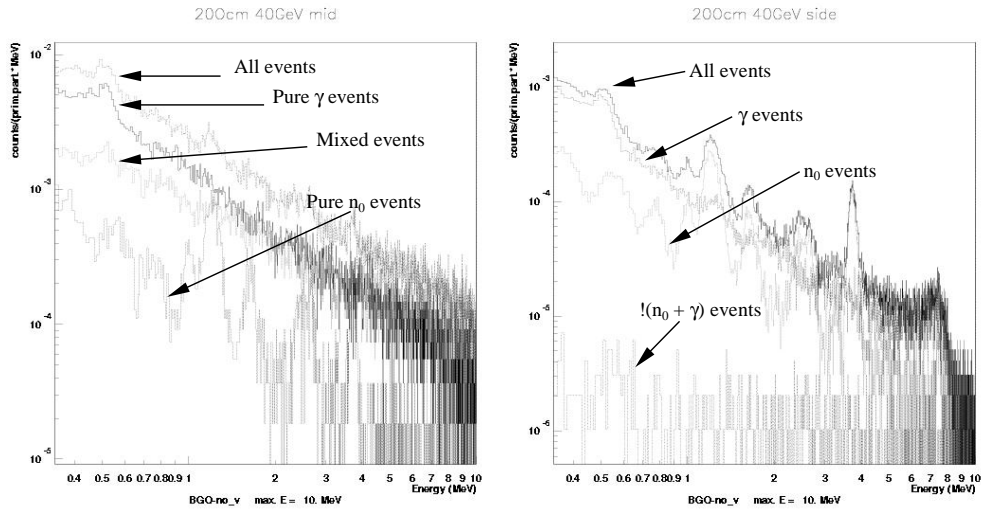
Particle type of mother particles	Mid position [%]	Side position [%]
Proton	0.6	0.6
Neutron	10.7	67.6
Positive pion	4.5	1.8
Negative pion	3.4	1.7
Positive kaon	0.3	0.1
Neutral pion	77.9	26.5
Others	2.6	1.7

hadronic interactions. The situation at the side position is different. Only 26% of the γ has a π^0 decay origin. In comparison to the mid position the π^0 interaction centre is so far away that in most cases only one γ produced by this electromagnetic shower reaches the BGO. The main portion of the photons originates from (n,γ) or (n,n',γ) reactions. The situation concerning the hadronic origin of the neutrons is similar in both cases. Neutrons behind the iron absorber are mainly produced by other neutrons.

Induced spectra in the BGO

The energy dependent spectra and the counting rate for the different scenarios can be obtained via the procedure explained in a previous section. Figure 8 shows the simulated BGO spectra in the mid and side position behind a 200 cm cast iron wall, which is irradiated by an 40 GeV/c hadron beam. In the mid position (left) the counting rate spectrum is divided into three main parts. These are counts induced by pure γ multi-events, pure neutron multi-events and mixed multi-events. The strongest influence on the counting rate is caused by the pure γ multi-events followed by mixed events. In mixed events, photons are very often accompanied by neutrons. The fact that the neutrons only have a 10% chance to interact in the BGO implies that the counts induced by mixed multi-events are dominated by photon interactions. Also, the shape of the mixed event spectrum is very similar to the pure photon spectrum. The influence of pure neutron events on the counting rate in this position is less than 10%. To obtain the shown spectrum at the side position the biased method, explained in a previous section, was used. In addition, the counts in this situation are mainly affected by γ events. But the influence of

Figure 8. Counting spectra induced in the BGO at mid (left) and side (right) position behind a 2 m cast iron absorber, which is irradiated by a 40 GeV/c hadron beam. The spectra are divided into their single components.



neutrons at this location is much stronger than in the mid position. Around 30% of the counts are caused by pure neutron events. The influence of the mixed events is inferior in this position, and is not shown in this picture (biased calculations do not produce multi-events). In both pictures the neutron induced counts add strong peaks to the whole spectrum. The main reason for this fact is that FLUKA uses cross-sections which provide a correct neutron induced energy deposition only in an average way over a high number of neutrons. These peaks show average energy deposition values, which are stored in the used cross-section. In the simulation a down-scattered neutron, starting from a given energy group, always induces a fixed average energy deposition. This amount of energy is an average value over all possible energy depositions, caused by neutrons of this energy group. However there is no distortion of the total counting rate induced by this procedure.

Comparison between measurements and simulations

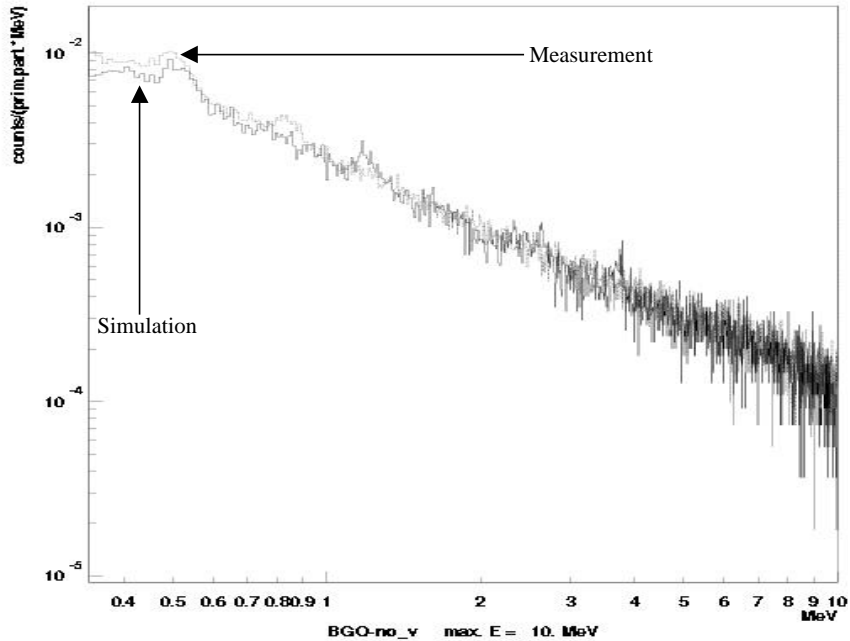
The rate comparison (0.35-9 MeV) between measurements and simulations can be found in Table 3. The results mostly agree within 20%. All rate simulations were performed in analogue mode. The shown simulation errors cover the statistical uncertainties of the calculations.

Table 3. Rate comparison between measurements and simulations

	Simulated rate per beam particle	Measured rate per beam particle
40 GeV/c		
200 cm mid	$(7.18 \pm 0.11) \cdot 10^{-3}$	$(7.66 \pm 0.23) \cdot 10^{-3}$
200 cm side	$(6.05 \pm 0.28) \cdot 10^{-4}$	$(7.02 \pm 0.25) \cdot 10^{-4}$
240 cm mid	$(1.58 \pm 0.05) \cdot 10^{-3}$	$(2.32 \pm 0.08) \cdot 10^{-3}$
240 cm side	$(1.86 \pm 0.15) \cdot 10^{-4}$	$(2.36 \pm 0.11) \cdot 10^{-4}$
120 GeV/c		
200 cm side	$(2.60 \pm 0.14) \cdot 10^{-3}$	$(2.66 \pm 0.12) \cdot 10^{-3}$
240 cm mid	$(7.68 \pm 0.22) \cdot 10^{-3}$	$(9.36 \pm 0.38) \cdot 10^{-3}$
240 cm side	$(7.87 \pm 0.87) \cdot 10^{-4}$	$(10.5 \pm 0.37) \cdot 10^{-4}$

In Figure 9 the simulated and measured spectrum comparison concerning the BGO counting rate observed in the mid position behind the 200 cm absorber, irradiated by 40 GeV/c hadron beam, are shown. In this position the influence of the neutrons is very weak. Therefore no distortion of the spectrum due to the neutron peaks is visible.

Figure 9. Comparison between measurement and simulation spectrum behind the 200 cm iron absorber, irradiated by a 40 GeV/c hadron beam. The BGO was located in mid position.



Conclusion

In order to verify the FLUKA predictions of the ATLAS hall background, benchmarking simulations concerning an ATLAS equivalent environment were performed. These simulations were compared with corresponding measurements performed in the H6 area at CERN. We found that the simulations agree with the measurements mostly within 25%. Therefore a decrease of the safety factor concerning the ATLAS background situation is justified. Further investigations will show to which value this factor will be lowered.

Acknowledgements

We would like to thank Heinz Vincke, Stefan Roesler and Alfredo Ferrari for many helpful discussions concerning simulation problems. Furthermore we are very grateful to Alfredo Ferrari and Paola Sala for providing the FLUKA code.

REFERENCES

- [1] “ATLAS, A General Purpose Experiment at LHC: ATLAS Technical Proposal”, CERN/LHCC/94-43, LHCC/P2 (1994).
- [2] A. Fassò, A. Ferrari, J. Ranft and P.R. Sala, “New Developments in FLUKA Modelling of Hadronic and EM Interactions”, in Proc. of SARE-3, KEK, Japan (1997).
- [3] H. Vincke, “FLUKACAD/PIPSICAD: A Three-dimensional Interface between FLUKA and AutoCAD”, these proceedings.

SESSION V

Dosimetry and Dose Calculations

Chairs: M. Pelliccioni, V. Batyaev

Dose Conversion Coefficients for “High-energy” Radiations

**FLUENCE-TO-EFFECTIVE DOSE CONVERSION COEFFICIENTS
FOR HIGH-ENERGY RADIATIONS CALCULATED WITH MCNPX**

Michele R. Sutton and Nolan E. Hertel
Georgia Institute of Technology

Laurie S. Waters
Los Alamos National Laboratory

Abstract

Fluence-to-dose conversion coefficients for the currently recommended protection quantity, effective dose, have been calculated with MCNPX for mono-energetic neutrons and photons with energies up to 2 GeV. The calculations were performed for four different geometrical irradiation conditions (anterior-posterior, posterior-anterior, left lateral and right lateral) and compared with recently published data sets by other authors.

Introduction

In practice, the radiation protection quantities are obtained from the energy-dependent fluence rate by folding it with fluence-to-dose conversion coefficients. Dose conversion coefficients form the basis for shielding analyses and occupational dose estimates during facility design. Due to the limited dosimetric information available for high-energy radiations, the ability to calculate the recommended protection quantities has been questioned. The need for additional conversion coefficient computations has been expressed by the ICRP and the high-energy accelerator community [1-3]. This need is becoming more apparent as projects such as human exploration of deep space and the Spallation Neutron Source (SNS) project become more developed.

Effective dose

Effective dose is a protection quantity defined by the ICRP as the sum of the weighted equivalent doses in all the tissues and organs of the body and is given by the expression:

$$E = \sum_T w_T \cdot H_T \quad (1)$$

where H_T is the equivalent dose in tissue or organ T and w_T is the weighting factor for tissue T . The human body as defined by the ICRP consists of 12 designated tissues and organs, and a remainder, which consists of nine additional organs. The recommended tissue weighting factors for these tissues and organs are shown in Table 1 [4].

Table 1. ICRP 60 tissue weighting factors

Tissue or organ	Tissue weighting factor, w_T
Gonads	0.20
Bone marrow (red)	0.12
Colon	0.12
Lung	0.12
Stomach	0.12
Bladder	0.05
Breast	0.05
Liver	0.05
Oesophagus	0.05
Thyroid	0.05
Skin	0.01
Bone surface	0.01
Remainder	0.05

The organ equivalent dose, H_T , is the absorbed dose in an organ or tissue multiplied by the relevant radiation-weighting factor. It is given by the expression:

$$H_{T,R} = w_R \cdot D_{T,R} \quad (2)$$

where w_R is the radiation weighting factor for radiation, R , and $D_{T,R}$ is the absorbed dose averaged over the tissue or organ, T , due to radiation R . (In the case of multiple radiation types, the absorbed dose would be subdivided by radiation type, each multiplied by its own radiation weighting factor and summed over all radiations.) The radiation-weighting factor is determined by the radiation type,

intensity and energy distribution incident on the body and is applied to the mean absorbed dose in the organ or tissue of interest. ICRP provides a continuous function as an approximation for its recommended set of neutron radiation weighting factors. It is:

$$w_R = 5 + 17 \exp \left[\frac{-(\ln(2E_n))^2}{6} \right] \quad (3)$$

where E_n is the neutron energy in MeV. The weighting factor for photons is unity [4].

Effective dose calculations

Effective dose conversion coefficients are calculated using anthropomorphic phantoms with the specified ICRP organs and tissues. The phantoms used in this work were the Pacific Northwest National Laboratory MIRD-based (Medical Internal Radiation Dose Committee) sex-specific phantoms.

The energy deposition tally was used in MCNPX [5] to calculate the absorbed dose in each organ for both the male and female phantom. The absorbed dose was multiplied by the radiation-weighting factor determined by Eq. 3 for neutrons and unity for photons to give the equivalent dose for each organ. The remainder dose incorporated footnote 3 of Table 2 in ICRP Publication 60.

Since tissue and organ dose data was calculated for both a male and female phantom the effective dose was determined using the following formula given in ICRP Publication 74:

$$E = w_{breast} H_{breast, female} + \sum_{T \neq breast} w_T \left[\frac{H_{T, male} + H_{T, female}}{2} \right] \quad (4)$$

where w_T represents the appropriate tissue-weighting factor shown in Table 1 [3].

The effective dose calculations were then divided by the total fluence in order to obtain the fluence-to-effective dose conversion coefficients. These calculations were performed for four irradiation geometries (AP, PA, LLAT and RLAT) for both neutrons and photons.

The neutron conversion coefficients were calculated using a version of the LA150N neutron cross-section library that is corrected for the “double counting” problem seen in the preliminary version and a “cross-over” energy of 150 MeV. The “cross-over” energy is the energy at which MCNPX switches from using the physical models of LAHET to the evaluated data in the nuclear data tables to transport neutrons [6]. Photon organ doses were calculated with and without electron transport.

Results and discussion

The neutron results for the four irradiation geometries are shown in Figure 1. The results of the neutron calculations have been compared with the limited number of published data sets by other authors [7,8]. A comparison for AP irradiation geometry is shown in Figure 2. The agreement with the published data is satisfactory up to 500 MeV. Above 500 MeV, the comparison with the data set published by Ferrari, Pelliccioni and Pillon shows some disagreement. The source of this disagreement is unknown and has been attributed to the differences in the transport codes. A comparison of the other irradiation geometries shows similar agreement. The organ and effective doses for each irradiation geometry are shown in Tables 2-5.

Figure 1. Neutron fluence-to-effective dose conversion coefficients calculated with a “cross-over” energy of 150 MeV in MCNPX for AP, PA, LLAT and RLAT irradiation geometries

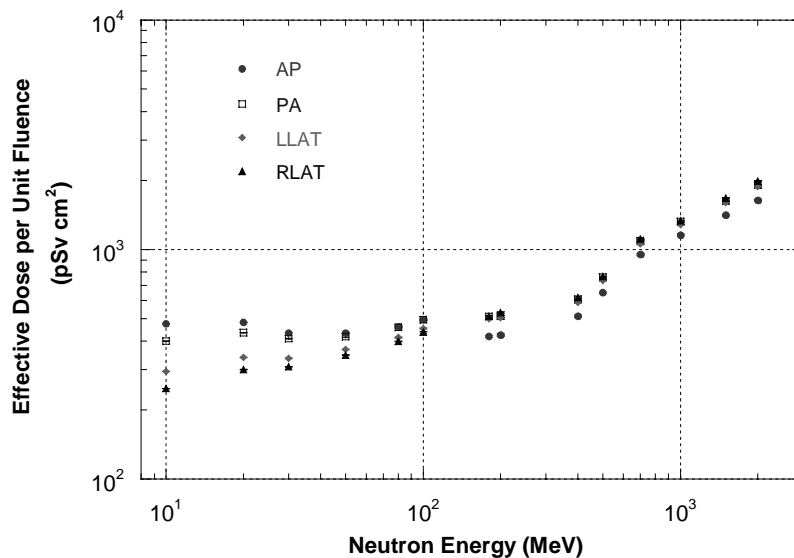
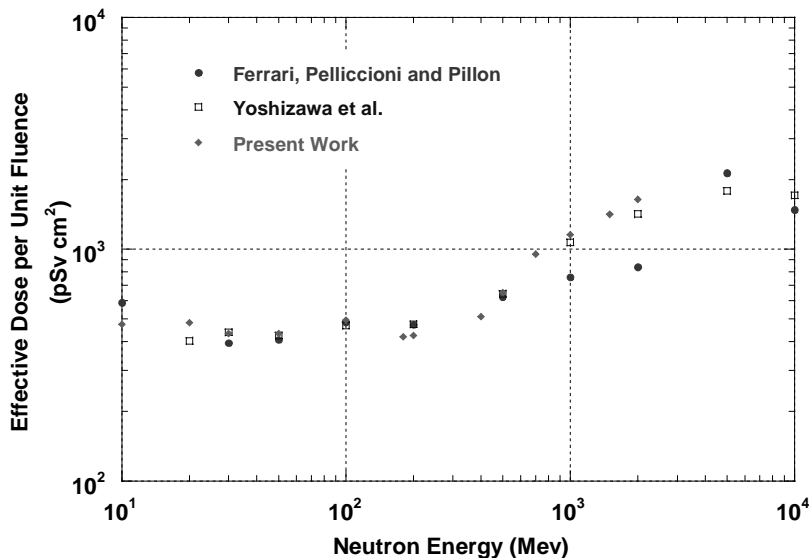


Figure 2. Comparison of neutron fluence-to-effective dose conversion coefficients for AP irradiation geometry with other authors [7,8]



The photon results for the four irradiation geometries are shown in Figure 3. The calculations of photon fluence-to-dose conversion coefficients were performed with and without electron transport. A comparison of the results with and without electron transport for AP irradiation is shown in Figure 4. As seen in Figure 4, electron transport is important for photon calculations above 10 MeV. The results of the photon calculations have been compared with the limited number of published data sets by other authors [9,10]. A comparison for AP irradiation geometry is shown in Figure 5. The agreement with the published data is good with the largest difference less than 20%. The organ and effective doses for each irradiation geometry are shown in Tables 6-9.

Figure 3. Photon fluence-to-effective dose conversion coefficients calculated with MCNPX for AP, PA, LLAT and RLAT irradiation geometries

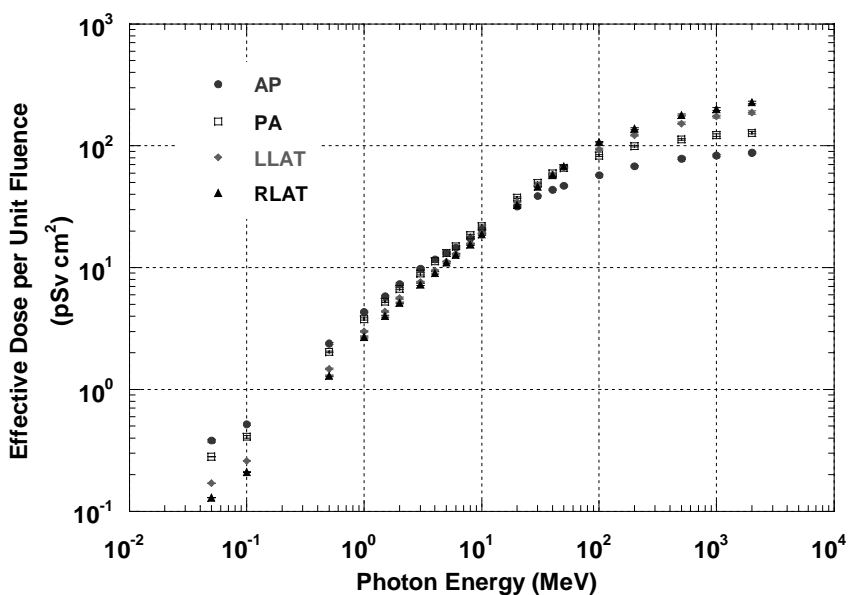


Figure 4. Comparison of photon fluence-to-effective dose conversion coefficients calculated with and without electron transport for AP irradiation

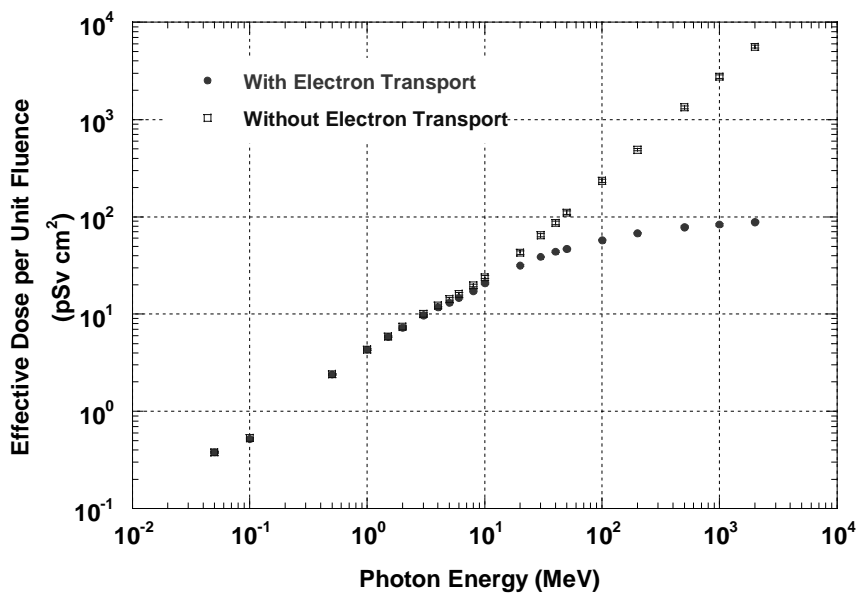
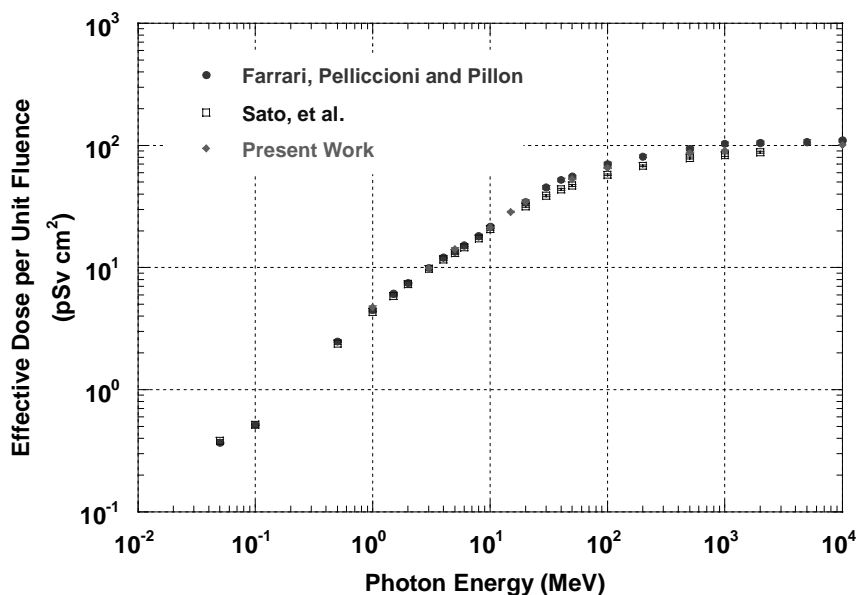


Figure 5. Comparison of photon fluence-to-effective dose conversion coefficients for AP irradiation geometry with other authors [9,10]



Summary

The conversion coefficients calculated with MCNPX are in reasonably good agreement with those calculated by other authors up to 2 GeV for neutrons and photons. Large differences between the neutron effective dose conversion coefficients at 1 GeV are observed between the present work and those of Ferrari, Pelliccioni and Pillon. The MCNPX results at these energies are in agreement with those of Yoshizawa, *et al.* This is not surprising since LAHET physics is used in MCNPX above 150 MeV, LAHET being a descendant of HETC. Such differences demonstrate the benefit of comparisons of high-energy codes being performed by the dosimetry workgroup at this meeting.

REFERENCES

- [1] International Commission on Radiation Protections, "Conversion Coefficients for Use in Radiological Protection Against External Radiation", ICRP Publication 74, 1997.
- [2] Simulation Accelerator Radiation Environments (SARE) IV, Knoxville, TN, 14-16 Sept. 1998.
- [3] The Ninth International Conference on Radiation Shielding (ICRS-9), Tsukuba, Ibaraki, Japan, 17-22 October 1999.
- [4] International Commission on Radiation Protections, "Recommendations of the ICRP", ICRP Publication 60, 1990.
- [5] H.G. Hughes, R.E. Prael, R.C. Little, "MCNPX – The LAHET/MCNP Code Merger", Los Alamos National Laboratory, XTM-RN (u) 97-012, 1997.
- [6] L.S. Waters, "MCNPX User's Manual", TPO-E83-G-UG-X-00001 Revision 0, Los Alamos National Laboratory, 1999.
- [7] A. Ferarri, M. Pelliccioni, M. Pillon, "Fluence to Effective Dose Conversion Coefficients for Neutrons Up to 10 TeV", *Rad. Prot. Dosim.*, 71, 165 (1997).
- [8] N. Yoshizawa, O. Sato, S. Takagi, S. Furihata, S. Iwai, T. Uehara, S. Tanaka, Y. Sakamoto, "External Radiation Conversion Coefficients Using Radiation Weighting Factor and Quality Factor for Neutron and Proton from 20 MeV to 10 GeV", *Nucl. Sci. Tech.*, 35, 928 (1998).
- [9] A. Ferarri, M. Pelliccioni, M. Pillon, "Fluence to Effective Dose Conversion Coefficients for Photons from 50 keV to 10 GeV", *Rad. Prot. Dosim.*, 67, 245 (1996).
- [10] O. Sato, S. Iwai, S. Tanaka, T. Uehara, Y. Sakamoto, N. Yoshizawa and S. Furihata, "Calculations of Equivalent Dose and Effective Dose Conversion Coefficients for Photons from 1 MeV to 10 GeV", *Rad. Prot. Dosim.*, 62, 119 (1995).

Table 2. Organ doses and effective dose per unit neutron fluence incident on an anthropomorphic phantom in AP geometry in pGy cm² and pSv cm² respectively. Neutron energy is in MeV.

	Energy	10.0	20.0	30.0	50.0	80.0	100.0	180.0
	Wr	8.81	6.76	6.04	5.50	5.23	5.16	5.05
Organ/Tissue	Wt							
Gonads	0.20	60.1	78.4	78.0	84.6	94.9	101.4	72.0
Red Bone Marrow	0.12	32.4	48.9	55.5	67.7	81.2	90.7	99.5
Colon	0.12	46.8	63.2	64.4	70.1	78.1	86.3	80.9
Lungs	0.12	54.2	71.9	72.4	79.2	89.5	96.9	86.5
Stomach	0.12	63.7	80.9	78.8	84.7	94.5	101.3	79.5
Bladder	0.05	63.1	81.0	78.4	84.1	92.8	100.1	83.7
Breast	0.05	63.2	78.8	74.9	79.8	83.5	87.2	53.5
Liver	0.05	57.1	75.7	75.8	82.5	92.6	99.9	91.1
Esophagus	0.05	42.9	62.8	68.2	76.1	87.1	100.0	114.7
Thyroid	0.05	64.8	80.7	76.9	81.1	85.8	89.9	56.6
Skin	0.01	51.3	68.8	67.9	71.8	75.5	79.8	65.6
Bone	0.01	37.3	53.4	58.2	69.4	82.3	90.9	87.9
Remainders	0.05							
Adrenals		33.4	54.8	63.8	69.0	84.1	96.9	116.7
Brain		45.3	63.1	65.2	75.0	87.0	94.6	88.7
Small Intestines		55.1	74.9	76.2	82.6	93.3	100.3	98.9
Kidneys		35.9	57.1	65.0	75.6	89.1	98.9	122.3
Muscle		52.2	71.0	72.2	79.8	89.3	96.1	91.3
Pancreas		52.6	73.2	74.8	82.6	93.7	100.2	107.9
Spleen		44.9	65.4	69.3	77.4	89.1	99.6	112.5
Thymus		65.9	82.7	77.2	88.9	96.8	105.3	70.3
Uterus		60.4	77.7	75.1	80.5	86.0	93.8	73.8
Effective Dose		475.1 +/- 0.2%	482.5 +/- 0.2%	432.8 +/- 0.5%	433.8 +/- 0.7%	462.8 +/- 0.8%	495.0 +/- 0.9%	418.7 +/- 1.1%

	Energy	200.0	400.0	500.0	700.0	1000.0	1500.0	2000.0
	Wr	5.04	5.01	5.01	5.00	5.00	5.00	5.00
Organ/Tissue	Wt							
Gonads	0.2	77.6	98.7	124.5	182.6	232.8	270.9	306.4
Red Bone Marrow	0.12	101.5	121.2	152.7	224.9	273.1	341.2	397.7
Colon	0.12	82.3	98.4	126.4	187.6	221.4	269.3	321.8
Lungs	0.12	87.5	104.0	132.5	191.0	231.7	287.3	328.4
Stomach	0.12	79.1	96.2	126.5	180.6	221.9	275.4	317.3
Bladder	0.05	84.0	99.7	125.6	184.6	224.4	278.1	324.3
Breast	0.05	54.0	62.4	81.5	114.3	144.3	175.0	202.5
Liver	0.05	90.8	109.2	138.3	198.8	243.6	298.3	346.9
Esophagus	0.05	112.3	134.8	163.3	250.7	291.9	362.5	429.1
Thyroid	0.05	53.7	70.4	86.4	137.1	155.1	190.3	236.0
Skin	0.01	66.4	79.2	98.6	143.1	171.5	211.2	244.2
Bone	0.01	88.5	106.2	134.1	196.8	239.1	299.7	348.9
Remainders	0.05							
Adrenals		115.3	141.6	179.0	274.9	318.2	396.4	452.2
Brain		87.5	98.1	122.2	176.5	210.2	261.6	298.9
Small Intestines		99.3	119.6	151.7	220.2	266.0	329.1	381.3
Kidneys		122.7	148.8	181.9	266.0	319.5	395.2	459.1
Muscle		91.5	109.5	137.9	200.1	241.6	298.7	344.5
Pancreas		108.5	125.0	159.6	241.4	287.9	358.5	408.8
Spleen		110.9	125.4	157.6	231.2	275.7	345.0	396.9
Thymus		75.9	88.0	117.8	159.2	211.5	249.8	292.4
Uterus		74.5	90.9	114.1	170.4	202.0	256.5	289.1
Effective Dose		424.9 +/- 1.1%	512.6 +/- 1.3%	649.6 +/- 1.0%	951.8 +/- 0.9%	1158.4 +/- 0.9%	1414.9 +/- 0.8%	1642.0 +/- 0.8%

Table 3. Organ doses and effective dose per unit neutron fluence incident on an anthropomorphic phantom in PA geometry in pGy cm² and pSv cm² respectively. Neutron energy is in MeV.

	Energy	10.0	20.0	30.0	50.0	80.0	100.0	180.0
	Wr	8.81	6.76	6.04	5.50	5.23	5.16	5.05
Organ/Tissue	Wt							
Gonads	0.20	44.8	66.0	70.8	78.3	92.6	102.8	113.6
Red Bone Marrow	0.12	44.1	59.4	62.4	72.5	84.3	91.6	77.4
Colon	0.12	41.8	59.0	61.7	67.5	75.3	84.2	88.3
Lungs	0.12	59.2	76.6	75.5	81.7	90.4	96.6	82.1
Stomach	0.12	41.2	62.3	67.9	76.8	89.5	98.6	117.2
Bladder	0.05	39.3	60.7	66.8	77.4	90.2	98.1	120.4
Breast	0.05	35.9	57.2	65.2	75.6	88.2	95.3	114.7
Liver	0.05	48.3	68.1	71.3	79.4	90.5	98.7	104.6
Esophagus	0.05	53.2	71.6	72.0	78.2	92.0	99.6	97.0
Thyroid	0.05	27.3	45.3	53.9	67.5	80.7	90.6	117.7
Skin	0.01	51.5	69.0	67.9	71.6	75.1	79.2	64.9
Bone	0.01	41.7	57.3	60.8	71.1	83.3	91.2	79.5
Remainders	0.05							
Adrenals		67.0	82.3	76.8	88.0	91.5	98.3	67.7
Brain		45.1	63.1	65.3	75.0	86.7	94.3	87.9
Small Intestines		48.6	68.7	72.5	80.6	91.5	99.6	108.7
Kidneys		67.1	83.4	78.8	84.6	94.9	100.4	70.0
Muscle		52.4	71.1	72.2	79.9	89.3	96.2	90.9
Pancreas		51.8	71.8	76.0	80.8	90.8	101.1	106.3
Spleen		61.4	78.7	77.0	82.0	91.4	99.3	83.7
Thymus		32.9	52.6	58.3	68.9	86.2	97.1	122.3
Uterus		43.0	64.2	69.8	79.6	92.2	99.2	117.3
Effective Dose		399.7 +/- 0.2%	434.4 +/- 0.2%	409.1 +/- 0.4%	417.9 +/- 0.7%	457.8 +/- 0.8%	494.5 +/- 0.8%	510.2 +/- 1.0%

	Energy	200.0	400.0	500.0	700.0	1000.0	1500.0	2000.0
	Wr	5.04	5.01	5.01	5.00	5.00	5.00	5.00
Organ/Tissue	Wt							
Gonads	0.2	115.9	136.3	167.6	246.8	301.5	301.5	435.4
Red Bone Marrow	0.12	77.9	94.1	120.5	177.0	217.4	217.4	314.6
Colon	0.12	92.0	107.4	134.7	196.6	241.1	241.1	344.2
Lungs	0.12	82.2	98.5	127.1	182.4	221.9	221.9	315.9
Stomach	0.12	118.1	141.9	176.7	250.7	300.2	300.2	433.8
Bladder	0.05	121.9	140.8	178.4	262.4	319.6	319.6	453.9
Breast	0.05	116.2	137.6	167.8	241.7	285.4	285.4	405.1
Liver	0.05	103.7	123.7	156.3	224.7	273.3	273.3	392.2
Esophagus	0.05	93.7	112.3	144.5	218.1	252.1	252.1	377.7
Thyroid	0.05	120.9	141.5	178.0	233.6	274.4	274.4	420.3
Skin	0.01	65.4	78.0	97.8	141.3	169.4	169.4	241.3
Bone	0.01	79.6	95.8	122.3	178.7	218.5	218.5	318.1
Remainders	0.05							
Adrenals		64.6	89.3	103.2	164.0	186.4	186.4	270.0
Brain		87.0	98.7	122.5	175.3	214.3	214.3	302.4
Small Intestines		109.5	132.1	168.9	244.4	296.4	296.4	421.6
Kidneys		68.8	89.2	112.4	162.1	200.3	200.3	283.2
Muscle		91.1	108.5	136.9	198.7	240.4	240.4	343.3
Pancreas		109.8	124.8	164.2	239.9	291.5	291.5	417.8
Spleen		81.5	98.1	126.4	189.1	225.0	225.0	320.5
Thymus		118.3	142.1	174.2	243.4	307.6	307.6	449.8
Uterus		117.1	145.6	173.8	252.4	304.8	304.8	435.6
Effective Dose		512.0 +/- 1.1%	607.2 +/- 1.0%	757.4 +/- 0.9%	1093.9 +/- 0.8%	1323.4 +/- 0.8%	1631.3 +/- 0.7%	1911.0 +/- 0.7%

Table 4. Organ doses and effective dose per unit neutron fluence incident on an anthropomorphic phantom in LLAT geometry in pGy cm² and pSv cm² respectively. Neutron energy is in MeV.

	Energy	10.0	20.0	30.0	50.0	80.0	100.0	180.0
	Wr	8.81	6.76	6.04	5.50	5.23	5.16	5.05
Organ/Tissue	Wt							
Gonads	0.20	27.5	45.1	52.9	66.8	80.8	92.7	110.9
Red Bone Marrow	0.12	28.0	42.7	49.5	62.5	77.2	86.3	93.6
Colon	0.12	35.8	51.4	56.0	64.4	73.4	80.8	91.6
Lungs	0.12	34.4	51.0	56.6	67.8	81.8	91.0	102.1
Stomach	0.12	46.3	65.4	68.6	77.6	89.9	98.0	100.4
Bladder	0.05	29.4	48.1	56.8	71.1	84.6	93.2	119.3
Breast	0.05	19.2	27.0	28.4	31.6	35.1	37.7	43.2
Liver	0.05	15.9	30.7	40.7	55.7	72.5	81.8	115.6
Esophagus	0.05	38.4	57.8	63.3	73.9	85.9	91.6	109.8
Thyroid	0.05	58.0	78.5	77.9	85.0	91.5	99.5	83.6
Skin	0.01	44.9	61.2	61.6	67.0	72.5	77.4	65.6
Bone	0.01	28.7	42.8	48.8	61.5	76.1	85.0	88.9
Remainders	0.05							
Adrenals		32.7	51.6	57.7	70.9	85.0	94.1	103.9
Brain		53.5	71.6	71.5	79.0	89.6	96.8	80.3
Small Intestines		28.9	46.8	54.7	67.6	81.1	90.7	117.0
Kidneys		32.5	50.4	56.9	68.0	82.2	91.4	105.1
Muscle		34.9	51.8	57.1	68.6	81.3	89.5	98.6
Pancreas		35.2	53.1	59.1	70.7	83.0	92.8	110.1
Spleen		51.5	69.7	71.2	79.5	92.5	100.0	91.4
Thymus		27.4	44.8	53.8	66.0	82.2	94.4	115.6
Uterus		27.8	45.5	53.8	67.0	79.1	88.8	107.6
Effective Dose		294.5 +/- 0.2%	338.9 +/- 0.2%	336.4 +/- 0.4%	367.1 +/- 0.5%	414.1 +/- 0.6%	453.5 +/- 0.7%	499.9 +/- 0.8%

	Energy	200.0	400.0	500.0	700.0	1000.0	1500.0	2000.0
	Wr	5.04	5.01	5.01	5.00	5.00	5.00	5.00
Organ/Tissue	Wt							
Gonads	0.2	110.5	129.7	162.0	230.8	282.5	348.4	419.2
Red Bone Marrow	0.12	95.9	114.7	143.4	210.9	256.8	327.6	385.8
Colon	0.12	92.4	104.7	132.0	188.2	233.7	286.7	338.1
Lungs	0.12	102.7	116.7	144.9	210.9	252.5	317.5	371.8
Stomach	0.12	100.2	118.8	148.9	213.5	258.2	323.8	366.6
Bladder	0.05	120.6	138.0	174.2	253.0	301.8	377.9	441.6
Breast	0.05	44.0	55.8	70.7	102.4	126.1	160.1	183.1
Liver	0.05	122.8	147.2	180.7	262.0	318.9	402.7	475.9
Esophagus	0.05	111.7	126.3	156.7	229.0	274.6	343.1	400.4
Thyroid	0.05	85.3	105.5	134.3	190.2	220.9	279.0	322.6
Skin	0.01	68.0	82.9	102.7	148.1	179.3	221.4	258.5
Bone	0.01	91.1	109.0	136.2	199.0	243.7	309.8	364.5
Remainders	0.05							
Adrenals		102.3	136.6	162.4	236.5	271.5	347.0	406.0
Brain		80.1	95.4	119.2	170.2	203.0	252.5	289.6
Small Intestines		119.5	139.3	172.7	250.7	305.3	383.8	454.2
Kidneys		108.6	130.7	160.0	233.2	282.9	354.0	417.7
Muscle		100.9	119.1	148.0	214.3	259.1	325.7	381.4
Pancreas		109.2	132.5	163.3	242.7	282.9	362.1	416.4
Spleen		90.2	110.1	137.1	193.8	239.4	293.7	341.9
Thymus		113.2	125.0	160.2	225.1	277.5	340.0	405.2
Uterus		109.0	127.8	157.2	229.5	278.5	353.9	414.2
Effective Dose		504.3 +/- 0.8%	587.7 +/- 0.7%	734.4 +/- 0.7%	1056.9 +/- 0.6%	1281.7 +/- 0.6%	1602.7 +/- 0.5%	1881.7 +/- 0.5%

Table 5. Organ doses and effective dose per unit neutron fluence incident on an anthropomorphic phantom in RLAT geometry in pGy cm² and pSv cm² respectively. Neutron energy is in MeV.

	Energy	10.0	20.0	30.0	50.0	80.0	100.0	180.0
	Wr	8.81	6.76	6.04	5.50	5.23	5.16	5.05
Organ/Tissue	Wt							
Gonads	0.20	27.2	45.3	53.1	66.4	79.5	88.9	111.8
Red Bone Marrow	0.12	28.0	42.7	49.5	62.4	77.0	86.1	93.7
Colon	0.12	13.1	26.1	35.1	48.0	62.2	70.1	98.8
Lungs	0.12	34.4	51.0	56.5	68.0	81.7	90.9	101.9
Stomach	0.12	16.0	31.4	41.7	56.6	73.8	83.8	117.6
Bladder	0.05	29.3	48.2	56.3	70.7	84.3	93.4	122.6
Breast	0.05	19.1	27.1	28.6	31.8	35.4	38.0	41.9
Liver	0.05	47.4	65.7	68.5	77.7	89.3	97.1	96.5
Esophagus	0.05	36.1	55.9	61.5	73.9	85.3	92.5	115.3
Thyroid	0.05	57.9	78.5	78.2	85.4	92.1	97.0	85.6
Skin	0.01	44.9	61.2	61.5	67.1	72.5	77.4	65.7
Bone	0.01	28.7	42.8	48.8	61.5	75.9	84.9	89.0
Remainders	0.05							
Adrenals		32.2	50.4	58.6	70.8	85.0	90.3	106.3
Brain		53.5	71.5	71.4	79.1	89.6	96.8	80.5
Small Intestines		27.6	45.2	53.4	66.6	80.2	90.1	118.5
Kidneys		32.4	50.3	57.0	68.5	82.7	92.1	106.5
Muscle		33.7	50.6	56.1	67.8	80.8	88.9	99.2
Pancreas		19.7	35.7	45.4	58.8	76.5	84.2	116.1
Spleen		12.4	25.8	36.1	52.6	68.8	77.9	115.0
Thymus		35.5	54.7	61.2	71.3	88.6	97.2	112.8
Uterus		27.9	45.8	54.4	66.5	79.5	87.6	108.1
Effective Dose		248.3 +/- 0.2%	300.1 +/- 0.2%	308.5 +/- 0.4%	347.0 +/- 0.5%	398.1 +/- 0.6%	436.8 +/- 0.7%	514.2 +/- 0.8%

	Energy	200.0	400.0	500.0	700.0	1000.0	1500.0	2000.0
	Wr	5.04	5.01	5.01	5.00	5.00	5.00	5.00
Organ/Tissue	Wt							
Gonads	0.2	116.8	133.5	159.5	237.4	277.8	345.5	420.8
Red Bone Marrow	0.12	95.8	114.3	143.8	210.9	256.5	327.5	385.2
Colon	0.12	108.6	127.3	159.8	229.3	284.0	349.3	425.8
Lungs	0.12	102.6	116.6	145.2	209.8	252.8	319.8	374.3
Stomach	0.12	124.5	146.0	181.8	262.6	317.8	403.4	475.5
Bladder	0.05	123.8	138.6	174.8	250.3	296.5	370.1	437.1
Breast	0.05	44.0	56.7	71.2	104.2	126.9	159.7	183.9
Liver	0.05	95.9	110.7	141.0	202.5	245.6	308.1	354.2
Esophagus	0.05	112.5	129.3	159.6	235.0	278.4	356.9	418.5
Thyroid	0.05	85.1	109.1	132.3	184.0	226.9	278.4	316.2
Skin	0.01	68.0	83.2	102.6	147.9	179.2	221.5	257.9
Bone	0.01	91.0	108.9	136.2	198.9	243.5	309.5	364.5
Remainders	0.05							
Adrenals		110.3	132.2	168.7	226.6	281.5	358.0	407.0
Brain		80.1	95.7	118.5	170.4	203.1	253.1	290.1
Small Intestines		120.3	141.6	174.8	253.6	307.0	389.3	462.7
Kidneys		106.9	131.0	161.5	233.9	283.6	355.8	412.6
Muscle		101.9	120.3	149.6	216.1	261.9	329.3	384.9
Pancreas		121.8	148.0	180.9	271.6	323.8	412.3	480.4
Spleen		124.9	149.0	184.8	272.8	332.8	421.3	499.2
Thymus		108.7	121.3	151.0	215.6	267.1	328.4	380.6
Uterus		108.2	128.8	161.1	230.1	278.4	350.9	414.2
Effective Dose		532.2 +/- 0.8%	617.5 +/- 0.7%	763.9 +/- 0.7%	1108.8 +/- 0.6%	1335.3 +/- 0.5%	1676.4 +/- 0.5%	1988.9 +/- 0.5%

Table 6. Organ doses and effective dose per unit photon fluence incident on an anthropomorphic phantom in AP geometry in pGy cm² and pSv cm², respectively. Photon energy is in MeV.

	Energy	0.05	0.1	0.5	1.0	1.5	2.0	3.0
	Wr	1.00	1.00	1.00	1.00	1.00	1.00	1.00
Organ/Tissue	Wt							
Gonads	0.20	0.40	0.59	2.79	4.77	5.99	8.16	10.84
Red Bone Marrow	0.12	0.48	0.56	1.88	3.55	4.97	6.24	8.39
Colon	0.12	0.26	0.42	1.92	3.61	5.03	6.36	8.63
Lungs	0.12	0.32	0.47	2.36	4.40	5.93	7.51	9.94
Stomach	0.12	0.44	0.61	2.70	4.78	6.53	7.74	10.56
Bladder	0.05	0.44	0.63	2.78	5.02	6.75	8.16	10.38
Breast	0.05	0.43	0.56	2.76	4.92	6.56	7.83	9.63
Liver	0.05	0.34	0.51	2.49	4.50	6.08	7.61	10.02
Esophagus	0.05	0.17	0.30	1.72	3.33	5.09	6.42	9.30
Thyroid	0.05	0.49	0.60	2.67	4.96	6.94	7.80	9.22
Skin	0.01	0.26	0.38	2.07	3.36	3.98	4.53	5.43
Bone	0.01	0.61	0.64	2.12	3.93	5.47	6.78	9.01
Remainders	0.05							
Adrenals		0.08	0.23	1.52	3.52	4.57	6.28	8.06
Brain		0.17	0.30	1.92	3.81	5.47	6.93	9.39
Small Intestines		0.32	0.50	2.39	4.43	6.04	7.32	9.68
Kidneys		0.11	0.25	1.64	3.32	4.66	6.07	8.41
Muscle		0.28	0.43	2.26	4.23	5.86	7.22	9.49
Pancreas		0.25	0.43	2.26	4.10	5.99	7.73	9.49
Spleen		0.19	0.33	2.03	3.91	5.43	6.69	9.05
Thymus		0.44	0.62	2.61	4.60	6.70	8.14	11.29
Uterus		0.42	0.58	2.55	4.26	5.56	6.52	8.92
Effective Dose		0.38 +/- 1.4%	0.52 +/- 1.4%	2.39 +/- 1.6%	4.33 +/- 1.9%	5.84 +/- 1.9%	7.33 +/- 2.1%	9.75 +/- 2.3%

	Energy	4.0	5.0	6.0	8.0	10.0	20.0	30.0
	Wr	1.00	1.00	1.00	1.00	1.00	1.00	1.00
Organ/Tissue	Wt							
Gonads	0.2	13.35	13.56	14.26	15.15	19.66	30.13	37.22
Red Bone Marrow	0.12	10.31	12.07	13.64	16.83	20.23	35.11	48.90
Colon	0.12	10.12	11.81	13.09	16.47	19.52	32.43	38.61
Lungs	0.12	11.95	14.09	16.03	20.05	23.58	36.43	43.60
Stomach	0.12	12.82	15.08	16.85	20.15	23.27	32.58	35.19
Bladder	0.05	12.23	13.86	15.93	18.93	21.94	29.50	33.33
Breast	0.05	10.73	11.67	12.30	13.34	14.31	15.57	16.12
Liver	0.05	12.33	14.41	16.28	20.03	23.11	35.40	42.25
Esophagus	0.05	10.34	11.69	14.84	17.83	21.73	39.28	56.65
Thyroid	0.05	10.13	12.04	13.61	15.20	16.62	16.07	15.77
Skin	0.01	6.24	7.18	7.91	9.43	11.05	18.84	26.34
Bone	0.01	10.99	12.80	14.44	17.70	21.05	34.24	44.09
Remainders	0.05							
Adrenals		11.70	11.99	14.94	19.20	25.10	41.06	54.99
Brain		11.52	13.66	15.60	19.17	23.00	37.52	48.01
Small Intestines		12.01	13.99	16.08	19.77	23.51	39.01	48.53
Kidneys		10.55	12.53	14.49	18.05	21.22	36.75	55.67
Muscle		11.41	13.15	14.66	17.54	20.40	32.07	41.16
Pancreas		10.86	12.80	14.07	19.00	22.51	42.35	55.10
Spleen		11.59	13.41	15.49	18.80	22.49	40.42	53.97
Thymus		13.57	14.85	16.22	21.24	22.07	27.06	27.71
Uterus		10.22	12.11	13.72	15.87	19.33	27.76	32.24
Effective Dose		11.67 +/- 2.3%	13.12 +/- 2.1%	14.63 +/- 1.9%	17.38 +/- 1.9%	20.65 +/- 2.0%	31.67 +/- 1.8%	38.63 +/- 1.7%

	Energy	40.0	50.0	100.0	200.0	500.0	1000.0	2000.0
	Wr	1.00	1.00	1.00	1.00	1.00	1.00	1.00
Organ/Tissue	Wt							
Gonads	0.2	39.46	37.90	43.33	55.50	69.79	62.99	72.26
Red Bone Marrow	0.12	59.69	68.10	91.17	110.89	130.62	140.65	150.82
Colon	0.12	43.80	47.29	57.62	65.29	72.77	81.96	78.41
Lungs	0.12	48.02	51.65	61.04	69.45	75.70	85.32	87.93
Stomach	0.12	37.08	38.51	45.40	49.50	52.26	56.46	59.65
Bladder	0.05	35.24	38.00	43.93	49.24	55.32	55.42	58.07
Breast	0.05	16.84	17.46	19.77	21.58	25.38	27.32	25.68
Liver	0.05	47.33	50.30	60.40	69.05	76.54	81.82	83.57
Esophagus	0.05	69.19	77.52	98.90	113.08	136.10	150.02	152.33
Thyroid	0.05	16.61	17.60	19.06	26.50	27.30	28.67	43.46
Skin	0.01	32.36	37.99	53.15	65.45	80.61	86.19	92.90
Bone	0.01	51.33	57.12	72.90	86.65	99.86	107.77	113.50
Remainders	0.05							
Adrenals		75.16	86.86	119.40	154.33	192.82	204.01	227.57
Brain		55.99	62.11	77.54	91.95	108.07	113.99	116.79
Small Intestines		53.72	57.76	69.92	81.06	90.45	95.08	95.39
Kidneys		71.40	81.50	110.62	136.73	162.77	175.20	181.57
Muscle		47.74	52.94	67.06	79.48	91.54	97.85	101.81
Pancreas		62.43	69.51	81.79	96.83	113.01	130.21	130.63
Spleen		62.58	71.69	90.91	105.42	119.88	124.76	134.46
Thymus		30.84	30.66	33.96	36.97	41.90	43.42	48.19
Uterus		34.24	38.72	45.65	51.35	52.58	59.22	56.46
Effective Dose		43.81 +/- 1.7%	46.87 +/- 1.5%	57.45 +/- 1.7%	67.99 +/- 1.5%	78.81 +/- 2.1%	83.15 +/- 2.6%	88.28 +/- 1.8%

Table 7. Organ doses and effective dose per unit photon fluence incident on an anthropomorphic phantom in PA geometry in pGy cm² and pSv cm², respectively. Photon energy is in MeV.

	Energy	0.05	0.1	0.5	1.0	1.5	2.0	3.0
	Wr	1.00	1.00	1.00	1.00	1.00	1.00	1.00
Organ/Tissue	Wt							
Gonads	0.20	0.16	0.31	1.97	3.43	4.89	6.60	8.64
Red Bone Marrow	0.12	0.90	0.89	2.51	4.43	5.97	7.31	9.58
Colon	0.12	0.18	0.34	1.81	3.48	4.81	6.11	8.09
Lungs	0.12	0.35	0.50	2.55	4.74	6.36	7.84	10.37
Stomach	0.12	0.16	0.31	1.82	3.53	5.05	6.37	8.76
Bladder	0.05	0.15	0.30	1.78	3.65	5.23	6.52	8.92
Breast	0.05	0.09	0.18	1.53	3.29	4.72	6.05	8.42
Liver	0.05	0.22	0.38	2.12	4.02	5.58	6.98	9.40
Esophagus	0.05	0.19	0.41	1.87	3.77	4.78	6.96	8.10
Thyroid	0.05	0.05	0.14	1.21	2.43	3.64	5.12	7.48
Skin	0.01	0.26	0.38	2.07	3.38	3.91	4.51	5.31
Bone	0.01	0.75	0.76	2.35	4.26	5.84	7.15	9.40
Remainders	0.05							
Adrenals		0.47	0.70	2.84	5.12	7.50	8.09	10.15
Brain		0.16	0.30	1.93	3.84	5.48	6.94	9.43
Small Intestines		0.19	0.39	2.13	3.92	5.44	6.84	9.34
Kidneys		0.46	0.62	2.80	4.93	6.57	8.03	10.72
Muscle		0.28	0.43	2.27	4.24	5.88	7.21	9.49
Pancreas		0.23	0.45	2.17	4.20	5.43	6.97	9.58
Spleen		0.39	0.55	2.66	4.66	6.28	7.47	10.26
Thymus		0.09	0.22	1.52	3.30	4.40	5.48	8.12
Uterus		0.16	0.32	1.82	3.62	5.20	6.28	8.85
Effective Dose		0.28 +/- 1.6%	0.41 +/- 1.4%	2.03 +/- 1.7%	3.79 +/- 1.7%	5.26 +/- 1.9%	6.71 +/- 2.0%	8.91 +/- 2.0%
	Energy	4.0	5.0	6.0	8.0	10.0	20.0	30.0
	Wr	1.00	1.00	1.00	1.00	1.00	1.00	1.00
Organ/Tissue	Wt							
Gonads	0.2	12.39	14.33	16.58	19.38	23.24	45.03	59.23
Red Bone Marrow	0.12	11.64	13.33	14.84	17.69	20.27	29.83	35.38
Colon	0.12	9.91	11.56	12.83	15.98	18.78	34.08	46.54
Lungs	0.12	12.56	15.00	16.94	20.67	24.05	33.72	38.15
Stomach	0.12	10.75	12.86	14.94	18.59	23.13	39.85	57.10
Bladder	0.05	10.98	12.52	14.09	17.71	20.97	38.04	54.79
Breast	0.05	10.21	11.83	13.64	16.81	20.68	37.84	54.16
Liver	0.05	11.62	13.77	15.65	19.52	22.91	38.40	50.39
Esophagus	0.05	10.24	12.73	15.05	19.34	22.51	41.25	55.72
Thyroid	0.05	9.90	11.27	12.34	17.70	22.31	38.74	57.81
Skin	0.01	6.14	7.03	7.70	9.28	10.99	18.37	25.83
Bone	0.01	11.40	13.19	14.80	17.91	20.92	32.11	39.01
Remainders	0.05							
Adrenals		13.12	12.19	12.97	15.54	17.56	22.24	23.78
Brain		11.60	13.77	15.81	19.34	23.01	37.49	48.40
Small Intestines		11.41	13.38	15.01	18.67	22.05	40.95	55.89
Kidneys		12.88	14.82	16.34	19.62	21.24	23.86	25.39
Muscle		11.40	13.15	14.70	17.56	20.45	32.09	41.17
Pancreas		11.70	13.40	15.91	19.97	24.19	42.47	55.12
Spleen		12.70	15.02	16.36	20.01	23.45	32.61	36.19
Thymus		10.90	11.00	12.75	17.81	21.17	37.92	58.37
Uterus		11.32	13.40	15.18	19.20	23.33	37.31	54.37
Effective Dose		11.3 +/- 2.2%	13.21 +/- 2.1%	14.97 +/- 2.1%	18.39 +/- 1.9%	21.93 +/- 1.8%	37.43 +/- 1.8%	49.61 +/- 1.5%
	Energy	40.0	50.0	100.0	200.0	500.0	1000.0	2000.0
	Wr	1.00	1.00	1.00	1.00	1.00	1.00	1.00
Organ/Tissue	Wt							
Gonads	0.2	71.60	78.19	96.22	116.03	129.35	131.07	144.95
Red Bone Marrow	0.12	39.77	42.77	52.31	61.40	69.14	74.46	78.49
Colon	0.12	54.24	61.44	75.92	87.32	100.96	113.12	114.19
Lungs	0.12	40.87	43.47	48.98	54.88	60.39	63.46	64.68
Stomach	0.12	69.43	78.31	104.65	123.59	139.69	153.90	164.23
Bladder	0.05	67.82	77.52	103.81	131.36	147.85	157.39	173.46
Breast	0.05	67.74	78.00	105.49	126.90	145.02	167.12	171.86
Liver	0.05	58.94	65.71	83.07	97.90	114.46	122.18	129.96
Esophagus	0.05	61.27	66.82	85.24	97.99	115.42	137.99	122.07
Thyroid	0.05	74.00	82.81	129.26	170.17	203.74	229.12	228.43
Skin	0.01	31.94	37.21	52.20	64.17	77.82	84.02	90.18
Bone	0.01	43.93	47.81	58.42	68.40	77.60	82.85	86.72
Remainders	0.05							
Adrenals		24.65	24.60	25.51	27.22	34.42	33.18	43.30
Brain		55.80	61.65	78.09	91.74	105.99	114.39	116.07
Small Intestines		64.96	72.27	91.35	107.24	123.17	131.76	134.34
Kidneys		26.40	27.77	31.51	35.29	40.26	39.11	39.33
Muscle		47.72	52.85	67.20	79.71	92.14	98.60	105.01
Pancreas		62.53	69.92	82.50	102.73	130.72	124.93	133.85
Spleen		38.36	40.66	46.21	51.73	56.36	56.06	42.78
Thymus		76.11	93.14	125.29	163.02	201.62	227.78	193.75
Uterus		67.66	75.06	97.90	115.17	133.48	140.69	146.65
Effective Dose		59.20 +/- 1.4%	65.81 +/- 1.4%	83.11 +/- 1.5%	99.31 +/- 1.6%	113.27 +/- 1.7%	122.54 +/- 2.0%	127.95 +/- 2.0%

Table 8. Organ doses and effective dose per unit photon fluence incident on an anthropomorphic phantom in LLAT geometry in pGy cm² and pSv cm², respectively. Photon energy is in MeV.

	Energy Wr	0.05 1.00	0.1 1.00	0.5 1.00	1.0 1.00	1.5 1.00	2.0 1.00	3.0 1.00
Organ/Tissue	Wt							
Gonads	0.20	0.09	0.18	1.17	2.50	4.01	5.48	7.20
Red Bone Marrow	0.12	0.39	0.44	1.61	3.15	4.54	5.80	7.93
Colon	0.12	0.13	0.26	1.51	2.90	4.09	5.32	7.18
Lungs	0.12	0.13	0.23	1.47	3.05	4.48	5.78	8.15
Stomach	0.12	0.22	0.36	1.97	3.85	5.30	6.72	9.01
Bladder	0.05	0.08	0.17	1.26	2.82	4.15	5.14	7.49
Breast	0.05	0.09	0.14	0.85	1.56	2.14	2.56	3.39
Liver	0.05	0.02	0.08	0.71	1.76	2.86	3.95	5.93
Esophagus	0.05	0.12	0.25	1.64	3.40	4.91	5.83	7.36
Thyroid	0.05	0.32	0.43	2.51	4.92	6.69	8.42	10.77
Skin	0.01	0.22	0.31	1.85	3.11	3.86	4.41	5.40
Bone	0.01	0.44	0.45	1.63	3.18	4.54	5.77	7.89
Remainders	0.05							
Adrenals		0.09	0.16	1.54	3.13	4.47	6.09	8.12
Brain		0.25	0.39	2.29	4.32	6.02	7.38	9.88
Small Intestines		0.09	0.19	1.27	2.68	3.95	5.23	7.46
Kidneys		0.11	0.20	1.46	2.98	4.35	5.77	8.13
Muscle		0.14	0.23	1.50	3.09	4.49	5.73	7.89
Pancreas		0.11	0.26	1.51	3.21	4.61	5.91	8.32
Spleen		0.25	0.41	2.26	4.28	5.97	7.67	10.18
Thymus		0.07	0.18	1.28	2.68	4.14	4.91	7.87
Uterus		0.07	0.16	1.25	2.82	4.19	5.55	7.62
Effective Dose		0.17 +/- 1.5%	0.26 +/- 1.3%	1.48 +/- 1.2%	3.00 +/- 1.4%	4.37 +/- 1.5%	5.63 +/- 1.7%	7.61 +/- 1.7%

	Energy Wr	4.0 1.00	5.0 1.00	6.0 1.00	8.0 1.00	10.0 1.00	20.0 1.00	30.0 1.00
Organ/Tissue	Wt							
Gonads	0.2	8.85	10.02	12.05	14.50	18.57	36.81	52.22
Red Bone Marrow	0.12	9.90	11.63	13.32	16.55	19.69	33.85	45.50
Colon	0.12	8.95	10.53	11.99	14.37	17.07	33.69	45.62
Lungs	0.12	10.28	12.23	14.11	17.41	21.08	37.92	51.16
Stomach	0.12	11.14	13.12	15.03	18.58	22.07	38.60	50.82
Bladder	0.05	9.26	10.83	12.61	15.94	19.30	35.33	53.23
Breast	0.05	4.05	4.67	5.24	6.11	7.12	10.91	15.05
Liver	0.05	7.72	9.40	11.11	14.28	17.54	32.39	47.21
Esophagus	0.05	10.34	13.56	15.25	17.66	22.13	36.81	52.54
Thyroid	0.05	12.89	15.97	17.77	20.82	24.17	33.38	38.05
Skin	0.01	6.23	7.02	7.76	9.18	10.69	18.03	24.70
Bone	0.01	9.80	11.55	13.10	16.08	19.07	32.11	42.91
Remainders	0.05							
Adrenals		10.72	12.15	14.67	17.82	21.84	37.36	55.84
Brain		12.03	14.02	15.83	19.14	22.38	34.05	40.53
Small Intestines		9.32	11.09	12.70	16.06	19.49	36.19	52.70
Kidneys		10.18	12.31	14.03	17.70	21.15	37.10	51.10
Muscle		9.81	11.57	13.17	16.24	19.27	32.58	44.72
Pancreas		9.57	12.40	13.07	18.33	21.12	38.31	53.97
Spleen		12.66	14.50	16.26	19.98	23.95	39.25	48.44
Thymus		9.51	11.13	13.74	15.03	19.51	37.99	50.71
Uterus		9.66	11.41	12.88	16.24	19.93	35.95	50.16
Effective Dose		9.49 +/- 1.6%	11.23 +/- 1.6%	12.95 +/- 1.6%	15.79 +/- 1.5%	19.16 +/- 1.5	34.48 +/- 1.3%	47.22 +/- 1.3%

	Energy Wr	40.0 1.00	50.0 1.00	100.0 1.00	200.0 1.00	500.0 1.00	1000.0 1.00	2000.0 1.00
Organ/Tissue	Wt							
Gonads	0.2	68.68	77.48	112.66	157.04	205.30	255.60	281.11
Red Bone Marrow	0.12	55.91	64.15	93.46	121.29	151.07	171.60	186.54
Colon	0.12	54.10	60.24	79.79	97.93	114.36	124.47	135.57
Lungs	0.12	63.19	72.98	106.10	136.90	163.98	178.54	197.96
Stomach	0.12	59.01	66.24	82.50	95.72	116.18	123.82	124.88
Bladder	0.05	69.38	81.10	118.81	153.39	191.29	204.82	219.96
Breast	0.05	19.08	21.96	32.07	38.75	51.81	57.77	63.77
Liver	0.05	63.22	78.20	138.52	198.32	274.88	322.95	370.62
Esophagus	0.05	66.75	72.08	97.99	120.26	146.49	152.37	156.04
Thyroid	0.05	41.85	42.43	44.47	51.72	48.94	49.26	20.24
Skin	0.01	31.11	37.05	59.24	83.28	112.81	129.73	145.29
Bone	0.01	52.21	60.17	89.04	118.31	152.82	175.72	195.83
Remainders	0.05							
Adrenals		65.28	71.46	113.64	138.07	157.57	177.55	165.98
Brain		44.76	46.78	56.09	64.58	73.42	76.37	79.57
Small Intestines		67.01	79.68	122.38	162.38	206.14	227.71	257.96
Kidneys		64.17	75.09	113.13	145.58	185.70	205.31	218.66
Muscle		55.47	64.82	97.54	129.77	166.56	188.18	208.01
Pancreas		68.57	79.22	111.99	146.50	188.00	190.67	206.35
Spleen		53.01	60.89	73.44	80.95	99.65	101.04	109.79
Thymus		67.40	72.40	110.99	137.02	179.17	212.64	185.15
Uterus		66.50	77.98	113.31	150.25	178.90	203.92	226.97
Effective Dose		58.52 +/- 1.2%	66.38 +/- 1.6%	94.10 +/- 1.5%	122.19 +/- 1.6%	152.84 +/- 2.4%	174.15 +/- 2.8%	187.78 +/- 3.4%

Table 9. Organ doses and effective dose per unit photon fluence incident on an anthropomorphic phantom in RLAT geometry in pGy cm² and pSv cm², respectively. Photon energy is in MeV.

	Energy	0.05	0.1	0.5	1.0	1.5	2.0	3.0
	Wr	1.00	1.00	1.00	1.00	1.00	1.00	1.00
Organ/Tissue	Wt							
Gonads	0.20	0.07	0.17	1.30	2.65	4.12	5.09	7.99
Red Bone Marrow	0.12	0.39	0.44	1.61	3.16	4.55	5.82	7.94
Colon	0.12	0.01	0.06	0.59	1.47	2.42	3.30	5.01
Lungs	0.12	0.13	0.23	1.47	3.05	4.47	5.78	8.15
Stomach	0.12	0.02	0.07	0.72	1.84	2.96	4.20	6.27
Bladder	0.05	0.08	0.17	1.26	2.82	4.03	5.24	7.38
Breast	0.05	0.10	0.15	0.84	1.55	2.17	2.61	3.40
Liver	0.05	0.22	0.37	2.03	3.89	5.43	6.88	9.24
Esophagus	0.05	0.11	0.22	1.60	3.16	4.79	5.64	7.20
Thyroid	0.05	0.32	0.43	2.51	5.06	6.78	8.52	10.48
Skin	0.01	0.22	0.31	1.85	3.12	3.84	4.41	5.36
Bone	0.01	0.44	0.45	1.63	3.18	4.53	5.78	7.90
Remainders	0.05							
Adrenals		0.08	0.18	1.39	2.96	4.55	6.02	8.46
Brain		0.25	0.39	2.28	4.34	6.02	7.36	9.87
Small Intestines		0.08	0.17	1.22	2.59	3.88	5.07	7.26
Kidneys		0.11	0.20	1.47	2.97	4.38	5.69	8.10
Muscle		0.13	0.22	1.45	3.01	4.40	5.62	7.77
Pancreas		0.03	0.09	0.85	1.93	3.17	4.12	6.44
Spleen		0.01	0.05	0.54	1.42	2.47	3.49	5.44
Thymus		0.13	0.25	1.62	3.63	4.39	5.81	7.90
Uterus		0.07	0.16	1.22	2.71	4.12	5.28	7.17
Effective Dose		0.13 +/- 1.8%	0.21 +/- 1.5%	1.30 +/- 1.5%	2.70 +/- 1.5%	4.00 +/- 1.7%	5.13 +/- 1.7%	7.28 +/- 1.9%
	Energy	4.0	5.0	6.0	8.0	10.0	20.0	30.0
	Wr	1.00	1.00	1.00	1.00	1.00	1.00	1.00
Organ/Tissue	Wt							
Gonads	0.2	9.00	11.95	13.50	15.38	19.66	33.31	52.51
Red Bone Marrow	0.12	9.82	11.68	13.33	16.50	19.74	33.83	45.63
Colon	0.12	6.73	8.07	9.53	11.99	14.97	27.62	40.75
Lungs	0.12	10.23	12.23	14.14	17.66	21.24	38.10	51.12
Stomach	0.12	8.03	9.70	11.35	14.60	17.74	32.62	48.53
Bladder	0.05	9.39	11.05	12.74	16.36	19.78	34.89	52.80
Breast	0.05	4.06	4.68	5.14	6.12	7.12	11.32	15.24
Liver	0.05	11.33	13.34	15.16	18.76	22.33	37.24	47.46
Esophagus	0.05	10.13	11.86	16.24	18.90	22.44	39.10	53.19
Thyroid	0.05	13.59	15.65	17.48	20.74	23.36	35.42	38.73
Skin	0.01	6.23	7.04	7.74	9.16	10.74	17.99	24.67
Bone	0.01	9.78	11.56	13.10	16.11	19.12	32.18	42.98
Remainders	0.05							
Adrenals		10.73	12.52	13.95	16.73	21.07	35.58	54.73
Brain		12.06	14.09	15.87	19.08	22.33	33.96	40.46
Small Intestines		9.05	10.87	12.50	15.76	19.16	35.70	51.94
Kidneys		10.18	11.93	13.59	17.19	21.03	36.85	51.60
Muscle		9.67	11.41	13.01	16.05	19.04	32.47	44.84
Pancreas		8.43	9.85	11.34	14.88	17.94	32.22	48.68
Spleen		7.03	8.90	9.94	13.28	16.15	31.35	46.59
Thymus		10.13	11.81	14.72	18.89	20.81	37.29	51.33
Uterus		8.77	10.70	11.79	15.18	19.22	34.85	49.25
Effective Dose		9.04 +/- 1.7%	10.98 +/- 1.9%	12.70 +/- 1.8%	15.48 +/- 1.7%	18.81 +/- 1.7%	32.65 +/- 1.3%	46.44 +/- 1.25
	Energy	40.0	50.0	100.0	200.0	500.0	1000.0	2000.0
	Wr	1.00	1.00	1.00	1.00	1.00	1.00	1.00
Organ/Tissue	Wt							
Gonads	0.2	63.23	76.99	125.71	145.08	194.17	222.38	271.39
Red Bone Marrow	0.12	55.80	64.17	93.24	120.71	150.96	171.04	185.25
Colon	0.12	54.21	68.22	120.76	174.04	233.24	271.58	315.96
Lungs	0.12	63.48	72.59	106.20	135.47	165.83	185.01	197.35
Stomach	0.12	63.57	81.71	140.34	196.11	267.03	295.49	338.88
Bladder	0.05	69.26	81.70	119.32	147.82	187.20	199.82	225.93
Breast	0.05	19.34	21.78	32.36	38.23	51.57	57.38	60.19
Liver	0.05	54.67	60.71	78.26	92.31	109.30	115.10	119.23
Esophagus	0.05	67.00	74.57	108.23	133.10	157.55	150.12	168.50
Thyroid	0.05	43.27	40.20	47.47	55.48	46.61	48.18	33.97
Skin	0.01	31.08	37.13	59.55	83.87	112.71	130.21	146.69
Bone	0.01	52.33	60.14	88.93	118.62	152.79	175.66	195.08
Remainders	0.05							
Adrenals		57.90	75.57	106.90	144.31	172.88	192.98	198.90
Brain		44.54	46.68	56.29	64.82	73.87	75.47	79.56
Small Intestines		66.67	80.08	124.69	164.39	210.62	239.80	262.81
Kidneys		63.68	75.81	114.01	143.98	183.30	209.21	210.87
Muscle		55.92	65.69	99.85	133.60	172.20	195.33	216.94
Pancreas		62.33	77.57	119.51	176.64	230.43	291.46	314.83
Spleen		61.64	77.07	145.60	219.50	309.65	361.12	414.07
Thymus		62.93	69.60	96.38	121.59	141.64	147.54	164.51
Uterus		66.51	76.72	116.15	142.60	181.73	201.88	218.70
Effective Dose		57.62 +/- 1.2%	68.31 +/- 1.6%	107.42 +/- 1.5%	138.45 +/- 1.4%	179.16 +/- 2.0%	200.72 +/- 2.6%	228.14 +/- 2.5%

**EVALUATION OF DOSE CONVERSION COEFFICIENTS
FOR HIGH-ENERGY RADIATION IN JAPAN AFTER SATIF-4**

Yukio Sakamoto, Shuichi Tsuda

Japan Atomic Energy Research Institute
Tokai-mura, Ibaraki 319-1195, Japan
E-mail: sakamoto@frs.tokai.jaeri.go.jp

Osamu Sato, Nobuaki Yoshizawa

Mitsubishi Research Institute Inc.
Otemachi, Chiyoda-ku, Tokyo 100-8141, Japan

Abstract

After SATIF-4, four activities of dose conversion coefficient evaluation for high-energy radiations were achieved by using an anthropomorphic model in Japan. The first was the evaluation of effective dose and ambient dose equivalent conversion coefficients for high-energy photon and the evaluation of dose contribution due to photonuclear reactions from high-energy photons. The second was the evaluation of effective dose for high-energy electrons. The third was the evaluation of effective dose and effective dose equivalents for high-energy alpha particles. The fourth was the trial evaluation for neutrons and protons up to 100 GeV.

The data of fluence to effective dose conversion coefficients for high-energy photons and electrons obtained using the EGS4 code were almost same as those evaluated by the FLUKA code system. On the other hand, the data for 10-100 GeV neutrons and protons obtained using the HERMES code system were smaller than those evaluated by the FLUKA code system for all irradiation geometries, and the difference was caused by the nuclear reaction model.

Introduction

For purposes of dose assessment and shielding designs concerning high-energy accelerators, high-flying aircraft and space vehicles, fluence to dose conversion coefficients are needed. As the data for high-energy radiations were not included in ICRP Publication 74, we began the evaluation of effective dose equivalent for high-energy radiations using the HERMES code system and the EGS4 code in conjunction with an anthropomorphic model. Fluence to dose conversion coefficients for photons, neutrons and protons up to 10 GeV have already been evaluated and reported at SATIF, SATIF-2, SATIF-3 and SATIF-4.

The data for various high-energy radiations such as electrons and alpha particles is required for the assessment of radiation in the upper atmosphere and space. Additionally, data for energy radiations above 10 GeV are needed for the 50 GeV accelerator shielding design which is the basis of the JAERI-KEK collaborative plan for a high intensity proton accelerator. The 50 GeV accelerator will be built at the Tokai Establishment of JAERI. For these reasons, the following four activities were undertaken in Japan after SATIF-4:

1. The evaluation of effective dose and ambient dose equivalent conversion coefficients for high-energy photons and the evaluation of dose contribution due to photonuclear reactions from high-energy photons.
2. The evaluation of effective dose for high-energy electrons.
3. The evaluation of effective dose and effective dose equivalents for high-energy alpha particles.
4. The trial evaluation for neutrons and protons up to 100 GeV.

Effective dose and ambient dose equivalent conversion coefficients for high-energy photons

Effective dose

The effective doses calculated in AP, PA, RLAT, LLAT, ROT and ISO geometries [1] using the EGS4 code [2] are compared in Figure 1. Below 10 MeV, the maximum effective dose is found at AP geometry. From 10-20 MeV, PA geometry shows the maximum effective doses, RLAT or LLAT for the energy from 50 MeV to 1 GeV, and ISO at 10 GeV. The contribution of each organ to effective doses in AP geometry calculated by the formula below can be seen in Figure 2.

$$\text{Contribution from tissue or organ } T = w_T H_T / E$$

where E is the effective dose. The contribution of tissue or organ near the irradiated surface is greater at low energy, such as a breast in AP geometry or a liver in RLAT geometry. At high energy, the contribution of the tissue or organ at the opposite side of irradiated surface becomes greater due to transport of secondary electrons.

Table 1 compares the effective doses [1] in AP geometry calculated with the EGS4 code [3], the FLUKA code [4] considering electron transport, and the data in ICRP 74 [5]. The effective doses in AP geometry in Ref. [3] are lower than those in Ref. [1] at 1 MeV and 3 MeV, and are systematically of higher energy. The difference is considered to come from the different anthropomorphic phantom models used in the two calculations. The phantom model in Ref. [1] had a half height of breast to represent the hermaphrodite, and the path length of photons in the breast may be shorter compared to

the calculation in Ref. [3]. At low energy, a shorter path length results in the smaller attenuation of photon fluence, and the absorbed dose will be higher in the breast and lungs. At high energy a fewer number of secondary electrons are produced with shorter path lengths, and the absorbed doses in the lungs will become lower. At 10 MeV, the results of Refs. [1] and [3] are systematically lower compared to ICRP 74 for all geometries. The reason will be the KERMA approximation used in the calculations on which ICRP 74 based. Except for AP geometry, effective doses at high energies (>10 MeV) in Ref. [1] agree well with the data in Ref. [3].

Ambient dose equivalents

Figure 3 shows the distribution of calculated ambient dose equivalents, $H^*(d)$ on the principal axis of the ICRU sphere [1]. Below 3 MeV, the maximum dose equivalents appear at the position nearest to the surface irradiated by the photon beam. From 3 MeV to 50 MeV, the dose equivalents have a peak in the ICRU sphere. Above 100 MeV, the dose equivalents monotonically increase with the depth, and the maximum dose equivalent is found near the surface opposite to the irradiated side.

$H^*(10)$, dose equivalents at 1 cm depth on the principal axis and H^*_{max} , the maximum dose equivalents in the ICRU sphere calculated with EGS4 code are compared with the values from ICRP 74 and calculations neglecting the transport of secondary particles (KERMA approximation). The $H^*(10)$ with KERMA approximation agreed well with those in ICRP 74 below 10 MeV. Above 3 MeV, the $H^*(10)$ with KERMA approximation exceed the values calculated with secondary particle transports. In this energy range, the maximum dose equivalents appear at a depth of more than 1 cm when the secondary particles are considered.

Figure 4 compares $H^*(10)$ and the maximum effective dose per unit fluence selected from AP, PA, LLAT, ERAT or ISO geometries at each energy. The depths in the ICRU sphere (d) are 1, 5, 10, 15 and 20 cm. $H^*(10)$ considering electron transports does not overestimate the effective doses at the energy above 5 MeV. $H^*(10)$ with KERMA approximation overestimates the effective dose by more than a factor of two at energies above 100 MeV. At energies above 50 MeV, the effective doses are exceeded by the ambient dose equivalents at a depth of 20 cm, $H^*(200)$, and the differences between the effective doses and $H^*(200)$ are almost constant at 33% above 1 GeV. The depth where the ambient dose equivalents are comparable to the effective doses varies up to 20 cm for photon energies up to 10 GeV, since the thickness of the anthropomorphic phantom is approximately 20 cm.

Dose contribution due to photonuclear reactions from high-energy photons

The spectra of secondary particles and the distribution of the photoneutron production rate in the 30 cm thick semi-infinite slab phantom were calculated from energy-differential photonuclear cross-sections and averaged photon fluences in the phantom [6]. The photon fluences were calculated using the EGS4 code to take secondary photons from the electromagnetic cascade into account. The spectra of secondary charged particles were calculated as the products of photonuclear cross-sections (preliminary version of JENDL Photonuclear Data File, JENDL-PDF [7]), secondary particle spectra and an averaged photon spectrum at all positions in the phantom. The photoneutron spectra were calculated as the averaged value in each 3 cm thick layer and used as the source spectra of neutron transport calculations.

Figure 5 shows the ratios of the dose equivalents deposited by photonuclear reactions to the total dose equivalents including the electromagnetic process. The contribution of photoneutrons to equivalent dose is about 0.2% at 30 MeV. It is smaller than the estimation by Allen, *et al.* [8] (1.0% to dose

equivalent) for photons from bremsstrahlung of 30 MeV electron. The difference is mainly due to the quality factor of neutrons and the assumption of neutron transport. Allen assumed that the quality factor of neutrons is always 20 and that the neutrons deposit whole kinetic energy at the point where photon neutrons are produced. In Sato's evaluation, the average quality factor for neutrons from 30 MeV photons are 11.1 and the neutron transport in the phantom was calculated using the HERMES code system [9].

The dose was neglected for the photonuclear reaction with photons above 140 MeV in Sato's calculations by the lack of the reaction cross-sections in JENDL-PDF. In $^{12}\text{C}(\gamma, n)$ cross-sections [10] up to 1 GeV calculated with MC-PHOTO [11] and PICA [12] it is shown that cross-sections above 140 MeV are comparable or greater than those at the energy of GDR (about 20 MeV). The photon fluences above 140 MeV amount to 17% for an incident photon energy of 10 GeV. The contribution of photons above 140 MeV are estimated to be a few ten per cent and the contribution of photonuclear reactions to absorbed dose and dose equivalents are underestimated for incident photons above 140 MeV.

Effective dose conversion coefficients for high-energy electrons

Effective dose

Figure 6 shows the effective dose conversion coefficients in various irradiation geometries [13] calculated using the EGS4 code. At 50 MeV, the effective doses are generally in agreement with irradiation geometries for the reason that the range of electrons with 50 MeV was semi-empirically estimated to be about 16 cm and nearly equal to the thickness of the phantom. Below 50 MeV, the maximum effective dose is found at AP geometry. Above 100 MeV, RLAT and ISO geometries show the maximum effective doses. The effective dose for ROT geometry is nearly averaged values for AP and LAT geometries. The difference of effective doses between RLAT and LLAT resulted from the position of the stomach (left) and the liver (right).

Figure 7 shows a comparison of effective doses with those calculated by Ferrari, *et al.* [14]. Tsuda, *et al.* assumed the contribution of photonuclear reaction below a photon energy of 140 MeV and established effective dose to be 10% for all irradiation geometries. The value of 10% is provisional, and is a rough value based on the discussion about the contribution of photonuclear reactions to the absorbed doses by charged particles below 140 MeV to compare with Ferrari's data. The effective dose conversion coefficients for the electromagnetic cascade shower in the energy range over 10 MeV were multiplied by 1.1. In the energy range below 10 MeV, effective dose is a good agreement with Ferrari's data and became nearly 10% larger than Ferrari's data over 10 MeV.

Dose contribution due to photonuclear reactions from high-energy electrons

Dose contribution due to photonuclear reactions from high-energy electrons was evaluated using the EGS4 code following the same procedure as for photons. The predominant charged particles were recoil ions for (γ, n) and (γ, p) reactions and protons for (γ, p) reactions, due to the larger cross-sections than for other reactions. The maximum ratio in the energy range up to 500 MeV was about 0.6%. In the other cases, the maximum ratio was 0.9% and 0.8% for ISO and ROT geometries, respectively. The averaged quality factors of charged particles produced by the photonuclear reactions can be roughly estimated to be 10 from Sato's calculation [6]. Then the contribution of photonuclear reaction to effective dose will be about 6%, 9% and 8% for AP, ISO and ROT geometries, respectively.

Fluence to dose conversion coefficients for high-energy alpha particles

Effective dose

Alpha particles are one of the main radiations in galactic cosmic rays (GCR). Yoshizawa, *et al.* [15] calculated fluence-to-effective dose conversion coefficients for high-energy alpha particles in AP, PA and ISO irradiation geometries. The results are shown in Figure 8. In ICRP 60 [16], w_R for alpha particles is recommended to be 20 in all energy regions.

Effective dose equivalent and mean quality factor

The fluence to effective dose equivalent conversion coefficients for high-energy alpha particles in AP, PA and ISO irradiation geometries were calculated using the Q-L relationship [16]. The effective dose equivalents for high-energy alpha particles are about ten times lower than effective dose. Mean quality factors, the effective dose equivalent divided by the effective absorbed dose, are shown in Figure 9 with radiation weighting factors (w_R). The w_R for alpha particles is about ten times larger than mean quality factors – about 50 MeV/nucleon (200 MeV in the total energy). For alpha particle calculations with HETC-3STEP, nuclear reactions are simply approximated as the sum of neutron and proton individual reactions [17]. It will be necessary to develop a new heavy ion transport code to estimate doses from heavy ion.

Trial estimation of fluence to dose conversion coefficients for neutrons and protons with energies up to 100 GeV

Average quality factors for high-energy charged particles

The EFQ5d code was revised to calculate the average quality factors of charged particles up to 100 GeV. In this code, the stopping power of protons up to 10 GeV was calculated by the SPAR code, and that of pions and muons was evaluated by the proton's value with the modification of mass correction of pions and muons. For heavy ions, the STOPPING code and SPAR were used below 10 MeV/nucleon and above 10 MeV/nucleon, respectively. The stopping power data of charged particles up to 100 GeV are also calculated by the same code as below 10 GeV, because the consistency of dose conversion coefficients is needed below and above 10 GeV. Figure 10 shows the average quality factors of protons, pion, alpha, ^{12}C and ^{16}O particles evaluated by the Q-L relationship in ICRP Pub. 60. Heavy charged particles such as ^{12}C and ^{16}O have average quality factors larger than 1.0 above 10 GeV.

Effective dose for high-energy neutrons

Figure 11 shows the fluence to effective dose for high-energy neutrons with Ferrari's results [18]. Our results above 10 GeV are smaller than Ferrari's, and this discrepancy is caused by the difference in the nuclear reaction model. We need the consideration for the scaling model for nuclear reaction calculations above 3.5 GeV nucleons.

Effective dose for high-energy protons

Figure 12 shows the fluence to effective dose for high-energy protons with Ferrari's results [19]. Our results above 10 GeV are also smaller than Ferrari's under the same circumstances in the case of neutrons. We need the same consideration for the scaling model.

Conclusions

After the SATIF-4 meeting, four evaluation activities concerning dose conversion coefficients for high-energy radiations were executed in Japan. The following results were obtained:

1. $H^*(10)$ is not a reasonable estimation of the effective dose for high-energy photons above 10 MeV. The radiation risk can be estimated with the maximum effective dose in various irradiation geometries instead of the operational quantities. The calculated contribution of photonuclear reactions to dose equivalent was 5% for a photon energy of 30 MeV, which is significant for high-energy photons when considering the secondary charged particles and recoil nuclei.
2. Fluence to effective dose conversion coefficients for electrons up to 10 GeV using the EGS4 code, including the charged particles produced by the photonuclear reactions, were generally in agreement with Ferrari's results using the FLUKA code. We need a more exact estimation using the averaged quality factors for charged particles due to photonuclear reactions.
3. From the comparison between w_R and mean quality factors concerning alpha particles, it was found that w_R is about 10 times larger than mean quality factors.
4. Fluence to effective dose conversion coefficients for neutrons and protons above 10 GeV are smaller than Ferrari's results and this discrepancy is caused by the difference in the nuclear reaction model.

REFERENCES

- [1] O. Sato, *et al.*, *J. Nucl. Sci. Tech.*, 36 [11], 977 (1999).
- [2] W.R. Nelson, H. Hirayama, W.O. Rogers, SLAC-265 (1985).
- [3] A. Ferrari, *et al.*, *Radiat. Prot. Dosim.*, 67 [4], 245 (1996).
- [4] A. Fassò, Proc. 2nd Workshop on Simulating Accelerator Radiation Environments, Geneva, Switzerland, 1995, OECD Publ. 158 (1997).
- [5] International Commission on Radiological Protection, "Conversion Coefficients for Use in Radiological Protection Against External Radiation", ICRP Publication 74, Pergamon Press, Oxford (1996).
- [6] O. Sato, *et al.*, *J. Nucl. Sci. Tech.*, Supplement 1, 861 (2000).
- [7] T. Fukahori, T. Murata, private communication.
- [8] P.D. Allen, M.A. Chaudi, *Phys. Med. Biol.*, 33 [9], 1017 (1988).

- [9] P. Close, *et al.*, KFA-IRE-EAN 12/88 (1988).
- [10] Y. Asano, private communication.
- [11] N. Kishida, JAERI-M 92-122 (1992).
- [12] T.A. Gabriel, M.P. Guthrie, O.W. Hermann, ORNL-4687 (1971).
- [13] S. Tsuda, A. Endo, Y. Yamaguchi, O. Sato, submitted for the proceedings of 10th Congress of International Radiation Protection Association (IRPA10) (2000).
- [14] A. Ferrari, *et al.*, *Radiat. Prot. Dosim.*, 69, 97 (1997).
- [15] N. Yoshizawa, *et al.*, *J. Nucl. Sci. Tech.*, Supplement 1, 865 (2000).
- [16] International Commission on Radiological Protection, “1990 Recommendations of the International Commission on Radiological Protection”, ICRP Publication 60, Pergamon Press, Oxford (1991).
- [17] T.W. Armstrong, *et al.*, *Nucl. Instr. Meth.*, 169, 161 (1980).
- [18] A. Ferrari, M. Pelliccioni, M. Pillon, *Radiat. Prot. Dosim.*, 71 [3], 165 (1997).
- [19] A. Ferrari, M. Pelliccioni, M. Pillon, *Radiat. Prot. Dosim.*, 71 [2], 85 (1997).

Table 1. Comparison of fluence to effective dose conversion coefficients of Sato, *et al.*[1], Ferrari, *et al.* [3] and data in ICRP 74 [5] in AP geometry

AP (anterio-posterior)		(Sv·cm ² /10 ¹² photons)	
Energy (MeV)	Present work	Ferrari, <i>et al.</i>	ICRP 74
1	4.58±0.4%	4.47±2.4%	4.48
3	9.92±0.5%	9.94±2.1%	9.89
5	13.4±0.8%	13.6±2.0%	14.0
10	20.8±0.7%	21.6±2.8%	23.8
15	28.4±0.7%		
20	33.5±0.6%	34.4±3.5%	
50	52.6±0.5%	55.5±2.4%	
100	66.1±0.5%	70.6±3.7%	
500	85.4±0.9%	93.7±3.6%	
1 000	91.3±0.8%	103±3.4%	
10 000	105±0.9%	110±3.0%	

Figure 1. Effective dose calculated in AP, PA, RLAT, LLAT, ROT and ISO geometries using the EGS4 code

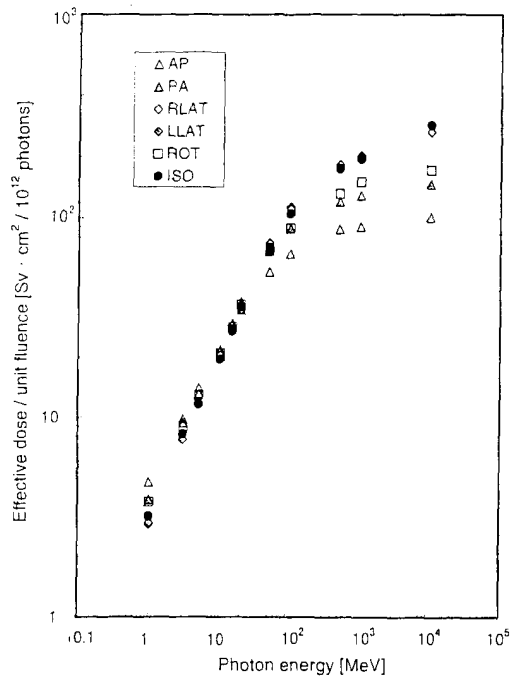


Figure 2. Contribution of each organ or tissue to effective dose in AP geometry

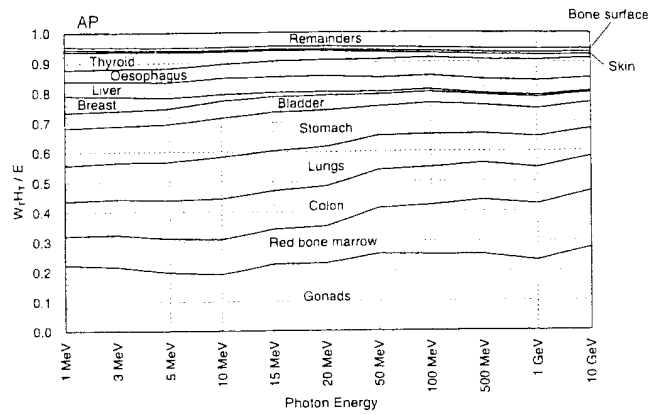


Figure 3. Dose equivalent distribution on the principal axis of the ICRU sphere calculated by using EGS4

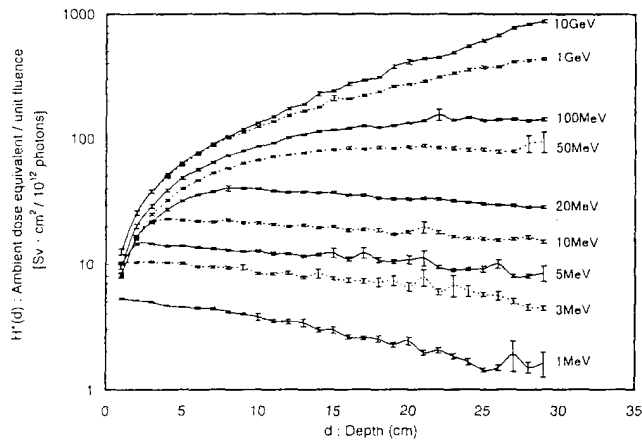


Figure 4. Comparison of the maximum effective doses and ambient dose equivalents, $H^*(d)$ at 1, 5, 10, 15 and 20 cm depth on the principal axis of the ICRU sphere

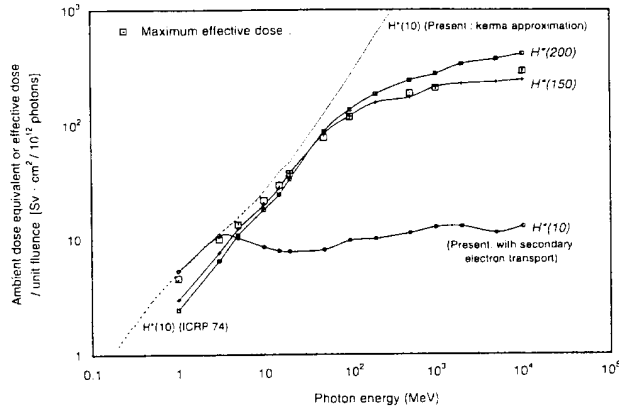


Figure 5. Ratios of dose equivalent deposited by photonuclear reactions to electromagnetic reactions

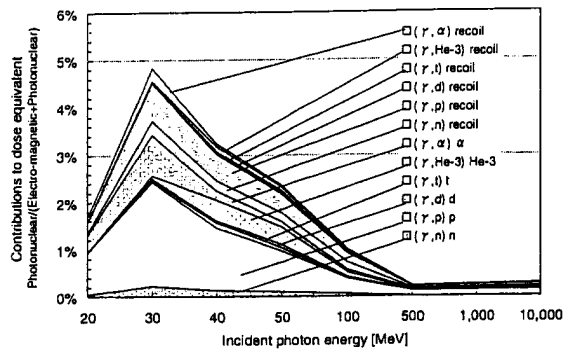


Figure 6. Effective dose per unit fluence as a function of incident electron energy

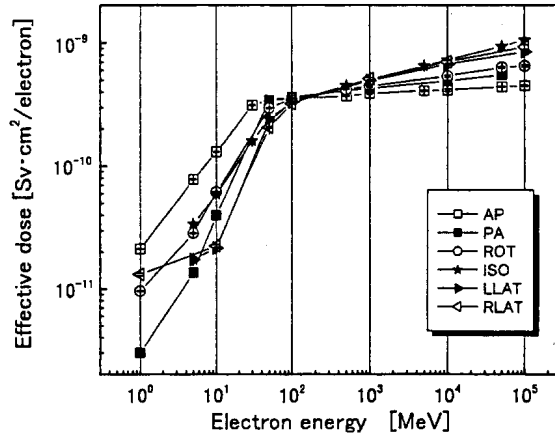


Figure 7. The comparison of effective doses with Ferrari's data

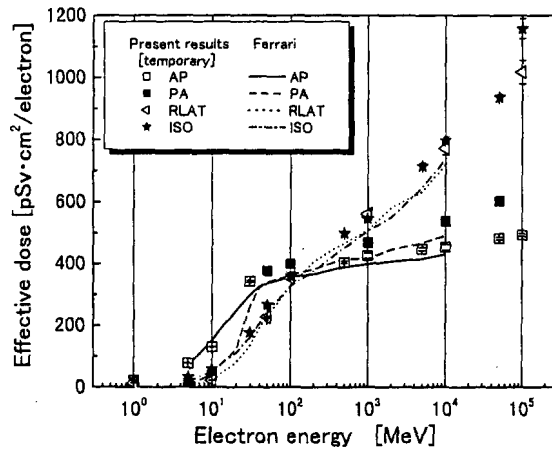


Figure 8. Fluence to effective dose and effective dose equivalent conversion coefficients calculated using w_R and Q-L relationship for alpha particle

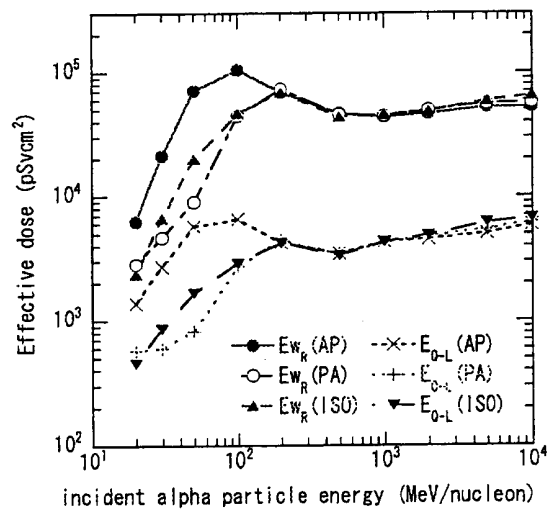


Figure 9. Mean quality factor of alpha particles for whole body and w_R given in ICRP 60

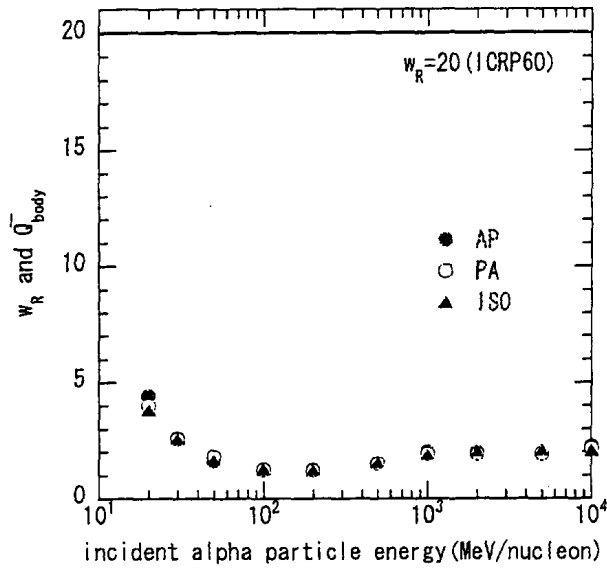


Figure 10. Average quality factors of protons, pion, alpha, carbon and oxygen particles evaluated by the Q-L relationship in ICRP 60

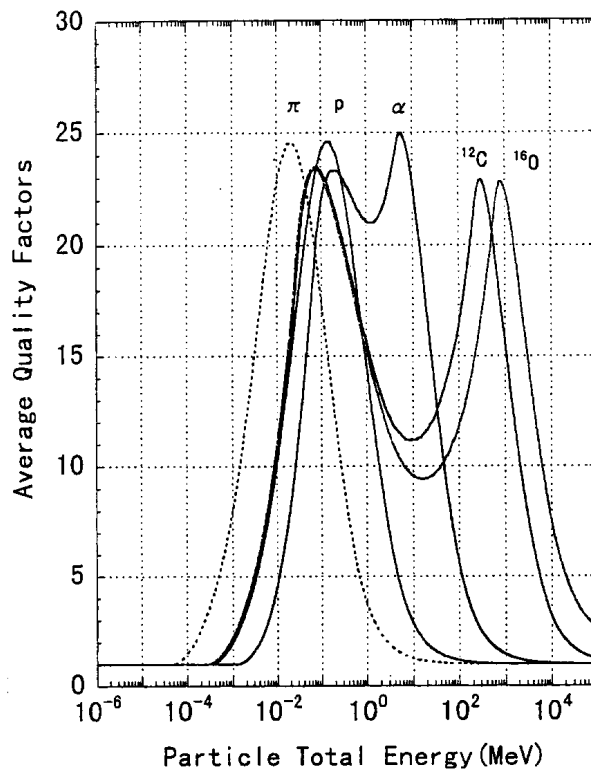


Figure 11. Fluence to effective dose conversion coefficients for high-energy neutrons

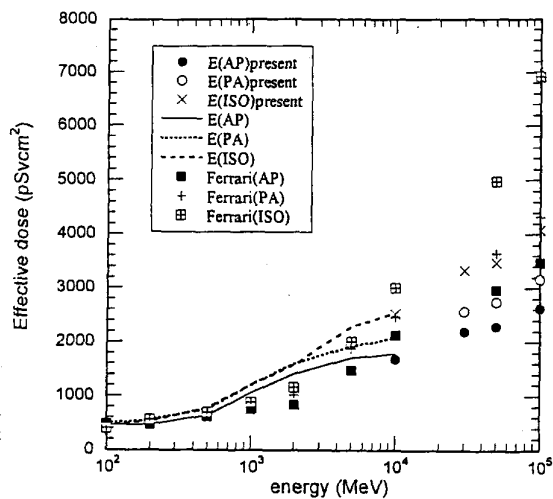
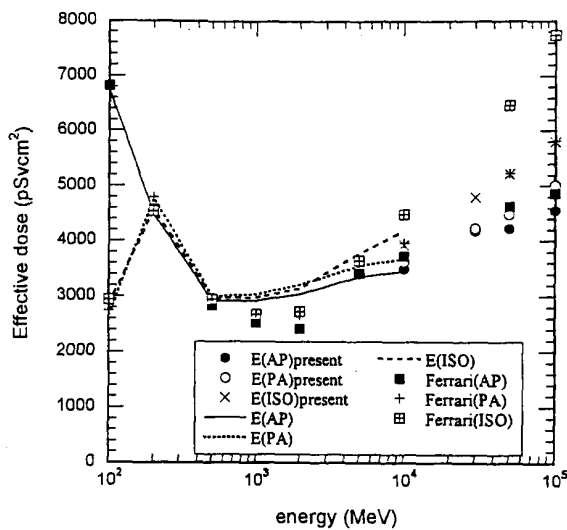


Figure 12. Fluence to effective dose conversion coefficients for high-energy protons



Anthropomorphic Computational Models

EFFECTIVE DOSE AND ORGAN DOSES DUE TO GAS BREMSSTRAHLUNG FROM ELECTRON STORAGE RINGS

Maurizio Pelliccioni

INFN, Laboratori Nazionali di Frascati, 00044 Frascati, Italy

Marco Silari, Luisa Ulrici

CERN, 1211 Geneva 23, Switzerland

Abstract

Bremsstrahlung on residual gas is an important source of beam losses in electron-positron storage rings. The bremsstrahlung photons are emitted in a narrow cone in the forward direction, which produces a “hot spot” of dose at the end of a straight section. Estimates of radiation hazard due to gas bremsstrahlung have so far been performed by calculating the maximum dose equivalent (MADE) or similar quantities. However, the use of quantities conceived for broad parallel beams in the case of very narrow beams significantly overestimates the organ doses and effective dose. In this paper a more sophisticated computational model was used to calculate values of effective dose and absorbed doses in various organs due to gas bremsstrahlung X-rays generated by 0.1-10 GeV electrons. The bremsstrahlung photons generated by the interaction of a mono-energetic electron beam in a 1 m long air target were made to impinge on a selected organ of an hermaphrodite anthropomorphic mathematical model placed at 1 and 10 m distances from the end of the target. Organ dose and effective dose were calculated for five representative organs, namely the right eye, ovaries, breast, testes and thyroid. Fits to the calculated values are given, as well as the dependence of photon fluence and dosimetric quantities on various parameters. The results are compared with previous estimates based on MADE and with values of ambient dose equivalent.

Introduction

Bremsstrahlung on residual gas is an important source of beam losses in high-energy electron/positron circular accelerators. The bremsstrahlung photons are emitted in a narrow cone in the forward direction; in the arcs this effect gives rise to a distributed radiation fan in the bending plane, whilst in the straight sections it generates a much more collimated radiation source. This narrow and concentrated radiation cone produces a “hot spot” of dose at the end of a straight section. In a collider, where the beams circulate on a closed orbit without being extracted, this can be a source of background in the experiments (see, for example, Ref. [1]) or cause radiation damage to electronic components, but does not constitute a radiological hazard. In a high-energy collider the radiation environment is in any case dominated by synchrotron radiation (in LEP, for example, this is up to several tens of grey per hour at 100 GeV beam operation [2]). On the other hand, in a synchrotron light source this concentrated source of bremsstrahlung X-rays may represent a serious radiation hazard, leading to personnel exposure, if channelled outside the accelerator through the beam lines down to the experimental areas. Gas bremsstrahlung and the associated photon-neutrons produced by interactions of the energetic X-rays with beam line components and photon stoppers may dictate in some instances the shielding requirements [3-7]. This phenomenon is of particular relevance for Φ -factories, which have a luminosity much higher than other electron storage rings [8].

Fluence rates and absorbed dose rates due to gas bremsstrahlung have been measured at several facilities [7,9-16] and calculated by various authors using both analytical and Monte Carlo methods [3-6,8,17-21]. Estimates of radiation hazard due to gas bremsstrahlung have so far been performed by calculating the maximum dose equivalent (MADE) or similar quantities. However, the use of quantities conceived for broad parallel beams in the case of very narrow beams significantly overestimates the organ doses and effective dose. The aim of the present paper is to provide – by using a more sophisticated computational model – values of effective dose and absorbed doses in various organs due to gas bremsstrahlung X-rays generated by 0.1-10 GeV electrons. This energy range covers accelerators from Φ -factories like DaΦne in Frascati to third generation synchrotron light sources such as ELETTRA in Trieste (2 GeV electrons), the European Synchrotron Radiation Facility in Grenoble (6 GeV), the Advanced Photon Source at Argonne National Laboratory (7 GeV) and SPring-8 in Japan, currently the facility with the highest stored electron energy (8 GeV). The calculations were performed with the latest version of the Monte Carlo transport code FLUKA (Fluka98) [22-23]. In the 0.1-1 GeV energy range the results are compared with previous estimates based on MADE [20] and with values of ambient dose equivalent.

Monte Carlo calculations

The calculations were made in two steps. First, the fluence rate of bremsstrahlung X-rays produced by interaction of a mono-energetic electron beam with an air target was calculated. In a second step this bremsstrahlung source was used to irradiate a selected organ of an anthropomorphic mathematical model (sometimes called “phantom”).

For the first step new calculations were made for electron energies of 5 and 10 GeV, using the same procedure adopted in Ref. [20] and briefly recalled here. For lower energies (0.1-1 GeV) the fluence rates of Ref. [20] were employed. In the simulations a storage ring straight section is modelled by an air target hit by a pencil electron beam. Although the actual composition of the residual gas is different from air, it has been shown that they are equivalent in terms of average values of the atomic number [17]. Because of the low interaction probability at the operating pressure of a storage ring (typically in the range of about 10^{-7} - 10^{-8} Pa or 10^{-9} - 10^{-10} torr), the calculations were performed with the gas density corresponding to atmospheric pressure and the results linearly scaled to a reference

pressure of 1.33×10^{-7} Pa (10^{-9} torr). The multiple scattering was suppressed in the FLUKA simulations because it is negligible at low operating pressures, while it is responsible for a large broadening of the beam at atmospheric pressure. It should be underlined that the above assumptions allow a correct simulation of the angular distribution of the emitted photons, avoiding fictitious widening due to scattering processes.

It has been shown before that in the energy range 0.1-1 GeV the photon fluence scales with length of the straight section, L , and distance from its end, d , according to a term of the form $L/d(L+d)$, to an accuracy better than 1% [20]. This dependence is verified for $L = 1-50$ m and $d = 1 - 500$ m; the minimum scoring distance required to avoid errors is 20 cm. For the present calculations the length of the straight section was set at $L = 1$ m, and the photon fluence was scored at distances $d = 1$ m and $d = 10$ m. At both distances scoring was performed in 14 concentric detectors of radius ranging from 5×10^{-4} cm to 10 cm. These scoring areas are small enough to avoid underestimates of the fluence but are sufficiently large to keep the computing time within reasonable values [12,20]. The energy cuts were set at 10 MeV for charged particles and at 10 keV for photons.

In Ref. [20] photon fluences were transformed into maximum dose equivalent using the conversion coefficients for broad parallel beam given in Ref. [24]. In the present work a more correct and sophisticated model was adopted in the second step of the simulations. The bremsstrahlung photons were made to impinge on a selected organ of an hermaphrodite anthropomorphic mathematical model placed at 1 and 10 m distances from the end of the straight section. The phantom was derived from the male phantom developed for MCNP by GSF-Forschungszentrum für Umwelt und Gesundheit (Germany) [25]. The MCNP phantom was translated in terms of bodies and regions appropriate for the combinatorial geometry of FLUKA [26], then the female organs (breast, ovaries, uterus) were added. Additional changes with respect to the original model concern the representation of bone surfaces and red bone marrow. Five representative organs were chosen as target organs for the present study, namely the right eye, ovaries, breast, testes and thyroid. The eye and they thyroid are the organs which are most likely to be irradiated in an accidental situation, whilst testes and ovaries are the most important ones from a radiation protection viewpoint (i.e. they have the largest values of the tissue weighting factor w_T defined below). Breast was chosen because it represents a case in which two target organs with different w_T values are irradiated simultaneously, since when breast is the target organ the lung is exposed at the same time. These five target organs should provide a fairly comprehensive picture of the different irradiation conditions, and the results can be used for a radiological estimation in case of a real exposure where a different organ may be involved. Both the dose to the target organs and the effective dose were calculated. Here we shall just recall that the effective dose E is the sum of the weighted equivalent doses H_T in all tissues and organs of the body [27]:

$$E = \sum_T w_T H_T \quad (1)$$

where H_T is in turn given by:

$$H_T = \sum_R w_R D_{T,R} \quad (2)$$

in which $D_{T,R}$ is the absorbed dose averaged over the tissue or organ T due to radiation R , and w_T and w_R are the tissue weighting factors and the radiation weighting factors, respectively, as provided by the International Commission on Radiological Protection [27]. For photons of any energy $w_R = 1$. For testes and ovaries $w_T = 0.2$, for lung $w_T = 0.12$, for breast and thyroid $w_T = 0.05$. There is no w_T value associated to the eye.

All results given in the next section are normalised to one circulating electron and to a pressure of 1.33×10^{-7} Pa (10^{-9} torr).

Results and discussion

An example of the bremsstrahlung photon source generated in the first simulation step is shown in Figures 1 and 2 for 1 GeV electrons and $d = 1$ m. Figure 1 shows the angular distribution of the integral fluence, while Figure 2 shows the photon spectral fluences in 9 out of the 14 detectors (the three inner ones and the two outer ones are not shown). First, it was verified that Eq. (1) of Ref. [20]:

$$\Phi = 1.9 \times 10^{-18} \left(\frac{K}{mc^2} \right)^2 \frac{L}{d(L+d)} I \frac{p}{p_0} \quad (3)$$

which was given for energies up to 1 GeV, is valid for energies up to 10 GeV. This is true for $d \geq 10$ m. Here K is the primary electron energy in MeV, I is the beam current in electrons per second, $p_0 = 1.33 \times 10^{-7}$ Pa, p is the operating pressure in Pa, d and L as defined above.

In the second step of the calculations, photons from the 14 regions of the source were sampled in position and energy and made to impinge on one of the five organs of the model selected as the target. Both the effective dose E and the organ dose D_T were determined. The calculated results are shown in Figures 3-6 for scoring distances of $d = 1$ m and $d = 10$ m from the end of a 1 m long straight section ($L = 1$ m). From Figures 3 and 4 one sees that above 200 MeV the dose to the ovaries exceeds the dose to the eye due to the effect of build-up. The effective dose (Figures 5 and 6) increases with the increasing organ weighting factor and with the decreasing mass of the target organ, as expected. By comparing Figures 3 and 4 one also sees that at high energy the values of D_T for any given organ are not much different for 1 m and 10 m distances. The same is valid for the effective doses (compare Figures 5 and 6). This can be explained by the fact that at high energies the beam is extremely well focussed and therefore its angular spreading with distance is very limited.

Figures 3-6 also show the fits to the calculated values according to the law:

$$\begin{aligned} D_T &= A_D + B_D \log K && \text{(Gy per electron) and} \\ E &= A_E + B_E \log K && \text{(Sv per electron)} \end{aligned} \quad (4)$$

where K is the energy of the circulating electron in GeV. The parameters of the fits for the various target organs are given in Table 1 along with their range of validity. At short distances ($d = 1$ m) Eq. (4) is generally valid over almost the entire energy range investigated, 0.1-10 GeV. At larger distances ($d = 10$ m) the fits tend to fail at the lower energy end, in particular in the case of the ovaries (for both D_T and E) and the right eye (for D_T). Very similar results are obtained by using in Eq. (4) the natural rather than the decimal logarithm (with a different set of fitting parameters A_D , B_D and A_E , B_E).

When the pencil photon beam hits the target organ, the rest of the phantom also absorbs a certain dose released by secondary radiation. The effective dose is thus the sum of a main contribution from the target organ and several minor contributions from the other tissues. The fraction of effective dose due to non-target organs is shown in Figures 7 and 8 for $d = 1$ m and $d = 10$ m, respectively. This fraction is relatively large for large organs (although for the breast this is essentially an artefact: a large fraction of the non-target dose is due to the lung which in practice is also target) and progressively decreases with organ size, being as low as a few per mil for the testes. This is easily explained by the fact that, as the beam is very small, the smaller the organ the larger the absorbed dose in the target (Figures 3 and 4). When the eye is the target organ there is no contribution to the effective dose from the target since there is no associated w_T value [27].

Table 1. Parameters A_D , B_D and A_E , B_E in Eq. (4). The energy range over which the fits are valid to better than 15% is given in the last column.

Organ dose D_T [Gy per electron]; $d = 1$ m			
Organ	A_D (Gy)	B_D (Gy)	Range of validity (GeV)
Breast	9.70E-27	5.06E-27	0.1-10
Ovaries	3.53E-25	3.53E-25	0.25-10
Testes	4.29E-26	2.56E-26	0.25-10
Thyroid	4.39E-26	2.75E-26	0.1-10
Right eye	2.63E-25	1.83E-25	0.25-10
Effective dose E [Sv per electron]; $d = 1$ m			
Organ	A_E (Sv)	B_E (Sv)	Range of validity (GeV)
Breast	1.91E-27	1.35E-27	0.1-10
Ovaries	7.08E-26	7.07E-26	0.25-10
Testes	8.60E-27	5.12E-27	0.25-10
Thyroid	2.32E-27	1.42E-27	0.1-10
Right eye	5.19E-28	3.87E-28	0.25-10
Organ dose D_T [Gy per electron]; $d = 10$ m			
Organ	A_D (Gy)	B_D (Gy)	Range of validity (GeV)
Breast	7.96E-27	6.79E-27	0.1-10
Ovaries	2.50E-25	3.71E-25	5-10
Testes	3.22E-26	3.40E-26	0.8-10
Thyroid	3.42E-26	3.33E-26	0.51-10
Right eye	1.56E-25	2.22E-25	5-10
Effective dose E [Sv per electron]; $d = 10$ m			
Organ	A_E (Sv)	B_E (Sv)	Range of validity (GeV)
Breast	1.70E-27	1.55E-27	0.25-10
Ovaries	5.04E-26	7.45E-26	5-10
Testes	6.46E-27	6.77E-27	0.51-10
Thyroid	1.88E-27	1.73E-27	0.25-10
Right eye	5.10E-28	4.28E-28	0.1-10

The linear dependence found previously (Eq. (2) of Ref. [20]) of maximum dose equivalent (MADE) on parameters d and L [i.e. $(L/d(L+d))$] is no longer valid for D_T and E . Similarly, there are no reasons to expect the same dependence on electron energy (i.e. $K^{2.67}$). This is in a way obvious and it is due to various reasons. First, D_T and E are totally different quantities with respect to MADE and the calculations are performed in a geometry (the mathematical model) which is quite different from the simplified phantom used to calculate MADE. Second (although less important), in Ref. [20] only the photon emission at 0° was considered, whilst in the present paper the total emission is taken into account in calculating E and D_T .

The dependence of organ doses and effective dose on parameters d and L was studied for one energy value, $K = 510$ MeV, and for one target organ, the ovaries. It was found that both D_T and E depend on d and L according to the law:

$$\left(\frac{Ld}{L+d} \right)^3 \quad (5)$$

valid in the range $d = 1 - 25$ m and $L = 1 - 50$ m, usually to within 15%. Eq. (5) is a weakly increasing function of d and L . Since it is symmetric in d and L , if one variable is kept constant, Eq. (5) tends to be an asymptotic value while increasing the second variable. If the phantom is placed at a given distance d from the end of the straight section, both the organ dose and the effective dose increase only smoothly with the length of the air target. This means that the most important contribution to the photon fluence comes from the last section of the target. On the other hand, if the length of the air target is kept constant, organ dose and effective dose again slowly increase with distance from the target. This is perhaps less intuitive to understand, but it can be explained by the high collimation of the photon beam, which practically stays centred on the target organ whatever the distance at which the phantom is located. For such a narrow beam, the distance from the target thus plays only a minor role. A complete assessment of this effect would require extending the present study to other electron energies and other organs.

To our knowledge there are no other studies reporting calculations of effective dose and organ doses for gas bremsstrahlung beams to which the present results could be directly compared. The available experimental data also usually refer to slab irradiation. A comparison can thus only be made with previous results given in terms of MADE. The values of effective dose calculated here are compared with the MADE previously estimated in the 0.1-1 GeV energy range [20] and to the ambient dose equivalent $H^*(10)$. Values of MADE are those calculated with Eq. (2) of Ref. [20]. Values of $H^*(10)$ were calculated by folding the photon fluences in the 14 detectors with the fluence to ambient dose equivalent conversion coefficients of Ref. [28] and taking the highest of the 14 values thus obtained. The results are compared in Table 2, where it is shown that MADE largely overestimates $H^*(10)$, which in turn largely overestimates the effective dose. This drastic reduction in the estimated risk yielded by the use of the effective dose can be explained by the fact that the beam is very narrow and is thus not irradiating the whole phantom but only a fraction of a selected organ. In a first approximation this purely geometric factor re-scales the dose by the ratio of the beam areas. In addition, the target organ is bigger (in some cases much bigger) than the detectors which intercept the largest fraction of the photon fluence (at each given distance the fluence is concentrated in a few detectors, the others contributing much less). In calculating MADE [20] the phantom was uniformly irradiated by the maximum fluence, whilst in the present calculations the maximum fluence is limited to a realistic surface area of the target organ, which may be as small as a fraction of mm^2 .

Conclusions

The radiological hazard posed by a narrow beam of high-energy photons generated by the interaction of an electron beam with the residual gas in an accelerator vacuum chamber has been assessed by Monte Carlo calculations. An anthropomorphic mathematical model has been employed to calculate values of effective dose and absorbed doses in five target organs (right eye, ovaries, breast, testes and thyroid). Gas bremsstrahlung X-rays generated by 0.1-10 GeV electrons were considered. A comparison of the present results with estimates based on MADE and ambient dose equivalent have shown that the use of the latter quantities leads to unrealistic overestimates of the radiological risk.

Table 2. Comparison of effective dose E and ambient dose equivalent $H^*(10)$ (as calculated in the present work) with maximum dose equivalent (MADE) [20]

All quantities are calculated at $d = 1$ m from the end of a 1 m long air target. Units are Sv per electron. The comparison is made in the range 0.1-1 GeV since previous MADE estimates were limited to this energy interval.

E_e (MeV)	E					$H^*(10)$	MADE
	Ovaries	Breast	Testes	Thyroid	Eye		
100	8.1×10^{-27}	6.0×10^{-28}	2.9×10^{-27}	8.6×10^{-28}	1.6×10^{-28}	7.4×10^{-26}	4.6×10^{-25}
250	2.6×10^{-26}	1.1×10^{-27}	5.7×10^{-27}	1.5×10^{-27}	2.9×10^{-28}	4.8×10^{-25}	5.3×10^{-24}
510	4.5×10^{-26}	1.5×10^{-27}	7.3×10^{-27}	1.9×10^{-27}	3.8×10^{-28}	4.3×10^{-24}	3.5×10^{-23}
800	6.2×10^{-26}	1.8×10^{-27}	8.6×10^{-27}	2.2×10^{-27}	4.7×10^{-28}	8.7×10^{-24}	1.2×10^{-22}
1 000	6.7×10^{-26}	1.8×10^{-27}	8.7×10^{-27}	2.3×10^{-27}	4.9×10^{-28}	1.1×10^{-23}	2.1×10^{-22}

Given the present lack of literature data on dosimetry of narrow gas bremsstrahlung beams, the five target organs selected for the present study should provide a fairly comprehensive picture of the different irradiation conditions which might be encountered. The present results along with the fits to the calculated values and the dependence of photon fluence and dosimetric quantities on the various parameters should be of help in estimating the radiological risk in case of an exposure where a different organ may be involved and under different conditions than those considered here.

REFERENCES

- [1] G. Von Holtey, *et al.*, *Nucl. Instr. and Meth.*, A 403 (1998), 205.
- [2] N. Conan, F. Pirote, M. Silari and L. Ulrici, Internal Report CERN TIS-RP/IR/99-32 (1999).
- [3] N.E. Ipe and A. Fassò, Proc. of the 8th International Conference on Radiation Shielding, Arlington (Texas, USA), 24-28 April 1994, American Nuclear Society (1994), 659.
- [4] N.E. Ipe and A. Fassò, *Nucl. Instr. and Meth.*, A 351 (1994), 534.
- [5] J.C. Liu, W.R. Nelson and K.R. Kase, *Health Phys.*, 68 (1995), 205.
- [6] Y. Asano and N. Sasamoto, *Radiat. Prot. Dosim.*, 82 (1999), 167.
- [7] M. Pisharody, E. Semones and P.K. Job, *Nucl. Instr. and Meth.*, A 430 (1999), 542.
- [8] A. Ferrari, L. Liberatori and M. Pelliccioni, *Health Phys.*, 68 (1995), 383.
- [9] A. Esposito and M. Pelliccioni, Proc. of the XX Midyear Topical Symposium of the Health Physics Society, Reno (USA), CONF-8602106 (1987), p. 495.
- [10] H. Hirayama, S. Ban and S. Miura, *Nucl. Sci. Eng.*, 96 (1987), 66.

- [11] S. Ban, H. Hirayama and S. Miura, *Health Phys.*, 53 (1987), 67.
- [12] A. Ferrari, M. Pelliccioni and P.R. Sala, *Nucl. Instr. and Meth.*, B 82 (1993), 32.
- [13] A. Esposito, A. Ferrari, L. Liberatori and M. Pelliccioni, *Nucl. Instr. and Meth.*, B 88 (1994), 345.
- [14] M. Pisharody, P.K. Job, S. Magill, J. Proudfoot and R. Stanek, *Nucl. Instr. and Meth.*, A 401 (1997), 442.
- [15] P.K. Job, M. Pisharody and E. Semones, *Nucl. Instr. and Meth.*, A 438 (1999), 540.
- [16] P.K. Job, M. Pisharody and E. Semones, Proc. of the 9th International Conference on Radiation Shielding, Tsukuba (Japan), 17-24 October 1999 (in press).
- [17] A. Rindi, *Health Phys.*, 42 (1982), 187.
- [18] S. Ban, H. Hirayama and S. Miura, *Health Phys.*, 57 (1989), 407.
- [19] G. Tromba and A. Rindi, *Nucl. Instr. and Meth.*, A 292 (1990), 700.
- [20] A. Ferrari, M. Pelliccioni and P.R. Sala, *Nucl. Instr. and Meth.*, B 83 (1993), 518.
- [21] A. Esposito, L. Liberatori, M. Pelliccioni, A. Ferrari and P.R. Sala, Proc. of the 1st Specialists Meeting on Shielding Aspects of Accelerators, Targets and Irradiation Facilities, Arlington (Texas, USA), 28-29 April 1994, NEA/OECD (1995), p. 227.
- [22] A. Fassò, A. Ferrari, J. Ranft and P.R. Sala, Proc. of the Third Workshop on Simulating Accelerator Radiation Environments (SARE-3), Tsukuba (Japan), H. Hirayama, ed., KEK Proceedings 97-5 (1997), 32.
- [23] A. Ferrari, T. Rancati and P.R. Sala, Proc. of the Third Workshop on Simulating Accelerator Radiation Environments (SARE-3), Tsukuba (Japan), H. Hirayama, ed., KEK Proceedings 97-5 (1997), 165.
- [24] D.W.O. Rogers, *Health Physics*, 46 (1984), 891.
- [25] R. Kramer, M. Zankl, G. Williams and G. Drexler, GSF-Forschungszentrum für Umwelt und Gesundheit, Neuherberger, GSF-Bericht S885 (1982).
- [26] M. Pelliccioni and M. Pillon, *Radiat. Prot. Dosim.*, 67 (1996), 253.
- [27] ICRP Publication 60, 1990 Recommendations of the International Commission on Radiological Protection, Pergamon Press (1991).
- [28] A. Ferrari and M. Pelliccioni, Proc. of the 8th International Conference on Radiation Shielding, Arlington (Texas, USA), 24-28 April 1994, American Nuclear Society (1994), 893.

Figure 1. Angular distribution of the integral fluence of the bremsstrahlung photons generated in 1 m long straight section by 1 GeV electrons

The target is air at a pressure of 1.33×10^{-7} Pa (10^{-9} torr). The fluence is scored at 1 m distance from the end of the straight section and is normalised to one circulating electron.

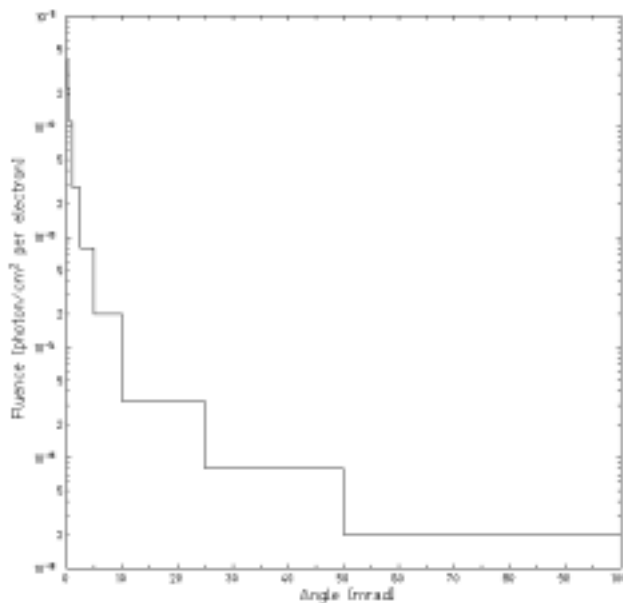


Figure 2. Photon spectral fluences in 9 out of the 14 detectors labelled by their angular coverage (the three inner ones and the two outer ones are not shown)

Same conditions as for Figure 1

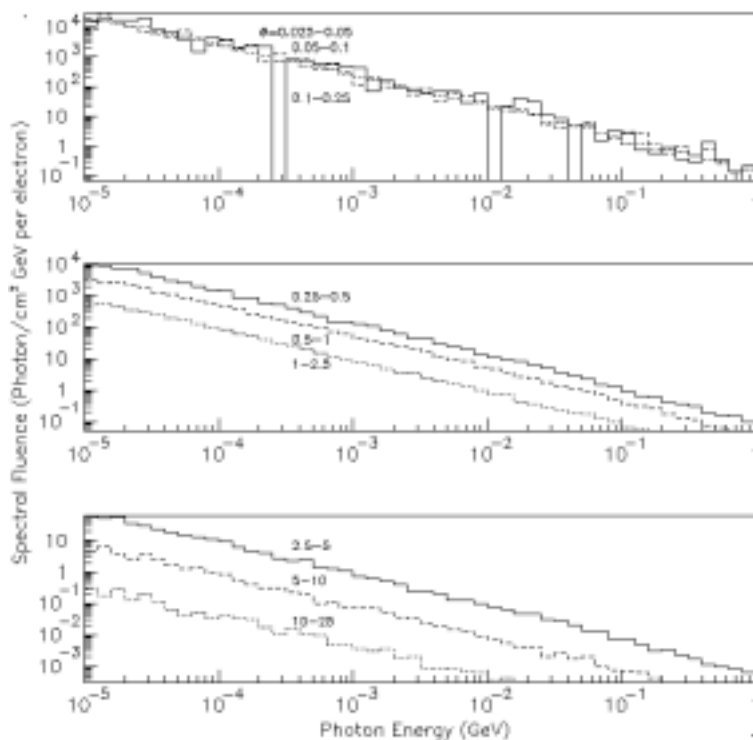


Figure 3. Dose to various target organs, D_T , with the phantom placed at a distance $d = 1$ m from the end of a 1 m long straight section

A fit according to the law $D_T = A_D + B_D \log K$ is shown. The parameters A_D and B_D are given in Table 1.

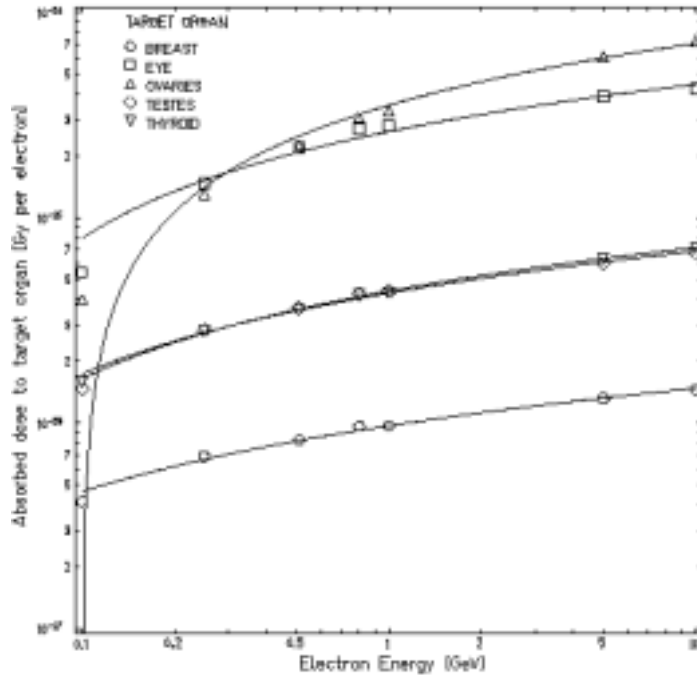


Figure 4. Dose to various target organs, D_T , with the phantom placed at a distance $d = 10$ m from the end of a 1 m long straight section

A fit according to the law $D_T = A_D + B_D \log K$ is shown. The parameters A_D and B_D are given in Table 1.

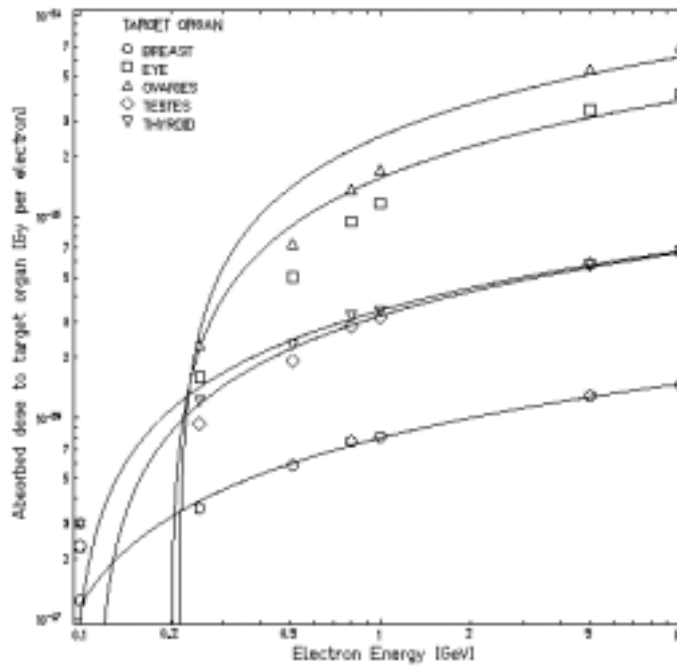


Figure 5. Effective dose E for various target organs, with the phantom placed at a distance $d = 1$ m from the end of a 1 m long straight section

A fit according to the law $E = A_E + B_E \log K$ is shown. The parameters A_E and B_E are given in Table 1.

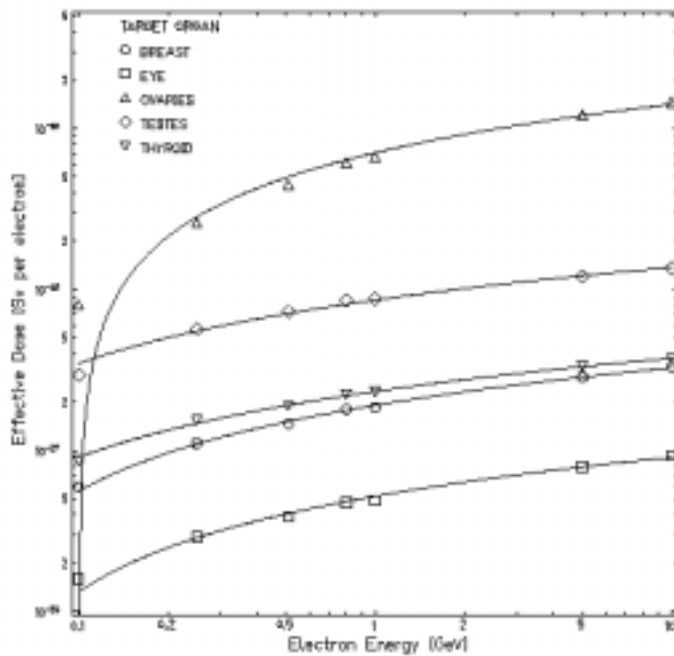


Figure 6. Effective dose E for various target organs, with the phantom placed at a distance $d = 10$ m from the end of a 1 m long straight section

A fit according to the law $E = A_E + B_E \log K$ is shown. The parameters A_E and B_E are given in Table 1.

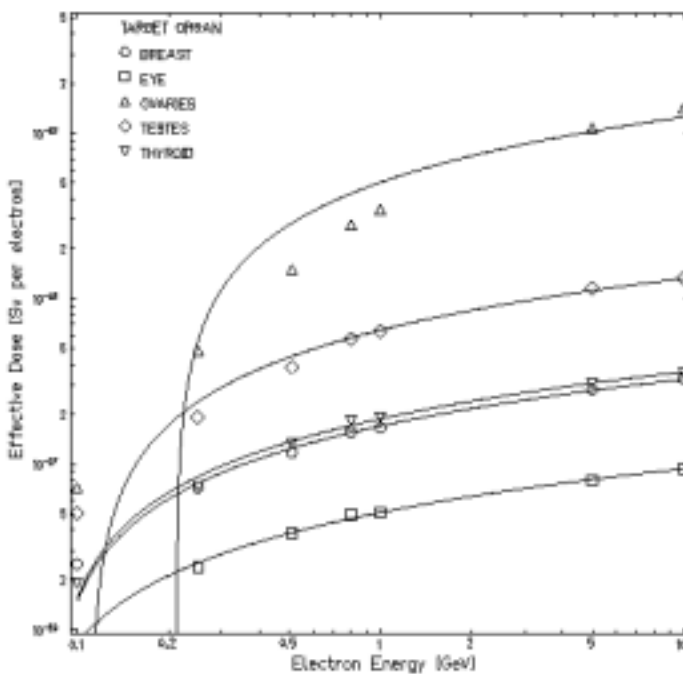


Figure 7. Fraction of effective dose due to non-target organs, for $d = 1$ m and for the five target organs

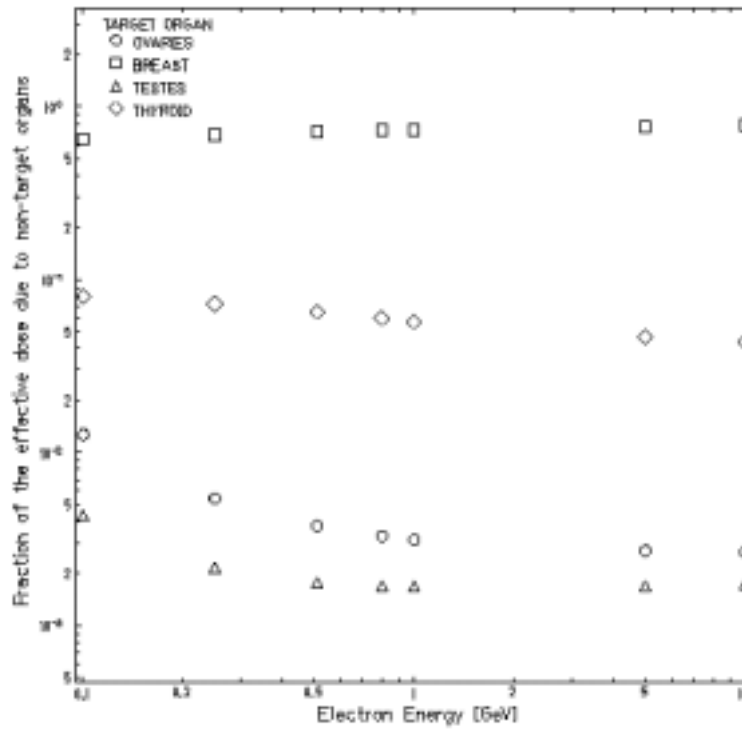
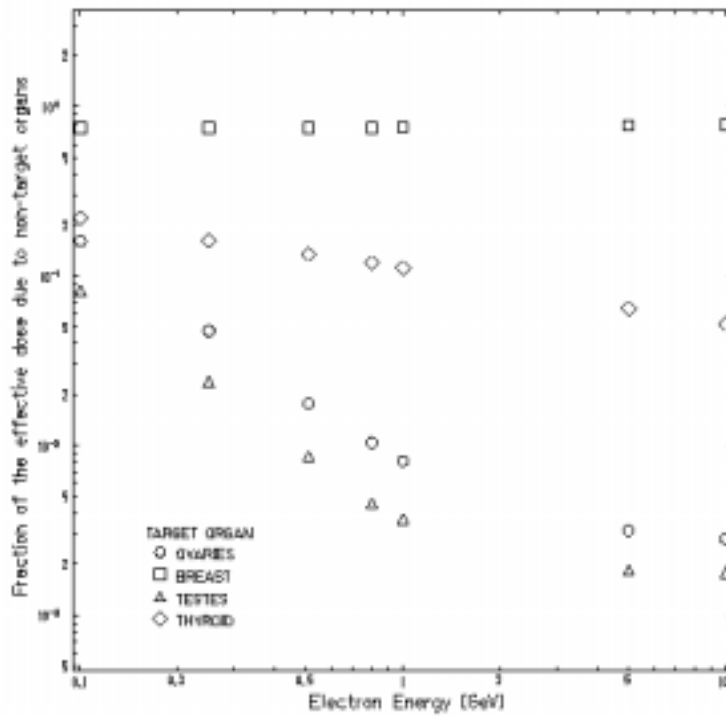


Figure 8. Fraction of effective dose due to non-target organs, for $d = 10$ m and for the five target organs



SESSION VI

Additional Topics

Chairs: B. Kirk, A. Leuschner

**PROGRESS REPORT ON THE COLLECTION OF COMPUTER CODES
AND DATA SETS FOR ACCELERATOR SHIELDING ANALYSIS**

Enrico Sartori and Pedro Vaz
OECD/NEA Data Bank
12, Boulevard des Iles
92130 Issy-les-Moulineaux, France

Jennifer B. Manneschildt, Hamilton T. Hunter and Bernadette L. Kirk
Radiation Safety Information Computational Centre (RSICC)
Oak Ridge National Laboratory
Oak Ridge, TN 37831-6362, USA

Abstract

The four specialists meetings on Shielding Aspects of Accelerators, Targets and Irradiation Facilities (SATIF-1, SATIF-2, SATIF-3 and SATIF-4) held in Arlington, Texas (1994), Geneva, Switzerland (1996), Sendai, Japan (1997) and Knoxville, Tennessee (1998) have produced an increasing interest in the collection of computer software and associated data sets for accelerator shielding. The Radiation Safety Information Computational Centre (RSICC) and the Nuclear Energy Agency Data Bank (NEA DB) continue to pursue the task of collecting these codes for the interest of the community.

Introduction

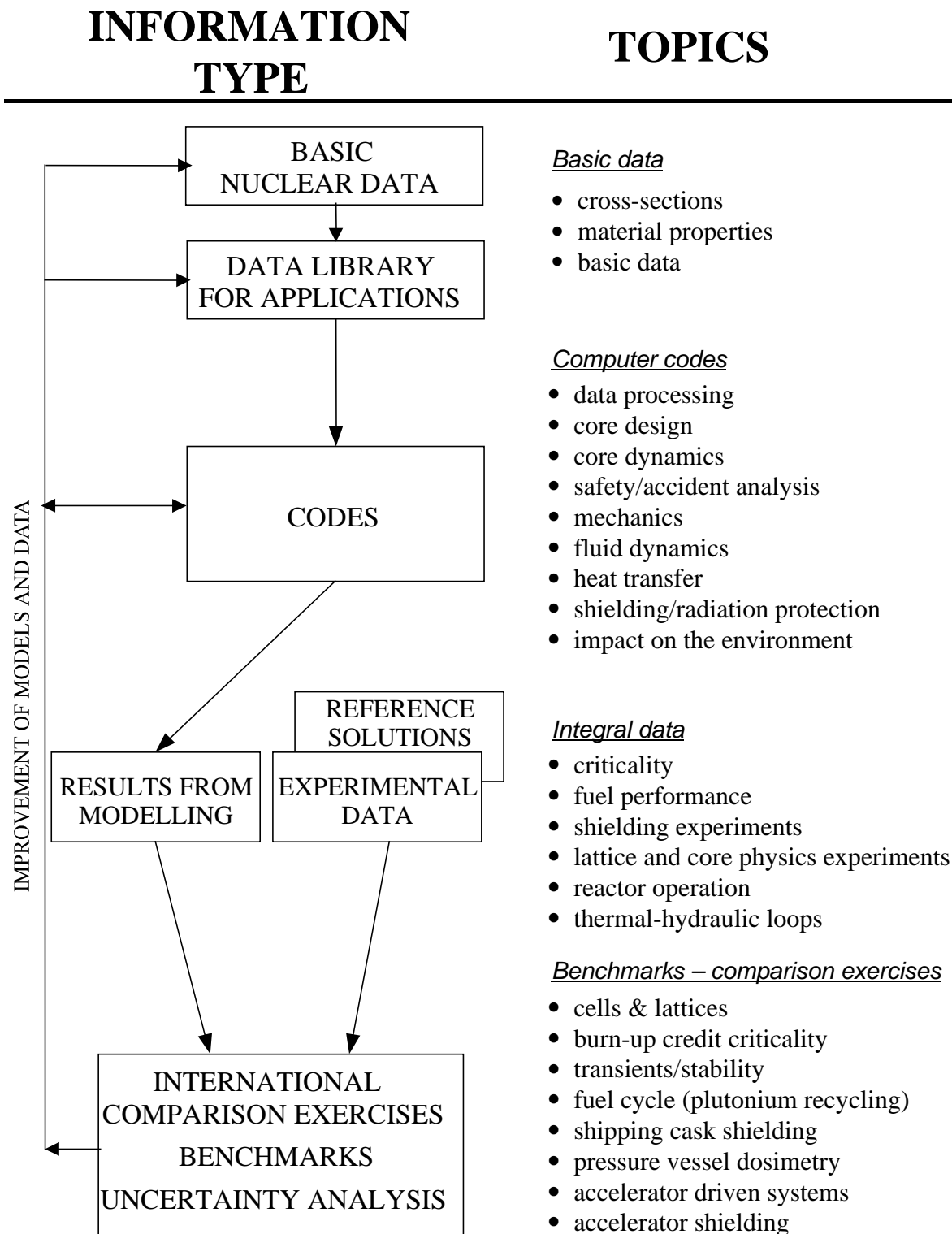
The Radiation Safety Information Computational Center (RSICC) and the OECD/NEA Data Bank have developed in close co-operation over the years an infrastructure that assures that the tools required for modelling in nuclear and radiation applications are made available to the international community. The three basic components needed by users for validation of modelling tools are:

1. *Basic nuclear data, derived application data libraries, group constants, continuous energy data.* The basic particle interaction data is described in numerical form in evaluated nuclear data libraries such as ENDF/B-VI, JEF-2, JENDL-3 and others. These libraries are very general and describe within the energy range considered (in most cases in the range of 10^{-5} - $20 \cdot 10^6$ eV but for some nuclides extended to $150 \cdot 10^6$ eV) all basic phenomena (neutron interaction cross-section, photon production, photon interaction cross-section, fission yields and radioactive decay data). These contain information in great detail and in a form not directly usable by computer codes. There is consequently a need to filter out relevant information and to condense it to a form appropriate for applications (e.g. multi-group cross-section libraries, continuous energy cross-section libraries, etc.). The computer code system most widely used for that purpose is NJOY.
2. *Computer codes carrying out different modelling aspects.* The computer codes used in most nuclear applications have the role of bridging the gap between the underlying microscopic phenomena and the macroscopic effects. They also accumulate, in a readily usable way using a mathematical and algorithmic language, the wealth of physics knowledge that science and technology have acquired during the last half century. In many cases these computer codes can have a relatively complex structure; in addition they also contain associated data libraries (for generic applications or project oriented), application dependent code/data sequences, test problems, etc. In some instances the basic nuclear data are directly generated from nuclear models rather than extracted from data libraries. This is relatively common for medium and high-energy particle transport.
3. *Integral experiments databases.* Integral experiments concern measurements on a system consisting of different components. The measured values describe the macroscopic behaviour of the system (e.g. attenuation of dose through a complex shield, level of reactivity of a reactor or a spent fuel transportation cask, decay heat, level of burn-up, etc.). They allow gauging the combined use of computational methods and basic data used to the real world values. They are the references needed for model development, verification and validation.

Integral experiments come with clearly stated and documented uncertainties in the form of confidence bounds of the measured values and a correlation matrix describing the relative independence of the measurements carried out. An integral experiment is complete if it includes a final phase of interpretation of the results. The interpretation is the part that gives insight into the phenomena and into the way they are appropriately modelled.

Computer codes and basic nuclear data have been thoroughly checked in a number of cases, be it known reference solutions or experiments. However, the number of possible combinations of their use is so big that a large and possibly comprehensive database of well-characterised experiments is needed. With such databases sufficient confidence can be built such that methods and procedures used for design, operation and safety analysis would be adequate. Figure 1 shows the interplay of the different components.

Figure 1. Procedures, data and computer codes for model validation and improvement



Progress since SATIF-4 (September 1998) – highlights

Since the SATIF-4 meeting in Knoxville, USA in September 1998, the following codes have been made available from either RSICC or NEA DB and which are relevant or of interest for modelling shielding aspects of accelerators, targets and irradiation facilities. [Note: computer code collection (CCC), peripheral shielding routine (PSR) and data library collection (DLC) are RSICC designations.]

- ABAREX (PSR-0248). An optical-statistical model program developed for the calculation and fitting of energy-averaged neutron cross-sections. One version is isotopic ABAREX, the other is elemental ABAREX, which is an extension designed for the interpretation of neutron interactions with elemental targets consisting of up to ten isotopes. The contributions from each of the isotopes of the element are explicitly dealt with and combined for comparison with the elemental observers.
- CHEMENGL/CHIMISTE (NEA-1561). Database on basic chemical and physical properties of the elements in the Mendeleev Table such as electric density and thermal conductivity, masses of isotopes and isomers, ionisation potential, etc. from H to Xc ($A = 112$). Improvements include crystallographic data, nuclear masses; information on solar abundance of elements has been added.
- DWBA98 (NEA-1209). The distorted wave Born approximation (DWBA) is used. DWBA98 includes a fully microscopic non-local optical model obtained with the description of the target by its occupation numbers and with the two-body interaction for the initial and final distorted waves. The effective interaction is input as a quasi-potential operator, which generates plane wave t - g -matrix elements equal to those generated from some nucleon nucleon potentials. The effective interaction may comprise central, tensor, (LS) , L^2 and $(LS)^2$ operator components with Yukawa form factors and complex density dependent strengths. Minimum relativity makes allowance for DWBA98 to be used for projectiles at low and medium energy.
- EAF 99 (NEA-1609). The European Activation File (EAF) is the collection of nuclear data that is required to carry out inventory calculations of materials that have been activated following exposure to neutrons. One of the components of EAF is the collection of neutron-induced cross-section data. The current release of the European Activation File, EAF-99, contains cross-section data of neutron-induced reactions for energies between 10^{-5} eV and 20 MeV and data for 98 elements from H to Fm, but excludes data for the short-lived radioactive elements At and Fr. There are a total of 766 target isotopes, including ground, first and second isomers, which have non-zero cross-sections (i.e. greater than 10^{-8} b) below an energy of 20 MeV. Cross-sections to and from isomeric states are listed separately in a pointwise format. This leads to a total of 12 468 reaction channels that contain data.
- EASY-97 (NEA-1564). The European Activation System (EASY) is a complete tool for the calculation of activation in materials exposed to neutrons. It can be used for any application (fusion, transmutation, fission and accelerator) where the neutron energy does not exceed 20 MeV. EASY-97 consists of the inventory code FISPACT-97, EAF-97 and the FENDL-2.0 activation file, which contains various libraries of nuclear data. FISPACT is an inventory code that solves a set of stiff first order differential equations by means of a numerical method.
- EMPIRE-II (IAEA1169). EMPIRE-II calculates nuclear reactions in the framework of combined optical, Multistep Direct (TUL), Multistep Compound (NVWY) and statistical (Hauser-Feshbach) models. The incident particle can be a nucleon or any nucleus (heavy ion).

Isomer ratios, residue production cross-sections and emission spectra for neutrons, protons, alpha-particles, gamma-rays and one type of light ion can be calculated. The energy range starts just above the resonance region for neutron induced reactions and extends up to several hundreds of MeV for the heavy ion induced reactions.

- GCASCAD (IAEA1362). GCASCAD is designed to calculate, using the statistical model, the gamma-ray branching ratios and the photon production cross-sections. The gamma-ray transmission coefficients are calculated using one of several possible forms for gamma-ray strength functions: Brink-Axel giant dipole model, Kopecky-Uhl generalised Lorentzian model, Weisskopf single-particle model. In the continuum part of level spectrum the level density is treated with the Gilbert-Cameron composite formula.
- JENDL-3.2 (NEA-1470). JENDL-3.2 (Japanese Evaluated Nuclear Data Library, Version 3, Revision 2) is an evaluated nuclear data library which consists of neutron nuclear data and secondary gamma-ray data for 340 nuclides for neutrons energies up to 70 MeV. Numerical data and graphs are included. The data stored are the original data and point-wise data (0 K and 300 K) of JENDL-3.2 and graphs of cross-sections.
- JENDL/D-99 (NEA-1624). Contains information for 47 nuclides and 67 reactions in both the SAND-II group structure and as 0 K processed point-wise energy files. The point-wise files also include unresolved resonance parameters for self-shielding calculations, but cross-sections are given explicitly in the point-wise format (MF=3).
- MARLOWE15 (PSR-0137). The MARLOWE program simulates atomic collisions in crystalline targets using the binary collision approximation. It follows out the consequences of launching an energetic atomic projectile, from either an external beam or an interior site, into a target. The program follows the slowing down of the primary particle and, if desired, that of all target particles which are displaced from their lattice sites, until they either leave their target or fall below a selected low kinetic energy.
- MCNP-4C (CCC-0700). MCNP is a general-purpose, continuous-energy, generalised geometry, time-dependent, coupled neutron-photon-electron Monte Carlo transport code system.
- MCNPDATA (DLC-0200). These cross-section libraries are released by Los Alamos National Laboratory for use with the MCNP-4C Monte Carlo code package.
- NJOY99 (PSR-0480). The NJOY nuclear data processing system is a modular computer code used for converting evaluated nuclear data for incident neutrons, photons and charged particles in the ENDF format into libraries useful for applications calculations. NJOY provides comprehensive capabilities for processing evaluated data, and it can serve applications ranging from continuous-energy Monte Carlo (MCNP), through deterministic transport codes (DANT, DOORS), to reactor lattice codes (WIMS, EPRI). NJOY handles a wide variety of nuclear effects, including resonances, Doppler broadening, heating (KERMA), radiation damage, thermal scattering (even cold moderators), gas production, neutrons and charged particles, photo-atomic interactions, self-shielding, probability tables, photon production and high-energy interactions (to 150 MeV).
- NMTC/JAERI-97 (NEA-0974). High-energy nuclear reactions induced by incident high-energy protons, neutrons and pions are simulated with the Monte Carlo method by the intra-nuclear nucleon-nucleon reaction probabilities based on an intra-nuclear nucleon cascade model of BERTINI followed by the particle evaporation including high-energy fission process.

An intra-nuclear cascade model (ISOBAR code) taking into account the in-medium nuclear effects and the pre-equilibrium calculation model based on the exciton one are also implemented for simulating the nuclear reactions. Inter-nuclear transport processes of the incident and secondary nucleons in macroscopic material regions are simulated with the Monte Carlo method and a continuous slowing down model for charged particles.

- NucDecayCalc (DLC-202). This database was designed to address needs concerning medical, environmental and occupational radiation protection. It contains the unabridged data used in preparing ICRP Publication 38. It consists of data on the energies and intensities of radiation emitted by the 825 radionuclides reported. The utility code DecayCalc extracts the decay data from the library for radionuclide(s) specified by the user. It computes the activities of radionuclides present after decay and ingrowth over a user-specified time period from 1 minute to 50 years. Decay data for any decay chain may be displayed and printed either in tabular form or graphically.
- NUCLEUS-CHART (NEA-1492). NUCLEUS is an interactive PC-based graphical viewer of NUBASE nuclear property data. NUBASE contains experimentally known nuclear properties, together with some values that have been estimated from extrapolation of experimental data for 3 039 nuclides. NUBASE also contains data on those isomeric states that have half-lives greater than 1 millisecond; there are 669 such nuclides of which 58 have more than one isomeric state.
- PCNUDAT32.2.8 (USCD1205). The PCNUDAT program gives access to nuclear data extracted from several databases. The data consists of nuclear level information, decay gamma information, nuclear ground/metastable state properties, nuclear radiation, thermal neutron cross-sections and resonance integrals.
- PHENOM/BCS-COLLI (IAEA1327). Empirical estimations of the rotational and vibrational enhancements in the nuclear level density obtained from the analysis of fragmentation cross-sections.
- RADDECAY (DLC-0134). RADDECAY is a data library of half-lives, radioactive daughter nuclides, probabilities per decay and decay product energies for alpha particles, positrons, electrons, X-rays and gamma-rays. The current database contains approximately 500 nuclides of interest in the nuclear fuel cycle, environmental problems, nuclear medicine, fusion reactor technology and radiological protection assessment.
- SCAT-2 (NEA-0829). SCAT-2 is designed as a fast, easy-to-use program to calculate total cross-sections, elastic scattering cross-sections and their angular distributions and transmission coefficients from the optical model of a spherical nucleus. The calculation is performed at a specified set of energies for one of the following incident particles: neutron, proton, deuteron, triton, helium-3, alpha or heavy ions.
- SOURCES4A (CCC-0661). Determines (α ,n); spontaneous fission; and (β ,n) delayed neutron sources and spectra due to the decay of radionuclides. The previous version, SOURCES3A, calculated (α ,n) source rate and spectra for three problem types: homogeneous medium, interface and α -beam problems. The new version, SOURCES4A, code will also calculate (α ,n) source rate and spectra in a thin neutron-producing region between two α -producing regions.
- SRIM2000 (NEA-0919). SRIM is a group of programs which calculate the stopping and range of ions (10 eV-2 GeV/amu) into matter. The transport of ions in matter (TRIM) will

accept complex targets made of compound materials with up to eight layers, each of different materials. It will calculate both the final 3-D distribution of the ions and also all kinetic phenomena associated with the ion's energy loss: target damage, sputtering, ionisation and phonon production. All target atom cascades in the target are followed in detail. It can be used for physics of recoil cascades, physics of sputtering, the stopping of ions in compounds and stopping powers for ions in gases. This includes radiation damage from neutron, electrons and photons.

- STAPREF (NEA-0461). Calculation of energy-averaged cross-sections for nuclear reactions with emission of particles and gamma rays and fission. The models employed are the evaporation model with inclusion of pre-equilibrium decay and a gamma-ray cascade model. Angular momentum and parity conservation are accounted for. Recent improvements include level density approach, generalised super-fluid model, Boltzmann-gas modelling of intrinsic state density and semi-empirical modelling of a few-quasi-particle effects in total level density at equilibrium and saddle deformations of actinide nuclei.
- STARCODES (PSR-0330). Collision stopping powers are calculated from the Bethe theory, with a density-effect correction evaluated according to Sternheimer. The stopping-power formula contains an important parameter, the mean excitation energy (I-value), which characterises the stopping properties of a material. The codes provide output for electrons in any stopping material (279 provided) and for protons and helium ions in 74 materials.
- SUS3D (NEA-1628). SUS3D calculates sensitivity coefficients for one-dimensional, two-dimensional and three-dimensional deterministic transport problems. Variance and standard deviation of detector responses or design parameters can be obtained using cross-section covariance matrices. In neutron transport problems, this code is able to perform sensitivity-uncertainty analysis for secondary angular distribution (SAD) or secondary energy distribution (SED).
- TART98 (CCC-0638). TART98 is a coupled neutron-photon, three-dimensional, combinatorial geometry, Monte Carlo transport code. It is a complete system assisting with input preparation, running Monte Carlo calculations, and analysis of output results. It can calculate: 1) static reactivity problems, 2) dynamic reactivity problems, 3) source problems involving any combination of neutron and/or photon sources. TART 98 uses the latest ENDF/B-VI, Release 5, neutron data and Evaluated Photon Data Library '97 (EPDL97).
- ZOTT99 (IAEA1371). Carries out data evaluation using partitioned least squares. Given an existing combined set $y(i)$ of differential and integral measurements with completely general covariances $c_{yy}(i,j)$ and a sensitivity matrix relating the expectation values of the various measurements, ZOTT obtains a new evaluation $y_p(i)$ with covariances $c_{y_p y_p}(i,j)$. The results $y_p(i)$ are minimum-variance linear unbiased estimators of the true values, $Expect[y(i)]$.

Please refer to Tables 1-4 for other programs and data libraries available at present. The enclosed lists cover only the subset of nuclear data and codes that are of interest to SATIF activities. Other codes and data of interest, especially involving modelling in nuclear fission and fusion applications can be searched by accessing the following internet pages on:

- Radiation Safety Information Computational Center: <http://www-rsicc.ornl.gov/rsic.html>.
- OECD/NEA Data Bank: <http://www.nea.fr/html/dbprog/>.

These web sites provide also brief description of the functions and the methods used in the computer codes and data.

Progress report on SINBAD, the shielding benchmarks database

The Shielding Integral Benchmark Archive and Database (SINBAD) is an electronic database [5] developed to store a variety of radiation shielding benchmark data. A new edition SINBAD2000 is being released and will contain the data described in Tables 14 and 15. This database is developed jointly by RSICC and the OECD/NEA Data Bank. More detailed information can be found at the following site: <http://www-rsicc.ornl.gov/BENCHMARKS/SINBAD.html>.

REFERENCES

- [1] Proceedings of the Specialists Meeting on Shielding Aspects of Accelerators, Targets and Irradiation Facilities, held in Arlington, Texas (USA), on 28-29 April 1994, published as an OECD document ISBN 92-64-14327-0.
- [2] Proceedings of the Second Specialists Meeting on Shielding Aspects of Accelerators, Targets and Irradiation Facilities (SATIF-2), held at CERN, Geneva (Switzerland), on 12-13 Oct. 1995, published as an OECD document ISBN 92-64-15287-3.
- [3] Proceedings of the Third Specialists Meeting on Shielding Aspects of Accelerators, Targets and Irradiation Facilities (SATIF-3), held at Tohoku University, Sendai, Japan, on 12-13 May 1997, published as an OECD document ISBN 92-64-16071-X.
- [4] Proceedings of the Fourth Specialists Meeting on Shielding Aspects of Accelerators, Targets and Irradiation Facilities (SATIF-4), held at Gatlinburg, TN, USA, on 17-18 September 1998, published as an OECD document ISBN: 92-64-17044-8.
- [5] “Shielding Experimental Benchmark Storage, Retrieval and Display System”, by H.T. Hunter, J.L. Parson, W.J. Marshall, E. Sartori and I. Kodeli, in Proceedings of Ninth International Conference on Radiation Shielding (ICRS9), October 17-22, 1999, Tsukuba, Japan, *Journal of Nuclear Science and Technology*, Supplement 1, March 2000.

Table 1. List of programs and data in alphabetical order

Name

Blank *Programs available.*

** *Programs known but not available.*

*** *Additions/updates since the SATIF-4 meeting.*

Identification

CCC-,PSR-,DLC- *Original packaging by RSICC.*

NESC *Original packaging by NESC (now ESTSC).*

USCD *Originated in US/Canada, packaged by NEA DB.*

NEA, IAEA *Original packaging by NEA DB.*

Blank *Acquisition sought.*

Name	Identification	Function
ABAREX ***	PSR-248	Optical statistical model to calculate energy averaged neutron induced reaction cross-sections
ACTIV-87	IAEA1275	Library with fast neutron activation cross-sections
AIRSCAT	CCC-0341	Dose rate from gamma air scattering, single scat. approx.
ALBEDO	NEA 1353	Gamma, neutron attenuation in air ducts
ALDOSE	CCC-0577	Calculates absorbed dose and dose equivalent rates as function of depth in water irradiated by alpha source
ALICE91 *	PSR-0146	Precompound/compound nuclear decay model
ALPHN	CCC-0612	Calculates the (alpha,n) production rate in a mixture receiving alpha particles from emitting actinides
AMALTHEE	NEA 0675	Emission spectra for n, p, d, h3, he3, alpha reaction
ANISN	CCC-0650	1-D Sn, n, gamma transport in slab, cylinder, sphere
ASOP	CCC-0126	1-D Sn shield calculation (new version for AIX and Linux)
ASTAR	IAEA1282	Calculates stopping power and range for alphas
ASTROS	CCC-0073	Primary/secondary proton dose in sphere/slab tissue
AUJP	IAEA0906	Optical potential parameters search by chi**2 method
BALTORO	NEA 0675	n, gamma transport perturbation from MORSE, ANISN calculation
BASACF	IAEA0953	Integral neutron adjustment and dosimetry
BERMUDA	NEA 0949	1-D,2-D,3-D n, gamma transport for shielding
BETA-2B	CCC-0117	MC time-dependent bremsstrahlung, electron transport
BETA-S3.1	CCC-657	Calculates beta decay source terms and energy spectra
BREESE	PSR-0143	Distribution function for MORSE from albedo data
BREMRAD	CCC-0031	External/internal bremsstrahlung
BRHGAM	CCC-0350	MC absorbed dose from x-rays in phantom
CADE	NEA 1020	Multiple particle emission cross-sections by Weisskopf-Ewing
CALOR95	CCC-0610	MC system for design, analysis of calorimeter system
CAMERA	CCC-0240	Radiation transport and computerised man model
CARP-82	PSR-0131	Multi-group albedo data using DOT angular flux results
CASCADE	CCC-0176	High-energy electron-photon transport in matter
CASIM	NESC0742	MC high energy cascades in complex shields
CCRMN	PSR-355	Computation of reactions of a medium-heavy nucleus with six light particles
CEM95	IAEA1247	MC calculation of nuclear reactions (Cascade Exciton Model)
CENDL	IAEA1256	Chinese Evaluated Nuclear Data Library (neutron, proton, deuteron, triton, He3 and He4)
CEPXS/ONELD	CCC-0544	1-D coupled electron photon multi-group transport
CFUP1	IAEA1266	n, charged-particle reaction of fissile nuclei E < 33 MeV
CHARGE-2/C	CCC-0070	Electron, p, heavy particle flux/dose behind shield
CHEMENGL(***)	NEA-1561	Chemical and physical properties of elements
CHUCK	USCD1021	N, charged particle cross-sections, coupled channel model
CMUP2	IAEA1265	Reaction cross-sections for n, p, d, t, He3, He4, E < 50 MeV
COLLI-PTB	NEA 1126	MC n fluence spectra for 3-D collimator system
COMNUC3B	PSR-0302	Compound nucleus interaction in n reactions
COVFILES	DLC-0091	Library of neutron cross-sections covariance data, useful to estimate radiation damage or heating
DANTSYS	CCC-0547	1-D, 2-D, 3-D Sn neutron, photon transport
DASH	CCC-0366	Void tracing Sn - MC coupling with fluxes from DOT
DCTDOS	CCC-0520	n, gamma penetration in composite duct system
DDCS	IAEA1290	Neutron, proton, deuteron, triton, He3, and alpha induced reactions of medium heavy nuclei up to 50 MeV
DISDOS	CCC-0170	Dose from external photons in phantom
DOORS3.2	CCC-0650	Discrete ordinates system for deep penetration neutron and gamma transport
DORT	CCC-0543	1-D 2-D Sn n, photon transport with deep penetration
DOSDAT-2	DLC-0079	Gamma, electron dose factors data lib. for body organs
DOSEDAT-DOE	DLC-0144	Dose rate factors for external photon, electron exposure

Table 1. List of programs and data in alphabetical order (continued)

Name	Identification	Function
DUST	CCC-0453	Albedo MC simulation of n streaming inducts
DWBA98(***)	NEA 1209	Distorted Wave Born Approximation nuclear model
DWUCK-4	NESC9872	Distorted Wave Born Approximation nuclear model
E-DEP-1	CCC-0275	Heavy ion energy deposition
EADL	DLC-0179	Library of atomic subshell and relaxation data
EAF99(***)	NEA-1609	Cross-section library for neutron induced activation materials
EASY-97 (***)	NEA-1564	European Neutron Activation System
ECIS-95	NEA 0850	Schrodinger/Dirac nuclear model with experimental fit
ECPL-86	DLC-0106	Evaluated charged particle cross-sections
EDMULT	NEA 0969	Electron depth dose in multi-layer slab absorbers
EEDL	DLC-179	Electron interaction cross-section from 10 eV to 100 GeV
EGS4	CCC-0331	MC electron photon shower simulation
ELBA	CCC-0119	Bremsstrahlung dose from electron flux on Al shield
ELPHIC-PC	IAEA1223	Statistical model MC simulation of heavy ion reaction
ELPHO	CCC-0301	MC muon, electron, positron generation from pions
ELTRAN	CCC-0155	MC 1-D electron transport
EMPIRE-MSC	IAEA1169	Multi-step compound nucleus/pre-equilibrium cross-sections
EMPIRE-II(***)	IAEA1169	Comprehensive nuclear model code, nucleons, ions induced cross-sections
ENLOSS	PSR-0047	Energy loss of charged particles
ENDLIB-97	DLC-0179	Coupled electron and photon transport library (in LLL ENDL format)
EPDL-97	DLC-0179	Photon interaction cross-sections library (10 eV to 100 GeV)
EPICSHOW-96.1	IAEA1285	Interactive Viewing of the Electron-Photon Interaction (10 eV < E < 1 GeV)
ERINNI	NEA 0815	Multiple cascades emission spectra by optical model
ESTAR	IAEA1282	Calculates stopping power and range for electrons
ETRAN	CCC-0107	MC electron, gamma transport with secondary radiation
EVA		Codes performing the nuclear evaporation processes (working on the output from ISABEL)
EVALPLOT	IAEA0852	Plots cross-sections in ENDF/B format, angular and energy distributions
EVAP_F **		Modified version of the Dresner evaporation code
EXIFONGAMMA	IAEA1211	n, alpha, proton, gamma emission spectra model
FALSTF	CCC-0351	n, gamma flux detector response outside cylindrical shields
FEM-RZ	NEA 0566	2-D multi-group n transport in r-z geometry
FGR-DOSE	DLC-0167	Library of dose coefficients for intake and exposure to radionuclides
FLEP	DLC-0022	Neutron, proton non-elastic cross-sections and spectra E < 400 MeV
FLUKA	CCC-0207	MC high energy extranuclear hadron cascades
FOTELP/EM	CCC-0581	MC photons, electrons and positron transport
FRITIOF (**)		Hadronic cascades in high-energy heavy ion collisions
FSMN	IAEA1264	Fission spectra by compound-nucleus optical model
FSXLIB-J3R2	NEA 1424	JENDL-3 Evaluated Nuclear Data File, fusion neutronics
G33-GP	CCC-0494	Multi-group gamma scattering using gp build-up factor
GAMMONE	NEA 0268	MC gamma penetration from various geometrical sources
GBANISN	CCC-0628	1-D neutron & gamma fluxes with group band fluxes
GCASCAD	IAEA1362	Gamma production cross-sections from statistical model
GEANT-CERN		
GGG-GP	CCC-0564	Multi-group gamma-ray scattering – build-up factors
GMA	PSR-367	Generalised least squares evaluation of related cross-sections
GNASH-FKK	PSR-0125	Multi-step direct and compound and Hauser Feshbach models
GNASH-LANL	PSR-0125	Pre-equilibrium/statistical cross-sections, emission spectra
GRACE-1	NESC0045	Multi-group gamma attenuation, dose in slab
GRAPE	NEA 1043	Precompound/compound nuclear reaction models
GRPANL	PSR-0321	Germanium gamma and alpha detector spectra unfolding
HELLO	DLC-0058	47 n, 21 gamma group coupled cross-sections from VITAMIN-C library
HERMES-KFA	NEA 1265	MC high-energy radiation transport
HERMES96b	NEA 1265	MC high-energy radiation transport
HETC NMTC	CCC-0178	MC high energy nucleon meson cascade transport
HETC-KFA	CCC-0496	MC high energy nucleon-meson cascades
HETC95 (**)		MC high energy nucleon-meson cascades and transport
HFMOD	IAEA1317	Elastic and inelastic cross-section calculation by Hauser-Feshbach and Moldauer
HFTT	IAEA0954	n cross-sections by compound-nucleus evaporation model
HIC-1	CCC-0249	MC heavy ion reactions at E>50 MeV/nucleon
HIJET (**)		Hadronic cascades in high-energy Heavy Ion Collisions
HILO86	DLC-0119	66 N, 22 gamma group cross-section lib. for ANISN-ORNL, DORT, MORSE-CGA
HILO86R	DLC-0187	66 N, 22 gamma group cross-section, up to 400 MeV (neutron) and 20 MeV (gamma)
HOMO	IAEA1253	Program for mixing/converting libraries in ANISN format

Table 1. List of programs and data in alphabetical order (continued)

Name	Identification	Function
HUGO-VI	DLC-0146	Photon interaction evaluated data library ENDF-6 format
ICOM	CCC-651	Calculate transport characteristics of ion radiation
IDC	CCC-0384	ICRP dosimetric calculational system
IHEAS-BENCH	NEA 1468	High-energy accelerator shielding benchmarks
IMPACTS	ESTS0005	Radiological assessment code
INFLTB	PSR-0313	Dosimetric mass energy transfer and absorption coefficients
ISABEL	NEA 1413	Intra-nuclear cascade model allowing hydrogen and helium ions and antiprotons as projectiles
ISAJET (**)		Hadronic cascades in high-energy heavy ion collisions
ISO-PC	CCC-0636	Kernel integration code system for general purpose isotope shielding
ITS-3.0	CCC-0467	MC system of coupled electron photon transport, photon, neutron dose in electron accelerator
K009	CCC-0062	Charged particle penetration – phantom quantum mechanical multi-step direct model
LA100	DLC-0168	Evaluated data library for n, p up to 100 MeV, ENDF-6 format
LAHET **		MC nucleon, pion, muons, tritons, He-3, alpha transport
LAHIMAC	DLC-0128	Neutron, gamma cross-sections - response functions, E<800MeV
LEP	DLC-0001	Results from intra-nuclear cascade and evaporation
LIMES	NEA 1337	Intermediate mass fragments in heavy ion nuclear reactions
LPPC	CCC-0051	Proton penetration, slab
LPSC	CCC-0064	p, n flux, spectra behind slab shield from p irradiation
LRSPC	CCC-0050	Range and stopping power calculator for ions
MAGIK	CCC-0359	MC for computing induced residual activation dose rates
MAGNA	NEA 0163	Dose rates from gamma source in slab or cylindrical shell shields
MARLOWE15(***)	PSR-0137	Atomic displacement cascades in solids
MARMER	NEA 1307	Point-kernel shielding, ORIGEN-S nuclide inventories
MATXS10	DLC-0176	Library with 30n-12gamma energy groups for particle transport codes
MATXS11	DLC-0177	Library with 80n-24gamma energy groups for particle transport codes
MCNP-4B2	CCC-0660	MC 3-D time-dependent coupled n, photon, electron transport
MCNP-4C(***)	CCC-0700	MC 3-D time-dependent coupled n, photon, electron transport
MCNPDATA(***)	DLC-0200	Cross-section data library for the MCNP-4C transport code
MCNP-VISED	PSR-358	Visual editor for MCNP input
MCNPXS	DLC-0189	Cross-section data for MCNP4B2
MCNPX		The LAHET/MCNP Code merger
MECC-7	CCC-0156	Medium energy intra-nuclear cascade model
MENSLIB	DLC-0084	Neutron 60 group cross-sections, E<60MeV
MERCURE-4	NEA 0351	MC 3-D gamma heating/gamma dose rate, fast flux
MEVDP	CCC-0157	Radiation transport in computerised anatomical man
MICAP	PSR-0261	MC ionisation chamber responses
MIRDOSE3.1	CCC-0528	Calculate internal dose estimates by the MIRD technique
MORSE-CGA	CCC-0474	MC n, gamma multi-group transport
MRIPP 1.0	CCC-0655	Magnetic resonance image phantom for in vivo measurements
MSM-SOURCE	PSR-0369	Estimate stopping characteristics of proton transmissions
MUONLM	NEA 1475	Calorimeter Interaction of Muons
MUP-2	IAEA0907	Fast n reaction cross-sections of medium-heavy nuclei
MUTIL	NEA-1451	Calculates the asymmetry factor of the Mott scattering of electrons and positrons by point nuclei
NDEM (**)		Generates a gamma-ray source from the de-excitation of residual nuclei
NESKA	NEA 1422	Electron, positron scattering from point nuclei
NFCLIST	ESTS0352	Radionuclide decay data tabulations (240 radionuclides)
NJOY-94.61	PSR-0171	n, p, photon evaluated data processing system
NJOY97.0	PSR-355	n, p, photon evaluated data processing system
NJOY99.0(***)	PSR-0480	Data processing system of evaluated nuclear data files ENDF format
NMTC/JAERI	NEA 0974	MC high-energy p, n, pion reactions
NMTC/JAERI-97(***)	NEA-0974	High-energy neutron, proton, pion reaction Monte Carlo simulation
NMF-90	IAEA1279	Database for neutron spectra unfolding
NUCDECAY	DLC-0172	Nuclear decay data for radiation dosimetry calculations
NucDecayCalc (***)	DLC-0202	Nuclear decay data for radiation dosimetry and retrieval program
NUCHART	IAEA1320	Nuclear properties and decay data chart
NUCLEUS		Nuclear spallation simulation and primary products
NUCLEUS-CHART(***)	NEA-1492	Interactive chart of nuclides
OPTMOD	IAEA1316	Elastic & total cross-section, polarisation calculations using the optical model
PACE2 (**)		Codes performing the nuclear evaporation processes (working on the output from ISABEL)
PALLAS-2DY	NEA 0702	2-D n ,gamma transport for fixed source
PCROSS	IAEA1220	Pre-equilibrium emission spectra in neutron reaction
PCNUDAT32.2.8(***)	USCD1205	Nuclear properties database & retrieval system

Table 1. List of programs and data in alphabetical order (continued)

Name	Identification	Function
PEGAS	IAEA1261	Unified model of particle and gamma emission reactions
PENELOPE	NEA 1525	Monte Carlo code for electron-photon transport
PEQAG-2	IAEA1185	Pre-equilibrium model nucleon, gamma spectra, cross-sections
PEREGRINE (**)		Used to model dose to humans from radiation therapy
PHENOM/BCS-COLL(***)	IAEA1327	Nuclear level density of excited nuclei
PHOTX	DLC-0136	Photon interaction cross-section library for 100 elements
PICA	CCC-0160	MC nuclear cascade reactions by the collision of photons (30 < E < 400 MeV) with nuclei
PIPE	NEA 0416	1-D gamma transport for slab, spherical shields
PLACID	CCC-0381	MC gamma streaming in cylindrical duct shields
PNESD	IAEA1235	Elastic cross-sections of 3 MeV to 1 000 MeV p on natural isotopes
POINT97	DLC-0192	Combination of resonance parameters and/or tabulated energy dependent evaluated cross-sections
POTAUS	IAEA1249	H through U ion ranges, stopping power for various materials
PREANG	NEA 0809	Nuclear model particle spectra, angular distribution
PRECO-D2	PSR-0226	Pre-equilibrium, direct reaction double differential cross-sections
PREM	NEA 0888	Nucleon emission pre-equilibrium energy spectra, cross-sections
PREPRO-96	CCC-351	Pre-processing code system for data in ENDF/B format
PSTAR	IAEA1282	Calculates stopping power and range for protons
PTRAN	CCC-0618	MC proton transport for 50 to 250 MeV
PUTZ	CCC-0595	Point-kernel 3-D gamma shielding
QAD-CGGP-A	CCC-0645	Fast neutron and gamma ray penetration in shields
QMD		Intra-nuclear cascade and classical molecular dynamics
RADCOMPT	PSR-0348	Sample analysis for alpha and beta dual channel detect
RADDECAY(***)	DLC-0134	Decay data library for radiological assessment
RADHEAT-V3	NEA 0467	Transport, heat, radiation damage cross-sections in reactor, shield
RAID	CCC-0083	Gamma, n scattering into cylindrical or multi-bend duct
RAF	IAEA1350	Neutron and proton radiative capture differential and integrated cross-section
REAC	CCC-0443	Activation and transmutation
REAC-2	NESC9554	Nuclide activation, transmutation
REAC*3	CCC-0443	Isotope activation and transmutation in fusion reactors
REBEL-3	IAEA0846	MC radiation dose to human organs
RECOIL/B	DLC-0055	Heavy charged particle recoil spectra lib. for radiation damage
REMIT	ESTS0579	Radiation exposure monitoring and inf. transmittal system
REPC	PSR-0195	Dose from protons in tissue
RESRAD5.82	CCC-0552	Calculation of residual radioactive material guidelines, site specific radiation doses and risks
SAM-CE	CCC-0187	MC time-dependent 3-D n ,gamma transport in complex geometry
SAMSY	IAEA0837	n, gamma dose rates, heat source for multi-layer shields
SAND-II	PSR-0345	Determines neutron energy spectra using multiple experimental activation detector data
SANDYL	CCC-0361	MC 3-D time-dependent gamma electron cascade transport
SCAP-82	CCC-0418	Scattering, albedo, point-kernel anal. in complex geometry
SCAT-2(***)	NEA-0829	Spherical optical model for light particles and heavy ions
SCINFUL	PSR-0267	MC response of scintillation neutron detector (incident neutron energies from 0.1 to 75 MeV)
SEECAL	CCC-0620	Age-dependent effective energies for 54 and 32 target regions in the human body (825 radionuclides)
SFERXS	NEA 1239	Photon absorption, coherent, incoherent cross-sections for shielding
SHIELD (**)	IAEA1287	Universal code for exclusive simulation of hadron cascades in complex macroscopic targets
SIGMA-A	DLC-0139	Photon interaction and absorption data 1 KeV-100 MeV
SINBAD97	DLC-191	Shielding INtegral Benchmark Archive DataBase
SINBAD2000		Shielding INtegral Benchmark Archive DataBase
SITHA (**)	IAEA1179	SIMulation Transport HAdron, calculates hadron transport
SKYIII-PC	CCC-0289	PC version of program SKYSHINE-III
SKYPORT	DLC-0093	Importance of n, photon skyshine dose from accelerators
SKYSHINE-KSU	CCC-0646	Computation of gamma skyshine doses by different methods
SNLRML	DLC-0178	Dosimetry library compendium
SNL/SAND-II	PSR-0345	Enhanced version of SAND-II
SOURCE (**)		Description of the proton transmission and generation of n source
SOURCESA4 (***)	CCC-661	(α ,n), spontaneous fission and (β ,n) delayed neutron sources and spectra due to decay in homog. media
SPACETRAN	CCC-0120	Radiation leakage from cylinder with ANISN flux
SPAR	CCC-0228	Stopping power and ranges from muons, pions, protons ions
SPARES	CCC-0148	Space radiation environment and shielding evaluation
SPEC	IAEA1332	Computation of neutron and charged particle reactions using optical and evaporation models
SPCHAIN (**)		Calculates accumulation and decay of nuclides
SPECTER-ANL	PSR-0263	n damage for material irradiation
SRIM-2000 ***	NEA 0919	Stopping power and ranges of ions (10 ev-2 GeV/amu)
STAC-8		Transmitted, absorbed power/spectrum – synchrotron radiation

Table 1. List of programs and data in alphabetical order (continued)

Name	Identification	Function
STAPRE-H95	IAEA0971	Evaporation, pre-equilibrium model reaction cross-sections
STAPREF(***)	NEA-0461	Nuclear reactions cross-sections by evaporation model, gamma-cascades
STARCODE(***)S	PSR-0330	Stopping power, ranges for electrons, protons, alpha
STOPOW	IAEA0970	Stopping power of fast ions in matter
STR92	ESTS1041	Energy deposition in accelerator ring components
STRAGL	CCC-0201	Energy loss straggling of heavy charged particles
SWIMS	ESTS0682	Angular dispersion of ion beams at small-angle incoherent multiple scattering by gaseous or solid media
TART98 ***	CCC-638	3-D MC transport program for neutrons and photons
TNG1	PSR-0298	N multi-step statistical model
TORT	CCC-0543	3-D Sn n, photon transport with deep penetration
TPASGAM	DLC-0088	Library with gamma-ray decay data for 1438 radionuclides
TRANSX2.15	PSR-0317	Code to produce neutron, photon transport tables for discrete ordinates and diffusion codes
TRAPP	CCC-0205	Proton and alpha transport, reaction products neglected
TRIPOLI-3		MC time-dependent 3-D N, gamma transport
TRIPOS	CCC-0537	MC ion transport
TWODANT-SYS	CCC-0547	1-D, 2-D multi-group Sn n, photon transport
UNGER	DLC-0164	Effective dose equivalent data for selected isotopes
UNIFY	IAEA1177	Fast n cross-sections, spectrum calculation for structural materials
UNSPEC	ESTS0827	X-ray spectrum unfolding using an iterative technique
VEGAS (**)		Intra-nuclear cascade code (from which ISABEL is derived)
VIRGIN	IAEA0932	Uncollided neutron flux and neutron reactions due through a neutron beam through any thickness of material
VITAMIN-E	DLC-0113	Cross-section data library with 174n-38gamma energy groups
VITAMIN-B6	DLC-0184	Cross-section data library with 199n-42gamma energy groups from ENDF/B-VI Release 3
XCOM	DLC-0174	Photon cross-sections from 1 KeV to 100 GeV
ZOTT99(***)	IAEA1371	Data evaluation using partitioned least squares

Table 2. Evaluated and processed data (cross-sections, dose conversion, ranges, stopping powers)

Name	Identification	Function
ACTIV-87	IAEA1275	Library with fast neutron activation cross-sections
CENDL	IAEA1256	Chinese Evaluated Nuclear Data Library (neutron, proton, deuteron, triton, He3 and He4)
COVFILES	DLC-0091	Library of neutron cross-sections covariance data, useful to estimate radiation damage or heating
DOSDAT-2	DLC-0079	Gamma, electron dose factors data lib. for body organs
DOSEDAT-DOE	DLC-0144	Dose rate factors for external photon, electron exposure
EADL	USCD1192	Library of atomic sub-shell and relaxation data
EAF99(***)	NEA-1609	Cross-section library for neutron induced activation materials
EASY-97 (***)	NEA-1564	European Neutron Activation System
ECPL-86	DLC-0106	Evaluated charged particle cross-sections
EEDL	USCD1193	Electron interaction cross-section from 10 eV to 100 GeV
ENDLIB-94	DLC-0179	Coupled electron and photon transport library (in LLL ENDL format)
ENDLIB-97	DLC-0179	Coupled electron and photon transport library (in LLL ENDL format)
EPDL-VI/MOD	USCD1187	Photon interaction cross-sections library (10 eV to 100 GeV)
FGR-DOSE	DLC-0167	Library of dose coefficients for intake and exposure to radionuclides
FLEP	DLC-0022	Neutron, proton non-elastic cross-sections and spectra E < 400 MeV
FSXLIB-J3R2	NEA 1424	JENDL-3 Evaluated Nuclear Data File, fusion neutronics
HILO86	DLC-0119	66 n, 22 gamma group cross-section lib. for ANISN-ORNL, DORT, MORSE-CGA
HILO86R	DLC-0187	66 n, 22 gamma group cross-sections, up to 400 MeV (neutron) and 20 MeV (gamma)
HELLO	DLC-0058	47 n, 21 gamma group coupled cross-section from VITAMIN-C library
HUGO-VI	DLC-0146	Photon interaction evaluated data library ENDF-6 format
IDC	CCC-0384	ICRP dosimetric calculational system
IHEAS-BENCH	NEA 1468	High-energy accelerator shielding benchmarks
JENDL-3.2(***)	NEA-1470	Cross-sections data library and plots for neutrons up to 70 MeV
JENDL/D-99(***)	NEA-1624	Dosimetry cross-section data library and plots for neutrons
LA100	DLC-0168	Evaluated data library for n, p up to 100 MeV, ENDF-6 format
LAHIMACK	DLC-0128	Multi-group neutron and gamma cross-sections up to 800 MeV
LEP	DLC-0001	Results from intra-nuclear cascade and evaporation
LRSPC	CCC-0050	Range and stopping power calculator
MATXS10	DLC-0176	Library with 30n-12gamma energy groups for particle transport codes
MATXS11	DLC-0177	Library with 30n-12gamma energy groups
MCNPDATA(***)	DLC-0105	Cross-section data library for the MCNP-4C transport code
MCNPXS	DLC-0189	Cross-section data for MCNP-4B2
MENSLIB	DLC-0084	Neutron 60 group cross-sections, E<60MeV
NJOY97.0	PSR-355	n, p, photon evaluated data processing system
NJOY99.0(***)	PSR-0480	Data processing system of evaluated nuclear data files ENDF format
NMF-90	IAEA1279	Database for neutron spectra unfolding
NUCDECAY	DLC-0172	Nuclear decay data for radiation dosimetry calculations
NucDecayCalc (***)	DLC-0202	Nuclear decay data for radiation dosimetry and retrieval program
NUCHART	IAEA1320	Nuclear properties and decay data chart
PCNUDAT32.2.8(***)	USCD1205	Nuclear properties database & retrieval system
PHOTX	DLC-0136	Photon interaction cross-section library for 100 elements
PNESD	IAEA1235	Elastic cross-sections of 3 MeV to 1000 MeV p on natural isotopes
POINT97	DLC-0192	Combination of resonance parameters and/or tabulated energy dependent evaluated cross-sections
RADEDECAY	DLC-0134	Decay data library for radiological assessment
RECOIL/B	DLC-0055	Heavy charged particle recoil spectra lib. for radiation damage
SFERXS	NEA 1239	Photon absorption, coherent, incoherent cross-sections for shielding
SIGMA-A	DLC-0139	Photon interaction and absorption data 1 KeV-100 MeV
SINBAD97	DLC-191	Shielding INtegral Benchmark Archive DataBase
SINBAD2000(**)		Shielding INtegral Benchmark Archive DataBase
SKYIII-PC	CCC-0289	PC version of program SKYSHINE-III
SKYPORT	DLC-0093	Importance of n, photon skyshine dose from accelerator
SKYSHINE-KSU	CCC-0646	Computation of gamma skyshine doses by different methods
SNLRML	DLC-0178	Dosimetry library compendium
SPAR	CCC-0228	Stopping power and ranges from muons, pions, protons, ions
SRIM-2000 ***	NEA 0919	Stopping power and ranges of ions (10 eV-2 GeV/amu) in matter
STARCODES(***)	PSR-0330	Stopping power, ranges for electrons, protons, alpha
STOPOW	IAEA0970	Stopping power of fast ions in matter
TPASGAM	DLC-0088	Library with gamma-ray decay data for 1438 radionuclides
UNGER	DLC-0164	Effective dose equivalent data for selected isotopes
VITAMIN-E	DLC-0113	Cross-section data library with 174n-38gamma energy groups
VITAMIN-B6	DLC-0184	Cross-section data library with 199n-42gamma energy groups derived from ENDF/B-VI Release 3
XCOM	DLC-0174	Photon cross-sections from 1 KeV to 100 GeV

Table 3. Cross-sections – spectra from nuclear models (for E > 20 MeV)

Name	Identification	Function
ALICE91	PSR-0146	Precompound/compound nuclear decay model
AMALTHEE	NEA 0675	Emission spectra for n, p, d, h3, he3, alpha reaction
ASOP	CCC-0126	1-D Sn shield calculation
AUJP	IAEA0906	Optical potential parameters search by chi**2 method
CADE	NEA 1020	Multiple particle emission cross-sections by Weisskopf-Ewing
CCRMN	IAEA1347	Computation of reactions of a medium-heavy nucleus with six light particles
CEM95	IAEA1247	MC calculation of nuclear reactions (Cascade Exciton Model)
CFUP1	IAEA1266	n, charged-particle reaction of fissile nuclei E < 33 MeV
CHUCK	USCD1021	n, charged particle cross-sections, coupled channel model
CMUP2	IAEA1265	Reaction cross-sections for n ,p, d, t, he3, he4, E < 50 MeV
COMNUC3B	PSR-0302	Compound nucleus interaction in n reactions
DWBA82	NEA 1209	Distorted Wave Born Approximation nuclear model
DWUCK-4	NESC9872	Distorted Wave Born Approximation nuclear model
ECIS-95 ***	NEA 0850	Schroedinger/Dirac nuclear model with experimental fit
ELPHIC-PC	IAEA1223	Statistical model MC simulation of heavy ion reaction
EMPIRE-MSC	IAEA1169	Multi-step compound nucleus/pre-equilibrium cross-sections
EMPIRE-II(***)	IAEA1169	Comprehensive nuclear model code, nucleons, ions induced cross-sections
ERINNI	NEA 0815	Multiple cascades emission spectra by optical model
EVA		Codes performing the nuclear evaporation processes
EVAP_F(**)		Modified version of the Dresdner evaporation code
EXIFONGAMMA	IAEA1211	n, alpha, proton, gamma emission spectra model
FRITIOF (**)		MC high-energy heavy ion collisions
GCASCAD(***)	IAEA1362	Gamma production cross-sections from statistical model
GNASH-FKK	PSR-0125	Multi-step direct and compound and Hauser-Feshbach models
GNASH-LANL	PSR-0125	Pre-equilibrium/statistical cross-sections, emission spectra
GRAPE	NEA 1043	Precompound/compound nuclear reaction models
HETC NMTC	CCC-0178	MC high energy nucleon meson cascade transport
HETC-KFA	CCC-0496	MC high energy nucleon-meson cascades
HETC95 (**)		MC high energy nucleon-meson cascades and transport
HFMOD	IAEA1317	Elastic and inelastic cross-section calculation by Hauser-Feshbach and Moldauer
HFTT	IAEA0954	n cross-section by compound-nucleus evaporation model
HIJET (**)		MC high-energy heavy ion collisions
ISABEL	NEA 1413	Intra-nuclear cascade model allowing hydrogen and helium ions and antiprotons as projectiles
ISAJET (**)		MC high-energy heavy ion collisions
KAPSIIES		Quantum mechanical multi-step direct model
LIMES	NEA 1337	Intermediate mass fragments in heavy ion nuclear reactions
MARLOWE15(***)	PSR-0137	Atomic displacement cascades in solids
MECC-7	CCC-0156	Medium energy intra-nuclear cascade model
MUP-2	IAEA0907	Fast n reaction cross-section of medium-heavy nuclei
MUTIL	NEA 1451	Calculates the asymmetry factor of the Mott scattering of electrons and positrons by point nuclei
NDEM (**)		Generates a gamma-ray source from the de-excitation of residual nuclei
NJOY-94.61	PSR-0171	n, p, photon evaluated data processing system
NJOY97.0	PSR-355	n, p, photon evaluated data processing system
NJOY99.0(***)	PSR-0480	Data processing system of evaluated nuclear data files ENDF format
NMTC/JAERI-97(***)	NEA 0974	MC high-energy p, n, pion reactions
NUCLEUS		Nuclear spallation simulation and primary products
OPTMOD	IAEA1316	Elastic and total cross-section, polarisation calculations using the optical model
PACE2 (**)		Codes performing the nuclear evaporation processes
PCROSS	IAEA1220	Pre-equilibrium emission spectra in neutron reaction
PEGAS	IAEA1261	Unified model of particle and gamma emission reactions
PEQAG-2	IAEA1185	Pre-equilibrium model nucleon, gamma spectra, cross-section
PHENOM/BCS-COLL	IAEA1327	Nuclear level density of excited nuclei
PREANG	NEA 0809	Nuclear model particle spectra, angular distribution
PRECO-D2	PSR-0226	Pre-equilibrium, direct reaction double differential cross-section
PREM	NEA 0888	Nucleon emission pre-equilibrium energy spectra, cross-section
QMD		Intra-nuclear cascade and classical molecular dynamics
RAF	IAEA1350	Neutron and proton radiative capture differential and integrated cross-section
REAC	CCC-0443	Activation and transmutation
REAC-2	NESC9554	Nuclide activation, transmutation
REAC*3	CCC-0443	Isotope activation and transmutation in fusion reactors
SOURCES4A (***)	CCC-661	Determine (α ,n), spontaneous fission and (β ,n) delayed
SPEC	IAEA1332	Computation of neutron and charged particle reactions using optical and evaporation models
STAPRE-H95	IAEA0971	Evaporation, pre-equilibrium model reaction cross-sections
STAPREF(***)	NEA-0461	Nuclear reactions cross-sections by evaporation model, gamma-cascades
TNG1	PSR-0298	n multi-step statistical model
UNIFY	IAEA1177	Fast n cross-section, spectrum calculation for structural materials

Table 4. Monte Carlo (MC) and deterministic radiation transport (neutron/photon)

Name	Identification	Function
ALBEDO	NEA 1353	Gamma, neutron attenuation in air ducts
ANISN	CCC-0254	1-D Sn, n, gamma transport in slab, cylinder, sphere
ASOP	CCC-0126	1-D Sn shield calculation
BALTORO	NEA 0675	n, gamma transport perturbation from MORSE, ANISN calculation
BASACF	IAEA0953	Integral neutron adjustment and dosimetry
BERMUDA	NEA 0949	1-D,2-D,3-D n gamma transport for shielding
BREESE	PSR-0143	Distribution function for MORSE from albedo data
CARP-82	PSR-0131	Multi-group albedo data using DOT angular flux results
COLLI-PTB	NEA 1126	MC n fluence spectra for 3-D collimator system
DANTSYS	CCC-0547	1-D, 2-D, 3-D Sn neutron, photon transport
DASH	CCC-0366	Void tracing Sn - MC COUPLING with fluxes from DOT
DCTDOS	CCC-0520	n, gamma penetration in composite duct system
DOORS3.2	CCC-0650	Discrete ordinates system for deep penetration neutron and gamma transport
DORT	CCC-0543	1-D 2-D Sn n, photon transport with deep penetration
DOMINO	PSR-0064	Coupling of Sn DOT with MC MORSE
DOT	CCC-0276	2-D Sn n, photon transport with deep penetration
DUST	CCC-0453	Albedo MC simulation of n streaming inducts
FALSTF	CCC-0351	n, gamma flux detector response outside cylindrical shields
FEM-RZ	NEA 0566	FEM 2-D multi-group n transport in r-z geometry
GBANISN	CCC-0628	1-D neutron and gamma fluxes with group band fluxes
GEANT-CERN		MC hadron shower simulation
MAGIK	CCC-0359	MC induced residual activation dose rates
MCNP-4A	CCC-0200	MC 3-D time-dependent coupled n, photon, electron transport
MCNP-4B	CCC-0660	MC 3-D time-dependent coupled n, photon, electron transport
MCNP-4B2	CCC-0660	MC 3-D time-dependent coupled n, photon, electron transport
MCNP-4C(***)	CCC-0700	Coupled neutron, photon, electron 3-D time dependent Monte Carlo transport calculations
MICAP	PSR-0261	MC ionisation chamber responses
MORSE-CGA	CCC-0474	MC n, gamma multi-group transport
PALLAS-2DY	NEA 0702	2-D n, gamma transport for fixed source
RADHEAT-V3	NEA 0467	Transport, heat, radiation damage cross-sections in reactor, shield
QAD-CGGP-A	CCC-0645	Fast neutron and gamma ray penetration in shields
RAID	CCC-0083	Gamma, n scattering into cylindrical or multi-bend duct
SAMSY	IAEA0837	n, gamma dose rates, heat source for multi-layer shields
SAM-CE	CCC-0187	MC time-dependent 3-D n, gamma transport in complex geometry
SCINFUL	PSR-0267	MC response of scintillation neutron detector (incident neutron energies from 0.1 to 75 MeV)
SCAP-82	CCC-0418	Scattering, albedo, point-kernel anal. in complex geometry
SNL/SAND-II	PSR-0345	Enhanced version of SAND-II
SPACETRAN	CCC-0120	Radiation leakage from cylinder with ANISN flux
SPECTER-ANL	PSR-0263	n damage for material irradiation
STAPREF(***)	NEA-0461	Nuclear reactions cross-sections by evaporation model, gamma-cascades
STARCODE(***)S	PSR-0330	Stopping power, ranges for electrons, protons, alpha
TORT	CCC-0543	3-D Sn n, photon transport with deep penetration
TRANSX	PSR-0317	Code to produce neutron, photon transport tables for discrete ordinates and diffusion codes
TRIPOLI-2	NEA 0874	MC time-dependent 3-D n, gamma transport
TWODANT-SYS	CCC-0547	1-D,2-D multi-group Sn n, photon transport
VIRGIN	IAEA0932	Uncollided neutron flux and neutron reactions due through a neutron beam through any thickness of material

Table 5. Monte Carlo (MC) and deterministic radiation transport (photon)

Name	Identification	Function
AIRSCAT	CCC-0341	Dose rate from gamma air scattering, single scat. approx.
GAMMONE	NEA 0268	MC gamma penetration from various geometrical sources
MERCURE-4	NEA 0351	MC 3-D gamma heating/gamma dose rate, fast flux
PLACID	CCC-0381	MC gamma streaming in cylindrical duct shields
BRHGAM	CCC-0350	MC absorbed dose from x-rays in phantom
BREMRAD	CCC-0031	External/internal bremsstrahlung
GRPANL	PSR-0321	Germanium gamma and alpha detector spectra unfolding
G33-GP	CCC-0494	Multi-group gamma scattering using gp build-up-factor
ISO-PC	CCC-0636	Kernel integration code system for general purpose isotope shielding
MAGNA	NEA 0163	Dose rates from gamma source in slab or cylindrical shell shields
MARMER	NEA 1307	Point-kernel shielding, ORIGEN-S nuclide inventories
PELSHIE	IAEA0855	Dose rates from gamma source, point-kernel method
PIPE	NEA 0416	1-D gamma transport for slab, spherical shields
PUTZ	CCC-0595	Point-kernel 3-D gamma shielding
STAC-8		Transmitted, absorbed power/spectrum – synchrotron radiation
UNSPEC	ESTS0827	X-ray spectrum unfolding using an iterative technique

Table 6. Monte Carlo (MC) and deterministic radiation transport (electron/photon)

Name	Identification	Function
BETA-2B	CCC-0117	MC time-dependent bremsstrahlung, electron transport
BETA-S3.1	CCC-0657	Calculates beta decay source terms and energy spectra
CASCADE	CCC-0176	High-energy electron-photon transport in matter
CEPXS ONELD	CCC-0544	1-D coupled electron photon multi-group transport
DOSDAT-2	DLC-0079	Gamma, electron dose factors data lib. for body organs
EDMULT	NEA 0969	Electron depth dose in multi-layer slab absorbers
EGS4	CCC-0331	MC electron photon shower simulation
ELBA	CCC-0119	Bremsstrahlung dose from electron flux on Al shield
EPICSHOW-96.1	IAEA1285	Interactive viewing of the electron-photon interaction ($10 \text{ eV} < E < 1 \text{ GeV}$)
ESTAR	IAEA1282	Calculates stopping power and range for electrons
ETRAN	CCC-0107	MC electron, gamma transport with secondary radiation
ELTRAN	CCC-0155	MC 1-D electron transport
FOTELP	CCC-0581	MC photons, electrons and positron transport
FOTELP/EM	CCC-0581	MC photons, electrons and positron transport
INFLTB	PSR-0313	Dosimetric mass energy transfer and absorption coefficients
ITS-3.0	CCC-0467	MC tiger system of coupled electron photon transport
MCNP-4A	CCC-0200	MC 3-D time-dependent coupled n, photon, electron transport
MCNP-4B	CCC-0660	MC 3-D time-dependent coupled n, photon, electron transport
MCNP-4C(***)	CCC-0700	MC 3-D time-dependent coupled n, photon, electron transport
PENELOPE	NEA 1525	Monte Carlo for electron-photon transport
SANDYL	CCC-0361	MC 3-D time-dependent gamma electron cascade transport

Table 7. Monte Carlo (MC) and deterministic radiation transport (proton)

Name	Identification	Function
ASTROS	CCC-0073	Primary/secondary proton dose in sphere/slab tissue
LPPC	CCC-0051	Proton penetration, slab
PSTAR	IAEA1282	Calculates stopping power and range for protons
PTRAN	CCC-0618	MC proton transport for 50 to 250 MeV
SOURCE (**)		Description of the proton transmission and generation of n source
TRAPP	CCC-0205	Proton and alpha transport, reaction products neglected

Table 8. Monte Carlo (MC) and deterministic radiation transport (alpha)

Name	Identification	Function
ALDOSE	CCC-0577	Absorbed dose and dose equivalent rates as function of depth in water irradiated by alpha source
ALPHN	CCC-0612	(alpha,n) production rate in a mixture from alpha emitting actinides
ASTAR	IAEA1282	Calculates stopping power and range for alphas
GRPANL	PSR-0321	Germanium gamma and alpha detector spectra unfolding
RADCOMPT	PSR-0348	Sample analysis for alpha and beta dual channel detectors

Table 9. Monte Carlo (MC) and deterministic radiation transport (nucleons/hadrons/cascades)

Name	Identification	Function
CALOR95		MC system for design, analysis of calorimeter system
CASIM	NESC0742	MC high energy cascades in complex shields
FLUKA	CCC-0207	MC high energy extranuclear hadron cascades
GEANT-CERN		MC hadron shower simulation
HERMES-KFA	NEA 1265	MC high-energy radiation transport
HERMES96b		Idem
HETC NMTC-97(***)	CCC-0178	MC high energy nucleon meson cascade transport
HETC-KFA	CCC-0496	MC high energy nucleon-meson cascade transport
LAHET		MC nucleon, pion, muons, tritons, He-3, alpha transport
LPSC	CCC-0064	p, n flux, spectra behind slab shield from p irradiation
NMTC/JAERI	NEA 0974	MC high-energy p, n, pion reactions
SITHA (**)	IAEA1179	Simulation Transport HAdron, used to calculate hadron transport
SHIELD (**)	IAEA1287	Hadron cascades in complex macroscopic targets

Table 10. Monte Carlo (MC) and deterministic radiation transport (heavy ions)

Name	Identification	Function
E-DEP-1	CCC-0275	Heavy ion energy deposition
ELPHIC-PC	IAEA1223	Statistical model MC simulation of heavy ion reaction
HIC-1	CCC-0249	MC heavy ion reactions at E > 50 MeV/nucleon
STRAGL	CCC-0201	Energy loss straggling of heavy charged particles
SWIMS	ESTS0682	Angular dispersion of ion beams at small-angle incoherent multiple scattering by gaseous or solid media
TRIPOS	CCC-0537	MC ion transport

Table 11. Monte Carlo (MC) and deterministic radiation transport (muons)

Name	Identification	Function
MUONLM	NEA 1475	calorimeter interaction of muons

Table 12. Monte Carlo (MC) and deterministic radiation transport (other cascades)

Name	Identification	Function
CHARGE-2/C	CCC-0070	Electron, p, heavy particle flux/dose behind shield
DDCS	IAEA1290	Neutron, proton, deuteron, triton, He3, and alpha induced reactions of medium heavy nuclei in the energy range up to 50 MeV
ELPHO	CCC-0301	MC muon, electron, positron generation from pions
IMPACTS-BRC	ESTS0005	Radiological assessment code
JENKINS		Photon, neutron dose in electron accelerator
PICA	CCC-0160	MC nuclear cascade reactions by the collision of photons (30 < E < 400 MeV) with nuclei
SPARES	CCC-0148	Space radiation environment and shielding evaluation

Table 13. Monte Carlo (MC) and deterministic radiation transport (anthropomorphic phantom modelling)

Name	Identification	Function
BRHGAM	CCC-0350	MC absorbed dose from x-rays in phantom
CAMERA	CCC-0240	Radiation transport and computerised man model
DISDOS	CCC-0170	Dose from external photons in phantom
K009	CCC-0062	Charged particle penetration – phantom
MEVDP	CCC-0157	Radiation transport in computerised anatomical man
MIRDOSE3.1	CCC-0528	Calculate internal dose estimates by the MIRD technique
MRIPP 1.0	CCC-0655	Magnetic resonance image phantom for <i>in vivo</i> measurements
PEREGRINE (**)		Used to model dose to humans from radiation therapy
REBEL-3	IAEA0846	MC radiation dose to human organs
REPC	PSR-0195	Dose from protons in tissue
SEECAL	CCC-0620	Computes age-dependent effective energies for 54 and 32 target regions in the human body (825 radionuclides)

Table 14. Benchmark data relative to reactor shields sets included in the SINBAD database

Name	Description
ASPIS-FE	Winfrith Iron Benchmark Experiment (ASPIS)
ASPIS-FE88	Winfrith Iron 88 Benchmark Experiment (ASPIS)
ASPIS-GRAPHITE	Winfrith Graphite Benchmark Experiment (ASPIS)
Winfrith H2O	Winfrith Water Benchmark Experiment
Winfrith PCA-REPLICA	Winfrith Water/Iron Benchmark Experiment
Winfrith NESDIP-2	Radial Shield of a PWR
Winfrith NESDIP-3	Radial Shield w/Cavity and Backing Shield of a PWR
EURACOS-FE	Ispra Iron Benchmark Experiment (EURACOS)
EURACOS-NA	Ispra Sodium Benchmark Experiment (EURACOS)
HARMONIE-NA	Cadarache Sodium Benchmark Experiment (HARMONIE)
JANUS-I	Fast Reactor w/Mild Steel, SS, and Concrete -Phase I
JANUS-VIII	Fast Reactor w/ Mild Steel, SS, Sodium, Polyethylene, Lead
KFK-FE	Karlsruhe Iron Sphere Benchmark Experiment
PROTEUS-FE	Wuerenlingen Iron Benchmark Experiment
PCA-PV	Pool Critical Assembly - Pressure Vessel Experiment (PCA)
SDT1	Iron Broomstick Benchmark Experiment (TSF-ORNL)
SDT2	Oxygen Broomstick Benchmark Experiment (TSF-ORNL)
SDT3	Nitrogen Broomstick Benchmark Experiment (TSF-ORNL)
SDT4	Sodium Broomstick Benchmark Experiment (TSF-ORNL)
SDT5	Stainless Steel Broomstick Benchmark Experiment (TSF-ORNL)
SDT 11	ORNL Neutron Transport in Iron and SS
SDT 12	ORNL Neutron Transport in Thick Sodium
SB2	Gamma Production Cross-Sections from Thermal Neutrons
SB3	Gamma Production Cross-Sections from Fast Neutron in 14 elements and SS
JASPER Axial Shield	Fast Reactor w/SS, B4C
JASPER Radial Shield	Fast Reactor w/SS, Graphite, B4C, and Sodium
JASPER Int. Heat Exch.	Fast Reactor w/Sodium, Spent Fuel, and B4C
Illinois Iron Sphere	Univ. of Illinois Iron Sphere

Table 15. Benchmark data sets relative to fusion shielding and accelerator shielding included in the SINBAD database

Name	Description
OKTAVIAN-Fe	Osaka Iron Sphere Benchmark Experiment
OKTAVIAN-Ni	Osaka Nickel Benchmark Experiment
OKTAVIAN-Al	Osaka Leakage Neutron and Gamma Spectra from Aluminum Sphere Pile
TUD Iron Slab	TU Dresden Iron Slab
TUD FNG Bulk Shield	TU Dresden FNG Bulk Shield
SB5	ORNL 14-MeV Neutron Stainless-Steel/Borated Polyethylene Slab Experiment
ENEA Bulk SS	FNG SS Bulk Shield Benchmark Experiment (Frascati)
ENEA Blanket	FNG ITER Blanket (VV+First Wall+Shield+TF Coil) (Frascati)
Accelerators:	
U. of Tokyo INS	Intermediate Energy Neutrons and Gamma-rays on Shielding Materials – 52 MeV and 65 MeV Protons
Osaka U. AVF	Penetration of Secondary Neutrons and Photons through Concrete, Fe, Pb, and C

FLUKACAD/PIPSICAD: THREE-DIMENSIONAL INTERFACES BETWEEN FLUKA AND AUTOCAD

Helmut Vincke
CERN, Switzerland

Abstract

FLUKA [1] is a widely used 3-D particle transport program. Up to now there was no possibility to display the simulation geometry or the calculated tracks in three dimensions. Even with FLUKA there exists only an option to picture two-dimensional views through the geometry used. This paper covers the description of two interface programs between the particle transport code FLUKA and the CAD program AutoCAD. These programs provide a three-dimensional facility not only for illustrating the simulated FLUKA geometry (FLUKACAD), but also for picturing simulated particle tracks (PIPSICAD) in a three-dimensional set-up. Additionally, the programming strategy for connecting FLUKA with AutoCAD is shown. A number of useful features of the programs themselves, but also of AutoCAD in the context of FLUKACAD and PIPSICAD, are explained.

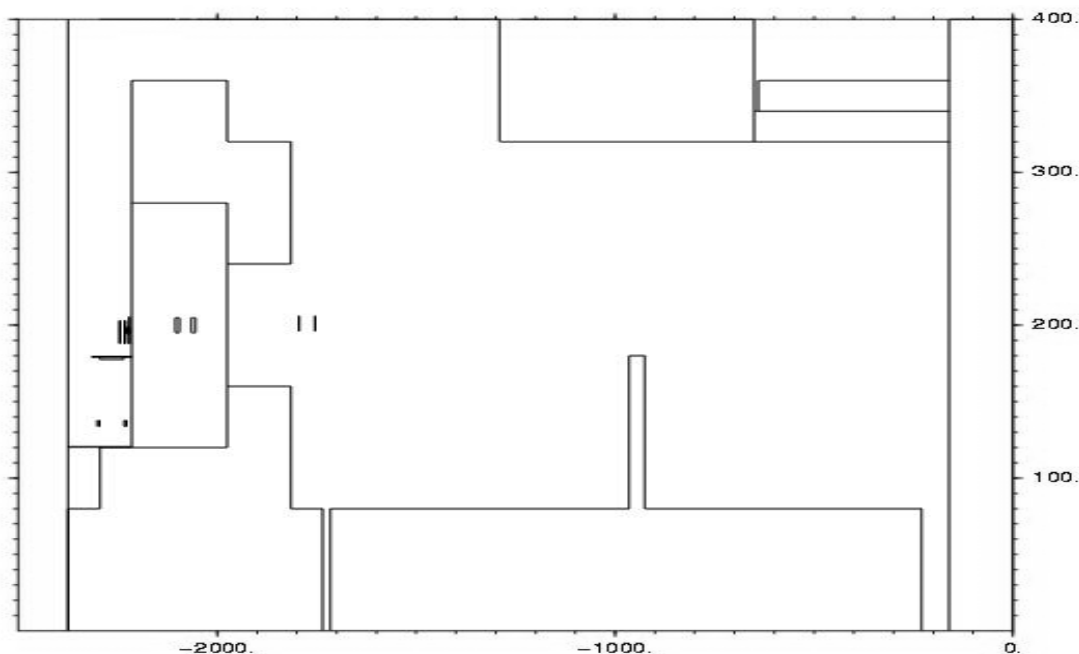
Introduction of FLUKA

FLUKA is a Monte Carlo particle transport program which can deal with more than 40 different kinds of particles. The covered energy range is between thermal energies and 1 000 TeV. The geometry description used in FLUKA is a kind of “combinatorial geometry”, which covers a specific number of three-dimensional basic bodies. These bodies can be combined with Boolean operators to set up more complicated constructions in so-called regions. The whole FLUKA geometry consists of a certain number of regions. To each region a material is assigned, which can be defined by the user. The particle transport simulation in FLUKA is similar to real life experiments. The path of the particles through the geometry is simulated according to the cross-sections, which are submitted via the region material compositions. A source particle is started in the existing geometry in a specified region. It keeps going until it crosses a boundary to an adjacent region, and it undertakes an interaction with a particle belonging to the regions’ matter or it decays. In case of inelastic reactions or decays, new particles can be produced. After the simulation of the path of the primary particle, the histories of the secondary particles have to be simulated as well. The simulation of a particle stops if the particle gets a lower energy than an energy which is submitted via a threshold or if it escapes from the system. All these history steps of particles can be written on a file via the FLUKA input card “dumpthem”.

Former possibility to display FLUKA geometries

A standard device of FLUKA for displaying geometries is Plotgeom. This program is included in FLUKA and can be accessed by using a FLUKA input card. The user specifies a two-dimensional cross-section through the geometry by giving its orientation with respect to the geometry co-ordinate axes and via submitting the desired co-ordinates of the corners of the picture. Figure 1 shows an example of a two-dimensional cross-section produced by Plotgeom.

Figure 1. Cross-section picture through the H6 area at CERN (August 1999), produced with Plotgeom



FLUKACAD: A solution for displaying FLUKA geometries in three dimensions

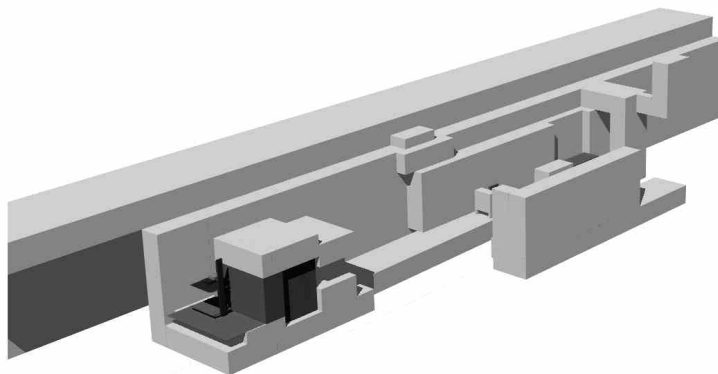
FLUKACAD is an interface program between FLUKA and AutoCAD. In comparison to Plotgeom, FLUKACAD produces a script file which is loaded in AutoCAD and creates a three-dimensional picture. The main features of this program in combination with AutoCAD are as follows:

- Once the 3-D picture is loaded in AutoCAD, each single region in this 3-D picture can be switched on and off (made visible or invisible).
- All regions which consist of the same type of material can be switched on and off together.
- The different FLUKA materials have different colours which can be adapted to very realistic material colours.
- The colour number of a region in AutoCAD correlates with the appropriate material number in FLUKA. Therefore all different materials can be recognised very easily.
- Once the script file is loaded, each detail in the geometry can be zoomed.
- The light which falls at the geometry can be chosen. The benefit of this feature is that very realistic pictures can be produced.
- The point of view at the geometry can be chosen and changed by the user without reproducing the whole 3-D geometry.
- Possible change between parallel projection and perspective view of the picture.
- Possibility to check geometry concerning overlapping regions and undefined areas (geometry debugging).
- All features of AutoCAD can be used to display the geometry.

As an example of the ability of FLUKACAD in combination with AutoCAD the same FLUKA geometry as already produced with Plotgeom (Figure 1) is shown in Figure 2.

Figure 2. Three-dimensional picture of H6 area at CERN (August 1999), produced with FLUKACAD + AutoCAD

For showing details inside the beam line, the roof and the side wall of the area were removed



Directions for use FLUKACAD in combination with AutoCAD

When FLUKACAD is started, the machine asks if the user wants to use the FLUKACAD command file “FILEDAT” to produce the AutoCAD script file. This file provides FLUKACAD with necessary information concerning the production of the script file. More details about “FILEDAT” can be found at the end of this chapter. In case the user denies the usage of the command file, the necessary commands to produce the script have to be submitted by hand. To receive this information the computer asks questions concerning the following topics:

1. Name of FLUKA input file.
2. Desired name of the AutoCAD script file.
3. The user can choose between drawing the whole geometry or only a part of it. In case only a few regions are to be drawn, FLUKACAD asks for the first and afterwards for the last region, which shall be displayed.
4. The program asks if one wants to split the produced output file. In case of geometries bigger than 30 regions it is recommended to choose the splitting option. The effect of this feature is that in case of big geometries the production of the drawing in AutoCAD is much faster.
5. After this step, one is asked whether FLUKACAD should calculate the proper beginning zoom factor for the AutoCAD session. If this factor is chosen wrongly, AutoCAD sometimes goes wrong. Therefore an automatic calculation performed by FLUKACAD is recommended.

Necessary steps for running the produced script file in AutoCAD

1. The next step is to start AutoCAD (English version) from scratch (AutoCAD14) or with the Prototype acad.dwg(AutoCAD13).
2. The command “Run Script” of the menu point “Tools” has to be chosen. Under this menu point the produced script has to be submitted.
3. In case the option of splitting was chosen, the computer produces a directory called “deleteme”. In this directory necessary files are temporarily stored. When AutoCAD has finished the production of the geometry, the computer asks the user whether the directory “deleteme” shall be deleted or not. The user has to confirm this command with yes. Otherwise this directory including all files has to be removed manually.

The file “FILEDAT” provides FLUKACAD with the answers to the necessary questions for producing an AutoCAD script file. These questions are asked by the machine in case the use of FILEDAT is refused (see above, points 1-5).

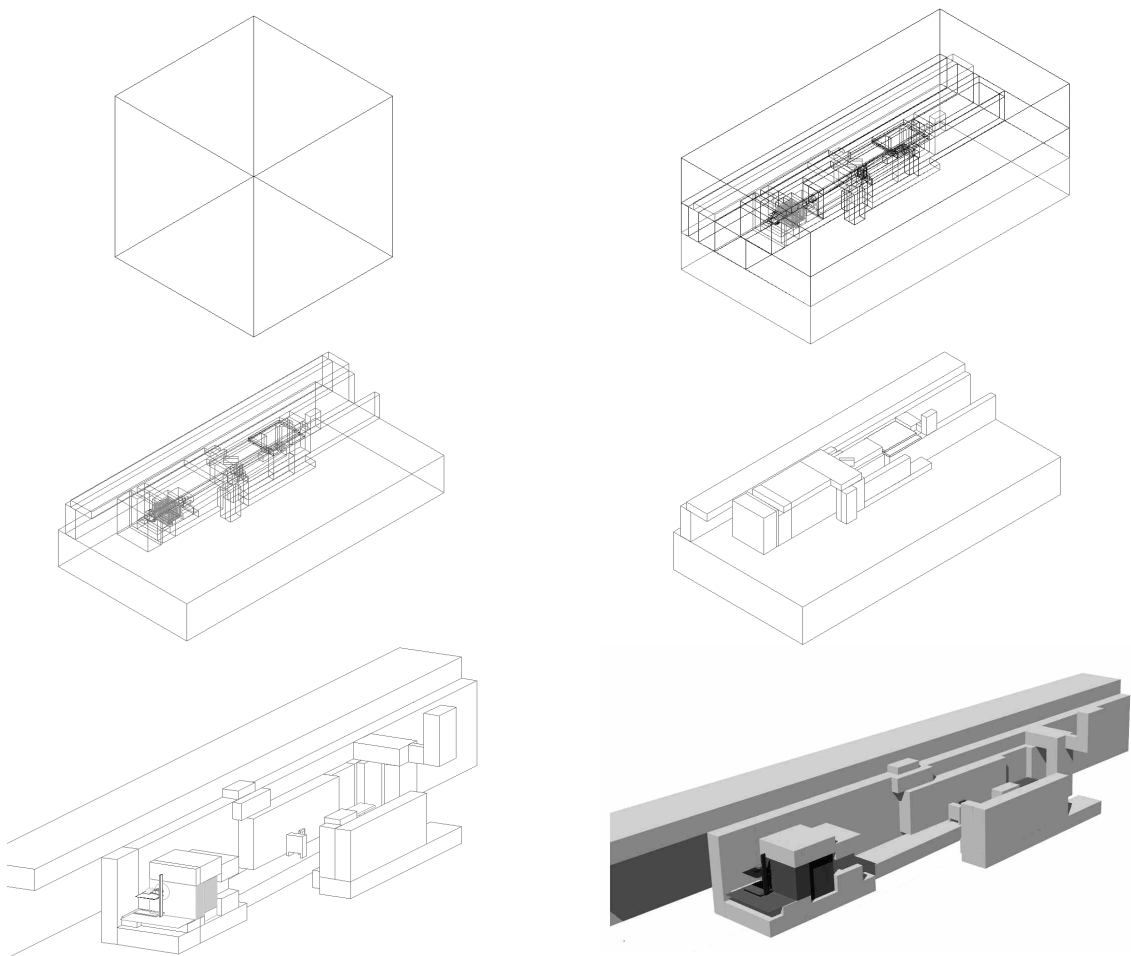
Contents of the file FILEDAT

Lines starting with a * are seen as comment lines. These lines can be removed or additional comment lines can be added. In between the comment lines, necessary information for FLUKACAD is submitted. This information can be adapted properly to the actual used geometry but the sequence of the commands must be provided in the shown order.

* name of input file for FLUKACAD
infile.inp
* name of Autocad file .scr
autocad.scr
* drawing all regions or not: 0=all 1=speciall regions
0
* region number of first region; if above 0 is chosen then meaningless
1
* region number of last region; if above 0 is chosen then meaningless
2
* splitting: 1=yes 0=no
0
* automatic zoom factor: 1=yes 0=no
1

Necessary steps to receive high quality pictures

The following picture sequence shows the different stages between loading a geometry and receiving a high quality picture in AutoCAD.



The first picture shows the AutoCAD display surface after loading the script. The cube shows the external void, which is in most cases much bigger than the actual geometry. After removing (AutoCAD command “freeze”) the void, followed by a zoom to the actual geometry, the second picture on the right is displayed on screen. At that level of production, all regions (including gas and internal void regions) can be seen in a transparent form. At this stage of the procedure a check concerning overlapping regions or undefined areas in the geometry is appropriate. These checks are done via the command “union” and “interfere” respectively. The command union unifies all regions. In case all points of the geometry are covered by regions, only one body (in this case a box) without any internal structure should remain. If the remaining body has an internal structure (= some areas are not defined inside the geometry), FLUKA would crash with use of this geometry. In case of performing the command “interfere”, AutoCAD recognises double defined areas (overlappings) and reports the result to the user. After selection and removing of all materials, which are in real life invisible (e.g. gases, voids), the third picture will be displayed on screen. The remained solid regions are still shown in a transparent form. With use of AutoCAD command “hide”, the fourth picture second row on the right) is produced. The next step is to remove parts, which hide the important part of the geometry (bottom left picture). After a change from parallel view to perspective view, an assignment of realistic colours to the materials, a proper selection of light sources followed by the AutoCAD command “render”, the last picture is displayed on screen.

Internal working strategy of FLUKACAD

When FLUKACAD is started the following procedures inside the program are performed:

1. The specified FLUKA input file is loaded.
2. The program tries to find the beginning of the body description in the input file. After this position is found, all bodies are stored in a matrix system, which covers the description of the single bodies with all their parameters.
3. Followed to the body readout, the program starts to read all “ASSIGNMAT” cards in the input file. This card assigns the used materials to the single parts (regions) of the geometry. Each material refers to a specific AutoCAD colour.
4. During the following step FLUKACAD starts to readout all regions, assembles the used bodies in the single regions and performs assignment of the already stored materials. The collected information is translated into an AutoCAD readable format and is written on the script file.
5. During the production of the script file, additional necessary AutoCAD set-up information for displaying the geometry are stored on the file.
6. The script file is saved with the desired filename.

PIPSICAD: Particle Identification Program for Simulated Interactions

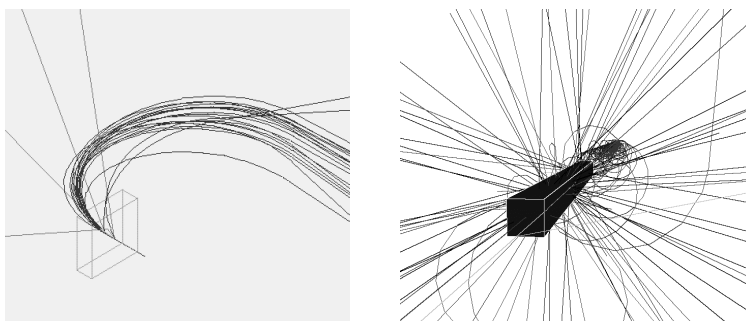
FLUKA has an option to write particle track data on a collision file, but there is no possibility to display these tracks, which are produced during the simulation procedure. This option of writing the collision file can be accessed via the FLUKA card “dumpthem” (with parameter WHAT(1) \geq 100). In this card one can choose whether only trajectories or local energy depositions or both shall be written on the file. PIPSICAD is like FLUKACAD an interface between FLUKA and AutoCAD. It reads information from the collision file (binary format) to generate a script file for displaying the produced tracks and energy depositions in AutoCAD.

Main features of PIPSICAD

- Via AutoCAD, PIPSICAD produces 3-D pictures of particle tracks and point energy depositions (generated by FLUKA). These pictures can either be displayed at a blank page or superimposed on an existing AutoCAD geometry.
- Energy depositions are shown as spheres with either fixed radii or with radii which correlate to the amount of the energy deposition.
- The picture can be displayed in parallel projection or perspective view. Furthermore the distance and the view direction to the drawn tracks and energy depositions can be selected by the user.
- Tracks and energy depositions in the 3-D picture are stored separately in AutoCAD layers and can be switched on and off (made visible or invisible).
- PIPSICAD can perform either a general readout of all particle types or a restricted readout of only one sort. In case all particles are drawn, the single particle types can be recognised and switched on and off during the AutoCAD session.
- Different energy ranges of the particles can be displayed with PIPSICAD. When PIPSICAD is started, it will ask for the desired energy range. That means that only particles (and energy depositions caused by these particles) within a chosen energy range are read from the collision file. A display of up to 10 particle script files with different energy ranges in the same AutoCAD drawing is possible.
- The FLUKA particle numbers of the different particles correlate to the AutoCAD colour numbers. For example a proton track (particle number in FLUKA = 1) will be displayed in red (AutoCAD colour number = 1)). The same is valid for the colours of the energy deposition spheres, which are caused by the specific particle.
- The particle tracks and energy depositions are stored separately in specified AutoCAD layers. The name of the single layers contains information about the stored particle contents.
- By means of the naming convention of the layers and the strategy of storing particle types with correlated AutoCAD colour numbers, an energy range and particle type selection of the tracks and energy deposition can be performed very easily during the AutoCAD session.

Figure 5. A proton beam hits an iron block (left) and a small iron target (right) respectively

Except for the half space in front of the target a magnetic field bends the charged particles according to their kinetic energy. The neutral particles (straight tracks) are not effected by the field.



Directions for use PIPSICAD in combination with AutoCAD

When PIPSICAD is started, the machine needs to obtain information concerning the production of the AutoCAD script file. This communication between the program and the user can be divided into the following stages:

1. A submission of the FLUKA Collision file and the desired AutoCAD script file name is requested.
2. The user has to choose between a readout covering all particle types or covering only a specified kind of particles.
3. The minimal and maximal energy of the particles which are read from the collision file have to be submitted. The user can choose between entering the total or the kinetic energy of the particles. These energy thresholds are expected in GeV.
4. The next stage deals with the number of energy dependent particle script files (0-9) which were already loaded into the AutoCAD geometry. This information is both necessary for the identification of the energy dependent particles in the picture and to prevent an overwriting of already existing AutoCAD layers. In case this information is not provided to AutoCAD, the program would try to renew existing layers and the loaded script in AutoCAD would stop immediately.
5. The following step concerns the point energy depositions. These interactions can be drawn as spheres with either a fixed radius or a radius which correlates to the amount of the deposited energy. In case the second option is chosen, a multiplication factor has to be submitted. This factor is multiplied with the energy deposition of this interaction. The result of this product provides the radius for the sphere which is drawn in AutoCAD.
6. The last question asked by PIPSICAD deals with the storage of particle tracks and point energy depositions in AutoCAD layers. Either each track and energy deposition is written on a separated layer or all tracks and energy depositions of the same kind are stored in a joint layer. If the first option is chosen, the assigned name of the layers can be interpreted in the following way:
 - In case of tracks: *name of loaded particles, number of previous loaded energy range sets, number of track.*
 - In case of Edeps: *COLL, number of prev. loaded energy range sets, ICODE, number of collision.*

If the second option is chosen the following layer name convention is performed:

- In case of tracks: *name of loaded particles, number of previous loaded energy range sets, particle number.*
- In case of Edeps: *COLL, number of previously loaded energy range sets, particle number which induced the collision_ICODE.*

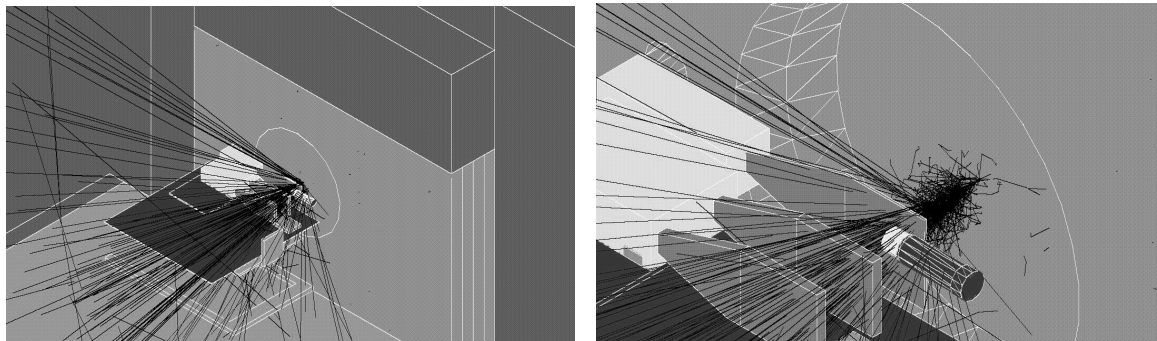
COLL means collision and ICODE is a number which is assigned from FLUKA to the different kinds of collisions. The meaning of the single numbers can be found in the FLUKA manual [1].

After performing this dialog, PIPSICAD will produce a script file which contains the FLUKA particle tracks and energy depositions in an AutoCAD readable format. For displaying the particle information in AutoCAD the following two steps have to be performed:

7. Either AutoCAD (English version) has to be started from scratch or an existing FLUKA geometry has to be loaded.
8. After running the produced script under “Run Script” of the menu “Tools”, AutoCAD displays the FLUKA particle information.

In FLUKA there exists the possibility to control the storing of particle data via a subroutine “mgdraw.f”. To change the default procedure so as to generate the collision file, this routine has to be modified and linked to FLUKA. More details concerning this procedure can be found in the FLUKA manual. Figure 6 shows an example of such a kind of modification in the context of PIPSICAD. In this case mgdraw.f was modified in such a way that FLUKA starts to write data on the collision file when a chosen collision at a specified point occurs. In this example the collision is a hadronic impact, which produces $2 \pi_0$ s. These π_0 generate a huge electromagnetic shower. Only the photons of this shower were displayed with PIPSICAD.

Figure 6. Electromagnetic shower (only photons shown) induced by a hadronic interaction inside the iron block hits a measurement construction including a BGO. The cascade itself can be seen after removing 20 cm of the inner iron part (right).



Restrictions of the programs

For using FLUKACAD, the geometry part of the input FLUKA file has to be stored within the FLUKA main input file. Also, possible modifications performed using the “lattice card” have to be introduced by hand after the geometry is loaded in AutoCAD.

Conclusion

FLUKACAD is an interface between FLUKA and AutoCAD which comes with a lot of useful features to generate three-dimensional geometry pictures in AutoCAD. PIPSICAD is an interface between the FLUKA collision file and AutoCAD. With FLUKACAD it is possible to develop FLUKA geometries much more quickly than before. With this program the user always has control with regard to the actual geometry and errors can be recognised much faster. PIPSICAD provides the possibility to control the particle histories of a run. Furthermore, a combination of both programs produces excellent three-dimensional pictures which should not be missed in a publication concerning FLUKA simulations.

REFERENCE

- [1] A. Fassò, A. Ferrari, J. Ranft and P.R. Sala, “New Developments in FLUKA Modelling of Hadronic and EM Interactions”, in proceedings of the SARE-3 workshop, KEK, Japan (1997).

DEVELOPMENT OF DUCT-III CODE FOR DUCT STREAMING CALCULATION UP TO 3 GeV

H. Nakano, R. Tayama, T. Tsukiyama, H. Handa, K. Hayashi

Hitachi Engineering Co., Ltd., Saiwai-cho, Hitachi-shi, Ibaraki 317-0073, Japan

K. Shin

Kyoto University, Sakyo-ku, Kyoto, 606-8317, Japan

H. Hirayama

High Energy Accelerator Research Organisation, Oho, Tsukuba, Ibaraki, 305-0801, Japan

H. Nakashima, F. Masukawa, N. Sasamoto, Y. Sakamoto

Japan Atomic Energy Research Institute, Tokai-mura, Ibaraki, 319-1195, Japan

K. Yamada, T. Abe

Start Com Co., Ltd., Hayamiya, Nerima-ku, Tokyo, 179-0085, Japan

Abstract

A simple and useful code for radiation streaming calculations known as DUCT-III, equipped with updated high-energy albedo data up to 3 GeV, has been developed. DUCT-III can treat cylindrical duct, rectangular duct, annulus and slit geometry. Multi-legged geometry is also available. As an output, we can obtain energy spectra at many positions along the duct centre axis.

We performed benchmark analyses with neutron streaming experiments at TIARA and NIMROD to validate the applicability of DUCT-III. The results were in agreement with the experiments for neutron dose equivalents and reaction rates with activation detectors. Therefore, the applicability of DUCT-III to the shielding design work of high-energy neutron facilities was validated.

Introduction

The evaluation of radiation streaming through a maze connected to the room entrance and piping, cable and air duct penetrations through the wall is important but time consuming with regard to the shielding design work of radiation facilities. A simple method is indispensable to check radiation streaming from many holes in the building one by one. Many sophisticated studies on radiation streaming have been carried out, and many semi-empirical equations [1-3] have been proposed up to now. If we limit our interest to high-energy neutron streaming from several tens MeV to a few GeV, however, there are not so many studies that apply a simple method. One of the exceptions is Tesch's equation [1]. This type of semi-empirical equation, though, does not consider the incident energies and also does not provide any information on the energy spectrum. To realise a simple but useful streaming calculation method for high-energy neutron facilities, we developed DUCT-III.

We performed benchmark analyses for radiation streaming of high-energy proton accelerator facilities to validate the applicability of DUCT-III. The benchmark analyses were carried out with neutron radiation streaming experiments at TIARA [4] and NIMROD [5].

Outline of DUCT-III code

A previous code, DUCT-II [6], was designated to estimate radiation streaming from neutrons of which energies are up to 14 MeV and gamma rays of which energies are up to 10 MeV. It can treat cylindrical duct, rectangular duct, annulus and slit geometry. Multi-legged geometry is also available. As an output, we can obtain energy spectra at many positions along the duct centre axis. This code uses a semi-empirical formulation [7] developed by one of the authors of this paper. The basis of the formulation is the albedo model. The formulation is made for the albedo components, i.e. multi-scattered neutrons or gamma rays due to those which enter into the duct through the entrance mouth. It is essentially energy independent and easy to expand to high-energy neutrons by changing the albedo data.

To provide the albedo data for the high-energy neutrons streaming up to a few GeV, we carried out neutron scattering calculations for concrete and iron. The concrete density is $2.15 \text{ g} \cdot \text{cm}^{-3}$ and the component is referred from ANL-5800 (type02-a) concrete [8]. The calculation was performed using NMTC/JAERI97 [9] for neutrons in an energy range from 3 GeV to 20 MeV, and using MCNP-4A [10] with JENDL-3.2 [11] for neutrons under 20 MeV.

Benchmark analyses

We performed benchmark analyses with the neutron radiation streaming experiments at TIARA and NIMROD. These calculation models are shown in Figures 1 and 2. Details of the experiments have been described in Refs. [2] and [3], respectively.

TIARA

Calculation

We carried out the benchmark analysis with the radiation streaming experiment at TIARA using DUCT-III. The experiment was performed with neutrons from a copper target (diameter: 80 mm, thickness: 12 mm) bombarded by 68 MeV protons at a labyrinth connected to the second light ion room (LIR2) of the Takasaki Ion Accelerator Facility for Advanced Radiation Application (TIARA) at the Japan Atomic Energy Research Institute (JAERI).

In the experiment, neutron dose equivalent rate distributions in the labyrinth were measured by a rem counter and a Bonner ball counter, thermal neutron flux by TLDs and the Bonner ball counter, and neutron flux above 0.1 MeV by a solid state nuclear track detector, a BC501A scintillation detector and a multi-moderate spectrometer. Figure 1 shows the horizontal and the vertical section view of TIARA (LIR2) and the connected access way of three legs of about 29 m long. The cross-sections of each leg are 1.5 m in width and 3.5 m in height for the first and second legs, and 3.0 m in height for the third leg. The labyrinth is surrounded by a concrete wall over 2 m thick. The concrete density is $2.41 \text{ g} \cdot \text{cm}^{-3}$. In this geometry, as the labyrinth encircles LIR2, the neutron components penetrating through bulk shield are not negligible compared with streaming radiation. The calculation of dose equivalent for the neutron component penetrating through bulk shield was carried out with PKN-H [12]. PKN-H is a simplified code based on a point kernel method which is able to calculate dose equivalent for bulk shield penetration. The energy group structure for PKN-H consists of 55 groups from 10^{-2} MeV neutrons to 400 MeV neutrons, which is based on that of HILO86 [13].

For evaluation using DUCT-III, it is assumed that an angular distributed source is set over the entrance surface of the labyrinth. DUCT-III can treat two angular distributed sources for rectangular duct. Their angle intervals are 0° , 28.5° and 90° relative to the line normal of the entrance surface. For this experiment, a most oblique angle relative to the line normal of the entrance surface is 35.6° , and the source does not face to the end of the first leg. The source intensity is therefore zero for the angle from 0 - 28.5° . The angular neutron source used in DUCT-III was calculated by MCNP-4B with HILO86.

Results and discussion

Figures 3-6 show calculated and measured attenuation curves of neutron dose equivalent rates with the rem counter and the Bonner ball counter, thermal neutron flux and neutron flux above 0.1 MeV in the labyrinth, respectively.

The calculated dose equivalent rates shown in Figure 3 were obtained by multiplying the neutron flux to dose equivalent conversion factors to the neutron energy spectra calculated by MCNP-4B and DUCT-III. The neutron energy dependent response functions of the rem counter were used as the above conversion factors. The results of DUCT-III and PKN-H are in good agreement with the measurements within -10% to +30% in the region from the entrance to about 14 m, i.e. in the first and the second legs, but tend to be larger than the measurements in the third leg. The results of DUCT-III and PKN-H reproduce approximately about two times as many as the measurements at the end of the third leg.

On the other hand, ICRP Publication 51 dose equivalent conversion factors [14] were used as the neutron flux to dose equivalent conversion factors in Figure 4. The results of DUCT-III and PKN-H are smaller than the measurements and the calculations with MCNP-4B in the region from the entrance to about 20 m. At the end of the third leg, however, the results of DUCT-III and PKN-H are in good agreement with those of MCNP-4B.

For thermal neutron flux (shown in Figure 5), the calculations with DUCT-III are almost in agreement with the measurements for the attenuation curves in the labyrinth, but these are a little larger than the measurements. The results with DUCT-III reproduce the measurements approximately within a factor of five at the end of the third leg.

The neutron flux above 0.1 MeV was measured in the region from the entrance to about 14 m, i.e. in the first and the second legs. Both measurements and calculations were normalised at the entrance of the labyrinth as shown in Figure 6. The calculations with DUCT-III are larger than those

with MCNP-4B in the third leg, although a little smaller in the first and second legs. The results of DUCT-III reproduce the measurements and the MCNP calculations approximately within a factor of three in the whole region of the labyrinth.

NIMROD

Calculation

The benchmark analysis with the radiation streaming experiment was also carried out at NIMROD using DUCT-III. The experiment was conducted with neutrons from a lead target (diameter: 10 mm, thickness: 50 mm) bombarded by 7 GeV protons at the synchrotron beam line for the NIMROD accelerator facility.

The measurements were performed in large concrete-lined tunnels. Attenuation curves of reaction rates with various activation detectors were obtained. In the benchmark analysis, the $^{197}\text{Au}(n,\gamma)^{198}\text{Au}$ reaction rates and the $^{12}\text{C}(n,2n)^{11}\text{C}$ reaction rates were calculated to compare the measured data with gold and carbon foils. The neutron cross-sections used for the $^{197}\text{Au}(n,\gamma)^{198}\text{Au}$ reaction are found in Ref. [15], and in Ref. [16] for the $^{12}\text{C}(n,2n)^{11}\text{C}$ reaction.

Figure 2 shows the calculational model of the straight and the bent tunnels connected to the synchrotron room. The cross-sections of each tunnel are 2.3 m in width and 2.3 m in height. Walls made of over 1 m thick ordinary concrete surround the tunnels. The concrete density is $2.3 \text{ g} \cdot \text{cm}^{-3}$. The component of the concrete is referred from ANL-5800 (type02-a) concrete. The source, assumed to be an isotropic point source and calculated by NMTC/JAERI97, combined JAM [17,18] and MCNP-4A. In the second leg, the neutron component penetrating through bulk shield was negligible compared with the streaming component.

Results and discussion

Figures 7 and 8 and Figures 9 and 10 show calculated and measured attenuation curves of activities with gold and carbon foils in the straight and the bent ducts, respectively. These are normalised at the entrance of each duct. For gold foils, the self-shielding effect was considered in the calculations, because absorption of the epithermal neutron flux due to the gold foils had an influence on the calculated results.

In the straight duct, the calculations for gold foils with DUCT-III reproduce the measurements and the calculations with the Monte Carlo code within -30% in the region from the entrance to about 15 m as shown in Figure 7. The results with DUCT-III, however, underestimate at the end of the duct because the reflection effects found there are not taken into account with DUCT-III. For carbon foils (Figure 8), the calculations with DUCT-III reproduce the measurements within +70% and the calculations with the Monte Carlo code within -40%.

In the bent duct (Figure 9), on the other hand, the calculated attenuation curves for gold foils with DUCT-III are in good agreement with the measured and the calculated ones obtained with the Monte Carlo code in the first leg, but the results with DUCT-III are a little smaller than those in the second leg. For carbon foils (shown in Figure 10), the results with DUCT-III tend to be a little larger than the measurements, but a little smaller than the calculations with the Monte Carlo code in the first leg. DUCT-III provides conservative results compared with the measurements and the Monte Carlo calculations in the second leg. At the end of the duct, the results with DUCT-III reproduce the measurements and the calculations with the Monte Carlo code within a factor of four.

Conclusions

A simple design code named DUCT-III with updated high-energy albedo data up to 3 GeV neutrons has been developed and tested with neutron streaming experiments at TIARA and NIMROD. The following results were obtained:

- DUCT-III reproduces the experiments with high accuracy for the attenuation curves of neutron dose equivalents in the labyrinth at TIARA.
- DUCT-III is in good agreement with the experiments for the thermal neutron flux distribution in the labyrinth at TIARA.
- DUCT-III is in good agreement with the experiments for the attenuation curves with gold foils except at the end of duct at NIMROD.
- DUCT-III gives conservative results compared with the experiments for the attenuation curves with carbon foils in the duct at NIMROD. At the end of that one, DUCT-III reproduces the measurements within a factor of four.

According to the above results, the applicability of DUCT-III to the shielding design work of high-energy neutron facilities has been validated.

REFERENCES

- [1] K. Tesch, *Particle Accel.*, 12, 169 (1982).
- [2] Y. Uwamino, T. Nakamura, T. Ohkubo, *Med. Phys.*, 13, 374 (1986).
- [3] K. Geobel, G.R. Stevenson, J.T. Routti, H.G. Vogt, "Evaluating Dose Rates Due to Neutron Leakage Through the Access Tunnels of the SPS", CERN Internal Report LAB II – RA/Note/75-10 (1975).
- [4] Su. Tanaka, *et al.*, to be submitted to *Health Physics*.
- [5] G.R. Stevenson, *et al.*, "An Experimental Study of Attenuation of Radiation in Tunnels Penetrating the Shield of an Extracted Beam of the 7 GeV Proton Synchrotron NIMROD", *Health Physics Pergamon Press* 1973, Vol. 24 (Jan.), pp. 87-93.
- [6] K. Hayashi, *et al.*, "DUCT-II and SHINE-II: Simple Design Code for Duct-streaming and Skyshine", JAERI-M 91-013 (1991).
- [7] K. Shin, "Semi-empirical Formula for Energy-space Distributions of Streamed Neutrons and Gamma Rays in Cylindrical Duct", *Journal of Nucl. Sci. & Tech.*, 25, 8-18 (1988).

- [8] Reactor Physics Constants ANL-5800 Second Edition, Argonne National Laboratory (1963).
- [9] H. Takeda, *et al.*, “An Upgraded Version of the Nucleon Meson Transport Code: NMTC/JAERI97”, JAERI Data/Code 98-005 (1998).
- [10] J.F. Briesmeister, “MCNP – A General Monte Carlo N-particle Transport Code, Version 4A”, LA-12625-M (1993).
- [11] T. Nakagawa, *et al.*, *J. Nucl. Sci. & Technol.*, 32, 1259 (1995).
- [12] H. Kotegawa, *et al.*, “PKN-H: A Point Kernel Shielding Code for Neutron Source Up to 400 MeV”, JAERI-Data/Code 95-004.
- [13] R.G. Alsmiller, Jr., J.M. Barish, J.D. Drischler, ORNL/TM-7818 (1981).
- [14] Data for Use in Protection Against External Radiation Annals of the ICRP, 17, No. 2/3 (1987).
- [15] JAERI Nuclear Data Centre, JENDL Dosimetry File 99, private communication (1999).
- [16] E. Kim, *et al.*, “Measurements of Neutron Spallation Cross-sections of ^{12}C and ^{209}Bi in the 20 to 150 MeV Energy Range”, *Nuclear Science and Engineering*, 129, 209-223 (1998).
- [17] K. Niita, *et al.*, “Analysis of the Proton-induced Reactions at 150 MeV-24 GeV by High-energy Nuclear Reaction Code JAM”, JAERI Tech 99-065 (1999) (in Japanese).
- [18] K. Niita, “High Energy Nuclear Reaction Code JAM”, Proc. of Symp. on Nucl. Data, JAERI, Tokai, 18-19 Nov. (1999).

Figure 1. Geometry for the calculational model at TIARA (LIR2) (unit: cm)

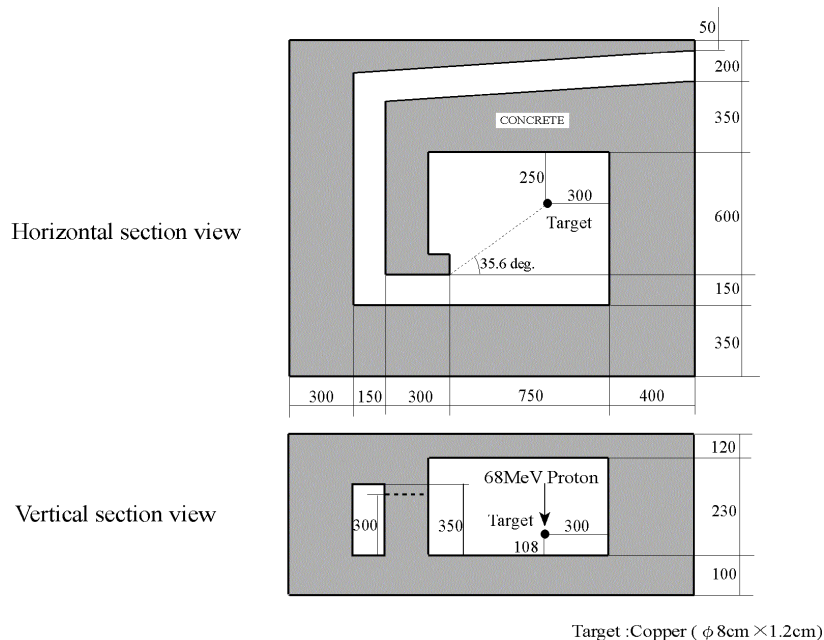


Figure 2. Geometry for the calculational model at NIMROD (unit: cm)

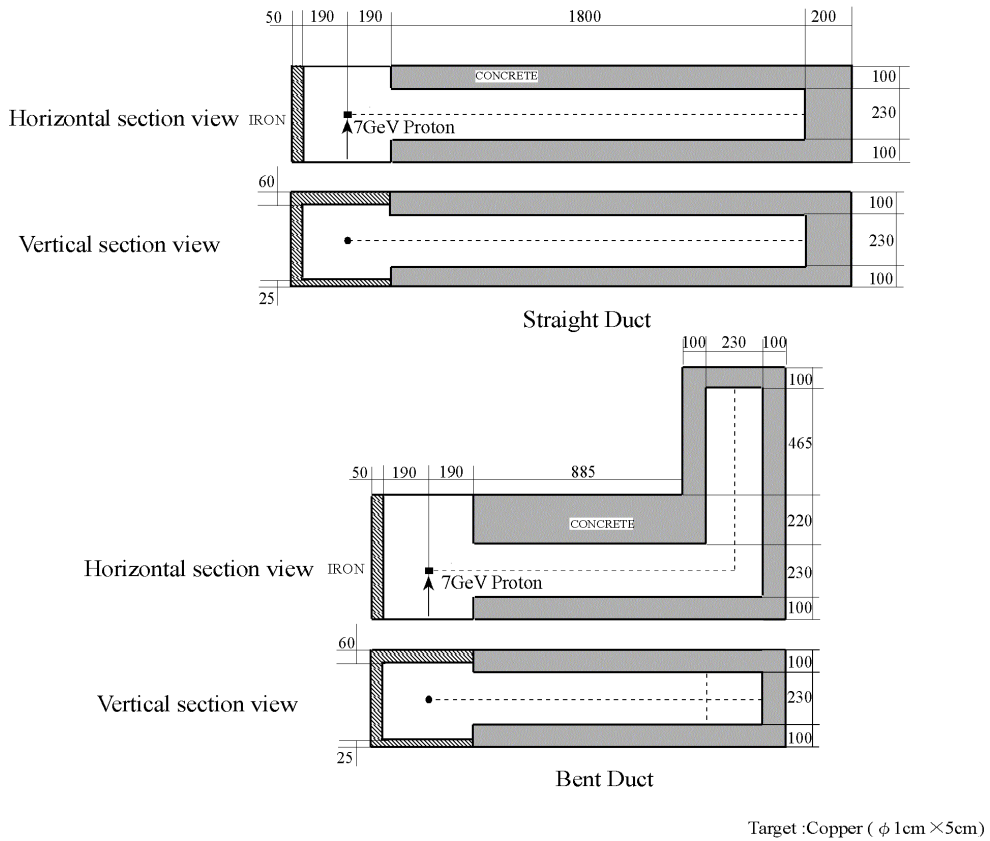


Figure 3. Comparison of calculated neutron dose equivalent rate distributions in the labyrinth at TIARA (LIR2) together with measured ones using the rem counter

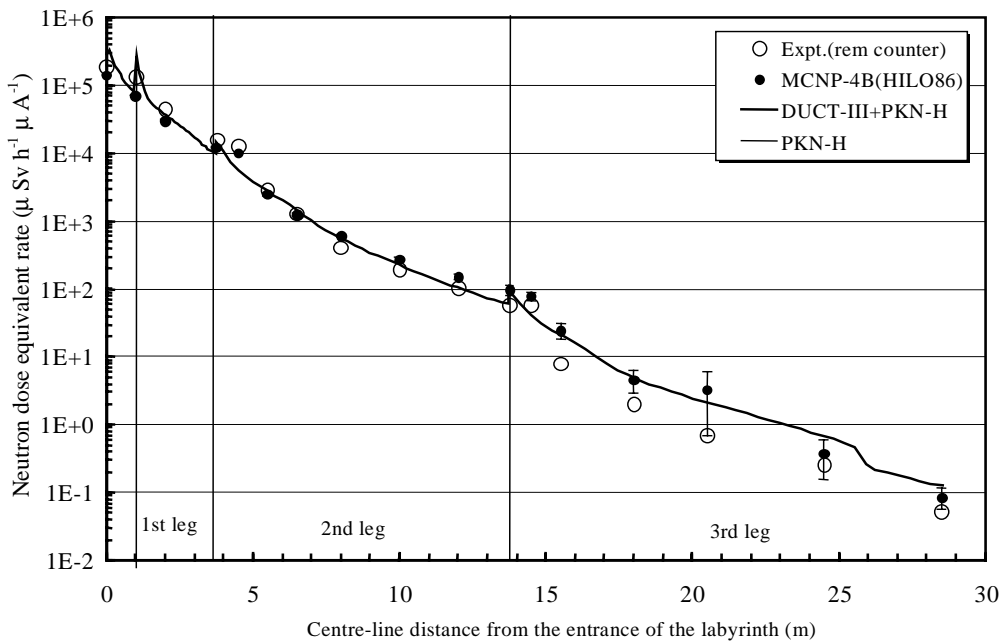


Figure 4. Comparison of calculated neutron dose equivalent rate distribution in the labyrinth at TIARA (LIR2) together with the Bonner ball counter

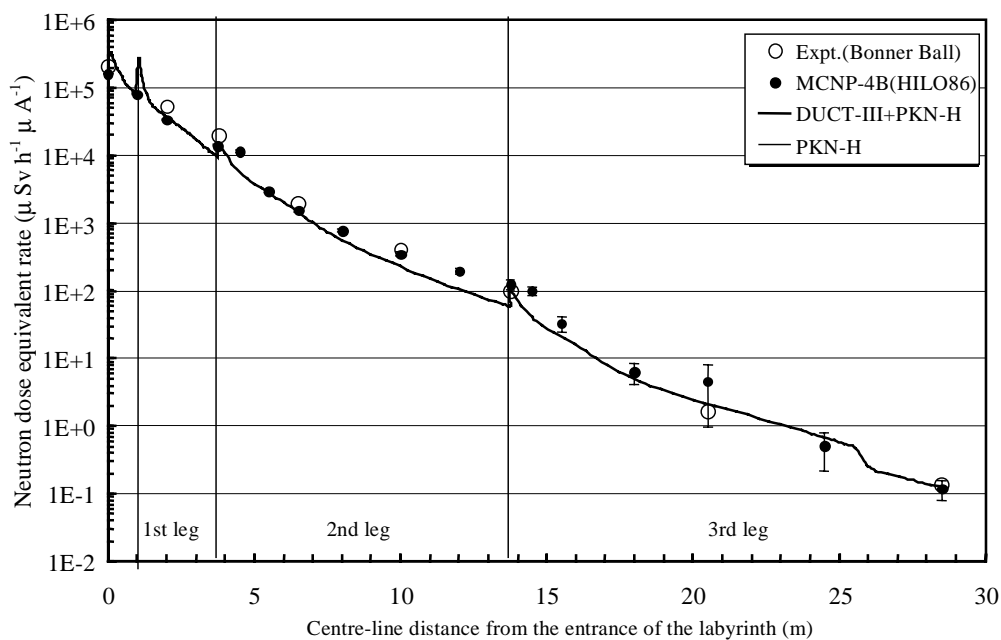


Figure 5. Comparison of calculated thermal neutron flux distribution in the labyrinth at TIARA (LIR2) together with measured ones using the TLDs and the Bonner ball counter

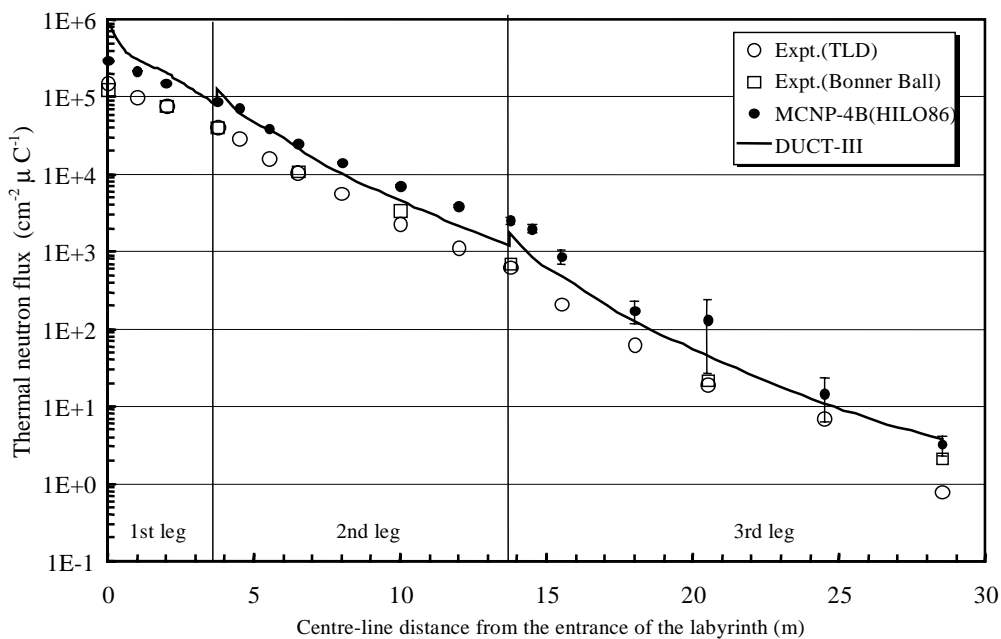


Figure 6. Comparison of calculated attenuation curves for neutron flux above 0.1 MeV in the labyrinth at TIARA together with measured ones using BC501A scintillation detector and the multi-moderate spectrometer, the solid state nuclear track detector

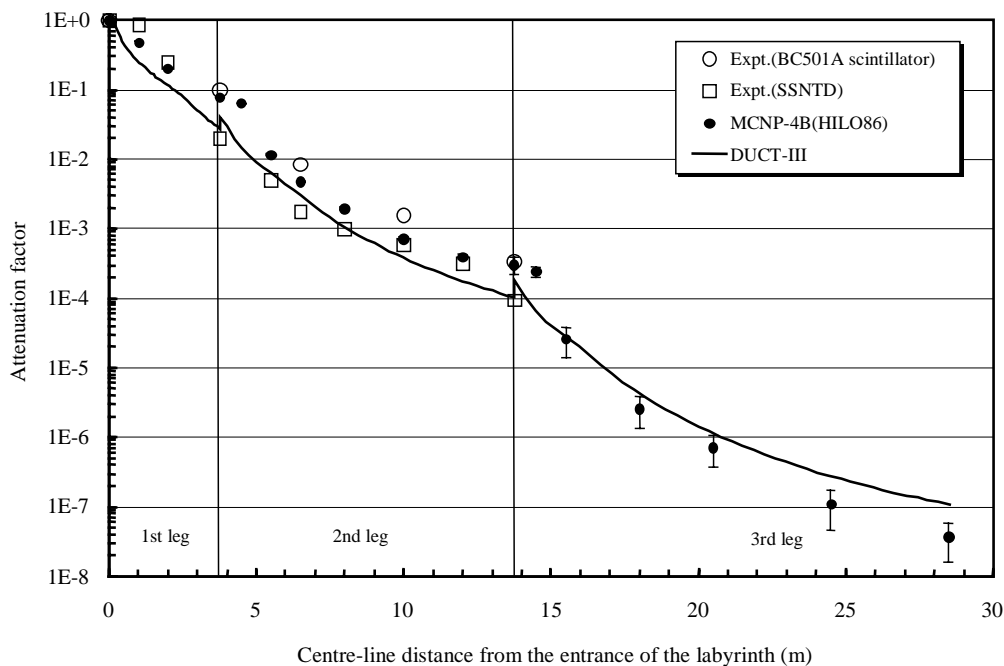


Figure 7. Comparison of calculated attenuation curves for the activities induced gold foils in the straight duct at NIMROD together with measured ones using the activation detector

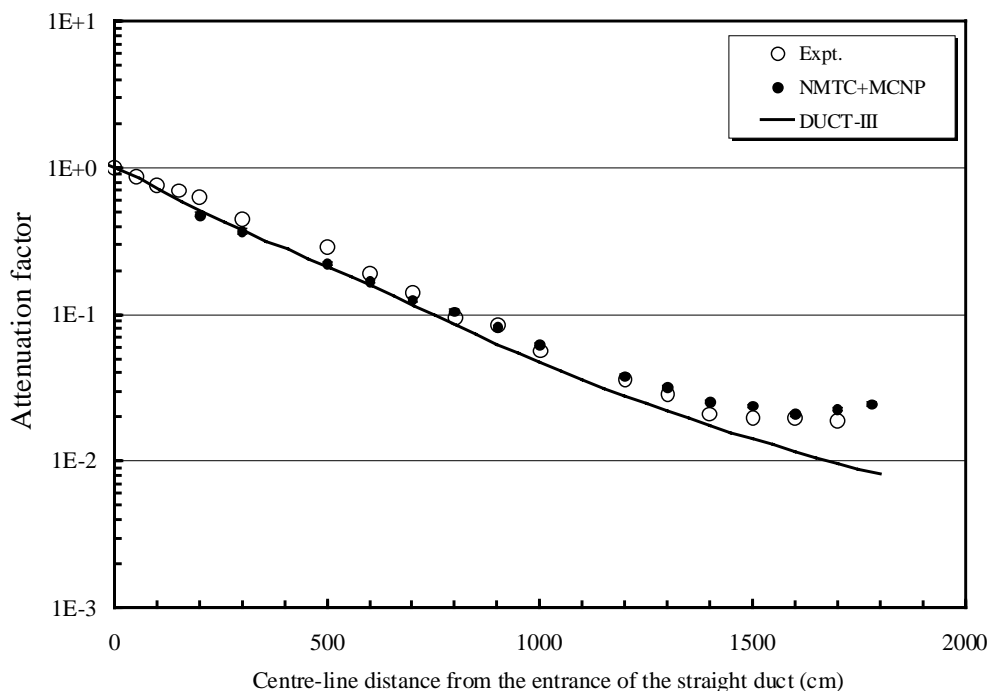


Figure 8. Comparison of calculated attenuation curves for the activities induced carbon foils in the straight duct at NIMROD together with measured ones using the activation detector

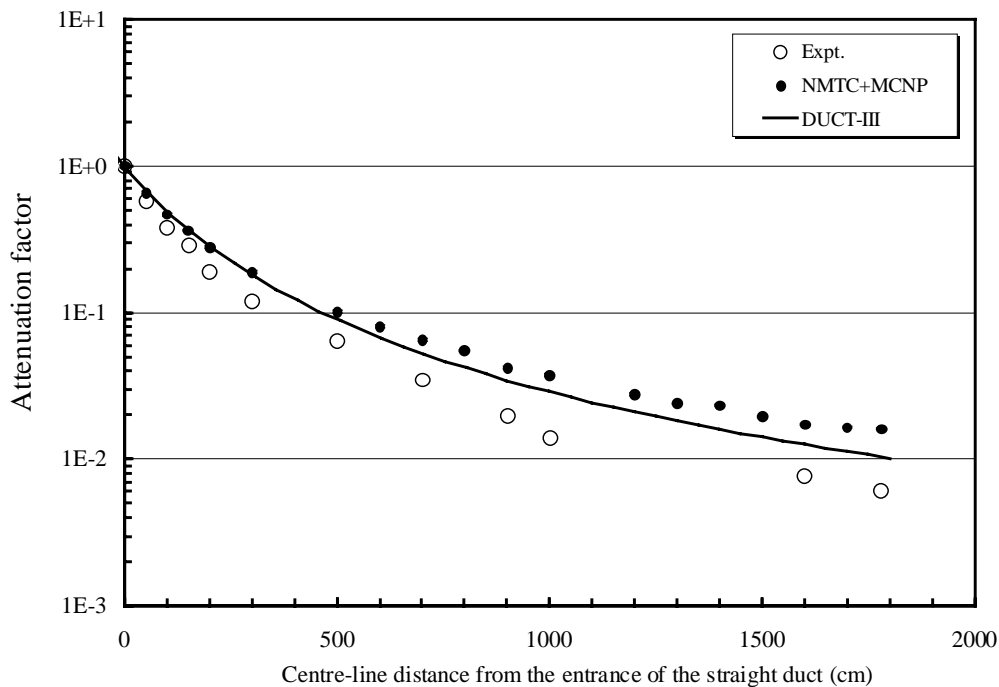


Figure 9. Comparison of calculated attenuation curves for the activities induced gold foils in the bent duct at NIMROD together with measured ones using the activation detector

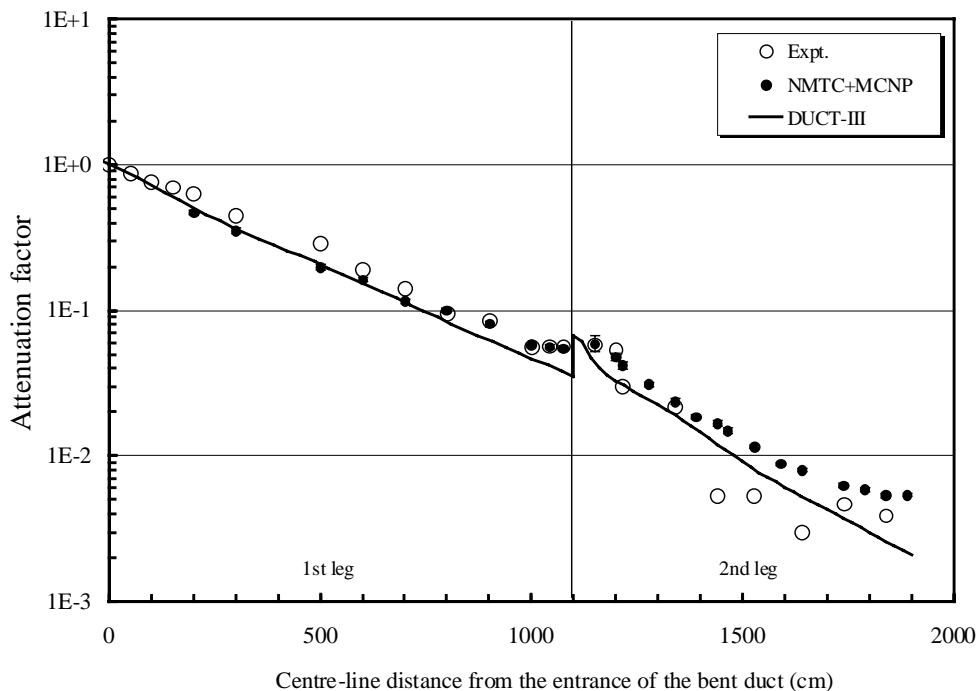
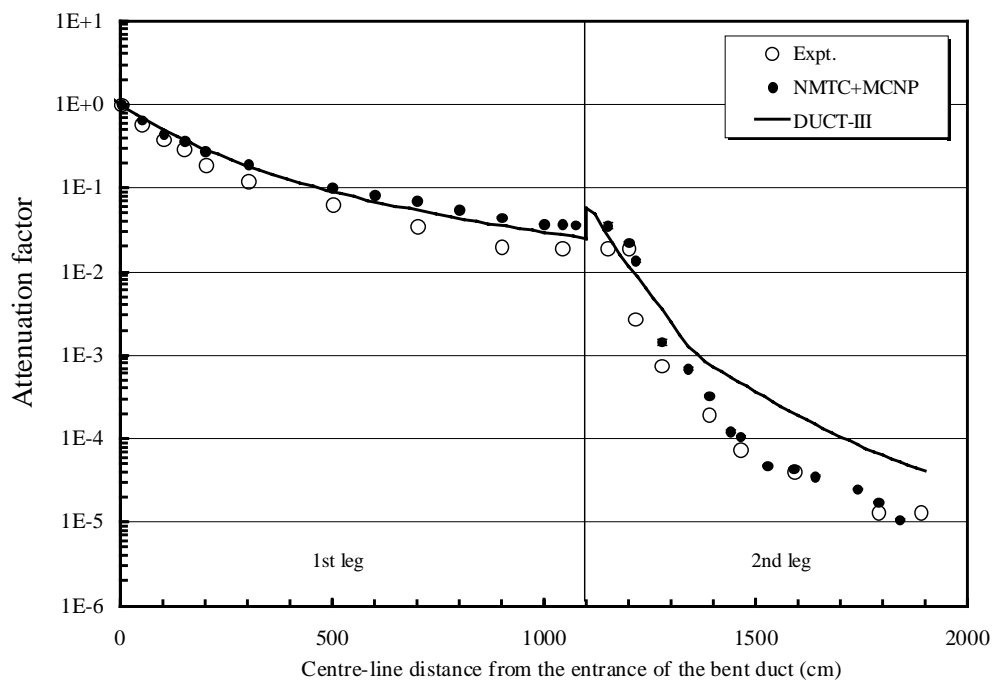


Figure 10. Comparison of calculated attenuation curves for the activities induced carbon foils in the bent duct at NIMROD together with measured ones using the activation detector



ON THE FUEL CYCLE AND NEUTRON FLUXES OF THE HIGH FLUX REACTOR AT ILL GRENOBLE

D. Ridikas, G. Fioni, P. Goberis, O. Déruelle, M. Fadil, F. Marie, S. Röttger
CEA Saclay, F-991191 Gif-sur-Yvette Cedex, France

H. Faust
Institut Laue-Langevin, Grenoble, France

Abstract

The fuel evolution and neutron fluxes of the high flux reactor at ILL Grenoble were investigated for the full fuel cycle. Two different code systems, namely MONTEBURNS and MCNP + CINDER'90, were employed for a realistic 3-D geometry description of the reactor core and experimental channels of interest. Both codes correctly reproduce the history of the fuel burn-up. Calculated neutron flux in the reactor core is $2.16 \times 10^{15} \frac{n}{s \text{ cm}^2}$ and decreases down to $1.65 \times 10^{15} \frac{n}{s \text{ cm}^2}$ and $6.7 \times 10^{14} \frac{n}{s \text{ cm}^2}$ in the experimental channels V4 and H9 respectively. Thermal neutron contribution is ~85.2% in V4 and ~98.3% in H9. We show that neutron fluxes in the experimental channels V4 and H9 are not perturbed/changed due to the burn-up of the fuel element and/or movement of the control rod. This result should simplify most of the irradiation experiments (and data analysis in particular), which employ the experimental channels as above.

Introduction

In the frame of the Mini-Inca project [1] – integral measurements relevant to nuclear waste transmutation systems – neutron beams delivered by the high flux reactor of the Institut Laue-Langevin in Grenoble [2] will be used, both for thermal and epithermal spectra. The choice of the ILL reactor for nuclear waste transmutation related projects is mainly due to its unique possibility to dispose of several different neutron spectra, obtained by changing the distance between the sample and the fuel element (core). It also provides very high thermal neutron flux ($\sim 10^{15} \frac{n}{s \text{ cm}^2}$), which makes possible high accuracy measurements in the thermal energy region with a very small amount of target material ($\sim 10 \mu\text{g}$) [1].

So far, there was no quantitative and consistent study of neutron fluxes delivered by the ILL reactor to the experimental channels. In principle, these fluxes may change due to the nuclear fuel burn-up and/or movement of the control rod during the full reactor cycle of ~ 50 days. There is no doubt that variable irradiation conditions could influence/complicate data analysis if neutron fluxes are considerably changed as a function of time.

Here we perform quantitative calculations of the fuel evolution and corresponding comparison (time dependence) of the neutron fluxes both in the reactor and experimental channels. A realistic 3-D geometry of the reactor core and experimental tubes of interest is modelled with two different code systems, namely MONTEBURNS and MCNP + CINDER'90.

Simulation codes and data libraries

Below we briefly describe the code systems employed to perform the fuel evolution and neutron flux calculations. By comparing the results obtained with two different codes we want to make sure that our simulations are reliable and self-consistent.

An automatic MONTEBURNS code

MONTEBURNS [3] was designed to link the Monte Carlo N-particle transport code MCNP [4] and the radioactive decay and burn-up code ORIGEN2 [5] into an automated tool. MCNP generates a statistical history for a neutron based random samples from probability distributions. These distributions are used in calculations to determine the type of interaction the particle undergoes at each moment of its life, the resulting energy of the particle it scatters, if it is absorbed, the number of particles that “leak” from the system because of geometry constraints, and the number of neutrons produced if the neutron causes a fission or (n,xn) reaction. The fluxes of neutrons determined in this way can then be used to tally a wide variety of information (reaction rates, heating rates, doses, etc.) for the system.

The main function of MONTEBURNS is to transfer one-group cross-sections and flux values from MCNP to ORIGEN2, and then transfer the resulting material compositions (after irradiation and/or decay) from ORIGEN2 back to MCNP in a repeated, cyclic fashion. ORIGEN2 performs burn-up calculations for MONTEBURNS using the matrix exponential method in terms of time-dependent formulation, destruction and decay concurrently. The nuclides contained in the ORIGEN2 databases have been divided into three segments: 130 actinides, 850 fission products and 720 activation products (a total of 1 700 nuclides) [5].

MONTEBURNS produces a large number of criticality and burn-up results based on various material feed/removal specifications, power and time intervals. The results obtained are more accurate

if long irradiation periods are broken up into several intervals of time because the physics and composition of materials in the system may change significantly with time. Not all isotopes produced during the burn-up step are transferred for a follow-up MCNP calculation. If an isotope contributes a large enough fraction to absorption or fission interactions, mass or atom density, then automatically the isotope is considered “important”. Flux and one-group, spectrum-averaged, cross-section tallies can then be performed in MCNP for these isotopes (except those for which no MCNP cross-section exist).

MONTEBURNS calculations are only as good as the MCNP cross-sections that are available to the user (e.g. see Refs. [6,7,8]). MONTEBURNS is also limited by the accuracy of the ORIGEN2 fission product yields and decay data library.

Manual coupling of MCNP and CINDER’90 codes

Instead of using MONTEBURNS, an interesting alternative is to run the CINDER’90 transmutation inventory code [9] coupled with MCNP because of increased output options, improved default cross-section sets (for 63-group neutron energies) and fission product yields, and possibly wider availability (e.g. handling of the spallation products in high-energy induced reactions). However, coupling of CINDER’90 to MCNP is not yet available in the automatic-cyclic fashion. Therefore, averaged 63-group neutron fluxes have to be recalculated with MCNP for each consequent burn-up step, for which MCNP materials are feeded manually as a result of the previous CINDER’90 burn-up output.

In brief, the temporal concentrations of nuclides depleted and produced in materials subject to irradiation are described by a large set of coupled differential equations, each nuclide’s concentration being determined by a history of gains from neutron absorption reactions (spallation, fission, (n,γ) , $(n,2n)$, etc.) and radioactive decay of parent nuclides, and losses from its own decay and particle absorption. The CINDER’90 code resolves nuclide couplings into linear chains, resulting in small independent sets of differential equations describing the rate of change of partial concentrations of nuclides in each chain. The solution of a large sets of differential equations is thus reduced to the solution of a number of small sets of differential equations. Because of the linear nature of the chain (a result of Markov like process), the generalised equations are solved sequentially for the partial concentration of each linear nuclide in the chain. Nuclide concentrations are then obtained by summing partial concentrations (see [9] for a more detailed description).

The CINDER’90 code has a library of 63-group cross-sections (to be compared with one-group cross-sections used by ORIGEN2). The library, known as LibB, of nuclear data used by CINDER’90, constantly growing in breadth and quality, now describes 3 400 nuclides in the range $1 \leq Z \leq 103$ including 1 325 fission products. CINDER’90 uses these data, e.g. ENDF/B-VI, Joint European Data File (JEF-1), European Activation File (EAF-3), Master Decay Library (MDL), GNASH code results, etc. [9].

The high flux reactor at ILL Grenoble

ILL reactor characteristics

The high flux reactor of the Institute Laue-Langevin (ILL) in Grenoble provides the highest thermal neutron flux in the world for research purposes. A single fuel element of highly enriched uranium (93%) is cooled and moderated by a flow of heavy water. The main reactor characteristics employed in our simulations are given in Table 1. More details can be found in Ref. [2].

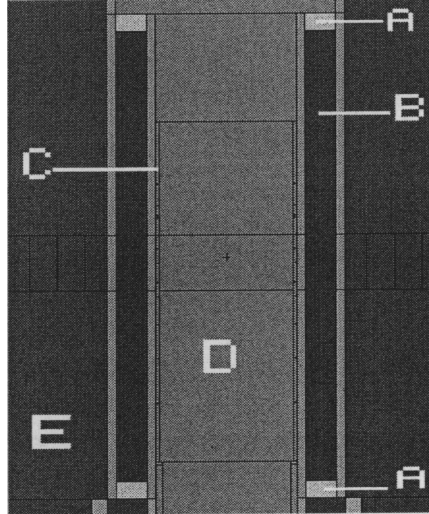
Table 1. Main characteristics of the high flux reactor at ILL Grenoble with highly enriched uranium fuel in equilibrium

Reactor thermal output	58 MW _{th}
Average reactor cycle	~50 days
Average core power density (W/cm ³)	1 253
Core geometrical parameters:	
– Core radius, inner/outer (cm)	14.0/19.5
– Core height (cm)	80.0
– Inner radius of reflector (cm)	11.9
– Axial reflector thickness (cm)	105.5
Control rod material	Natural Ni
Initial fuel isotopic composition (%):	
– ²³⁵ U	93
– ²³⁸ U	7
Core fuel inventory (g)	~8 600
B-10 zone inventory (g)	~7.8

In Figure 1 we present the major elements of the reactor geometry used for neutron flux estimations with the MCNP code. MCNP is run in the mode of the criticality eigenvalue (k_{eff}) problem.

Figure 1. A representation of the major elements of the reactor geometry

The following notation is employed: A – borated zones, B – reactor core, C – control rod, D – inner reflector region, E – outer reflector region. Note: all elements have cylindrical geometry and are symmetric along the central reactor axis.



The control rod changes its position (moves down) as a function of time (as a function of the evolution of the fuel composition) in order to keep $k_{eff} \sim 1$. A position of the control rod at any time t is known experimentally for 50 days of the reactor cycle [2]. We have followed this dependence during our simulations by changing the MCNP input file. One should note that the anti-reactivity of the control rod changes due to the irradiation from one cycle to another cycle. Therefore, depending on how many times (cycles) the same control rod was used, its position dependence might change. As a matter of fact, the control rod is replaced by a new one once per year.

Our calculations show that the worth of the control rod is ~16 500 pcm. Another ~5 500 pcm is due to upper and lower borated zones of the reactor (see Figure 1). These values are in good agreement with the ones reported in [2], i.e. 17 300 pcm and 4 500 pcm correspondingly.

A formulation of the problem

As we have already mentioned, the main goal of this study is to estimate the change (if any) of the neutron fluxes both in absolute value and energy due to the fuel evolution and/or movement of the control rod of the reactor. Of course, the “theoretical” reactor should stay in equilibrium ($k_{\text{eff}} = 1$) or as close to the equilibrated system as possible during the fuel cycle we want to simulate. Another interest is related to the validation/comparison of two different evolution codes, namely ORIGEN2 and CINDER’90.

We use both MONTEBURNS and MCNP + CINDER’90 code systems for the material evolutions of the fuel (core) and two borated zones as shown in Figure 1. Reactor power is kept constant at 58 MW_{th} by means of an automatic renormalisation (if needed) of the neutron flux. The absolute value of the neutron flux is calculated using the following expression [3]:

$$\phi = \phi_n \times C = \phi_n \times \frac{\nu P (10^6 \text{ W/MW})}{(1.602 \times 10^{-13} \text{ J/MeV}) k_{\text{eff}} Q_{\text{ave}}} \quad (1)$$

where ν is an average number of neutrons produced per fission, P is a reactor power (in MW) defined by user, k_{eff} is an effective neutron multiplication factor given by MCNP and Q_{ave} is an average recoverable energy per fission, while ϕ_n stands for an average neutron flux obtained from the MCNP output file and normalised per source neutron.

Fifty days fuel cycle is then divided into 13 smaller intervals for which k_{eff} and fluxes in the reactor areas of interest are recalculated with new/updated material compositions (if these are considered “important” according to the conditions we have discussed in the previous section).

Simulation results

Fuel burn-up and k_{eff} of the reactor

The history of the fuel burn-up is presented in Tables 2-3. In addition to the evolution of ^{235}U , ^{238}U and ^{239}Pu we also represent the evolution of ^{135}Xe and ^{149}Sm (here as fission products and major neutron poisons) in the fuel element. The calculated burn-up of ^{235}U is nearly 47.5% with MONTEBURNS and 46.6% with MCNP + CINDER’90. These numbers are in reasonable agreement with burn-up rates given in Ref. [2], namely 36% on average and a possible maximum burn-up of 70% during the full reactor cycle.

Table 2 also gives the calculated average flux intensities both in the fuel element (core) and in the experimental tubes V4 and H9 at their lowest/end positions (to be discussed in the following section).

Figure 2 represents the evolution of k_{eff} during the full reactor cycle. In order to keep the k_{eff} constant, the movement of the control rod should compensate the fuel burn-up (see Table 2), which is consistently reproduced by both simulations. This also proves that the evolution of the fuel and borated zones is done correctly.

Table 2. Reactor full cycle history (MONTEBURNS simulation). The eigenvalue problem for k_{eff} with MCNP has been run with 125 000 source neutrons.

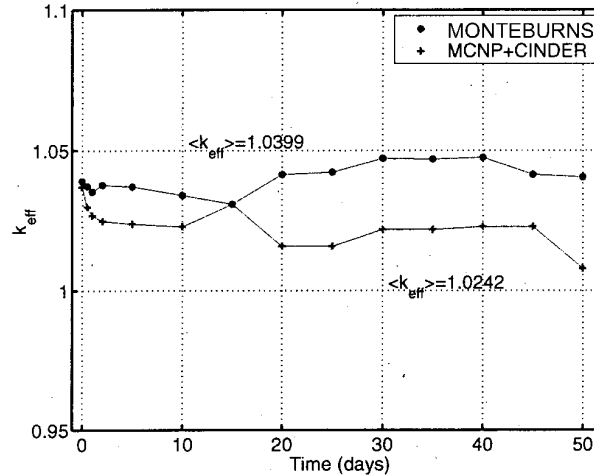
Time, days	k_{eff}	ϕ_n (core), $10^{15} \frac{n}{s \text{ cm}^2}$	ϕ_n (V4), $10^{15} \frac{n}{s \text{ cm}^2}$	ϕ_n (H9), $10^{15} \frac{n}{s \text{ cm}^2}$	^{235}U (g)	^{238}U (g)	^{239}Pu (g)	^{135}Xe (g)	^{149}Sm (g)
0.0	1.039	2.25	1.88	0.79	7 970	607	0.00	0.000	0.00
0.5	1.037	2.30	1.71	0.78	7 930	607	0.01	0.045	0.01
1.0	1.035	2.27	1.71	0.72	7 890	607	0.05	0.055	0.02
2.0	1.038	2.27	1.65	0.75	7 820	606	0.27	0.060	0.08
5.0	1.037	2.28	2.00	0.74	7 590	604	1.54	0.062	0.26
10	1.034	2.30	1.88	0.75	7 210	600	4.36	0.058	0.36
15	1.031	2.30	1.75	0.75	6 830	596	7.15	0.054	0.37
20	1.041	2.31	1.74	0.74	6 450	592	9.64	0.051	0.37
25	1.042	2.32	1.70	0.76	6 070	589	11.7	0.047	0.37
30	1.047	2.32	1.71	0.77	5 690	585	13.3	0.044	0.36
35	1.047	2.36	1.78	0.74	5 310	581	14.7	0.041	0.36
40	1.048	2.39	1.66	0.72	4 940	577	15.8	0.038	0.35
45	1.042	2.43	1.98	0.79	4 560	573	16.5	0.035	0.34
50	1.041	2.46	1.83	0.77	4 180	570	16.8	0.031	0.33
Average	1.040	2.32	1.78	0.76					

Table 3. Reactor full cycle history (MCNP + CINDER'90 simulation). The eigenvalue problem for k_{eff} with MCNP has been run with 2 000 000 source neutrons.

Note: k_{eff} values and fluxes were not calculated at $t = 25, 35$ and 45 days

Time, days	k_{eff}	^{235}U (g)	^{238}U (g)	^{239}Pu (g)	^{135}Xe (g)	^{149}Sm (g)
0.0	1.037	7 970	607	0.00	0.000	0.00
0.5	1.030	7 929	607	0.00	0.049	0.01
1.0	1.027	7 891	607	0.03	0.064	0.04
2.0	1.025	7 818	607	0.09	0.069	0.11
5.0	1.024	7 596	606	0.46	0.067	0.30
10	1.023	7 229	605	1.27	0.064	0.40
15	1.031	6 874	604	2.09	0.061	0.42
20	1.016	6 536	603	2.82	0.058	0.43
25	–	6 136	602	3.44	0.054	0.40
30	1.022	5 760	601	4.02	0.051	0.42
35	–	5 360	600	4.47	0.046	0.40
40	1.023	4 989	599	4.89	0.043	0.41
45	–	4 607	598	5.16	0.039	0.38
50	1.008	4 255	597	5.42	0.036	0.39
Average	1.024					

Figure 2. A variation of k_{eff} as a function of time during fuel cycle

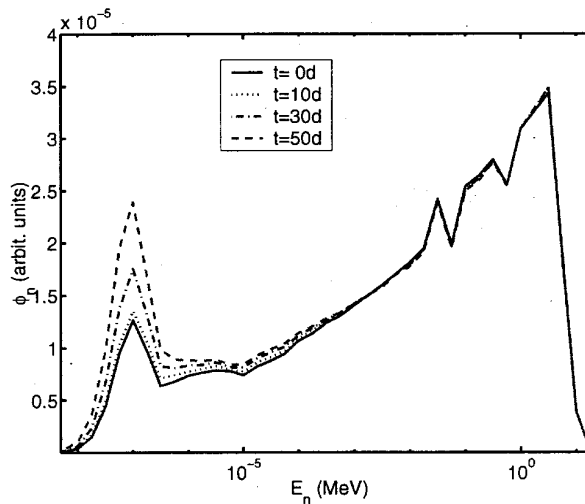


The only big difference (between the two codes) in the material composition of the fuel is seen from the evolution of ^{239}Pu (compare the corresponding columns in Tables 2-3). The total mass of ^{239}Pu predicted by MONTEBURNS is three times higher than the same quantity obtained with CINDER'90. This disagreement between the two codes still has to be understood, even though such a small mass of ^{239}Pu has no/little influence on the fuel cycle of the ILL reactor.

Neutron fluxes in the core

The main goal of this study was to estimate possible changes of the neutron fluxes due to the movement of the control rod and fuel burn-up. The time-dependent energy distributions of the neutron flux are presented in Figure 3. These curves stand for the average neutron flux in the fuel element (core). It is clearly seen that there are more (by ~7%) thermal neutrons ($E_n < 1 \text{ eV}$) at the end of the fuel cycle, while the relative weight of the energetic neutrons has decreased correspondingly.

Figure 3. A variation of the average neutron spectrum inside the fuel element (core) during the reactor cycle of 50 days. The spectra presented are at time $t = 0, 10, 30$ and 50 days.



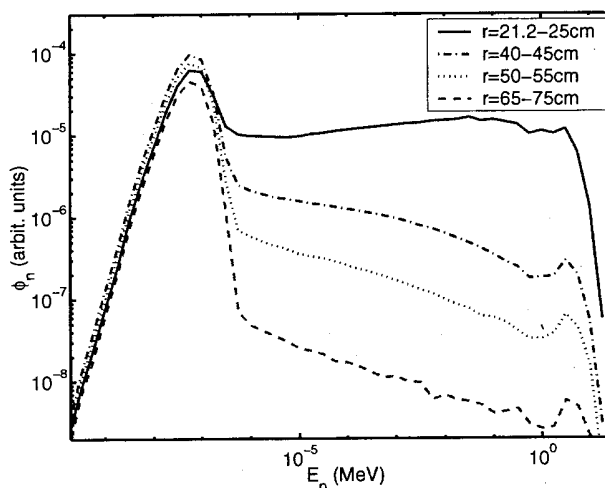
The “thermalisation” of the neutron flux in the core is mainly due to the movement of the control rod; in this way more thermal neutrons can be re-scattered back to the fuel element from the inner reflector region (D₂O). We remind here that the control rod moves down and at the end of the fuel cycle is completely withdrawn from the active zone (see Figure 1 for a geometry of the core). In addition, the decrease/saturation of ¹³⁵Xe (T_{1/2} = 9.1 h) and ¹⁴⁹Sm concentrations (being the major poisons of thermal neutrons) will also have non-negligible effect on the neutron energy spectra. The corresponding concentrations of Xe and Sm are given in Tables 2-3 for the full reactor cycle.

Neutron fluxes in the external moderator and experimental channels

Inside the external reflector tank of the reactor, neutrons are moderated by the heavy water, where the scattering length is about 20 cm. The moderator partly reflects the thermalised neutrons towards the fuel element. It is evident that different neutron spectra will be present at different distances from the core (with an increase of the moderation as a function of the distance). Starting from about 60 cm from the fuel element edge, the spectrum is essentially a Maxwellian distribution at the moderator temperature.

In Figure 4 we present the neutron fluxes calculated at different distances from the central axis of the reactor core. Thermal neutrons become dominant (>90%) at about 40 cm (dashed-dotted line). As close as at 5-10 cm from the reactor core, nearly ~56% of the neutrons are still epithermal and/or fast (solid line).

Figure 4. Neutron spectra in the external reflector for different radial distance r from the central axis of the core



The schemes of the installation of an inclined V4 and horizontal H9 beam tubes are presented on the left and right part of Figure 5, respectively. This particular geometry has been used for our simulations with the MCNP code.

The transmutation samples can be positioned at different distances along the experimental channels (V4 and H9) to have access to variable neutron fluxes. For comparison in Figure 6 we show calculated neutron fluxes in the lowest/end positions of V4 and H9 beam tubes, where flux intensities of $1.78 \times 10^{15} \frac{n}{s \text{ cm}^2}$ and $7.6 \times 10^{14} \frac{n}{s \text{ cm}^2}$ respectively are predicted at the nominal reactor power of 58 MW_{th}. These values are the neutron fluxes averaged over entire fuel cycle (see Table 2).

Figure 5. Positions of V4 (vertical) and H9 (horizontal) experimental tubes with respect to the fuel element (core)

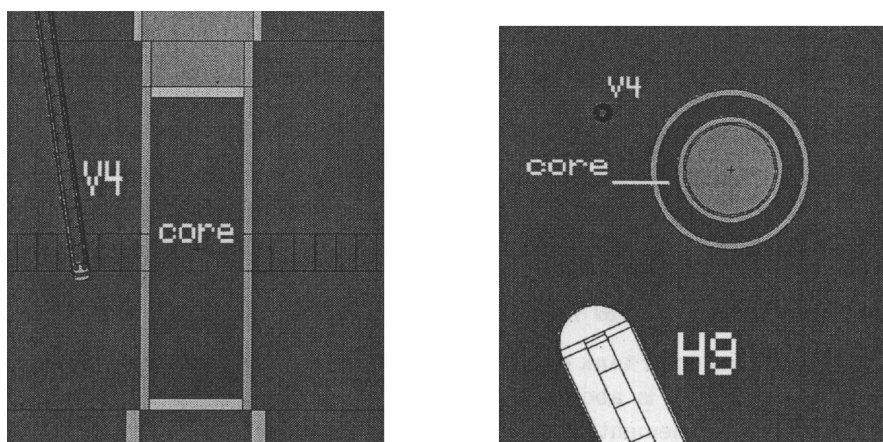
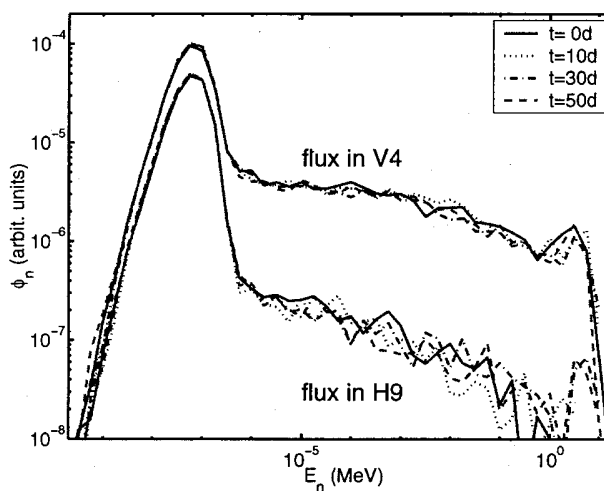


Figure 6. Calculated neutron fluxes at the lowest/end positions of the experimental beam channels V4 and H9 depending on time t (days) of the reactor cycle (also see Figure 5)



As long as the energy spectra of neutrons are concerned, we found that the flux in H9 is more thermalised (~ 98.3) if compared to the flux in V4 ($\sim 85.2\%$). The calculated change (due to fuel burn-up and movement of the control rod) of the thermal part of the flux is not higher than 1% in both channels. We reiterate that inside the fuel element at the end of the fuel cycle the contribution of the thermal neutrons was increased by $\sim 7\%$ as shown in Figure 3. However, in the external reflector (including experimental channels) most of the epithermal and fast neutrons leaving the reactor core become thermal, and this already small change of $\sim 7\%$ becomes relatively less important further away from the reactor core.

We should note at this point that the fluxes calculated in H9 experimental channel are by $\sim 25\%$ higher than the corresponding experimentally measured values, namely $5.5\text{-}5.9 \times 10^{14} \frac{n}{s \text{ cm}^2}$ with 10% uncertainty [10]. We believe that the major reason for overestimation of this flux in absolute value was due to many other experimental channels [2] which were not taken into account in our simulated geometry. Secondly, only after all calculations had been finished did we have realise that the mass of ^{235}U in the initial fuel load (see Table 1) was not taken correctly, i.e. 8.0 kg of ^{235}U instead of

8.6 kg [2]. Finally, the calculated average neutron fluxes correspond to the H9 experimental channel filled with heavy water but not with air as was the case during the experiment [10]. Therefore, we performed a new calculation (at time $t = 0$ days), this time with a correct mass of ^{235}U and no heavy water in the experimental tube H9. The calculated flux decreased by 15%, i.e. from $7.9 \times 10^{14} \frac{n}{s \text{ cm}^2}$ down to $6.7 \times 10^{14} \frac{n}{s \text{ cm}^2}$, which is in better agreement with the experimentally obtained value. A similar decrease was predicted for the flux in the experimental channel V4, specifically from $1.88 \times 10^{15} \frac{n}{s \text{ cm}^2}$ down to $1.65 \times 10^{15} \frac{n}{s \text{ cm}^2}$.

Finally, we add that the above correction for the absolute value of the neutron fluxes does not change the conclusions we made concerning the energy spectra of neutrons during the fuel cycle. However, the fuel burn-up would be slightly smaller than the presently predicted value of $\sim 47\%$.

Conclusions

We have performed a quantitative calculation of the evolution of the fuel and fluxes of the high flux reaction at ILL Grenoble for its full reactor cycle. The simulations were done with two different code systems: MONTEBURNS (MCNP + ORIGEN2) and MCNP + CINDER'90. The major difference between the two codes is that the first is based on one-group neutron cross-section libraries while the second uses 63-group neutron data.

Both codes correctly reproduce the history of the fuel cycle ($k_{\text{eff}} \sim 1$ at all times within 50 days) and give a similar fuel burn-up of $\sim 47\%$. Calculated average neutron flux (corrected as discussed above) in the reactor core is $2.16 \times 10^{15} \frac{n}{s \text{ cm}^2}$ and decreases to $1.65 \times 10^{15} \frac{n}{s \text{ cm}^2}$ and $6.7 \times 10^{14} \frac{n}{s \text{ cm}^2}$ in the experimental channels V4 and H9 respectively at the lowest/end positions. Thermal neutron ($E_n < 1 \text{ eV}$) contribution is $\sim 85.2\%$ in V4 and 98.3% in H9.

In both experimental channels (V4 and H9) there were no important changes (within 1%) in the energy spectra of the neutrons due to fuel evolution and/or movement of the control rod. On the other hand, the contribution of the thermal neutrons increased by 7% in the fuel element (core) itself at the end of the reactor cycle.

We conclude that neutron fluxes in the experimental channels V4 and H9 are not perturbed/changed due to the burn-up of the fuel element and/or movement of the control rod. We believe that this result simplifies most of the irradiation experiments (and data analysis in particular) which employ the experimental channels as above. The Mini-Inca project is one of them.

Finally, this work serves as a validation study of two different evolution codes, namely ORIGEN2 and CINDER'90. It also gives us confidence to employ them for the simulations of different critical or sub-critical systems related to nuclear waste transmutation. The calculations along these lines are in progress.

REFERENCES

- [1] G. Fioni, *et al.*, “Mini-Inca: Integral Measurements Relevant for Nuclear Waste Transmutation Systems”, Proposition au Conseil Scientifique et Technique, SPhN CEA/Saclay, France (December 1998).
- [2] “Rapport de Sûreté du Réacteur à Haut Flux”, Vol. 4, Institut Max von Laue – Paul Langevin (Grenoble, 1971).
- [3] H.R. Trellue and D.I. Poston, “User’s Manual, Version 2.0 for MONTEBURNS, Version 5B”, Los Alamos National Laboratory, pre-print LA-UR-99-4999 (1999); H.R. Trellue, private communication (April 2000).
- [4] J. Briesmeister for Group X-6, “MCNP-A, A General Monte Carlo Code for Neutron and Photon Transport”, Version 4A, Los Alamos National Laboratory, pre-print LA-12625-M (1993).
- [5] RSIC Computer Code Collection, “ORIGEN 2.1 – Isotope Generation and Depletion Code Matrix Exponential Method”, Radiation Shielding Information Center, report CCC-371 (1991).
- [6] ENDF/B-VI, “The US Evaluated Neutron Nuclear Data Library for Neutron Reactions”, IAEA Vienna, IAEA-NDS-100, Rev. 6 (1995).
- [7] JENDL-3.2, “The Japanese Evaluated Nuclear Data Library”, IAEA Vienna, IAEA-NDS-110, Rev. 5 (1994).
- [8] JEF-2.2, “The Evaluated Neutron Nuclear Data Library of the NEA Data Bank”, IAEA Vienna, IAEA-NDS-120, Rev. 3 (1996).
- [9] W.B. Wilson, T.R. England and K.A. Van Riper, “Status of CINDER’90 Codes and Data”, Los Alamos National Laboratory, preprint LA-UR-99-361 (1991), submitted to Proc. of 4th Workshop on Simulating Accelerator Radiation Environments, 13-16 September 1998, Knoxville, Tennessee, USA; W.B. Wilson, private communication (March 2000).
- [10] F. Gunsing, G. Fioni, “Neutron Flux Determination from Iron Monitors for the ²⁴¹Am Transmutation Experiment”, CEA report, DAPNIA/SPhN 98-07 (1998).

SHIELDING ASPECTS OF A TOKAMAK REACHING IGNITION

Sofia Rollet and Paola Batistoni

ENEA, Energy Research Centre
Via E. Fermi 27, I-00044 Frascati (Roma), Italy

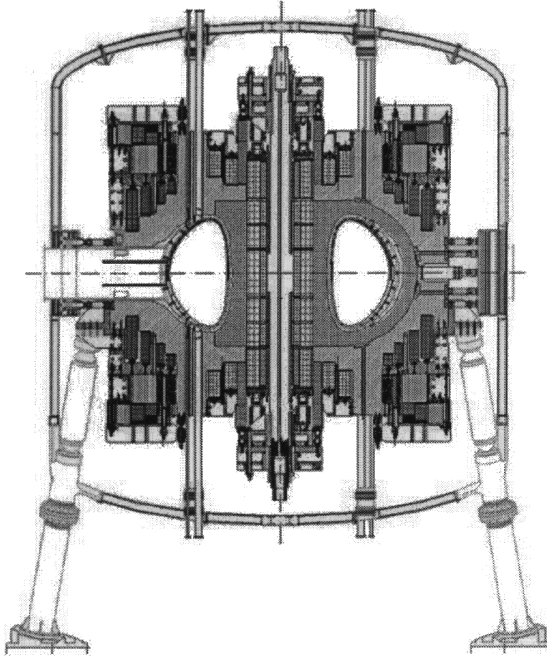
Abstract

The Ignitor experiment is designed to produce deuterium-tritium (DT) plasmas in which ignition can take place and the physics of α -particles can be studied. After a first period of aneutronic operation, a second phase in deuterium with 2.5 MeV neutron production rate up to 10^{17} n/s is planned. This will be followed by operations at increasing percentages of tritium, leading to short but intense 14 MeV neutron production, up to $\approx 3 \times 10^{19}$ n/s. To calculate the neutron fluxes in all the machine components, a detailed description of the actual Ignitor machine is implemented in the MCNP-4B Monte Carlo code. These fluxes are then used as input for the FISPACT-99 code for the analysis of the activation at the end of life (EOL) and at intermediate times for safety assessment purposes. The estimated neutron emission pulse results in rather modest neutron fluences ($\approx 10^{18}$ n/cm² on the first wall at EOL). The shielding strategy and possible solutions to prevent/reduce the activation of the cryostat are presented.

Introduction

Ignitor (Figure 1) is a proposed experiment [1] designed to produce deuterium-tritium plasmas where ignition can take place and the physics of α -particles can be studied.

Figure 1. The Ignitor experiment layout



Dimensions: 7.5 m height, 7 m diameter

Major radius $R = 1.32$ m

Minor radii $a, b = 0.47$ m, 0.87 m

Toroidal field $B_T = 13$ T

Toroidal current $I_p = 12$ MA

Plasma volume $V_0 \approx 10$ m³

Plasma surface $S_0 \approx 36$ m²

It is a compact, high magnetic field tokamak with a toroidal field of 13 T, the major radius is $R = 1.32$ m, the minor radii are $a = 0.47$ and $b = 0.87$ m. After a first phase with pure deuterium (DD) plasma and 2.5 MeV neutron production rate up to 10^{17} n/s, operations with deuterium-tritium plasma (DT) at increasing percentages of tritium are planned, leading to short (4 s) but intense 14 MeV neutron production, up to 3×10^{19} n/s, corresponding to a fusion power of 90 MW. As compared to demonstration reactor experiments, characterised by large volume and long pulse duration, the Ignitor neutron emission results in a rather more modest fluence but in a comparable neutron flux on the first wall ($\approx 10^{14}$ n/s per cm²), inducing a considerable activation in the device components.

As in the present fusion experiments, access to the tokamak hall cannot be allowed during machine operation due to the neutron emission. However, in Ignitor the level of neutron emission is such that the induced activation of the materials could permanently forbid access to the machine. The main objective of the shielding study is thus to provide protection for the personnel from the inner activated components and to reduce the activation of the external cryostat as much as possible.

Calculation and results

The complex layout of the Ignitor experiment is described in detail with the use of the 3-D geometry capability of the MCNP-4B [2] Monte Carlo code. Only a 24th of the machine is described in the model, taking into account the symmetry planes and using the reflectivity boundary conditions. Figure 2 shows a plot of two-dimensional slice through the equatorial plane and Figure 3 shows an enlargement of the same cut only with the outboard region. A vertical cut through the toroidal magnet

Figure 2. Ignitor geometry simulated in the MCNP code: horizontal cut through the equatorial plane. Inboard, plasma and outboard region.

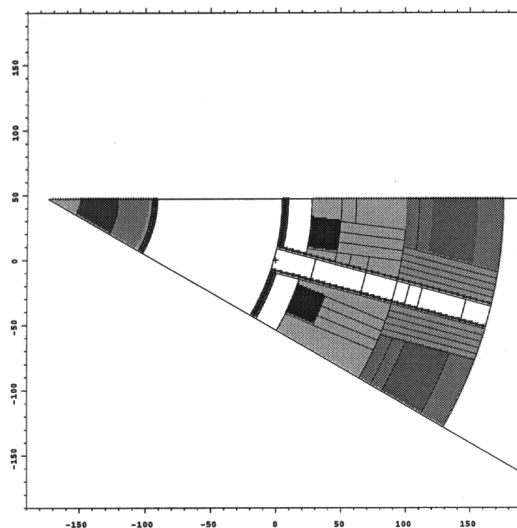
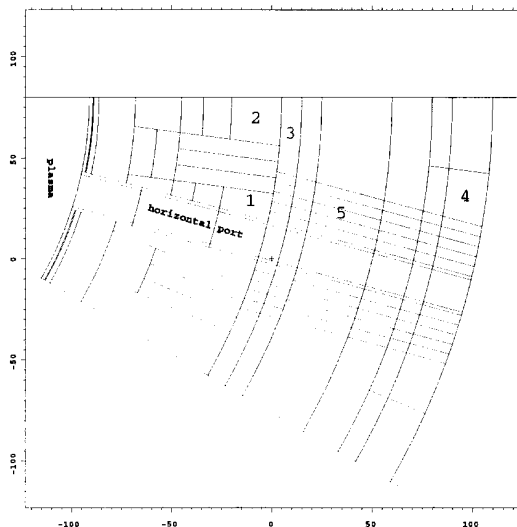


Figure 3. Ignitor geometry simulated in the MCNP code: horizontal cut through the equatorial plane. Enlargement of the outboard region with the shielding.



and through the horizontal and vertical ports is shown in Figures 4 and 5, respectively. The neutron fluxes calculated with MCNP are then used as input for the FISPACT-99 code [3] to calculate the induced activation of the materials and the resulting contact dose rates at the end of life and intermediate times during operations. The adopted agenda foresees ten years of operation: DD would begin during the second year, full DT (50/50%) operations by the fourth year. A total of 10^{21} 2.5 MeV (DD) neutrons and 10^{23} 14.1 MeV (DT) neutrons are produced.

The C-clamps are the mechanical structures surrounding the toroidal magnet to withstand the relevant loads and are made of stainless steel (AISI316). They are considered from a radiation protection point of view because they are the most external components inside the cryostat and they are the first the personnel will be in contact if any maintenance or repair is planned inside the cryostat.

Figure 4. Ignitor geometry simulated in the MCNP code: vertical cut through the toroidal magnet

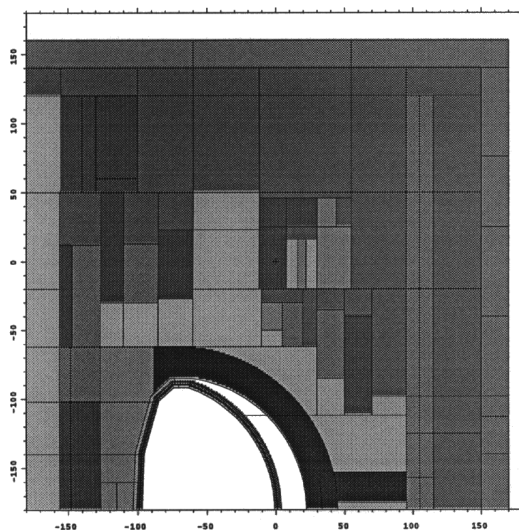
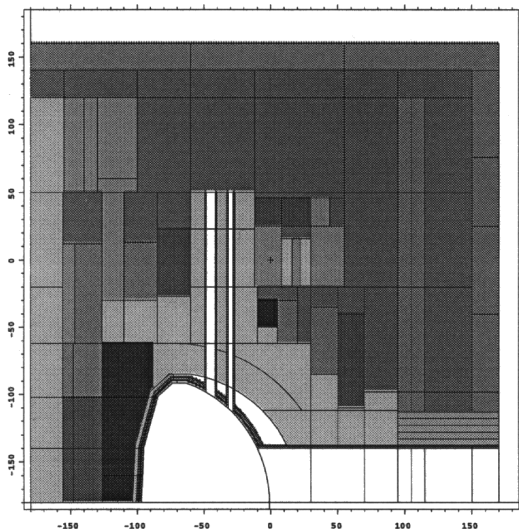


Figure 5. Ignitor geometry simulated in the MCNP code: vertical cut through the vertical and horizontal port



The neutron flux, shown in Figure 6, was calculated in the external part of the C-clamp (position 2 of Figure 3) located behind 50 cm of bulky components with respect to the neutron source (the plasma region). The resulting contact dose rate is given in Figure 7, showing that it is larger than the allowed limit of 100 $\mu\text{Sv/h}$. Such a limit is derived assuming that, given the ICRP limits of 100 mSv in five years, never exceeding 50 mSv per year [5], an average exposure of 200 h/y per person is permitted. The dose rate level falls below the limit after about one year of cooling time, if no cobalt is present in the steel, or after about 20 years if 0.04% of cobalt is contained as an impurity, due to the contribution of ^{60}Co ($T_{1/2} \approx 5.2$ years) produced in (n,γ) reactions on ^{59}Co . The streaming of fast neutrons through the horizontal ports gives rise to a higher neutron flux, especially in the fast energy range ($E \geq 1$ MeV), in the C-clamp close to the port (position 1 in Figure 3) as shown in Figure 8.

Figure 6. The neutron spectrum in the C-clamp far from the port

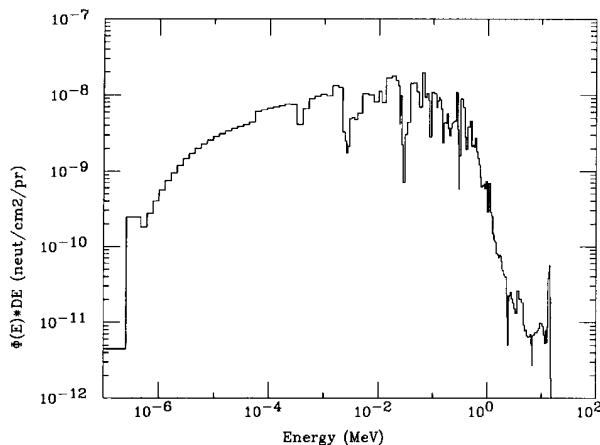


Figure 7. Contact dose rate versus cooling time in the C-clamp far from the port at the end of life. The dashed curve is obtained with 0.04% of Co addition as impurity in the material composition.

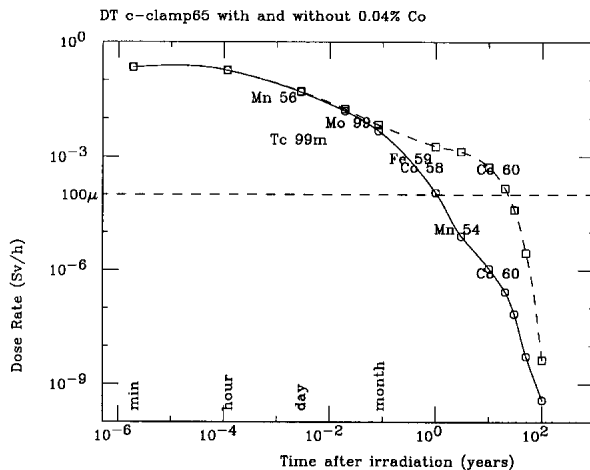
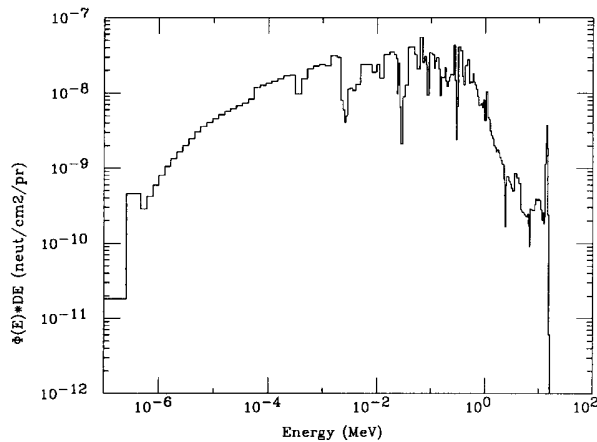
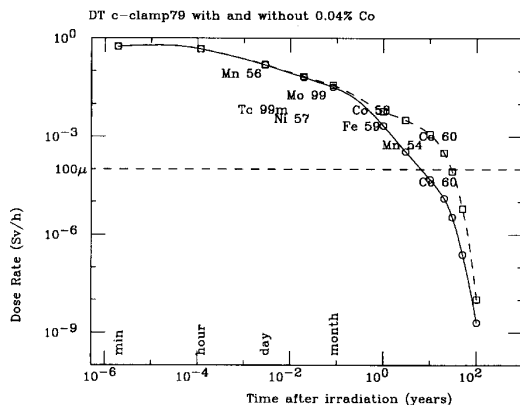


Figure 8. The neutron spectrum in the C-clamp close to the port



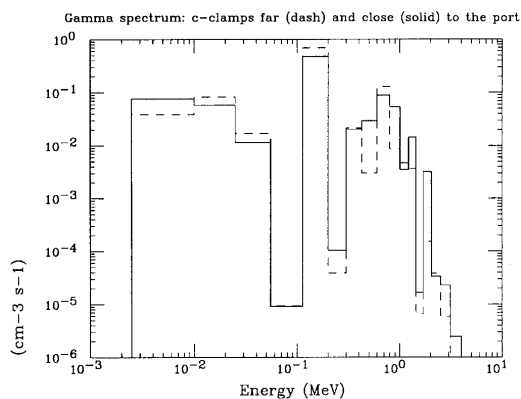
In this case the resulting dose rate (Figure 9) falls below the limit after about eight years of cooling time (if no cobalt is present in the steel), while no significant difference is observed if the cobalt is present. After seven days of cooling time, the major contribution to the dose is due to ^{58}Co ($T_{1/2} \approx 70$ days) produced in (n,p) reactions on ^{58}Ni , and to ^{99}Mo ($T_{1/2} \approx 3$ days) produced in (n, γ) reactions on ^{99}Mo .

Figure 9. Contact dose rate versus cooling time in the C-clamp close to the port at the end of life. The dashed curve is obtained with 0.04% of Co addition as impurity in the material composition.

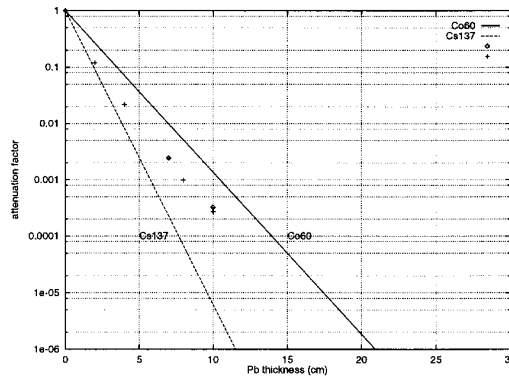


The decay γ -ray spectra in both the C-clamps are reported in Figure 10. In order to obtain an estimate of the shield needed to stop these gamma rays, the spectra given in this figure were used as a source in a simple geometry and the attenuation in a high-Z shield (i.e. lead) was calculated using MCNP. The attenuation factor obtained is shown in Figure 11, compared to the attenuation of a standard ^{137}Cs ($E = 0.66$ MeV) and ^{60}Co ($E = 1.25$ MeV) γ sources. At the end of life, assuming that high performance discharges are concentrated in the last operation phase, the contact dose rate at the C-clamp far from the port could be as high as 7×10^{-2} Sv/h after one day of cooling time. In this case, the high-Z shield should provide an attenuation factor of about 700 to have the dose rate below the limit in a reasonable cooling time. Based on the simple calculations described above this can be accomplished, for instance, by a 7 cm thick lead shield (11 cm close to the port). This additional shield can be located inside the cryostat, close to the C-clamp (position 3 in Figure 3) in order to limit as much as possible its size and weight and to avoid any impact on diagnostics and auxiliary systems outside the cryostat.

Figure 10. Gamma-ray spectra inside the C-clamp: far (dashed) and near (solid) to the port



**Figure 11. Gamma-rays attenuation in lead ($\rho = 11.35 \text{ g/cm}^2$):
for ^{137}Co and ^{60}Co sources and for the Figure 10 spectra**



Moving further apart from the machine the next structure we are dealing with is the cryostat, which is also the first structure the personnel come into contact working in the tokamak hall. We have calculated the neutron flux in the cryostat (Figure 12) at the equatorial level (position 4 in Figure 3), when no shield is present and when different kinds of shields are considered. The consequent neutron spectra could differ by many orders of magnitude in the thermal region (Figure 12), while in the high-energy region the differences are smaller (Figure 13). As a consequence, the corresponding activation of the cryostat metallic structure does not differ significantly with or without the high-Z shield (Figure 14). As expected, the most important contribution to the neutron flux comes from the port, as is clearly visible in Figure 15, where the neutron spectra in the cryostat without any shielding is presented with the real port configuration (upper curve) or filling the port with a totally absorbing material (lower curve).

The shielding must then be improved adding a collar wrapping the port (region 5 in Figure 3), reducing as much as possible the contribution of the fast neutrons to the cryostat activation. The collar must be a mixture of low-Z material (such as CH_2) to moderate the fast neutrons, with an absorbing element (such as B). The effect of the collar on the cryostat dose rate is shown in Figure 16, where it can be seen that the cooling time needed for the dose rate to fall below the allowed limit is reduced from about one year to about four months. This is a reasonable time at the end of the machine lifetime but, more importantly, the cooling time needed during the machine life is also acceptable, being of the order of one month after one year of DT operation (Figure 17). This is also true even adding the Co as impurity in the material, since the most important contribution to the dose is due to ^{58}Co (deriving from ^{58}Ni) in both cases.

Figure 12. Thermal neutron spectra in the cryostat with different kinds of shielding

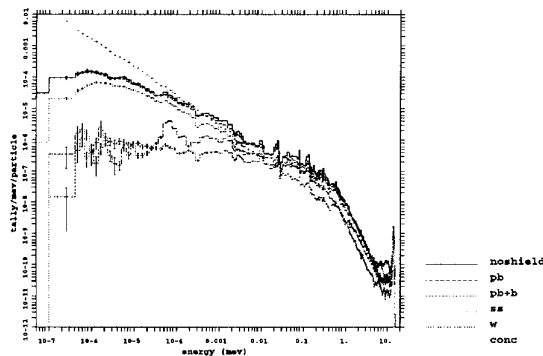


Figure 13. Fast neutron spectra in the cryostat with different kinds of shielding

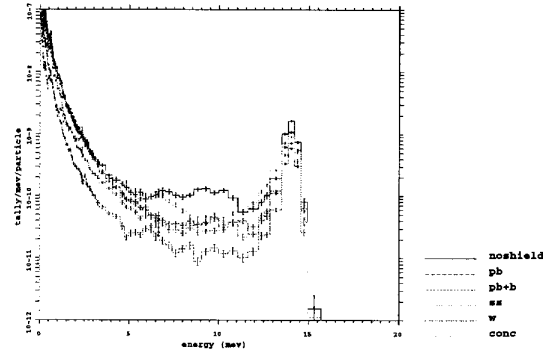


Figure 14. Contact dose rate versus cooling time in the cryostat at the equatorial level with different kinds of shielding materials

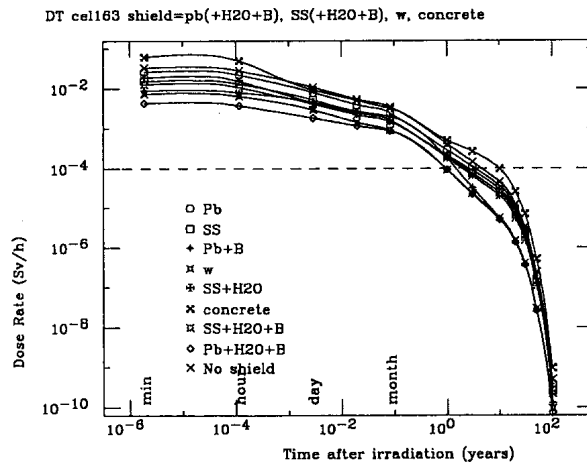


Figure 15. Neutron spectra in the cryostat without any shielding, with (upper curve) and without (lower) the contribution of neutrons streaming along the port

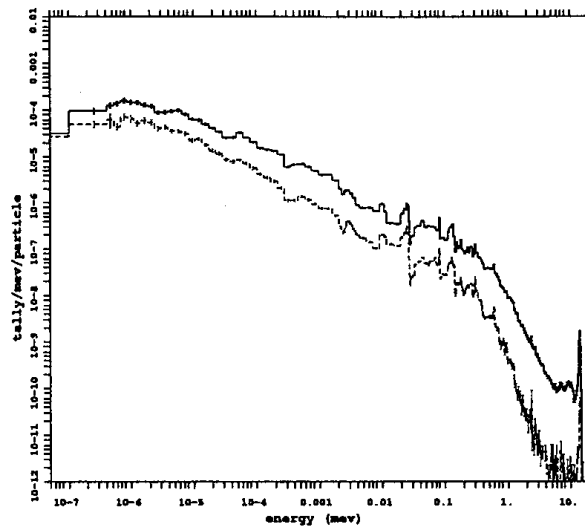


Figure 16. Contact dose rate versus cooling time in the cryostat without any shielding, with a lead shield and with a CH₂ + B collar

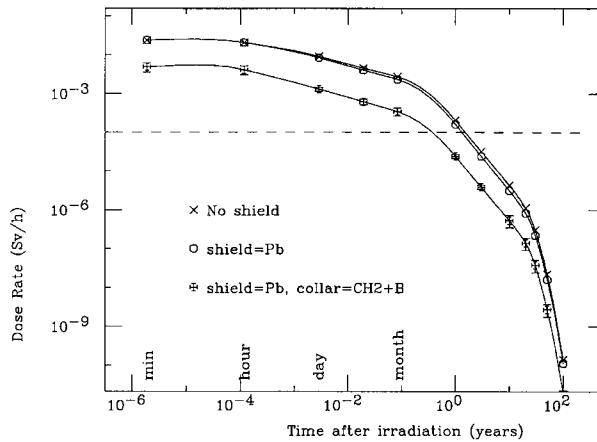
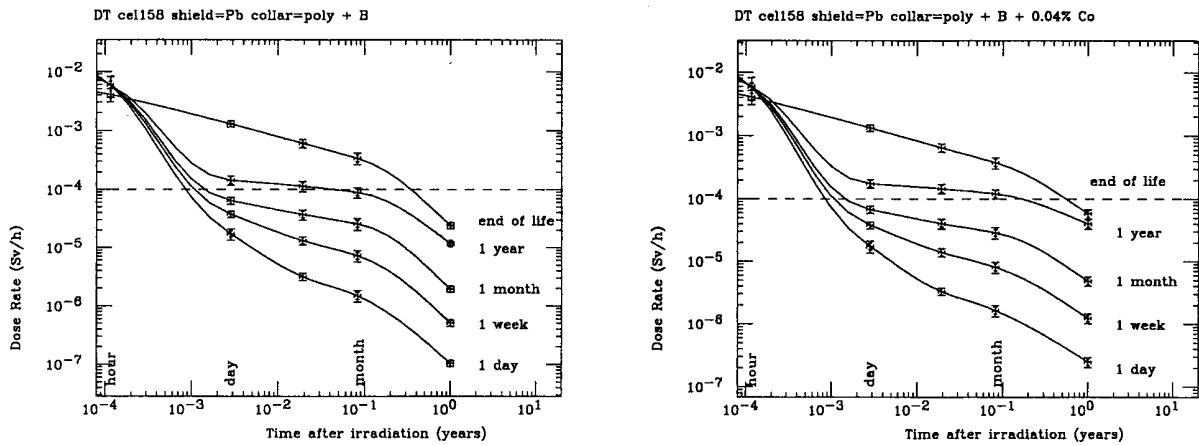


Figure 17. Contact dose rate versus cooling time in the cryostat with the complete shielding after one day, one week, one month and one year of DT operation (left). The same but with a 0.04% of Co added as impurity (right).



Conclusions

The study presented in this paper addresses the problem of additional radiation shielding in a compact fusion experiment such as Ignitor operating with DT plasmas. In order to maintain the possibility to access the machine and operate on the diagnostics systems installed on it during the whole lifetime, an accurate nuclear analysis has been performed to discover critical aspects and provide solutions. As the activation of the external components of the device was found to be higher than acceptable levels, a high-Z shield was studied to protect the personnel from the decay γ emitted from these components. A major contribution to the activation of these components is due to the neutron streaming through the horizontal port. In order to reduce this contribution the adoption of a low-Z collar was adopted and optimised.

REFERENCES

- [1] B. Coppi, *et al.*, “Ignitor Program: Engineering Design Description, Vol. II”, RLE Report PTP 96/03 (1996).
- [2] “MCNP: A General Purpose Monte Carlo N-particle Transport Code (Version 4B)”, J. Briesmeister, ed., LA-12625-M, Los Alamos National Laboratory Report (1997).
- [3] R.A. Forrest and J-Ch. Sublet, “FISPACT-99 User Manual”, UKAEA-FUS-407 Report (1998).
- [4] S. Rollet, P. Batistoni and R. Forrest, “Activation Analysis for the Ignitor Tokamak”, accepted for publication in *Fus. Eng. and Des.* (2000).
- [5] ICRP Recommendation, ICRP Publication No. 60, Annals of ICRP Vol. 21, N. 1-3 (1990).

EVALUATION OF NUCLEAR DATA FOR RADIATION SHIELDING BY MODEL CALCULATIONS AND INTERNATIONAL CO-OPERATION ASPECTS

Elisabetta Canetta*, Giuseppe Maino and Enzo Menapace

ENEA, Applied Physics Division
Via Don G. Fiammelli, 2, I-40129 Bologna, Italy

Abstract

The matter is reviewed, also following previous discussions at ICRS-9, concerning evaluation and related theoretical activities on nuclear data for radiation shielding within the framework of international co-operation initiatives, according to recognised needs and priorities. Both cross-section data – for reactions induced by neutrons and photons – and nuclear structure data have been considered. In this context, main contributions and typical results are presented from theoretical and evaluation activities at the ENEA Applied Physics Division, especially concerning neutron induced reaction data up to 20 MeV and photonuclear reaction data such as photon absorption and (gamma,n) cross-sections. Relevant aspects of algebraic nuclear models and of evaporation and pre-equilibrium models are discussed.

* ENEA fellowship.

Introduction to general aspects and data needs

In a recent review [1] of both the matter and the related needs and priorities presented at the Ninth International Conference on Radiation Shielding in Tsukuba, the main aspects of the international co-operation have been discussed according to the initiatives carried out in recent years by the NEA Nuclear Science Committee, particularly the working parties on nuclear data intercomparison (presently that of the WPEC), as they are intended to produce more accurate and reliable experimental and evaluated nuclear data, in particular for the purposes of radiation shielding [2], and also with respect to the SARE/SATIF initiative [3]. In fact, the same international co-operation, as discussed by the same review, is founded on the evaluation intercomparison based on theoretical and experimental activities (mainly inelastic scattering high-resolution measurements) and on the validation (with respect to benchmark shielding experiments) of the existing evaluated data (from the principal files such as ENDF/B, JEFF, JENDL and the ones produced from IAEA related countries) on shielding and structure materials for general or multiple applications, particularly the SARE/SATIF ones. In the same context, it has been recognised that new measurements (also to parameterise the nuclear models) and evaluations are mainly needed in the intermediate energy region (i.e. above 20 MeV up to several GeV) with regard to neutron, proton, light-ion and pion induced reactions (with special care to photon emission data) and especially to photonuclear data (mainly photoabsorption and neutron production cross-sections), to bremsstrahlung yields and angular distributions and to radioactive isotope production data. As for the photonuclear data aspects, the state of the art of the present evaluated libraries with respect to the present needs, including the ones expressed in previous SATIF meetings, has been reviewed in Ref. [4], also for the purposes of the WPEC initiative. Furthermore, more and new shielding benchmark experiments are done or specifically requested to be performed, mainly for data validation in the intermediate energy region, concerning iron, structure (target, etc.) and concrete materials, with main reference to proton, ion and electron accelerators, for applications relevant to basic physics and applied research (namely on accelerator-driven systems and intense spallation neutron sources, free electron lasers, synchrotron radiation facilities, material irradiation fields, etc.) and also to recent and new developments in radiotherapy and high technology fields. Moreover, reliable basic data are required for both the correct estimate of the activation rates in structure components and other relevant materials, and their impact on the environment and the planned activities on the irradiation facilities. Accordingly, as a complement to the ongoing or planned experimental activities, physically meaningful calculations of the requested basic data are needed through consistent models and codes and their appropriate parameterisation, as the most reliable approach to valuable evaluations of the data for national and international libraries, following the priorities shown by the existing requests, also expressed in the previous SARE/SATIF meetings.

Nuclear model aspects and results

Consequently, in previous years, significant contributions have been produced at ENEA to the international co-operation aimed to the development of physical models and computing codes for the theoretical estimate of basic data, and for their validation and parameterisation with respect to reliable experimental values and selected benchmarks. Recognising the need for reliable and consistent theoretical calculations in order to support and qualify the data evaluation processes, above all when the experimental values are scarce or lacking or even discrepant, special efforts have been devoted to investigate most crucial topics and parameters in cross-section calculations, particularly concerning energy and angular distributions of emitted particles and gamma-rays in the continuum energy region of main impact in transport calculations for radiation shielding. To this purpose, the activities have been referred to international co-operation initiatives, such as (on the NEA side) the above-mentioned WPEC (in particular, the working group on nuclear models), the model code intercomparison on selected benchmarks and (on the IAEA side) the “Reference Nuclear Parameter Library” project and

the co-ordinated research projects on photon production data and on photonuclear reaction data, both of extreme relevance to shielding purposes. In this context, close collaborations have been established with specialists of the universities and of the National Institute of Nuclear Physics (INFN), in Italy, and of the major institutes and laboratories abroad, where expert groups are active in the nuclear model field. Theoretical activities at the ENEA have been mainly devoted to:

- Calculations of inelastic scattering cross-sections (possibly including the direct ones, to rotational and vibrational band levels, by deformed optical model) and related angular distributions and angle integrated energy spectra of the scattered particles and of the emitted gamma-rays (as for the relevant case in Figure 1) requested for deep transmission analysis, attenuation and dose rate estimate inside the structure and shield materials.
- Theoretical prediction of discrete level structure data, in order to interpolate and extrapolate the existing experimental values from nuclear measurements (compiled by the international libraries, particularly by the ENSDF), as needed for reaction cross-section calculations (with concern to the transitions to discrete levels in the residual nucleus) and for estimating energy and relative intensity of the emitted gamma-rays; to this aim, algebraic models have been developed and parameterised with respect to recent measurements which have been made within selected collaborations with the INFN.
- Produce physically meaningful and consistent level density values, mainly investigating and estimating the “level density” parameters (requested in the simplified semi-empirical formalisms commonly adopted for cross-section calculations, both in the evaporation and pre-equilibrium model methods) and their dependence on the excitation energy and angular momentum of the nucleus, as they are crucial and very sensitive parameters in producing evaluated data in the continuum energy region, especially for shielding calculation purposes; by the ENEA adopted approach, as discussed in Ref. [5], advanced superfluid BCS model calculations have been performed to deduce a physically meaningful behaviour of the level density in extended excitation energy intervals in comparison with the few existing experimental values (from discrete levels, resolved resonances and emission spectra); then, the approximation formula by means of the above semi-empirical law and suitable parameters is obtained.
- The computational estimate of the requested cross-section values by a validated approach, based on the equilibrium and pre-equilibrium models (taking into account the above predictions of the level structures) and on satisfactory approximation of the existing and critically evaluated experiments, with special concern to the prediction of the angular and energy correlated (“double-differential”) distributions of the emitted particles and gammas, as basic physical quantities of main impact on shielding estimates, and consequently on the design aspects and the related costs.
- The prediction of very important photonuclear data, such as photoabsorption and (gamma,n) cross-section values, through advanced algebraic models, mainly as reference calculations with respect to the commonly adopted formalisms and systematics, as shown and discussed in the following sections.

Data evaluation activities and results

Evaluation activities at the ENEA on materials relevant to radiation shielding and activation estimate concerned neutron data up to 20 MeV for the nuclides of the structure natural elements,

mainly natural isotopes of Fe and Cr, as steel components, and of Al, Si, Cu, Mo, V as further relevant materials of primary interest. Within the framework of the international co-operation projects in the field, these evaluations allowed significant contributions to the JEF and EFF evaluated data libraries, then to the joint JEFF library, and to the selection for the IAEA FENDL library, also for the sake of the intercomparison with the other major files such as ENDF/B and JENDL within the WPEC. Accordingly, for relevant structure materials and critically selected evaluations, group libraries (at the requested temperature and dilution parameter values), including gamma production data, were obtained for applications in dosimetry studies of present interest (e.g. in Refs. [5,6]) by the FLUKA Monte Carlo code. Mainly the evaluations of the most important data for shielding purposes (such as total, elastic and inelastic scattering and photon production cross-sections and energy-angular double differential distributions of emitted particles and gammas) and for material activation estimate, are based on reliable selected experimental data and on the above theoretical models (for fitting the data, covering the gaps and possibly solve discrepancies). Recent experiments concerned:

- The high resolution measurements of Fe, Al and ^{208}Pb inelastic scattering cross-sections and the those of Cr natural isotopes activation cross-sections, at IRMM, Geel.
- The double-differential scattering measurements for Ti, V, Cr, Fe at PTB, Braunschweig.

In the cases where the fine structure from the experiments could not be fitted by model calculations, in lack of resonance or “pseudo-resonance” parameters (as for ^{56}Fe inelastic scattering and total cross-sections measurements at IRMM, presented and discussed at the NEA WPEC), an empirical approximation of the cross-section structure was assumed in the evaluation to account for self-shielding effects in transport calculations. In fact, by adopting this fine structure in the evaluated data in deterministic for Monte Carlo transport calculations, the results from a number of benchmark shielding experiments were reasonably reproduced, particularly the ones from deep neutron penetration measurements for SS at the Frascati 14 MeV Neutron Generator (FNG) performed at the Neutronics Section of the ENEA Fusion Division, as discussed in the framework of the JEFF project, within the actions for validating the evaluated files for shielding calculations. Concerning the validation of the activation libraries for fusion, specifically those of the European EAF and the IAEA-FENDL-A, the intercomparison was referred to decay heat calculations with respect to a series of measurements performed at the JAERI Fusion Neutronics Source (FNS) in the framework of the ITER Project. The results of Ref. [7] have been discussed within the EFF Project, showing the most crucial discrepancies between the different basic data affecting the macroscopic results and also the impact on the overall decay estimate from the adopted group structure in the processed libraries. Therefore specific improvements on selected cross-sections and the appropriate group structure in the calculations were deduced.

Traditionally, collective properties of nuclei have been mainly formulated in terms of geometrical models and, therefore, giant resonances have also been described within this framework, soon after the discovery of large peaks in the nuclear photoabsorption cross-sections between 10 and 30 MeV. Classical models of the isovector giant dipole resonance (GDR) were developed by Goldhaber and Teller, and Steinwedel and Jensen, respectively, based on the common assumption that the neutron fluid (incompressible or not according to the latter or former model) vibrates against the proton fluid. For medium and heavy mass nuclei, the GDR excitation energy is a mixture of Goldhaber-Teller and Steinwedel-Jensen laws. Furthermore, the geometrical model applied to giant resonances have been extended by the Frankfurt group, headed by Greiner. His dynamical collective model couples giant resonance degrees of freedom to surface degrees of freedom and is thus able to explain the fragmentation of the GDR in several components. The well-known splitting of GDR in two components in deformed nuclei arises because of the ground state stable deformation; in the case of prolate nuclei, the higher-energy peak is about twice than the lower one since it is doubly degenerate, due to rotations

around the symmetry axis. On the other hand, from a microscopic point of view, the GDR states have angular momentum and parity quantum numbers, $J^\pi = 1^-$ and isospin, $T = 1$ in even-even nuclei, and originate from coherent excitations of many nucleons across a major shell closure, with typical energies of $1\hbar\omega$. As a consequence, the electromagnetic (dipole) transition probabilities from nuclear ground state to GDR components have a collective strength one or two orders of magnitude larger than the single-particle transition strength. Moreover, the GDR motion shows a remarkable regularity along all the periodic table, its excitation energy slowly varying with mass number. Since $1\hbar\omega$ excitations involve promotions of nucleons across major shells, a complete description of GDR states within the usual shell-model framework is a formidable task if one considers nuclei far away from closed-shell configurations. In fact, the numerical difficulties related to this approach are cumbersome and yet above the present capabilities of parallel computers. In order to predict photoabsorption cross-sections in the GDR region, one has to resort both to geometrical and algebraic models. In particular, the algebraic approach is well suited since it allows us to emphasise the main characteristics of collective motions and drastically simplify the problem from a computational point of view. Moreover, the algebraic models can be simply related to the geometrical aspects, by considering the semi-classical limit associated to the topology coupled to the algebraic structure, and interpreted microscopically starting from a simplistic model, for instance, thus linking together these two main facets of nuclear structure. In the last twenty years remarkable success has been gained by the Interacting Boson Model (IBM) [8,9] of nuclear structure in reproducing many spectroscopic properties of nuclei far from closed shells at low energy. Moreover, the model has been suitably extended to the description of isoscalar and isovector resonances through the introduction of additional degrees of freedom [10]. In the following sections we illustrate results obtained for GDR excitations, together with the relevant formalism.

The IBM model

The algebraic structure underlying the Interacting Boson Model (IBM), or, more generally, the Interacting Boson-Fermion Model (IBFM), for the description of both even-even, odd-mass and odd-odd nuclei, is provided by the following group product:

$$U_\pi(6) \otimes U_\nu(6) \otimes U_p \left(\sum_{j_p=1}^{N_p} (2j_p + 1) \right) \otimes U_n \left(\sum_{j_n=1}^{N_n} (2j_n + 1) \right) \quad (1)$$

while the basis states, in the second quantisation formalism, are defined according to the relevant decomposition chain [8]. Here, π and ν refer, respectively, to the proton and neutron degree of freedom, and j_p (j_n) is the angular momentum value of the proton (neutron) single-particle orbitals accessible to the unpaired particle, whose number is given by N_p (N_n). Collective states of even-even nuclei can be constructed in terms of a system of N interacting bosons with angular momenta $J^\pi = 0^+$ and 2^+ (s and d bosons, respectively). From a microscopic point of view, these bosons correspond to correlated pairs of nucleons, namely two neutrons, two protons, or one neutron and one proton, in the valence shells. The Hamiltonian, including boson and fermion degrees of freedom, for the description of correlated pairs and unpaired nucleons, respectively, has the general form:

$$\hat{H} = \hat{H}_B(\pi, \nu) + \hat{H}_F(p, n) + \hat{V}_{BF}(\pi, \nu, p, n) \quad (2)$$

where $\hat{H}_B(\pi, \nu)$ is the usual Talmi expression for the IBM-2 Hamiltonian [9,11,12,13]:

$$\hat{H}_B(\pi, \nu) = \epsilon_\pi \hat{n}_{d_\pi} + \epsilon_\nu \hat{n}_{d_\nu} + k \hat{Q}_\pi^{(2)} \cdot \hat{Q}_\nu^{(2)} + \hat{M}_{\pi\nu} + \hat{V}_{\pi\pi} + \hat{V}_{\nu\nu} \quad (3)$$

In Eq. (3), n_{d_ρ} ($\rho = \pi, \nu$) represents the one-body term originating from the pairing between identical nucleons, while $\hat{Q}_\pi^{(2)}$ ($\rho = \pi, \nu$) is the quadrupole operator. $\hat{M}_{\pi\nu}$ [Eq. (3)] is the so-called Majorana term ruling the mixed-symmetry states [9], and the $\hat{V}_{\rho\rho}$ ($\rho = \pi, \nu$) corresponds to the residual interaction between bosons of the same kind*. The purely fermionic part of the Hamiltonian (2) is given by:

$$\hat{H}_F(p, n) = \sum_{j_p} E_{j_p} \hat{n}_{j_p} + \sum_{j_n} E_{j_n} \hat{n}_{j_n} + \hat{V}_F(p, n) \quad (4)$$

where E_{j_ρ} is the energy of a quasiparticle in the j orbital, evaluated in the standard BCS approximation, and \hat{n}_{j_ρ} is the corresponding quasiparticle number operator, $\hat{n}_{j_\rho} = \sum_{m_\rho=-j_\rho}^{j_\rho} a_{j_\rho m_\rho}^\dagger a_{j_\rho m_\rho}$. Moreover, the two-body residual interaction between the unpaired neutron and proton has been chosen in the very simple form:

$$\begin{aligned} \hat{V}_F(p, n) = & (\alpha_1 + \alpha_2 \vec{\sigma}_n \cdot \vec{\sigma}_p) \delta(\vec{r}_n - \vec{r}_p) \delta(r_p - R_0) + \alpha_3 r_n^2 r_p^2 Y^{(2)}(\Omega_n) \cdot Y^{(2)}(\Omega_p) \\ & + \alpha_4 \frac{e^{-(r/r_0)^2}}{r^2} [3(\vec{\sigma}_n \cdot \vec{r})(\vec{\sigma}_p \cdot \vec{r}) - (\vec{\sigma}_p \cdot \vec{\sigma}_n) r^2] \end{aligned} \quad (5)$$

with $\vec{r} = \vec{r}_n - \vec{r}_p$, R_0 nuclear radius, $\vec{\sigma}_\rho$ spin operator and $Y^{(2)}$ spherical harmonics of rank two. Eq. (5) is a combination of a surface delta interaction, including a spin-spin part, a quadrupole-quadrupole long-range force and a short-range tensor part; this form has been previously used in Ref. [14] in order to reproduce the semi-empirical matrix elements of the effective two-nucleon interaction deduced from direct-transfer measurements. Finally, the boson-fermion interaction has the following expression:

$$\hat{V}_{BF}(\pi, \nu, p, n) = \hat{V}_{BF}^m + \hat{V}_{BF}^q + \hat{V}_{BF}^{exc} \quad (6)$$

where, in order to reduce the number of adjustable parameters, a simplified form has been introduced on the basis of microscopic considerations [8] in the frame of a generalised seniority treatment of quasiparticles in the valence shells. Eq. (6) has been used in many analyses of spectra of odd-mass nuclei in the IBFM-2 approach and consists of a monopole-monopole term:

$$\hat{V}_{BF}^m = \sum_{j_p} A_{j_p} \hat{n}_{j_p} \cdot \hat{n}_{j_p} + \sum_{j_n} A_{j_n} \hat{n}_{j_n} \cdot \hat{n}_{j_n} \quad (7)$$

a quadrupole-quadrupole part:

$$\hat{V}_{BF}^q = \sum_{j_p, j_{p'}} \Gamma_{j_p, j_{p'}} \hat{Q}_\nu^{(2)} \cdot \hat{q}_{j_p, j_{p'}} + \sum_{j_n, j_{n'}} \Gamma_{j_n, j_{n'}} \hat{Q}_\nu^{(2)} \cdot \hat{q}_{j_n, j_{n'}} \quad (8)$$

with $q_{j_\rho, j_{\rho'}} = (a_{j_\rho}^\dagger \times a_{j_{\rho'}})^{(2)}$ and an exchange interaction which takes into account the Pauli principle, arising from the fact that bosons approximate correlated nucleon pairs:

* For the explicit formulae of the operators in Eq. (3), we refer to Ref. [12].

$$\begin{aligned}
\hat{V}_{BF}^{exc} = & (s_{\pi}^{\dagger} \times \tilde{d}_{\pi})^{(2)} \cdot \left\{ \sum_{j_n, j'_n, j''_n} \Lambda_{j_n, j'_n, j''_n}^{j''_n} : \left[(d_{\nu}^{\dagger} \times \tilde{a}_{j_n}^{\dagger})^{(j_n)} \times (\tilde{s}_{\nu} \times a_{j'_n}^{\dagger})^{(j'_n)} \right]^{(2)} : \right\} \\
& + (s_{\nu}^{\dagger} \times \tilde{d}_{\nu})^{(2)} \cdot \left\{ \sum_{j_p, j'_p, j''_p} \Lambda_{j_p, j'_p, j''_p}^{j''_p} : \left[(d_{\pi}^{\dagger} \times \tilde{a}_{j_p}^{\dagger})^{(j_p)} \times (\tilde{s}_{\pi} \times a_{j'_p}^{\dagger})^{(j'_p)} \right]^{(2)} : \right\} \\
& + h.c.
\end{aligned} \tag{9}$$

where $::$ denotes the normal ordering. The number of Λ and Γ parameters can be greatly reduced on the assumption of a microscopic model which gives [15]:

$$\Gamma_{j_p, j'_p} = (u_{j_p} u_{j'_p} - v_{j_p} v_{j'_p}) \mathcal{Q}_{j_p, j'_p} \Gamma_p \tag{10}$$

$$\mathcal{Q}_{j_p, j'_p} = \left\langle l_p, j_p, \frac{1}{2} \parallel Y^{(2)} \parallel l'_p, j'_p, \frac{1}{2} \right\rangle \tag{11}$$

$$\Lambda_{j_p, j'_p}^{j''_p} = -\sqrt{\frac{10}{N_p(2j_p+1)}} (u_{j_p} v_{j'_p} + v_{j'_p} u_{j_p}) \mathcal{Q}_{j_p, j'_p} \beta_{j_p, j'_p} \Lambda_p \tag{12}$$

where u_j and v_j are the BCS quasiparticle occupation probabilities. Finally, the β coefficients are related to the microscopic structure of d bosons and, in general, are given by the following approximate expressions [15]:

$$\beta_{j_p, j'_p} = \frac{1}{E_{j_p} + E_{j'_p} - \hbar\omega} (u_{j_p} v_{j'_p} + v_{j_p} u_{j'_p}) \mathcal{Q}_{j_p, j'_p} \tag{13}$$

where E_j and $E_{j'}$ are quasiparticle energies and $\hbar\omega$ is the difference between the energies of correlated nucleon pairs with angular momentum $L = 0$ and $L = 2$; this term can be estimated from the excitation energy of the lowest 2^+ state in the nearest semi-magic nucleus.

As for the electromagnetic transitions, the relevant operators are given by one-body terms at the first order as usually made in the IBFM treatment, an hypothesis which represents – in general – a satisfactory approximation:

$$\hat{T}(L) = \hat{T}_B(L) + \hat{T}_p(L) + \hat{T}_n(L) \tag{14}$$

where the boson operators are defined in Ref. [9] and the fermion operators have the general structure [13]:

$$\hat{T}_k(L) = \sum_{j \leq j'} \frac{e_{jj'}^{(L)}}{1 + \delta_{jj'}} \left[(a_j^{\dagger} \times \tilde{a}_{j'}^{\dagger})^{(L)} + (-1)^{j-j'} (a_{j'}^{\dagger} \times \tilde{a}_j^{\dagger})^{(L)} \right] \quad (k = n, p) \tag{15}$$

Here, the single-particle matrix elements are, for $L = E2$:

$$e_{jj'}^{(2)} = -e_k \frac{1}{\sqrt{5}} (u_j u_{j'} - v_j v_{j'}) \left\langle l, \frac{1}{2}, j \parallel r^2 Y^{(2)} \parallel l', \frac{1}{2}, j' \right\rangle \tag{16}$$

and for $L = M1$:

$$e_{j'j}^{(1)} = -\frac{1}{\sqrt{3}}(u_j u_{j'} + v_j v_{j'}) \left\langle l, \frac{1}{2}, j \parallel g_l \bar{l} + g_s \bar{s} \parallel l', \frac{1}{2}, j' \right\rangle \delta_{ll'} \quad (17)$$

Analogous expressions hold for higher multipolarities.

The dipole IBM approach

Differently from low-energy collective levels, the giant resonance states originate from a coherent superposition of particle-hole excitations across major-shell closures where the single-particle orbitals generally have opposite parities. In IBM language, the GDR excitations can be thus described in terms of a $J^\pi = 1^-$ boson (p boson) whose creation and annihilation operators generate a $U(3)$ algebra [10]. Since the p boson collective excitation leading to GDR states is characterised by isospin $t = 1$ and third component, $t_z = 0$, in the case of photon absorption an obvious choice for the relevant isospin group symmetry is $SU(3)$. Thus, the nuclear collective excitations, including the GDR states, are given by the direct product of the above-discussed symmetry groups, $U_B^{(sd)}(6) \otimes U_B^{(p)}(3) \otimes SU_T^{(sd)}(3) \otimes SU_T^{(p)}(3)$, where the indices have the usual meaning, already defined in this article. The high-energy, GDR states are then obtained by coupling the irreducible representations (irreps) that describe the low-lying IBM-3 states to the total symmetric irrep, (1,0), of the dipole collective excitation. The corresponding phenomenological Hamiltonian is discussed in full details in Ref. [10] and it will not be recalled here. The nuclear eigenvalue problem is then solved numerically, on the basis provided by the previous equation, by means of a suitable computation code and the algorithmic procedure developed in Refs. [10,11] and summarised in the following section. In this way, both energies and eigenfunctions are obtained for the collective low-lying and GDR excitations. Introducing a standard form of the IBM total isovector E1 transition operator [10], it is a simple matter to estimate the reduced matrix elements for dipole transitions between these states, too. The relevant Hamiltonian, which couples low-energy with GDR degrees of freedom, reads as:

$$H_{sdp} = b_0 [d^+ x \tilde{d}]^{(0)} \cdot [p^+ x \tilde{p}]^{(0)} + b_1 [d^+ x \tilde{d}]^{(1)} \cdot [p^+ x \tilde{p}]^{(1)} + b_2 \tilde{Q}^{(2)} \cdot [p^+ x \tilde{p}]^{(0)} \quad H = H_{sd} + \epsilon_p \hat{n}_p + H_{sdp}$$

The b coefficients are free parameters to be adjusted on the basis of available experimental information, in the present phenomenological approach. In principle, they could be deduced microscopically by a correspondence between IBM and shell model. The free p boson energy, ϵ_p , is assumed to follow the semi-empirical law $\approx A^{-1/3}$ MeV. The dominant term is the quadrupole-quadrupole interaction whose strength is mainly responsible for the GDR fragmentation. The complexity of the problem is largely reduced with respect to shell-model calculations, even in a suitable truncated basis. Dimensions of the involved matrices in the algebraic IBM approach range from 5-10 up to one hundred. In addition to the Hamiltonian, one needs a boson dipole operator in order to evaluate the transition probabilities between low-energy states and GDR components. The simplest choice is $D^{(1)} = D_0 [p^+ x \tilde{p}]^{(1)}$, where D_0 is a suitable adjustable parameter. With these ingredients, it is possible to evaluate excitation energies and transition strengths for GDR states of even-even nuclei far from closed shells. Before this, in order to compare the IBM predictions about GDR fragmentation and transition probabilities with experimental data, an intrinsic width must be associated with each calculated GDR component. These widths arise from the coupling of GDR states to more complicated nuclear configurations, as 2p-2h doorway states or the continuum. Since these configurations lie outside the IBM model, their effect has to be accounted on a phenomenological ‘‘ad hoc’’ manner, as made in the Frankfurt dynamical model, by means of a semi-empirical power law. As a significant

example, Figure 2 shows instead the calculated photoabsorption cross-sections of a few light and medium mass nuclei in the GDR energy region, in comparison with the experimental data. The different isospin contributions to the total cross-section are outlined and the overall agreement is striking, provided the very simple computational structure of the model previously described. It is worth mentioning that the adjustable parameters of the phenomenological $s - p - d$ Hamiltonian are constant or vary slightly with the mass number, thus allowing us confidence in applications of this model to nuclear reactions other than photonic (electromagnetic) processes such as muon nuclear capture.

REFERENCES

- [1] E. Menapace, Proc. Ninth International Conference on Radiation Shielding, Tsukuba (1999), published in *Journal of Nuclear Science and Technology – Suppl.* 1 (March 2000), pp. 68-72.
- [2] T. Nakamura, T. Fukahori and E. Menapace, Proc. Intern. Conference on Nuclear Data for Science and Technology, Trieste (1997), p. 1478.
- [3] SATIF-4, Proc. of the Knoxville Workshop (1998).
- [4] E. Menapace and A. Musumeci, JEF/DOC-812, NEA Project report (1999).
- [5] M. Frisoni, E. Menapace, A. Musumeci, E. Spezi and M. Vaccari, Proc. ANS Meeting on Nuclear Applications of Accelerator Technology, Albuquerque (1997), p. 190.
- [6] M. Frisoni, E. Menapace, A. Musumeci, G.C. Panini and M. Vaccari, Proc. International Conference on Nuclear Data for Science and Technology, Trieste (1997), p. 1317.
- [7] G. Cambi, D. Cepraga, M. Frisoni and E. Menapace, EFF-DOC-654 (1998).
- [8] F. Iachello and P. Van Isacker, “The Interacting Boson-Fermion Model”, Cambridge University Press (1987).
- [9] F. Iachello and A. Arima, “The Interacting Boson Model”, Cambridge University Press (1987).
- [10] G. Maino, in “Dynamical Symmetries and Chaotic Behaviour in Physical Systems”, World Scientific, Singapore (1991), p. 141; id., in “The Physics of Complex Systems”, IOS Press, Amsterdam (1997), p. 637; G. Maino, A. Ventura and L. Zuffi, *Phys. Rev.*, C37, 1379 (1988); G. Maino, *Phys. Rev.*, C40, 988 (1989); E. Bortolani, G. Maino, *Comp. Phys. Comm.* 70, 207 (1992); id., *Phys. Rev.* C43, 353 (1991); L. Zuffi, G. Maino, A. Ventura, *Phys. Rev.*, C44, 285 (1991); G. Maino, A. Ventura, L. Zuffi, *Phys. Rev.*, C46, 1725 (1992).
- [11] G. Maino, *Int. J. Mod. Phys.*, E6, 287 (1997).
- [12] E. Canetta, G. Maino, *Int. J. Mod. Phys.*, E8, 321 (1999).

- [13] S.C. Fultz, R.A. Alvarez, B.L. Berman, M.A. Kelly, D.R. Lasher, T.W. Phillips and J. McElhinney, *Phys. Rev.*, C4, 149 (1971).
- [14] R.E. Pywell and M.N. Thompson, *Nucl. Phys.*, A318, 461 (1979); S. Oikawa and K. Shoda, *ibid.* A277, 301 (1977).
- [15] P. Carlos, H. Beil, R. Bergère, J. Fagot, A. Leprêtre, A. Veyssiére and G.V. Solodukhov, *Nucl. Phys.*, A258, 365 (1976); B.S. Ishkhanov, I.M. Kapitonov, E.V. Lazutin, I.M. Piskarev and O.P. Shevchenko, *Yad. Fiz.*, 20, 433 (1974), engl. transl. *Sov. J. Nucl. Phys.*, 20, 233 (1974).
- [16] S.S. Verbitskii, A.M. Lapik, B.S. Ratner and A.N. Sergievski and A.N. Sergievskii, *ibid.* 28, 1441 (1978), engl. transl. *ibid.* 28, 741 (1978).

Figure 1. Gamma-ray spectrum from ^{52}Cr (n,n',gamma) reaction, versus incident neutron energy and emitted photon energy, by means of model calculations within the ENEA evaluation activity for relevant structural materials

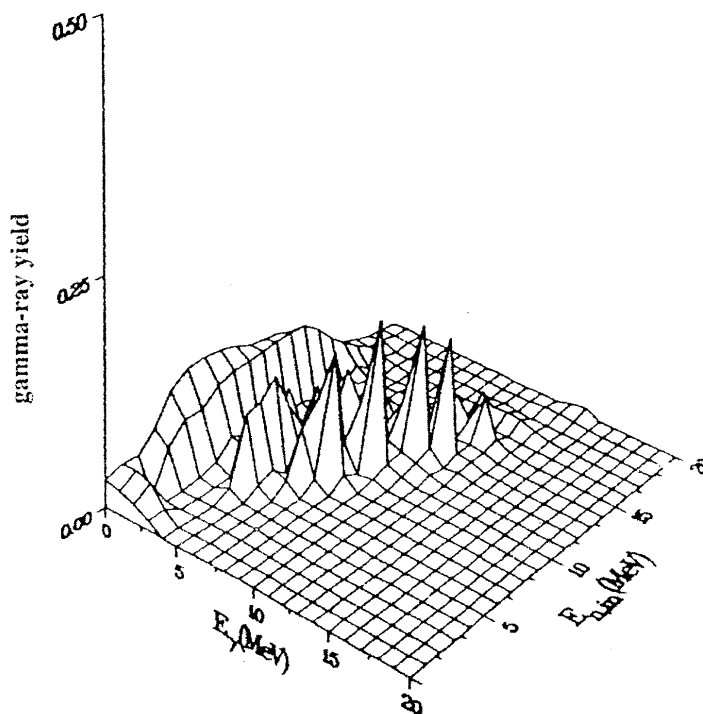
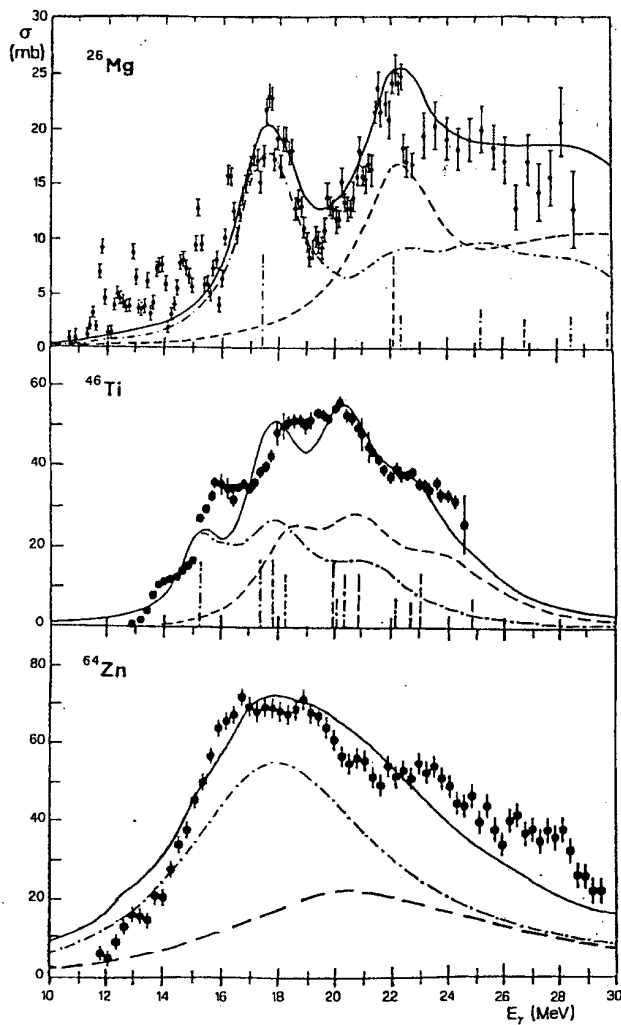


Figure 2. Experimental and theoretical (IBM-3) photoabsorption cross-sections of $N > Z$ nuclei in the giant dipole resonance region

(Upper) ^{26}Mg ; expt. data from Ref. [3], dotted-dashed line, $T = 1$ component; dashed line, $T = 2$ component; solid line, total cross-section. (Middle) ^{46}Ti ; expt. data from Ref. [14], dotted-dashed line, $T = 1$ component; dashed line, $T = 2$ component; solid line, total cross-section. (Lower) ^{64}Zn ; expt. data from Ref. [15], dotted-dashed line, $T = 2$ component; dashed line, $T = 3$ component; solid line, total cross-section. Bars at the bottom of the upper and middle figures represent the calculated dipole strengths in arbitrary units.



LIST OF PARTICIPANTS

AUSTRALIA

* MUKHERJEE, Bhaskar
ANSTO – Safety Division
PMB-1
Menai, NSW 2234
Tel: +61 2 9717 3404
Fax: +61 2 9389 8444
Eml: mukherjee@ieee.org

BELGIUM

CUGNON, Joseph
Physics Department B5
University of Liège
B-4000 Sart Tilman Liège 1
Tel: +32 43663601
Fax: +32 43663672
Eml: J.Cugnon@ulg.ac.be

FRANCE

CLAPIER, Francois
Ingénieur de Radioprotection
CNRS-IN2P3
Institut Physique Nucléaire
SPR
F-91406 Orsay
Tel: +33 (1) 6915 7170
Fax: +33 (1) 6915 6470
Eml: clapier@ipno.in2p3.fr

DUARTE, Helder
CEA Bruyères-le-Châtel
BP 12
F-91191 Bruyères-le-Châtel
Tel: +33 (1) 69 26 42 82
Fax: +33 (1) 69 26 70 63
Eml: duarte@bruyeres.cea.fr

DUCAUZE, Marie
CEA Bruyères-le-Châtel
BP 12
F-91680 Bruyères-le-Châtel
Tel: +33 (1) 69 26 56 07
Fax: +33 (1) 69 26 70 63
Eml: ducauze@bruyeres.cea.fr

FREHAUT, Joel
Service de Physique Nucléaire
CEA/Bruyères-le-Châtel
BP N° 12
F-91680 Bruyères-le-Châtel
Tel: +33 (1) 69 26 47 23
Fax: +33 (1) 69 26 70 63
Eml: joel.frehaut@cea.fr

GALIN, Joel
GANIL
BP-5027
F-14076 Caen Cedex 05
Tel: +33 (2) 31 45 45 74
Fax: +33 (2) 31 45 46 65
Eml: galin@ganil.fr

LERAY, Sylvie
CEA Saclay
DAPNIA/SPhN
F-91191 Gif-sur-Yvette Cedex

Tel: +33 (1) 69 08 83 61
Fax: +33 (1) 69 08 75 84
Eml: sleray@cea.fr

LETOURNEAU, Alain
GANIL
BP 5027
F-14076 Caen Cedex 5

Tel: +33 (2) 31 45 45 49
Fax: +33 (2) 31 45 46 65
Eml: letourneau@ganil.fr

PAUWELS, Nicolas
CNRS-IN2P3
Institut Physique Nucléaire
SPR
F-91406 Orsay

Tel: +33 (1) 69 15 62 67
Fax: +33 (1) 69 15 45 16
Eml: pauwels@ipno.in2p3.fr

RIDIKAS, Danas
CEA Saclay
DSM/DAPNIA/SPhN
F-91191 Gif-sur-Yvette Cedex

Tel: +33 (1) 69087847
Fax: +33 (1) 69087584
Eml: ridikas@cea.fr

TOCCOLI, Cécile
Commissariat à l'Énergie Atomique
DIF/DPTA/SPN
BP 12
F-91680 Bruyères-le-Châtel

Tel: +33 (1) 69 26 49 92
Fax: +33 (1) 69 26 70 63
Eml: cecile.toccoli@cea.fr

VOLANT, Claude
DAPNIA/SPhN
CEA Saclay
F-91191 Gif-sur-Yvette Cedex

Tel: +33 (1) 69 08 55 85
Fax: +33 (1) 69 08 75 84
Eml: cvolant@cea.fr

GERMANY

FILGES, Detlef
Institut für Kernphysik
Forschungszentrum Jülich GmbH
D-52425 Jülich

Tel: +49 (2461) 61 5232
Fax: +49 (2461) 61 3930
Eml: d.filges@fz-juelich.de

GOLDENBAUM, F.
Institut für Kernphysik
Forschungszentrum Jülich GmbH
D-52425 Jülich

Tel: +49 (2461) 61 4250
Fax: +49 (2461) 61 3930
Eml: F.Goldenbaum@fz-juelich.de

HERBACH, Claus-Michael
Hahn-Meitner-Institute Berlin
Glienickestr. 100
D-14109 Berlin

Tel: +49 8062 2717
Fax: +49 8062 2293
Eml: herbach@hmi.de

HILSCHER, Dietrich
Hahn-Meitner-Institut Berlin
Glienickestr. 100
D-14109 Berlin

Tel: +49 8062 2718
Fax: +49 8062 2293
Eml: hilscher@hmi.de

JAHNKE, Ulrich
Hahn-Meitner-Institut Berlin
Glienicke str.100
D-14109 Berlin

Tel: +49 8062 2727
Fax: +49 8062 2293
Eml: Jahnke@hmi.de

LEUSCHNER, Albrecht
Deutsches Elektronen-Synchrotron
DESY
Notkestrasse 85
D-22607 Hamburg

Tel: +49 (0) 40 8998 2043
Fax: +49 (0) 40 8998 3282
Eml: Albrecht.Leuschner@desy.de

* MARES, Vladimir
GSF
Institute of Radiation Protection
Ingolstaedter Landstr. 1
D-85764 Neuherberg

Tel: +49 (89) 5996 838 or 3187 2652
Fax: +49 (89) 5996 840 or 3187 3323
Eml: mares@gsf.de

MICHEL, Rolf
Zentrum für Strahlenschutz
und Radiokologie der
Universitaet Hannover (ZSR)
Am Kleinen Felde 30
D-30167 Hannover

Tel: +49 (171) 644 2719
Fax: +49 (511) 762 3319
Eml: michel@mbox.zsr.uni-hannover.de

NEEF, Ralf D.
Institut für Kernphysik
Forschungszentrum Jülich GmbH
D-52425 Jülich

Tel: +49 (2461) 61 62 24
Fax: +49 (2461) 61 39 30
Eml: r.d.neef@fz-juelich.de

SCHAAL, Hartwig
Institut für Kernphysik
Forschungszentrum Jülich GmbH
D-52425 Jülich

Tel: +49 (2461) 61 4004
Fax: +49 (2461) 61 3930
Eml: h.schaal@fz-juelich.de

STERZENBACH, Guenter
Institut für Kernphysik
Forschungszentrum Jülich GmbH
D-52425 Jülich

Tel: +49 (2461) 61 4612
Fax: +49 (2461) 61 3930
Eml: G.Sterzenbach@fz-juelich.de

TICHTCHENKO, Vladimir
Hahn-Meitner-Institute Berlin
Glienickestr. 100
D-14109 Berlin

Tel: +49 8062 2717
Fax: +49 8062 2293
Eml: tichtchenko@hmi.de

WOHLMUTHER, M.
Institut für Kernphysik
Forschungszentrum Jülich GmbH
D-52425 Jülich

Tel: +49 (2461) 61 3415
Fax: +49 (2461) 61 3930
Eml: M.Wohlmuther@fz-juelich.de

ISRAEL

YARIV, Yair
Soreq Nuclear Research Centre
Yavne 81800

Tel: +972 8 943 4789
Fax: +972 8 943 4157
Eml: Yariv@ndc.soreq.gov.il

ITALY

MENAPACE, Enzo
ENEA CRE Clementel
Applied Physics Division
via Don G. Fiammelli 2
I-40128 Bologna

Tel: +39 051 60 98 239
Fax: +39 051 60 98 359
Eml: menapace@bologna.enea.it

PELLICIONI, Maurizio
INFN
Laboratori Nazionali di Frascati
Casella Postale 56
I-00044 Frascati (Roma)

Tel: +39 (06) 940 32246
Fax: +39 (06) 940 32364
Eml: maurizio.pellicioni@lnf.infn.it

ROLLET, Sofia
CRE-ENEA
ENEA Fusion Division
via E. Fermi 27
I-00044 Frascati (Roma)

Tel: +39(0)6 94005825
Fax: +39(0)6 94005314
Eml: rollet@frascati.enea.it

ZAFIROPOULOS, Demetre
Head of Radiation Protection Service
INFN Laboratori Nazionali di Legnaro
via Romea, 4
I-35020 Legnaro-Padova

Tel: +39 049 8068394
Fax: +39 049 8068889
Eml: zafirooulos@lnl.infn.it

JAPAN

HAYASHI, Katsumi
Hitachi Engineering Company
3-2-1 Saiwai-cho
Hitachi-shi
Ibaraki-ken 317-0065

Tel: +81 (294) 21 7330
Fax: +81 (294) 23 6619
Eml: k_hayashi@psg.hitachi-hec.co.jp

HIRAYAMA, Hideo
KEK, High Energy Accelerator
Research Organisation
Oho 1-1
Tsukuba-shi
Ibaraki-ken 305-0801

Tel: +81 (298) 64 5489
Fax: +81 (298) 64 1993
Eml: hideo.hirayama@kek.jp

NAKAMURA, Takashi
Cyclotron and Radioisotope Centre
Tohoku University
Aramaki, Aoba, Aoba-ku
Sendai 980-8578

Tel: +81 (22) 217 7805
Fax: +81 (22) 217 7809
Eml: nakamura@cyric.tohoku.ac.jp

NAKANE, Yoshihiro
Centre for Neutron Science
JAERI
Tokai-mura, Naka-gun
Ibaraki-ken 319-1195

Tel: +81 (29) 282 6329
Fax: +81 (29) 282 6496
Eml: nakane@shield4.tokai.jaeri.go.jp

NAKAO, Noriaki
KEK, High Energy Accelerator
Research Organisation
1-1 Oho
Tsukuba-shi, Ibaraki-ken 305-0801

Tel: +81 (298) 79 6004
Fax: +81 (298) 64 4051
Eml: noriaki.nakao@kek.jp

SAKAMOTO, Yukio
External Dosimetry Laboratory
Department of Health Physics
JAERI
Tokai-mura, Naka-gun
Ibaraki-ken 319-1195

Tel: +81 (29) 282 5803
Fax: +81 (29) 282 6063
Eml: sakamoto@frs.tokai.jaeri.go.jp

* SHIN, Kazuo
Dept. of Nuclear Engineering
Kyoto University
Yoshida
Sakyo-ku
Kyoto 606-8501

Tel: +81 (75) 753 5825
Fax: +81 (75) 753 5845
Eml: shin@nucleng.kyoto-u.ac.jp

YOSHIZAWA, Nobuaki
Mitsubishi Research Institute
3-6, Otenachi 2-Chome
Chiyoda-ku
Tokyo, 100-8141

Tel: +81 (3) 3277 0772
Fax: +81 (3) 3277 3480
Eml: yoshizaw@mri.co.jp

THE NETHERLANDS

* KONING, Arjan
NRG Nuclear Research and
Consultancy Group
Building 34.333
Westerduinweg 3, P.O. Box 25
NL-1755 ZG Petten

Tel: +31 (224) 56 4051
Fax: +31 (224) 56 3490
Eml: koning@nrg-nl.com

RUSSIAN FEDERATION

BATYAEV, Vyacheslav F.
Institute for Theoretical and
Experimental Physics
B. Cheremushkinskaya 25
117259 Moscow

Tel: +7 (095) 123 6383
Fax: +7 (095) 127 0543
Eml: vfb@itep.ru

TITARENKO, Yuri
Institute for Theoretical and
Experimental Physics
B. Cheremushkinskaya 25
117259 Moscow

Tel: +7 095 123 6383
Fax: +7 095 127 0543
Eml: Yury.Titarenko@itep.ru

ZHIVUN, Valery M.
Institute for Theoretical and
Experimental Physics
B. Cheremunshkinskaya 25
117259 Moscow

Tel: +7 095 123 6383
Fax: +7 095 127 0543
Eml: zhivun@mail.ru

SLOVENIA

KODELI, Ivan
Institut Josef Stefan
Jamova 39
1000 Ljubljana

Tel: +386 (61) 188 5412
Fax: +386 (61) 161 2335
Eml: ivan.kodeli@ijs.si

UNITED STATES OF AMERICA

* HERTEL, Nolan E.
George Woodroof School of
Mechanical Engineering
Georgia Institute of Technology
900 Atlantic Dr.
Atlanta, GA 30332-0405

Tel: +1 (404) 894 3601
Fax: +1 (404) 894 9325
Eml: nolan.hertel@me.gatech.edu

IPE, Nisy E.
SLAC
Radiation Physics Dept. MS-48
2575 Sand Hill Road
Menlo Park, CA 94025

Tel: +1 (650) 926 4324
Fax: +1 (650) 926 3569
Eml: ipe@slac.stanford.edu

KIRK, Bernadette L.
Radiation Safety Information
Computational Center
Oak Ridge National Laboratory
Post Office Box 2008
Oak Ridge, TN 37831-6362

Tel: +1 (865) 574 6176
Fax: +1 (865) 574 6182
Eml: blk@ornl.gov

MASHNIK, Stepan
Nuclear Physics Group, T-16
MS B283
Los Alamos National Laboratory
Los Alamos, NM 87545

Tel: +1 (505) 667 9946
Fax: +1 (505) 667 1931
Eml: mashnik@t2y.lanl.gov

ROESLER, Stefan
SLAC
P.O. Box 4349, MS-48
Stanford, CA 94309

Tel: +1 650 926 2048
Fax: +1 650 926 3569
Eml: sroesler@slac.stanford.edu

ROKNI, Sayed H.
Radiation Physics Department
SLAC
P.O.Box 4349, MS 48
Stanford, CA 94309

Tel: +1 (650) 926 3544
Fax: +1 (650) 926 3569
Eml: rokni@slac.stanford.edu

SUTTON, Michele
Georgia Institute of Technology
Neely Nuclear Research Center
900 Atlantic Drive
Atlanta, Georgia 30332-0425

Tel: +1 (404) 894 3600
Fax: +1 (404) 894 9325
Eml: sutton@nukeisit.gatech.edu

* WATERS, Laurie S.
MS H816
Los Alamos National Lab.
Los Alamos, NM 87544

Tel: +1 (505) 665 4127
Fax: +1 (505) 667 7443
Eml: lsw@lanl.gov

INTERNATIONAL ORGANISATIONS

BERKVEN, Paul
ESRF, European Synchrotron
Radiation Facility
BP 220
6 rue Jules Horowitz
F-38043 Grenoble Cedex

Tel: +33 (4) 76 88 20 71
Fax: +33 (4) 76 88 24 18
Eml: berkvens@esrf.fr

SARTORI, Enrico
OECD/NEA Data Bank
Le Seine-Saint Germain
12 boulevard des Iles
F-92130 Issy-les-Moulineaux

Tel: +33 (1) 45 24 10 72/78
Fax: +33 (1) 45 24 11 10/28
Eml: sartori@nea.fr

VAZ, Pedro
OECD/NEA Data Bank
Le Seine-Saint Germain
12 boulevard des Iles
F-92130 Issy-les-Moulineaux

Tel: +33 (1) 45 24 10 74
Fax: +33 (1) 45 24 11 10
Eml: vaz@nea.fr

* FERRARI, Alfredo
CERN – SL Division
Bldg. 864-2-D05
CH-1211 Genève 23
Tel: +41 (22) 76 76119
Fax: +41 (22) 76 77555
Eml: alfredo.ferrari@cern.ch

KADI, YACINE
CERN
Emerging Energy Technologies
SL Division
CH-1211 Genève 23
Tel: +41 (22) 7679569
Fax: +41 (22) 7677555
Eml: Yacine.Kadi@cern.ch

LACOSTE, Veronique
CERN
SL/EET Division
CH-1211 Genève 23
Tel: +41 (22) 767 8165
Fax: +41 (22) 767 7555
Eml: veronique.lacoste@cern.ch

SILARI, Marco
CERN
TIS-RP
CH-1211 Genève 23
Tel: +41 (22) 767 3937
Fax: +41 (22) 767 5700
Eml: marco.silari@cern.ch

ULRICI, Luisa
CERN
CH-1211 Genève 23
Tel: +41 (22) 767 21 51
Fax: +41 (22) 767 57 00
Eml: Luisa.Ulrici@cern.ch

VINCKE, Heinz
CERN
CH-1211 Genève 23
Tel: +41 (22) 767 8864
Fax: +41 (22) 767 9080
Eml: Heinz.Vincke@cern.ch

VINCKE, Helmut
CERN – EP Division
CH-1211 Genève 23
Tel: +41 (22) 767 12 78
Fax: +41 (22) 767 12 20
Eml: Helmut.Vincke@cern.ch

* *Regrets not being able to attend*

ALSO AVAILABLE

NEA Publications of General Interest

- 1999 Annual Report* (2000) *Free: available on Web.*
NEA News
ISSN 1605-9581 Yearly subscription: FF 240 US\$ 45 DM 75 £ 26 ¥ 4 800
Geologic Disposal of Radioactive Waste in Perspective (2000)
ISBN 92-64-18425-2 Price: FF 130 US\$ 20 DM 39 £ 12 ¥ 2 050
Radiation in Perspective – Applications, Risks and Protection (1997)
ISBN 92-64-15483-3 Price: FF 135 US\$ 27 DM 40 £ 17 ¥ 2 850
Radioactive Waste Management in Perspective (1996)
ISBN 92-64-14692-X Price: FF 310 US\$ 63 DM 89 £ 44

Nuclear Science

- Pyrochemical Separations* (2001)
ISBN 92-64-18443-0 Price: FF 500 US\$ 66 DM 149 £ 46 ¥ 7 230
Core Monitoring for Commercial Reactors: Improvements in Systems and Methods (2000)
ISBN 92-64-17659-4 Price: FF 460 US\$ 71 DM 137 £ 44 ¥ 7 450
Shielding Aspects of Accelerators, Targets and Irradiation Facilities (SATIF-4)(1999)
ISBN 92-64-17044-8 Price: FF 500 US\$ 88 DM 149 £ 53 ¥ 10 300
3-D Radiation Transport Benchmarks for Simple Geometries with Void Regions
(2000) *Free on request.*
Benchmark Calculations of Power Distribution Within Fuel Assemblies
Phase II: Comparison of Data Reduction and Power Reconstruction Methods in Production Codes
(2000) *Free on request.*
Benchmark on the VENUS-2 MOX Core Measurements
(2000) *Free on request.*
Calculations of Different Transmutation Concepts: An International Benchmark Exercise
(2000) *Free on request.*
Prediction of Neutron Embrittlement in the Reactor Pressure Vessel: VENUS-1 and VENUS-3 Benchmarks
(2000) *Free on request.*
Pressurised Water Reactor Main Steam Line Break (MSLB) Benchmark
(2000) *Free on request.*

International Evaluation Co-operation (*Free on request*)

- Volume 1: *Comparison of Evaluated Data for Chromium-58, Iron-56 and Nickel-58* (1996)
Volume 2: *Generation of Covariance Files for Iron-56 and Natural Iron* (1996)
Volume 3: *Actinide Data in the Thermal Energy Range* (1996)
Volume 4: *²³⁸U Capture and Inelastic Cross-Sections* (1999)
Volume 5: *Plutonium-239 Fission Cross-Section between 1 and 100 keV* (1996)
Volume 8: *Present Status of Minor Actinide Data* (1999)
Volume 12: *Nuclear Model to 200 MeV for High-Energy Data Evaluations* (1998)
Volume 13: *Intermediate Energy Data* (1998)
Volume 14: *Processing and Validation of Intermediate Energy Evaluated Data Files* (2000)
Volume 15: *Cross-Section Fluctuations and Shelf-Shielding Effects in the Unresolved Resonance Region* (1996)
Volume 16: *Effects of Shape Differences in the Level Densities of Three Formalisms on Calculated Cross-Sections* (1998)
Volume 17: *Status of Pseudo-Fission Product Cross-Sections for Fast Reactors* (1998)
Volume 18: *Epithermal Capture Cross-Section of ²³⁵U* (1999)

Order form on reverse side.

OECD PUBLICATIONS, 2, rue André-Pascal, 75775 PARIS CEDEX 16
PRINTED IN FRANCE
(66 2001 07 1 P) ISBN 92-64-18691-3 – No. 51899 2001